

JULY 2021

**AJNR**

VOLUME 42 • PP 1183-1358

# AJNR

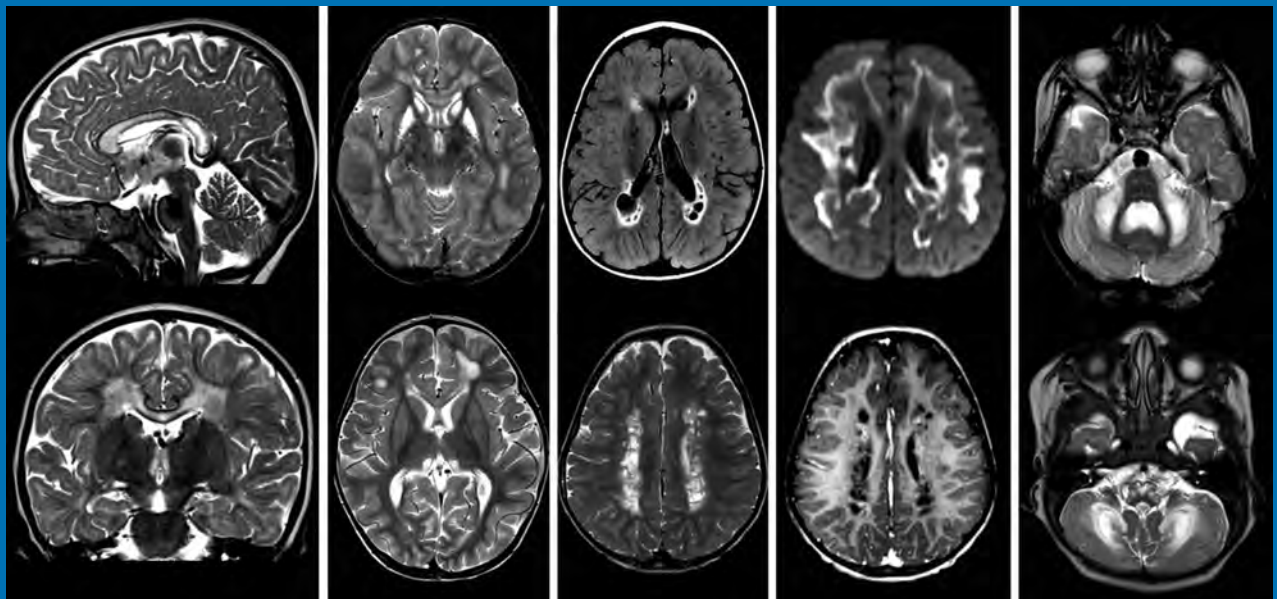
## AMERICAN JOURNAL OF NEURORADIOLOGY

JULY 2021  
VOLUME 42  
NUMBER 7  
WWW.AJNR.ORG

THE JOURNAL OF DIAGNOSTIC AND  
INTERVENTIONAL NEURORADIOLOGY

Imaging patterns of mitochondrial leukodystrophies  
Endovascular technique to treat spinal arteriovenous fistulas  
Iatrogenic foreign materials associated with retrieved clot tissue  
Cerebral venous thrombosis in COVID-19

Official Journal ASNR • ASFNR • ASHNR • ASPNR • ASSR



# FRED™

Flow Re-Direction  
Endoluminal Device

---

## FLOW DIVERSION.



## SIMPLIFIED.

---



**MicroVention Worldwide**  
**Innovation Center**  
35 Enterprise  
Aliso Viejo, CA 92656 USA  
**MicroVention UK Limited**  
**MicroVention Europe S.A.R.L.**  
**MicroVention Deutschland GmbH**  
**Web**

PH +1 714.247.8000

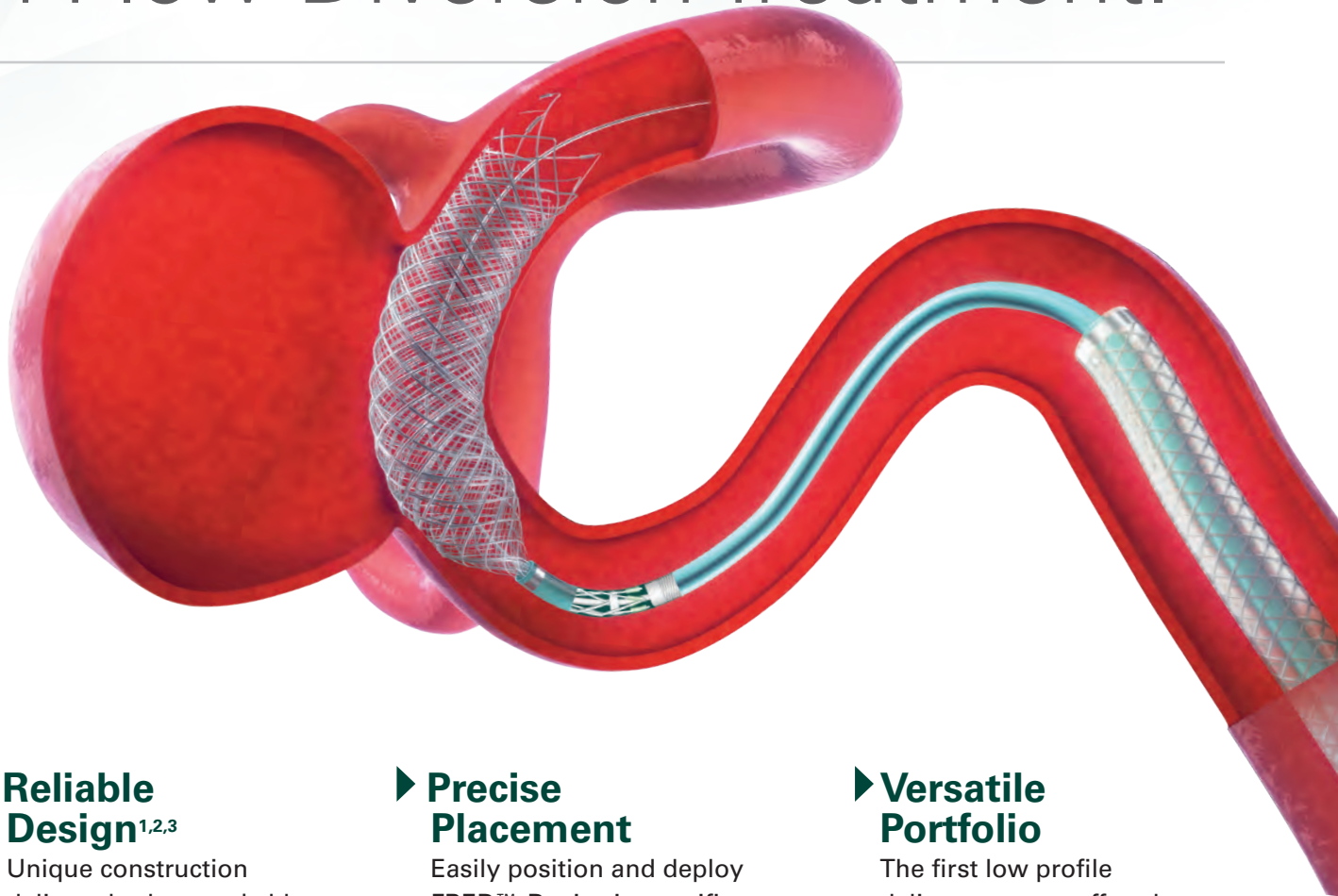
PH +1 44 (0) 191 258 6777

PH +33 (1) 39 21 77 46

PH +49 211 210 798-0

[microvention.com](http://microvention.com)

# The New Standard of **Ease and Simplicity** in Flow Diversion Treatment.



## ► **Reliable Design**<sup>1,2,3</sup>

Unique construction delivers both remarkable ease of use and excellent flow diversion<sup>1,2,3</sup>

## ► **Precise Placement**

Easily position and deploy FRED™ Device in specific, targeted locations<sup>4,5,6</sup>

## ► **Versatile Portfolio**

The first low profile delivery system offered in combination with large diameter and long length options

#### References:

1. TR11-211 2. TR13-171 3. TR15-055 4. TR13-192 5. TR15-072 6. TR19-145

The Flow Re-Direction Endoluminal Device (FRED™) System is indicated for use in the internal carotid artery from the petrous segment to the terminus for the endovascular treatment of adult patients (22 years of age or older) with wide-necked (neck width  $\geq 4$  mm or dome-to-neck ratio  $< 2$ ) saccular or fusiform intracranial aneurysms arising from a parent vessel with a diameter  $\geq 2.0$  mm and  $\leq 5.0$  mm.

Use of the FRED™ System is contraindicated under these circumstances: Patients in whom anticoagulant, anti-platelet therapy, or thrombolytic drugs are contraindicated. Patients with known hypersensitivity to metal such as nickel-titanium and metal jewelry. Patients with anatomy that does not permit passage or deployment of the FRED™ System. Patients with an active bacterial infection. Patients with a pre-existing stent in place at the target aneurysm. Patients in whom the parent vessel size does not fall within the indicated range. Patients who have not received dual anti-platelet agents prior to the procedure. For complete indications, contraindications, potential complications, warnings, precautions, and instructions, see instructions for use (IFU provided in the device).

**RX Only:** Federal (United States) law restricts this device to sale by or on the order of a physician.

MICROVENTION™ and FRED™ are registered trademarks of MicroVention, Inc. in the United States and other jurisdictions. © 2020 MicroVention, Inc. 04/2020.

# Dotarem®

(gadoterate meglumine) Injection

MR

Comparison of Dotarem® to Gadavist® for Overall Visualization and Characterization in the MRI Diagnosis of Primary Brain Tumors



Despite the difference in relaxivity between these 2 GBCAs

## There Is No Measurable Difference in Clinical Benefit Observed Between Dotarem® and Gadavist®<sup>2</sup>



as demonstrated by the **REMIND Study**, a multicenter, double-blind, randomized, controlled intraindividual crossover study.<sup>2</sup>

**This study “demonstrates the non-inferiority of gadoterate meglumine [Dotarem®] versus gadobutrol [Gadavist®] for overall visualization and characterization of primary brain tumors despite quantitative mean lesion percentage enhancement being higher with gadobutrol”.<sup>2</sup>**

- For all readers in the REMIND Study, more than 90% of patient images were scored with good or excellent overall lesion visualization and characterization with either Dotarem® or Gadavist®.<sup>2</sup>
- The REMIND Study also confirmed low incidence of immediate reported AEs with Dotarem® and with Gadavist®, as shown in multiple previous studies.<sup>2,3,4</sup>
- Dotarem® is an imaging contrast with macrocyclic and ionic structure for high thermodynamic and kinetic stability.<sup>5,6</sup>
- Dotarem® is not only trusted for high molecular stability<sup>5,6</sup>; the REMIND Study demonstrates that it is as effective as Gadavist® for MRI diagnosis of primary brain tumors.<sup>2</sup>

Please see Important Safety information on opposite page. For more information on Dotarem®, please see Full Prescribing Information including Boxed Warning and Medication Guide.



Scan the code to learn more or visit [www.Dotarem-us.com/Remind-Study](http://www.Dotarem-us.com/Remind-Study)

## IMPORTANT SAFETY INFORMATION

### WARNING: NEPHROGENIC SYSTEMIC FIBROSIS (NSF)

Gadolinium-based contrast agents (GBCAs) increase the risk for NSF among patients with impaired elimination of the drugs. Avoid use of GBCAs in these patients unless the diagnostic information is essential and not available with non-contrast MRI or other modalities. NSF may result in fatal or debilitating fibrosis affecting the skin, muscle and internal organs.

- The risk for NSF appears highest among patients with:
  - Chronic, severe kidney disease (GFR < 30 mL/min/1.73m<sup>2</sup>), or
  - Acute kidney injury.
- Screen patients for acute kidney injury and other conditions that may reduce renal function. For patients at risk for chronically reduced renal function (e.g. age > 60 years, hypertension, diabetes), estimate the glomerular filtration rate (GFR) through laboratory testing.
- For patients at highest risk for NSF, do not exceed the recommended DOTAREM dose and allow a sufficient period of time for elimination of the drug from the body prior to any re-administration.

### INDICATIONS AND USAGE

DOTAREM® (gadoterate meglumine) injection is a prescription gadolinium-based contrast agent indicated for intravenous use with magnetic resonance imaging (MRI) in brain (intracranial), spine and associated tissues in adult and pediatric patients (including term neonates) to detect and visualize areas with disruption of the blood brain barrier (BBB) and/or abnormal vascularity.

### CONTRAINDICATIONS

History of clinically important hypersensitivity reactions to DOTAREM.

### WARNINGS AND PRECAUTIONS

- Hypersensitivity Reactions: Anaphylactic and anaphylactoid reactions have been reported with DOTAREM, involving cardiovascular, respiratory, and/or cutaneous manifestations. Some patients experienced circulatory collapse and died. In most cases, initial symptoms occurred within minutes of DOTAREM administration and resolved with prompt emergency treatment.
- Before DOTAREM administration, assess all patients for any history of a reaction to contrast media, bronchial asthma and/or allergic disorders. These patients may have an increased risk for a hypersensitivity reaction to DOTAREM.
- Administer DOTAREM only in situations where trained personnel and therapies are promptly available for the treatment of hypersensitivity reactions, including personnel trained in resuscitation.
- Gadolinium Retention: Gadolinium is retained for months or years in several organs. The highest concentrations have been identified in the bone, followed by brain, skin, kidney, liver and spleen. The duration of retention also varies by tissue, and is longest in bone. Linear GBCAs cause more retention than macrocyclic GBCAs.
- Consequences of gadolinium retention in the brain have not been established. Adverse events involving multiple organ systems have been reported in patients with normal renal function without an established causal link to gadolinium retention.
- Acute Kidney Injury: In patients with chronically reduced renal function, acute kidney injury requiring dialysis has occurred with the use of GBCAs. The risk of acute kidney injury may increase with increasing dose of the contrast agent; administer the lowest dose necessary for adequate imaging.
- Extravasation and Injection Site Reactions: Ensure catheter and venous patency before the injection of DOTAREM. Extravasation into tissues during DOTAREM administration may result in tissue irritation.

### ADVERSE REACTIONS

- The most common adverse reactions associated with DOTAREM in clinical trials were nausea, headache, injection site pain, injection site coldness and rash.
- Serious adverse reactions in the Postmarketing experience have been reported with DOTAREM. These serious adverse reactions include but are not limited to: arrhythmia, cardiac arrest, respiratory arrest, pharyngeal edema, laryngospasm, bronchospasm, coma and convulsion.

### USE IN SPECIFIC POPULATIONS

- **Pregnancy:** GBCAs cross the human placenta and result in fetal exposure and gadolinium retention. Use only if imaging is essential during pregnancy and cannot be delayed.
- **Lactation:** There are no data on the presence of gadoterate in human milk, the effects on the breastfed infant, or the effects on milk production. However, published lactation data on other GBCAs indicate that 0.01 to 0.04% of the maternal gadolinium dose is present in breast milk.
- **Pediatric Use:** The safety and efficacy of DOTAREM at a single dose of 0.1 mmol/kg has been established in pediatric patients from birth (term neonates ≥ 37 weeks gestational age) to 17 years of age based on clinical data. The safety of DOTAREM has not been established in preterm neonates. No cases of NSF associated with DOTAREM or any other GBCA have been identified in pediatric patients age 6 years and younger.

You are encouraged to report negative side effects of prescription drugs to the FDA. Visit [www.fda.gov/medwatch](http://www.fda.gov/medwatch) or call 1-800-FDA-1088.

Please see the full Prescribing Information, including Boxed Warning and the patient Medication Guide, for additional important safety information.

**References:** **1.** Dotarem [package insert]. Princeton, NJ: Guerbet LLC; Oct 2019. **2.** Maravilla K et al. Comparison of Gadoterate Meglumine and Gadobutrol in the Diagnosis of Primary Brain Tumors: A Double-Blind Randomized Controlled Intraindividual Crossover Study (the REMIND Study). 2017 June 29. doi: 10.3174/ajnr.A5316. [Epub ahead of print]. **3.** de Kerviler E et al. Adverse reactions to gadoterate meglumine: review of over 25 years of clinical use and more than 50 million doses. Invest Radiol 2016;51:544–51 CrossRef Medline. **4.** Endrikat J et al. Safety of gadobutrol: results from 42 clinical phase II to IV studies and postmarketing surveillance after 29 million applications. Invest Radiol 2016;51: 537–43 CrossRef Medline. **5.** Port M et al. Efficiency, thermodynamic and kinetic stability of marketed gadolinium chelates and their possible clinical consequences: a critical review. Biometals. 2008;21: 469–90. **6.** Frenzel T et al. Stability of gadolinium-based magnetic resonance imaging contrast agents in human serum at 37°C. Invest Radiol. 2008;43:817–828.

DOTAREM® is a registered trademark of Guerbet and is available by prescription only.

Gadavist® is a registered trademark of the Bayer group of companies, and is available by prescription only.

# We're Inside Every Great Neuroradiologist!

## ASNR MEMBERS RECEIVE

### *American Journal of Neuroradiology (AJNR)*

The leading neuroradiology research journal, published monthly

### *Neurographics*

Bimonthly educational journal with CME for members

### **ASNR Annual Meeting**

Discounts for members on the field's premier conference

### **eCME**

Online collection of lectures and articles with SA-CME and Category 1 credit

### **Advocacy**

Coding/reimbursement, quality standards and practice guidelines; demonstrating neuroradiology's value!

### **Networking**

Access to 5,000 peers

... And More!

**Join the leaders in neuroradiology today!**

**Learn more at [www.asnr.org/join](http://www.asnr.org/join)**

# ASNR

## American Society of Neuroradiology

800 Enterprise Dr., Suite 205, Oak Brook, IL 60523 • (630)574-0220 • [membership@asnr.org](mailto:membership@asnr.org) • [www.asnr.org](http://www.asnr.org)

# Explore the New ASNR Career Center



Your Premier Resource for Professional Development

- Access to jobs in the National Healthcare Career Network
- Confidential resume posting
- One-time free resume review
- Professional online profile
- Saved jobs capability

Start here: [careers.asnr.org](http://careers.asnr.org)

**ASNR**  
American Society of Neuroradiology



# Simplify the MOC Process



# Manage your CME Credits Online

## CMEgateway.org

### Available to Members of Participating Societies

American Board of Radiology (ABR)  
American College of Radiology (ACR)  
American Roentgen Ray Society (ARRS)  
American Society of Neuroradiology (ASNR)  
Commission on Accreditation of Medical  
Physics Educational Programs, Inc. (CAMPEP)  
Radiological Society of North America (RSNA)  
Society of Interventional Radiology (SIR)  
SNM  
The Society for Pediatric Radiology (SPR)

### It's Easy and Free!

Log on to CME Gateway to:

- View or print reports of your CME credits from multiple societies from a single access point.
- Print an aggregated report or certificate from each participating organization.
- Link to SAMs and other tools to help with maintenance of certification.

### American Board of Radiology (ABR) participation!

By activating ABR in your organizational profile, your MOC-fulfilling CME and SAM credits can be transferred to your own personalized database on the ABR Web site.

### Sign Up Today!

go to [CMEgateway.org](http://CMEgateway.org)

# AJNR *go green*

***AJNR* urges American Society of Neuroradiology members to reduce their environmental footprint by voluntarily suspending their print subscription.**

The savings in paper, printing, transportation, and postage directly fund new electronic enhancements and expanded content.

The digital edition of *AJNR* presents the print version in its entirety, along with extra features including:

- Publication Preview
- Case Collection
- Podcasts
- The *AJNR* News Digest
- The *AJNR* Blog

It also reaches subscribers much faster than print. An electronic table of contents will be sent directly to your mailbox to notify you as soon as it publishes.

Readers can search, reference, and bookmark current and archived content 24 hours a day on [www.ajnr.org](http://www.ajnr.org).

ASNR members who wish to opt out of print can do so by using the *AJNR* Go Green link on the *AJNR* Website (<http://www.ajnr.org/content/subscriber-help-and-services>). Just type your name in the email form to stop print and spare our ecosystem.



# MIDRC

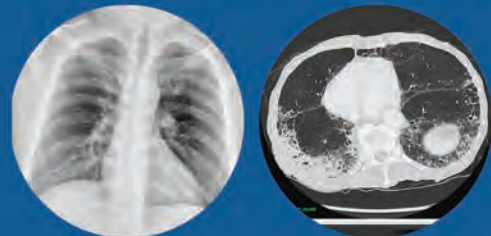
MEDICAL IMAGING AND DATA RESOURCE CENTER.

## Medical Imaging in the Fight against COVID-19 Call for Contributions

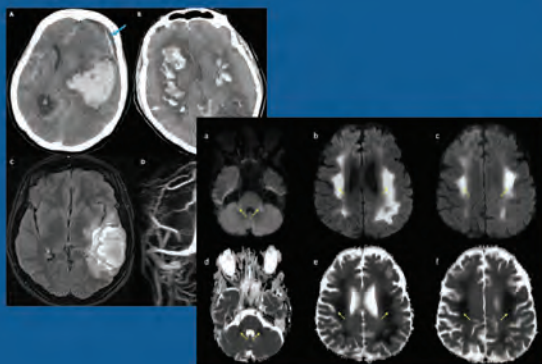
The Medical Imaging and Data Resource Center (MIDRC) is a multi-organizational initiative in the fight against the ongoing worldwide pandemic co-led by the ACR®, the RSNA, and the AAPM and is hosted at the University of Chicago.



The primary goal is to accelerate machine learning research by creating a high quality COVID-19 image commons linked to relevant clinical data made available as a public resource.



ASNR has teamed up with MIDRC to advance the understanding of the neuroimaging manifestations of COVID-19 and to enhance the MIDRC image commons.



- To ensure success, MIDRC encourages all institutions and hospitals, both small and large, to donate their COVID-19 medical images and data to the cause.
- MIDRC provides a HIPAA-compliant mechanism to securely submit medical images and clinical metadata, and is committed to helping institutions throughout the submission process.

*Visit [midrc.org](http://midrc.org) for more information*



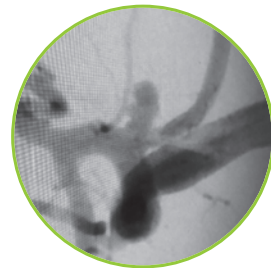
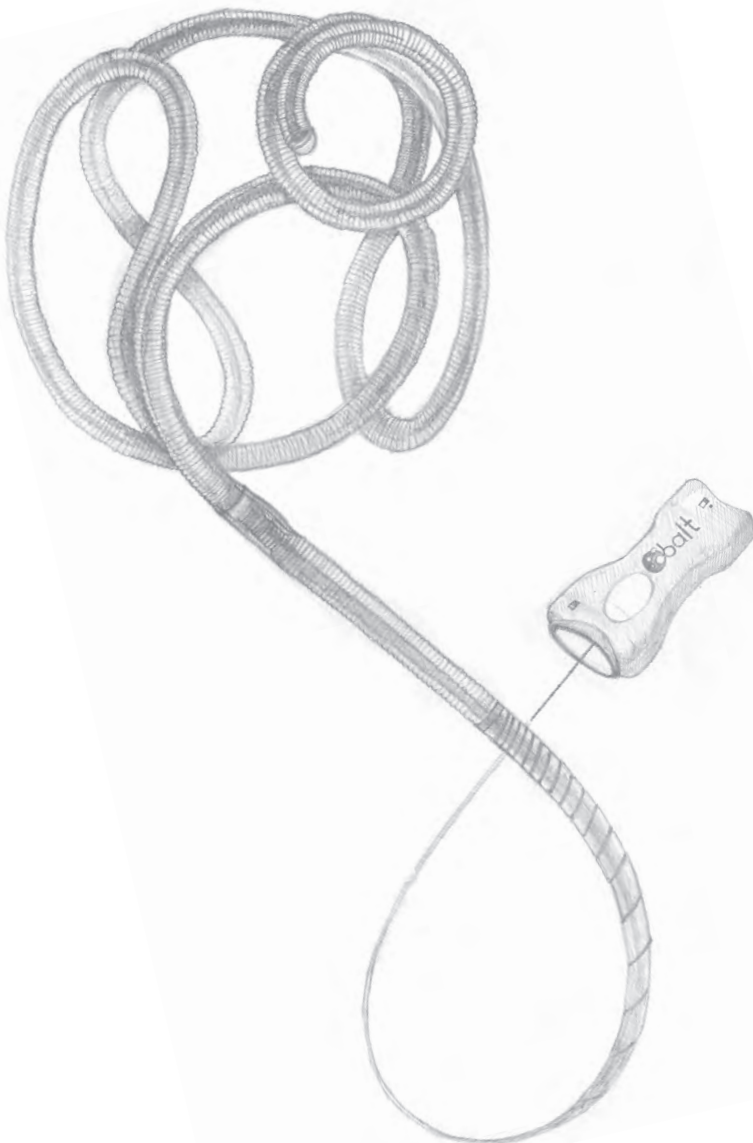
THE UNIVERSITY OF  
**CHICAGO**



National Institute of Biomedical Imaging and Bioengineering  
*Creating Biomedical Technologies to Improve Health*

# OPTIMAX

**FEEL THE DIFFERENCE:  
VOLUME, SOFTNESS AND STABILITY**



**Complete and Unique Offerings:**

The only large volume coil available in a **Super Soft** configuration in 1mm to 3.5mm diameters, including half sizes.

Visit our products page at [www.Balt-USA.com](http://www.Balt-USA.com) to learn more.

**Balt USA**

29 Parker, Irvine, CA 92618  
tel 949.788.1443 fax 949.788.1444

[balt-usa.com](http://balt-usa.com)

©2021 BALT USA MKTG-250 Rev. A

 **balt**  
inspiring innovation

# TAKE A NEW **APPROACH** TO RADIAL

## Rist™ Radial Access System

**The Rist™ Radial Access System** features the first guide catheter designed for the unique demands of accessing the neurovasculature through the radial pathway.<sup>1,2</sup>



**See Rist™ in action.**

Scan code with your smart phone or visit  
[medtronic.com/TakeANewApproach](https://www.medtronic.com/TakeANewApproach)

1. INCTR-12549 2. INCTR-12736

**CAUTION:** Federal (USA) law restricts this device to sale by or on the order of a physician. Indications, contraindications, warnings and instructions for use can be found on the product labeling supplied with each device. The Rist™ 079 Radial Access Guide Catheter is indicated for the introduction of interventional devices into the peripheral, coronary, and neuro vasculature. The Rist™ Radial Access Selective Catheter is indicated for the introduction of interventional devices into the peripheral, coronary and neuro vasculature. It can be used to facilitate introduction of diagnostic agents in the neuro vasculature. It is not intended to facilitate introduction of diagnostic agents in coronary or peripheral arteries.

© 2021 Medtronic. All rights reserved. Medtronic, Medtronic logo and Further, Together are trademarks of Medtronic. All other brands are trademarks of a Medtronic company. UC202119233 EN

**Medtronic**

# AJNR

## AMERICAN JOURNAL OF NEURORADIOLOGY

JULY 2021  
VOLUME 42  
NUMBER 7  
WWW.AJNR.ORG

Publication Preview at [www.ajnr.org](http://www.ajnr.org) features articles released in advance of print. Visit [www.ajnrblog.org](http://www.ajnrblog.org) to comment on AJNR content and chat with colleagues and AJNR's News Digest at <http://ajnrdigest.org> to read the stories behind the latest research in neuroimaging.

1183 **PERSPECTIVES** *K.L. Mani*

### REVIEW ARTICLE

-  1184 **MR-Eye: High-Resolution Microscopy Coil MRI for the Assessment of the Orbit and Periorbital Structures, Part 2: Clinical Applications** *N.W. Dobbs, et al.* **HEAD & NECK**

### GENERAL CONTENTS

-   1190 **Modelling the Anatomic Distribution of Neurologic Events in Patients with COVID-19: A Systematic Review of MRI Findings** *N. Parsons, et al.* **ADULT BRAIN**
-   1196 **Cerebral Venous Thrombosis in COVID-19: A New York Metropolitan Cohort Study** *F. Al-Mufti, et al.* **ADULT BRAIN**
-  1201 **Variability of Normal Pressure Hydrocephalus Imaging Biomarkers with Respect to Section Plane Angulation: How Wrong a Radiologist Can Be?** *P. Ryska, et al.* **ADULT BRAIN**
-   1208 **Acceleration of Brain TOF-MRA with Compressed Sensitivity Encoding: A Multicenter Clinical Study** *J. Ding, et al.* **ADULT BRAIN**
-   1216 **Relationship between Shear Stiffness Measured by MR Elastography and Perfusion Metrics Measured by Perfusion CT of Meningiomas** *T. Takamura, et al.* **ADULT BRAIN FUNCTIONAL**
-  1223 **Unraveling Deep Gray Matter Atrophy and Iron and Myelin Changes in Multiple Sclerosis** *G. Pontillo, et al.* **ADULT BRAIN FUNCTIONAL**
-   1231 **MRI-Visible Perivascular Spaces in the Centrum Semiovale Are Associated with Brain Amyloid Deposition in Patients with Alzheimer Disease-Related Cognitive Impairment** *H.J. Kim, et al.* **ADULT BRAIN**
-   1239 **Iatrogenic Foreign Materials Associated with Retrieved Clot Tissue via Mechanical Thrombectomy** *M. Abbasi, et al.* **INTERVENTIONAL**
-    1250 **Novel Human Acute Ischemic Stroke Blood Clot Analogs for In Vitro Thrombectomy Testing** *S.T. Fitzgerald, et al.* **INTERVENTIONAL**
-   1258 **Refractory Stroke Thrombectomy: Prevalence, Etiology, and Adjunctive Treatment in a North American Cohort** *R.N. Abdalla, et al.* **INTERVENTIONAL**
-   1264 **Carotid Stenting without Embolic Protection Increases Major Adverse Events: Analysis of the National Surgical Quality Improvement Program** *P. Nazari, et al.* **INTERVENTIONAL**

AJNR (Am J Neuroradiol ISSN 0195-6108) is a journal published monthly, owned and published by the American Society of Neuroradiology (ASNR), 800 Enterprise Drive, Suite 205, Oak Brook, IL 60523. Annual dues for the ASNR include approximately 21% for a journal subscription. The journal is printed by Intellicor Communications, 330 Eden Road, Lancaster, PA 17601; Periodicals postage paid at Oak Brook, IL and additional mailing offices. Printed in the U.S.A. POSTMASTER: Please send address changes to American Journal of Neuroradiology, P.O. Box 3000, Denville, NJ 07834, U.S.A. Subscription rates: nonmember \$410 (\$480 foreign) print and online, \$320 online only; institutions \$470 (\$540 foreign) print and basic online, \$935 (\$1000 foreign) print and extended online, \$380 online only (basic), \$825 online only (extended); single copies are \$35 each (\$40 foreign). Indexed by PubMed/MEDLINE, BIOSIS Previews, Current Contents (Clinical Medicine and Life Sciences), EMBASE, Google Scholar, HighWire Press, Q-Sensei, RefSeek, Science Citation Index, SCI Expanded, Meta/CZI, ReadCube, and Semantic Scholar. Copyright © American Society of Neuroradiology.

-   1270 **Pressure Cooker Technique for Endovascular Treatment of Spinal Arteriovenous Fistulas: Experience in 15 Cases** *F. Clarençon, et al.* **INTERVENTIONAL**
-  1276 **Endovascular Treatment of Small and Very Small Intracranial Aneurysms with the Woven EndoBridge Device** *J.-B. Girot, et al.* **INTERVENTIONAL**
- 1282 **Arterial and Venous 3D Fusion AV-3D-DSA: A Novel Approach to Cerebrovascular Neuroimaging** *E. Raz, et al.* **INTERVENTIONAL**
- 1285 **Carotid Intraplaque Hemorrhage and Stenosis: At What Stage of Plaque Progression Does Intraplaque Hemorrhage Occur, and When is It Most Likely to Be Associated with Symptoms?** *A.S. Larson, et al.* **EXTRACRANIAL VASCULAR**
- 1291 **Commentary**  
**Another Step toward the Understanding of Carotid Artery Pathology** *A. Podlasek, et al.*
-   1293 **Asynchrony in Peritumoral Resting-State Blood Oxygen Level–Dependent fMRI Predicts Meningioma Grade and Invasion** *P.B. Wu, et al.* **FUNCTIONAL ADULT BRAIN**
-  1299 **Resting-State Functional MRI for Determining Language Lateralization in Children with Drug-Resistant Epilepsy** *N.L. Phillips, et al.* **FUNCTIONAL PEDIATRICS**
-  1305 **Comparison of Readout-Segmented Echo-Planar Imaging and Single-Shot TSE DWI for Cholesteatoma Diagnostics** *M. Wiesmueller, et al.* **HEAD & NECK**
-  1313 **Optimal Duration of MRI Follow-up to Safely Identify Middle Ear Residual Cholesteatoma** *A.-L. Fourez, et al.* **HEAD & NECK**
-   1320 **Assessment of MR Imaging and CT in Differentiating Hereditary and Nonhereditary Parangliomas** *Y. Ota, et al.* **HEAD & NECK**
-   1327 **Quantitative Susceptibility Mapping of Venous Vessels in Neonates with Perinatal Asphyxia** *A.M. Weber, et al.* **PEDIATRICS FUNCTIONAL**
-    1334 **Imaging Patterns Characterizing Mitochondrial Leukodystrophies** *S.D. Roosendaal, et al.* **PEDIATRICS**
- 1341 **CT Cervical Spine Fracture Detection Using a Convolutional Neural Network** *J.E. Small, et al.* **SPINE**
-    1348 **T1 Mapping for Microstructural Assessment of the Cervical Spinal Cord in the Evaluation of Patients with Degenerative Cervical Myelopathy** *G. Baucher, et al.* **SPINE FUNCTIONAL**
- 1358 **35 YEARS AGO IN AJNR**

#### ONLINE FEATURES

#### MEMORIAL

- E36 **Robert A. Zimmerman, MD** *T.P. Naidich, et al.*

#### LETTERS

-  E37 **Virtual Biopsy: A Reality Thanks to Advances in Radiology** *M.F.V.V. Aragao, et al.*
-  E39 **Leptomeningeal Enhancement Due to COVID-19 on 3D-FLAIR and T1 Black-Blood MR Imaging Sequences** *G. Velonakis, et al.*
-  E42 **Reply** *E. Gulko, et al.*

**E43** **Expediting Care and Improving Patient Experience: Imaging after Subdural Contrast Injection during Myelography** *M.U. Antonucci, et al.*

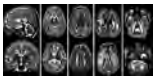
**E45** **Reply** *D. Shlapak*

**E46** **The True Potential of Artificial Intelligence for Detection of Large-Vessel Occlusion: The Role of M2 Occlusions** *S.P.R. Luijten, et al.*

**E47** **Reply** *A. Yahav-Dovrat, et al.*

**BOOK REVIEWS** *R.M. Quencer, Section Editor*

Please visit [www.ajnrblog.org](http://www.ajnrblog.org) to read and comment on Book Reviews.



Imaging Patterns  
Characterizing  
Mitochondrial  
Leukodystrophies by  
Roosendaal et al.



Indicates Editor's  
Choices selection



Indicates Fellows'  
Journal Club selection



Indicates open access to non-  
subscribers at [www.ajnr.org](http://www.ajnr.org)



Indicates article with  
supplemental online data



Indicates article with  
supplemental online video



Evidence-Based  
Medicine Level 1



Evidence-Based  
Medicine Level 2

### EDITOR-IN-CHIEF

**Jeffrey S. Ross, MD**

Professor of Radiology, Department of Radiology,  
Mayo Clinic College of Medicine, Phoenix, AZ

### SENIOR EDITORS

**Harry J. Cloft, MD, PhD**

Professor of Radiology and Neurosurgery,  
Department of Radiology, Mayo Clinic College of  
Medicine, Rochester, MN

**Christopher G. Filippi, MD**

Professor and Alice Ettinger-Jack R. Dreyfuss  
Chair of Radiology,  
Tufts University School of Medicine,  
Radiologist-in-Chief  
Tufts University Medical Center, Boston, MA

**Thierry A.G.M. Huisman, MD**

Radiologist-in-Chief, Texas Children's Hospital,  
Houston, TX

**Yvonne W. Lui, MD**

Associate Professor of Radiology,  
Chief of Neuroradiology,  
New York University School of Medicine,  
New York, NY

**C.D. Phillips, MD, FACR**

Professor of Radiology, Weill Cornell Medical  
College, Director of Head and Neck Imaging,  
New York-Presbyterian Hospital, New York, NY

**Lubdha M. Shah, MD, MS**

Professor of Radiology and Director of Spine  
Imaging, University of Utah Department of  
Radiology and Imaging Sciences, Salt Lake City, UT

### STATISTICAL SENIOR EDITOR

**Bryan A. Comstock, MS**

Senior Biostatistician,  
Department of Biostatistics,  
University of Washington, Seattle, WA

### ARTIFICIAL INTELLIGENCE DEPUTY EDITOR

**Peter D. Chang, MD**

Assistant Professor-in-Residence,  
Departments of Radiological Sciences,  
Computer Sciences, and Pathology,  
Director, Center for Artificial Intelligence in  
Diagnostic Medicine (CAIDM),  
University of California, Irvine, Irvine, CA

### EDITORIAL BOARD

Ashley H. Aiken, Atlanta, GA

Lea M. Alhilali, Phoenix, AZ

Mohammed A. Almekhlafi, Calgary, Alberta,  
Canada

Joachim Berkefeld, Frankfurt, Germany

Aashim Bhatia, Pittsburgh, PA

Waleed Brinjikji, Rochester, MN

Judah Burns, New York, NY

Danielle Byrne, Dublin, Ireland

Federico Cagnazzo, Montpellier, France

J. Levi Chazen, New York, NY

James Y. Chen, San Diego, CA

Gloria C. Chiang, New York, NY

Daniel Chow, Irvine, CA

Kars C.J. Compagne, Rotterdam, The Netherlands

Arturo Consoli, Suresnes, France

Seena Dehkharghani, New York, NY

Nilesh K. Desai, Houston, TX

Yonghong Ding, Rochester, MN

Birgit Ertl-Wagner, Toronto, Ontario, Canada

Clifford J. Eskey, Hanover, NH

Massimo Filippi, Milan, Italy

Nils D. Forkert, Calgary, Alberta, Canada

Ana M. Franceschi, New York, NY

Frank Gaillard, Melbourne, Australia

Joseph J. Gemmete, Ann Arbor, Michigan

Wende N. Gibbs, Phoenix, AZ

Philipp Gölitz, Erlangen, Germany

Brent Griffith, Detroit, MI

Joseph M. Hoxworth, Phoenix, Arizona

Raymond Y. Huang, Boston, MA

Gábor Janiga, Magdeburg, Germany

Christof Karmonik, Houston, TX

Timothy J. Kaufmann, Rochester, MN

Hillary R. Kelly, Boston, MA

Toshibumi Kinoshita, Akita, Japan

Alexander W. Korutz, Chicago, IL

Stephen F. Kralik, Houston, TX

Alexander Lerner, Los Angeles, CA

Yinsheng Li, Madison, WI

Franklin A. Marden, Chicago, IL

Markus A. Möhlenbruch, Heidelberg, Germany

Kambiz Nael, Los Angeles, CA

Renato Hoffmann Nunes, Sao Paulo, Brazil

Sasan Partovi, Cleveland, OH

Johannes A.R. Pfaff, Salzburg, Austria

Laurent Pierot, Reims, France

Alireza Radmanesh, New York, NY

Prashant Raghavan, Baltimore, MD

Eytan Raz, New York, NY

Paul M. Ruggieri, Cleveland, OH

Sebastian Schafer, Madison, WI

Maksim Shapiro, New York, NY

Timothy Shepherd, New York, NY

James Shin, New York, NY

Mark S. Shiroishi, Los Angeles, CA

Bruno P. Soares, Baltimore, MD

Jason F. Talbott, San Francisco, CA

Ruth Thiex, Everett, Washington

Vincent Thijs, Melbourne, Victoria, Australia

Anderanik Tomasian, Los Angeles, CA

Fabio Triulzi, Milan, Italy

Anja G. van der Kolk, Utrecht, the Netherlands

Arastoo Vossough, Philadelphia, PA

Elysa Widjaja, Toronto, Ontario, Canada

Leonard Yeo, Singapore

Woong Yoon, Gwangju, South Korea

David M. Yousem, Evergreen, CO

Carlos Zamora, Chapel Hill, NC

Chengcheng Zhu, Seattle, WA

### EDITORIAL FELLOW

Matthew D. Alvin, Baltimore, MD

### SPECIAL CONSULTANTS TO THE EDITOR

#### AJNR Blog Editor

Neil Lall, Denver, CO

#### Case of the Month Editor

Nicholas Stence, Aurora, CO

#### Case of the Week Editors

Matylda Machnowska, Toronto, Ontario, Canada

Anvita Pauranik, Calgary, Alberta, Canada

Vinil Shah, San Francisco, CA

#### Classic Case Editor

Sandy Cheng-Yu Chen, Taipei, Taiwan

#### Health Care and Socioeconomics Editor

Pina C. Sanelli, New York, NY

#### Physics Editor

Greg Zaharchuk, Stanford, CA

#### Podcast Editor

Courtney Tomblinson, Nashville, TN

#### Deputy Podcast Editor

Kevin Hiatt, Winston-Salem, NC

#### Twitter Editor

Roger Jordan, Houston, TX

### Official Journal:

American Society of Neuroradiology

American Society of Functional Neuroradiology

American Society of Head and Neck Radiology

American Society of Pediatric Neuroradiology

American Society of Spine Radiology

Founding Editor  
Juan M. Taveras

Editors Emeriti  
Mauricio Castillo, Robert I. Grossman,  
Michael S. Huckman, Robert M. Quencer

Managing Editor  
Karen Halm

Assistant Managing Editor  
Laura Wilhelm

Executive Director, ASNR  
Mary Beth Hepp



Title: Summer morning on the Long Island Sound.

*Kalpana L. Mani, MD, MEd, University Radiology Group, East Brunswick, NJ*

# MR-Eye: High-Resolution Microscopy Coil MRI for the Assessment of the Orbit and Periorbital Structures, Part 2: Clinical Applications

 N.W. Dobbs,  M.J. Budak,  R.D. White, and  I.A. Zealley



## ABSTRACT

**SUMMARY:** In the first part of this 2-part series, we described how to implement microscopy coil MR imaging of the orbits. Beyond being a useful anatomic educational tool, microscopy coil MR imaging has valuable applications in clinical practice. By depicting deep tissue tumor extension, which cannot be evaluated clinically, ophthalmic surgeons can minimize the surgical field, preserve normal anatomy when possible, and maximize the accuracy of resection margins. Here we demonstrate common and uncommon pathologies that may be encountered in orbital microscopy coil MR imaging practice and discuss the imaging appearance, the underlying pathologic processes, and the clinical relevance of the microscopy coil MR imaging findings.

**ABBREVIATIONS:** BCC = basal cell carcinoma; MC-MR imaging = microscopy coil MR imaging

In the first part of this 2-part series, we described how to implement microscopy coil MR imaging (MC-MR imaging) of the orbits and described pearls and pitfalls of the technique that were acquired from experience at our institution (Ninewells Hospital, Dundee). We have demonstrated that submillimeter depiction of orbital structures using MC-MR imaging generates images that provide functional and clinically relevant anatomy of the orbit and orbital content.

As well as being a useful anatomic educational tool, MC-MR imaging has many applications in clinical practice. The key principle in ophthalmic surgery is to preserve vision.<sup>1</sup> Preoperative imaging already aids this via its depiction of compartmental lesion location, guiding the most appropriate anatomic corridor to avoid manipulation of the optic and oculomotor nerves.<sup>1</sup> With the superior tissue contrast that MC-MR imaging offers compared with conventional MR imaging and CT,<sup>2,3</sup> MC-MR imaging increases confidence in lesion location and extent into different orbital compartments. Furthermore, by accurately demonstrating deep tissue tumor extension, the ophthalmic surgeons at our institution think they can better plan surgical procedures, preserving structures that

are difficult or impossible to reconstruct, while, at the same time, maximizing the accuracy of resection margins.

Furthermore, through an understanding of the orbital pathologies and their appearance on MC-MR imaging, a greater degree of confidence can be assured to diagnoses that are suspected clinically.<sup>4</sup> This can help guide the surgeon and patient toward conservative management when appropriate, avoiding an inappropriate resection or damage to vital orbital structures or, conversely, demonstrate the need for more extensive resection when necessary.<sup>4</sup> Although it may not always reveal additional information that would alter clinical management, MC-MR imaging will provide the radiologist and the surgeon with the highest resolution imaging of the pathology. By providing the highest resolution imaging the first time around, MC-MR imaging provides the best value to the patient by improving the clinician's confidence and minimizing the necessity for recalls and further clarification.

This article does not set out an exhaustive catalogue of orbital pathology but does provide examples that highlight the benefits of MC-MR imaging of the orbits. We describe common and uncommon pathologies that may be encountered in orbital MC-MR imaging practice and discuss the imaging findings together with a description of the underlying pathologic processes and the clinical relevance of the MC-MR imaging findings.

### Basal Cell Carcinoma

Basal cell carcinoma (BCC) is the most common skin malignancy, with its incidence rising with increasing age.<sup>5-7</sup> Although the tumor only very rarely metastasizes,<sup>7</sup> it is locally invasive, creating "rodent ulcers," which, with time, may become very large

Received July 18, 2019; accepted after revision December 20, 2020.

From the Department of Clinical Neuroscience (N.W.D.), Royal Hospital for Children and Young People, Edinburgh, UK; Qscan Radiology Clinics (M.J.B.), Brisbane, Queensland, Australia; Department of Clinical Radiology (R.D.W.), University Hospital of Wales, Cardiff, UK; and Department of Clinical Radiology (I.A.Z.), Ninewells Hospital, Dundee, UK.

Please address correspondence to Nicholas W. Dobbs, MBBS, Department of Clinical Neuroscience, Royal Hospital for Children and Young People, Edinburgh, United Kingdom; e-mail: nicholas.dobbs@nhslothian.scot.nhs.uk

 Indicates open access to non-subscribers at [www.ajnr.org](http://www.ajnr.org)

<http://dx.doi.org/10.3174/ajnr.A7080>

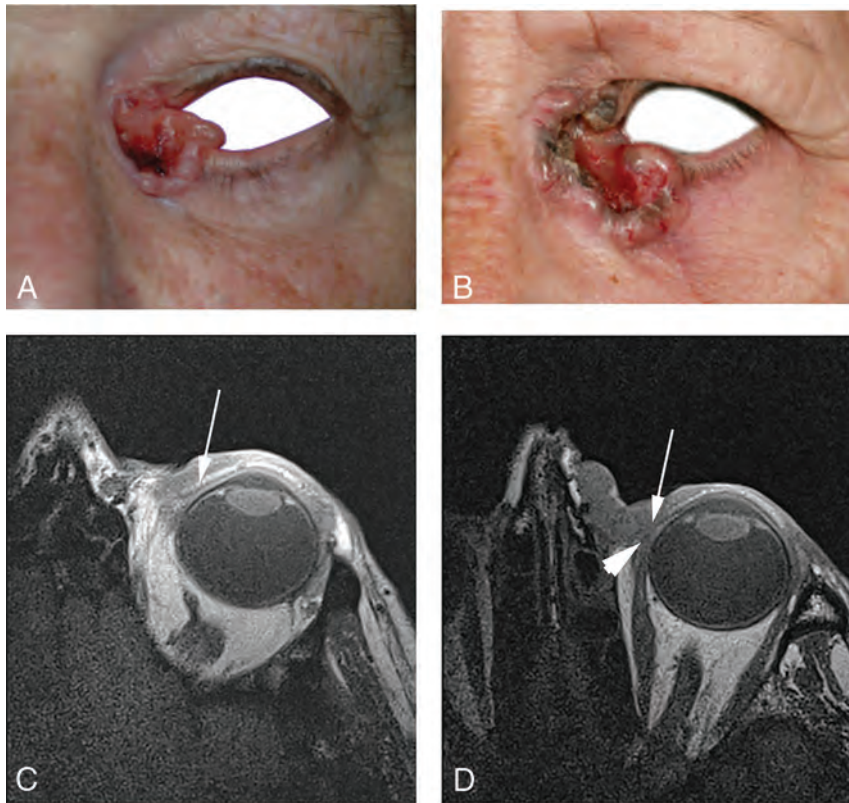


**FIG 1.** BCC of the left medial canthus in 2 elderly women. A, Clinical photograph of case 1. B, Clinical photograph of case 2, which appears superficially similar to the first case. C, T1-weighted axial MC-MR imaging of case 1 demonstrates that the superior tarsal plate is intact (*arrow*) and not invaded by tumor. D, T1-weighted axial MC-MR imaging of case 2 demonstrates full-thickness tumor invasion of the superior tarsal plate (*arrow*), requiring complex oculoplastic reconstruction surgery to optimize eyelid function after resection of the tumor. The tumor also abuts the tendinous insertion of the medial rectus muscle (*arrowhead*), but there was no invasion of this found during the operation.

and invade critical deep structures.<sup>8-11</sup> BCCs are associated with the stochastic effects of exposure to ultraviolet radiation, tending to occur in sun-exposed areas.<sup>7</sup>

The medial canthus of the eye is a common but sometimes surgically challenging site for BCC resection.<sup>9,10,12,13</sup> This issue is because the complex anatomy of the eyelids and tear ducts in this region may require complex reconstructive surgery<sup>10-12</sup> and reliable clinical assessment of the deep lesion extent is impossible,<sup>10,11</sup> with subclinical tumor extension being one of the main features found in recurrent BCC.<sup>14</sup> When reporting MC-MR imaging, we accurately describe the extent of tissue invasion. This description allows preoperative planning of the surgical field, aiming to minimize the extent of surgery to preserve eye and tear duct function, while maximizing clear resection margins.

Invasion of the superior tarsal plate in the upper eyelid is a key determinant of the subsequent complexity of reconstruction.<sup>12,13,15</sup> If this is spared, then surgical defects can usually be closed directly.<sup>12</sup> However, if tarsal plate involvement mandates the creation of a full-thickness surgical defect, then the tarsal plate needs to be reconstructed. This reconstruction necessitates repair by oculoplastic surgeons using a variety of different techniques, including the Cutler-Beard bridge flap, in which conchal cartilage

from the ear is grafted into the surgical defect to deliver the stability necessary for a functional eyelid.<sup>12,15,16</sup> Tarsal plate invasion is difficult to determine clinically, as shown in Fig 1. However, involvement of the tarsal plate and other important structures is exquisitely depicted on T1-weighted MC-MR imaging sequences, allowing advanced surgical planning to ensure that appropriately skilled surgical personnel are present for reconstruction and wound closure.

### **Dermoid Cyst**

Dermoid cysts are benign lesions that arise from rests of embryonic epithelium, which are abnormally sequestered into embryologic sites of fusion and may be encountered as incidental findings.<sup>17,18</sup> However, they may present due to cyst growth causing mass effect or following cyst rupture and subsequent induction of a local inflammatory response.<sup>17,19</sup>

Dermoid cysts are lined by squamous epithelium and may also contain skin appendages, including hair follicles, sebaceous glands, and sweat glands, features that differentiate dermoid from epidermoid cysts.<sup>18,20</sup> These pathologic features are mirrored in the imaging, with MC-MR imaging demonstrating a well-defined, extraocular mass with components of varying signal

return depending on their contents. Most telling is the sebaceous component, which returns high signal on T1-weighted imaging, with signal drop-out on fat-saturated T1-weighted imaging.<sup>21</sup> This appearance is demonstrated in Fig 2.

Surgical treatment for orbital dermoid cysts is primarily cosmetic, usually to reduce the degree of proptosis associated with the mass effect. Surgery is also indicated when the mass impairs eye movement or when rupture causes orbital inflammation.<sup>22</sup> MC-MR imaging is useful for preoperative planning through its demonstration of deep lesion extent; superficial lesions can be easily and completely excised, whereas deep lesions may require complex deep orbital dissection.<sup>22-24</sup>

### **Melanoma**

Uveal melanoma is the most common intraocular malignant tumor of adulthood.<sup>25,26</sup> Nevertheless, it remains relatively uncommon, with an annual incidence of 6 per million population.<sup>25,27</sup> Diagnosis and staging of uveal melanoma are usually purely clinical, with the use of ophthalmoscopy and slit lamp biomicroscopy.<sup>26,28</sup> However, when there is secondary orbital melanoma, either as local spread or recurrence or as a true metastasis, imaging with MC-MR imaging can add value.<sup>29,30</sup>

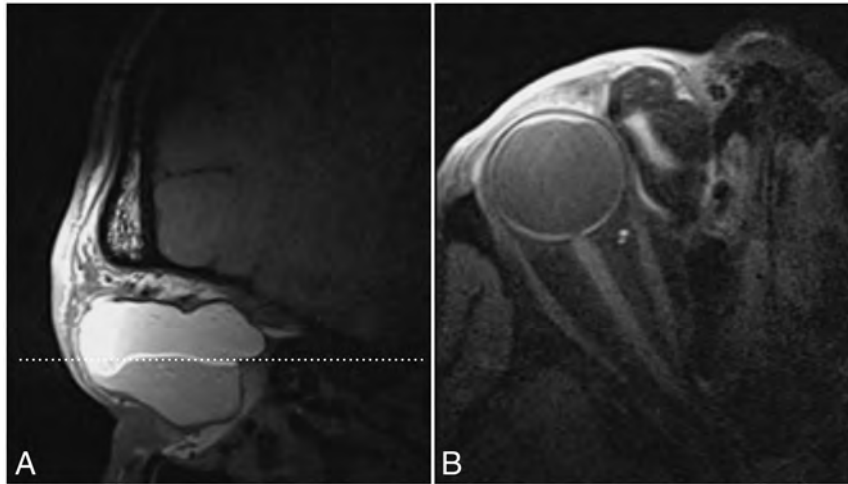


**FIG 2.** Dermoid cyst in the superonasal quadrant of the orbit in a 46-year-old man who had presented with slowly progressive swelling on the medial aspect of the right globe. A, T1-weighted sagittal MC-MR imaging demonstrates a superior layer of high signal intensity and an inferior layer of lower intensity. The acquisition plane of B is denoted by the *dotted line*. B, Fat-saturated T1-weighted axial MC-MR imaging shows signal drop-out of the superior layer, confirming fat content and reinforcing the preoperative diagnosis of dermoid cyst.

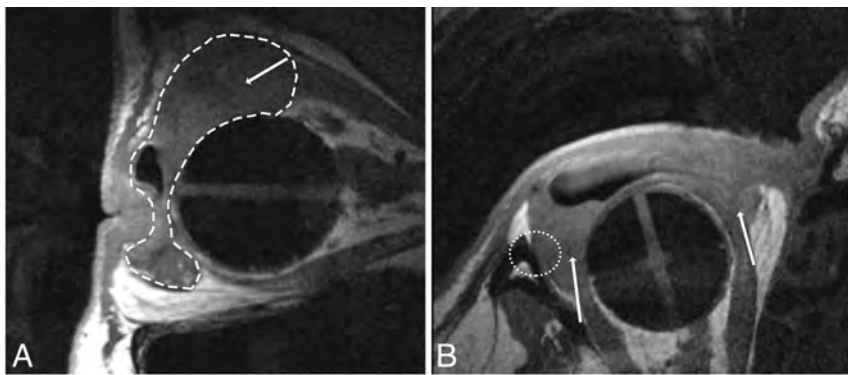


**FIG 3.** Intraorbital melanoma metastasis in an elderly woman with previous enucleation for primary iris melanoma. T1-weighted sagittal MC-MR imaging (A) and T1-weighted axial MC-MR imaging (B) demonstrate a bilobed mass (*dashed white line*) involving the extraocular muscles (*arrows*) and abutting the periosteum of the lateral orbital wall (*dotted white circle*). The tarsal plate was also invaded. Surgical resection margins were planned accordingly, with clear margins confirmed on histologic examination of the resection specimen.

Secondary orbital melanoma has a propensity to involve the extraocular muscles.<sup>29-31</sup> The detailed depiction of the extent of tumor invasion provided by MC-MR imaging facilitates surgical planning to ensure full clearance. The case shown in Fig 3 demonstrates periosteal involvement, and surgical margins were adjusted accordingly.

### Lacrimal Gland Prolapse

The lacrimal glands contain both lymphoid and epithelioid tissues and so may be affected by a diverse range of pathologic processes.<sup>32</sup> The presentation of lacrimal disorders typically involves nonspecific swelling of the outer aspect of the upper eyelid; clarifying the cause of localized palpebral swelling on clinical grounds alone is challenging.<sup>32,33</sup> We have found that MC-MR imaging

can assist with diagnosis and devising appropriate treatment, including the planning of surgical excision when appropriate.

An interesting and unusual lacrimal cause of lateral upper eyelid swelling is a prolapse of otherwise-normal lacrimal tissue, surrounded by fat, under the superior orbital rim. While this is a relatively reassuring diagnosis, the surgical management of lacrimal gland prolapse can be challenging. Macroscopically, the prolapsed lacrimal tissue resembles hypertrophied fat, which can lead to an inadvertent lacrimal resection during blepharoplasty, with subsequent aqueous tear deficiency and resultant damage to the surface of the eye.<sup>34,35</sup> MC-MR imaging evaluation of palpebral swelling can alert ophthalmic surgeons to this diagnosis, as was the case in Fig 4, and help avoid inadvertent lacrimal gland resection.

### Venous Malformation

Venous malformations, previously known as cavernous malformations, are the most common orbital vascular lesions of adulthood. Typically, they present with painless proptosis or may occasionally be diagnosed as an incidental finding on head imaging for other indications.<sup>36</sup>

Rapidly progressive proptosis due to a venous malformation has been described in both puberty and pregnancy.<sup>37</sup> The accelerated growth of the malformations in pregnancy has been attributed to the increase in serum concentrations of vascular endothelial growth factor, which occurs with the progression of pregnancy, because im-

munohistochemical studies have shown that venous malformations express vascular endothelial growth factor receptors.<sup>38</sup> These observations support the hypothesis of a hormone-driven and angiogenic cytokine-mediated growth pattern.<sup>36</sup>

The nature of the underlying pathologic processes that lead to the development of venous malformations is a controversial topic, with some sources postulating a purely venous origin while others suggest that they are a form of low-flow arteriovenous malformation with a fibrous pseudocapsule.<sup>36,39,40</sup> Nevertheless, they have a characteristic appearance that facilitates the radiologic diagnosis. They are typically well-defined, lobulated masses, with signal isointense to muscle on T1-weighted acquisitions and hyperintense to muscle on T2-weighted acquisitions. This appearance is demonstrated in Fig 5.

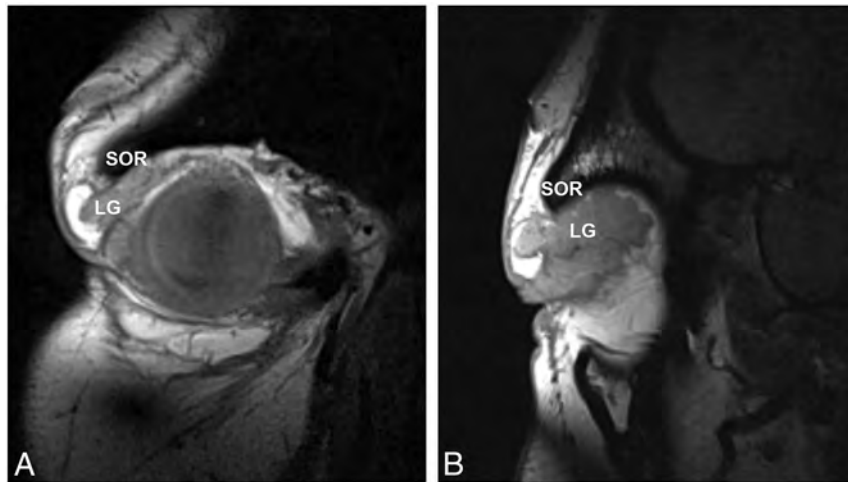


**FIG 4.** Lacrimal gland prolapse in a 27-year-old woman who had presented with palpebral swelling of uncertain origin. T1-weighted coronal MC-MR imaging (A) and T1-weighted sagittal MC-MR imaging (B) demonstrate prolapse of the lacrimal gland (LG) under the superior orbital rim (SOR). The patient was reassured and discharged from the clinic. Should future blepharoplasty be considered, intraoperative repositioning of the gland would be incorporated into the surgical planning.<sup>16</sup>

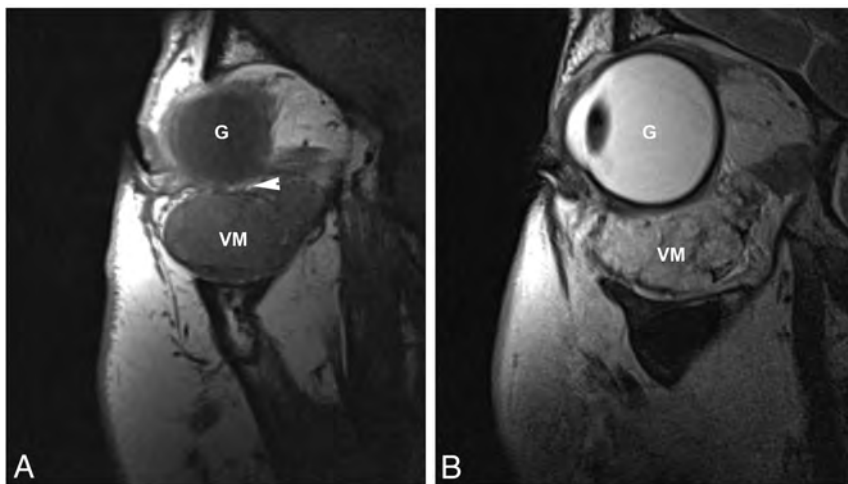


**FIG 5.** Venous malformation in a middle-aged woman. T1-weighted sagittal MC-MR imaging (A) and T2-weighted sagittal MC-MR imaging (B) demonstrate a well-defined, lobulated mass (VM) with signal isointense to muscle on T1-weighted acquisitions and signal hyperintense to muscle on T2-weighted acquisitions. A clean fat plane (*arrowhead*) separates the lesion from the globe (G), in keeping with a fibrous pseudocapsule. Such narrow fat planes would not be resolved on head coil MR imaging. Despite close proximity, neither the rectus muscles nor the tarsal plate was involved, and the lesion was surgically removed intact.

### Lymphatic Malformation

Lymphatic malformations are benign lesions that tend to be diagnosed in early childhood. They are nonencapsulated and consist of multiple lymph-filled channels of various caliber, separated by fine septa.<sup>36</sup> As slow-growing lesions, they usually present with gradual onset and progressive proptosis but can present with more sudden proptosis in the case of intralesional hemorrhage.<sup>41</sup> Management is often conservative, and traditionally surgery was considered when the degree of proptosis caused distress on cosmetic grounds or if the intraorbital involvement impaired eye movement and visual

acuity. However, the lesions often insinuate between the compartments of the orbit and can be intricately related to the extraocular muscles and optic nerve. This feature makes complete surgical excision challenging, with recurrence common.<sup>36,41</sup> Thus, percutaneous sclerotherapy is now thought an excellent treatment option for the condition because it has been shown to be safe and effective.<sup>41</sup> In Fig 6, a recurrent lymphatic malformation is demonstrated, with MC-MR imaging as part of the work-up before bleomycin sclerotherapy.

### Summary

Cross-sectional imaging is already in use for orbital abnormalities,<sup>27,36</sup> and MC-MR imaging of the orbits has been previously described but with rather limited clinical application.<sup>2,42-44</sup> However, the high spatial resolution of MC-MR imaging facilitates assessment of lesions and their relationship to normal anatomic structures in detail sufficient to more confidently and accurately guide the therapeutic approach. MC-MR imaging is particularly valuable for depicting tumor invasion of critical small structures such as the tarsal plates and for depicting clean fat planes between important structures or obliteration of these planes due to tumor invasion. Thus, MC-MR imaging can be implemented for imaging of orbital mass lesions in routine clinical practice. Furthermore, while diagnoses are usually established on clinical grounds, we have observed that characteristic MC-MR imaging appearances of several orbital pathologies can facilitate diagnosis in some unusual cases.

The added value of MC-MR imaging over conventional MR imaging is clear in many of the cases presented. We accept that in some cases, patients would have been managed appropriately with conventional CT or MR imaging. However, until an imaging investigation is performed, it may not be clear whether a particular case will benefit from high-resolution imaging. We are aware of the need to provide the best value for patients. We suggest that by performing MC-MR imaging as the first-line investigation, we are delivering the best value to patients by providing the highest resolution imaging the first time around and avoiding the delay, inconvenience, and expense of recalls for clarification. Furthermore, the surgeons

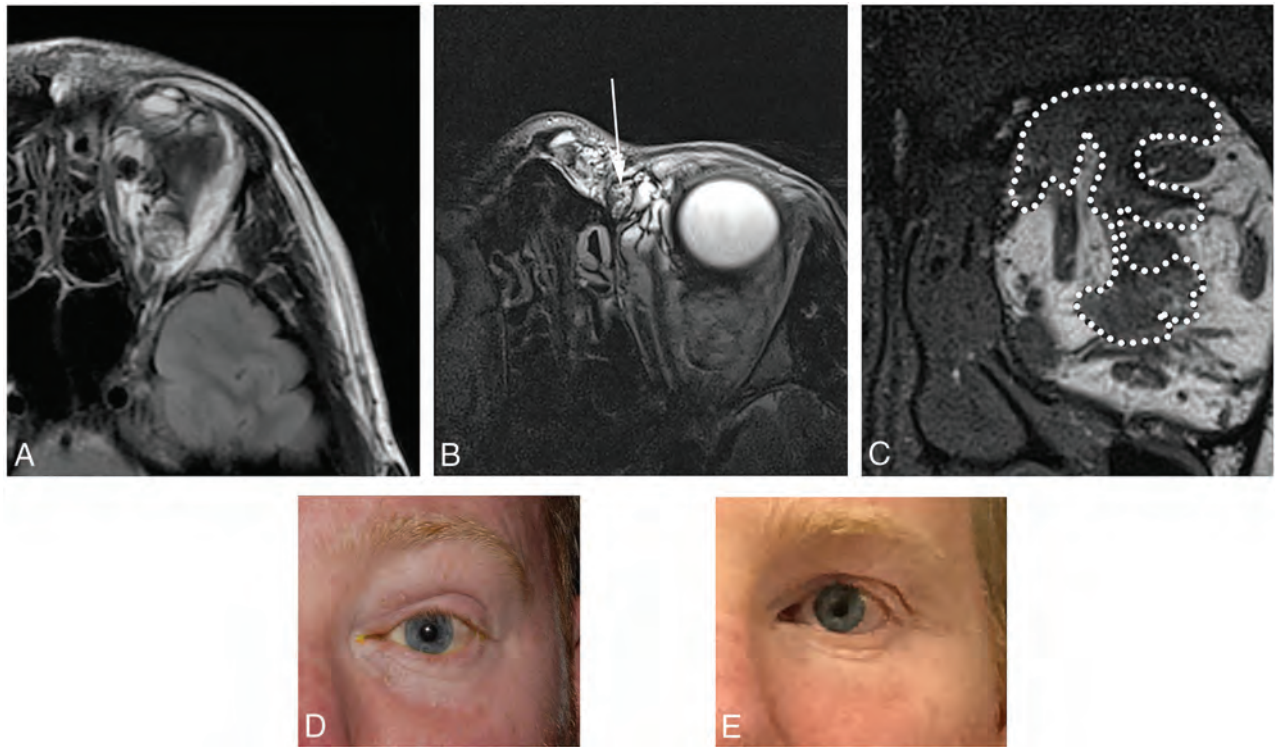


**FIG 6.** A persistent lymphatic malformation in a middle-aged man who had undergone multiple previous operations and steroid injections. MC-MR imaging was performed to guide definitive management. A, Conventional head coil T2-weighted axial MR imaging demonstrates the lymphatic malformation, but the clarity of depiction of the lesion margins and relationships is insufficient to guide treatment. T2-weighted axial MC-MR imaging (B) demonstrates the lesion's characteristic appearance (arrow) and T1-weighted coronal MC-MR imaging (C) demonstrates the lesion (dotted white line) extending from the periorbital soft tissues into the orbit and intraconally, an extent of involvement that precludes safe surgical intervention. Consequently, bleomycin sclerotherapy was performed with pretreatment (D) and posttreatment photography (with the patient's permission) (E) demonstrating aesthetic improvement.

with whom we work have become accustomed to high-resolution MC-MR imaging of orbital pathologies and indicate that they find that these images allow them to better visualize what they will encounter at the operation and how best to plan their procedures.

As well as providing a descriptive radiologic report, we encourage review of the images alongside the ophthalmic, oculo-plastic, or dermatologic surgeons. This collegial approach helps the radiologist understand the clinically and surgically pertinent findings and helps the surgeon by delineating the often-complex anatomic relationships between orbital lesions and surrounding structures. This close clinical liaison builds a mutually beneficial interdisciplinary relationship and increases the appropriateness and utility of referrals for MC-MR imaging, leading to better informed treatment plans and optimization of patient outcomes.

Disclosures: Ian A. Zealley—UNRELATED: Employment: National Health Service Tayside, Comments: This is the health service that employs me to perform clinical work. Expert Testimony: legal firms, Comments: expert opinion provided in relation to litigation not related to the work presented for publication; Travel/Accommodations/Meeting Expenses Unrelated to Activities Listed: various medical education meetings, Comments: support from meeting organizers to present lectures on various subjects.

## REFERENCES

1. Paluzzi A, Gardner PA, Fernandez-Miranda JC, et al. "Round-the-Clock" surgical access to the orbit. *J Neurol Surg B Skull Base* 2015;76:12–24 CrossRef Medline

2. Georgouli T, James T, Tanner S, et al. High-resolution microscopy coil MR-Eye. *Eye (Lond)* 2008;22:994–96 CrossRef Medline
3. Budak MJ, Weir-McCall JR, Yeap PM, et al. High-resolution microscopy-coil MR imaging of skin tumors: techniques and novel clinical applications. *Radiographics* 2015;35:1077–90 CrossRef Medline
4. Lin LK, Reznick A, Mukundan G, et al. Pictorial review of histopathologically diagnosed orbital tumors. *American Journal of Ophthalmic Clinical Trails* 2019;2:1–9 CrossRef
5. Reinau D, Surber C, Jick SS, et al. Epidemiology of basal cell carcinoma in the United Kingdom: incidence, lifestyle factors, and comorbidities. *Br J Cancer* 2014;111:203–06 CrossRef Medline
6. Apalla Z, Lallas A, Sotiriou E, et al. Epidemiological trends in skin cancer. *Dermatol Pract Concept* 2017;7:1–6 CrossRef Medline
7. Kim DP, Kus KJ, Ruiz E. Basal cell carcinoma review. *Hematol Oncol Clin North Am* 2019;33:13–24 CrossRef Medline
8. Kasper M, Jaks V, Hohl D, et al. Basal cell carcinoma: molecular biology and potential new therapies. *J Clin Invest* 2012;122:455–63 CrossRef Medline
9. Shi Y, Jia R, Fan X. Ocular basal cell carcinoma: a brief literature review of clinical diagnosis and treatment. *Onco Targets Ther* 2017;10:2483–89 CrossRef Medline
10. Slutsky JB, Jones EC. Periocular cutaneous malignancies: a review of the literature. *Dermatol Surg* 2012;38:552–69 CrossRef Medline
11. Leibovitch I, McNab A, Sullivan T, et al. Orbital invasion by periocular basal cell carcinoma. *Ophthalmology* 2005;112:717–23 CrossRef Medline
12. Ahmad J, Mathes DW, Itani KM. Reconstruction of the eyelids after Mohs surgery. *Semin Plast Surg* 2008;22:306–18 CrossRef Medline
13. Actis AG, Actis G. Reconstruction of the upper eyelid with flaps and free grafts after excision of basal cell carcinoma. *Case Rep Ophthalmol* 2011;2:347–53 CrossRef Medline

14. Malhotra R, Huilgol SC, Huynh NT, et al. **The Australian Mohs database, Part I: periocular basal cell carcinoma experience over 7 years.** *Ophthalmology* 2004;111:624–30 CrossRef Medline
15. Irvine F, McNab AA. **Technique for reconstruction of upper lid marginal defects.** *Br J Ophthalmol* 2003;87:279–81 CrossRef Medline
16. Cutler NL, Beard C. **A method for partial and total upper lid reconstruction.** *Am J Ophthalmol* 1955;39:1–7 CrossRef Medline
17. Shields JA, Kaden IH, Eagle RC, et al. **Orbital Dermoid Cysts: Clinicopathologic Correlations, Classification, and Management: The 1997 Josephine E. Schueler Lecture.** *Ophthalmic Plast Reconstr Surg* 1997;13:265–76 CrossRef Medline
18. Shields JA, Shields CL. **Orbital cysts of childhood—classification, clinical features, and management.** *Surv Ophthalmol* 2004;49:281–99 CrossRef Medline
19. Bonavolontà G, Tranfa F, de Conciliis C, et al. **Dermoid cysts: 16-year survey.** *Ophthalmic Plast Reconstr Surg* 1995;11:187–92 CrossRef Medline
20. Smirniotopoulos JG, Chiechi MV. **Teratomas, dermoids, and epidermoids of the head and neck.** *Radiographics* 1995;15:1437–55 CrossRef Medline
21. Chung EM, Murphey MD, Specht CS, et al. **From the Archives of the AFIP; Pediatric orbit tumors and tumorlike lesions: osseous lesions of the orbit.** *Radiographics* 2008;28:1193–1214 CrossRef Medline
22. Chaudhry IA. **Management of deep orbital dermoid cysts.** *Middle East Afr J Ophthalmol* 2008;15:43–45 CrossRef Medline
23. Lane CM, Ehrlich WW, Wright JE. **Orbital dermoid cyst.** *Eye (Lond)* 1987;1(Pt 4):504–11 CrossRef Medline
24. Cavazza S, Laffi GL, Lodi L, et al. **Orbital dermoid cyst of childhood: clinical pathologic findings, classification and management.** *Int Ophthalmol* 2011;31:93–97 CrossRef Medline
25. Egan KM, Seddon JM, Glynn RJ, et al. **Epidemiologic aspects of uveal melanoma.** *Surv Ophthalmol* 1988;32:239–51 CrossRef Medline
26. Mellen PL, Morton SJ, Shields CL. **American Joint Committee on Cancer Staging of Uveal Melanoma.** *Oman J Ophthalmol* 2013;6:116–18 CrossRef Medline
27. Tailor TD, Gupta D, Dalley RW, et al. **Orbital neoplasms in adults: clinical, radiologic, and pathologic review.** *Radiographics* 2013;33:1739–58 CrossRef Medline
28. Shields JA, Shields CL, De Potter P, et al. **Diagnosis and treatment of uveal melanoma.** *Semin Oncol* 1996;23:763–67 Medline
29. Rosenberg C, Finger PT. **Cutaneous malignant melanoma metastatic to the eye, lids, and orbit.** *Surv Ophthalmol* 2008;53:187–202 CrossRef Medline
30. Rose AM, Cowen S, Jayasena CN, et al. **Presentation, treatment, and prognosis of secondary melanoma within the orbit.** *Front Oncol* 2017;7:125 CrossRef Medline
31. Conill C, Morilla I, Malvehy J, et al. **Secondary orbital metastases from cutaneous melanoma.** *Melanoma Res* 2004;14:437–38 CrossRef Medline
32. Hughes GK, Miszkiel KA. **Imaging of the lacrimal gland.** *Semin Ultrasound CT MR* 2006;27:476–91 CrossRef Medline
33. Mohan S, Hegde A, Tchoyoson Lim CC. **Lacrimal glands: size does matter!** *Middle East Afr J Ophthalmol* 2011;18:328–30 CrossRef Medline
34. Massry GG. **Prevalence of lacrimal gland prolapse in the functional blepharoplasty population.** *Ophthalmic Plast Reconstr Surg* 2011;27:410–13 CrossRef Medline
35. Hundal KS, Mearza AA, Joshi N. **Lacrimal gland prolapse in blepharochalasis.** *Eye (Lond)* 2004;18:429–30 CrossRef Medline
36. Smoker WR, Gentry LR, Yee NK, et al. **Vascular lesions of the orbit: more than meets the eye.** *Radiographics* 2008;28:185–204; quiz 325 CrossRef Medline
37. Zauberman H, Feinsod M. **Orbital hemangioma growth during pregnancy.** *Acta Ophthalmol (Copenh)* 1970;48:929–33 CrossRef Medline
38. Nagasaka M, Naganuma H, Satoh E. **Growth potential of orbital cavernous hemangioma suggested by vascular endothelial growth factor and its receptor flk-1.** *Neurol Med Chir (Tokyo)* 2007;47:5–10 CrossRef Medline
39. Ansari SA, Mafee MF. **Orbital cavernous hemangioma: role of imaging.** *Neuroimaging Clin N Am* 2005;15:137–58 CrossRef Medline
40. Rootman J. **Vascular malformations of the orbit: hemodynamic concepts.** *Orbit* 2003;22:103–20 CrossRef Medline
41. Barnacle AM, Theodorou M, Maling SJ, et al. **Sclerotherapy treatment of orbital lymphatic malformations: a large single-centre experience.** *Br J Ophthalmol* 2016;100:204–08 CrossRef Medline
42. Hoffmann KT, Hosten N, Lemke AJ, et al. **Septum orbitale: high-resolution MR in orbital anatomy.** *AJNR Am J Neuroradiol* 1998;19:91–94 Medline
43. Kau HC, Tsai CC, Ortube MC, et al. **High-resolution magnetic resonance imaging of the extraocular muscles and nerves demonstrates various etiologies of third nerve palsy.** *Am J Ophthalmol* 2007;143:280–87 CrossRef Medline
44. Clark RA, Demer JL. **Magnetic resonance imaging of the globe-tendon interface for extraocular muscles: is there an “arc of contact”?** *Am J Ophthalmol* 2018;194:170–81 CrossRef Medline

# Modelling the Anatomic Distribution of Neurologic Events in Patients with COVID-19: A Systematic Review of MRI Findings

 N. Parsons,  A. Outsikas,  A. Parish,  R. Clohesy,  F. D'Aprano,  F. Toomey,  S. Advani, and  G.R. Poudel



## ABSTRACT

**BACKGROUND:** Neurologic events have been reported in patients with coronavirus disease 2019 (COVID-19). However, a model-based evaluation of the spatial distribution of these events is lacking.

**PURPOSE:** Our aim was to quantitatively evaluate whether a network diffusion model can explain the spread of small neurologic events.

**DATA SOURCES:** The MEDLINE, EMBASE, Scopus, and LitCovid data bases were searched from January 1, 2020, to July 19, 2020.

**STUDY SELECTION:** Thirty-five case series and case studies reported 317 small neurologic events in 123 unique patients with COVID-19.

**DATA ANALYSIS:** Neurologic events were localized to gray or white matter regions of the Illinois Institute of Technology (gray-matter and white matter) Human Brain Atlas using radiologic images and descriptions. The total proportion of events was calculated for each region. A network diffusion model was implemented, and any brain regions showing a significant association ( $P < .05$ , family-wise error-corrected) between predicted and measured events were considered epicenters.

**DATA SYNTHESIS:** Within gray matter, neurologic events were widely distributed, with the largest number of events (~10%) observed in the bilateral superior temporal, precentral, and lateral occipital cortices, respectively. Network diffusion modeling showed a significant association between predicted and measured gray matter events when the spread of pathology was seeded from the bilateral cerebellum ( $r = 0.51$ ,  $P < .001$ , corrected) and putamen ( $r = 0.4$ ,  $P = .02$ , corrected). In white matter, most events (~26%) were observed within the bilateral corticospinal tracts.

**LIMITATIONS:** The risk of bias was not considered because all studies were either case series or case studies.

**CONCLUSIONS:** Transconnectome diffusion of pathology via the structural network of the brain may contribute to the spread of neurologic events in patients with COVID-19.

**ABBREVIATIONS:** COVID-19 = coronavirus disease 2019; IIT = Illinois Institute of Technology; NDM = network diffusion model; SARS-CoV-2 = Severe Acute Respiratory Syndrome coronavirus 2

The coronavirus disease 2019 (COVID-19) is caused by Severe Acute Respiratory Syndrome coronavirus 2 (SARS-CoV-2).<sup>1</sup> Typically, patients with COVID-19 present with fever, cough, fatigue, and dyspnea, with approximately 20% of cases developing severe life-threatening disease.<sup>1</sup> Extrapulmonary symptoms are also being reported, including altered consciousness, seizures, and focal neurologic injuries, raising concerns of the long-term neurologic sequelae of COVID-19.<sup>2-7</sup> As of October 15, 2020, >38.4

million cases and 1.1 million deaths have been reported globally, with cases rising rapidly in the United States, India, and Brazil.<sup>8</sup>

Neurologic symptoms in patients with COVID-19 are linked to a broad range of acute neurologic events from large ischemic strokes to small and localized hemorrhages, vascular thrombosis, and microbleeds.<sup>9</sup> The presence of cerebral microbleeds (small 2- to 5-mm perivascular hemosiderin deposits) are also being reported and are presumed to be features of small-vessel disease.<sup>10,11</sup> These smaller neurologic events can manifest as

Received January 14, 2021; accepted after revision February 17.

From the Cognitive Neuroscience Unit (N.P.), School of Psychology (N.P., A.O., A.P., R.C.), and School of Medicine (F.T.), Deakin University, Melbourne, Australia; Melbourne School of Psychological Sciences (F.D.), The University of Melbourne, Melbourne, Australia; Department of Neurology (F.D.), Royal Melbourne Hospital, Melbourne, Australia; Social Behavioural Research Branch (S.A.), National Human Genome Research Institute, National Institutes of Health, Bethesda, Maryland; and Department of Health Sciences (G.R.P.), Mary Mackillop Institute for Health Research, Australian Catholic University, Melbourne, Australia.

Please address correspondence to Govinda R. Poudel, MD, Mary Mackillop Institute for Health Research, 215 Spring St, Melbourne, Australia; e-mail: govinda.poudel@acu.edu.au; @Govinrp

 Indicates open access to non-subscribers at [www.ajnr.org](http://www.ajnr.org)

 Indicates article with online supplemental data.

<http://dx.doi.org/10.3174/ajnr.A7113>

FLAIR signal abnormalities in either gray or white matter or localized signal changes as measured with T1-weighted, susceptibility-weighted, and diffusion-weighted MR imaging.<sup>9,12,13</sup> Most importantly, such neurologic events are known to be associated with long-term impacts on brain function<sup>14,15</sup> and may therefore reflect a selective vulnerability of brain regions to COVID-19.

These neurologic events are anatomically distributed throughout both cortical and deep subcortical structures.<sup>6,16-18</sup> However, these distributions are not well-understood and may benefit from mathematic modeling to characterize the pattern of distribution and potential epicenters of spread. For instance, network diffusion models (NDMs) can emulate the pattern of pathologic spread via white matter pathways in the brain and have been useful in modeling the cerebral distribution of pathology in other progressive, degenerative neurologic conditions.<sup>19,20</sup> However, to date, there has been no application of any mathematic model to assess and map the distribution of neurologic events associated with COVID-19.

This systematic review aims to shed light on the distribution of COVID-19-related neurologic events within gray matter. Subsequently, we summarized recent literature on neurologic events, mapped the spatial distribution of neurologic events, and used the NDM to model the anatomic distribution of gray matter events in patients with COVID-19.

## MATERIALS AND METHODS

### Protocol Registration

This systematic review was registered with the international prospective register of systematic reviews (PROSPERO: registration No. CRD42020201161) and conducted according to Preferred Reporting Items for Systematic Reviews and Meta-Analyses (PRISMA) guidelines.

### Search Strategy

We searched MEDLINE, EMBASE, Scopus, and LitCovid data bases from January 1, 2020, to July 19, 2020, by “nervous system” OR “CNS” AND “MR imaging” OR “MR imaging” OR “hypointensities” OR “microbleeds” OR “cerebral microbleeds” OR “microhemorrhages.” Additional studies were identified by manually searching the reference lists of relevant articles. The search strategy is outlined in the Online Supplemental Data in a PRISMA flow chart. This search was conducted with the help of a health science librarian.

### Selection Criteria

We included case reports, case series, and observational studies published in peer-reviewed journals and preprints available in English that identified small neurologic events in patients with COVID-19 using MR imaging. Articles without full texts and studies in patients without laboratory-confirmed COVID-19 diagnoses were excluded. Any studies that reported only large cerebrovascular events (such as strokes, infarcts) and diffuse pathology (nonspecific) were also excluded.

### Data Extraction

Two independent reviewers screened articles by title and abstract for relevance. These studies were then screened for eligibility for

inclusion by full-text evaluation. For each included article, 2 independent reviewers extracted data (A.P., R.C.). Disagreements were collaboratively resolved within the team. Instructions detailing the type of information to be extracted and how to record, categorize, or code this information were also discussed among team members. The following information was extracted from each article: 1) country, first author, and year of publication; 2) sample characteristics (sample size, age group, and sex distribution); 3) study design; 4) clinical symptoms; 5) reason for brain imaging; 6) type of MR imaging performed; 7) imaging findings; and 8) relevant conclusions to assist article interpretation. Two additional reviewers (F.D., F.T.) then validated all the extracted data and the eligibility of each included article.

### Neuroimaging Data Synthesis and Coding

Two expert reviewers (N.P., G.R.P.) screened each included article to identify the location, distribution, and number of neurologic events. These events ranged from microbleeds (observed in SWI or T2\* gradient recalled-echo images), white matter hyperintensities (FLAIR images), small lesions, or signal changes in diffusion-weighted imaging within the gray or white matter. For each article, events were manually localized to gray or white matter regions on the basis of available MR images and/or radiologic descriptions. The Desikan-Killiany gray matter atlas incorporating 84 brain regions was used to label any events located within the gray matter. Of the 41 gray matter regions that were impacted, ~70% of the regions had an exact match with the labels used in the atlas (eg, putamen, caudate, cerebellum, precentral/postcentral gyri, and so forth). The remaining labels that did not directly match or were broad (eg, basal ganglia, occipitoparietal, temporal, frontal) were localized using the combination of description and MR images available (based on agreement between 2 neuroimaging experts and 1 physician; Online Supplemental Data). White matter bundles from the Illinois Institute of Technology (IIT) Human Brain Atlas were used to label any events located within the white matter. The FSLeys neuroimaging software from the FMRIB Software Library (<https://fsl.fmrib.ox.ac.uk/fsl/fslwiki/FSLeys>) was then used to visualize white matter tracts and gray matter areas from the IIT atlas. Any patient with COVID-19 with nonspecific neuropathologic findings (eg, juxtacortical white matter) or without an accompanying MR image or description was excluded from further analyses. This data-encoding process generated 2 tables for gray and white matter regions with columns corresponding to each article and rows corresponding to the name of the region/bundle (Online Supplemental Data). Each cell in the table provided information on the number of cases corresponding to a localized neurologic event. A third independent reviewer (F.T.) validated the encoded data, and any discrepancies were discussed and addressed.

### Neuroimaging Data Visualization

The proportion of events  $\left(\frac{\text{number of events}}{\text{total cases}} \times 100\right)$  pertaining to each encoded region within the IIT Desikan-Killiany gray matter atlas and IIT white matter bundles was used for visualization. Gray matter events were visualized using MRICroGL software (<https://www.nitrc.org/projects/mricrogl/>). White matter events

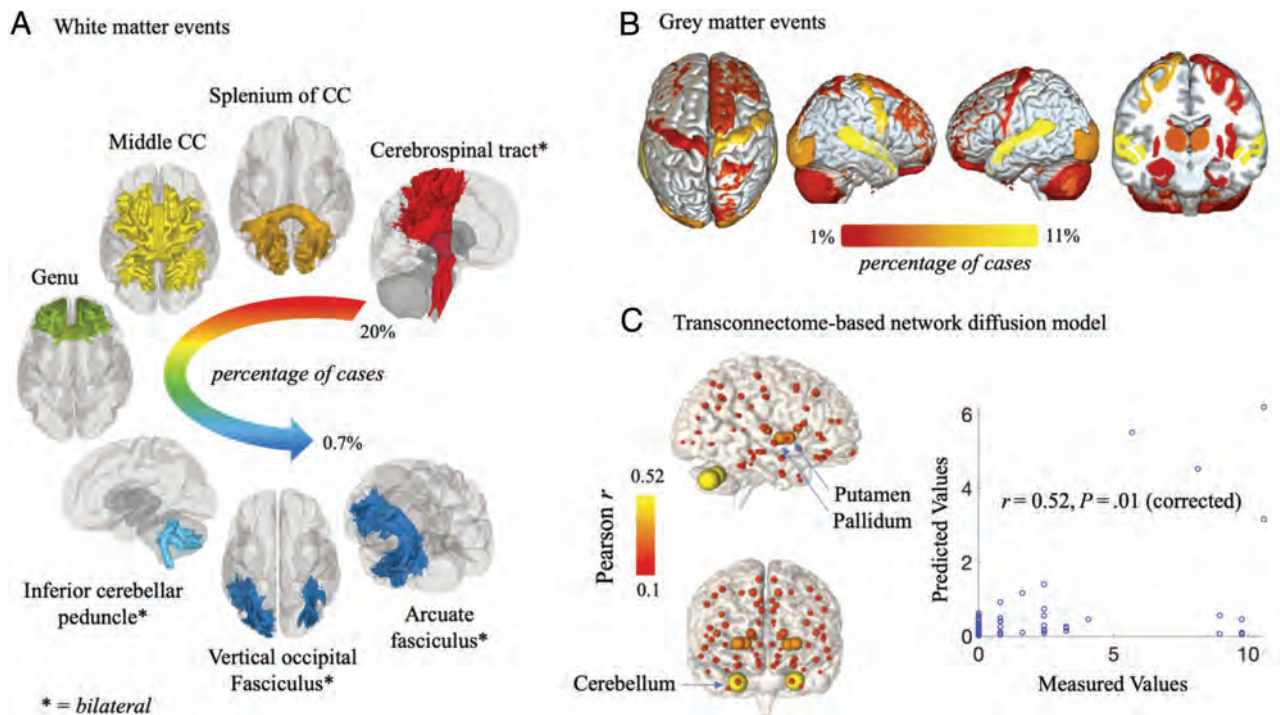


**FIG 1.** Visualization of the spatial distribution of neurologic events and network diffusion modeling. (A) The highest proportions of events occur in white matter areas such as the corticospinal tract. (B) In gray matter, the most affected regions are the bilateral superior temporal cortices, precentral cortices, and pallidum. (C) A network diffusion model using structural connectivity edge weights successfully predicts the spread of neurologic events. (C) The epicenters of spread that showed the most significant association between predicted and measured distribution of events are the bilateral cerebellum and putamen. CC indicates corpus callosum.

were visualized using Matlab 2018a (MathWorks) and the CONN toolbox, Version 19b (<https://web.conn-toolbox.org/>).

### Network Diffusion Model of Spread

A graph theoretic meta-analysis model was used to test whether the spatial distribution of small neurologic events in the brain can be explained by a spread via the structural connectome of the brain (source code available at: <https://github.com/govin2000/covidspread>). NDM was used per previous protocols that identified a spatial pattern of pathology in the brain.<sup>19,20</sup> The NDM models the hypothetic distribution of pathology in a brain network (given by a connectome  $C$ ) across time by linear diffusion, given by  $x(t) = e^{-\beta H t} x_0$ , where  $x_0$  is the initial pattern of the neurologic events at  $t = 0$ ,  $H$  is the degree normalized graph Laplacian, and is a diffusivity constant. The unit of the model's diffusion time ( $t$ ) is assumed to be days (given the likely progression of 5–14 days) for the diffusivity constant of 1 per day.  $x(t)$  is a vector of distribution of pathology in the brain when diffusion is seeded from a given region provided by an initial condition  $x_0$ . We used a repeat seeding approach, which has previously been used to identify potential epicenters of the spread of neuropathology. The IIT ( $84 \times 84$ ) connectivity matrix was used for the NDM simulation.

The NDM generates a vector of distribution of pathology  $x(t)$  across time. We expect that  $x(t)$  should correlate with the distribution of neurologic events. Thus, the Pearson correlation coefficient strength and  $P$  values were calculated between the empiric proportions of events measured using the systematic review

method (described above) and  $x(t)$  at all model timepoints ( $t$ ). This process was repeated for all bilateral regions (42 bilateral regions) within the IIT Desikan-Killiany gray matter atlas. The region that showed the largest significant ( $P < .05$ , family-wise error-corrected for 84 regions) association with measured neurologic events was defined as the seed region.

### RESULTS

The systematic search yielded 461 articles, of which 62 were eligible for full-text assessment (Online Supplemental Data; PRISMA flow diagram). Of these, 28 were excluded; these were commentaries, response letters, and review articles proposing SARS-CoV-2 nervous system invasion but lacking clinical findings. A total of 35 publications reporting small neurologic events in patients with COVID-19 were evaluated. Of these, 35 provided specific anatomic detail required for meta-analysis and modeling. These articles contributed 123 unique patients, with a total of 317 neurologic events (Online Supplemental Data). Of these, 91 patients had gray matter changes, 95 patients had white matter changes, and 72 patients had confirmed cerebral microbleeds. Further details on the presentation of gray and white matter events, and the frequency of symptoms can be found in the Online Supplemental Data.

### Spatial Distribution of Neurologic Events

Figure 1A, -B depicts the spatial distribution of white and gray matter neurologic events. White matter events were observed within 11 of 42 white matter bundles from the IIT atlas. The highest percentage (26%) of events was observed within the bilateral

corticospinal tracts, composed of white matter fibers that connect the primary motor cortex and basal ganglia. The splenium and middle of the corpus callosum were affected in 14% and 9% of the cases, respectively. The remaining tracts showed white matter events in <9% of cases. Of the cerebral microbleeds observed, a similar pattern emerged, in which the largest proportion of cerebral microbleeds was also found in the middle corpus callosum, followed by the splenium of the corpus callosum. Gray matter events were spatially distributed among 41 brain regions within the Desikan-Killiany atlas. The highest proportions (~10%) of events were observed in the bilateral superior temporal, precentral, and lateral occipital cortices. Subcortical events were most frequently identified in the pallidum.

### **Network Diffusion Model Findings**

Each of the 84 regions within the IIT Desikan-Killiany gray matter atlas was used as a potential seed for the spread of pathology across time. Figure 1C shows a glass-brain visualization of the best fit (maximum Pearson correlation coefficient value) between empiric events and predicted values determined using the NDM. A significant fit was achieved when seeding the spread from the bilateral cerebellum (Pearson  $r=0.52$ ,  $P<.001$ , corrected) and the putamen ( $r=0.4$ ,  $P=.02$ , corrected). Other basal ganglia structures also showed moderate associations ( $r>0.3$ ) but were not significant after correction. The spatial distribution of the fit in all regions reflects the consequence of network spread, originating from each of the included regions. The association between empiric events and predicted events was low ( $r<0.2$ ) when the Euclidian distance between regions was used as network edges instead of structural connectivity (Online Supplemental Data).

## **DISCUSSION**

Patients with COVID-19 are vulnerable to acute neuropathology, commonly in the form of small neurologic and cerebrovascular events. We systematically reviewed articles reporting localized MR imaging findings in patients with COVID-19 and spatially encoded them onto a common gray and white matter atlas. We then investigated whether the spatial distribution of these events follows a cortical or subcortical pattern that can be explained by a linear diffusion-based model of pathologic spread. We found the epicenters of this spread to be the cerebellum and putamen.

### **Neurologic Events in White and Gray Matter**

White matter events were identified most frequently in the corticospinal tract and corpus callosum. The corticospinal tract is a major white matter pathway connecting critical subcortical brain regions such as the basal ganglia and thalamus and, thus, facilitates information related to voluntary motor control. As a result, diffuse aberrations in the corticospinal tract are associated with motor symptoms such as tendon reflexes, ankle clonus, and bilateral extensor plantar reflexes, which have been commonly reported in patients with COVID-19.<sup>21</sup> Similarly, the corpus callosum plays an important role in interhemispheric communication, which can result in a disconnection syndrome and broad neurocognitive deficits.<sup>22</sup>

In gray matter regions, events were identified most frequently in the temporal and precentral gyrus as well as the bilateral thalamus. Alterations in thalamocortical connectivity can disrupt the regulation of consciousness and arousal.<sup>23</sup> Thus, acute events in these regions may explain symptoms such as confusion, disorientation, agitation, and loss of consciousness.<sup>10,24</sup> Despite their acute manifestation, the accumulation of neurologic events in subcortical structures and consequent disruption to distal cortical regions can increase susceptibility to cognitive impairment and decline, which have ramifications for long-term cognitive prognosis.<sup>25,26</sup>

### **Infiltration and Spread Mechanism: Olfactory Pathway**

Patients with neurologic symptoms also presented with anosmia, encephalopathy, seizures, and changes in vision including cortical blindness and visual confabulation.<sup>27-29</sup> Alterations in olfaction may therefore have a neurologic basis, particularly in light of the identified pathology implicating the olfactory bulb in clinical imaging, including the presence of microbleeds among these patients. It is plausible that these symptoms relate closely to the mode of infiltration of SARS-CoV-2, with a potential mechanism being direct injury to the nervous system via angiotensin-converting enzyme 2 receptor expression on nerve cells, including the olfactory bulb.

Given the potential for SARS-CoV-2 neurotropism, neuropathology in the piriform cortex could be caused initially by the introduction of a virus through a direct axonal connection with the olfactory bulb. Although we were not able to mathematically model the piriform cortex specifically within the Desikan-Killiany brain atlas, we found only 7 patients from 3 studies who presented with small lesions within this cortex (olfactory bulb). Indeed, some have found intranasal infection of other coronaviruses such as SARS-CoV in the respiratory tract, which were subsequently neuroinvasive.<sup>30</sup> However, this mechanism remains to be established in the newly discovered SARS-CoV-2.

### **Infiltration and Spread Mechanism: Axonal Transport**

An important question arises from our finding of the cerebellum and putamen as the seeds of spread—that is, how likely is it that these are indeed epicenters? Herein, note that NDMs are high-level generative models and only model the macroscopic consequences of the pathology in gray matter regions, and that the NDM does not require that the seed region itself presents with the highest number of pathologic events. Indeed, a neurobiologic explanation for the identification of these seed regions is beyond the scope of this article. Therefore, the mechanism underpinning the potential spread from these sites and subsequent distribution of SARS-CoV-2 throughout the brain remains to be thoroughly examined. However, while the cerebellum and putamen may serve as epicenters, SARS-CoV-2 may then travel to cortical sites such as the precentral gyrus via retrograde transsynaptic transmission through the corticospinal tract by hijacking axonal transport mechanisms.<sup>22</sup> While in transit, direct neuronal or endothelial cell disruption may exacerbate the systemic pathophysiology, facilitating cerebrovascular complications and mixed type I/II respiratory failure.<sup>3,22</sup>

Indeed, the first site of infection of other SARS-CoV viruses is the epithelial cells of the respiratory tract, where they bind to

angiotensin-converting enzyme 2 receptors;<sup>31</sup> however, angiotensin-converting enzyme 2 is also expressed on nerve cells. Therefore, coronaviruses may easily be transported to infect the endothelial cells of the blood-brain barrier.<sup>31</sup> However, SARS-CoV-2 has rarely been isolated from CSF samples, precluding the characterization of its neurotropism and direct role in neurologic event pathogenesis.

### **Neuroinflammation and Cytokine Storm**

Other proposed pathologic mechanisms may explain the distribution of neurologic events, including neuroinflammatory responses and cytokine- and hypoxia-induced injury.<sup>3</sup> Emerging evidence is characterizing COVID-19 as a vascular disease, a hyperinflammatory response with an ensuing cytokine storm and coagulopathy that may synergistically contribute to neurologic event pathogenesis.<sup>2,3</sup> COVID-19-associated coagulopathy occurs proportional to disease severity and leads to treatment-resistant thrombotic and hemorrhagic events, characterized by D-dimer elevation with prothrombin prolongation and thrombocytopenia.

Furthermore, cytokine- and hypoxia-induced injury to the corpus callosum, particularly the splenium, has been reported in critical illness, including acute respiratory distress syndrome and high-altitude cerebral edema, potentially contributing to a vulnerability in COVID-19.<sup>17</sup> Hypoxia directly induces chemical and hydrostatic endothelial cell disruption, promoting vascular permeability and hence contributing to neurologic event pathogenesis.<sup>32</sup> Relative to the cortex, the thalamus, basal ganglia, and deep white matter are poorly perfused due to their watershed end-arterial vascular architecture, which could exacerbate their baseline hypoxic vulnerability and ultimately promote subcortical neurologic events. While the pathogenesis of white matter hyperintensities remains under debate, roles for hypoxia, immune activation, endothelial cell dysfunction, and altered metabolism have been posited, not dissimilar to the neuropathologic associations of COVID-19.<sup>15,18,33</sup>

### **Clinical Relevance**

In addition to their acute manifestations, the accumulation of neurologic events in subcortical structures and consequent disruption of distal cortical regions may lead to microstructural injury, independently contributing to cognitive impairment and dementia—a clinically impacting patient morbidity.<sup>11,34</sup> Microbleeds and white matter hyperintensities also signify a hemorrhage-prone brain, which is more susceptible to larger neurologic events such as ischemic stroke and intracranial hemorrhage, whereby patients demonstrate worse deterioration from premonitory functioning and increased mortality.<sup>17</sup> Indeed, in patients with COVID-19, the presence of small neurologic events has been associated with increased disease severity, the length of hospital admission, mortality, and worse functional status on discharge.<sup>35</sup> Given the established adverse effects of small neurologic events and these early findings, the potential long-term cognitive and cerebrovascular impact on patients with COVID-19 may become more apparent with time. If found, careful consideration should be given to the prescription of anticoagulation, given that these neurologic events suggest a propensity for further hemorrhage.

### **Limitations**

This review has several important limitations. First, we translated neurologic events into a standard MR imaging atlas space using a partly qualitative method, whereby these pathologies were localized using the radiologic description of the location or MR images when available. While this method may lack specificity, we used multiple neuroimaging and medical experts and included only data with specific spatial information or MR images. Thus, the partly qualitative nature of the translation should be considered with caution while interpreting our findings. Furthermore, the white matter tracts used to visualize the summary of the white matter findings are only coarse grain reorientations. Given that few tracts (eg, corpus callosum) completely match the labels used in the atlas, we localized events on the basis of the descriptions and available MR images regarding approximate corresponding tracts. Second, most of the included articles were cross-sectional case studies and hence cannot directly attribute the observed neuropathology to SARS-CoV-2.

The question remains as to whether neurologic events are the direct consequence of viral infection/sequelae or instead indicate an underlying propensity for neurologic events in these patients.<sup>36</sup> To answer this question, studies must use large samples in which a specific etiology can be isolated in a case-control, longitudinal design.<sup>36</sup> These etiologies must be separated into those of unrelated vascular origin and those that may be a direct consequence of viral infection. Therein, an additional challenge ensues: to determine whether there are, indeed, overlapping or isolated pathologies in patients with COVID-19. This question could be approached by including patients with previous MR images, in whom existing pathology can essentially be modelled out. We acknowledge that some of the neurologic events included in our study may be explained by the healthy ageing process, whereby white matter hyperintensities are correlated with age.<sup>14</sup> Furthermore, IIT tractography data were used for visualization of abnormalities in the white matter. Because only a few labels (eg, corpus callosum) completely match the names of the tracts, the locations are only approximate. Hence, the findings regarding white matter changes, for example, white matter hyperintensities in the centrum semi-ovale, should be interpreted with caution.

### **CONCLUSIONS**

Patients with COVID-19 exhibit acute neuropathologic and cerebrovascular events. These events occur predominantly in white matter tracts such as the corticospinal tract and corpus callosum, as well in gray matter areas such as the pallidum, putamen, thalamus, and cerebellum. These aberrations likely contribute to altered thalamocortical connectivity and may disrupt the regulation of consciousness and arousal. The accumulation of these events in subcortical structures and the consequent disruption to distal regions may ultimately increase susceptibility to cognitive impairment and decline—having significant long-term cognitive ramifications. Given the prevalence and severity of these manifestations, clinicians should consider having a low threshold for investigating neurologic symptoms and monitoring potential long-term sequelae in patients with COVID-19.

## REFERENCES

1. Grant MC, Geoghegan L, Arbyn M, et al. **The prevalence of symptoms in 24,410 adults infected by the novel coronavirus (SARS-CoV-2; COVID-19): a systematic review and meta-analysis of 148 studies from 9 countries.** *PLoS One* 2020;15:e0234765 CrossRef Medline
2. Aghagholi G, Gallo Marin B, Katchur NJ, et al. **Neurological involvement in COVID-19 and potential mechanisms: a review.** *Neurocrit Care* 2020 Jul 13. [Epub ahead of print] CrossRef Medline
3. Ellul M, Benjamin L, Singh B, et al. **Neurological associations of COVID-19.** *Lancet Neurol* 2020;19:767–83 CrossRef Medline
4. Mao L, Jin H, Wang M, et al. **Neurologic manifestations of hospitalized patients with coronavirus disease 2019 in Wuhan, China.** *JAMA Neurol* 2020;77:683–90 CrossRef Medline
5. Varatharaj A, Thomas N, Ellul MA, et al. **CoroNerve Study Group. Neurological and neuropsychiatric complications of COVID-19 in 153 patients: a UK-wide surveillance study.** *Lancet Psychiatry* 2020;7:875–82 CrossRef Medline
6. Radmanesh A, Derman A, Lui YW, et al. **COVID-19-associated diffuse leukoencephalopathy and microhemorrhages.** *Radiology* 2020;297:E223–27 CrossRef Medline
7. Kremer S, Lersy F, de Seze J, et al. **SFNR-COVID Group. Brain MRI findings in severe COVID-19: a retrospective observational study.** *Radiology* 2020;297:E242–51 CrossRef Medline
8. WHO Coronavirus (COVID 19) Dashboard. <https://covid19.who.int/>. Published 2020. Accessed October 15, 2020
9. Katal S, Balakrishnan S, Gholamrezaezhad A. **Neuroimaging findings in COVID-19 and other coronavirus infections: a systematic review in 116 patients.** *J Neuroradiol* 2021;48:43–50 CrossRef Medline
10. Kremer S, Lersy F, Anheim M, et al. **Neurologic and neuroimaging findings in COVID-19 patients: a retrospective multicenter study.** *Neurology* 2020;95:e1868–82 CrossRef Medline
11. Hernandez-Fernandez F, Valencia HS, Barbella-Aponte RA, et al. **Cerebrovascular disease in patients with COVID-19: neuroimaging, histological and clinical description.** *Brain* 2020;143:3089–3103 CrossRef Medline
12. Politi LS, Salsano E, Grimaldi M. **Magnetic resonance imaging alteration of the brain in a patient with coronavirus disease 2019 (COVID-19) and anosmia.** *JAMA Neurol* 2020;77:1028–29 CrossRef Medline
13. Kandemirli SG, Dogan L, Sarikaya ZT, et al. **Brain MRI findings in patients in the intensive care unit with COVID-19 infection.** *Radiology* 2020;297:E232–35 CrossRef Medline
14. Debette S, Markus H. **The clinical importance of white matter hyperintensities on brain magnetic resonance imaging: systematic review and meta-analysis.** *BMJ* 2010;341:c3666 CrossRef Medline
15. Wardlaw JM, Valdés Hernández MC, Muñoz-Maniega S. **What are white matter hyperintensities made of? Relevance to vascular cognitive impairment.** *J Am Heart Assoc* 2015;4:e001140 CrossRef Medline
16. Fitsiori A, Pugin D, Thieffry C, et al. **Unusual microbleeds in brain MRI of Covid-19 patients.** *J Neuroimaging* 2020;30:593–97 CrossRef
17. Cannac O, Martinez-Almoyna L, Hraiech S. **Critical illness-associated cerebral microbleeds in COVID-19 acute respiratory distress syndrome.** *Neurology* 2020;95:498–99 CrossRef Medline
18. Scullen T, Keen J, Mathkour M, et al. **Coronavirus 2019 (COVID-19)-associated encephalopathies and cerebrovascular disease: the New Orleans experience.** *World Neurosurg* 2020;141:e437–46 CrossRef Medline
19. Poudel GR, Dominguez JF, Verhelst H, et al. **Network diffusion modeling predicts neurodegeneration in traumatic brain injury.** *Ann Clin Transl Neurol* 2020;7:270–79 CrossRef Medline
20. Poudel GR, Harding IH, Egan GF, et al. **Network spread determines severity of degeneration and disconnection in Huntington's disease.** *Hum Brain Mapp* 2019;40:4192–4201 CrossRef Medline
21. Payus AO, Lin CL, Noh MM, et al. **SARS-CoV-2 infection of the nervous system: a review of the literature on neurological involvement in novel coronavirus disease (COVID-19).** *Bosn J Basic Med Sci* 2020;20:283–92 CrossRef Medline
22. DosSantos MF, Devalle S, Aran V, et al. **Neuromechanisms of SARS-CoV-2: a review.** *Front Neuroanat* 2020;14:37 CrossRef Medline
23. Edlow BL, Takahashi E, Wu O, et al. **Neuroanatomic connectivity of the human ascending arousal system critical to consciousness and its disorders.** *J Neuropathol Exp Neurol* 2012;71:531–46 CrossRef Medline
24. Afshar H, Yassin Z, Kalantari S, et al. **Evolution and resolution of brain involvement associated with SARS-CoV2 infection: a close clinical-paraclinical follow up study of a case.** *Mult Scler Relat Disord* 2020;43:102216 CrossRef Medline
25. Ding J, Sigurðsson S, Jónsson PV, et al. **Space and location of cerebral microbleeds, cognitive decline, and dementia in the community.** *Neurology* 2017;88:2089–97 CrossRef Medline
26. Wang Y, Jiang Y, Suo C, et al. **Deep/mixed cerebral microbleeds are associated with cognitive dysfunction through thalamocortical connectivity disruption: the Taizhou Imaging Study.** *Neuroimage Clin* 2019;22:101749 CrossRef Medline
27. Bonardel C, Bonnerot M, Ludwig M, et al. **Bilateral posterior cerebral artery territory infarction in a SARS-Cov-2 infected patient: discussion about an unusual case.** *J Stroke Cerebrovasc Dis* 2020;29:105095 CrossRef Medline
28. Guillan M, Villaceros-Alvarez J, Bellido S, et al. **Unusual simultaneous cerebral infarcts in multiple arterial territories in a COVID-19 patient.** *Thromb Res* 2020;193:107–09 CrossRef Medline
29. Novi G, Rossi T, Pedemonte E, et al. **Acute disseminated encephalomyelitis after SARS-CoV-2 infection.** *Neurol Neuroimmunol Neuroinflamm* 2020;77:e797 CrossRef Medline
30. Netland J, Meyerholz DK, Moore S, et al. **Severe acute respiratory syndrome coronavirus infection causes neuronal death in the absence of encephalitis in mice transgenic for human ACE2.** *J Virol* 2008;82:7264–75 CrossRef Medline
31. Desforges M, Le Coupanec A, Dubeau P, et al. **Human coronaviruses and other respiratory viruses: underestimated opportunistic pathogens of the central nervous system?** *Viruses* 2019;12:14 CrossRef Medline
32. Bailey DM, Bärtsch P, Knauth M, et al. **Emerging concepts in acute mountain sickness and high-altitude cerebral edema: from the molecular to the morphological.** *Cell Mol Life Sci* 2009;66:3583–94 CrossRef Medline
33. Wang Y, Liu G, Hong D, et al. **White matter injury in ischemic stroke.** *Prog Neurobiol* 2016;141:45–60 CrossRef Medline
34. Martinez-Ramirez S, Greenberg SM, Viswanathan A. **Cerebral microbleeds: overview and implications in cognitive impairment.** *Alzheimers Res Ther* 2014;6:33 CrossRef Medline
35. Agarwal S, Jain R, Dogra S, et al. **Cerebral microbleeds and leukoencephalopathy in critically ill patients with COVID-19.** *Stroke* 2020;51:2649–55 CrossRef Medline
36. Lu Y, Li X, Geng D, et al. **Cerebral micro-structural changes in COVID-19 patients: an MRI-based 3-month follow-up study.** *EclinicalMedicine* 2020;25:100484 CrossRef Medline

# Cerebral Venous Thrombosis in COVID-19: A New York Metropolitan Cohort Study

F. Al-Mufti, K. Amuluru, R. Sahni, K. Bekelis, R. Karimi, J. Ogulnick, J. Cooper, P. Overby, R. Nuoman, A. Tiwari, K. Berekashvili, N. Dangayach, J. Liang, G. Gupta, P. Khandelwal, J.F. Dominguez, T. Sursal, H. Kamal, K. Dakay, B. Taylor, E. Gulko, M. El-Ghanem, S.A. Mayer, and C. Gandhi



## ABSTRACT

**BACKGROUND AND PURPOSE:** Severe Acute Respiratory Syndrome coronavirus 2 (SARS-CoV-2) infection is associated with hypercoagulability. We sought to evaluate the demographic and clinical characteristics of cerebral venous thrombosis among patients hospitalized for coronavirus disease 2019 (COVID-19) at 6 tertiary care centers in the New York City metropolitan area.

**MATERIALS AND METHODS:** We conducted a retrospective multicenter cohort study of 13,500 consecutive patients with COVID-19 who were hospitalized between March 1 and May 30, 2020.

**RESULTS:** Of 13,500 patients with COVID-19, twelve had imaging-proved cerebral venous thrombosis with an incidence of 8.8 per 10,000 during 3 months, which is considerably higher than the reported incidence of cerebral venous thrombosis in the general population of 5 per million annually. There was a male preponderance (8 men, 4 women) and an average age of 49 years (95% CI, 36–62 years; range, 17–95 years). Only 1 patient (8%) had a history of thromboembolic disease. Neurologic symptoms secondary to cerebral venous thrombosis occurred within 24 hours of the onset of the respiratory and constitutional symptoms in 58% of cases, and 75% had venous infarction, hemorrhage, or both on brain imaging. Management consisted of anticoagulation, endovascular thrombectomy, and surgical hematoma evacuation. The mortality rate was 25%.

**CONCLUSIONS:** Early evidence suggests a higher-than-expected frequency of cerebral venous thrombosis among patients hospitalized for COVID-19. Cerebral venous thrombosis should be included in the differential diagnosis of neurologic syndromes associated with SARS-CoV-2 infection.

**ABBREVIATIONS:** COVID-19 = coronavirus disease 2019; CVST = cerebral venous sinus thrombosis; CVT = cerebral venous thrombosis; SARS-CoV-2 = Severe Acute Respiratory Syndrome coronavirus 2

Coronavirus disease 2019 (COVID-19) is predominantly an acute respiratory disease caused by a single-stranded RNA virus known as severe acute respiratory syndrome coronavirus 2

(SARS-CoV-2), which originated in Wuhan, China.<sup>1</sup> The virus possesses a spike protein that binds to angiotensin-converting enzyme receptors, expressed on respiratory epithelium, facilitating entry into the host cell.<sup>2–4</sup> Susceptibility of organ systems to this virus may depend on the extent of expression of angiotensin-converting enzyme receptors on cell surfaces. These receptors are expressed on endothelial cells, pericytes, macrophages, glial cells, and cardiac myocytes.<sup>2–4</sup> Viral entry into these cells can lead to diverse manifestations such as acute respiratory distress syndrome, acute kidney injury, transaminitis, cardiac injury, and neurologic complications.<sup>3–6</sup>

Neurologic symptoms include headache, confusion, hypogeusia, hyposmia, myalgias, and delirium, while neurologic complications include acute ischemic stroke, encephalitis, and Guillain-Barre syndrome.<sup>3,6–8</sup> Postmortem data have revealed cerebral edema and partial neuronal degeneration in some patients as well.<sup>9</sup>

Early evidence suggests an increased risk of acute ischemic stroke in patients with COVID-19, which has been linked to a hypercoagulable state that can develop in some patients with

Received December 12, 2020; accepted after revision February 23, 2021.

From the Departments of Neurosurgery (F.A.-M., R.S., J.C., P.O., R.N., J.F.D., T.S., E.G., S.A.M., C.G.) and Neurology (F.A.-M., R.S., J.O., H.K., K.D., E.G., S.A.M., C.G.), Westchester Medical Center at New York Medical College, Valhalla, New York; Department of Neurosurgery (K. Bekelis), Catholic Health Services and Good Samaritan Hospital, West Islip, New York; Department of Neurosurgery (R.K.), Hackensack University Medical Center, Hackensack, New Jersey; Department of Neurosurgery (A.T., K. Berekashvili), New York University, New York, New York; Department of Neurosurgery (N.D., J.L.), Icahn School of Medicine at Mount Sinai, New York, New York; Department of Neurological Surgery (G.G., P.K., B.T.), Rutgers University, New Brunswick, New Jersey; Department of Neurology (M.E.-G.), University of Arizona-Tucson, Tucson, Arizona; and Department of Radiology (K.A.), Goodman Campbell Brain and Spine, Indianapolis, Indiana.

Please address correspondence to Fawaz Al-Mufti, MD, Westchester Medical Center at New York Medical College School of Medicine, 100 Woods Rd, Macy Pavilion 1331, Valhalla, NY 10599; e-mail: Fawaz.Al-Mufti@wmchealth.org

Indicates open access to non-subscribers at www.ajnr.org

Indicates article with online supplemental data.

<http://dx.doi.org/10.3174/ajnr.A7134>

COVID-19.<sup>10</sup> It remains unknown whether infection with the SARS-CoV-2 virus can also lead to cerebral venous thrombosis (CVT).

## MATERIALS AND METHODS

We conducted a retrospective multicenter cohort study of 13,500 consecutive patients with COVID-19 who were hospitalized between March 1 and May 30, 2020, in 6 academic, tertiary care facilities that are also designated as comprehensive stroke centers in the New York City metropolitan area. The number of hospital beds ranged from 500 to 1100. The patients were identified by conducting a retrospective review of prospectively maintained stroke data bases in each of these collaborating centers. The goal of our study was to characterize the frequency and demographic and clinical characteristics of hospitalized patients with SARS-CoV-2 who developed CVT. This study was approved by the individual enrolling hospitals' institutional review board centers.

### Clinical Management

Clinical management of CVT conformed to the American Heart Association/American Stroke Association and Society of Neurointerventional Surgery guidelines.<sup>11,12</sup> The diagnostic criteria and classification of COVID-19 severity was defined by the American Thoracic Society criteria.<sup>13</sup>

### Data Collection

Comprehensive data on each patient were collected, including demographics, medical history, baseline clinical status, imaging results and treatment, and complications during hospitalization. Clinical data for COVID-19 diagnosis and management were retrieved from the medical records as well, which included demographic features, medical history, clinical symptoms, laboratory findings, lung CT findings on admission, treatment regimens, and clinical outcomes. Prior prothrombotic risk was defined as any history of a clinically significant thromboembolic event.

### Clinical and Radiologic Variables

The diagnosis of the CVT was established by admission CT or MR venography. All included patients also underwent a noncontrast CT of the head. In patients with intracranial hemorrhages, hematoma volumes were measured using the ABC/2 technique modified for ellipsoid chronic subdural hematoma (cSDH).<sup>14</sup> The diagnosis was confirmed following adjudication by a cerebrovascular specialist and a neuroradiologist.

## RESULTS

During the study period, of 13,500 patients with COVID-19 admitted to 6 different New York metropolitan tertiary care centers, 12 patients (8.8:10,000) had imaging-proved CVT. The demographic and clinical characteristics of our patients are summarized in the Online Supplemental Data.

The mean age in our cohort was 48 years (95% CI, 36–62 years) (interquartile range, 31–63 years) with 25% of patients younger than 25 years of age. Men accounted for 66% (8/12) of cases. 50% of the patients (6/12) were White. Prior prothrombotic risk was identified in only 17% (2/12) of patients (breast cancer and deep vein thrombosis). However, traditional cardiovascular risk factors

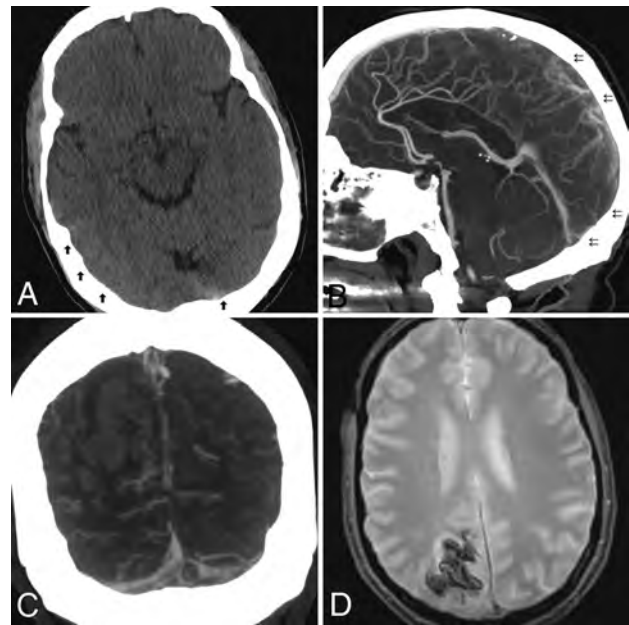


**FIG 1.** A, NCCT shows hyperdense thrombus in the region of the torcula and subtle cortical hyperdensity along the right temporo-occipital region (arrows). Sagittal (B) and coronal MIP (C) reformatted images of CTA show multiple filling defects along the posterior superior sagittal sinus (double arrows), torcula, and right transverse sinus. Note a parenchymal hematoma in the right occipital lobe. D, MR imaging of the brain; gradient recalled-echo sequence shows thrombus in the sagittal sinus and associated parenchymal hematoma.

(hypertension, hyperlipidemia, diabetes, smoking) were identified in 58% (7/12) of patients.

Neurologic symptoms secondary to CVT occurred within 24 hours of the onset of the respiratory and constitutional symptoms (fever, cough, dyspnea, myalgia, and fatigue) in 58% (7/12) of patients. Of the remaining patients, 25% (3/12) developed CVT symptoms between 24 and 72 hours from symptom onset, and 16% (3/12) manifested CVT between 3 and 7 days from symptom onset.

Headache was the most common clinical neurologic symptom noted in 85% (10/12) of patients. Both seizures and hemiparesis occurred in 42% of patients. Cortical signs such as aphasia, neglect, or hemianopia were noted in only 25% of patients. Fever or cough was the most common symptom attributed to the COVID-19 infection and was noted in 75% (9/12) of patients.

Neuroimaging demonstrated focal brain injury in 75% of patients. Isolated hemorrhage ( $n = 4$ ), venous infarction ( $n = 2$ ), or venous infarction with hemorrhagic changes ( $n = 3$ ) was about equally represented. Vessel imaging identified dural venous sinus thrombosis in 83% (10/12) of patients and isolated cortical vein thrombosis in 16% (2/12) of patients. Multiple dural sinuses were involved in 41% (5/12) of patients (Fig 1).

Anticoagulation was administered to 83% (10/12) of patients. Two patients were treated with endovascular thrombolysis (Fig 2). Hemicraniectomy was also performed in 2 patients. Of the 2 patients who did not receive treatment for their CVT, one patient died; and the second patient, who had a cortical vein as well as a nonocclusive superior sagittal sinus thrombosis, refused treatment.

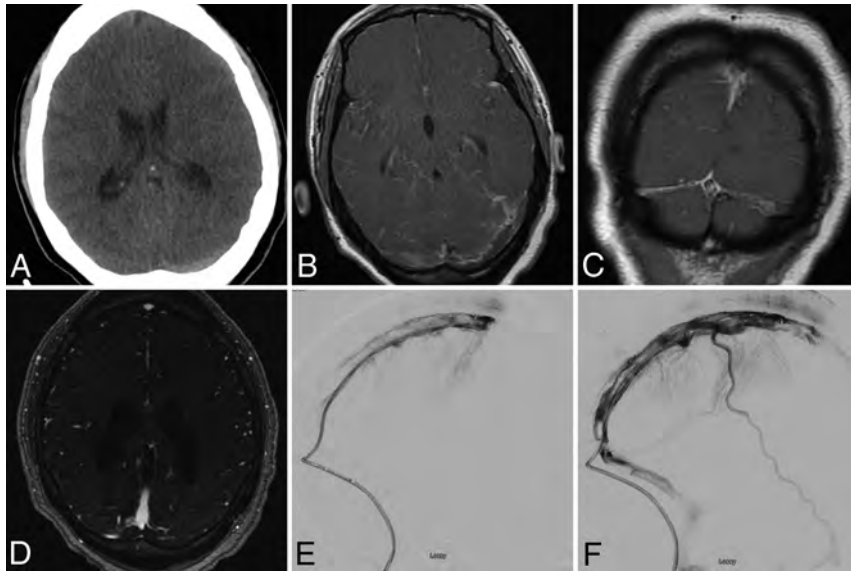


**FIG 2.** A, NCCT shows a subtle hyperdense thrombus in left transverse sinus. MR imaging of the brain: T1 postgadolinium images in axial (B) and sagittal (C) projections and MRV (D) with gadolinium showing sinus thrombosis of the torcula with extension to the bilateral, left-greater-than-right, transverse sinuses. E, Endovascular microcatheter venogram shows progression of thrombus throughout superior sagittal sinus. F, A postinterventional venogram shows improved patency after mechanical thrombectomy.

Although all patients met the criteria for admission to the intensive care unit, mechanical ventilation was required in 41% of patients (5/12), and the median duration of ventilation was 15 days. One patient required a tracheostomy, while the remaining patients were successfully extubated. Acute renal failure was noted in 33% (4/12), acute liver failure occurred in 25% (3/12), and 8% (1/12) developed superimposed sepsis. One patient developed concomitant deep vein thrombosis. Hydroxychloroquine with or without azithromycin was administered to half (6/12) of the patients. No patients received steroids or remdesivir. Three patients (25%) were discharged home. Half (6/12) of patients were transferred to a rehabilitation facility (5 to acute rehabilitation and 1 patient to subacute rehabilitation). The mortality rate in our cohort was 25% (3/12).

## DISCUSSION

Our findings on CVT in the setting of COVID-19, pooled from 6 tertiary care centers in the New York metropolitan area, demonstrate the predominance of individuals younger than 25 years of age in 25% of cases, with a male preponderance. Only 1 patient in our cohort was African American, despite the fact that Black individuals are more severely affected by severe COVID-19. In terms of risk factors, traditional thrombogenic risk factors were identified in only 1 of 12 patients, and 7 of 12 had traditional cardiovascular risk factors. Most patients (10 of 12) presented with headache, and half presented with seizures or unilateral weakness. This presentation is in addition to the fever and cough attributed to COVID-19 infection in 9 of 12 patients, with 5 of 12 requiring mechanical ventilation. Neuroimaging was significant for brain injury, including hemorrhage, venous infarction, venous infarction with hemorrhagic

changes, dural venous sinus thrombosis, and isolated cortical vein thrombosis in most (9 of 12) patients. Ten of 12 patients were treated with anticoagulation, 2 with endovascular thrombolysis, 2 with hemicraniectomy, and 6 with hydroxychloroquine with or without azithromycin. Of the 2 patients who did not receive treatment for their CVT, one died; the other patient, who had a cortical vein as well as a nonocclusive superior sagittal sinus thrombosis, refused treatment.

We collected our cases during the height of the COVID-19 pandemic (March through May 2020). During this 3-month period, CVT was diagnosed in 12 of 13,500 hospitalized patients with COVID-19, for a frequency of 0.088 per million. By contrast, the reported incidence of CVT in the general population is 5 per million annually.<sup>11</sup> The higher-than-expected rate of CVT among hospitalized patients with COVID-19, along with the well-established hypercoagulability that is known to occur with SARS-CoV-2 infection, supports a causal effect.

The literature demonstrates that 36%–59% of patients with COVID-19 have neurologic complications.<sup>1,2</sup> Ischemic stroke incidence is estimated to be in the range of 5%, with a recent study demonstrating an unusual presentation of young patients with COVID-19 with arterial stroke.<sup>2,5</sup> By contrast, cerebral venous sinus thrombosis (CVST) associated with COVID-19 is an exceedingly rare occurrence, with only 57 reports available at the time this writing (Online Supplemental Data).<sup>15–43</sup> The average age of these previously reported patients is 53.5 years (range, 23–72 years), which is in agreement with our findings. Although we report a male preponderance, these 57 cases demonstrate an equal distribution of male and female patients. A direct comparison between our patients and those reported in the Online Supplemental Data is challenging in light of the substantial heterogeneity of demographic and clinical characteristics of patients with COVID-19 with CVST. Most previously reported patients had clinical CVST in a delayed fashion from initial symptoms attributable to COVID-19, whereas more than half of our patients presented with CVT concomitant with respiratory and constitutional symptoms. Because headache can be a common symptom of viral illnesses including COVID-19, diagnosis can often be elusive or delayed until symptoms worsen.<sup>7</sup> Patients with either no or minimal systemic and respiratory symptoms may first come to medical attention when they present with seizures or other symptoms attributed to the venous sinus thrombosis and are ultimately found to have COVID-19 infection.<sup>8</sup>

While treatment guidelines for patients with COVID-19-related strokes are emerging, it is unclear whether any intervention can prevent these outcomes.<sup>43</sup> Although anticoagulation is

being used prophylactically at many centers to prevent the thrombotic complications related to COVID-19, its benefit in stroke prevention remains to be seen. Two of our patients were on anticoagulation when their strokes were detected, and in one of those patients, the anticoagulation may have contributed to hemorrhagic conversion.

There have been several proposed mechanisms of neurologic manifestations following infection with coronaviruses.<sup>44</sup> The virus may initially invade endothelial cells through angiotensin-converting enzyme receptors.<sup>45</sup> The presence of viral elements within endothelial cells and an accumulation of inflammatory cells, with evidence of inflammatory cell death, have been demonstrated in patients with COVID-19.<sup>44</sup> Inflammation of endothelial cells may cause cellular dysfunction, leading to either disruption of stable atherosclerotic plaque or circulatory changes in vascular beds, through a thrombogenic microvascular environment, manifesting as stroke, pulmonary embolism, or myocardial infarction. Critical SARS-CoV-2 infection is almost always accompanied by a significant proinflammatory response, which can activate the coagulation cascade through various pathways, leading to a profound prothrombotic state. This is consistent with 5 of 12 patients in our cohort having elevated D-dimer levels.

SARS-CoV-2 infection has also been linked to alternative and lectin complement cascade activation.<sup>46</sup> These complement complexes can deposit on endothelial cells, leading to cellular damage, and can initiate a thrombotic microangiopathy.<sup>47</sup> The presence of antiphospholipid antibodies and lupus antibodies has also been described in patients with COVID-19, though their clinical significance remains unknown.<sup>48</sup>

Several caveats and weaknesses of this study deserve mention. Complete screening for pre-existing hypercoagulable states was not performed in all patients. However, the temporal association of CVT with respiratory and constitutional symptoms of COVID-19 in more than half of our patients suggests a causal effect. It is possible that some patients with CVT due to COVID-19 were not included in this series because their symptoms or signs were not properly diagnosed or charted. We were unable to compare baseline demographic and disease-related features between the CVT patient population and the main cohort of patients with COVID-19; this comparison might have allowed us to confirm male sex and identify other risk factors for CVT. Similarly, we also were unable to provide an estimate of the frequency of CVT among patients with COVID-19 who underwent brain imaging. Because all our patients were sick enough to be admitted to the hospital, multiple confounding factors could have contributed to our observed complications and outcomes. Additionally, because our sample of patients with confirmed CVT is limited to patients with COVID-19 who had neurologic issues, we are unable to assess the frequency of CVT in the overall COVID-19 cohort. It is also difficult to compare the incidence of CVT in the COVID-19 cohort with that of the general population due to differences in demographics between our cohort and the general population. Finally, the small number of included patients and restriction of our study population to the New York metropolitan area may limit the generalizability of our findings to other regions throughout the world. Larger analyses of this

complication, such as a pooled meta-analysis, are warranted in the future, especially when more data become available.

## CONCLUSIONS

SARS-CoV-2 has already infected millions of patients worldwide. Dreaded thrombotic complications, including CVST, have been reported in patients with SARS-CoV-2. As more reports of COVID-related CVST become available, it is hoped that our understanding of which patients are most at risk and the ideal treatment and prevention strategies can be elucidated.

Disclosures: Priyank Khandelwal—UNRELATED: Grants/Grants Pending: Feasibility of the Infinity Catheter for transradial neurology procedures; Payment for Lectures Including Service on Speakers Bureaus: American College of Cardiology meeting.

## REFERENCES

1. Wang HY, Li XL, Yan ZR, et al. **Potential neurological symptoms of COVID-19.** *Ther Adv Neurol Disord* 2020;13:175628642091783 CrossRef Medline
2. Mao L, Jin H, Wang M, et al. **Neurologic manifestations of hospitalized patients with coronavirus disease 2019 in Wuhan, China.** *JAMA Neurol* 2020;77:683–90 CrossRef Medline
3. Zhou F, Yu T, Du R, et al. **Clinical course and risk factors for mortality of adult inpatients with Covid-19 in Wuhan, China: a retrospective cohort study.** *Lancet* 2020;395:1054–62 CrossRef Medline
4. Lu R, Zhao X, Li J, et al. **Genomic characterisation and epidemiology of 2019 novel coronavirus: implications for virus origins and receptor binding.** *Lancet* 2020;395:565–74 CrossRef Medline
5. Mankad K, Perry MD, Mirsky DM, et al. **COVID-19: a primer for neuroradiologists.** *Neuroradiology* 2020;62:647–48 CrossRef Medline
6. Baig AM, Khaleeq A, Ali U, et al. **Evidence of the COVID-19 virus targeting the CNS: tissue distribution, host-virus interaction, and proposed neurotropic mechanisms.** *ACS Chem Neurosci* 2020;11:995–98 CrossRef Medline
7. Ruan Q, Yang K, Wang W, et al. **Clinical predictors of mortality due to COVID-19 based on an analysis of data of 150 patients from Wuhan, China.** *Intensive Care Med* 2020;46:846–48 CrossRef Medline
8. Li YC, Bai WZ, Hashikawa T. **The neuroinvasive potential of SARS-CoV2 may play a role in the respiratory failure of COVID-19 patients.** *J Med Virol* 2020;92:552–55 CrossRef Medline
9. Xu Z, Shi L, Wang Y, et al. **Pathological findings of COVID-19 associated with acute respiratory distress syndrome.** *Lancet Respir Med* 2020;8:420–22 CrossRef Medline
10. Oxley TJ, Mocco J, Majidi S, et al. **Large-vessel stroke as a presenting feature of Covid-19 in the young.** *N Engl J Med* 2020;382:e60 CrossRef Medline
11. Saposnik G, Barinagarrementeria F, Brown RD Jr, et al. American Heart Association Stroke Council and the Council on Epidemiology and Prevention, **Diagnosis and management of cerebral venous sinus thrombosis. a statement for healthcare professionals from the American Heart Association/American Stroke Association.** *Stroke* 2011;42:1158–92 CrossRef Medline
12. Lee SK, Mokin M, Hetts SW, et al. Society of NeuroInterventional Surgery. **Current endovascular strategies for cerebral venous thrombosis: report of the SNIS Standards and Guidelines Committee.** *J Neurointerv Surg* 2018;10:803–10 CrossRef Medline
13. Jamil S, Mark N, Carlos G, et al. **Diagnosis and management of COVID-19 disease.** *Am J Respir Crit Care Med* 2020;201:P19–20 CrossRef Medline
14. Kothari RU, Brott T, Broderick JP, et al. **The ABCs of measuring intracerebral hemorrhage volumes.** *Stroke* 1996;27:1304–05 CrossRef Medline

15. Dahl Cruz F, Guevara Dalrymple N, López Hernández N. **Cerebral venous thrombosis and SARS-CoV-2 infection** [in Spanish]. *Rev Neurol* 2020;70:391 CrossRef Medline
16. Hughes C, Nichols T, Pike M, et al. **Cerebral venous sinus thrombosis as a presentation of COVID-19**. *Eur J Case Rep Intern Med* 2020;7:001691 CrossRef Medline
17. Garaci F, Di Giuliano F, Picchi E, et al. **Venous cerebral thrombosis in COVID-19 patient**. *J Neurol Sci* 2020;414:116871 CrossRef Medline
18. Poillon G, Obadia M, Perrin M, et al. **Cerebral venous thrombosis associated with Covid-19 infection: causality or coincidence?** *J Neuroradiol* 2021;48:121–24 CrossRef Medline
19. Hemasian H, Ansari B. **First case of Covid-19 presented with cerebral venous thrombosis: a rare and dreaded case**. *Rev Neurol (Paris)* 2020;176:521–23 CrossRef Medline
20. Klein D, Libman R, Kirsch C, et al. **Cerebral venous thrombosis: a typical presentation of COVID-19 in the young**. *J Stroke Cerebrovasc Dis* 2020;29:104989 CrossRef Medline
21. Cavalcanti DD, Raz E, Shapiro M, et al. **Cerebral venous thrombosis associated with COVID-19**. *AJNR Am J Neuroradiol* 2020;41:1–7 CrossRef Medline
22. Li Y, Li M, Wang M, et al. **Acute cerebrovascular disease following COVID-19: a single center retrospective, observational study**. *Stroke Vasc Neurol* 2020;5:279–84 CrossRef Medline
23. Baudar C, Duprez T, Kassab A, et al. **COVID-19 as triggering co-factor for cortical cerebral venous thrombosis?** *J Neuroradiol* 2021;48:65–67 CrossRef Medline
24. Bolaji P, Kukoyi B, Ahmad N, et al. **Extensive cerebral venous sinus thrombosis: a potential complication in a patient with COVID-19 disease**. *BMJ Case Rep* 2020;13:e236820 CrossRef Medline
25. Chougar L, Mathon B, Weiss N, et al. **Atypical deep cerebral vein thrombosis with hemorrhagic venous infarction in a patient positive for COVID-19**. *AJNR Am J Neuroradiol* 2020;41:1377–79 CrossRef Medline
26. Chow LC, Chew LP, Leong TS, et al. **Thrombosis and bleeding as presentation of COVID-19 infection with polycythemia vera: a case report**. *SN Compr Clin Med* 2020 Oct 4. [Epub ahead of print] CrossRef Medline
27. Haroon KH, Muhammad A, Hussain S, et al. **COVID-19 related cerebrovascular thromboembolic complications in three young patients**. *Case Rep Neurol* 2020;12:321–28 CrossRef Medline
28. Hoelscher C, Sweid A, Ghosh R, et al. **Cerebral deep venous thrombosis and COVID-19: case report**. *J Neurosurg* 2020 Sep 4. [Epub ahead of print] CrossRef Medline
29. Kananah MF, Thomas T, Sharma K, et al. **Arterial and venous strokes in the setting of COVID-19**. *J Clin Neurosci* 2020;79:60–66 CrossRef Medline
30. Keaney K, Mumtaz T. **Cerebral venous thrombosis in patients with severe COVID-19 infection in intensive care**. *Br J Hosp Med (Lond)* 2020;81:1–4 CrossRef Medline
31. Koh JS, De Silva DA, Quek AM, et al. **Neurology of COVID-19 in Singapore**. *J Neurol Sci* 2020;418:117118 CrossRef Medline
32. Malentacchi M, Gned D, Angelino V, et al. **Concomitant brain arterial and venous thrombosis in a COVID-19 patient**. *Eur J Neurol* 2020;27:e38–39 CrossRef Medline
33. Mowla A, Shakibajahromi B, Shahjouei S, et al. **Cerebral venous sinus thrombosis associated with SARS-CoV-2; a multinational case series**. *J Neurol Sci* 2020;419:117183 CrossRef Medline
34. Rifino N, Censori B, Agazzi E, et al. **Neurologic manifestations in 1760 COVID-19 patients admitted to Papa Giovanni XXIII Hospital, Bergamo, Italy**. *J Neurol* 2020 Oct 7. [Epub ahead of print] CrossRef Medline
35. Rouyer O, Pierre-Paul IN, Balde A, et al. **High prevalence of deep venous thrombosis in non-severe COVID-19 patients hospitalized for a neurovascular disease**. *Cerebrovasc Dis Extra* 2020 Dec 7. [Epub ahead of print] CrossRef Medline
36. Roy-Gash F, Marine DM, Jean-Michel D, et al. **COVID-19-associated acute cerebral venous thrombosis: clinical, CT, MRI and EEG features**. *Crit Care* 2020;24:419 CrossRef Medline
37. Shahjouei S, Naderi S, Li J, et al. **Risk of stroke in hospitalized SARS-CoV-2 infected patients: a multinational study**. *EBioMedicine* 2020;59:10293 CrossRef Medline
38. Siegler JE, Cardona P, Arenillas JF, et al. **Cerebrovascular events and outcomes in hospitalized patients with COVID-19: the SVIN COVID-19 Multinational Registry**. *Int J Stroke* 2020 Sep 30. [Epub ahead of print] CrossRef Medline
39. Sugiyama Y, Tsuchiya T, Tanaka R, et al. **Cerebral venous thrombosis in COVID-19-associated coagulopathy: a case report**. *J Clin Neurosci* 2020;79:30–02 CrossRef Medline
40. Thompson A, Morgan C, Smith P, et al. **Cerebral venous sinus thrombosis associated with COVID-19**. *Pract Neurol* 2020 Oct 8. [Epub ahead of print] CrossRef Medline
41. Trimaille A, Curtiaud A, Marchandot B, et al. **Venous thromboembolism in non-critically ill patients with COVID-19 infection**. *Thromb Res* 2020;193:166–69 CrossRef Medline
42. Tu TM, Goh C, Tan YK, et al. **Cerebral venous thrombosis in patients with COVID-19 infection: a case series and systematic review**. *J Stroke Cerebrovasc Dis* 2020;29:105379 CrossRef Medline
43. Qureshi AI, Abd-Allah F, Alsenani F, et al. **Management of acute ischemic stroke in patients with COVID-19 infection: report of an international panel**. *Int J Stroke* 2020;15:540–54 CrossRef Medline
44. Wu Y, Xu X, Chen Z, et al. **Nervous system involvement after infection with COVID-19 and other coronaviruses**. *Brain Behav Immun* 2020;87:18–22 CrossRef Medline
45. Chen L, Li X, Chen M, et al. **The ACE2 expression in human heart indicates new potential mechanism of heart injury among patients infected with SARS-CoV-2**. *Cardiovasc Res* 2020;116:1097–1100 CrossRef Medline
46. Magro C, Mulvey JJ, Berlin D, et al. **Complement associated microvascular injury and thrombosis in the pathogenesis of severe COVID-19 infection: a report of five cases**. *Transl Res* 2020;220:1–13 CrossRef Medline
47. Noris M, Galbusera M, Gastoldi S, et al. **Dynamics of complement activation in aHUS and how to monitor eculizumab therapy**. *Blood* 2014;124:1715–26 CrossRef Medline
48. Zhang Y, Xiao M, Zhang S, et al. **Coagulopathy and antiphospholipid antibodies in patients with Covid-19**. *N Engl J Med* 2020;382:e38 CrossRef Medline

# Variability of Normal Pressure Hydrocephalus Imaging Biomarkers with Respect to Section Plane Angulation: How Wrong a Radiologist Can Be?

P. Ryska, O. Slezak, A. Eklund, J. Salzer, J. Malm, and J. Zizka



## ABSTRACT

**BACKGROUND AND PURPOSE:** Systematic analysis of angulation-related variability of idiopathic normal pressure hydrocephalus imaging biomarkers has not been published yet. Our aim was to evaluate the variability of these radiologic biomarkers with respect to imaging plane angulation.

**MATERIALS AND METHODS:** Eighty subjects (35 with clinically confirmed idiopathic normal pressure hydrocephalus and 45 age- and sex-matched healthy controls) were prospectively enrolled in a 3T brain MR imaging study. Two independent readers assessed 12 radiologic idiopathic normal pressure hydrocephalus biomarkers on sections aligned parallel or perpendicular to the bicallosal, bicommissural, hypophysis-fastigium, and brain stem vertical lines, respectively.

**RESULTS:** Disproportionately enlarged subarachnoid space hydrocephalus, simplified callosal angle, frontal horn diameter, z-Evans Index, and cella media vertical width did not show significant systematic differences in any of 6 section plane combinations studied. The remaining 7 biomarkers (including the Evans Index and callosal angle) showed significant differences in up to 4 of 6 mutually compared section plane combinations. The values obtained from sections aligned with the brain stem vertical line (parallel to the posterior brain stem margin) showed the most deviating results from other section angulations.

**CONCLUSIONS:** Seven of 12 idiopathic normal pressure hydrocephalus biomarkers including the frequently used Evans Index and callosal angle showed statistically significant deviations when measured on sections whose angulations differed or did not comply with the proper section definition published in the original literature. Strict adherence to the methodology of idiopathic normal pressure hydrocephalus biomarker assessment is, therefore, essential to avoid an incorrect diagnosis. Increased radiologic and clinical attention should be paid to the biomarkers showing low angulation-related variability yet high specificity for idiopathic normal pressure hydrocephalus-related morphologic changes such as the z-Evans Index, frontal horn diameter, or disproportionately enlarged subarachnoid space hydrocephalus.

**ABBREVIATIONS:** BVR = brain-to-ventricle ratio; CA = callosal angle; CMW = cella media vertical width; CTR = cella media-to-temporal horn ratio; DESH = disproportionately enlarged subarachnoid space hydrocephalus; EI = Evans Index; FHD = frontal horn diameter; FHVD = frontal horn vertical diameter; HC = healthy control; Hy-Fa = hypophysis-fastigium; iNPH = idiopathic normal pressure hydrocephalus; ISD = inner skull diameter; MSID = maximum supratentorial intracranial diameter; PBSM = posterior brain stem margin; simpCA = simplified callosal angle; SVW = supraventricular brain vertical width; THW = temporal horn vertical width; ZEI = z-Evans Index

The prevalence of idiopathic normal pressure hydrocephalus (iNPH) may be as high as 0.5% in the population older than 65 years of age, and iNPH has emerged as a significant health issue for the aging population in developed countries. The

symptoms include gait disturbance, memory impairment, and urinary incontinence. Underdiagnosed iNPH entails missed opportunities for successful ventricular shunt treatment.<sup>1,2</sup>

Numerous linear, angular, and volumetric measurements; relative indexes; CSF flow studies; as well as visual semiquantitative or qualitative parameters have been proposed as radiologic biomarkers of iNPH.<sup>3-15</sup> Most of the iNPH imaging biomarkers have originally been defined by their authors using arbitrary or proprietary settings in terms of defining section planes and/or measurement techniques, which, in many cases, do not comply with the routines of daily radiologic practice. This issue particularly applies to the use of the bicommissural plane, which is rarely used in routine practice because the anatomic landmarks are subtle and, therefore, difficult to apply.

Received July 2, 2020; accepted after revision January 13, 2021.

From the Department of Diagnostic Radiology (P.R., O.S.), University Hospital Hradec Kralove, Hradec Kralove, Czech Republic; Department of Diagnostic Radiology (O.S.), Charles University, Faculty of Medicine, Hradec Kralove, Czech Republic; and Departments of Radiation Sciences (A.E.), Pharmacology and Clinical Neuroscience (J.S., J.M.), Section of Neurology, and Imaging and Functional Medicine (J.Z.), University Hospital of Umeå, Umeå, Sweden.

Please address correspondence to Jan Zizka, MD, University Hospital of Umeå, Umeå, Sweden; e-mail: jan.zizka@regionvasterbotten.se

Indicates open access to non-subscribers at www.ajnr.org

<http://dx.doi.org/10.3174/ajnr.A7095>

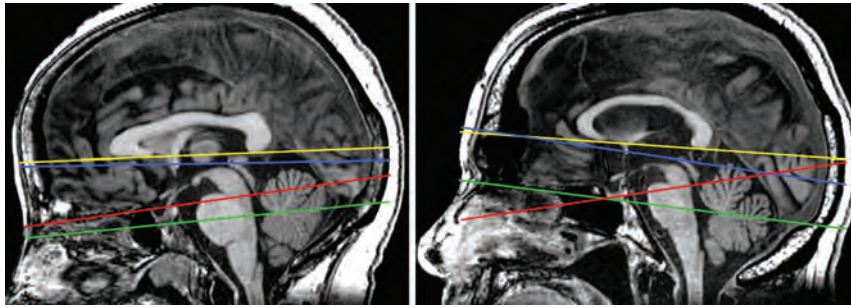


**FIG 1.** Definition of standard transverse imaging planes: bicallosal (yellow), bicommissural (blue), Hy-Fa (green), and perpendicular to the posterior brain stem margin (red), shown on midsagittal MR images of 2 different individuals. Note the differences in their mutual alignment between the 2 subjects.

Various institutions have been using different definitions of standard imaging planes for decades. For example, a “standard” transverse CT or MR imaging plane can be angulated according to at least 5 different section definitions. Such interinstitutional differences may lead to different outcomes of iNPH imaging studies.

The frequently used Evans Index (EI, originally defined on pneumoencephalograms in 1942) was not initially intended for use with cross-sectional imaging.<sup>16</sup> The Evans Index was secondarily adopted for transverse CT sections aligned parallel to orbitomeatal line in 1976 and subsequently transferred into MR imaging, without a particular respect for the transverse plane definition.<sup>17</sup> Even recently published studies often do not precisely define anatomic landmarks used for angulation of transverse or coronal sections in the methodology section. Such methodologic inconsistencies might have contributed to widely differing diagnostic performances of iNPH biomarkers reported by various authors.<sup>3-5,8-12</sup>

A systematic evaluation of the variability of iNPH biomarkers related to imaging plane definition (bicallosal, bicommissural, hypophysis-fastigium [Hy-Fa], brain stem vertical line, and so forth) has not been published so far. The aim of this study was to assess the variability of individual iNPH cross-sectional imaging biomarkers with respect to different imaging plane angulations.

## MATERIALS AND METHODS

### Study Population

Eighty subjects were prospectively enrolled in the study: 35 subjects with clinically confirmed iNPH (25 men and 10 women; mean age, 74.0 [SD, 7.2] years) and 45 sex- and age-matched healthy controls (HCs: 32 men and 13 women; mean age, 72.6 [SD, 5.7] years).

Patient history, neurologic objective findings, and brain MR imaging were used for diagnosing iNPH in accordance with the international iNPH guidelines.<sup>18</sup> Six subjects with iNPH (17%) showed signs of dementia (Mini-Mental State Examination scores, 20–24 points), and 15 subjects (43%) had mild cognitive impairment (Mini-Mental State Examination scores, 24–27 points). All patients except one were able to walk 10 m with or without an assistive device. In addition, all patients underwent a CSF dynamic investigation (including estimation of CSF outflow resistance) and a short-term tap test, which had positive findings in 19 patients (54%). Eighty-nine percent of patients (31/35) were

categorized as having probable iNPH, and 11% (4/35), as having possible iNPH. Subjects with significant neurologic comorbidities or a known etiology of NPH (secondary NPH) were not included in the study.

The healthy control group comprised sex- and age-matched volunteers primarily recruited through an advertisement in a local newspaper who showed no signs of neurologic, psychiatric, or advanced atherosclerotic disease on a subsequent clinical examination performed by a neurologist. We applied the following exclusion

criteria: medications influencing the central nervous system or blood coagulation; electrocardiogram evidence of arrhythmia, left ventricular hypertrophy, or myocardial infarction; a history and/or clinical or radiologic signs of neurologic disease (including ventriculomegaly, stroke, tremor, ataxia, walking/balance difficulties); significant cardiovascular disease; diabetes mellitus;  $\geq 2$  ancillary vascular risk factor (smoking, hypertension, hyperlipidemia); ongoing infectious disease; known serious disease that may reduce life expectancy; and contraindications to MR imaging. Cognition, balance, and gait were tested using the Mini-Mental State Examination ( $>27$  points required) and the one-legged balancing test (30 seconds), tandem stand (10 seconds), Timed Up-and-Go test, and 300-m walk test. Of 59 screened subjects, 50 passed the clinical evaluation and underwent brain MR imaging. Five subjects were subsequently excluded from participating in the study due to MR imaging findings of cortical infarctions ( $n = 3$ ), cerebellar tonsillar herniation ( $n = 1$ ), and subdural hygroma ( $n = 1$ ). Thus, the HC group consisted of 45 individuals.

The study was approved by the Umeå University institutional review board. Signed informed consent was obtained from all participants of the study.

### MR Image Acquisition and Analysis

All subjects were examined on a 3T MR imaging system by means of a 3D T1-weighted spoiled gradient-echo imaging sequence with a voxel size of 0.49 mm<sup>3</sup>. Multiplanar reformats parallel and perpendicular to the bicallosal, bicommissural, Hy-Fa, and brain stem vertical line were obtained.

Anonymized MR imaging data were independently evaluated by 2 observers: a senior radiology resident with 5 years of radiology training and a neuroradiologist with 21 years of clinical experience. Both readers were blinded to clinical data.

### Definition of Anatomic Planes on Midsagittal Sections

Inferior margins of the rostrum and splenium of the corpus callosum were used as anatomic landmarks for defining the bicallosal plane (Fig 1). The anterior and posterior commissure defined the bicommissural plane. The inferior pituitary gland margin and the apex of the fourth ventricle defined the hypophysis-fastigium (Hy-Fa) plane. The brain stem vertical line (ie, fourth ventricle floor plane) was parallel to the posterior brain stem margin (PBSM).

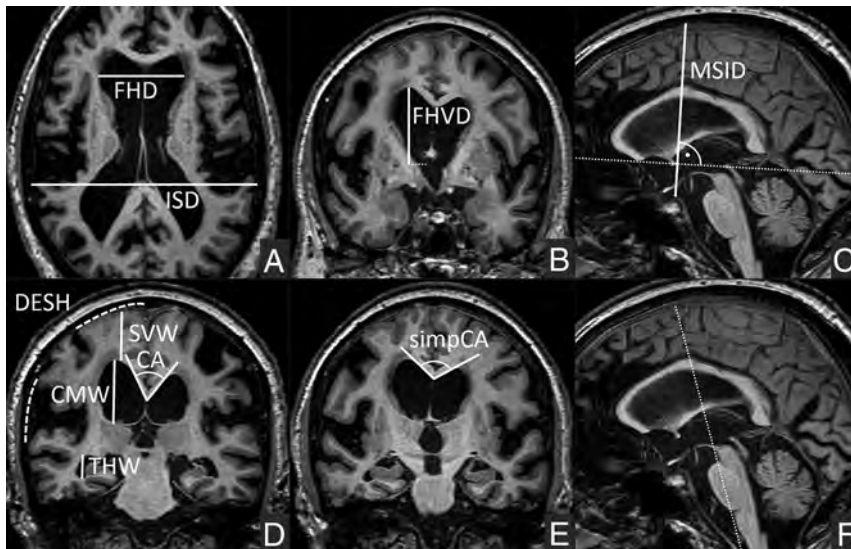


**FIG 2.** Graphic representation of biomarker measurements. A, Maximum frontal horn diameter (FHD) and inner skull diameter (ISD). B, Frontal horn vertical diameter (FHVD) measured to the midpoint of the foramen of Monro. C, Maximum supratentorial intracranial diameter (MSID) measured perpendicular to the bicommissural line (dotted line). D, Maximum vertical widths of the supraventricular brain (SVW), cella media (CMW), and temporal horn (THW), respectively; callosal angle (CA); and DESH (curved dashed lines, rated as severe, grade 2 in this case) measured on the coronal section passing through the posterior commissure. E, Simplified callosal angle (simpCA) measured at the corpus callosum midpoint on the coronal section paralleling the PBSM (F, dotted line). Note that for each biomarker, 4 measurement values have been obtained from 4 different sections (as defined in Fig 1). To keep the illustration simple, we show measurements on sections aligned parallel and perpendicular to the bicommissural line, except for the simpCA (E and F). For details, see the Materials and Methods section.

### iNPH Biomarker Definitions

Ten previously published radiologic measures as well as 4 calculated indexes<sup>5-7,12,16-21</sup> were individually evaluated on transverse/coronal imaging sections of 4 different angulations (bicallosal, bicommissural, Hy-Fa, and PBSM) (Fig 2): The frontal horn diameter (FHD) was defined by the maximum distance between the lateral margins of the frontal ventricular horns on the respective transverse sections.<sup>16,17</sup> The inner skull diameter (ISD) was defined by the maximum lateral-to-lateral distance between the inner laminae of the parietal bones on the same transverse sections that were used for FHD measurements.<sup>16,17</sup> The frontal horn vertical diameter (FHVD) was defined by the maximum z-axis (vertical) diameter of the frontal horns measured at the level of the foramen of Monro, ie, the vertical distance between the ceiling of the lateral ventricle and the midpoint of the foramen of Monro on 4 coronal sections.<sup>7</sup> The maximum supratentorial intracranial diameter (MSID) was measured bone-to-bone on the midsagittal section; the measurement line was drawn parallel to the coronal plane used for FHVD measurement.<sup>7</sup>

The maximum vertical width of the supraventricular brain (SVW; width of brain tissue superior to the ventricle), the cella media of the lateral ventricle (CMW), and the temporal horn (THW) were measured on 4 coronal sections passing through the posterior commissure (modified from Yamada et al<sup>12</sup>). Depending on the degree of ventricular dilation, the THW was measured either superior to the hippocampus only (if the hippocampus completely covered the floor of the temporal horn) or superior + lateral + inferior to the hippocampus (if the dilated temporal horn extended below the level of the hippocampus).

Disproportionately enlarged subarachnoid space hydrocephalus (DESH) referred to visual semiquantitative assessment of the disproportion between enlarged volumes of subarachnoid spaces at the Sylvian fissure and decreased volumes at the superior parasagittal convexity on the respective coronal sections passing through the posterior commissure.<sup>19,20</sup> DESH was rated as follows: no disproportion = 0, mild-to-moderate disproportion = 1, severe disproportion = 2 (Figs 2 and 3). A single enlarged sulcus in otherwise reduced subarachnoid spaces did not alter the rating because it was known to be a relatively common feature of iNPH.<sup>19</sup> In rare cases when the Sylvian fissure was narrower than the parasagittal convexity sulci, findings were rated as -1 or -2, respectively.

The callosal angle (CA) was defined by 2 lines tangentially aligned with the superior-medial walls of the lateral ventricles on the coronal sections passing through the posterior commissure.<sup>5</sup> The simplified callosal angle (simpCA) was assessed on the coronal sections passing through the corpus callosum midpoint, which was

identified on the midsagittal section. The angle was drawn with the vertex placed in the inferior point of the corpus callosum and the sides tangential to the lateral ventricles.<sup>6</sup>

In addition, 4 calculated indexes (ratios) derived from the above-mentioned linear measurements were assessed on 4 differently angulated transverse/coronal sections: The Evans Index (EI) was defined as the FHD divided by the ISD obtained from the same section.<sup>16,17</sup> The z-Evans Index (ZEI) was defined as the FHVD divided by the MSID.<sup>7</sup> The brain-to-ventricle ratio (BVR) was defined as the ratio between the SVW and the CMW.<sup>12</sup> The cella media-to-temporal horn ratio (CTR) was defined as the ratio between the CMW and THW. In cases of ventricular asymmetry, the hemisphere with a larger cella media was used for all measurements.

Note that the inner skull diameter and maximum supratentorial intracranial diameter were neither considered nor evaluated as iNPH biomarkers, yet they were prerequisites for calculating the EI or ZEI, respectively.

### Data Analysis

Interrater agreement was studied by means of the intraclass correlation coefficient for a 2-way random effects model and absolute agreement. Correlation coefficient analysis of each biomarker was based on measurements from all 4 planes, giving a total of  $n = 320$  ( $4 \times 80$ ) measurements per biomarker. Results of the reliability analysis were presented as intraclass correlation coefficients with 95% confidence intervals for 2 independent raters.

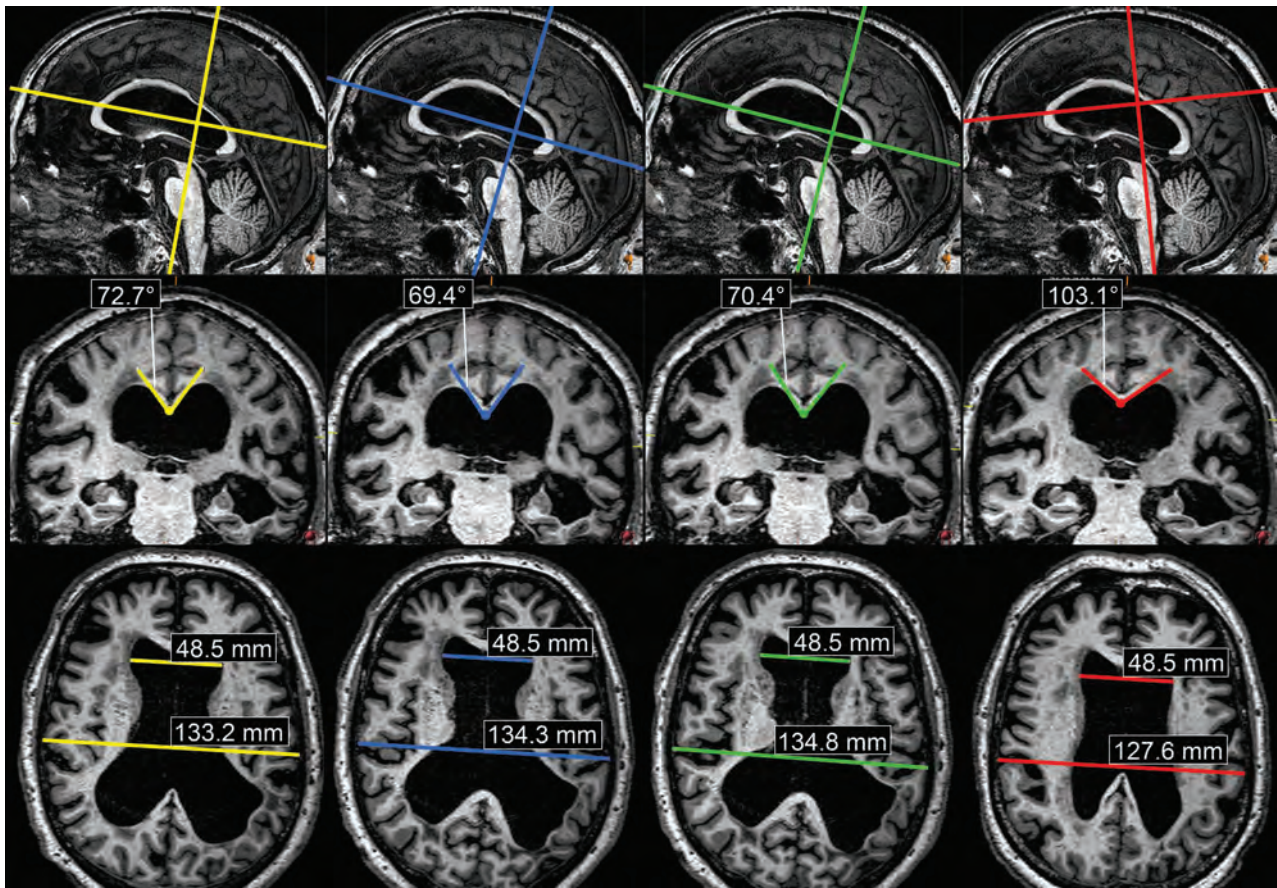


**FIG 3.** Variability of the CA (*middle row*) and EI (*lower row*) as measured on bicallosal (yellow), bicommissural (blue), Hy-Fa (green), and PBSM (red) sections of a single subject with iNPH. The CA yields 73°, 69°, 70°, and 103° in the 4 respective planes (maximum percentage difference of 39.5%). The EI shows a less variable range of values: 0.364, 0.361, 0.359, and 0.380, respectively (maximum difference of 5.7%). *Color lines* on the sagittal sections (*upper row*) refer to the alignment of the respective coronal and transverse sections below. The disproportion between Sylvian and parasagittal convexity subarachnoid spaces (DESH) has been rated moderate in this case (grade 1).

To assess whether individual biomarkers showed systematic differences when measured on sections with different angulations, we used 2-way repeated measures ANOVA (Huynh-Feldt correction) with angulation as a within-subjects factor and disease status (iNPH/HC) as a between-subjects factor, including the angulation by disease status interaction term (angulation iNPH/HC). For biomarkers that showed statistically significant dependence on angulation in the repeated measures ANOVA, we analyzed the pair-wise comparison among angulation planes. Means  $\pm$  standard errors of paired differences were calculated and presented ( $n = 80$ ) for the paired tests that were significant. A Bonferroni correction was used for the pair-wise comparisons. The level of statistical significance was set to  $P < .05$ .

## RESULTS

The interrater agreement analysis yielded reliable agreement for DESH (intraclass correlation coefficient = 0.851; 95% CI, 0.752–0.903) and excellent agreement for the remaining 11 biomarkers (intraclass correlation coefficients ranging from 0.963 to 0.997; 95% CI within  $\pm 0.011$  for all biomarkers). Because all intraclass correlation coefficients were highly significant ( $P < .001$ ), averaged values from both raters were used in all subsequent analyses.

When we compared the values of individual biomarkers obtained from differently angulated sections, DESH, simplified CA,

FHD, ZEI, and CMW did not show significant systematic differences in the repeated measures ANOVA (Table 1, column 5: “Angulation”). The remaining 7 biomarkers showed significant differences between up to 3 (eg, EI) or even 4 (eg, CA) mutually compared section pairs (Table 2). The biomarker values obtained from sections aligned parallel or perpendicular to the fourth ventricle floor (PBSM) showed the most deviating results from other section angulations. The lowest biomarker variability was found when comparing the results obtained from those section pairs: bicallosal and Hy-Fa or bicommissural and Hy-Fa; these combinations of sections significantly differed in a single biomarker only (BVR or THW, respectively; see Table 2, columns 3 and 5).

The angulation by the iNPH/HC interaction term was significant for the THW and CA, ie, dependence on angulation differed between the iNPH and HC groups for the THW and CA only, with the effects being larger for iNPH in both cases (Table 1, column 6: “Angulation iNPH/HC”). Differences of biomarker values between the iNPH and HC groups were significant ( $P < .001$ ) for all 12 biomarkers evaluated (Table 1, column 4: “iNPH/HC”).

Graphic examples of the variability of the EI and CA measured on 4 standardized imaging sections of the same subject are presented in Fig 3.

**Table 1: Variability of iNPH biomarkers with respect to imaging plane angulation<sup>a</sup>**

Biomarker	Mean		Repeated Measures ANOVA (P Values)		
	HC	iNPH	iNPH/HC	Angulation	Angulation iNPH/HC
DESH	0.12	1.31	<.001	.463	.463
simpCA	129.8	98.2	<.001	.264	.950
FHD	39.1	51.2	<.001	.151	.757
ZEI	0.286	0.420	<.001	.075	.792
CMW	17.4	34.5	<.001	.056	.49
BVR	2.44	0.92	<.001	.005	.106
THW	7.6	12.5	<.001	.002	.026
CTR	2.33	2.86	<.001	.002	.235
EI	0.293	0.384	<.001	<.001	.971
FHVD	25.7	38.8	<.001	<.001	.059
CA	116.6	74.7	<.001	<.001	<.001
SVW	39.6	30.9	<.001	<.001	.288

**Note:**—HC indicates healthy control; iNPH, idiopathic normal pressure hydrocephalus.

<sup>a</sup>Please refer to the Results section for detailed explanation. Two-way repeated measures ANOVA: angulation is a within-subjects factor (Angulation), and disease status is a between-subjects factor (iNPH/HC). Angulation by disease status interaction term (Angulation iNPH/HC) is significant for THW and CA only, with larger effects observed in the iNPH group for both biomarkers. Data are sorted in descending angulation *P* value order (column 5: "Angulation"). Decreasing *P* values indicate increasing statistical differences between measurements obtained at different section planes.

**Table 2: Pair-wise comparisons between different planes performed with Bonferroni correction for biomarkers showing significant dependence on angulation (*P* < .05) in the repeated measures ANOVA (as per Table 1)<sup>a</sup>**

Biomarker	Bi-Call, Bi-Comm	Bi-Call, Hy-Fa	Bi-Call, PBSM	Bi-Comm, Hy-Fa	Bi-Comm, PBSM	Hy-Fa, PBSM
DESH	NS	NS	NS	NS	NS	NS
simpCA	NS	NS	NS	NS	NS	NS
FHD	NS	NS	NS	NS	NS	NS
ZEI	NS	NS	NS	NS	NS	NS
CMW	NS	NS	NS	NS	NS	NS
BVR	NS	.007	.009	NS	NS	<.001
THW	NS	-0.04 ± 0.01	0.07 ± 0.02	.002	.014	0.11 ± 0.02
CTR	NS	NS	NS	0.24 ± 0.06	0.32 ± 0.10	NS
EI	NS	NS	<.001	NS	<.001	<.001
FHVD	NS	NS	-0.005 ± 0.001	NS	-0.005 ± 0.001	-0.005 ± 0.001
CA	.013	NS	-0.52 ± 0.17	NS	-0.92 ± 0.20	-0.79 ± 0.17
SVW	-1.94 ± 0.61	NS	-7.06 ± 0.87	NS	-9.01 ± 1.07	-8.24 ± 0.91
	-0.45 ± 0.16		0.97 ± 0.28		1.42 ± 0.30	1.26 ± 0.32

**Note:**—Bi-Call indicates bicallosal; Bi-Comm, bicommissural; Hy-Fa, hypophysis-fastigium; PBSM, posterior brain stem margin; NS, not significant.

<sup>a</sup>*P* values (upper digit) and means ± standard errors of paired differences are calculated (*n* = 80) and presented for those paired tests that are statistically significant.

## DISCUSSION

Various linear, angular, volumetric, or index measurements have been proposed as radiologic biomarkers of iNPH in multiple studies.<sup>3,5-10,12,13,15,16</sup> However, consensus on which biomarker is the most sensitive, specific, and accurate has not been reached.

Much less attention has been paid to standardization of biomarker measurements and their reliability with respect to imaging plane angulation. Ishii et al<sup>5</sup> arbitrarily decided to use the bicommissural plane for CA measurements, stating that CAs varied on each plane, but they did not provide any further details. Cagnin et al<sup>6</sup> tested callosal angle variability with respect to different section angulations on a limited group of 5 subjects. Toma et al<sup>9</sup> showed that the EI varied depending on both the CT section level and angulation in a study of 10 patients with NPH; the researchers concluded that comparing the EI on CT scans obtained at different

institutions using different protocols may result in inaccurate assessment of disease progression. Nonetheless, systematic comparison of biomarker variability with respect to different imaging plane angulations or robustness against angulation-related bias has not been published.

### Angulation-Related Variability

Our results show that both the EI and CA, the most frequently used biomarkers for iNPH assessment, are subject to significant systematic differences when assessed on sections of different angulations. Because most CT and MR imaging brain studies primarily do not contain coronal sections aligned perpendicular to the bicommissural line, precise CA values cannot be obtained unless a 3D set of volumetric data is available and supplementary multiplanar reformatting is performed. This requirement is easily

achievable in properly and prospectively designed research studies such as Miskin et al,<sup>3</sup> Yamada et al,<sup>7</sup> and Agerskov et al,<sup>22</sup> however, it does not comply with the reality of routine clinical practice in which the CA is frequently measured on the readily available, yet inappropriately angulated, coronal section (typically the PBSM). According to our results, this issue may lead to incorrect diagnostic conclusions. As shown in Fig 3, the CA value correctly obtained from the coronal section perpendicular to the bicommissural line is pathologically decreased to 69° in this subject, whereas the value obtained from the readily available “standard” coronal section aligned parallel to the PBSM yields 103°, which may be misinterpreted as a normal finding.

Similarly, if EI values are compared on cross-sectional studies of the same subject using various definitions of transverse planes, the differences obtained may be subject to a methodologic error rather than to the natural evolution of ventriculomegaly. This phenomenon might have contributed to the failure of the EI to correctly identify subjects with iNPH in a large study of 390 patients in which CT and MR imaging studies from 5 institutions using different protocols were retrospectively evaluated.<sup>8</sup> Although the EI may show significant differences when measured on variously angulated transverse sections, the exact definition of the transverse plane used for EI evaluation has been missing in multiple research studies published such as Kojoukhova et al,<sup>8</sup> Bao et al,<sup>10</sup> and Reinard et al.<sup>11</sup> It remains debatable whether small statistical differences found in the EI are relevant in the setting of daily clinical routine; nonetheless, they may be of significance at least in those cases in which the EI approaches the cutoff value.

On the contrary, DESH, simplified CA, FHD, ZEI, and CMW did not show statistically significant differences related to varying section angulation (Tables 1 and 2) and proved to be insensitive to plane-tilting differences, which would predispose them better for comparing iNPH imaging studies performed at different institutions using different protocols. DESH proved to be the biomarker least prone to angulation-related variability, which might be attributed to its semiquantitative nature based on visual relative assessment of subarachnoid spaces.

The FHD also showed insignificant variability of results obtained at various section angulations. Owing to the lateral convex geometry of the frontal horns, the maximum FHD would remain unchanged over a wide range of section angulations. Besides, the FHD scored comparably with the EI in a recent study on the diagnostic performance of 15 iNPH biomarkers.<sup>21</sup> This finding has further raised the question of whether a simple linear measure such as the FHD could possibly replace the more complicated index measurement of the EI which, in addition, shows significant variability when measured on different transverse sections. The reason for the increased EI variability is that although its numerator (FHD) remains constant at the level of maximum frontal horn diameter, the denominator (inner skull diameter) varies on differently angulated sections, which all intersect at the FHD level. As shown in the example in Fig 3, the FHD remains the same at all angulations (48.5 mm), whereas the inner skull diameter ranges between 127.6 and 134.8 mm.

Unlike the EI, the ZEI has not shown significant variability when assessed on different section planes using repeated measures ANOVA. Furthermore, the ZEI has shown better discriminatory

power between subjects with iNPH and HCs than the EI in the recent study.<sup>21</sup>

When comparing the CA<sup>5</sup> with the simplified CA<sup>6</sup>, the former (assessed at the posterior commissure) shows substantially increased variability at different angulations. This is because the angle formed by the medial walls of the lateral ventricles progressively varies near the ventricular trigones (and posterior commissure) but is relatively constant at the midportion of the corpus callosum, making the simplified CA at this location less susceptible to angulation-related deviations. Because the cerebral “uplift” and “wrapping” of the lateral ventricles around the posterior falx belong to the imaging hallmarks of iNPH,<sup>12,20,23</sup> the changes of the ventricular geometry as well as the resulting CA angulation-related variability tend to be accentuated in subjects with iNPH. This tendency is in accordance with the analysis of the disease status interaction term in which the dependence on angulation has differed between the iNPH and HC groups, most significantly for CA ( $P < .001$ ), with larger effects observed in the iNPH group (Table 1, column “Angulation iNPH/HC”). Post hoc analysis within the iNPH group showed that the SD of CA values obtained on 4 coronal planes yielded 10.3° (intraindividual differences of CA values ranged between 2° and 40°), whereas the SD within the HC group was significantly lower (5.8°; intraindividual range, 1°–26°).

Coronal sections aligned parallel with the brain stem vertical line (PBSM) showed the highest CA deviations from the prescribed bicommissural plane. Considering that the PBSM serves as the standard coronal imaging section at many institutions, improper-yet-not-rare assessment of the CA on PBSM sections may induce significant bias (Table 2 and Fig 3) and should be avoided. This observation should certainly not discourage radiologists from using the CA in routine practice because the CA has shown high discriminatory power between HCs and iNPH, surpassing, for example, the EI or the simplified CA,<sup>21</sup> yet it emphasizes that complying with the proper measurement methodology is essential.

### Study Limitations

This study was not intended to suggest new imaging standards, evaluate the importance of radiologic biomarkers as supplementary tests for predicting outcome of CSF shunt surgery, or determine which plane or biomarker is the most accurate one. Instead, we have tried to investigate how different standards of section positioning affect individual iNPH biomarkers and whether inappropriate cross-sectional plane angulation may significantly influence iNPH biomarker measurements.

The diagnosis of iNPH was established on the basis of the international iNPH guideline;<sup>18</sup> therefore, the EI of >0.3 was already used as a preselecting criterion. On the contrary, ventriculomegaly and EI increase are common in the overall elderly population,<sup>4</sup> which enhances the diagnostic benefits of more iNPH-specific biomarkers such as the ZEI, DESH, or CA.

The orbitomeatal plane was not included in the assessment, possibly being viewed as a limitation of the study, but there were several reasons for this exclusion: Its use has gradually decreased with advancements of multidetector CT scanner technology, offering unprecedented multiplanar reformatting capabilities yet restricting gantry tilt options. Also, this plane cannot be precisely defined on cross-sectional MR images, reducing its reproducibility on MR imaging.

Our study cohort represented a highly selective sample of the elderly population comprising subjects with iNPH or HCs only. However, systematic comparison of angulation-related biomarker variability, which was the main objective of this study, should not be significantly influenced by this study design.

## CONCLUSIONS

Seven of 12 iNPH biomarkers studied, including the frequently used EI and CA, show statistically significant deviations when measured on sections whose angulation differs from the original section definition. Strict adherence to the originally prescribed methodology of iNPH biomarker assessment (such as measuring the CA strictly on the coronal section oriented perpendicular to the bicommissural line) is considered essential to avoid incorrect diagnostic results. Volume acquisition of a 3D image dataset should be considered the standard of care in assessing patients for iNPH (as well as other dementias) on both CT and MR imaging because it provides the opportunity for reformatting correctly angulated section planes, thus complying with the proper measurement technique for each particular biomarker.

More radiologic as well as research attention should be paid to those biomarkers, which are the least sensitive to angulation-related differences such as DESH, ZEI, or CMW; in addition, these biomarkers have also shown high discriminatory power between iNPH and HCs in a recently published study.<sup>21</sup> If further research proves that these biomarkers show high diagnostic accuracy for iNPH as well as insensitivity to angulation-related bias, it would yield benefits for daily radiologic practice and potentially aid in designing the future versions of iNPH diagnostic guidelines.

Different institutions worldwide use various definitions of transverse and coronal brain imaging sections. Comparing CT or MR imaging studies from different sources using different protocols is not only arduous and less precise but may also lead to biased results when sections with improper angulation are used for assessment of specific biomarkers. Viewed from a broader perspective, a systematic effort to standardize and unify cross-sectional imaging plane definitions would bring substantial benefits extending far beyond the radiologic community.

Disclosures: Jonatan Salzer—UNRELATED: Consultancy: Mabion SA, Comments: consultancy fees\*; Grants/Grants Pending: Synapsys, Interacoustics, Comments: material research support.\* \*Money paid to the institution.

## REFERENCES

1. Brean A, Eide PK. **Prevalence of probable idiopathic normal pressure hydrocephalus in a Norwegian population.** *Acta Neurol Scand* 2008;118:48–53 CrossRef Medline
2. Isaacs AM, Riva-Cambria J, Yavin D, et al. **Age-specific global epidemiology of hydrocephalus: systematic review, meta-analysis and global birth surveillance.** *PLoS ONE* 2018;13:e0204926 CrossRef Medline
3. Miskin N, Patel H, Franceschi AM, et al. Alzheimer's Disease Neuroimaging Initiative. **Diagnosis of normal-pressure hydrocephalus: use of traditional measures in the era of volumetric MR imaging.** *Radiology* 2017;285:197–205 CrossRef Medline
4. Ambarki K, Israelsson H, Wählin A, et al. **Brain ventricular size in healthy elderly: comparison between Evans Index and volume measurement.** *Neurosurgery* 2010;67:94–99 CrossRef Medline
5. Ishii K, Kanda T, Harada A, et al. **Clinical impact of the callosal angle in the diagnosis of idiopathic normal pressure hydrocephalus.** *Eur Radiol* 2008;18:2678–83 CrossRef Medline
6. Cagnin A, Simioni M, Tagliapietra M, et al. **A simplified callosal angle measure best differentiates idiopathic-normal pressure hydrocephalus from neurodegenerative dementia.** *J Alzheimers Dis* 2015;46:1033–38 CrossRef Medline
7. Yamada S, Ishikawa M, Yamamoto K. **Optimal diagnostic indices for idiopathic normal pressure hydrocephalus based on the 3D quantitative volumetric analysis for the cerebral ventricle and subarachnoid space.** *AJNR Am J Neuroradiol* 2015;36:2262–69 CrossRef Medline
8. Kojoukhova M, Koivisto AM, Korhonen R, et al. **Feasibility of radiological markers in idiopathic normal pressure hydrocephalus.** *Acta Neurochir* 2015;157:1709–18 CrossRef Medline
9. Toma AK, Holl E, Kitchen ND, et al. **Evans' index revisited: the need for an alternative in normal pressure hydrocephalus.** *Neurosurgery* 2011;68:939–44 CrossRef Medline
10. Bao J, Gao Y, Cao Y, et al. **Feasibility of simple linear measurements to determine ventricular enlargement in patients with idiopathic normal pressure hydrocephalus.** *J Craniofac Surg* 2016;27:e462–65 CrossRef Medline
11. Reinard K, Basheer A, Phillips S, et al. **Simple and reproducible linear measurements to determine ventricular enlargement in adults.** *Surg Neurol Int* 2015;6:59 CrossRef Medline
12. Yamada S, Ishikawa M, Yamamoto K. **Comparison of CSF distribution between idiopathic normal pressure hydrocephalus and Alzheimer disease.** *AJNR Am J Neuroradiol* 2016;37:1249–55 CrossRef Medline
13. Sasaki M, Honda S, Yuasa T, et al. **Narrow CSF space at high convexity and high midline areas in idiopathic normal pressure hydrocephalus detected by axial and coronal MRI.** *Neuroradiology* 2008;50:117–22 CrossRef Medline
14. Bradley WG Jr. **CSF flow in the brain in the context of normal pressure hydrocephalus.** *AJNR Am J Neuroradiol* 2015;36:831–38 CrossRef Medline
15. Benedetto N, Gambacciani C, Aquila F, et al. **A new quantitative method to assess disproportionately enlarged subarachnoid space (DESH) in patients with possible idiopathic normal pressure hydrocephalus: the SILVER index.** *Clin Neurol Neurosurg* 2017;158:27–32 CrossRef Medline
16. Evans WA Jr. **An encephalographic ratio for estimating ventricular enlargement and cerebral atrophy.** *Arch Neuropsych* 1942;47:931–37
17. Synek V, Reuben JR, Du Boulay GH. **Comparing Evans' index and computerized axial tomography in assessing relationship of ventricular size to brain size.** *Neurology* 1976;26:231–33 CrossRef Medline
18. Relkin N, Marmarou A, Klinge P, et al. **Diagnosing idiopathic normal-pressure hydrocephalus.** *Neurosurgery* 2005;57:S4–16 CrossRef Medline
19. Kitagaki H, Mori E, Ishii K, et al. **CSF spaces in idiopathic normal pressure hydrocephalus: morphology and volumetry.** *AJNR Am J Neuroradiol* 1998;19:1277–84 Medline
20. Hashimoto M, Ishikawa M, Mori E, et al. Study of INPH on neurological improvement (SINPHONI). **Diagnosis of idiopathic normal pressure hydrocephalus is supported by MRI-based scheme: a prospective cohort study.** *Cerebrospinal Fluid Res* 2010;7:18 CrossRef Medline
21. Ryska P, Slezak O, Eklund A, et al. **Radiological markers of idiopathic normal pressure hydrocephalus: relative comparison of their diagnostic performance.** *J Neurol Sci* 2020;408:116581 CrossRef Medline
22. Agerskov S, Wallin M, Hellström P, et al. **Absence of disproportionately enlarged subarachnoid space hydrocephalus, a sharp callosal angle, or other morphologic MRI markers should not be used to exclude patients with idiopathic normal pressure hydrocephalus from shunt surgery.** *AJNR Am J Neuroradiol* 2019;40:74–79 CrossRef Medline
23. Virhammar J, Laurell K, Cesarini KG, et al. **The callosal angle measured on MRI as a predictor of outcome in idiopathic normal-pressure hydrocephalus.** *J Neurosurg* 2014;120:178–84 CrossRef Medline

# Acceleration of Brain TOF-MRA with Compressed Sensitivity Encoding: A Multicenter Clinical Study

J. Ding, Y. Duan, Z. Zhuo, Y. Yuan, G. Zhang, Q. Song, B. Gao, B. Zhang, M. Wang, L. Yang, Y. Hou, J. Yuan, C. Feng, J. Wang, L. Lin, and Y. Liu



## ABSTRACT

**BACKGROUND AND PURPOSE:** The clinical practice of three-dimensional TOF-MRA, despite its capability in brain artery assessment, has been hampered by the relatively long scan time, while recent developments in fast imaging techniques with random undersampling has shed light on an improved balance between image quality and imaging speed. Our aim was to evaluate the effectiveness of TOF-MRA accelerated by compressed sensitivity encoding and to identify the optimal acceleration factors for routine clinical use.

**MATERIALS AND METHODS:** One hundred subjects, enrolled at 5 centers, underwent 8 brain TOF-MRA sequences: 5 sequences using compressed sensitivity encoding with acceleration factors of 2, 4, 6, 8, and 10 (CS2, CS4, CS6, CS8, and CS10), 2 using sensitivity encoding with factors of 2 and 4 (SF2 and SF4), and 1 without acceleration as a reference sequence (RS). Five large arteries, 6 medium arteries, and 6 small arteries were evaluated quantitatively (reconstructed signal intensity, structural similarity, contrast ratio) and qualitatively (scores on arteries, artifacts, overall image quality, and diagnostic confidence for aneurysm and stenosis). Comparisons were performed among the 8 sequences.

**RESULTS:** The quantitative measurements showed that the reconstructed signal intensities of the assessed arteries and the structural similarity consistently decreased as the compressed sensitivity encoding acceleration factor increased, and no significant difference was found for the contrast ratios in pair-wise comparisons among SF2, CS2, and CS4. Qualitative evaluations showed no significant difference in pair-wise comparisons among RS, SF2, and CS2 ( $P > .05$ ). The visualization of all the assessed arteries was acceptable for CS2 and CS4, while 2 small arteries in images of CS6 were not reliably displayed, and the visualization of large arteries was acceptable in images of CS8 and CS10.

**CONCLUSIONS:** CS4 is recommended for routine brain TOF-MRA with balanced image quality and acquisition time; CS6, for examinations when small arteries are not evaluated; and CS10, for fast visualization of large arteries.

**ABBREVIATIONS:** ACA = anterior cerebral artery; BA = basilar artery; CR = contrast ratio; CS = compressed sensing; L = left; R = right; RS = reference sequence without SENSE or CS-SENSE acceleration; RSI = reconstructed signal intensity; SENSE = sensitivity encoding; SF = SENSE technique with acceleration factors; SSIM = structural similarity index; VA = vertebral artery; PCA = posterior cerebral artery

TOF-MRA is a noninvasive routine clinical method that does not require intravenous contrast agents or exposure to radiation for brain artery assessment.<sup>1-3</sup> Previous studies have

demonstrated its high diagnostic efficacy in detecting cerebrovascular diseases, which is comparable with that of DSA, and TOF-MRA has been used to replace DSA in the diagnosis of cerebrovascular diseases for a range of clinical practices.<sup>2-5</sup> However, the relatively long scan time of conventional TOF-MRA can potentially result in an uncomfortable experience for patients and increased motion artifacts in images.<sup>6-8</sup> Parallel imaging techniques such as sensitivity encoding (SENSE) and generalized

Received October 25, 2020; accepted after revision January 10, 2021.

From the Department of Radiology (J.D., Y.D., Z.Z., J.Y., C.F., Y.L.), Beijing Tiantan Hospital, Capital Medical University, Beijing, China; Department of Radiology (Y.Y., G.Z.), Beijing Royal Integrative Medicine Hospital, Beijing, China; Department of Radiology (Q.S., B.G.), the First Affiliated Hospital of Dalian Medical University, Dalian, China; Department of Radiology (B.Z., M.W.), The Affiliated Drum Tower Hospital of Nanjing University Medical School, Jiangsu, China; Department of Radiology (L.Y., Y.H.), Shengjing Hospital of China Medical University, Shenyang, China; and Philips Healthcare (J.W., L.L.), Beijing, China.

This work was supported by the National Science Foundation of China (Nos. 81870958 and 81571631), the Beijing Natural Science fund (No.7133244), and the Beijing Nova Program (xx2013045).

Paper previously presented, in part, at: Annual Meeting of the International Society for Magnetic Resonance in Medicine and the Society for MR Radiographers and Technologists, August 8-14, 2020; Virtual.

Please address correspondence to Yaou Liu, MD, PhD, Department of Radiology, Beijing Tiantan Hospital, Capital Medical University, No.119, West Southern 4th Ring Rd, Fengtai District, Beijing, 100070, China; e-mail: yaouliu80@163.com

Indicates open access to non-subscribers at [www.ajnr.org](http://www.ajnr.org)

Indicates article with online supplemental data.

<http://dx.doi.org/10.3174/ajnr.A7091>

autocalibrating partially parallel acquisition have been implemented in clinical practice in the past 2 decades for MR imaging acceleration.<sup>9,10</sup> However, the acceleration capability of parallel imaging is limited by the number of receive coils, and the acceleration factor rarely goes beyond 4 in clinical setups due to potential imaging artifacts and signal-to-noise ratio concerns.<sup>10,11</sup>

The compressed sensing (CS) technique by pseudorandom  $k$ -space undersampling has shown its potential in fast MR imaging with a relatively high acceleration factor and suppressed imaging artifacts.<sup>6,12-15</sup> Previous studies have shown that CS-accelerated TOF-MRA outperforms traditional parallel imaging through quantitative image evaluation, and the CS-accelerated sequence has been applied for evaluating cerebral artery malformations, aneurysms, and stenoses.<sup>6,16-18</sup> In previous studies of CS TOF-MRA, most cerebral aneurysms were recognized using a CS factor of 5 or 8 with 10 iterations.<sup>6</sup> The diagnostic quality of several distal arterial branches could be maintained on images with a CS factor of up to 6<sup>12</sup> and improved visualization of small collaterals in equivalent time (factor of 3); or equivalent results with a shorter scan time (factor of 5) could be achieved by CS in comparison with parallel imaging.<sup>18</sup> However, most of these studies were performed at a single center or with a small number of subjects, and there has been no consensus on the optimal CS acceleration factor for 3D TOF-MRA. Therefore, a more comprehensive study is required to verify the effectiveness of CS on TOF-MRA and to identify the optimal CS acceleration factors for routine clinical use, preferably in a multicenter study with more subjects.

In this work, we aimed to evaluate the effectiveness of CS-accelerated TOF-MRA and identify the optimal CS acceleration factors for clinical use in a cohort of 100 subjects from 5 centers by systematically evaluating the image quality and diagnostic efficacy of CS-accelerated TOF-MRA with 5 different acceleration factors ranging from 2 to 10. These findings were compared with results obtained by conventional SENSE with 2 acceleration factors and a nonaccelerated sequence.

## MATERIALS AND METHODS

### Ethics

This multicenter study was approved by the relevant institutional review boards. Informed consent was obtained from all participants.

### Study Population

Between March 2019 and January 2020, we prospectively and consecutively enrolled participants at 5 different hospitals (located in different cities in China): center 1: Beijing Tiantan Hospital, Capital Medical University, in Beijing, 26 cases; center 2: Beijing Royal Integrative Medicine Hospital, in Beijing, 30 cases; center 3: The Affiliated Drum Tower Hospital of Nanjing University Medical School, in Nanjing, 23 cases; center 4: the First Affiliated Hospital of Dalian Medical University, in Dalian, 15 cases; and center 5: Shengjing Hospital of China Medical University, in Shenyang, 14 cases. The inclusion criteria were as follows: 1) older than 18 years of age, and 2) healthy volunteers or participants suspected or confirmed of having cerebrovascular diseases. The exclusion criteria are included in Fig 1.

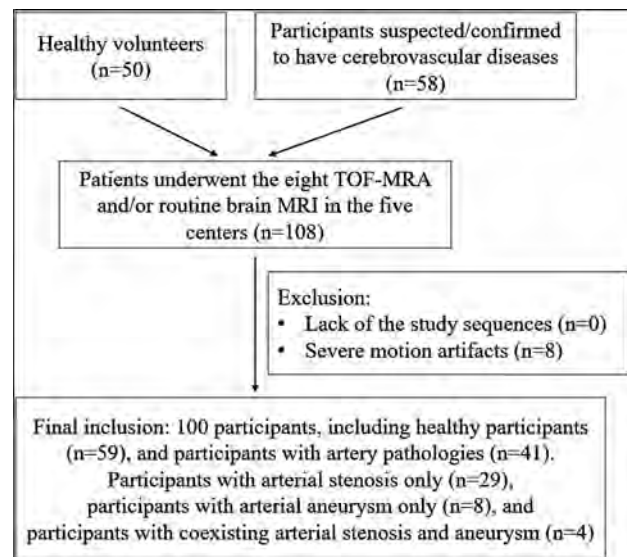


FIG 1. Flow chart for participant inclusion.

### MR Imaging Protocols

Each participant was scanned head-first in the supine position at 3T (Ingenia CX; Philips Healthcare) at 1 of the 5 centers where the MR imaging systems were located, with a 32-channel head coil using compressed SENSE as the acceleration technique<sup>19,20</sup> (a combination of CS and SENSE, hereafter referred to as CS-SENSE) with the reconstruction algorithm shown in Equation 1, which essentially followed the technique described by Lustig and Pauley:<sup>21</sup>

$$p = \min \left( \sum_{i=1}^{n_{\text{coils}}} \| m_{d,i} - E S_{d,i} p \|^2 + \lambda_1 \| R^{-1/2} p \|^2 + \lambda_2 \| \Psi p \|_1 \right)$$

where  $p$  is the image to be reconstructed;  $m_{d,i}$  is the measured value for a given coil element after noise decorrelation;  $E$  is the undersampled Fourier operator defined by the subsampling pattern;  $S_{d,i}$  is the coil sensitivity for a given coil element after noise decorrelation (obtained with the SENSE reference scan);  $\lambda_1$  is the regularization factor for balancing between data consistency and prior knowledge of image content;  $R$  is coarse resolution data from the integrated body coil obtained with the SENSE reference scan (used to constrain the solution during the regularization process);  $\lambda_2$  is the regularization factor to balance the sparsity constrain and data consistency in the iterative solution; and  $\Psi$  is the sparsity transform into the wavelet domain.

Each participant underwent 8 customized 3D TOF-MRA protocols (predesigned and optimized at Beijing Tiantan Hospital and then replicated on the MR imaging systems of other hospitals) in a random order. First, a routine brain MR imaging, including transverse T2-weighted TSE, sagittal 3D T1 turbo-field echo (known as MPRAGE), sagittal 3D-FLAIR, DWI, and SWI, was performed for all participants with suspected or confirmed cerebrovascular diseases, and after a period of 5–10 minutes, the 8 TOF-MRA sequences were additionally scanned. For healthy volunteers, routine brain MR imaging was optional, but the 8 TOF-MRA images were required. Among the 8 protocols, 5 used

CS-SENSE with acceleration factors of 2, 4, 6, 8, and 10 (denoted as CS2, CS4, CS6, CS8, and CS10, respectively); 2 used the conventional SENSE technique with acceleration factors of 2 and 4 (denoted as SF2 and SF4, respectively); and 1 was a reference protocol without SENSE or CS-SENSE acceleration (denoted as RS). A 3D FOV was used to cover most cerebral arteries and the pericallosal artery branches, including the intracranial segment of the bilateral ICAs, the anterior cerebral artery (ACA, A1–A3 segments), the MCA (M1–M4 segments), the distal bilateral vertebral arteries (VAs, at least half of the V4 segment), the basilar artery (BA), and the posterior cerebral artery (PCA, P1–P3 segments). A saturation band was placed above the FOV to suppress the signals from veins. The parameters for the 8 MRA protocols are listed in the Online Supplemental Data. The reconstruction was performed in real-time during the scan and did not affect the workflow of the hospital.

### Image Evaluation

Images were transferred to the IntelliSpace Portal, Version 7.0 (Philips Healthcare) workstation and processed before evaluations. First, all images were checked visually to exclude data with insufficient quality due to unacceptable motion artifacts. Second, image realignment was performed using SPM 12 ([www.fil.ion.ucl.ac.uk/spm/](http://www.fil.ion.ucl.ac.uk/spm/)) for images acquired by the 8 sequences on the same subject. Third, the patient and sequence information was removed from all images. Finally, quantitative and qualitative assessments were performed.

Quantitative image evaluations were performed on Matlab R2016b (MathWorks). Because the iterative reconstruction of CS-SENSE can result in artificial reduction of noise in MR images, it would be inaccurate to use classic measurement approaches for calculating the signal-to-noise ratio and/or contrast-to-noise ratio. Instead, the reconstructed signal intensities (RSIs) of 11 cerebral arteries, WM, and CSF were extracted from the source image-based ROIs drawn by a neuroradiologist (Y.D., with >10 years of experience). For the signal intensity measurements of the arteries, WM, and CSF for each subject, ROIs were placed on the same slices of the 8 TOF-MRA source images. ROIs of the ACA, MCA, or PCA (such as the A1, M1, and P1 segments) were drawn in the proximal segment, while ROIs of the ICA and VA (such as C7 and V4) were drawn in the distal segment. In the case of stenosis, slight anatomic variation, or occlusion, the proximal or distal segment with maximal display in the same section of the 8 TOF-MRA source images was selected for ROI measurements. The signal of the corpus callosum was used to represent the WM signal.<sup>22</sup> The CSF signal was mainly acquired from the lateral ventricle. The contrast ratios (CRs) between assessed arteries and WM ( $CR_{artery/wm}$ ) and between assessed arteries and CSF ( $CR_{artery/csf}$ ) were calculated in Equation 2 as<sup>23</sup>

$$CR_{tissue1/tissue2} = \frac{|\mu_{tissue1} - \mu_{tissue2}|}{\sqrt{\sigma_{tissue1}^2 + \sigma_{tissue2}^2}}$$

where  $\mu_{tissue1}$  and  $\mu_{tissue2}$  are the ROI-based mean signal intensities of 2 specific tissues, with  $\sigma_{tissue1}$  and  $\sigma_{tissue2}$  as the corresponding variances. The assessed cerebral arteries included the left and right ICAs (LICA, RICA), ACAs (LACA, RACA), MCAs (LMCA, RMCA), VAs (LVA, RVA), PCAs (LPCA and RPCA), and the BA. In addition, the structural similarity index (SSIM)<sup>24</sup> was calculated

to measure the image similarity between each of the 7 accelerated scans and the RS scan.<sup>20</sup>

The whole MIP radial axis in the foot-head direction (radial angle = 12°, fifteen projections in total, no preprocessing) was used for visual depiction of the cerebral arteries. Qualitative image evaluation was performed independently by 2 neuroradiologists (J.Y. and C.F., with >8 years of experience who were blinded to the patient information and imaging parameters). The image quality; visualization of large, medium, and small arteries; and diagnostic confidence of arterial pathologies for all 8 protocols were assessed according to the scoring system listed in the Online Supplemental Data.<sup>15</sup> Before the evaluation, the 2 neuroradiologists completed a training session with 5 patients on the evaluation of the imaging findings.<sup>14</sup> The mean scores of the 2 readers were used for subsequent statistical analyses.

Nonvisible distal arteries or branches due to severe stenosis or occlusion were excluded from further analyses, but the normal arteries in the same patient were still included. The criteria were as follows: protocols with mean scores for large and medium arteries of  $\geq 3$ , small arteries of  $\geq 2$ , artifacts of  $\geq 2$ , overall image quality of  $\geq 3$ , and diagnostic confidence of  $\geq 2$  were considered acceptable for clinical setup.

### Statistical Analysis

Statistical analyses were performed using Matlab R2016b (MathWorks). Repeated measures ANOVA tests were performed for the RSIs, CRs, and SSIM among the 8 sequences, while differences between each pair of protocols were evaluated by multiple comparisons with *P* values corrected by the Bonferroni correction. The interobserver reliability on qualitative evaluation was assessed through the Cohen  $\kappa$  test (excellent agreement if  $\kappa > 0.9$ , good agreement if  $\kappa > 0.6$ ). Qualitative scores from all sequences were tested using the Friedman test, and multiple comparisons between each pair of the 8 sequences were performed with *P* values corrected by the Bonferroni correction. For all tests, *P* < .05 was considered statistically significant.

## RESULTS

### Participant Cohort

A total of 108 participants from the 5 centers were initially recruited. Data from 8 participants were excluded due to motion artifacts. Finally, 100 participants (46 men and 54 women; mean age, 52.9 [SD, 16.5] years; age range, 23–88 years) were enrolled (Fig 1). Fifty-nine participants had no artery pathologies and included 50 healthy volunteers and 9 participants from the suspected group. Forty-one participants showed artery pathologies, including arterial stenosis only (*n* = 29), arterial aneurysm only (*n* = 8), or coexisting arterial stenosis and an aneurysm (*n* = 4). The locations of the arterial stenoses and aneurysms are listed in the Online Supplemental Data.

### Quantitative Measurements

**RSIs and SSIM.** For all assessed arteries, WM, and CSF, significant differences were observed for RSIs among the 8 protocols (*P* < .05), as well as the SSIM among the 7 accelerated protocols (*P* < .05). For each artery, WM, or CSF, as the SENSE or CS-SENSE acceleration factor increased, the mean reconstructed signal

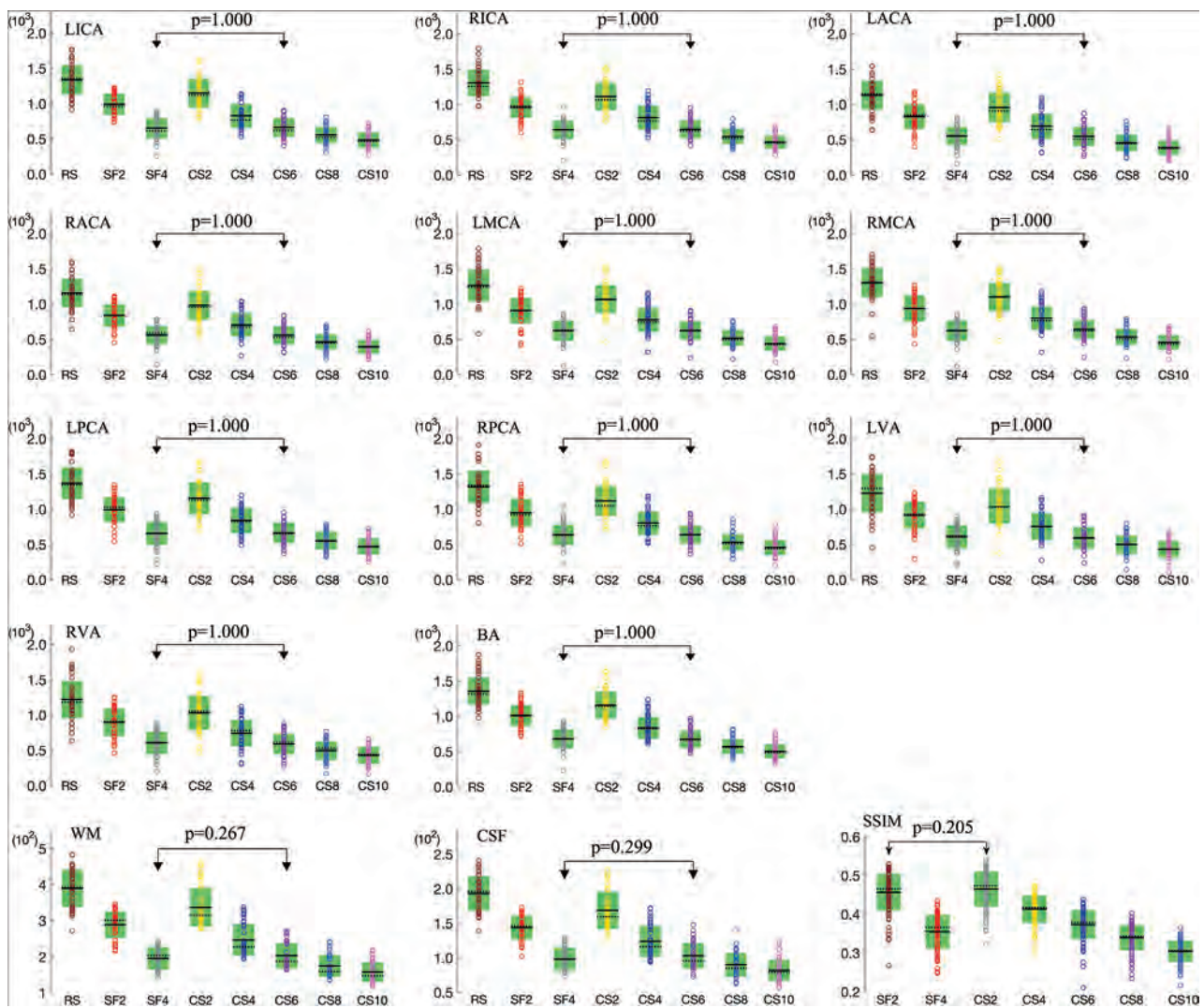


**FIG 2.** Measured RSIs for 11 arteries (LICA, RICA, LACA, RACA, LMCA, RMCA, LPCA, RPCA, LVA, RVA, and BA), WM, and CSF by the 8 sequences; and the SSIM values for the 7 accelerated scans with reference to the RS scan (circles indicate individual measurements; black lines, mean values; dotted black lines, median values; and green boxes, SD). Pairs without significant differences ( $P > .05$ ) are connected with double arrow lines because the  $P$  values in other pairs were all .000.

intensity gradually decreased, and significant differences were found between any 2 of the 8 protocols ( $P < .05$ , Fig 2) except between SF4 and CS6. The SSIM also decreased as the SENSE or CS-SENSE acceleration factor increased, and no significant difference was found between the SF2 and CS2 scans ( $P > .05$ , Fig 2).

**Contrast Ratio.** The mean  $CR_{artery/wm}$  and  $CR_{artery/csf}$  values decreased slightly and gradually for most arteries when the CS-SENSE acceleration factor increased (Online Supplemental Data). Differences were found among the 8 MRA sequences for the CRs using repeated measures ANOVA. Comparisons between any 2 of the 8 sequences are listed in the Online Supplemental Data. No significant difference was found for the CRs between any pairs of SF2, CS2, and CS4.

### Qualitative Assessments

Good or excellent agreement was reached between the 2 readers for scoring artery visualization ( $\kappa \geq 0.812$ ), artifacts ( $\kappa \geq 0.922$ ),

overall image quality ( $\kappa \geq 0.901$ ), and diagnostic confidence ( $\kappa \geq 0.894$ ).

**Visualization of the Assessed Arteries.** Significant differences were found for the scores of all arteries among the 8 protocols ( $P < .05$ , Online Supplemental Data). No significant difference was found in pair-wise comparison between RS, SF2, and CS2 for all arteries ( $P > .05$ , Online Supplemental Data). Images of RS, SF2, CS2, and CS4 were acceptable for the assessment of all arteries. Visualization of 2 small arteries (left anterior choroidal artery [LACHA] and right anterior choroidal artery [RACHA]) became less reliable (mean score  $< 2$ , Online Supplemental Data) in CS6 images. Reliable visualization of large arteries was still maintained on images of CS8 and CS10 (mean scores  $> 3$ ) but not for some medium-sized and all the small-sized arteries.

**Artifacts and Overall Image Quality.** A typical artifact generated by SENSE was observed in SF4, and speckled noise was found in

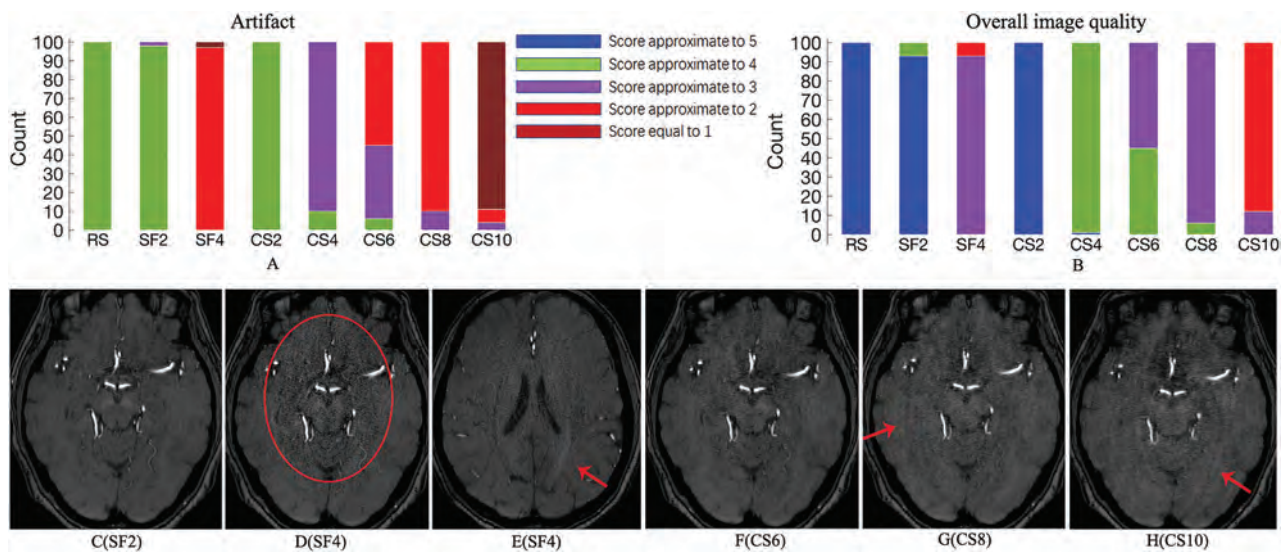


**FIG 3.** Subject count of scores for the 8 protocols about the artifacts (A) and overall image quality (B) and transverse images of different protocols from 1 healthy subject (C–H). Speckled noise is found in the center region of SF4 image (red circle, D) compared with SF2 (C), and the SENSE artifact is observed in SF4 (red arrow, E, different section from D). Curved striped pattern artifacts are obvious for CS8 (G) and CS10 (H) (red arrows), but negligible for CS6 (F).

the center region of images with SF4 (Fig 3D, -E). Curved striped pattern artifacts were obvious for CS8 and CS10 (Fig 3G, -H). For scores of artifacts and overall image quality, no significant differences were found in pair-wise comparisons among RS, SF2, and CS2 (Online Supplemental Data), and the mean scores decreased gradually as the SENSE or CS-SENSE acceleration factor increased (Fig 3).

**Diagnostic Confidence for Arterial Aneurysm and Stenosis.** No significant difference in the diagnostic confidence was found in the pair-wise comparisons among RS, SF2, and CS2 for either arterial stenosis or an aneurysm ( $P > .05$ , Fig 4A, -B). All arterial aneurysms (with diameters ranging from approximately 3 to 8 mm and positions listed in Online Supplemental Data) and most cases of arterial stenosis were well-diagnosed with RS, SF2, and CS2 (nearly all scores were equal to 3 and were considered acceptable), diagnosed with relative certainty with CS4 and CS6 (most scores were equal to 2 and the others were equal to 3, acceptable), and unclearly diagnosed with SF4, CS8, and CS10 (most the scores were  $<2$ ). Notably, the stenoses in the large arteries (listed in the Online Supplemental Data) could be successfully diagnosed on images of all 8 sequences. The zoomed MIP images obtained by the 8 sequences for 1 patient with mild stenosis in the BA (Fig 4C, -J) and for another patient with a tiny arterial aneurysm of the right ICA (Fig 4K, -R) are shown.

## DISCUSSION

In this study, the CS-SENSE technique with 5 different acceleration factors was evaluated for brain 3D TOF-MRA in a cohort of 100 patients with images collected from multiple centers. A reference sequence without acceleration and 2 sequences using the conventional SENSE technique were included for comparison. CS-SENSE with an acceleration factor of 4 could provide balanced image quality and acquisition times.

Obviously reduced image information was found from the quantitative measurements (tendency of RSIs or SSIM) when the CS-SENSE acceleration factors gradually increased from 2 to 10. The possible reason was that sparser data sampling was achieved for scans with higher acceleration factors.<sup>13</sup> Although the mean  $CR_{artery/wm}$  and  $CR_{artery/csf}$  values slowly decreased as the CS-SENSE factor increased, no significant difference was found between CRs for any pairs of SF2, CS2, and CS4, which indicated that imaging contrasts (between assessed arteries and WM/CSF) of CS4 were comparable with those of CS2 and SF2, despite the increased acceleration factor.

CS2 could generate images with almost equally acceptable quality compared with RS but with a reduction of 47.95% in scan time, considering both the comparisons of the qualitative and quantitative assessments. As the CS-SENSE acceleration factor increased from 2 to 4 though there were obvious decreases in some quantitative and qualitative assessments, images of both CS2 and CS4 achieved acceptable image quality through qualitative evaluations, including the visualization of all arteries, qualitative scores of artifacts and overall image quality, and diagnostic confidence of stenosis or aneurysm, according to the criteria in this study. In this sense, CS4 yielded image quality lower than that of CS2, which was a natural outcome of exaggerated under-sampling, but CS4 images were still acceptable for diagnosis from all the perspectives under evaluation in our study.

Given the reduced scan time (reduced by 48.68%) compared with CS2, CS4 could be a practical setup in routine clinical scanning. As the CS-SENSE acceleration factor increased from 4 to 6, visualization of the large and medium arteries was still acceptable, agreeing with the previous study by Yamamoto et al.<sup>12</sup> However, visualization of 2 small arteries (LACHA and RACHA) became unacceptable according to the criteria in this study, which might render CS6 unpromising for examinations of some small arterial disorders, such as the evaluation of small intracranial

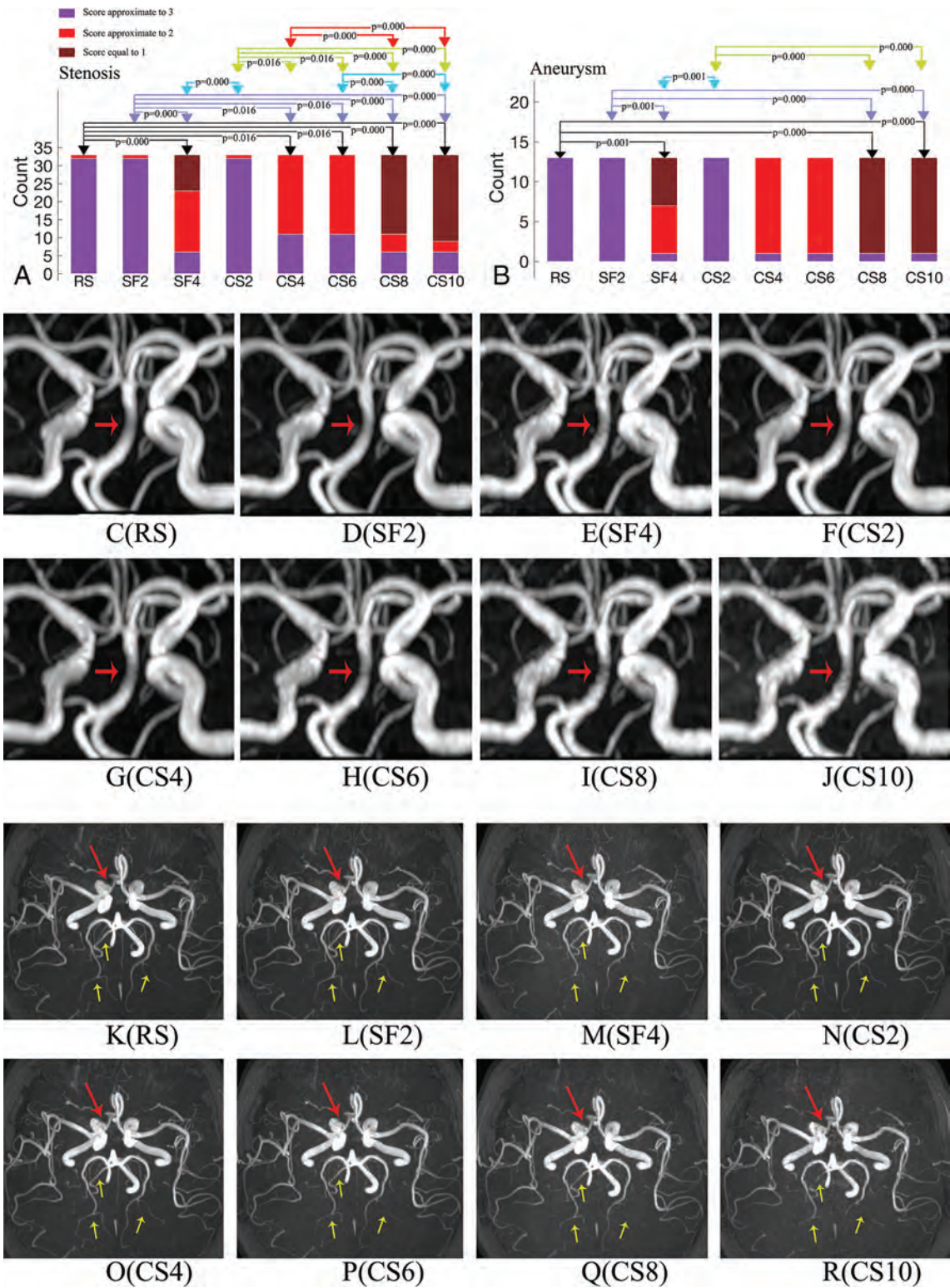


**FIG 4.** Patient count of scores for the 8 protocols of the arterial stenosis (A) and aneurysms (B). Groups with significant differences ( $P < .05$ ) are connected by *double arrow lines*. Zoomed MIP images obtained by the 8 sequences for 1 patient with mild stenosis (anterior view). The BA has a smooth boundary and uniform signal distribution in the region of the stenosis (*red arrow*) in images of RS (C), SF2 (D), and CS2 (F); it is visually acceptable in images of CS4 (G) and CS6 (H), but with rough boundaries and granulated signal distributions in images of SF4 (E), CS8 (I), and CS10 (J). Zoomed MIP images obtained by the 8 sequences for a patient with a tiny arterial aneurysm in the eye segment of right ICA (inferior view). The arterial aneurysm has an explicit boundary (*red arrow*) and can be well-diagnosed in RS (K), SF2 (L), CS2 (N), CS4 (O), and CS6 (P) (mean score = 3) and can be diagnosed with relative certainty in CS8 (Q) and SF4 (M) (mean score = 2); but the boundary becomes rough and unclear in CS10 (R). Additionally, 3 distal arterial branches were marked by *yellow arrows* in each image (K–R). These arterial branches are clear and continuous in RS (K), SF2 (L), CS2 (N), CS4 (O), and CS6 (P), but become discontinuous or even invisible in SF4 (M), CS8 (Q), and CS10 (R).

vasculature and arteriovenous malformations in challenging regions of the skull base.

As the acceleration factor increased to 8 or 10, visualization of small and medium arteries became unacceptable and the diagnostic confidence of arterial stenosis and aneurysms also became less convincing (the small size of aneurysms in this study and excessive sparsity of CS-SENSE might be possible reasons for the misdiagnosis of arterial aneurysms in large arteries). Moreover, curved striped pattern artifacts became obvious, the boundaries of the arteries became rougher, and some small arteries became discontinuous or missing in images. All these factors increase the potential risk of misdiagnosis or unclear diagnosis of possible pathologies. Nevertheless, reliable visualization for large arteries and a high diagnostic rate for all 5 stenoses in large arteries could be achieved by CS10. Considering the unprecedented short scan time (48 seconds), CS10 might be a fast approach for visualization or stenosis screening for large arteries (eg, ICA occlusion for emergency intravascular intervention).

Although conventional SENSE-accelerated TOF-MRA (such as SF2) is clinically effective and widely used for the noninvasive evaluation of cerebrovascular pathology, the long scan duration and vulnerability to motion artifacts can still be problematic for its clinical applications.<sup>25,26</sup> From both qualitative assessments and quantitative measurements, no significant difference was found between CS2 and SF2. The RSIs of assessed arteries, WM, and CSF in images in CS4 were obviously lower than those in SF2 due to the sparse sampling for CS-SENSE; however, the CRs were basically equivalent. Furthermore, considering the acceptable visualization of assessed arteries, overall image quality, relatively certain diagnostic confidence of arterial stenosis and aneurysm, and reduced scan time (reduced by 46.33% compared with SF2), CS4 could be considered a better choice than SF2 in routine clinical settings. Additionally, the overall performance of CS4 was much better than that of SF4. Even for CS6, the RSIs for all assessed arteries, the mean scores for most arteries (14/17, 82%) and the mean scores of artifacts (2.51 versus 1.97), and the overall image quality (3.45 versus 2.93) were still higher than those with SF4. Moreover, the diagnostic confidence for arterial aneurysms and stenosis with CS6 was higher than that with SF4. These observations suggest the use of higher acceleration factors with CS-SENSE in TOF-MRA clinical setups than with conventional SENSE, which was consistent with previous studies.<sup>8,12</sup>

Speckled noise and SENSE artifacts were commonly observed in the central part of TOF-MRA images with SF4, which was also mentioned in previous studies,<sup>8</sup> while these SENSE ghost artifacts were rarely seen on the CS-SENSE images. However, in this study, curved striped pattern artifacts were observed when the CS-SENSE acceleration factor was >6 (obvious in CS8 and CS10), especially around the skull boundaries. The possible origin of these curved striped pattern artifacts was thought to be related to the phase-encoding direction and sparse sampling, possibly derived from the outer edge of the skull.<sup>18</sup>

The current study has several limitations. First, the final diagnosis of the arterial pathologies was confirmed by comprehensive consideration of the MRA images, the routine MR images (T1, T2, FLAIR, DWI, and SWI), and any other available clinical data. DSA was not considered essential in this study due to its invasive

procedure. Furthermore, several studies have verified a good correlation between MRA and DSA.<sup>4,5,27</sup> Second, only 2 cerebrovascular pathologies (arterial stenosis and aneurysm) were assessed in this study. The performance of MRA with different CS-SENSE acceleration factors for other possible vessel pathologies (eg, vascular malformation) still merits further investigation. Additionally, the influence of CS-SENSE on the diameters of aneurysms or rates of stenosis was not included in the study, which would also be considered in future studies. Third, no comparison was performed among different centers in this study. Fourth, the number of iterations in the CS reconstruction that might have influenced the image quality<sup>6</sup> was not included. Fifth, only 1 neuroradiologist was chosen for ROI drawing. Although we believe that the neuroradiologist with >10 years of experience was professional in drawing ROIs,  $\geq 2$  readers would be better. Sixth, spiral TOF-MRA, which potentially delivers high-quality intracranial vessel imaging at a short scan time, was not included for comparison in the study<sup>28,29</sup> and will be studied in future work.

## CONCLUSIONS

The CS-SENSE technique with an acceleration factor of 4 is generally acceptable for brain 3D TOF-MRA in clinical setups at 3T with balanced image quality and acquisition times (117 seconds), while CS6 (79 seconds) can be used for examinations in which small arteries are not evaluated and CS10 (48 seconds) may be suitable for fast visualization of large arteries.

## ACKNOWLEDGMENTS

We thank Rongkai Ju and Yishi Wang for support in writing this article.

Disclosures: Jiazheng Wang—UNRELATED: Employment: Philips Healthcare. Liangjie Lin—UNRELATED: Employment: Philips Healthcare.

## REFERENCES

1. Chung MS, Jung SC, Kim SO, et al. **Intracranial artery stenosis: diagnosis by using two-dimensional spatially selective radio-frequency excitation pulse MR imaging.** *Radiology* 2017;284:834–43 CrossRef Medline
2. Mandell DM, Mossa-Basha M, Qiao Y, et al. Vessel Wall Imaging Study Group of the American Society of Neuroradiology. **Intracranial Vessel Wall MRI: Principles and Expert Consensus Recommendations of the American Society of Neuroradiology.** *AJNR Am J Neuroradiol* 2017;38:218–29 CrossRef Medline
3. Park JE, Jung SC, Lee SH, et al. **Comparison of 3D magnetic resonance imaging and digital subtraction angiography for intracranial artery stenosis.** *Eur Radiol* 2017;27:4737–46 CrossRef Medline
4. Debrey SM, Yu H, Lynch JK, et al. **Diagnostic accuracy of magnetic resonance angiography for internal carotid artery disease: a systematic review and meta-analysis.** *Stroke* 2008;39:2237–48 CrossRef Medline
5. van Rooij WJ, Sprengers ME, de Gast AN, et al. **3D rotational angiography: the new gold standard in the detection of additional intracranial aneurysms.** *AJNR Am J Neuroradiol* 2008;29:976–79 CrossRef Medline
6. Fushimi Y, Fujimoto K, Okada T, et al. **Compressed sensing 3-dimensional time-of-flight magnetic resonance angiography for cerebral aneurysms: optimization and evaluation.** *Invest Radiol* 2016;51:228–35 CrossRef Medline

7. Li B, Li H, Dong L, et al. **Fast carotid artery MR angiography with compressed sensing based three-dimensional time-of-flight sequence.** *Magn Reson Imaging* 2017;43:129–35 CrossRef Medline
8. Lin Z, Zhang X, Guo L, et al. **Clinical feasibility study of 3D intracranial magnetic resonance angiography using compressed sensing.** *J Magn Reson Imaging* 2019;50:1843–51 CrossRef Medline
9. Bhagat YA, Emery DJ, Naik S, et al. **Comparison of generalized autocalibrating partially parallel acquisitions and modified sensitivity encoding for diffusion tensor imaging.** *AJNR Am J Neuroradiol* 2007;28:293–98 Medline
10. Preibisch C, Wallenhorst T, Heidemann R, et al. **Comparison of parallel acquisition techniques generalized autocalibrating partially parallel acquisitions (GRAPPA) and modified sensitivity encoding (mSENSE) in functional MRI (fMRI) at 3T.** *J Magn Reson Imaging* 2008;27:590–98 CrossRef Medline
11. Larkman DJ, Nunes RG. **Parallel magnetic resonance imaging.** *Phys Med Biol* 2007;52:R15–55 CrossRef Medline
12. Yamamoto T, Fujimoto K, Okada T, et al. **Time-of-flight magnetic resonance angiography with sparse undersampling and iterative reconstruction: comparison with conventional parallel imaging for accelerated imaging.** *Invest Radiol* 2016;51:372–78 CrossRef Medline
13. Lustig M, Donoho D, Pauly JM. **Sparse MRI: the application of compressed sensing for rapid MR imaging.** *Magn Reson Med* 2007;58:1182–95 CrossRef Medline
14. Lu SS, Qi M, Zhang X, et al. **Clinical evaluation of highly accelerated compressed sensing time-of-flight MR angiography for intracranial arterial stenosis.** *AJNR Am J Neuroradiol* 2018;39:1833–38 CrossRef Medline
15. Greve T, Sollmann N, Hock A, et al. **Highly accelerated time-of-flight magnetic resonance angiography using spiral imaging improves conspicuity of intracranial arterial branches while reducing scan time.** *Eur Radiol* 2020;30:855–65 CrossRef Medline
16. Zhang X, Cao YZ, Mu XH, et al. **Highly accelerated compressed sensing time-of-flight magnetic resonance angiography may be reliable for diagnosing head and neck arterial steno-occlusive disease: a comparative study with digital subtraction angiography.** *Eur Radiol* 2020;30:3059–65 CrossRef Medline
17. Suh CH, Jung SC, Lee HB, et al. **High-resolution magnetic resonance imaging using compressed sensing for intracranial and extracranial arteries: comparison with conventional parallel imaging.** *Korean J Radiol* 2019;20:487–97 CrossRef Medline
18. Yamamoto T, Okada T, Fushimi Y, et al. **Magnetic resonance angiography with compressed sensing: an evaluation of Moyamoya disease.** *PLoS One* 2018;13:e0189493 CrossRef Medline
19. Geerts-Ossevoort L, de Weerd E, Duijndam A, et al. **Compressed SENSE. Speed done right. Every time.** Philips Healthcare, Netherlands, 2018. <https://philipsproductcontent.blob.core.windows.net/assets/20180109/619119731f2a42c4acd4a863008a46c7.pdf>. Accessed May 1, 2020
20. Bratke G, Rau R, Weiss K, et al. **Accelerated MRI of the lumbar spine using compressed sensing: quality and efficiency.** *J Magn Reson Imaging* 2019;49:e164–75 CrossRef Medline
21. Lustig M, Pauly JM. **SPIRiT: Iterative self-consistent parallel imaging reconstruction from arbitrary k-space.** *Magn Reson Med* 2010;64:457–71 CrossRef Medline
22. Okubo G, Okada T, Yamamoto A, et al. **MP2RAGE for deep gray matter measurement of the brain: a comparative study with MPRAGE.** *J Magn Reson Imaging* 2016;43:55–62 CrossRef Medline
23. Altahawi FF, Blount KJ, Morley NP, et al. **Comparing an accelerated 3D fast spin-echo sequence (CS-SPACE) for knee 3-T magnetic resonance imaging with traditional 3D fast spin-echo (SPACE) and routine 2D sequences.** *Skeletal Radiol* 2017;46:7–15 CrossRef Medline
24. Wang Z, Bovik AC, Sheikh HR, et al. **Image quality assessment: from error visibility to structural similarity.** *IEEE Trans Image Process* 2004;13:600–12 CrossRef Medline
25. Willinsky RA, Taylor SM, TerBrugge K, et al. **Neurologic complications of cerebral angiography: prospective analysis of 2,899 procedures and review of the literature.** *Radiology* 2003;227:522–28 CrossRef Medline
26. Wu H, Block WF, Turski PA, et al. **Noncontrast-enhanced three-dimensional (3D) intracranial MR angiography using pseudocontinuous arterial spin labeling and accelerated 3D radial acquisition.** *Magn Reson Med* 2013;69:708–15 CrossRef Medline
27. Borisch I, Horn M, Butz B, et al. **Preoperative evaluation of carotid artery stenosis: comparison of contrast-enhanced MR angiography and duplex sonography with digital subtraction angiography.** *AJNR Am J Neuroradiol* 2003;24:1117–22 Medline
28. Sartoretti T, van Smoorenburg L, Sartoretti E, et al. **Ultrafast intracranial vessel imaging with non-Cartesian spiral 3-dimensional time-of-flight magnetic resonance angiography at 1.5 T.** *Invest Radiol* 2020;55:293–303 CrossRef Medline
29. Sartoretti T, Sartoretti E, Schwenk A, et al. **Clinical feasibility of ultrafast intracranial vessel imaging with non-Cartesian spiral 3D time-of-flight MR angiography at 1.5T: an intra-individual comparison study.** *PLoS One* 2020;15:e0232372 CrossRef Medline

# Relationship between Shear Stiffness Measured by MR Elastography and Perfusion Metrics Measured by Perfusion CT of Meningiomas

T. Takamura, U. Motosugi, M. Ogiwara, Y. Sasaki, K.J. Glaser, R.L. Ehman, H. Kinouchi, and H. Onishi



## ABSTRACT

**BACKGROUND AND PURPOSE:** When managing meningiomas, intraoperative tumor consistency and histologic subtype are indispensable factors influencing operative strategy. The purposes of this study were the following: 1) to investigate the correlation between stiffness assessed with MR elastography and perfusion metrics from perfusion CT, 2) to evaluate whether MR elastography and perfusion CT could predict intraoperative tumor consistency, and 3) to explore the predictive value of stiffness and perfusion metrics in distinguishing among histologic subtypes of meningioma.

**MATERIALS AND METHODS:** Mean tumor stiffness and relative perfusion metrics (blood flow, blood volume, and MTT) were calculated (relative to normal brain tissue) for 14 patients with meningiomas who underwent MR elastography and perfusion CT before surgery (cohort 1). Intraoperative tumor consistency was graded by a neurosurgeon in 18 patients (cohort 2, comprising the 14 patients from cohort 1 plus 4 additional patients). The correlation between tumor stiffness and perfusion metrics was evaluated in cohort 1, as was the ability of perfusion metrics to predict intraoperative tumor consistency and discriminate histologic subtypes. Cohort 2 was analyzed for the ability of stiffness to determine intraoperative tumor consistency and histologic subtypes.

**RESULTS:** The relative MTT was inversely correlated with stiffness ( $P = .006$ ). Tumor stiffness was positively correlated with intraoperative tumor consistency ( $P = .01$ ), while perfusion metrics were not. Relative MTT significantly discriminated transitional meningioma from meningothelial meningioma ( $P = .04$ ), while stiffness did not significantly differentiate any histologic subtypes.

**CONCLUSIONS:** In meningioma, tumor stiffness may be useful to predict intraoperative tumor consistency, while relative MTT may potentially correlate with tumor stiffness and differentiate transitional meningioma from meningothelial meningioma.

**ABBREVIATIONS:** BF = blood flow; BV = blood volume; CUSA = Clarity Ultrasonic Surgical Aspirator System; MRE = MR elastography; PCT = perfusion CT; rBF = relative BF; rBV = relative BV; rMTT = relative MTT

Meningioma is the most common primary intracranial tumor with an incidence of approximately 8 cases per 10,000 persons per year.<sup>1</sup> Radiosurgery, chemotherapy, or arterial embolization play supplementary roles, though surgical resection is the primary treatment for meningiomas. Tumor consistency is recognized as a major

indicator of complete resection for meningiomas.<sup>2</sup> To date, various imaging modalities including T2-weighted images, diffusion MR imaging measurements, and magnetization transfer imaging have been investigated to predict meningioma consistency.<sup>3</sup> However, there have been conflicting results, and no widely accepted method has been established.

MR elastography (MRE) is a dynamic MR imaging-based technique used for the noninvasive measurement of the mechanical properties of soft tissue *in vivo*.<sup>4</sup> Recently, the mechanical properties of the brain have been studied in normal aging,<sup>5-9</sup> Alzheimer disease,<sup>6,10,11</sup> Parkinson disease,<sup>12</sup> frontotemporal dementia,<sup>6</sup> normal pressure hydrocephalus,<sup>6</sup> and brain tumors,<sup>13</sup> including meningiomas.<sup>14-17</sup> More recently, slip interface imaging using specialized processing of MRE data was shown to provide a dynamic measure of adherence between the tumor and the adjacent brain tissue.<sup>18</sup>

The global shear modulus of soft biologic tissue can be influenced by the scale of perfusion,<sup>19</sup> which relates to the topology

Received June 20, 2020; accepted after revision January 10, 2021.

From the Department of Radiology (T.T.), Shizuoka General Hospital, Shizuoka, Japan; Department of Radiology (T.T.), Juntendo University, Tokyo, Japan; Department of Radiology (U.M.), Kofu-Kyoritsu Hospital, Yamanashi, Japan; Departments of Neurosurgery (M.O., H.K.) and Radiology (Y.S., H.O.), University of Yamanashi, Yamanashi, Japan; and Department of Radiology (K.J.G., R.L.E.), Mayo Clinic College of Medicine, Rochester, Minnesota.

This work was supported, in part, by the National Institutes of Health, R37 EB001981.

Please address correspondence to Tomohiro Takamura, MD, PhD, Department of Radiology, Shizuoka General Hospital, 4-27-1 Kita Aoi-ku, Shizuoka City 420-8527, Japan; e-mail: t-takamura@i.shizuoka-pho.jp

Indicates open access to non-subscribers at www.ajnr.org

Indicates article with online supplemental data.

<http://dx.doi.org/10.3174/ajnr.A7117>

and geometry of microvessels,<sup>20</sup> indicating a potential effect of perfusion on the macroscopic viscoelastic response of brain tissue. Previous MRE studies have indicated a close correlation between tissue perfusion and mechanical properties in the brain<sup>21,22</sup> and abdominal organs.<sup>23</sup> Moreover, in investigations of the pathologic determinants underpinning MRE data,<sup>24,25</sup> microvascular density, which is related to perfusion metrics,<sup>21</sup> has been shown to contribute to the stiffness of soft brain tumor models in mice. Nevertheless, the perfusion conditions and mechanical properties of meningiomas have not been concurrently analyzed. Meningioma consistency and histologic subtype are indispensable factors influencing operative strategy and patient counseling. Recently, MRE has been increasingly recognized as a useful indicator of meningioma consistency,<sup>14-17</sup> while perfusion metrics provide physiologic and functional information about the tumor microenvironment. Because stiffness and perfusion status are intricately related, MRE and perfusion metrics may serve to preoperatively characterize the viscoelastic properties of meningiomas and further develop clinically applicable predictors for intraoperative tumor consistency. Relatively few studies have reported the relationship between stiffness<sup>16</sup> or perfusion metrics<sup>26-28</sup> and histologic subtype, and no definite association has been established. Investigating the relationship of stiffness and perfusion metrics to intraoperative meningioma consistency and histologic subtypes may contribute to understanding and objective comparison of these techniques and provide valuable information affecting risk assessment, patient management, and workflow optimization.

The purposes of this study were the following: 1) to investigate the correlation between stiffness and perfusion metrics, 2) to evaluate whether preoperative MRE and perfusion metrics could predict intraoperative tumor consistency, and 3) to explore the predictive value of stiffness and perfusion metrics in distinguishing among histologic subtypes of meningiomas.

## MATERIALS AND METHODS

### Subjects

This retrospective study was approved by institutional review board of University of Yamanashi Hospital. Between May 2017 and September 2019, twenty-seven meningiomas of 27 patients who underwent MRE and received pathologic confirmation of meningioma with subsequent radical resection were included in this study. For the correlation analysis between stiffness measured by MRE and perfusion metrics measured by perfusion CT (PCT), between perfusion metrics and intraoperative tumor consistency, as well as group analysis of pathologic subtype for perfusion metrics, patients were excluded under the following circumstances: 1) Preoperative endovascular embolization for tumors was performed, 2) tumors were clinically confirmed as locally recurring, 3) tumors were resected en bloc without the use of air aspiration or the Clarity Ultrasonic Surgical Aspirator System (CUSA; Integra LifeSciences), 4) there was no available PCT examination within 12 weeks of the MRE examination, or 5) PCT data were not successfully analyzed by the Perfusion Mismatch Analyzer software (PMA; ASIST Group). Of the 27 patients, we excluded 13 patients: Seven underwent endovascular embolization, 1 was a local recurrence case, 3 lacked an available PCT examination, and

2 were excluded because their PCT data were not successfully analyzed by the PMA software. Additionally, 1 of the 3 patients lacking an available PCT examination had undergone en bloc resection. The reason for the PCT data miscalculation by the PMA software in 1 case was the irregular arterial attenuation curve due to the presence of metal-related artifacts from previously implanted clips for a cerebral aneurysm independent of the meningioma. The reason for the other case was unclear.

Of these 13 excluded patients, 4 patients (2 lacked an available PCT and 2 whose PCT data were not successfully analyzed) who did not fulfill the following exclusion criteria (ie, 1) preoperative endovascular embolization for tumors was performed, 2) the tumors were clinically confirmed as locally recurring and, 3) the tumors were resected en bloc without the use of air aspiration or the CUSA) were additionally included in the correlation analysis between stiffness and intraoperative tumor consistency as well as the group analysis of pathologic subtype for stiffness because they were considered to have no intervention during the period between the MRE examination and the operation. Finally, 14 patients were included for the correlation analysis between stiffness and perfusion metrics, between perfusion metrics and intraoperative tumor consistency, and the group analysis of pathologic subtype for perfusion metrics (cohort 1), while 18 patients were included for the correlation analysis between stiffness and intraoperative tumor consistency and the group analysis of pathologic subtype for stiffness (cohort 2).

### Surgical Assessment of Tumor Consistency

Intraoperative tumor consistency was defined on the basis of the CUSA amplitude applied for tumor removal. The CUSA amplitude setting was determined in 10 steps and ranged from 10% to 100%. These values were consistently chosen by 1 operating neurosurgeon (M.O.) for all cases. The intraoperative tumor consistency score was defined as a value of 1/10 of the CUSA amplitude (eg, a CUSA amplitude of 50% was defined as score 5). If the tumor was removed solely by using air aspiration without the use of CUSA, the intraoperative tumor consistency score was defined as score 0. If >1 CUSA setting was used for tumor removal, the mean value of the intraoperative tumor consistency scores was applied.

### PCT Technique

The PCT examination was performed using a 320-section multi-detector row CT scanner (Aquilion ONE; Toshiba). For the perfusion scan, 70 mL of nonionic iodinated contrast medium, iopamidol (370 mg I/mL, Imeron; Eisai) was injected at a rate of 5 mL/s through the right antecubital vein. A total of 20 volumes covering the whole brain was acquired; each volume comprised 320 images of 0.5 mm-thick sections that covered a total of 16 cm of the head in the superior-inferior direction. The first volume was acquired with an acquisition delay of 5 seconds after the injection of contrast media, allowing the acquisition of baseline images without contrast enhancement, which were used as a mask for obtaining bone subtraction. Next, 10 volumes of the brain were acquired starting at 12 seconds after the injection of contrast media at a sampling interval of 1 volume every 1 second. Then, 5 volumes were acquired starting at 22 seconds after the

injection at a sampling interval of 1 volume every 2 seconds. Subsequently, 3 volumes were acquired starting at 35 seconds after the injection at a sampling interval of 1 volume every 3 seconds. Finally, 1 volume was acquired at 47 seconds.

Block circulant singular value decomposition perfusion maps, including tumor blood flow (BF), blood volume (BV), and MTT, were calculated directly from the residue function using the PMA software. Nonparenchymal vascular voxels were automatically excluded by temporal intensity thresholding. Arterial voxels were identified automatically by identifying the vascular voxels with the earliest peak enhancement. The arterial and venous reference voxels were selected automatically under supervision. All perfusion maps were converted to 2-mm section thickness using nearest-neighbor interpolation.

### MRE Technique

MRE data acquisition was conducted with a spin-echo EPI MRE sequence<sup>5,6,10,11,29,30</sup> on a 3T MR imaging scanner (Discovery 750; GE Healthcare). Shear waves were introduced into the brain with a soft pillowlike passive driver designed for brain MRE that was placed under the subject's head within a 32-channel phased array coil. A pneumatic actuator (Resoundant)<sup>31</sup> that was placed outside the MR imaging examination room produced pneumatic pressure waves and vibrated the brain at a mechanical frequency of 60 Hz. 3D wavefield imaging was repeated to capture motion along the positive and negative x, y, and z directions through 6 phase offsets to observe wave propagation in time. The imaging parameters were as follows: axial slices, TR = 3600 ms, TE = 62 ms, no signal averaging, FOV = 24 × 24 cm<sup>2</sup>, acquisition matrix = 128 × 128, parallel imaging acceleration factor = 3, section thickness = 3 mm with no section gap, and acquisition time = about 5 minutes. Depending on the subject, 48–50 sections were acquired to cover the entire brain.

Stiffness maps were automatically created on the MR imaging scanner using a previously described pipeline.<sup>9</sup> In brief, stiffness maps were generated in 3 steps. In the first step, the temporal harmonic of the curl of the displacement images was calculated. In the second step, the results were smoothed with quartic smoothing kernels of the form  $(1-x^2)^2 \times (1-y^2)^2 \times (1-z^2)$ , where x, y, and z are linearly spaced from -1 to 1. In the third step, the first-harmonic curl wave information was calculated using a direct inversion of the Helmholtz wave equation. The complex shear modulus values were then median-filtered using a 3 × 3 × 3 median filter. Next, shear stiffness maps (elastograms), ie, the magnitude of the complex shear modulus, were created on the scanner, from which regional stiffness information could be measured.

### Image Processing

ROIs of the tumor were manually drawn on the magnitude images for the MRE and on the delayed postcontrast images for the PCT by a board-certified neuroradiologist with 10 years of experience, blinded to the surgical findings (T.T.). For MRE, the ROI used for reporting tumor stiffness was eroded by 3 voxels from every edge to remove edge artifacts; this procedure was previously reported as a method to minimize partial volume effects and edge-related bias.<sup>31</sup>

For perfusion metrics, we normalized the absolute quantified BF, BV, and MTT values using the brain mask created by manually contouring the brain parenchyma excluding the CSF on the delayed postcontrast images to increase the robustness of regional physiologic measures by removing variations due to the arterial input function<sup>32</sup> and variations in cardiac output.<sup>33</sup>

Maps of BF, BV, and MTT (defined as relative BF [rBF], relative BV [rBV], and relative MTT [rMTT], respectively) were calculated by dividing each voxel value by the mean value of the brain mask. The tumor volume was computed from the tumor ROI drawn on MRE magnitude images.

### Statistical Analysis

Correlations between stiffness and the perfusion metrics rBF, rBV, and rMTT; stiffness and the intraoperative tumor consistency score; and the perfusion metrics rBF, rBV, and rMTT and the intraoperative tumor consistency score were evaluated using the Spearman rank correlation test.

On the basis of the results of correlation analyses, patients in cohort 1 were also grouped according to the median value of stiffness in our cohort into the “high-stiffness” group ( $\geq 2.9$  kPa) or the “low-stiffness” group ( $< 2.9$  kPa). The receiver operating characteristic curve was used to investigate the predictive ability of perfusion metrics for tumor stiffness. Cutoff values of perfusion metrics were determined by maximizing the Youden index on the estimated curves. Tumor stiffness and perfusion metrics among the histologic subtypes were analyzed using a nonparametric analysis of variance (Kruskal-Wallis test) and the Steel-Dwass test for post hoc comparisons.  $P < .05$  was considered statistically significant (2-tailed). All statistical analyses were performed using commercial software (JMP, Version 13.0.0; SAS Institute).

## RESULTS

Patient demographics, tumor location, tumor volume, intraoperative tumor consistency score, histologic subtype, and cohort are summarized in the Online Supplemental Data. In 7 of 18 meningiomas in cohort 2, two different CUSA settings were used; therefore, the mean intraoperative tumor consistency score was applied. The mean age of the 18 patients (14 women) was 62.8 (SD, 15.3) years, and the median intraoperative tumor consistency score was 3 (range, 1–8). All cases required the use of CUSA for tumor removal. MRE measured the mean stiffness as 3.12 (SD, 1.23) kPa, and the median mean stiffness was 2.89 kPa for 18 meningiomas. The mean values of rBF, rBV, and rMTT for cohort 1 were 3.37 (SD, 2.56), 3.95 (SD, 3.19), and 1.13 (SD, 0.17), respectively.

Correlations between perfusion metrics and stiffness are shown in Fig 1. rMTT was inversely correlated with stiffness ( $r = -0.69$ ,  $P = .006$ ) (Fig 1C). However, rBF and rBV were not significantly correlated with tumor stiffness (Fig 1A, -B).

A plot of mean tumor stiffness versus the intraoperative tumor consistency score is shown in Fig 2. Stiffness was significantly positively correlated with intraoperative tumor consistency ( $r = 0.59$ ,  $P = .01$ ) (Fig 2). There was no correlation between all perfusion metrics (rBF, rBV, and rMTT) and the intraoperative tumor consistency score.

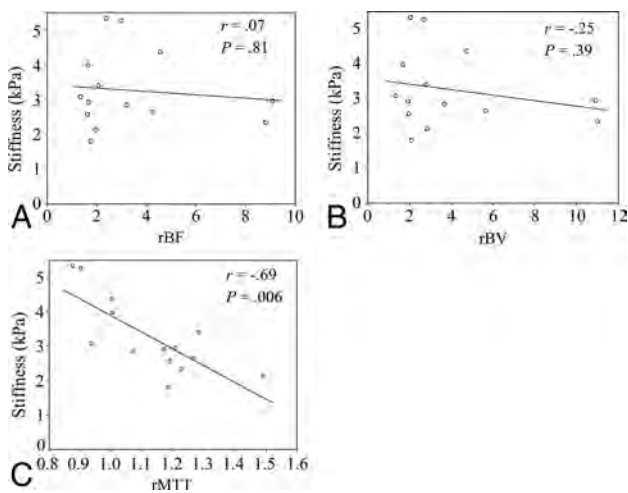


**FIG 1.** Scatterplot along with the least squares fitted line of tumor stiffness (kilopascal) measured using MRE and perfusion metrics measured using PCT in 14 patients with meningiomas. Graphs show stiffness versus rBF (A), rBV (B), and rMTT (C).

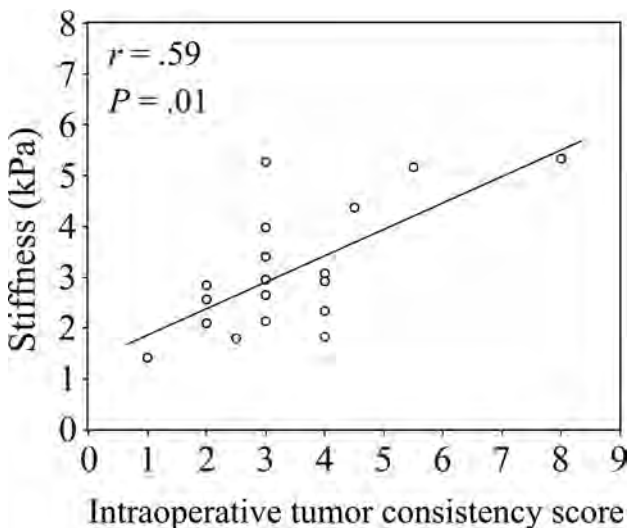


**FIG 2.** Scatterplot along with the least squares fitted line of tumor stiffness (kilopascal) measured using MRE and the intraoperative tumor consistency score in 18 patients with meningiomas.

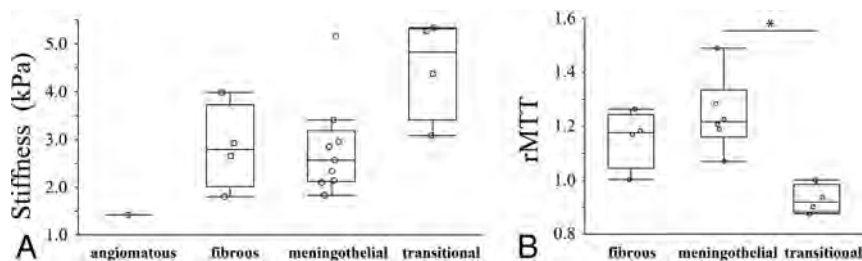


**FIG 3.** Boxplot of stiffness (kilopascal) (A) and rMTT (B) among histologic subtypes of meningioma. The lower and upper hinges of the boxes represent the 25th and 75th percentiles, respectively. The line within the box denotes the 50th percentile (median), and the whiskers indicate the maximum and minimum values. The asterisk indicates  $P < .05$  for post hoc comparisons (Steel-Dwass test).

Receiver operating characteristic analysis revealed that rMTT was a good predictor of tumors in the high-stiffness group (stiffness  $\geq 2.9$  kPa) (area under the receiver operating characteristic curve = 0.81,  $P = .02$ ). By means of a cutoff value of  $< 1.00$ , the sensitivity and specificity of rMTT for predicting tumors with high stiffness were 62.5% (5/8) and 100% (6/6), respectively.

Of the 18 meningiomas in cohort 2, nine meningothelial meningiomas, 4 fibrous meningiomas, 4 transitional meningiomas, and 1 angiomatous meningioma were pathologically confirmed, while 6 meningothelial meningiomas, 4 fibrous meningiomas, and 4 transitional meningiomas were pathologically confirmed for 14 meningiomas in cohort 1. Results from the Kruskal-Wallis test revealed significant differences in stiffness ( $P = .04$ ) (Fig 3A) and rMTT ( $P = .01$ ) (Fig 3B) among meningioma subtypes. However, there were no significant differences in rBF and rBV among meningioma subtypes. The intraoperative tumor consistency score also showed no significant differences with respect to meningioma subtypes for both cohort 1 and cohort 2. Post hoc analysis revealed that the rMTT of the transitional meningiomas was significantly lower than that of the meningothelial meningiomas ( $P = .04$ ) (Fig 3B).

Three representative meningioma cases are shown in the Online Supplemental Data. The stiffness maps (second row) and rMTT maps (bottom row) demonstrate a trend whereby rMTT decreased as stiffness increased. The rBF and rBV of a 42-year-old woman with a transitional meningioma, with a stiffness of 5.34 kPa (right column), were lower than those of a 72-year-old woman with a fibrous meningioma and stiffness of 2.65 kPa (left column). However, the rBF and rBV of the transitional meningioma of the 42-year-old woman (right column) were higher than those of a fibrous meningioma of a 62-year-old man (middle column), indicating that rBF and rBV were not necessarily correlated with the stiffness value.

## DISCUSSION

In this study, we demonstrated that rMTT measured by PCT was negatively correlated with tumor stiffness, but rBF and rBV were not. We also found that the meningioma stiffness and the intraoperative tumor consistency score were positively correlated.

An increased pathologic grading of fibrosis has been demonstrated to cause an increase in intraoperative tumor consistency in meningiomas.<sup>34</sup> Conversely, perfusion conditions, including BF or BV, are also important factors that influence stiffness. For example, increased viscoelastic parameters are correlated with increased BF in the brain<sup>21,22</sup> and increased BV in the liver.<sup>23</sup> In addition, perfusion metrics, including BV<sup>35</sup> or BF,<sup>36</sup> are positively correlated with microvascular density in meningiomas. Collectively, perfusion metrics including BF and BV and fibrosis may both intrinsically increase meningioma stiffness. Results from a previous animal experiment that used sonographic elastography indicated that vessel density and

stiffness were negatively correlated in a stiff tumor model with increasing amounts of collagen; however, vessel density and stiffness were positively correlated in a soft-tumor model with perfused cores and less collagen.<sup>25</sup> These results suggest that the degree of contribution of vascular density or fibrosis to tumor stiffness may vary according to the balance of pathologic contents. The complex relationship between vascular and fibrosis content may explain the lack of a positive correlation between BF and BV and stiffness in this study.

A marked correlation between rMTT and stiffness was observed in this study. Despite the widespread application in stroke imaging, the concept of MTT has not been as fully studied as BV in the context of oncologic imaging. MTT can be defined as the average time taken for blood to transfer between arterial inflow and venous outflow; therefore, increased MTT indicates a slow flow rate and a delayed exit of contrast agent into the venous system among tumors. MTT depends on the pathway taken by the blood traveling from arteries to veins, which depends on local tissue hemodynamics due to vascular network patterns. One possible explanation for the significant negative correlation between stiffness and rMTT in our study is that the difference in contrast agent excretion conditions due to the complexity of the intratumoral vascular pathway derived from architectural distortions caused by fibrosis within the tumor may be related to stiffness changes.

It is useful for neurosurgeons to know the stiffness of a meningioma before the operation because strategies and equipment are not the same for patients with stiff and soft tumors. Consistent with our results, previous studies have reported that MRE-measured meningioma stiffness is positively correlated with the tumor consistency assessed by a similar 5-point scale determined by surgeons.<sup>14-16</sup> In our criteria, we applied the mean value of the CUSA setting for tumors with 2 distinct consistency components (7 cases) whose value was considered to be derived from both components of the tumor. However, because the tumor margins were removed to create the final ROI, peripheral regions, such as the site of attachment of the meningioma to the dura, were not included in the stiffness measurements. Thus, the reported stiffness was likely biased toward the central areas. Therefore, the reported stiffness of internally heterogeneous tumors may have been underestimated or overestimated when the stiffer components were peripherally or centrally biased, respectively. The CUSA setting is probably not always a proper indicator of the tumor consistency. Nevertheless, our grading system highlights the possibility of estimating the CUSA settings required for tumor removal, which may be useful for the preoperative planning of meningiomas.

In this study, rMTT showed no significant correlation with intraoperative tumor consistency. A plausible explanation for the discrepancy in diagnostic ability between stiffness and rMTT might be the potentially superior diagnostic ability of MRE for intraoperative tumor consistency, in addition to reproducibility differences among the techniques. The within-subject coefficient of variation for brain shear stiffness of normal brain tissue was reportedly 1.8%–3.5% at the same mechanical frequency (60 Hz) as in our study;<sup>37</sup> however, MTT measured by PCT for normal brain tissue was reported as 8.8%.<sup>38</sup> Therefore, the potentially

higher variability expected in the reported rMTT value might lead to a lower correlation with intraoperative tumor consistency, especially with our small sample size and our scoring system, which was highly subdivided into the 11-point scale. This scoring system may have been sensitive to intraoperator variability in CUSA setting determination.

Although stiffness was highly correlated with rMTT, stiffness of the transitional meningioma and meningothelial meningioma was not significantly different, contrary to rMTT. One possible explanation for this discrepancy might be related to our postprocessing method for MRE. Because we eroded the tumor margins to create the final ROI for MRE, the reported stiffness would be biased toward the central tumor area and might not be adequately reflecting the mechanical properties of the whole tumor. In the case with considerably higher stiffness (5.17 kPa) than other cases of meningothelial meningiomas (Fig 3A), the 18th case in the Online Supplemental Data, the CUSA setting at the central area was 90%, while it was 20% in the periphery. This finding suggests that the reported stiffness was overestimated relative to the entire tumor. Another factor might be the limited statistical power due to the small sample size included in each histologic subtype and the relatively large number of subgroups. However, Sakai et al<sup>16</sup> suggested that MRE may be able to distinguish relatively firm meningiomas, such as fibrous and transitional meningiomas, from relatively soft meningiomas, such as meningothelial meningiomas; however, statistical analyses were not performed in that study. Moreover, although there was only 1 case, the stiffness of an angiomatous meningioma, typically a soft tumor,<sup>39</sup> was the lowest in all cases in our study (Fig 3A). These findings may suggest the potential relationship between stiffness and histologic subtype in meningioma. Further research with a larger sample size and a more devised postprocessing method reducing edge-related artifacts<sup>31</sup> is required to elucidate whether MRE has a potential ability to predict pathologic meningioma subtypes.

To characterize the relationship between perfusion metrics and subtypes, Zhang et al<sup>26</sup> used dynamic susceptibility contrast perfusion MR imaging and reported that the tumoral BV of angiomatous meningiomas was significantly higher than that of meningothelial, fibrous, or anaplastic meningiomas. Additionally, Kimura et al<sup>28</sup> used spin-labeling perfusion MR imaging and reported that the BF was significantly increased in angiomatous meningiomas compared with that in fibrous and meningothelial meningiomas. Nevertheless, these reports focused on the differentiation between angiomatous meningioma, which is typically a soft and vascular-rich tumor,<sup>39</sup> and other subtypes that are not as vascular. However, as discussed above, the relationship between fibrosis and vascular density may confound each other in a complex manner; therefore, we cannot apply their results to our comparison between consistency and perfusion metrics.

This study had several limitations. First, the number of subjects was small, particularly the number of subjects with high intraoperative tumor consistency. Therefore, the current results might be too susceptible to outlier data to be clinically meaningful. Future prospective studies with larger sample sizes and more uniformly distributed data are necessary to confirm our preliminary results. Second, although we used an intraoperative tumor

consistency score based on the CUSA setting that was applied for tumor removal in an effort to establish a quantitative method, the use of this analysis with the erosion of edge pixels from the ROIs to manage edge artifacts may have resulted in a disagreement between intraoperative assessment and imaging parameters based on the location of stiffer/softer components in internally heterogeneous tumors. Therefore, applying a method that accounts for spatial variability in the stiffness or perfusion metrics and allows a more detailed comparison based on each distinct component of the tumor is preferable. Third, our study lacked an examination of the histopathologic components corresponding to tumor stiffness and perfusion metrics. An investigation of the histopathologic determinants underpinning stiffness or perfusion metrics, including collagenous content, cellular architecture (including cellular arrangement, size, or density), and vascular density/network conditions is required in future work.

## CONCLUSIONS

This study demonstrated the relationship between stiffness and perfusion metrics, the correlation between stiffness and intraoperative tumor consistency, and the differences in perfusion metrics among common histologic subtypes of meningiomas. The results show that tumor stiffness may be useful to predict intraoperative tumor consistency, rMTT may correlate with tumor stiffness, and rMTT may be potentially useful to differentiate histologic subtypes in meningioma.

Disclosures: Kevin J. Glaser—RELATED: Grant: National Institutes of Health, Comments: R37-EB001981\*; Comments: The Mayo Clinic and Kevin J. Glaser have intellectual property rights and a financial interest related to magnetic resonance elastography technology. Richard L. Ehman—RELATED: Grant: National Institutes of Health, Comments: R37 EB001981\*; Other Relationships: The Mayo Clinic and Richard L. Ehman have intellectual property rights and a financial interest in magnetic resonance elastography technology. \*Money paid to the institution.

## REFERENCES

- Louis DN, Perry A, Reifenberger G, et al. **The 2016 World Health Organization Classification of Tumors of the Central Nervous System: a summary.** *Acta Neuropathol* 2016;131:803–20 CrossRef Medline
- Kendall B, Pulicino P. **Comparison of consistency of meningiomas and CT appearances.** *Neuroradiology* 1979;18:173–76 CrossRef Medline
- Shiroishi MS, Cen SY, Tamrazi B, et al. **Predicting meningioma consistency on preoperative neuroimaging studies.** *Neurosurg Clin N Am* 2016;27:145–54 CrossRef Medline
- Muthupillai R, Lomas DJ, Rossman PJ, et al. **Magnetic resonance elastography by direct visualization of propagating acoustic strain waves.** *Science* 1995;269:1854–57 CrossRef Medline
- Arani A, Murphy MC, Glaser KJ, et al. **Measuring the effects of aging and sex on regional brain stiffness with MR elastography in healthy older adults.** *Neuroimage* 2015;111:59–64 CrossRef Medline
- ElSheikh M, Arani A, Perry A, et al. **MR elastography demonstrates unique regional brain stiffness patterns in dementias.** *AJR Am J Roentgenol* 2017;209:403–08 CrossRef Medline
- Hiscox LV, Johnson CL, McGarry MD, et al. **High-resolution magnetic resonance elastography reveals differences in subcortical gray matter viscoelasticity between young and healthy older adults.** *Neurobiol Aging* 2018;65:158–67 CrossRef Medline
- Sack I, Streitberger KJ, Krefling D, et al. **The influence of physiological aging and atrophy on brain viscoelastic properties in humans.** *PLoS One* 2011;6:e23451 CrossRef Medline
- Takamura T, Motosugi U, Sasaki Y, et al. **Influence of age on global and regional brain stiffness in young and middle-aged adults.** *J Magn Reson Imaging* 2020;51:727–33 CrossRef Medline
- Murphy MC, Huston J 3rd, Jack CR Jr, et al. **Decreased brain stiffness in Alzheimer's disease determined by magnetic resonance elastography.** *J Magn Reson Imaging* 2011;34:494–98 CrossRef Medline
- Murphy MC, Jones DT, Jack CR Jr, et al. **Regional brain stiffness changes across the Alzheimer's disease spectrum.** *Neuroimage Clin* 2016;10:283–90 CrossRef Medline
- Lipp A, Trbojevic R, Paul F, et al. **Cerebral magnetic resonance elastography in supranuclear palsy and idiopathic Parkinson's disease.** *Neuroimage Clin* 2013;3:381–87 CrossRef Medline
- Bunevicius A, Schregel K, Sinkus R, et al. **REVIEW: MR elastography of brain tumors.** *Neuroimage Clin* 2020;25:102109 CrossRef Medline
- Hughes JD, Fattahi N, Van Gompel J, et al. **Higher-resolution magnetic resonance elastography in meningiomas to determine intra-tumoral consistency.** *Neurosurgery* 2015;77:653–58; discussion 658–59 CrossRef Medline
- Murphy MC, Huston J 3rd, Glaser KJ, et al. **Preoperative assessment of meningioma stiffness using magnetic resonance elastography.** *J Neurosurg* 2013;118:643–48 CrossRef Medline
- Sakai N, Takehara Y, Yamashita S, et al. **Shear stiffness of 4 common intracranial tumors measured using MR elastography: comparison with intraoperative consistency grading.** *AJNR Am J Neuroradiol* 2016;37:1851–59 CrossRef Medline
- Xu L, Lin Y, Han JC, et al. **Magnetic resonance elastography of brain tumors: preliminary results.** *Acta Radiol* 2007;48:327–30 CrossRef Medline
- Yin Z, Hughes JD, Glaser KJ, et al. **Slip interface imaging based on MR-elastography preoperatively predicts meningioma-brain adhesion.** *J Magn Reson Imaging* 2017;46:1007–16 CrossRef Medline
- Parker KJ. **Experimental evaluations of the microchannel flow model.** *Phys Med Biol* 2015;60:4227–42 CrossRef Medline
- Le Bihan D. **Theoretical principles of perfusion imaging: application to magnetic resonance imaging.** *Invest Radiol* 1992;27:(Suppl 2):6–11 CrossRef Medline
- Chatelin S, Humbert-Claude M, Garteiser P, et al. **Cannabinoid receptor activation in the juvenile rat brain results in rapid biomechanical alterations: neurovascular mechanism as a putative confounding factor.** *J Cereb Blood Flow Metab* 2016;36:954–64 CrossRef Medline
- Hetzer S, Birr P, Fehlnr A, et al. **Perfusion alters stiffness of deep gray matter.** *J Cereb Blood Flow Metab* 2018;38:116–25 CrossRef Medline
- Dittmann F, Tzschatzsch H, Hirsch S, et al. **Tomoelastography of the abdomen: tissue mechanical properties of the liver, spleen, kidney, and pancreas from single MR elastography scans at different hydration states.** *Magn Reson Med* 2017;78:976–83 CrossRef Medline
- Jamin Y, Boulton JK, Li J, et al. **Exploring the biomechanical properties of brain malignancies and their pathologic determinants in vivo with magnetic resonance elastography.** *Cancer Res* 2015;75:1216–24 CrossRef Medline
- Riegler J, Labyed Y, Rosenzweig S, et al. **Tumor elastography and its association with collagen and the tumor microenvironment.** *Clin Cancer Res* 2018;24:4455–67 CrossRef Medline
- Zhang H, Rodiger LA, Shen T, et al. **Perfusion MR imaging for differentiation of benign and malignant meningiomas.** *Neuroradiology* 2008;50:525–30 CrossRef Medline
- Zikou A, Alexiou GA, Goussia A, et al. **The role of diffusion tensor imaging and dynamic susceptibility perfusion MRI in the evaluation of meningioma grade and subtype.** *Clin Neurol Neurosurg* 2016;146:109–15 CrossRef Medline
- Kimura H, Takeuchi H, Koshimoto Y, et al. **Perfusion imaging of meningioma by using continuous arterial spin-labeling: comparison with dynamic susceptibility-weighted contrast-enhanced MR images and histopathologic features.** *AJNR Am J Neuroradiol* 2006;27:85–93 Medline

29. Fattahi N, Arani A, Perry A, et al. **MR elastography demonstrates increased brain stiffness in normal pressure hydrocephalus.** *AJNR Am J Neuroradiol* 2016;37:462–67 CrossRef Medline
30. Huston J 3rd, Murphy MC, Boeve BF, et al. **Magnetic resonance elastography of frontotemporal dementia.** *J Magn Reson Imaging* 2016;43:474–78 CrossRef Medline
31. Murphy MC, Huston J 3rd, Jack CR Jr, et al. **Measuring the characteristic topography of brain stiffness with magnetic resonance elastography.** *PLoS One* 2013;8:e81668 CrossRef Medline
32. Kamath A, Smith WS, Powers WJ, et al. **Perfusion CT compared to H(2) (15)O/O (15)O PET in patients with chronic cervical carotid artery occlusion.** *Neuroradiology* 2008;50:745–51 CrossRef Medline
33. Klotz E, König M. **Perfusion measurements of the brain: using dynamic CT for the quantitative assessment of cerebral ischemia in acute stroke.** *Eur J Radiol* 1999;30:170–84 CrossRef Medline
34. Phuttharak W, Boonrod A, Thammaroj J, et al. **Preoperative MRI evaluation of meningioma consistency: a focus on detailed architectures.** *Clin Neurol Neurosurg* 2018;169:178–84 CrossRef Medline
35. Shi R, Jiang T, Si L, et al. **Correlations of magnetic resonance, perfusion-weighted imaging parameters and microvessel density in meningioma.** *J BUON* 2016;21:709–713 Medline
36. Koizumi S, Sakai N, Kawaji H, et al. **Pseudo-continuous arterial spin labeling reflects vascular density and differentiates angiomatous meningiomas from non-angiomatous meningiomas.** *J Neurooncol* 2015;121:549–56 CrossRef Medline
37. Huang X, Chafi H, Matthews KL 2nd, et al. **Magnetic resonance elastography of the brain: a study of feasibility and reproducibility using an ergonomic pillow-like passive driver.** *Magn Reson Imaging* 2019;59:68–76 CrossRef Medline
38. Lee TY, Nabavi DG, Lee DH, et al. **Quantitative CT perfusion measurement: normal values and reproducibility in man.** *Stroke* 2000;32:344–45 [https://www.ahajournals.org/doi/10.1161/str.32.suppl\\_1.344-e](https://www.ahajournals.org/doi/10.1161/str.32.suppl_1.344-e). Accessed April 15, 2020
39. Maiuri F, Iaconetta G, de Divitiis O, et al. **Intracranial meningiomas: correlations between MR imaging and histology.** *Eur J Radiol* 1999;31:69–75 CrossRef Medline

# Unraveling Deep Gray Matter Atrophy and Iron and Myelin Changes in Multiple Sclerosis

G. Pontillo, M. Petracca, S. Monti, M. Quarantelli, C. Criscuolo, R. Lanzillo, E. Tedeschi, A. Elefante, V. Brescia Morra, A. Brunetti, S. Coccozza, and G. Palma

## ABSTRACT

**BACKGROUND AND PURPOSE:** Modifications of magnetic susceptibility have been consistently demonstrated in the subcortical gray matter of MS patients, but some uncertainties remain concerning the underlying neurobiological processes and their clinical relevance. We applied quantitative susceptibility mapping and longitudinal relaxation rate relaxometry to clarify the relative contribution of atrophy and iron and myelin changes to deep gray matter damage and disability in MS.

**MATERIALS AND METHODS:** Quantitative susceptibility mapping and longitudinal relaxation rate maps were computed for 91 patients and 55 healthy controls from MR images acquired at 3T. Applying an external model, we estimated iron and myelin concentration maps for all subjects. Subsequently, changes of deep gray matter iron and myelin concentration (atrophy-dependent) and content (atrophy-independent) were investigated globally (bulk analysis) and regionally (voxel-based and atlas-based thalamic subnuclei analyses). The clinical impact of the observed MRI modifications was evaluated via regression models.

**RESULTS:** We identified reduced thalamic ( $P < .001$ ) and increased pallidal ( $P < .001$ ) mean iron concentrations in patients with MS versus controls. Global myelin and iron content in the basal ganglia did not differ between the two groups, while actual iron depletion was present in the thalamus ( $P < .001$ ). Regionally, patients showed increased iron concentration in the basal ganglia ( $P \leq .001$ ) and reduced iron and myelin content in thalamic posterior-medial regions ( $P \leq .004$ ), particularly in the pulvinar ( $P \leq .001$ ). Disability was predicted by thalamic volume ( $B = -0.341$ ,  $P = .02$ ), iron concentration ( $B = -0.379$ ,  $P = .005$ ) and content ( $B = -0.406$ ,  $P = .009$ ), as well as pulvinar iron ( $B = -0.415$ ,  $P = .003$ ) and myelin ( $B = -0.415$ ,  $P = .02$ ) content, independent of atrophy.

**CONCLUSIONS:** Quantitative MRI suggests an atrophy-related iron increase within the basal ganglia of patients with MS, along with an atrophy-independent reduction of thalamic iron and myelin correlating with disability. Absolute depletions of thalamic iron and myelin may represent sensitive markers of subcortical GM damage, which add to the clinical impact of thalamic atrophy in MS.

**ABBREVIATIONS:** DD = disease duration; DGM = deep gray matter; EDSS = Expanded Disability Status Scale; HC = healthy controls; MNI = Montreal Neurological Institute; QSM = quantitative susceptibility mapping; RI = longitudinal relaxation rate; T2-LL = T2 lesion load

Along with atrophy,<sup>1</sup> several pathologic variations have been demonstrated in the deep gray matter (DGM) of MS patients by means of advanced MRI techniques.<sup>2</sup> Among these, recent

quantitative susceptibility mapping (QSM) studies explored magnetic susceptibility alterations of subcortical GM,<sup>3-5</sup> because such changes might reflect iron accumulation and depletion, which play an important role in MS pathophysiology<sup>6</sup> and seem to relate to motor and cognitive disability.<sup>4,5</sup>

Nonetheless, when drawing inferences on the relevance of DGM iron modifications in MS as measured by QSM, some considerations are needed. Indeed, brain magnetic susceptibility is also influenced by other molecules (primarily myelin, quantitatively assessable through the estimation of the longitudinal relaxation rate [R1]<sup>7,8</sup>) whose spatial distribution remarkably overlaps with iron patterns.<sup>9,10</sup> Furthermore, susceptibility changes can differ across distinct subregions of DGM nuclei, which show intrinsic structural heterogeneity.<sup>11</sup> Finally, the observed modifications may partially reflect atrophy-related epiphenomena rather than actual increases of iron load.<sup>12</sup>

Received July 17, 2020; accepted after revision January 11, 2021.

From the Departments of Advanced Biomedical Sciences (G.P., E.T., A.E., A.B., S.C.) and Neurosciences and Reproductive and Odontostomatological Sciences (M.P., C.C., R.L., V.B.M.), University "Federico II," Naples, Italy; and Institute of Biostructure and Bioimaging, (S.M., M.Q., G.P.) National Research Council, Naples, Italy.

Paper previously presented, in part, at: Annual Meeting of the European Society of Neuroradiology, October 1-4, 2020; Virtual, Lisbon, Portugal.

The data that support the findings of this study are available from the corresponding author on reasonable request.

S. Coccozza and G. Palma share senior authorship.

Please address correspondence to Arturo Brunetti, MD, Department of Advanced Biomedical Sciences, University "Federico II," Via Pansini, 5, 80131, Naples, Italy; e-mail: brunetti@unina.it; @NeuroN\_Lab

Indicates article with online supplemental data.

<http://dx.doi.org/10.3174/ajnr.A7093>

Here we performed a multimodal (QSM and R1 relaxometry) investigation of DGM, computing in vivo iron- and myelin-specific maps to disentangle the contribution of atrophy and iron and myelin (concentration and content) abnormalities to subcortical GM damage in patients with MS at both global (bulk analysis) and regional (voxel-based and thalamic subnuclei ROI analyses) levels, simultaneously exploring their relationship with clinical disability.

We hypothesized that: 1) modifications of DGM iron and myelin in MS would be partially accounted for by the presence of atrophy; 2) subregional analyses would show a heterogeneous spatial distribution of iron and myelin changes; 3) these alterations would predict clinical disability independent of atrophy.

## MATERIALS AND METHODS

### Subjects

In this prospective cross-sectional study, from December 2013 to April 2015, we enrolled patients with MS diagnosed according to the 2010 McDonald criteria,<sup>13</sup> along with age- and sex-comparable healthy controls (HC). Exclusion criteria were as follows: age below 18 or above 65 years; other pre-existing major systemic, psychiatric, or neurologic disorders; the presence of relapse and/or steroid treatment in the 30 days preceding MRI. Patients' clinical disability was quantified using the Expanded Disability Status Scale (EDSS) score,<sup>14</sup> while disease course was classified according to Lublin.<sup>15</sup>

### Standard Protocol Approvals, Registrations, and Patient Consents

The study was conducted in compliance with the ethical standards, approved by the University of Naples "Federico II" Ethics Committee, and written informed consent was obtained from all subjects according to the Declaration of Helsinki.

### MRI Data Acquisition and Map Generation

All MRI examinations were performed on the same 3T scanner (Magnetom Trio; Siemens) and included a 3D T1-weighted sequence for volumetric analyses, a 3D T2-weighted FLAIR sequence for quantifying demyelinating lesion load (T2-LL), and two double-echo spoiled gradient-echo sequences for computing QSM and the R1 map. Details about sequence parameters are available in Online Supplemental Data, while a complete description of QSM and R1 map extraction procedures is available in previous works.<sup>16,17</sup> Iron and myelin concentration maps were derived from QSM and the R1 map by inverting an external affine model estimated in a previous ex vivo MRI-pathology correlation study at 7T:<sup>9</sup>

$$QSM(ppm) = 1.43 \times 10^{-4} \times Fe \left( \frac{mg}{kg[DW]} \right) - 6.85 \times 10^{-2} \times My(MVF[DW]) - 2.5 \times 10^{-2}$$

$$R1(s^{-1}) = 2.23 \times 10^{-4} \times Fe \left( \frac{mg}{kg[DW]} \right) + 1.07 \times My(MVF[DW]) - 1.13,$$

where MVF indicates the myelin volume fraction, and DW, dry weight.

The 3T R1 map was converted into an expected map at 7T according to Rooney et al,<sup>18</sup> while susceptibility values were

considered independent from field strength. To provide a common and biologically plausible range of values, we referenced iron and myelin concentration maps to mean ventricular CSF (automatically segmented on T1-weighted scans and assumed to correspond to zero concentrations) values averaged across all subjects.

### Bulk, Voxel-Based, and Thalamic Subnuclei ROI Analyses

A detailed description of all MRI processing steps is available in the Online Supplemental Data, with a flow chart summarizing the pipeline depicted in the Online Supplemental Data.

Briefly, for the bulk analysis, demyelinating lesions were segmented on FLAIR images, and lesion masks were used to fill T1-weighted images. Then, basal ganglia structures (caudate nucleus, putamen, and globus pallidus) and the thalamus were segmented on filled T1-weighted anatomic scans using the FMRIB Integrated Registration and Segmentation Tool (FIRST; <http://fsl.fmrib.ox.ac.uk/fsl/fslwiki/FIRST>),<sup>19</sup> with segmentation masks used to obtain volume and mean iron and myelin concentrations for each DGM structure. In addition, to obtain a measure intrinsically adjusted for the presence of atrophy, we computed iron mass and myelin mass as measures of total iron and myelin content, respectively, as described by Hernandez-Torres et al.<sup>12</sup> Furthermore, as an ancillary analysis, the portion of MRI contrast attributable to iron or myelin was computed separately for each DGM structure based on the models in Stuber et al<sup>9</sup> and the estimated iron and myelin values.

For the voxel-based analysis, we adapted a previously described pipeline.<sup>20</sup> Briefly, QSM and R1 maps of all subjects were used to build study-specific multicontrast templates using ANTs (Version 2.3.1; <http://stnava.github.io/ANTs>).<sup>21</sup> The study-specific QSM template was then coregistered to the reference QSM atlas in the Montreal Neurological Institute (MNI) space,<sup>22</sup> and the resulting transformations were used to bring each subject's iron and myelin maps into the standard space. To take into account the effect of regional atrophy at the voxel level, we also computed modulated iron and myelin maps by scaling with the amount of volume changes due to spatial registration. Both modulated (reflecting local iron/myelin content) and unmodulated (reflecting local iron/myelin concentration) spatially normalized maps were smoothed with a 1-mm full width at half maximum isotropic Gaussian kernel before entering the statistical analysis.<sup>23</sup>

Finally, parallel to the voxelwise examination, subregional iron and myelin changes were also investigated with an ROI-based approach: thalamic subnuclei ROIs derived from the QSM atlas (ie, anterior, lateral, medial, midline nuclear groups; pulvinar; and internal medullary lamina)<sup>22</sup> were warped in each subject's native space to extract volume and iron and myelin values for each subregion.

### Statistical Analysis

Unless otherwise specified, statistical analyses were performed using the Statistical Package for the Social Sciences (SPSS, Version 25.0; IBM) with a significance level of  $\alpha = .05$ , and the Benjamini-Hochberg procedure was adopted for controlling the false discovery rate. Before running parametric analyses, we preliminarily verified linear model assumptions.

Between-group differences in terms of age and sex were evaluated using the Student *t* and Fisher exact tests, respectively. For

the bulk analysis, modifications of each DGM structure volume, mean iron/myelin concentrations, and total iron/myelin content were assessed with age- and sex-corrected ANCOVA. A similar approach was replicated for the thalamic subnuclei ROI analysis.

For the voxel-based analysis, the FSL Randomise tool (<http://fsl.fmrib.ox.ac.uk/fsl/fslwiki/Randomise/UserGuide>) was used to conduct between-group comparisons restricted to DGM: maps were fed into voxelwise cross-subject nonparametric analyses based on permutations, including age and sex as nuisance covariates, and controlling the family-wise error rate at the cluster level using the threshold-free cluster enhancement approach,<sup>23</sup> with an extent threshold of  $\kappa = 100$  voxels (0.1 mL) to avoid possible false-positive results due to minor registration errors.

**Table 1: Demographic, clinical, and conventional MRI characteristics of the studied population<sup>a</sup>**

	MS (n = 91)	HC (n = 55)	P Value (MS vs HC)
Age (yr)	38.3 (SD, 11.1)	41.6 (SD, 13.9)	.14
Female sex <sup>b</sup>	54 (59.3)	27 (49.1)	.23
Use of DMT <sup>b</sup>	83 (91.2)	—	—
Progressive course <sup>b</sup>	20 (22.0)	—	—
DD (yr)	11.2 (SD, 7.0)	—	—
EDSS <sup>c</sup>	3.5 (2.5–4.5)	—	—
T2-LL (mL)	11.4 (SD, 13.3)	—	—
Normalized brain volume (mL)	1485.8 (SD, 88.6)	1552.9 (SD, 76.4)	<.001
Normalized GM volume (mL)	755.6 (SD, 62.8)	794.7 (SD, 57.5)	<.001
Normalized WM volume (mL)	730.2 (SD, 36.5)	758.2 (SD, 31.7)	<.001

**Note:**— indicates not applicable; DMT, disease-modifying treatment.

<sup>a</sup> Unless otherwise indicated, data are expressed as means (SD). Between-group differences regarding MRI measures are adjusted for age and sex.

<sup>b</sup> Data are the number of subjects, with percentages in parentheses.

<sup>c</sup> Data are medians, with interquartile range in parentheses.

When regional differences emerged, the corresponding first eigenvariate was extracted from the cluster and corrected for the effect of age and sex measured in HC. The relationship between the obtained *z* scores and EDSS, disease duration (DD), and disease course was assessed via correlation analyses. Similarly, adjusted *z* scores of other MRI features that were significantly altered at the between-group analyses were entered in preliminary correlation analyses.

Finally, the value as clinical disability predictors of MRI variables correlating with EDSS was tested with hierarchic linear regression analyses using bootstrap with 5000 resamples, including age- and sex-adjusted whole-brain normalized volume and T2-LL in the first block and adjusted *z* scores of individual MRI features in

the second block. To test the ability of iron and myelin changes to predict disability independent of atrophy, we repeated the same regression analyses after including the volume of the corresponding DGM structure in the first block.

## RESULTS

### Subjects

Ninety-one patients with MS (71 with relapsing-remitting, with 20 progressive forms; 38.3 [SD, 11.1] years of age; male/female ratio = 37/54) were enrolled, along with 55 HC (41.6 [SD, 13.9] years of age; male/female ratio =

**Table 2: Results of the ANCOVA analyses for the between-group comparisons regarding DGM structures<sup>a</sup>**

	MS (n = 91)	HC (n = 55)	Cohen's <i>D</i>	<i>F</i>	<i>P</i> Value
Normalized volume (mL)					
Thalamus	19.2 (SD, 2.8)	21.7 (SD, 1.9)	1.14	45.75	<.001
Caudate	8.7 (SD, 1.5)	9.7 (SD, 1.3)	0.88	27.10	<.001
Putamen	12.6 (SD, 1.9)	13.8 (SD, 1.6)	0.82	23.83	<.001
Globus pallidus	4.5 (SD, 0.6)	4.9 (SD, 0.4)	0.76	20.55	<.001
Iron concentration (mg/kg[DW])					
Thalamus	5 (SD, 59)	38 (SD, 51)	0.62	13.64	<.001
Caudate	310 (SD, 103)	271 (SD, 76)	0.40	5.55	.02 <sup>b</sup>
Putamen	276 (SD, 112)	243 (SD, 94)	0.51	8.94	.03 <sup>b</sup>
Globus pallidus	786 (SD, 135)	697 (SD, 128)	0.68	16.51	<.001
Myelin concentration (MVF[DW])					
Thalamus	0.24 (SD, 0.06)	0.22 (SD, 0.08)	0.19	1.25	.27
Caudate	0.19 (SD, 0.06)	0.20 (SD, 0.08)	0.06	0.10	.76
Putamen	0.23 (SD, 0.06)	0.22 (SD, 0.08)	0.09	0.29	.59
Globus pallidus	0.21 (SD, 0.06)	0.20 (SD, 0.08)	0.11	0.49	.48
Iron content (μg)					
Thalamus	0.2 (SD, 1.1)	0.8 (SD, 1.1)	0.63	13.93	<.001
Caudate	2.7 (SD, 1.0)	2.6 (SD, 0.8)	0.03	0.04	.84
Putamen	3.4 (SD, 1.4)	3.3 (SD, 1.2)	0.25	2.13	.15
Globus pallidus	3.5 (SD, 6.8)	3.4 (SD, 6.9)	0.14	0.75	.39
Myelin content (mL)					
Thalamus	4.6 (SD, 1.4)	4.8 (SD, 1.7)	0.21	1.51	.22
Caudate	1.7 (SD, 0.8)	1.9 (SD, 0.7)	0.29	2.94	.09
Putamen	2.9 (SD, 1.0)	3.1 (SD, 1.0)	0.19	1.32	.25
Globus pallidus	0.9 (SD, 0.3)	1.0 (SD, 0.4)	0.09	0.34	.56

**Note:**—degrees of freedom (*df*), 141.

<sup>a</sup> Descriptive statistics (mean [SD]) for DGM-related MRI features are reported, along with the effect sizes (Cohen's *D*), test statistics (*F*), and exact probability (*P* value) values regarding between-group (MS versus HC) comparisons.

<sup>b</sup> Not significant after false discovery rate correction.

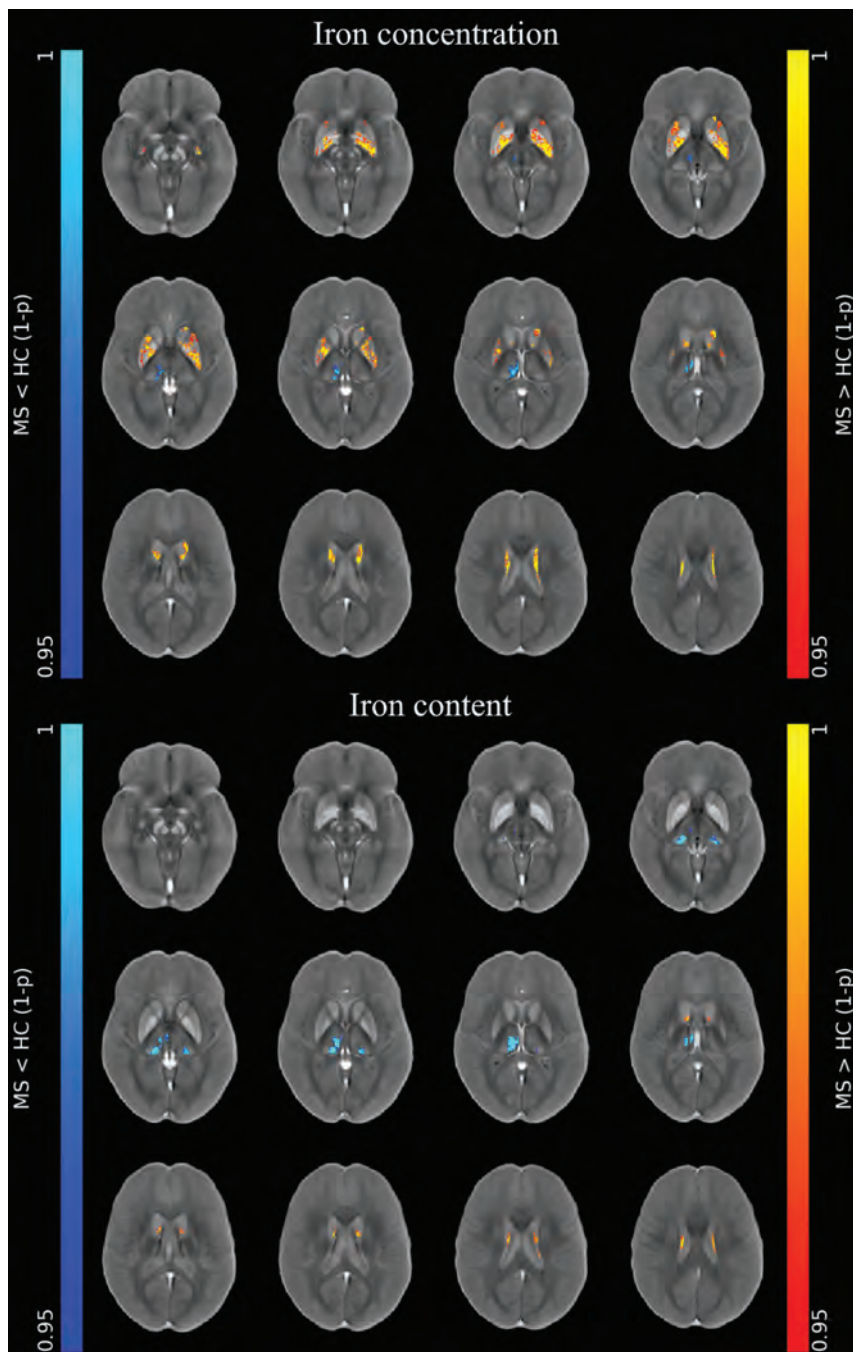


**FIG 1.** Image shows voxelwise analyses of iron maps. Clusters of significant between-group differences regarding unmodulated (*top panel*) and modulated (*lower panel*) iron maps for both the MS>HC (red-yellow, according to  $1 - P$  value) and MS<HC (blue-light blue, according to  $1 - P$  value) contrasts are presented, superimposed on the QSM template in the MNI space. Reprinted by permission from Springer Nature Customer Service Center GmbH: Springer Nature, Neuroradiology, European Society of Neuroradiology 2020, Copyright 2020, Springer-Verlag GmbH Germany, part of Springer Nature.

28/27). The mean DD for the whole cohort of patients was 11.2 (SD, 7.0) years, while the median EDSS score was 3.5 (interquartile range = 2.5–4.5). Eighty-three patients (91.2%) were under immunomodulatory treatment with either interferon- $\beta$ -1a (23.1%), interferon- $\beta$ -1b (11.0%), glatiramer acetate (3.3%), fingolimod (20.9%), teriflunomide (1.1%), or natalizumab (31.9%). Patients showed a mean T2-LL of 11.4 (SD, 13.3) mL and lower

normalized GM, WM, and whole-brain volumes (all  $P$ s < .001) compared with HC.

Demographic and clinical variables along with MRI-derived brain volumes of all subjects included in the study are reported in Table 1.

### **Between-Group Comparisons Regarding DGM Structures**

Patients showed significantly lower volumes of all DGM structures (all  $P$ s < .001). In comparison with HC, the mean iron concentration was reduced in the thalamus ( $P$  < .001) and increased in the globus pallidus ( $P$  < .001), caudate nucleus ( $P$  = .02, not significant after false discovery rate correction) and putamen ( $P$  = .03, not significant after false discovery rate correction). When we looked at the total iron content, no significant difference emerged for any of the basal ganglia structures, while an actual iron depletion was found in the thalamus ( $P$  < .001). Regarding myelin, no significant between-group differences emerged in terms of mean concentration, while the global myelin content of all DGM structures was lower in patients compared with HC, even if this difference did not reach statistical significance.

Detailed results of the between-group bulk analysis are reported in Table 2.

As for the ancillary analysis, QSM was mainly influenced by iron concentration in the basal ganglia (contrast portion  $\geq$  91%), with a slightly lower iron dependence in the thalamus (88% of the contrast attributable to iron, 12% to myelin). R1 contrast was highly influenced by iron concentration in the globus pallidus (contrast portion = 92%), with progressively increasing myelin dependence in the putamen, caudate nucleus, and thalamus (58% of the contrast caused by myelin, 42% by iron) (Online Supplemental Data).

At the voxel-based analyses (Online Supplemental Data), clusters of increased iron concentration encompassing the bilateral basal ganglia emerged in patients compared with HC ( $P$   $\leq$  .001), with only small clusters of increased local iron content in the body of the caudate nucleus bilaterally ( $P$   $\leq$  .005) (Fig 1). Conversely, clusters of reduced iron concentration and local content emerged in the posterior and medial regions of the thalami

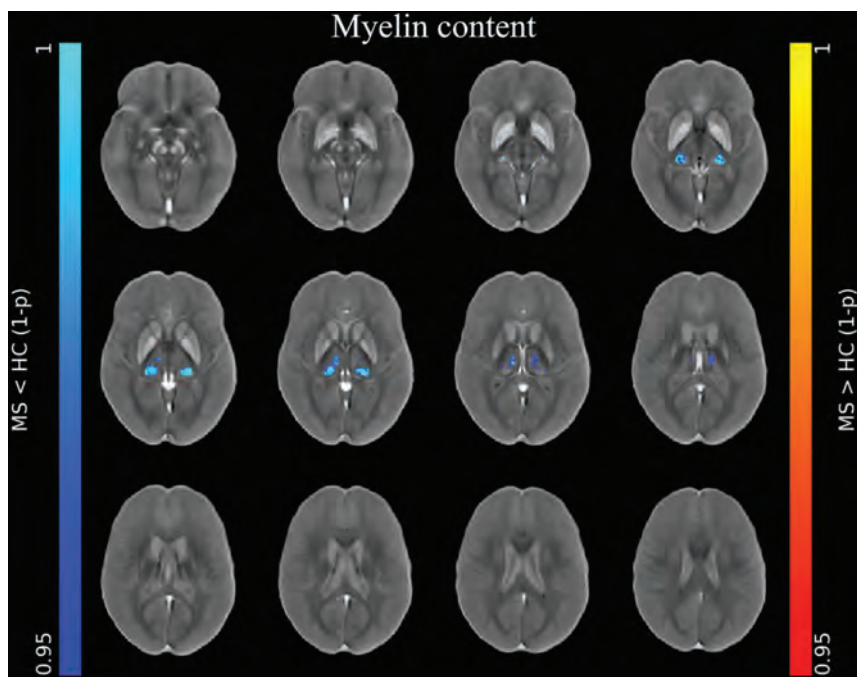


**FIG 2.** Image shows voxelwise analyses of myelin maps. Clusters of significant between-group difference regarding modulated myelin maps for the MS<HC (blue-light blue, according to 1 - P value) contrast are presented, superimposed on the QSM template in the MNI space. No significant differences emerged for the MS>HC contrast or for unmodulated myelin maps. Reprinted by permission from Springer Nature Customer Service Center GmbH: Springer Nature, Neuroradiology, European Society of Neuroradiology 2020, Copyright 2020, Springer-Verlag GmbH Germany, part of Springer Nature.

( $P \leq .004$ ) in patients compared with HC, along with a similar pattern of reduced local myelin content ( $P \leq .004$ ) (Figs 1 and 2).

In accordance with the results of the voxel-based investigation, the thalamic subnuclei ROI analysis of patients with MS compared with HC showed, along with significant atrophy of almost all subregions, reduced iron concentration and content in the pulvinar, midline, and medial nuclear groups and reduced myelin content in the pulvinar (Fig 3 and Online Supplemental Data).

#### **Relationship between DGM-Related MRI Features and Clinical Data**

Results of the preliminary correlation analyses exploring the relationship between MRI variables and clinical data are reported in the Online Supplemental Data. Briefly, significant associations emerged between DGM volume and iron and myelin levels and disease duration and course (with higher DD and progressive course: increasing DGM atrophy and basal ganglia iron concentration and reduced iron concentration and iron and myelin content in the thalamus). When we explored the relationship between MRI metrics and the EDSS score, thalamic volume ( $B = -0.341$ ,  $P = .02$ ) and iron concentration ( $B = -0.379$ ,  $P = .005$ ) and content ( $B = -0.406$ ,  $P = .009$ ) significantly predicted clinical disability, with a specific role for reduced volume ( $B = -0.310$ ,  $P = .03$ ) and iron ( $B = -0.415$ ,  $P = .003$ ) and myelin ( $B = -0.415$ ,  $P = .02$ ) content in the pulvinar (Online Supplemental Data). When we included the volume of the corresponding DGM structure in the model, reduced

iron and myelin levels in posteromedial subregions of the thalamus still provided additional value in the prediction of clinical disability (Online Supplemental Data).

#### **DISCUSSION**

In this study, the analysis of iron- and myelin-specific maps identified higher iron levels in the basal ganglia of patients with MS compared with HC, most likely reflecting atrophy-related condensation rather than iron accumulation, along with actual iron depletion and demyelination in subnuclei of the thalamus. Atrophy and reduction of thalamic iron and myelin content (particularly in the pulvinar) were all independently associated with higher clinical disability in patients with MS.

Direct (i.e. histopathology) and indirect (i.e. iron-sensitive MRI techniques)<sup>24</sup> evidence of increased iron levels in the basal ganglia has been extensively documented in both healthy aging<sup>22,25</sup> and CNS disease including MS,<sup>4,26</sup> supposedly reflecting neurodegeneration.<sup>6</sup> Increased

iron concentration may generally be caused by an actual deposition of iron or by the removal of non-iron-containing tissue components, resulting in iron condensation. In our data, the observed discrepancy between the increased mean iron concentration in the basal ganglia of patients compared with HC and the similarity of iron content values among groups, along with the significant DGM volume loss observed in patients with MS, suggest an atrophy-related epiphenomenon rather than absolute iron accumulation, as already hypothesized.<sup>12</sup> Nevertheless, higher iron levels could nurture a vicious circle contributing to neurodegeneration (and atrophy) through iron-related toxicity mechanisms.<sup>6</sup>

Conversely, we found reduced thalamic iron concentration, corresponding to an actual iron-depletion phenomenon. Discordant evidence exists regarding thalamic iron dynamics in MS, with reports of both increased<sup>3</sup> and decreased<sup>11</sup> levels. This inconsistency may relate to methodologic differences in addition to the unusual aging trajectory of thalamic iron concentration in HC, with an initial rise (peaking around 30 years) followed by a slow decrease at later ages.<sup>22,25</sup> Indeed, recent QSM studies consistently demonstrated reduced thalamic iron in adult patients with MS compared with HC.<sup>2,4,11</sup> Actually, the thalamus has a peculiar morphofunctional architecture, with more abundant WM fibers and iron-rich oligodendrocytes compared with the basal ganglia so that its changes in MS may rather resemble those of normal-appearing WM:<sup>27</sup> chronic microglial activation may induce thalamic oligodendroglial damage and death, with subsequent iron

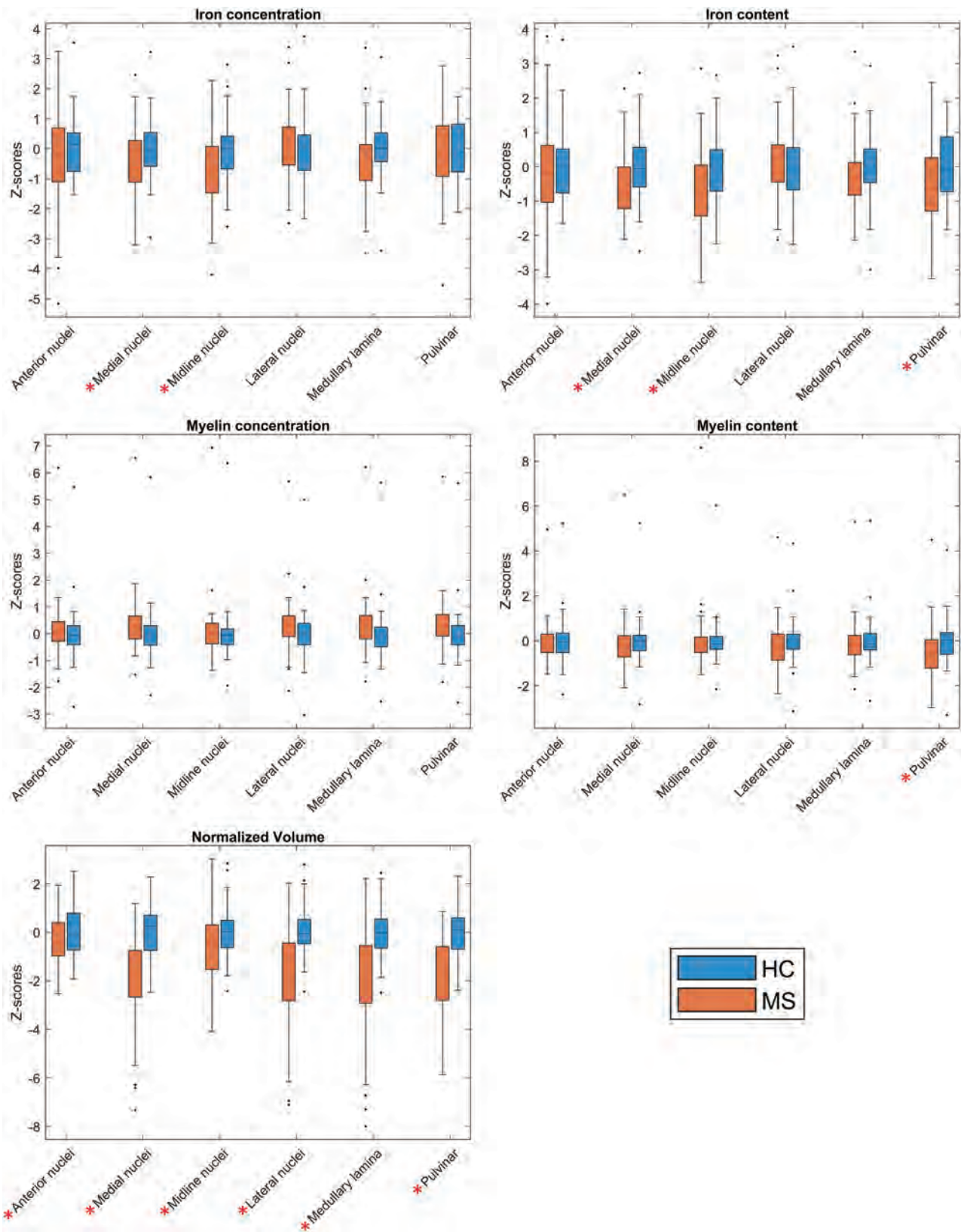


**FIG 3.** Between-group comparisons of MRI features regarding thalamic subnuclei. Boxplots at the y-axis show z scores (adjusted for the effect of age and sex in HC) of iron concentration and content (*upper panel*), myelin concentration and content (*middle panel*), and normalized volume (*lower panel*) of the corresponding thalamic subregions shown at the x-axis for both the MS and HC groups. Red asterisks mark significant between-group differences.

depletion, reducing axonal protection and neuronal repair and eventually leading to neurodegeneration.<sup>6,11</sup> Furthermore, its rich connectivity profile might make the thalamus particularly prone to secondary neurodegeneration effects from remote injury in other brain areas via deafferentation mechanisms, along with a neuroinflammatory microglial response spreading through corticothalamic tracts.<sup>11</sup>

When looking at myelin, between-group differences in terms of both mean concentration and global content were not statistically significant, in apparent contrast to the known occurrence of the demyelination phenomena in the DGM of patients with MS.<sup>26</sup> Indeed, the simultaneous presence of volume shrinkage and demyelination in subcortical GM structures may leave myelin concentrations unaffected (or even paradoxically increased), while the relatively low (compared with iron) myelin content of DGM structures, along with its heterogeneous spatial distribution, may reduce the statistical power of the bulk analysis, as also suggested by the results of the subregional investigations.

Results of the ancillary analysis confirm that QSM contrast highly depends on iron levels in subcortical GM.<sup>3</sup> Nevertheless, its combination with another quantitative MRI contrast (i.e. R1) may allow more specific mapping of tissue iron, especially in regions with higher myelin concentration (e.g. the thalamus). Furthermore, we showed how R1 contrast is strongly influenced by the high iron levels observed in DGM,<sup>18</sup> so it may not be a valid myelin marker in subcortical GM as it is in WM<sup>7</sup> or cortical GM.<sup>8</sup> Thus, the combination of multiple quantitative MRI contrasts may ensure more specific characterization of the demyelination phenomena occurring in the DGM of patients with MS.<sup>26</sup>

Voxel-based and atlas-based ROI analyses indicated iron and myelin depletion in the posterior and medial subnuclei of the thalamus, with prominent involvement of the pulvinar, further advocating a central role for remote injury in driving thalamic damage. Indeed, the pulvinar is the largest of thalamic association areas, participating in a dense cortico-pulvinar-cortical circuitry subtending different brain functions,<sup>28</sup> including the processing of visual information along visual pathways, which are known to be commonly involved in MS.<sup>29</sup>

When we explored the relationship with clinical data, along with atrophy, iron (increased concentration in the basal ganglia and reduced concentration and content in the thalamus) and myelin (reduced content in specific thalamic subregions) modifications were also associated with DD and a progressive course, supporting their role as disease-related neurodegeneration markers.

Furthermore, reductions of thalamic volume, iron and myelin content individually contributed to the prediction of the EDSS score in addition to conventional MRI markers of disease (i.e. whole-brain volume and T2-LL), once again confirming the clinical relevance of thalamic damage in the MS brain.<sup>2,4</sup> Most interesting, when we included thalamic volume in the predictive models, measures of both global and subregional thalamic iron and myelin decrease still provided significant extra value in explaining disability. Hence, thalamic iron and myelin depletion might reflect partially atrophy-independent pathologic processes, possibly expressing changes in oligodendroglial and microglial compartments that precede and/or concur with volume loss, thus

potentially representing sensitive and clinically relevant markers of subclinical inflammation.

Some limitations of this study should be acknowledged, partly related to iron/myelin estimation methods. First, the traditional myelin-iron model of MRI contrast may not be an accurate approximation of reality, particularly in the presence of other paramagnetic (e.g. gadolinium-based contrast agents<sup>30,31</sup>) or diamagnetic (e.g. calcium<sup>32</sup>) tissue components,<sup>10</sup> which are known to potentially accumulate in DGM structures. Furthermore, neurobiologic inferences might be hindered by additional confounding factors related to the adoption of external parameters, including issues of parameter conversion across field strengths<sup>18</sup> and intrinsic limitations of ex vivo/in vivo results matching (e.g. fixation- and temperature-dependence of MRI signal). However, while our approach to iron and myelin estimation cannot be considered purely quantitative in nature, the obtained values fall in plausible ranges according to reference studies,<sup>25,27</sup> supporting the validity of the proposed method for the pseudoquantitative evaluation of iron and myelin in clinical settings. Also, even if we were aware of the effect of iron concentration on T1 contrast and related automatic segmentations,<sup>18</sup> we preferred adopting a robust and widely used method based solely on T1-weighted scans,<sup>19</sup> thus keeping the volumetric quantification of DGM structures independent from the estimation of iron and myelin levels. Finally, longitudinal studies including extensive clinical and neuropsychological evaluations are encouraged to disentangle the causal relationship between iron and myelin modifications and atrophy in subcortical GM and to explore the potential of these metrics to outperform other established MRI measures of neurodegeneration (i.e. global/regional brain atrophy) as markers of disease progression and disability predictors.

## CONCLUSIONS

Our study sheds further light on iron and myelin modifications in the DGM of patients with MS, demonstrating an atrophy-related iron increase within the basal ganglia and a reduction of iron and myelin content within thalamic subnuclei, which correlates with clinical disability and may prove useful as a sensitive and partially atrophy-independent marker of subcortical GM damage.

## ACKNOWLEDGMENTS

Statistical analysis was conducted by Giuseppe Pontillo, MD, Department of Advanced Biomedical Sciences, University “Federico II,” Naples, Italy.

Disclosures: Maria Petracca—UNRELATED: Travel/Accommodations/Meeting Expenses Unrelated to Activities Listed: Novartis. Roberta Lanzillo—UNRELATED: Board Membership: Merck, Biogen, Novartis, Roche; Consultancy: Merck, Biogen, Novartis, Roche; Expert Testimony: Biogen; Payment for Lectures Including Service on Speakers Bureaus: Roche, Biogen, Merck, Novartis; Payment for Development of Educational Presentations: Roche, Biogen, Merck, Novartis. Vincenzo Brescia Morra—UNRELATED: Payment for Lectures Including Service on Speakers Bureaus: Novartis, Biogen, Genzyme, Teva Pharmaceutical Industries, Almirall, Bayer AG, Merck. Sirio Coccozza—UNRELATED: Board Membership: Amicus Therapeutics; Payment for Lectures Including Service on Speakers Bureaus: Sanofi.

## REFERENCES

1. Eshaghi A, Prados F, Brownlee WJ, et al. **MAGNIMS study group. Deep gray matter volume loss drives disability worsening in multiple sclerosis.** *Ann Neurol* 2018;83:210–22 CrossRef Medline
2. Pontillo G, Coccozza S, Lanzillo R, et al. **Determinants of deep gray matter atrophy in multiple sclerosis: a multimodal MRI study.** *AJNR Am J Neuroradiol* 2019;40:99–106 CrossRef Medline
3. Langkammer C, Liu T, Khalil M, et al. **Quantitative susceptibility mapping in multiple sclerosis.** *Radiology* 2013;267:551–59 CrossRef Medline
4. Zivadinov R, Tavazzi E, Bergsland N, et al. **Brain iron at quantitative MRI is associated with disability in multiple sclerosis.** *Radiology* 2018;289:487–96 CrossRef Medline
5. Fujiwara E, Kmech JA, Cobzas D, et al. **Cognitive implications of deep gray matter iron in multiple sclerosis.** *AJNR Am J Neuroradiol* 2017;38:942–48 CrossRef Medline
6. Stephenson E, Nathoo N, Mahjoub Y, et al. **Iron in multiple sclerosis: roles in neurodegeneration and repair.** *Nat Rev Neurol* 2014;10:459–68 CrossRef Medline
7. O'Muircheartaigh J, Vavasour I, Ljungberg E, et al. **Quantitative neuroimaging measures of myelin in the healthy brain and in multiple sclerosis.** *Hum Brain Mapp* 2019;40:2104–16 CrossRef Medline
8. Lutti A, Dick F, Sereno MI, et al. **Using high-resolution quantitative mapping of R1 as an index of cortical myelination.** *Neuroimage* 2014;93(Pt 2):176–88 CrossRef Medline
9. Stuber C, Morawski M, Schafer A, et al. **Myelin and iron concentration in the human brain: a quantitative study of MRI contrast.** *Neuroimage* 2014;93(Pt 1):95–106 CrossRef Medline
10. Moller HE, Bossoni L, Connor JR, et al. **Iron, myelin, and the brain: neuroimaging meets neurobiology.** *Trends Neurosci* 2019;42:384–401 CrossRef Medline
11. Schweser F, Raffaini Duarte Martins AL, Hagemeyer J, et al. **Mapping of thalamic magnetic susceptibility in multiple sclerosis indicates decreasing iron with disease duration: a proposed mechanistic relationship between inflammation and oligodendrocyte vitality.** *Neuroimage* 2018;167:438–52 CrossRef Medline
12. Hernandez-Torres E, Wiggermann V, Machan L, et al. **Increased mean R2\* in the deep gray matter of multiple sclerosis patients: have we been measuring atrophy?** *J Magn Reson Imaging* 2019;50:201–08 CrossRef Medline
13. Polman CH, Reingold SC, Banwell B, et al. **Diagnostic criteria for multiple sclerosis: 2010 revisions to the McDonald criteria.** *Ann Neurol* 2011;69:292–302 CrossRef Medline
14. Kurtzke JF. **Rating neurologic impairment in multiple sclerosis: an Expanded Disability Status Scale (EDSS).** *Neurology* 1983;33:1444–52 CrossRef Medline
15. Lublin FD. **New multiple sclerosis phenotypic classification.** *Eur Neurol* 2014;72 Suppl 1:1–5 CrossRef Medline
16. Palma G, Tedeschi E, Borrelli P, et al. **A novel multiparametric approach to 3D quantitative MRI of the brain.** *PLoS One* 2015;10:e0134963 CrossRef Medline
17. Monti S, Borrelli P, Tedeschi E, et al. **RESUME: turning an SWI acquisition into a fast qMRI protocol.** *PLoS One* 2017;12:e0189933 CrossRef Medline
18. Rooney WD, Johnson G, Li X, et al. **Magnetic field and tissue dependencies of human brain longitudinal 1H2O relaxation in vivo.** *Magn Reson Med* 2007;57:308–18 CrossRef Medline
19. Patenaude B, Smith SM, Kennedy DN, et al. **A Bayesian model of shape and appearance for subcortical brain segmentation.** *Neuroimage* 2011;56:907–22 CrossRef Medline
20. Hanspach J, Dwyer MG, Bergsland NP, et al. **Methods for the computation of templates from quantitative magnetic susceptibility maps (QSM): toward improved atlas- and voxel-based analyses (VBA).** *J Magn Reson Imaging* 2017;46:1474–84 CrossRef Medline
21. Avants BB, Tustison NJ, Song G, et al. **A reproducible evaluation of ANTs similarity metric performance in brain image registration.** *Neuroimage* 2011;54:2033–44 CrossRef Medline
22. Zhang Y, Wei H, Cronin MJ, et al. **Longitudinal atlas for normative human brain development and aging over the lifespan using quantitative susceptibility mapping.** *Neuroimage* 2018;171:176–89 CrossRef Medline
23. Smith SM, Nichols TE. **Threshold-free cluster enhancement: addressing problems of smoothing, threshold dependence and localisation in cluster inference.** *Neuroimage* 2009;44:83–98 CrossRef Medline
24. Stuber C, Pitt D, Wang Y. **Iron in multiple sclerosis and its noninvasive imaging with quantitative susceptibility mapping.** *Int J Mol Sci* 2016;17:100 CrossRef Medline
25. Hallgren B, Sourander P. **The effect of age on the non-haem iron in the human brain.** *J Neurochem* 1958;3:41–51 CrossRef Medline
26. Haider L, Simeonidou C, Steinberger G, et al. **Multiple sclerosis deep grey matter: the relation between demyelination, neurodegeneration, inflammation and iron.** *J Neurol Neurosurg Psychiatry* 2014;85:1386–95 CrossRef Medline
27. Hametner S, Endmayr V, Deistung A, et al. **The influence of brain iron and myelin on magnetic susceptibility and effective transverse relaxation: a biochemical and histological validation study.** *Neuroimage* 2018;179:117–33 CrossRef Medline
28. Benarroch EE. **Pulvinar: associative role in cortical function and clinical correlations.** *Neurology* 2015;84:738–47 CrossRef Medline
29. Poretto V, Petracca M, Saiote C, et al. **A composite measure to explore visual disability in primary progressive multiple sclerosis.** *Mult Scler J Exp Transl Clin* 2017;3:2055217317709620 CrossRef Medline
30. Coccozza S, Pontillo G, Lanzillo R, et al. **MRI features suggestive of gadolinium retention do not correlate with Expanded Disability Status Scale worsening in multiple sclerosis.** *Neuroradiology* 2019;61:155–62 CrossRef Medline
31. Tedeschi E, Palma G, Canna A, et al. **In vivo dentate nucleus MRI relaxometry correlates with previous administration of gadolinium-based contrast agents.** *Eur Radiol* 2016;26:4577–84 CrossRef Medline
32. Harder SL, Hopp KM, Ward H, et al. **Mineralization of the deep gray matter with age: a retrospective review with susceptibility-weighted MR imaging.** *AJNR Am J Neuroradiol* 2008;29:176–83 CrossRef Medline

# MRI-Visible Perivascular Spaces in the Centrum Semiovale Are Associated with Brain Amyloid Deposition in Patients with Alzheimer Disease–Related Cognitive Impairment

H.J. Kim, H. Cho, M. Park, J.W. Kim, S.J. Ahn, C.H. Lyoo, S.H. Suh, and Y.H. Ryu



## ABSTRACT

**BACKGROUND AND PURPOSE:** The association of perivascular spaces in the centrum semiovale with amyloid accumulation among patients with Alzheimer disease–related cognitive impairment is unknown. We evaluated this association in patients with Alzheimer disease–related cognitive impairment and  $\beta$ -amyloid deposition, assessed with [ $^{18}$ F] florbetaben PET/CT.

**MATERIALS AND METHODS:** MR imaging and [ $^{18}$ F] florbetaben PET/CT images of 144 patients with Alzheimer disease–related cognitive impairment were retrospectively evaluated. MR imaging–visible perivascular spaces were rated on a 4-point visual scale: a score of  $\geq 3$  or  $< 3$  indicated a high or low degree of MR imaging–visible perivascular spaces, respectively. Amyloid deposition was evaluated using the brain  $\beta$ -amyloid plaque load scoring system.

**RESULTS:** Compared with patients negative for  $\beta$ -amyloid, those positive for it were older and more likely to have lower cognitive function, a diagnosis of Alzheimer disease, white matter hyperintensity, the *Apolipoprotein E*  $\epsilon 4$  allele, and a high degree of MR imaging–visible perivascular spaces in the centrum semiovale. Multivariable analysis, adjusted for age and *Apolipoprotein E* status, revealed that a high degree of MR imaging–visible perivascular spaces in the centrum semiovale was independently associated with  $\beta$ -amyloid positivity (odds ratio, 2.307; 95% CI, 1.036–5.136;  $P = .041$ ).

**CONCLUSIONS:** A high degree of MR imaging–visible perivascular spaces in the centrum semiovale independently predicted  $\beta$ -amyloid positivity in patients with Alzheimer disease–related cognitive impairment. Thus, MR imaging–visible perivascular spaces in the centrum semiovale are associated with amyloid pathology of the brain and could be an indirect imaging marker of amyloid burden in patients with Alzheimer disease–related cognitive impairment.

**ABBREVIATIONS:** AD = Alzheimer disease; ADCI = AD-related cognitive impairment; *APOE* = *Apolipoprotein E*; BAPL =  $\beta$ -amyloid plaque load; [ $^{18}$ F] FBB = [ $^{18}$ F] florbetaben; MMSE = Mini-Mental State Examination; PVS = perivascular spaces; PVS-CS = perivascular spaces in the centrum semiovale; SUVr = standardized uptake value ratios; WMH = white matter hyperintensity

Accumulating evidence suggests that MR imaging–visible perivascular spaces (PVS) are not innocent lesions but may be a neuroimaging marker of cerebral small-vessel disease.<sup>1–3</sup> The

perivascular space is a potential space filled with interstitial fluid surrounding penetrating vessels. It is involved in the drainage of interstitial fluid and solutes from the brain.<sup>4</sup> Therefore, several clinical conditions that reduce the clearance of solutes from the brain interstitial fluid such as aging, hypertension, and inflammation can result in MR imaging–visible PVS.<sup>5</sup> MR imaging–visible PVS are also associated with various diseases, such as traumatic brain injury, Parkinson disease, and dementia.<sup>6–9</sup> The location of MR imaging–visible PVS is an important factor to consider when predicting disease status because MR imaging–visible PVS in the basal ganglia may be associated with markers of arteriolosclerosis, whereas MR imaging–visible PVS in the centrum semiovale (PVS-CS) are linked to diseases involving amyloid pathology, such as Alzheimer disease (AD) and cerebral amyloid angiopathy.<sup>10,11</sup>

Many different studies on cerebral amyloid angiopathy have demonstrated a strong relationship between MR imaging–visible PVS-CS and cerebral amyloid angiopathy.<sup>12–15</sup> Some studies have

Received June 18, 2020; accepted after revision January 21, 2021.

From the Departments of Nuclear Medicine (H.J.K., Y.H.R.), Neurology (H.C., C.H.L.), and Radiology (M.P., J.W.K., S.J.A., S.H.S.), Gangnam Severance Hospital, Yonsei University College of Medicine, Seoul, South Korea; and Department of Nuclear Medicine (H.J.K.), Yongin Severance Hospital, Yonsei University College of Medicine, Yongin-si, South Korea. H.J. Kim and H. Cho contributed equally to this work.

This research was supported by the Basic Science Research Program through the National Research Foundation of Korea funded by the Ministry of Education, Science and Technology (NRF-2017RID1A1B03034388), the National Research Foundation of Korea grant funded by the Korean government (Ministry of Science and ICT) (No. NRF-2020R1C1C1005724), and Yonsei University College of Medicine (6-2019-0059).

Please address correspondence to Mina Park, MD, Department of Radiology, Gangnam Severance Hospital, Yonsei University College of Medicine, Eonju-ro 211, Gangnam-gu, Seoul, South Korea; e-mail: to.minapark@yuhs.ac

Indicates open access to non-subscribers at www.ajnr.org

Indicates article with online supplemental data.

<http://dx.doi.org/10.3174/ajnr.A7155>

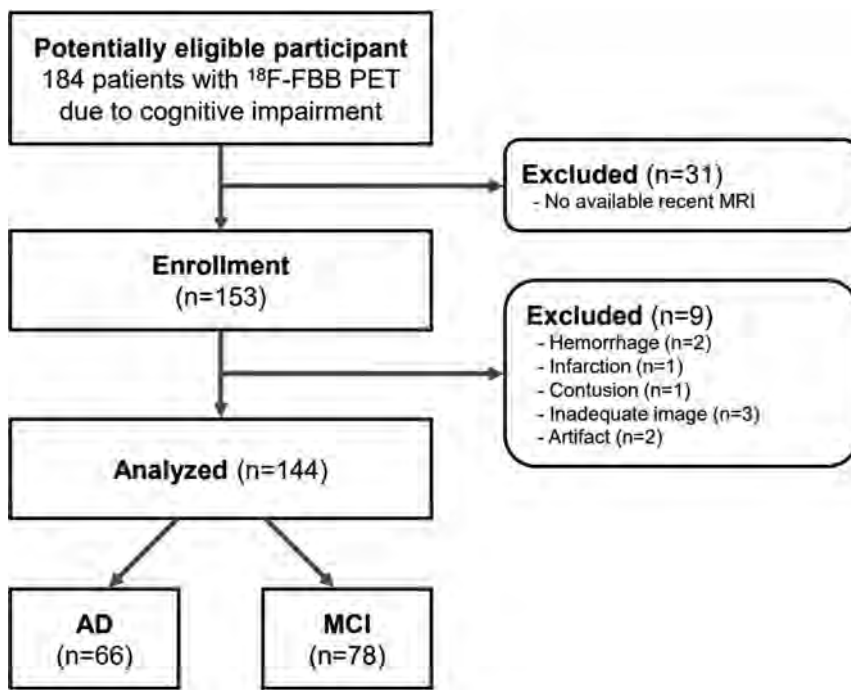


**FIG 1.** Patient-inclusion flowchart.

suggested that the dilation of PVS and failure in the drainage of interstitial fluid may result from deposition of  $\beta$ -amyloid in the cortical and leptomeningeal arteries.<sup>16</sup> Furthermore, evidence indicates that MR imaging–visible PVS-CS are associated with in vivo  $\beta$ -amyloid deposition in the brain, based on amyloid PET scanning,<sup>14,17</sup> which enables the visualization of brain amyloid deposition and measures the distribution and density of  $\beta$ -amyloid plaques.<sup>18</sup>

Failure in the perivascular clearance of  $\beta$ -amyloid may also be involved in the accumulation of  $\beta$ -amyloid in AD.<sup>19</sup> In patients with AD, MR imaging–visible PVS-CS may reflect impaired perivascular clearance of  $\beta$ -amyloid, and several studies have indicated a link between MR imaging–visible PVS and AD.<sup>7,20</sup> However, unlike evidence for the association between MR imaging–visible PVS-CS and cerebral amyloid angiopathy, scant evidence exists regarding the association between  $\beta$ -amyloid deposition and MR imaging–visible PVS in the population with dementia.

Several compounds labeled with radioisotopes have been developed to image amyloid deposition. In patients with cognitive impairment, PET scans using these tracers are widely used for diagnosis and follow-up.<sup>21</sup> Among the radiopharmaceuticals, [<sup>18</sup>F] florbetaben ([<sup>18</sup>F] FBB) is widely used for PET imaging to evaluate AD and other causes of dementia. [<sup>18</sup>F] FBB has a proper half-life and also allows high-resolution image acquisition, diagnostic capability, and quantification.<sup>22</sup> For these reasons, [<sup>18</sup>F] FBB is suitable for evaluating amyloid accumulation and its association with enlarged PVS in patients with dementia.

We hypothesized that MR imaging–visible PVS-CS would be associated with brain amyloid deposition in cognitively impaired patients, as it is in patients with cerebral amyloid angiopathy. We also evaluated the association using [<sup>18</sup>F] FBB, a PET radiotracer

that labels in vivo amyloid deposits, in patients with cognitive impairment.

## MATERIALS AND METHODS

### Participants

The need for written informed consent from patients was waived by the institutional review board of Gangnam Severance Hospital due to the retrospective nature of this study. Data were reviewed from 153 consecutive patients with cognitive impairment and clinical indications of AD-related cognitive impairment (ADCI). All patients underwent an [<sup>18</sup>F] FBB PET/CT and brain MR imaging within a 3-month interval from June 2017 to July 2019. Of the 153 patients with ADCI, we excluded 3 patients with inadequate image acquisition, 2 with image artifacts, 2 with intracranial hemorrhage, 1 with a large territorial infarction, and 1 with an old traumatic contusion. Therefore, 144 patients with ADCI were finally included in the analysis; among them, 66 patients had probable AD and 78

had mild cognitive impairment. Figure 1 shows the patient-inclusion flowchart. The criteria for probable AD, proposed by the National Institutes of Neurological and Disorders and Stroke and by the Alzheimer's Disease and Related Disorders Association<sup>23</sup>, and the Petersen criteria,<sup>24</sup> were used for the clinical diagnosis of mild cognitive impairment.

### Clinical Evaluation

We assessed all available patient information, such as basic demographic characteristics, other medical conditions (including a history of vascular risk factors), global cognitive assessment scores (eg, Clinical Dementia Rating Scale–Sum of Boxes score, Mini-Mental State Examination [MMSE] score, and a standardized neuropsychological battery called the Seoul Neuropsychological Screening Battery<sup>25</sup>), and *Apolipoprotein E (APOE)  $\epsilon$ 4* genotyping. *APOE* genotyping was performed using the polymerase chain reaction. Individuals with at least 1  $\epsilon$ 4 allele were classified as *APOE  $\epsilon$ 4*-positive.

### MR Imaging Acquisition and Analysis

The MR imaging sequences were performed on a 3T scanner (Discovery MR750; GE Healthcare) with a 16-channel head coil. All patients underwent axial T2-weighted imaging, sagittal T1-weighted imaging, sagittal 3D-FLAIR, and axial 3D susceptibility-weighted angiography. Axial 2D T2-weighted images were acquired using the FSE sequence (TR/TE, 5320/102 ms; flip angle, 142°; section thickness, 4 mm; gap, 1 mm; FOV, 230 mm; matrix, 352 × 352). The actual TR/TE ranged from 5289/104 ms to 6028/97 ms due to the autoTR setting and specific absorption rate adjustment. Sagittal 3D T1-weighted images were obtained using the 3D fast-spoiled gradient echo sequence (TR/TE, 8.2/3.2 ms;

flip angle, 12°; section thickness, 1 mm; FOV, 240 mm; matrix, 256 × 256). Sagittal 3D-FLAIR images were obtained using the Cube sequence (GE Healthcare) (TR/TE, 6000/89 ms; TI, 1741 ms; section thickness, 1.2 mm; FOV, 260 mm; matrix, 256 × 224). Axial 3D susceptibility-weighted angiography images were obtained using the following parameters: TR/TE, 30.9/23.4 ms, 46.8 ms, and 70.2 ms; flip angle, 10°; section thickness, 2 mm; gap, 1 mm; FOV, 230 mm; and matrix, 320 × 224.

The PVS that were visible on MR imaging were assessed in line with the STandards for ReportIng Vascular changes on nEuroimaging recommendations.<sup>26</sup> Based on the axial T2-weighted MR images, MR imaging-visible PVS were rated in the basal ganglia and centrum semiovale using a validated 4-point visual rating scale: 0 = no PVS; 1 = ≤10 PVS; 2 = 11–20 PVS; 3 = 21–40 PVS; and 4 = ≥40 PVS.<sup>12,27</sup> The numbers refer to MR imaging-visible PVS on 1 side of the brain (ie, the side/section with the highest number of PVS after all relevant slices for each anatomic area were reviewed). We prespecified a dichotomized classification of MR imaging-visible perivascular space degree as “high degree” (ie, score of >2) or “low degree” (ie, score of ≤2). This definition is in line with the perivascular space burden used in previous studies and may be characteristic of amyloid pathology.<sup>10,12</sup>

White matter hyperintensities (WMHs) were defined as hyperintense white matter lesions on FLAIR images based on the STandards for ReportIng Vascular changes on nEuroimaging criteria and were graded using the Fazekas scale as “deep WMHs” (0 = absent; 1 = punctate; 2 = early confluent; 3 = confluent) or “periventricular WMHs” (0 = absent; 1 = caps or pencil-thin lining; 2 = smooth halo; 3 = irregular WMHs extending into the deep white matter).<sup>26,28</sup> The total Fazekas score was calculated by adding the periventricular and deep WMH scores. A score of >3 was considered WMH-positive.<sup>28</sup> Lacunes were defined as small lesions that were hypointense on T1-weighted images and hyperintense on T2-weighted images and had perilesional halos on FLAIR images.<sup>26</sup> Microbleeds were defined as small signal voids with associated blooming on susceptibility-weighted angiography images. The presence and number of lacunes and microbleeds were recorded as previously described.<sup>26</sup>

### **[<sup>18</sup>F] FBB PET Imaging Acquisition and Analysis**

PET images were obtained using a Biograph mCT PET/CT scanner (Siemens). At 90 minutes after we injected 307.0 (SD, 32.2) MBq of [<sup>18</sup>F] FBB, PET data were acquired for 20 minutes. After we conducted attenuation and scatter correction, 3D-PET images were reconstructed in a 256 × 256 × 223 matrix with a voxel size of 1.591 × 1.591 × 1 mm using the ordered-subsets expectation maximization algorithm.

We defined the results of amyloid PET as “positive” when the visual assessment of [<sup>18</sup>F] FBB PET was scored as 2 or 3 on the brain  $\beta$ -amyloid plaque load (BAPL) scoring system based on the following: 1 = no tracer uptake, 2 = moderate tracer uptake, and 3 = pronounced tracer uptake.<sup>29,30</sup> The decision was based on visual assessment of each section on the axial plane. All scans were independently evaluated by 2 experienced nuclear medicine physicians, who reread all the studies while blinded to the original clinical reports and clinical information and reached a consensus.

In addition to the visual assessment, we also performed a semi-quantitative analysis to evaluate the cortical [<sup>18</sup>F] FBB retention in the PET/CT scans, as follows: Cortical regional standardized uptake value ratios (SUVr) were calculated for each patient in the 6 cortical ROIs (frontal, parietal, lateral temporal, precuneus, and anterior and posterior cingulate cortex regions). We used the cerebellar gray matter as the reference for SUVr calculation. The global composite florbetaben SUVr was calculated as the average of the SUVr value in each ROI.<sup>29,31</sup> On the basis of the SUVr analysis, an [<sup>18</sup>F] FBB PET was defined as positive (SUVr-positive) when the global composite florbetaben SUVr was >1.42, which was assessed against the histopathologic determination of  $\beta$ -amyloid in previous research.<sup>32</sup>

### **Statistical Analyses**

Baseline characteristics were compared using the  $\chi^2$  or Fisher exact test for categorical variables, independent *t* tests for normally distributed continuous variables, and Mann-Whitney *U* tests for continuous variables that were not normally distributed. MR imaging-visible PVS in both the basal ganglia and centrum semiovale were considered categorical variables, respectively. They were subdivided by severity, as described previously. We explored the independent and pathophysiologically relevant predictors of brain amyloid deposition using logistic regression analyses based on our prespecified hypothesis and the results of univariable analyses (including variables with *P* < .05). Multivariable logistic regression analyses, including age, sex, *APOE*  $\epsilon$ 4 allele status, and high degree of MR imaging-visible PVS-CS were performed. The variables of interest in univariable analysis were included in the multivariable models using the enter method. Positive WMH was not included in the analysis because it was significantly associated with a high degree of MR imaging-visible PVS-CS (*P* < .001, based on the  $\chi^2$  test).

### **Random Forests Analysis**

A total of 13 demographic and radiologic features, excluding WMH, were evaluated; these features included age, sex, hypertension, diabetes, hyperlipidemia, previous stroke, *APOE*  $\epsilon$ 4 allele, MR imaging-visible PVS in the basal ganglia, MR imaging-visible PVS-CS, lacunes, cortical superficial siderosis, lobar cerebral microbleeds, and deep cerebral microbleeds. The random forests model was trained with demographic and radiologic features to classify the amyloid positivity of the brain. The diagnostic ability of the random forests model using receiver operating characteristic analysis and the area under the receiver operating characteristic curve was calculated.

## **RESULTS**

### **Study Participants**

In this study, the total number of patients with ADCI was 144, comprising 67 patients with a BAPL score of one, 11 with a BAPL score of 2, and 66 with a BAPL score of 3. On the basis of the criteria of the BAPL scoring system, 67 patients were negative for  $\beta$ -amyloid deposition and 77 were positive for it. According to the SUVr analysis, 74 patients were negative for  $\beta$ -amyloid deposition and 70 patients were positive for it.

Among the 144 patients with ADCI, 3 had a PVS in the basal ganglia score of zero, 85 had a score of 1 in MR imaging-visible PVS in the basal ganglia, 32 had a score of two, 17 had a score of 3, and 7 had a score of 4 in terms of MR imaging-visible PVS in the basal ganglia. With regard to MR imaging-visible PVS-CS, 15 patients with ADCI had a score of one, 57 had a score of two, 56 had a score of 3, and 16 had a score of 4.

### Comparison between Groups Positive and Negative for $\beta$ -Amyloid

Age was significantly older in the patients positive for  $\beta$ -amyloid deposition than in patients negative for it (mean, 75.4 [SD,

7.6] years versus 71.3 [SD, 10.6] years;  $P = .010$ ). The prevalence of the *APOE*  $\epsilon 4$  allele ( $P = .001$ ), WMH ( $P = .013$ ), and AD ( $P < .001$ ) was higher in patients with  $\beta$ -amyloid positivity than in patients with  $\beta$ -amyloid negativity. The patients with  $\beta$ -amyloid positivity had poorer cognitive function on the MMSE ( $P < .001$ ), the Clinical Dementia Rating Scale ( $P = .019$ ), and the Clinical Dementia Rating Scale-Sum of Boxes ( $P < .001$ ) compared with patients with  $\beta$ -amyloid negativity (Table 1). A high degree of MR imaging-visible PVS-CS existed more frequently among patients with  $\beta$ -amyloid positivity than in patients with  $\beta$ -amyloid negativity (48/77 [62.3%] versus 24/67 [35.8%];  $P = .002$ ), whereas a high degree of MR imaging-visible PVS

in the basal ganglia did not differ between groups positive and negative for  $\beta$ -amyloid (13/77 [16.9%] versus 11/67 [16.4%],  $P = .297$ ) (Fig 2). Representative examples of PVS patterns with the corresponding [ $^{18}$ F] FBB PET findings are presented in Fig 3.

### Quantitative SUVr Analysis

In the SUVr analysis, 43/70 (61.4%) with global composite SUVr positivity were classified as having a high degree of MR imaging-visible PVS-CS compared with 29/74 (39.2%) with SUVr negativity ( $P = .008$ ), and the high degree of MR imaging-visible PVS in the basal ganglia did not differ between the SUVr-positive and SUVr-negative groups (12/70 [17.1%] versus 12/74 [16.2%],  $P = .881$ ). The global composite SUVr was significantly higher in patients with a high degree of MR imaging-visible PVS-CS than in those with a low degree (1.52 versus 1.37,  $P = .005$ ). In region-based analysis, all 6 ROIs showed statistically significant differences. The frontal (1.56 versus 1.37,  $P = .004$ ), parietal (1.50 versus 1.38,  $P = .009$ ), lateral temporal (1.31 versus 1.19,  $P = .008$ ), precuneus (1.60 versus 1.43,  $P = .008$ ), anterior cingulate (1.47 versus 1.36,  $P = .044$ ), and posterior cingulate (1.69 versus 1.52,  $P = .004$ ) regions showed higher SUVr values in the patients with a high degree of MR imaging-visible PVS-CS than in those a low degree, respectively.

**Table 1: Baseline characteristics of the groups positive and negative for brain  $\beta$ -amyloid**

	Amyloid-Negative	Amyloid-Positive	P Value
(No.) (%)	67 (46.5%)	77 (53.5%)	
Age (mean) (SD) (yr)	71.3 (10.6)	75.4 (7.6)	.010
Female sex (No.) (%)	44 (65.7%)	44 (57.1%)	.297
Hypertension (No.) (%)	25 (37.3%)	36 (46.8%)	.254
Diabetes mellitus (No.) (%)	10 (14.9%)	16 (20.8%)	.364
Hyperlipidemia (No.) (%)	9 (13.4%)	11 (14.3%)	.883
Previous stroke (No.) (%)	7 (10.4%)	4 (5.2%)	.238
<i>APOE</i> $\epsilon 4$ presence (No.) (%)	13 (19.4%)	33 (42.9%)	.001
High degree of MR imaging-visible PVS-CS (No.) (%)	24 (35.8%)	48 (62.3%)	.002
High degree of MR imaging-visible PVS-BG (No.) (%)	11 (16.4%)	13 (16.9%)	.297
AD (No.) (%)	19 (28.4%)	47 (61.0%)	<.001
MMSE (median) (IQR)	26 (23–28)	24 (20–26)	<.001
CDR (median) (IQR)	0.5 (0.5–0.5)	0.5 (0.5–1.0)	.019
CDR-SB (median) (IQR)	1.5 (0.5–3.0)	3.0 (1.5–4.5)	<.001
Lacunae (median) (IQR)	0 (0–0)	0 (0–0)	.778
cSS present (No.) (%)	1 (1.5%)	6 (7.8%)	.081
Lobar CMB (median) (IQR)	0 (0–0)	0 (0–1)	.117
Deep CMB (median) (IQR)	0 (0–0)	0 (0–0)	.160
WMH presence (No.) (%)	27 (40.3%)	47 (61.0%)	.013

**Note:**—IQR indicates interquartile range; PVS-BG, perivascular space in the basal ganglia; CMB, cerebral microbleed; CDR, Clinical Dementia Rating Scale; CDR-SB, Clinical Dementia Rating Scale-Sum of Boxes; cSS, cortical superficial siderosis.

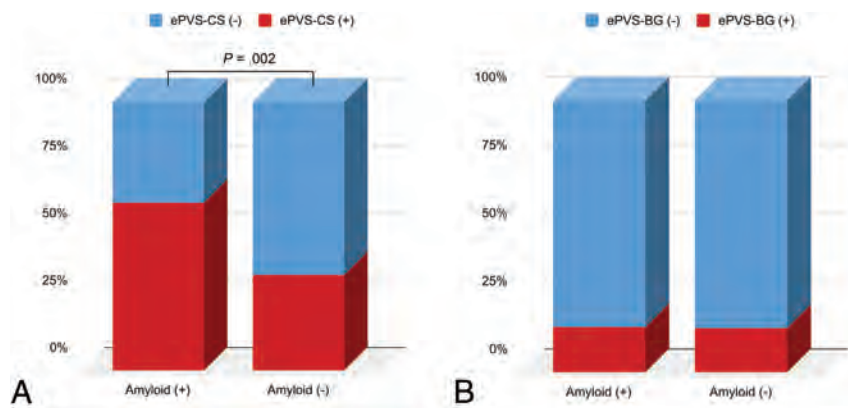


**FIG 2.** Comparisons of the presence of MR imaging-visible PVS-CS (A) and MR imaging-visible PVS in the basal ganglia (B) based on the  $\beta$ -amyloid status. The enlarged perivascular spaces in the centrum semiovale (ePVS-CS) were significantly higher in the patient group positive for  $\beta$ -amyloid than in the patient group negative for it, whereas the high degree of enlarged perivascular spaces in the basal ganglia (ePVS-BG) did not differ between the groups positive and negative for  $\beta$ -amyloid.

### MR Imaging-Visible PVS as a Predictor of $\beta$ -Amyloid Positivity

In the univariate logistic regression analysis, a high degree of MR imaging-visible PVS-CS was a positive predictor of  $\beta$ -amyloid positivity based

on the BAPL scoring system (OR, 2.966; 95% CI, 1.503–5.851;  $P = .002$ ) (Table 2). After adjustment, a high degree of MR imaging-visible PVS-CS remained independently associated with  $\beta$ -amyloid PET positivity (OR, 2.307; 95% CI, 1.036–5.136;  $P = .041$ ), as well as the presence of the *APOE*  $\epsilon 4$  allele (OR, 4.583; 95% CI, 1.945–10.796;  $P < .001$ ) and older age (OR, 1.050; 95% CI, 1.004–1.098;  $P = .034$ ).

The random forests model with 13 variables showed an area under the curve of 0.985 (95% CI, 0.964–1.000) with an accuracy of 0.971 (95% CI, 0.931–1.000), sensitivity of 1.000 (95% CI, 1.000–

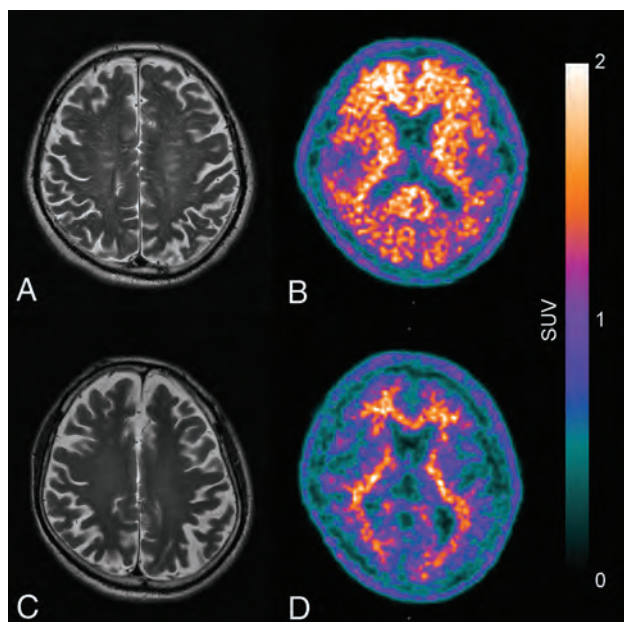


**FIG 3.** Examples of perivascular space patterns with the corresponding  $[^{18}\text{F}]$  FBB PET image. The axial T2-weighted MR imaging shows a high degree of MR imaging-visible PVS-CS (A), and the corresponding  $[^{18}\text{F}]$  FBB PET (B) shows pronounced  $\beta$ -amyloid deposition. Axial T2-weighted MR imaging shows a low degree of MR imaging-visible PVS-CS (C) and the  $[^{18}\text{F}]$  FBB PET scan (D) shows low  $\beta$ -amyloid deposition.

1.000), and specificity of 0.985 (95% CI, 0.964–1.000). We observed that MR imaging-visible PVS-CS ranked as the third most important variable after *APOE* 4 and age (Online Supplemental Data).

#### Comparisons between Patients with High and Low Degrees of MR Imaging-Visible PVS-CS among Patients Positive for $\beta$ -Amyloid

Among the 77 patients with ADCI with  $\beta$ -amyloid positivity, 70.8% of the patients with a high degree of MR imaging-visible PVS-CS had a higher proportion of positive WMHs (34/48), whereas 44.8% (13/29) of patients with a low degree of MR imaging-visible PVS-CS had positive WMHs ( $P = .023$ ). The frequency of lobar microbleeds was also higher in patients with ADCI and  $\beta$ -amyloid positivity than among patients with ADCI and  $\beta$ -amyloid negativity ( $P = .007$ ). Other parameters such as age, MMSE score, lacunes, deep microbleeds, sex, hypertension, diabetes mellitus, hyperlipidemia, previous stroke, the presence of an *APOE*  $\epsilon 4$  allele, or final diagnosis were not significantly different between the patients with high and low degrees of MR imaging-visible PVS-CS (Online Supplemental Data).

#### Comparisons between Patients with High and Low Degrees of MR Imaging-Visible PVS-CS among Patients Negative for $\beta$ -Amyloid

Among 67 patients with ADCI with  $\beta$ -amyloid negativity, the patients with a high degree of MR imaging-visible PVS-CS ( $n = 24$ ) were older compared with patients with a low degree of MR imaging-visible PVS-CS ( $n = 43$ ) (mean, 76.5 [SD, 9.8] years versus 68.3 [SD, 10.0] years;  $P = .002$ ). Furthermore, the patients with a high degree of MR imaging-visible PVS-CS had lower MMSE scores compared with those with a low degree of MR imaging-visible PVS-CS (23.8 [SD, 4.0] versus 26.1 [SD, 3.7],  $P = .018$ ). The patients with a high degree of MR imaging-visible PVS-CS compared with patients with a low degree of MR imaging-visible PVS-CS had a higher prevalence of hypertension (54.2% versus 27.9%,  $P = .033$ ), positive WMHs (58.3% versus 30.2%,  $P = .025$ ), final diagnosis of probable AD (45.8% versus

**Table 2: Logistic regression analysis for the predictors of  $\beta$ -amyloid positivity**

	Univariable		Multivariable	
	OR (95% CI)	P Value	OR (95% CI)	P Value
Age (yr)	1.051 (1.012–1.092)	.010	1.050 (1.004–1.098)	.034
Sex				
Female	Reference group			
Male	1.435 (0.729–2.823)	.296	1.561 (0.699–3.489)	.278
Hypertension (present)	1.475 (0.757–2.875)	.254		
Diabetes (present)	1.495 (0.627–3.564)	.364		
Hyperlipidemia (present)	1.074 (0.416–2.774)	.883		
Previous stroke (present)	0.470 (0.131–1.681)	.245		
<i>APOE</i> $\epsilon 4$ allele (present)	3.526 (1.630–7.627)	.001	4.583 (1.945–10.796)	<.001
High degree of MR imaging-visible PVS-CS (score, $\geq 3$ )	2.966 (1.503–5.851)	.002	2.307 (1.036–5.136)	.041
High degree of MR imaging-visible PVS-BG (score, $\geq 3$ )	1.034 (0.429–2.492)	.940		
WMH (present)	2.321 (1.188–4.533)	.014		
Lacunes (for 1 number higher)	0.937 (0.726–1.209)	.618		
cSS (present)	5.577 (0.654–47.565)	.116		
Lobar CMB (present)	1.100 (0.934–1.295)	.253		
Deep CMB (present)	0.688 (0.428–1.108)	.124		

**Note:**—CMB indicates cerebral microbleed; cSS, cortical superficial siderosis; MRI-visible PVS-BG, enlarged perivascular space in the basal ganglia; MRI-visible PVS-CS, enlarged perivascular space in the semi ovale.

18.6%,  $P = .018$ ), and a higher number of lobar microbleeds (median, 0 [interquartile range, 0–0] versus 0 [interquartile range, 0–1];  $P = .007$ ). Other results are presented in the Online Supplemental Data.

## DISCUSSION

In this retrospective study, we hypothesized that MR imaging-visible PVS-CS would be associated with brain amyloid deposition in patients with ADCI. We found that a high degree of MR imaging-visible PVS-CS were independently associated with  $\beta$ -amyloid accumulation, as assessed by [ $^{18}\text{F}$ ] FBB PET scanning, even after adjusting for previously known clinical risk factors. Our findings support the evidence that MR imaging-visible PVS-CS are associated with the amyloid pathology of the brain and could be an indirect imaging marker of amyloid burden in the brains of patients with ADCI.

PVS become visible on MR imaging when enlarged and can be detected in individuals of all ages; however, MR imaging-visible PVS are more frequently found with aging.<sup>17,33</sup> A recent meta-analysis, including a total of 8395 individuals, showed strong evidence for the association with age and MR imaging-visible PVS in the basal ganglia, as well as in the centrum semiovale.<sup>33</sup> On the other hand, a greater number of MR imaging-visible PVS can also be associated with various pathologic conditions. Accumulating evidence shows that MR imaging-visible PVS-CS, in particular, are associated with amyloid-associated pathology; several different studies have demonstrated an association with the presence of AD and MR imaging-visible PVS-CS,<sup>7,20,34</sup> though the mechanisms of MR imaging-visible PVS-CS remain poorly understood. However, our observation suggests a potential pathophysiologic link between AD and MR imaging-visible PVS, in that progressive  $\beta$ -amyloid deposition in the vascular wall or brain cortex may interfere with the perivascular drainage of interstitial fluid and ultimately cause retrograde perivascular space dilation in the white matter.<sup>35</sup> Consequently, the visibility of MR imaging-visible PVS is increased on MR imaging and appears as spaces with a signal intensity similar to that of CSF, resulting in a high burden of MR imaging-visible PVS.<sup>8</sup> Consistent with this hypothesis, a post-mortem study of AD demonstrated that the degree of white matter PVS on histopathologic examination was positively correlated with cortical  $\beta$ -amyloid deposition,<sup>16</sup> which is in line with our observation. Therefore, visible PVS on brain MR imaging may result from abnormal amyloid accumulation in the cortex and cortical/leptomeningeal vessels.

Recently, advances in bioimaging and radiochemistry have enabled the in vivo imaging of  $\beta$ -amyloid deposits of AD, and this could be beneficial in aiding the early diagnosis of AD, compared with the use of clinical symptoms alone.<sup>36–38</sup> Furthermore, the use of biomarkers may also identify individuals who could benefit from disease-modifying therapies in AD. On the basis of our results, MR imaging-visible PVS alone cannot be an alternative to an amyloid PET scan; however, MR imaging-visible PVS-CS could be a useful indirect marker of amyloid deposition and may also be helpful in determining which patients with cognitive impairment are most likely to benefit from a biomarker test. These approaches may decrease the unnecessary patient burden and the costs of clinical practice and clinical trials.

To date, unlike the evidence for the cerebral amyloid angiopathy population,<sup>14,17</sup> scarce evidence exists regarding the association between AD and the in vivo amyloid burden, as assessed with PET. A previous study, with results conflicting with ours, showed that there was no association between MR imaging-visible PVS and amyloid burden in patients with dementia.<sup>7</sup> However, several considerable differences were found in terms of the study methodology, which may lead to different study outcomes.<sup>7</sup> First, the aforementioned study included a population with AD and vascular cognitive impairment, unlike our ADCI population. Because they included a large vascular dementia population, the heterogeneity of the diagnosis and probable higher severity of small-vessel disease in the population may lead to different results between the 2 studies. The amyloid-negative group in the aforementioned study had an inevitably higher WMH volume load, which may result in the misdiagnosis of MR imaging-visible PVS and ultimately interfere with the evaluation of the association between MR imaging-visible PVS and amyloid positivity. Furthermore, the different cutoff values for MR imaging-visible PVS scores may also lead to different study results. Those investigators considered score 2 (11–20 PVS) as a moderate pathologic condition, whereas we considered score 2 as a low degree of MR imaging-visible PVS. We believe that due to the wider area of the centrum semiovale compared with the basal ganglia and consequent higher number of PVS in the centrum semiovale than in basal ganglia, when one focuses on PVS in the centrum semiovale, score 2 should be considered a lower degree of PVS as it has been in other studies.<sup>10,12</sup>

Most interesting, we found that the group negative for  $\beta$ -amyloid had many different clinical variables that may be associated with a high degree of MR imaging-visible PVS-CS, such as aging, hypertension, and lower cognitive function in addition to AD pathology, lobar microbleeds, and the presence of WMHs. Therefore, we hypothesized that in patients with ADCI with lower amyloid burden, the presence of an MR imaging-visible PVS may have multifactorial causes, such as arterial stiffness and atrophy,<sup>39,40</sup> whereas in patients with ADCI and a high amyloid burden, MR imaging-visible PVS are primarily caused by amyloid accumulation. However, this hypothesis needs further validation.

In multivariate analysis, MR imaging-visible PVS-CS, *APOE*  $\epsilon 4$  allele presence, and older age were significantly related to  $\beta$ -amyloid PET positivity, as analyzed by the BAPL scoring system. The visual assessment of [ $^{18}\text{F}$ ] FBB PET images has achieved high diagnostic accuracy, with the neuropathology assessments offering good reliability and efficacy.<sup>41,42</sup> We believe that using the BAPL scoring system to evaluate  $\beta$ -amyloid deposition can achieve accurate and reproducible assessments of [ $^{18}\text{F}$ ] FBB PET data. Also, a semi-quantitative analysis by SUVr cutoff classification was performed to obtain a significant result. Bullich et al<sup>31</sup> reported a good agreement between florbetaben PET quantification and histopathologic amyloid plaque density (92% sensitivity and 96% specificity) and visual read results by experts (percentage agreement = 94%~97%). They emphasized the robustness of visual analysis performed by expert readers, as well as the additional contribution that optimized relative FBB uptake quantification may have for the detection of  $\beta$ -amyloid plaques.

Our study had some limitations. First, it was a retrospective observational study and may have selection bias. Our findings require external validation in larger cohorts. We also did not quantitatively assess the MR imaging-visible PVS burden in both the centrum semiovale and basal ganglia. Therefore, whether MR imaging-visible PVS in both the centrum semiovale and basal ganglia are consistent and good estimators of the whole-PVS load in the brain remains uncertain. Standardized, fully automated, and reliable whole-brain assessment techniques for PVS volume quantification are needed to generalize the results of our study.

## CONCLUSIONS

The findings of this study provide further supporting evidence that MR imaging-visible PVS-CS are a key imaging marker of amyloid pathology when assessed by amyloid PET scans in patients with ADCI. Our findings raise the possibility that MR imaging-visible PVS-CS in patients with ADCI are also a consequence of amyloid deposition in the cortical and vascular amyloid processes.

## REFERENCES

- Doubal FN, MacLulich AM, Ferguson KJ, et al. **Enlarged perivascular spaces on MRI are a feature of cerebral small vessel disease.** *Stroke* 2010;41:450–54 CrossRef Medline
- Brown R, Benveniste H, Black SE, et al. **Understanding the role of the perivascular space in cerebral small vessel disease.** *Cardiovasc Res* 2018;114:1462–73 CrossRef Medline
- Zhu YC, Tzourio C, Soumare A, et al. **Severity of dilated Virchow-Robin spaces is associated with age, blood pressure, and MRI markers of small vessel disease: a population-based study.** *Stroke* 2010;41:2483–90 CrossRef Medline
- Weller RO, Hawkes CA, Kalaria RN, et al. **White matter changes in dementia: role of impaired drainage of interstitial fluid.** *Brain Pathol* 2015;25:63–78 CrossRef Medline
- Wardlaw JM, Benveniste H, Nedergaard M, et al. **Colleagues from the Fondation Leducq Transatlantic Network of Excellence on the Role of the Perivascular Space in Cerebral Small Vessel Disease. Perivascular spaces in the brain: anatomy, physiology and pathology.** *Nat Rev Neurol* 2020;16:137–53 CrossRef Medline
- Park YW, Shin NY, Chung SJ, et al. **Magnetic resonance imaging-visible perivascular spaces in basal ganglia predict cognitive decline in Parkinson's disease.** *Mov Disord* 2019;34:1672–79 CrossRef Medline
- Banerjee G, Kim HJ, Fox Z, et al. **MRI-visible perivascular space location is associated with Alzheimer's disease independently of amyloid burden.** *Brain* 2017;140:1107–16 CrossRef Medline
- Smeijer D, Ikram MK, Hilal S. **Enlarged perivascular spaces and dementia: a systematic review.** *J Alzheimers Dis* 2019;72:247–56 CrossRef Medline
- Inglese M, Bomszyk E, Gonen O, et al. **Dilated perivascular spaces: hallmarks of mild traumatic brain injury.** *AJNR Am J Neuroradiol* 2005;26:719–24 Medline
- Martinez-Ramirez S, Pontes-Neto OM, Dumas AP, et al. **Topography of dilated perivascular spaces in subjects from a memory clinic cohort.** *Neurology* 2013;80:1551–56 CrossRef Medline
- Charidimou A, Meegahage R, Fox Z, et al. **Enlarged perivascular spaces as a marker of underlying arteriopathy in intracerebral haemorrhage: a multicentre MRI cohort study.** *J Neurol Neurosurg Psychiatry* 2013;84:624–29 CrossRef Medline
- Charidimou A, Boulouis G, Pasi M, et al. **MRI-visible perivascular spaces in cerebral amyloid angiopathy and hypertensive arteriopathy.** *Neurology* 2017;88:1157–64 CrossRef Medline
- van Veluw SJ, Biessels GJ, Bouvy WH, et al. **Cerebral amyloid angiopathy severity is linked to dilation of juxtacortical perivascular spaces.** *J Cereb Blood Flow Metab* 2016;36:576–80 CrossRef Medline
- Raposo N, Planton M, Payoux P, et al. **Enlarged perivascular spaces and florbetapir uptake in patients with intracerebral hemorrhage.** *Eur J Nucl Med Mol Imaging* 2019;46:2339–47 CrossRef Medline
- Martinez-Ramirez S, van Rooden S, Charidimou A, et al. **Perivascular spaces volume in sporadic and hereditary (Dutch-Type) cerebral amyloid angiopathy.** *Stroke* 2018;49:1913–19 CrossRef Medline
- Roher AE, Kuo YM, Esh C, et al. **Cortical and leptomeningeal cerebrovascular amyloid and white matter pathology in Alzheimer's disease.** *Mol Med* 2003;9:112–22 CrossRef Medline
- Charidimou A, Hong YT, Jager HR, et al. **White matter perivascular spaces on magnetic resonance imaging: marker of cerebrovascular amyloid burden?** *Stroke* 2015;46:1707–09 CrossRef Medline
- Rowe CC, Ackerman U, Browne W, et al. **Imaging of amyloid beta in Alzheimer's disease with 18F-BAY94-9172, a novel PET tracer: proof of mechanism.** *Lancet Neurol* 2008;7:129–35 CrossRef Medline
- Hawkes CA, Jayakody N, Johnston DA, et al. **Failure of perivascular drainage of beta-amyloid in cerebral amyloid angiopathy.** *Brain Pathol* 2014;24:396–403 CrossRef Medline
- Ramirez J, Berezuk C, McNeely AA, et al. **Visible Virchow-Robin spaces on magnetic resonance imaging of Alzheimer's disease patients and normal elderly from the Sunnybrook Dementia Study.** *J Alzheimers Dis* 2014;43:415–24 CrossRef Medline
- Marcus C, Mena E, Subramaniam RM. **Brain PET in the diagnosis of Alzheimer's disease.** *Clin Nucl Med* 2014;39:e413–22; quiz e23–26 CrossRef Medline
- Murphy MP, LeVine H 3rd. **Alzheimer's disease and the amyloid-beta peptide.** *J Alzheimers Dis* 2010;19:311–23 CrossRef Medline
- McKhann G, Drachman D, Folstein M, et al. **Clinical diagnosis of Alzheimer's disease: report of the NINCDS-ADRDA Work Group under the auspices of Department of Health and Human Services Task Force on Alzheimer's Disease.** *Neurology* 1984;34:939–44 CrossRef Medline
- Petersen RC, Smith GE, Waring SC, et al. **Mild cognitive impairment: clinical characterization and outcome.** *Arch Neurol* 1999;56:303–08 CrossRef Medline
- Ahn HJ, Chin J, Park A, et al. **Seoul Neuropsychological Screening Battery-dementia version (SNSB-D): a useful tool for assessing and monitoring cognitive impairments in dementia patients.** *J Korean Med Sci* 2010;25:1071–76 CrossRef Medline
- Wardlaw JM, Smith EE, Biessels GJ, et al. **STandards for Reporting Vascular changes on nEuroimaging (STRIVE v1). Neuroimaging standards for research into small vessel disease and its contribution to ageing and neurodegeneration.** *Lancet Neurol* 2013;12:822–38 CrossRef Medline
- MacLulich AM, Wardlaw JM, Ferguson KJ, et al. **Enlarged perivascular spaces are associated with cognitive function in healthy elderly men.** *J Neurol Neurosurg Psychiatry* 2004;75:1519–23 CrossRef Medline
- Fazekas F, Chawluk JB, Alavi A, et al. **MR signal abnormalities at 1.5 T in Alzheimer's dementia and normal aging.** *AJR Am J Roentgenol* 1987;149:351–56 CrossRef Medline
- Barthel H, Gertz HJ, Dresel S, et al. **Cerebral amyloid-beta PET with florbetaben (18F) in patients with Alzheimer's disease and healthy controls: a multicentre phase 2 diagnostic study.** *Lancet Neurol* 2011;10:424–35 CrossRef Medline
- Lopresti BJ, Klunk WE, Mathis CA, et al. **Simplified quantification of Pittsburgh Compound B amyloid imaging PET studies: a comparative analysis.** *J Nucl Med* 2005;46:1959–72 CrossRef Medline
- Bullich S, Seibyl J, Catafau AM, et al. **Optimized classification of (18F)-Florbetaben PET scans as positive and negative using an SUVR quantitative approach and comparison to visual assessment.** *Neuroimage Clin* 2017;15:325–32 CrossRef Medline
- Duara R, Loewenstein DA, Lizarraga G, et al. **Effect of age, ethnicity, sex, cognitive status and APOE genotype on amyloid load and the threshold for amyloid positivity.** *Neuroimage Clin* 2019;22:101800 CrossRef Medline

33. Francis F, Ballerini L, Wardlaw JM. **Perivascular spaces and their associations with risk factors, clinical disorders and neuroimaging features: a systematic review and meta-analysis.** *Int J Stroke* 2019;14:359–71 CrossRef Medline
34. Chen W, Song X, Zhang Y; Alzheimer's Disease Neuroimaging Initiative. **Assessment of the Virchow-Robin Spaces in Alzheimer disease, mild cognitive impairment, and normal aging, using high-field MR imaging.** *AJNR Am J Neuroradiol* 2011;32:1490–95 CrossRef Medline
35. Weller RO, Djuanda E, Yow HY, et al. **Lymphatic drainage of the brain and the pathophysiology of neurological disease.** *Acta Neuropathol* 2009;117:1–14 CrossRef Medline
36. Palmqvist S, Zetterberg H, Mattsson N, et al. Alzheimer's Disease Neuroimaging Initiative. **Detailed comparison of amyloid PET and CSF biomarkers for identifying early Alzheimer disease.** *Neurology* 2015;85:1240–49 CrossRef Medline
37. Buchhave P, Minthon L, Zetterberg H, et al. **Cerebrospinal fluid levels of beta-amyloid 1-42, but not of tau, are fully changed already 5 to 10 years before the onset of Alzheimer dementia.** *Arch Gen Psychiatry* 2012;69:98–106 CrossRef Medline
38. Hansson O, Zetterberg H, Buchhave P, et al. **Association between CSF biomarkers and incipient Alzheimer's disease in patients with mild cognitive impairment: a follow-up study.** *Lancet Neurol* 2006;5:228–34 CrossRef Medline
39. Hughes TM, Craft S, Lopez OL. **Review of 'the potential role of arterial stiffness in the pathogenesis of Alzheimer's disease.'** *Neurodegener Dis Manag* 2015;5:121–35 CrossRef Medline
40. Adams HH, Hilal S, Schwingenschuh P, et al. **A priori collaboration in population imaging: the Uniform Neuro-Imaging of Virchow-Robin Spaces Enlargement Consortium.** *Alzheimers Dement (Amst)* 2015;1:513–20 CrossRef Medline
41. Minoshima S, Drzezga AE, Barthel H, et al. **SNMMI Procedure Standard/EANM Practice Guideline for Amyloid PET Imaging of the Brain 1.0.** *J Nucl Med* 2016;57:1316–22 CrossRef Medline
42. Seibyl J, Barthel H, Stephens A, et al. **Reliability, reproducibility and efficacy of the 18F florbetaben  $\beta$ -amyloid PET scan visual assessment method as trained via a computer-based instructional tool.** *J Nucl Med* 2013;54(Suppl 2):300

# Iatrogenic Foreign Materials Associated with Retrieved Clot Tissue via Mechanical Thrombectomy

M. Abbasi, D. Dai, Y. Liu, S. Fitzgerald, R. Kadirvel, L.E. Savastano, H. Cloft, D.F. Kallmes, and W. Brinjikji



## ABSTRACT

**BACKGROUND AND PURPOSE:** Hydrophilic polymers and polytetrafluoroethylene liners, commonly used in the construction of endovascular devices, occasionally separate from devices with subsequent embolization. We determined the frequency of such materials in thrombus specimens retrieved by mechanical thrombectomy in patients with stroke.

**MATERIALS AND METHODS:** We retrospectively reviewed H&E–stained thrombus sections for presence and types of foreign materials. We identified 4 types of foreign materials—Type I: material was light green with refraction and had a homogeneous texture; type II: material was light gray and/or dark gray, thin, and loose or attenuated in texture; type III: material was light green with refraction, solitary in texture, irregular in shape, and was often associated with round or oval bubblelike particles and/or diffuse black particles; and type IV: material had homogeneous texture and was light pink or red. In addition, polymer materials from different layers of used mechanical thrombectomy catheters were compared with the foreign materials found in thrombus specimens.

**RESULTS:** A total of 101 thrombi were evaluated. Foreign materials were found in 53 (52.5%) thrombus samples. The most common type was type I (92%), followed by type II (30%). The histopathologic features of the polymer materials from mechanical thrombectomy catheters were similar to the foreign materials found in thrombus specimens. The inner polytetrafluoroethylene liner and coating layer of catheters resembled type I and type II of the foreign materials, respectively.

**CONCLUSIONS:** Foreign polymer materials are present in approximately half of retrieved thrombi, most commonly polytetrafluoroethylene from catheter liners and less from hydrophilic coatings.

**ABBREVIATIONS:** ASP = aspiration; MT = mechanical thrombectomy; PTFE = polytetrafluoroethylene

Neuroendovascular catheters are constructed with various polymers aimed at improving lubricity, including polytetrafluoroethylene (PTFE) liners and hydrophilic coatings. The benefits of these materials include low coefficients of friction, improved trackability during the endovascular procedure, easy lesion passage, and vasospasm prevention.<sup>1</sup> However, introduction of such foreign material to the body is associated with some risks. Many reports have suggested that foreign materials could dissociate from catheters with subsequent distal embolization and microinfarctions.<sup>2,3</sup>

In the current study, we performed histologic examination of 101 thrombus specimens to evaluate how often polymer materials are liberated from catheters. All of the thrombus samples were retrieved by mechanical thrombectomy (MT) from patients with large-vessel occlusion stroke. To confirm the source of the foreign materials observed in thrombi, we examined the histologic appearance of each polymer layer of the aspiration catheters commonly used in thrombectomy, and compared the histology with that of the foreign materials observed in thrombus specimens.

Received November 18, 2020; accepted after revision January 30, 2021.

From the Departments of Radiology (M.A., D.D., Y.L., S.F., R.K., L.E.S., H.C., D.F.K., W.B.) and Neurosurgery (L.E.S.), Mayo Clinic, Rochester, Minnesota.

This study is supported by the National Institutes of Health grant (No. R01 NS105853).

Please address correspondence to Daying Dai, MD, PhD, Department of Radiology, Mayo Clinic, 200 First St SW, Rochester, MN 55905; e-mail: dai.daying@mayo.edu

Indicates open access to non-subscribers at [www.ajnr.org](http://www.ajnr.org)

<http://dx.doi.org/10.3174/ajnr.A7106>

## MATERIALS AND METHODS

### Patient Population

After independent review board approval, 101 thrombus samples retrieved from patients with acute ischemic stroke from our center were collected for conventional, histopathologic evaluation. Demographic data were collected. Procedural data including thrombectomy approach (aspiration [ASP], stent retriever, and a

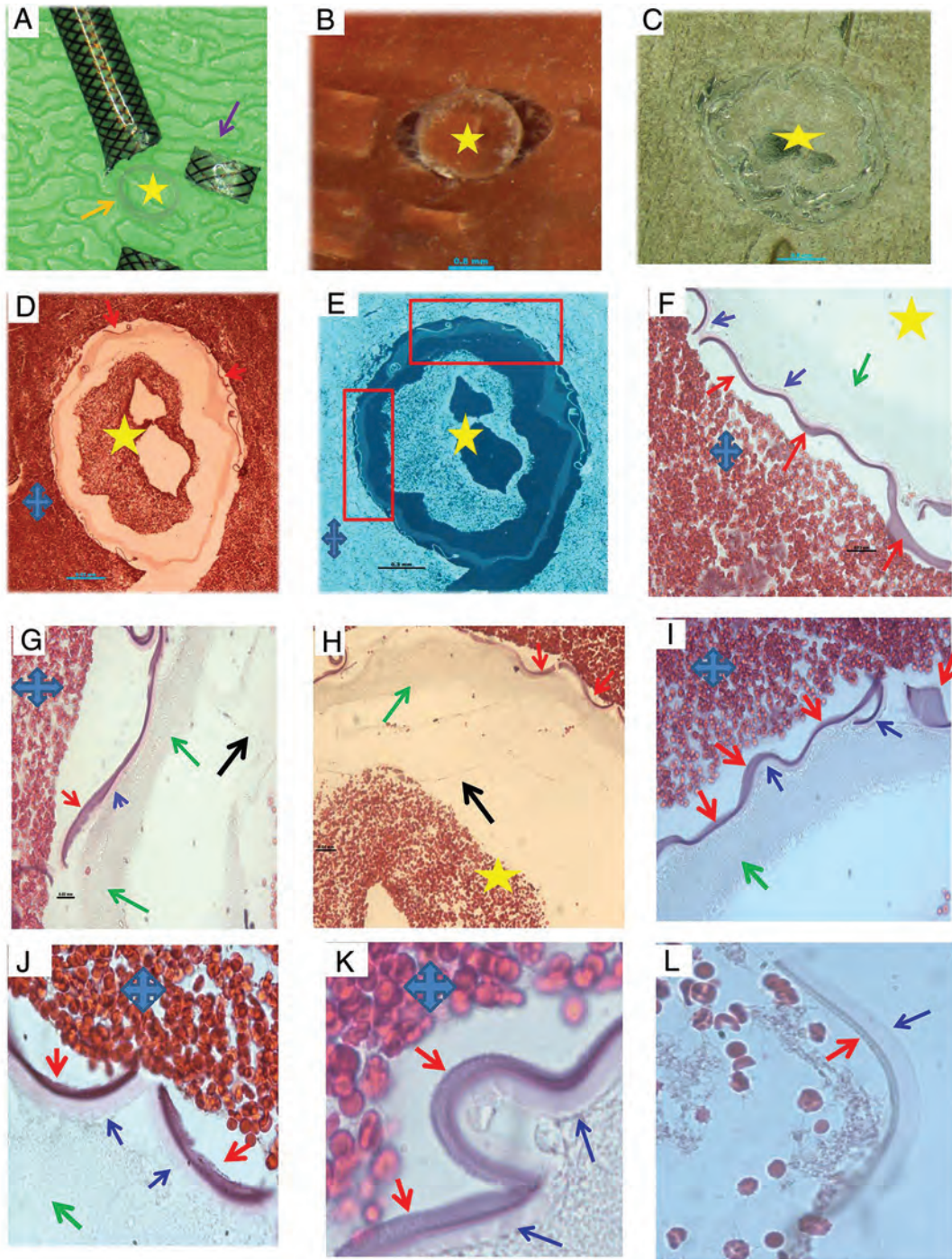


**FIG 1.** Histologic processing of cross-section of MT catheter. A, Macro photograph of the Sofia catheter, showing the catheter is cut into pieces in coronary plane (arrows), with removal of metal scaffold for further histology processing (orange arrow) (asterisk: lumen side). B, Macro photograph of catheter piece in image A mixed with clot analog tissue (asterisk: lumen side). C, Macro photograph showing the catheter piece mixed with clot tissue embedded in paraffin after tissue processing; catheter piece remains in the coronal orientation (asterisk: lumen side). D, Low-magnification microphotograph of H&E-stained catheter piece from image C (blue cross: the surrounding clot; yellow asterisk: the lumen/inner side of catheter; red arrows: outer layer surface-coating material that is next to the surrounding clot tissue). E, Reverse image of image D, showing each layer of the catheter, in relation to the lumen and outside surrounding clot tissue (yellow star: lumen side; blue cross: surrounding clot tissue). F-I, High magnification of microphotograph taken from the red rectangular area in image E, showing each layer of the catheter materials from the outer layer surface (red arrows), middle layer (blue arrows and green arrows) to the inner liner layer (black arrow) (H&E, original magnification  $\times 400$ ; yellow star: the lumen side of catheter; blue cross: the surrounding clot analog tissue). J-L, Microphotographs taken with oil lens, showing the surface-coating material (red arrows), its subsequent layer (blue arrows), and deeper layer (green arrow). The surface-coating material appears to be light gray, gray-pink, or lightly stained; attenuated or loose in texture; and with varied shape, same as the type II foreign material found in the patient clot tissue (Fig 6). The layer that is immediately underneath the coating layer appears to be homogeneous in texture, light pink, or pale in color (blue arrows). It is similar to the type IV foreign material observed in the patient clot tissue (Fig 8) (H&E, oil lens  $\times 100$ ).

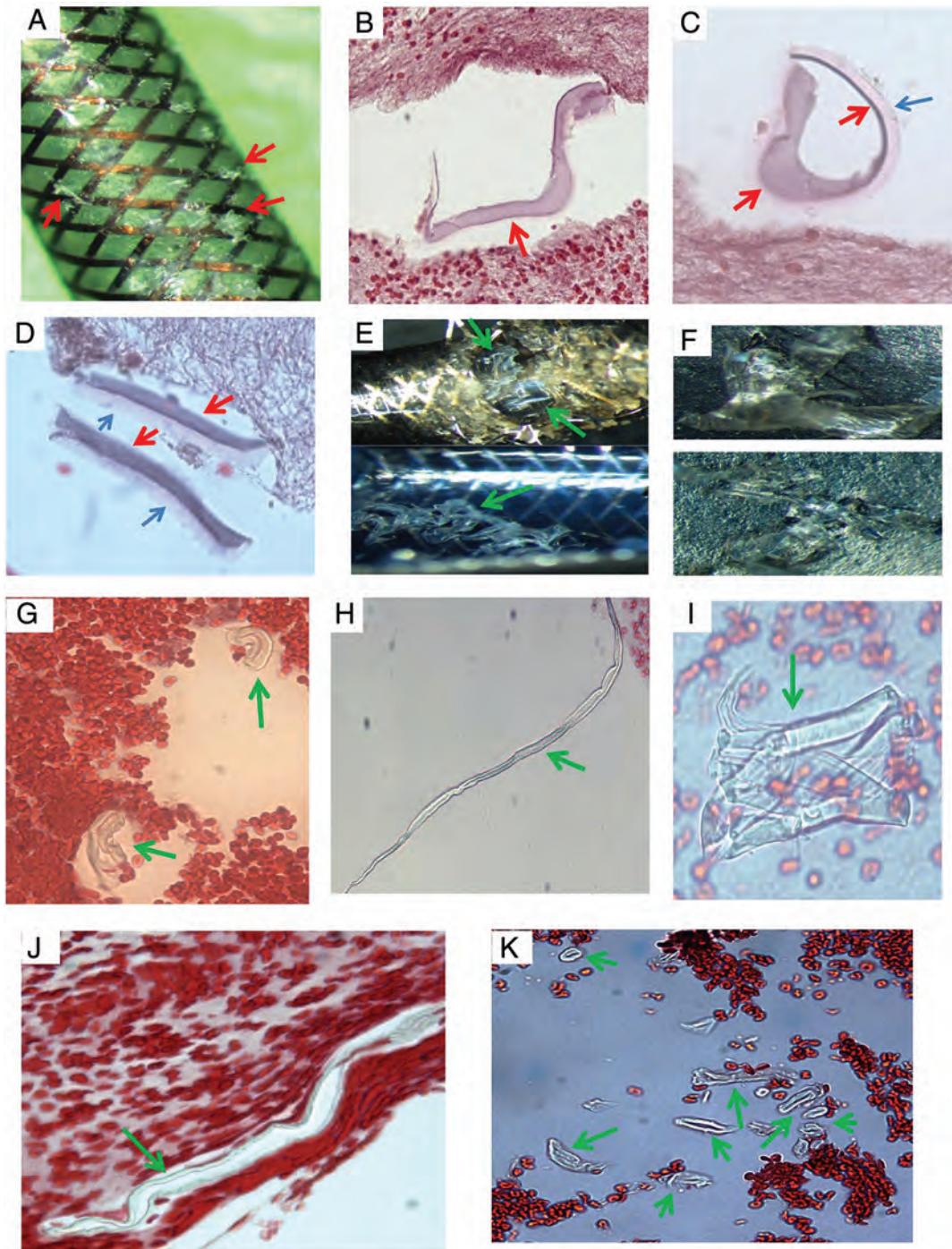


**FIG 2.** Histologic appearance of scratched surface and inner layer of MT catheter. *A*, Macrophotograph of the Sofia catheter, showing the scratched surface pieces (*red arrows*). *B–D*, Microphotograph of scratched pieces from image *A* associated with clot analog tissue, showing the surface-coating material, which appears to be varied in shape and texture following tissue processing (*red arrows*), and which is similar to the material seen in the cross-section experiment, (Fig 1). The layer immediately underneath the surface-coating material is also present (*blue arrow*), which appears to be a different shape, light pink/red, and has a homogeneous texture. It is similar to the material seen in the cross-section (Fig 1, *blue arrow*), and type IV foreign material (Fig 8) found in the patient clot tissue as well. *E*, Macrophotograph of Sofia and Fubuki catheters, showing the scratched liner layer material in situ (*green arrows*; upper—Sofia; lower—Fubuki). *F*, Macrophotograph of the manually torn off liner material pieces from image *E*, showing the similar gross appearance to that of the PTFE material (Fig 4). These pieces were crushed into small pieces for further routine, histologic processing, similar to the surface scratched material mentioned in Fig 1. *G–I*, Microphotograph of torn off liner pieces from *F* (upper), showing the material that appears to be varied in shape, color, and texture because of processing. These could be tube-like, long stripe, or an irregular solid mass, with refraction and light green outline. Those features are the same as what is seen from the PTFE material (Fig 4), and the type I material found in the patient clot (Fig 5). *J* and *K*, Representative microphotograph of scratched, torn off liner pieces from *F* (lower), showing the material that appears to be long, or short, or small tubular in shape, and light green, as shown with the PTFE material (Fig 4) and type I foreign material found in the patient clot tissue (Fig 5).

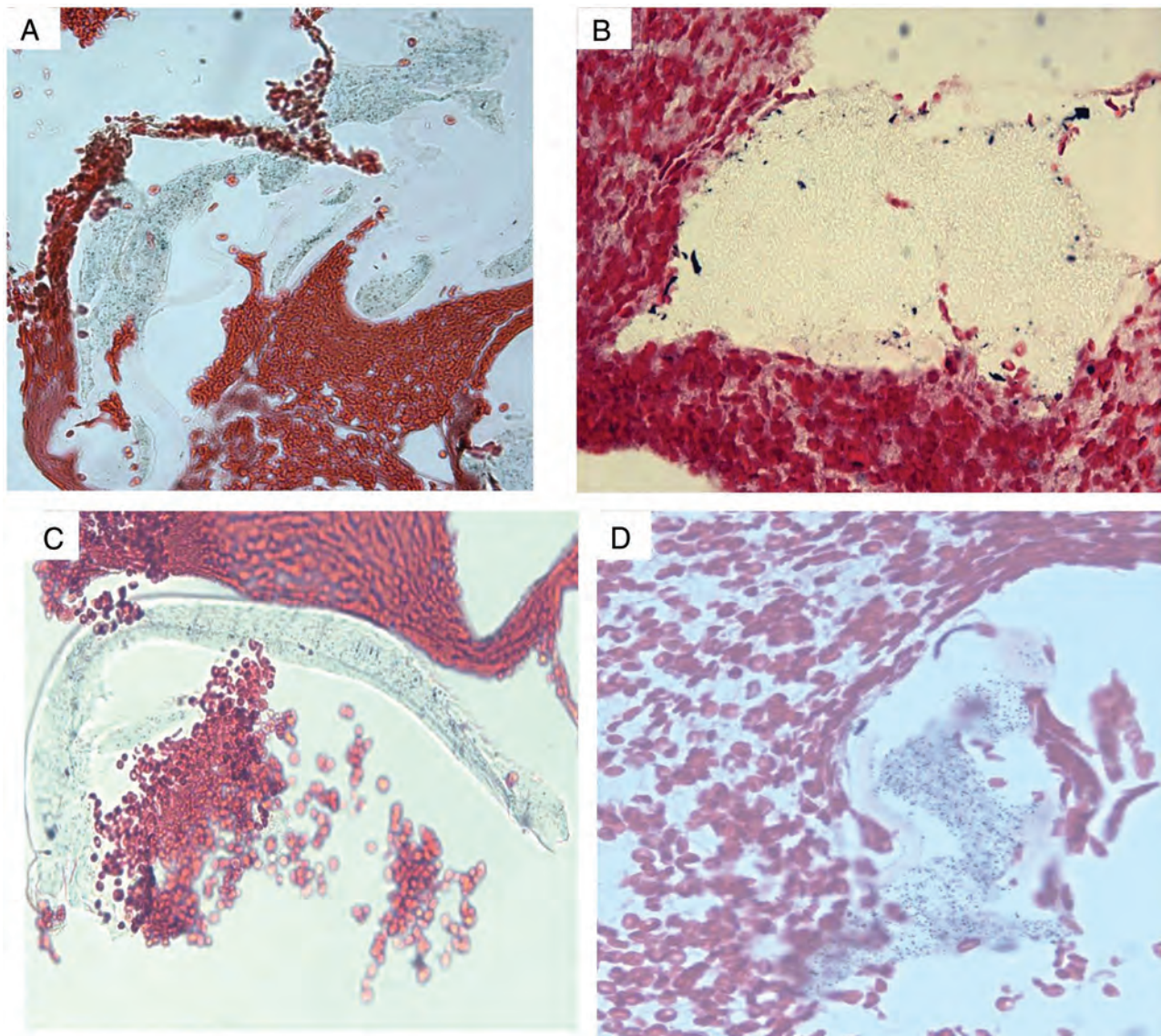


**FIG 3.** Representative microphotographs of scratched pieces of different layers rather than the surface or inner layer. Microphotographs showing the different materials of MT catheter, rather than the surface-coating material and inner liner materials shown in Figs 1 and 2. The similar foreign material is found in the patients' retrieved clot tissue (type III, Fig 7) (H&E, original magnification  $\times 400$ ).

combination), number of device passes, and list of devices (particularly catheters used for thrombectomy) were collected.

#### **Histopathologic Evaluation of Retrieved Thrombi**

Immediately after MT, thrombus samples were placed in 10% natural buffered formalin for at least 24 hours for fixation. After macrophotography, thrombus samples went through routine lab tissue processing as described by Fitzgerald et al.<sup>4</sup> Samples were then embedded in paraffin and sectioned in 3- to 5- $\mu$ m thickness. At least 2 serial sections from each sample were stained with H&E. In addition, 2 serial sections were stained with Martius Scarlet Blue for clot composition analysis.<sup>5</sup> All H&E-stained slides were evaluated by an experienced pathologist (D.D., with more than 18 years of experience) for the presence and the types of foreign materials in thrombus samples. Based on the color and texture of foreign materials in H&E-stained slides, 4 types of

foreign materials were categorized and defined as the following types. Type I: materials were light green with refraction and had homogeneous texture. Type II: materials were light gray or dark gray, thin, and loose or attenuated in texture. Type III: materials were light green with refraction, solitary in texture, irregular in shape, and were often associated with round or oval bubblelike particles and/or diffused black particles. Type IV: Materials had homogeneous texture, and they were light pink or red. Foreign materials observed under light microscopy were photographed and recorded for each sample. The location where the foreign material was observed was also recorded as within the clot tissue or alongside the tissue edge.

Each individual foreign material piece or pool of foreign material pieces on each slide of the patient was measured using Image-Pro 10 (Media Cybernetic). The average size (length  $\times$  width) was used as representative for each type, respectively.

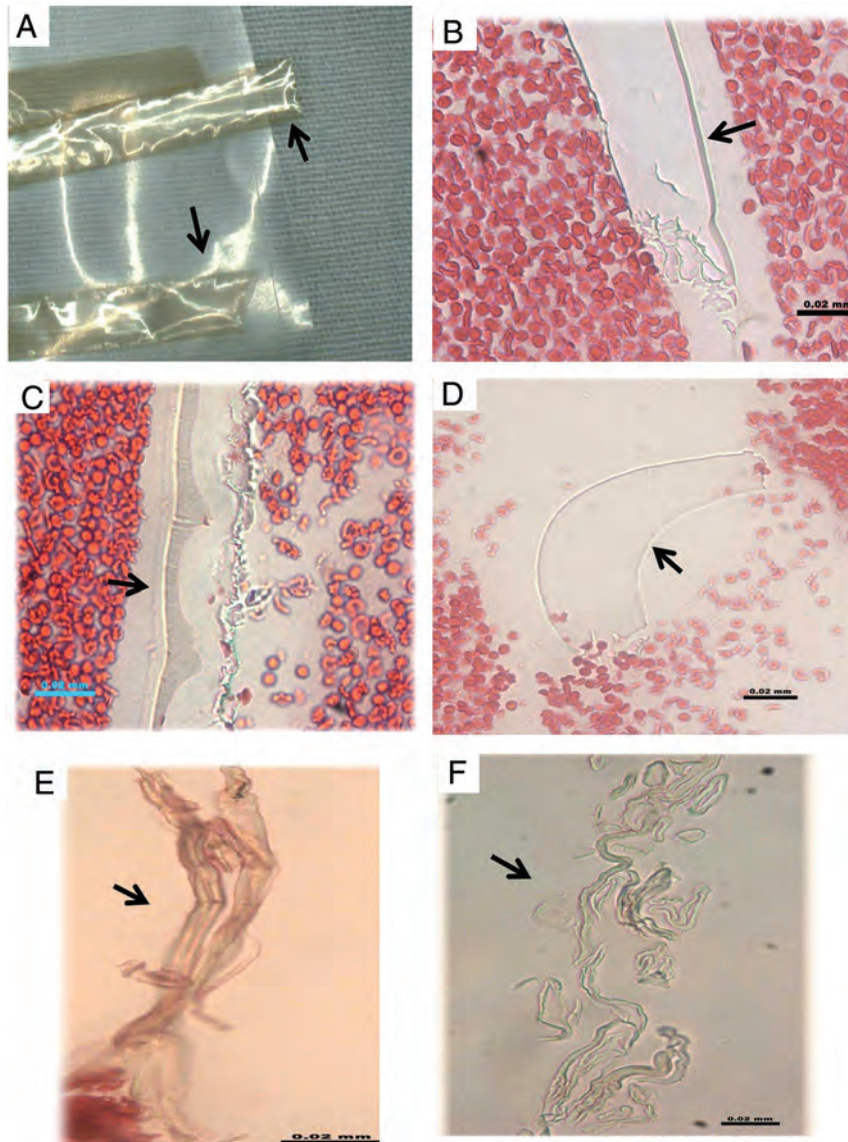


**FIG 4.** Histologic features of donated PTFE material. A, Macrophotograph of the PTFE liner material provided by manufacturer sponsor. B–F, Microphotographs of the scratched PTFE pieces in H&E–stained slides. The material appears to have varied shape. It is either a mass with solid, homogeneous texture associated with refraction, and light green edge (B–D), or long strips or tubes with light green outline (E and F). Those features are the same as the scratched inner layer of catheters (Fig 2), and type I material found in the patient clot tissue as well (Fig 5) (B–F, H&E, original magnification  $\times 400$ ).

#### **Histopathologic Features of Polymer Materials Used in Catheters for MT**

To determine the source of the foreign materials seen in the patients' thrombus samples, we evaluated the histologic appearance of the polymer materials of 2 commonly used catheters for MT at our institution: the Sofia suction catheter (MicroVent) and Fubuki guide catheter (Asahi Intecc). Catheters were collected after MT procedures and were carefully cleaned, dried, and sterilized. Under a dissecting microscope, the catheter wall was cut into pieces in a coronal plane, followed by removal of metal pieces (Fig 1A). The catheter pieces were then mixed with human blood in a coronal (cross) orientation, followed by a clot analog formation protocol, using a method described by Fitzgerald et al.<sup>6</sup> The catheter piece associated with the clot analog was processed, embedded, sectioned, and stained in the same manner as

the retrieved thrombi from patients (Fig 1). Each layer of polymeric materials from the catheter on the H&E–stained slide was visually compared with the foreign materials found in the patients' thrombus specimens. Manual scratching of the catheter, layer by layer, and starting from the very outer layer to the lumen inner layer longitudinally, was also performed under dissection microscope. The scratched material pieces from each layer were mixed with clot analog, and processed in the same way as above. The materials scratched from each layer of catheter on the H&E–stained slide were also visually compared with the layer at the cross/coronal section of the catheter, and the patient clot tissue as well (Figs 2 and 3).

The PTFE material that constructs the liner layer of the catheters was also provided specifically for the current study by the manufacturer sponsor. This material was manually scratched,

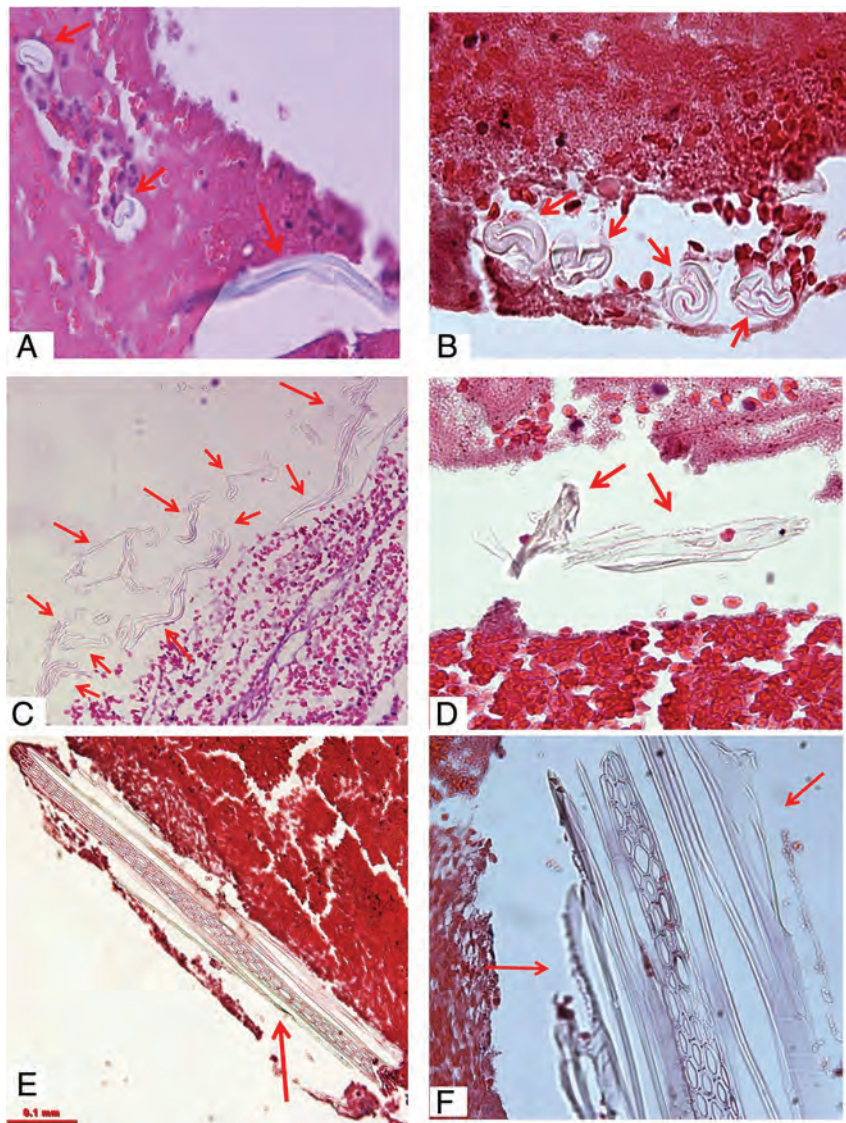


**FIG 5.** Representative microphotographs of type I foreign material found in patient clot tissue. *A*, Individual foreign material pieces separately embedded within the clot tissue (arrows). They appear to be small, ringlike, or long tubelike in shape, and light green (H&E, original magnification  $\times 400$ ). *B*, The cluster of foreign material pieces (arrows). Individual pieces appear to be wormlike with refraction and a light green outline (H&E, original magnification  $\times 400$ ). *C*, Multiple pieces of material associated with clot tissue. They are long or short stripes or pieces, with refraction, and green outline (arrows) (H&E, original magnification  $\times 200$ ). *D*, Irregular, solid pieces of material, with refraction, and light green outline (H&E, original magnification  $\times 400$ ). *E* and *F*, Large piece of polymer material surrounded with clot tissue (arrows). It appears to be long strips or ringlike circle, and solid homogeneous mass with refraction, with light green outline (H&E, original magnification  $\times 200$  [*E*],  $\times 400$  [*F*]).

torn off into pieces, and subsequently processed for histologic evaluation like the catheters mentioned above. The morphologic features (Fig 4) of the PTFE liner were also compared with foreign material found in the patient clot tissue and the material scratched from the catheters.

#### **Association of Thrombus Composition with the Presence of Foreign Materials**

Our experienced pathologist (D.D., with 18 years of lab-working experience) also evaluated the correlation between thrombus

composition and the presence of foreign materials to see whether a higher percentage of any of the components, particularly fibrin and platelet, results in a higher likelihood of materials release from catheters. In addition, we evaluated any inflammatory response to the foreign materials presented in the clot. Acute inflammatory response was defined as the presence of polymorphonuclear neutrophil, monocytes reacting to foreign materials.<sup>7</sup>

#### **Association of the Presence of Foreign Material with MT Approach and Angiographic Outcome**

The association of an MT approach (ASP or a combination of ASP and stent retriever) with the angiographic outcome using the final modified TICI reperfusion score and the number of device passes with the presence of foreign material found in the clot tissue was also evaluated.

#### **Statistical Analysis**

All statistical analyses were performed with the SPSS software package, v.24 for Windows (IBM). For descriptive analysis, categorical variables were presented as a percentage. The student *t* test and  $\chi^2$  test were used for inferential analysis. The level of significance was  $P < .05$ .

#### **RESULTS**

A total of 101 thrombi were retrieved from patients. The mean age for patients was 65.9 years (SD, 11.9) years. Fifty-six patients (55%) were men. The most common thrombectomy approach was ASP in 58% of patients, followed by combination of ASP and stent retrievers (31%).

The average number of passes to achieve successful revascularization (TICI 2b) was 2.2 (SD, 1.2). Overall, the median number of passes was 2 (IQR = 1–2).

#### **Histopathologic Features of Foreign Materials Found in Thrombi**

Foreign materials were found in 53 (52.5%) of 101 thrombus samples. The foreign materials were categorized into 4 types

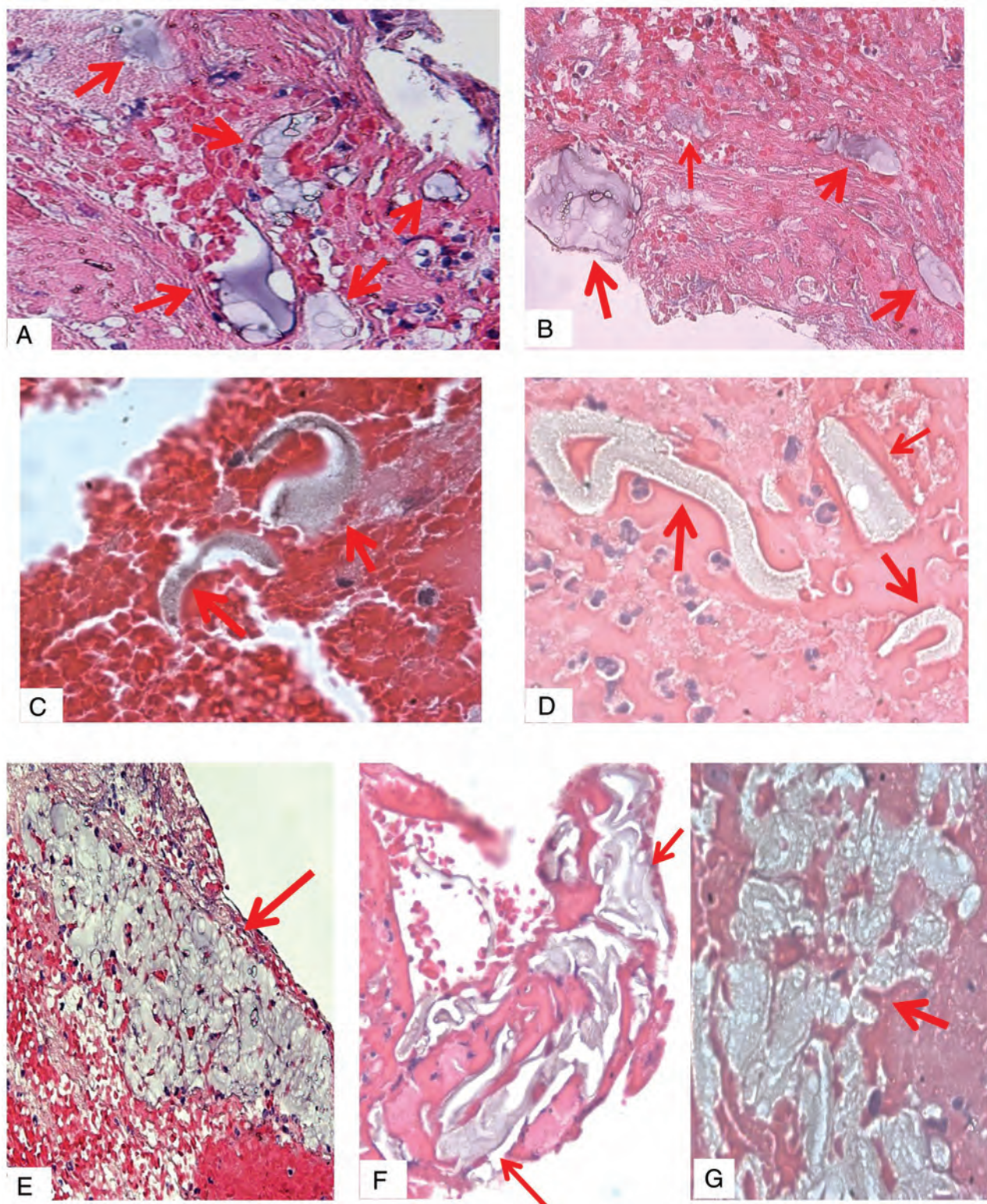


**FIG 6.** Representative microphotographs of type II foreign material found in patient clot tissue. A and B, Multiple pieces of foreign material embedded within clot tissue (*arrows*). They appear to be light gray or dark gray; thin or attenuated in texture (H&E, original magnification  $\times 400$ ). C and D, Foreign material pieces embedded within clot tissue, which appear to be denser and solid in texture (*arrows*), compared with that in A and B. They are wormlike or irregular in shape, gray or light gray (H&E, original magnification oil lens  $\times 100$ ). E–G, Cluster of the foreign material pieces, as a pool surrounded with clot tissue (H&E, original magnification  $\times 200$  [E],  $\times 400$  [F and G]).

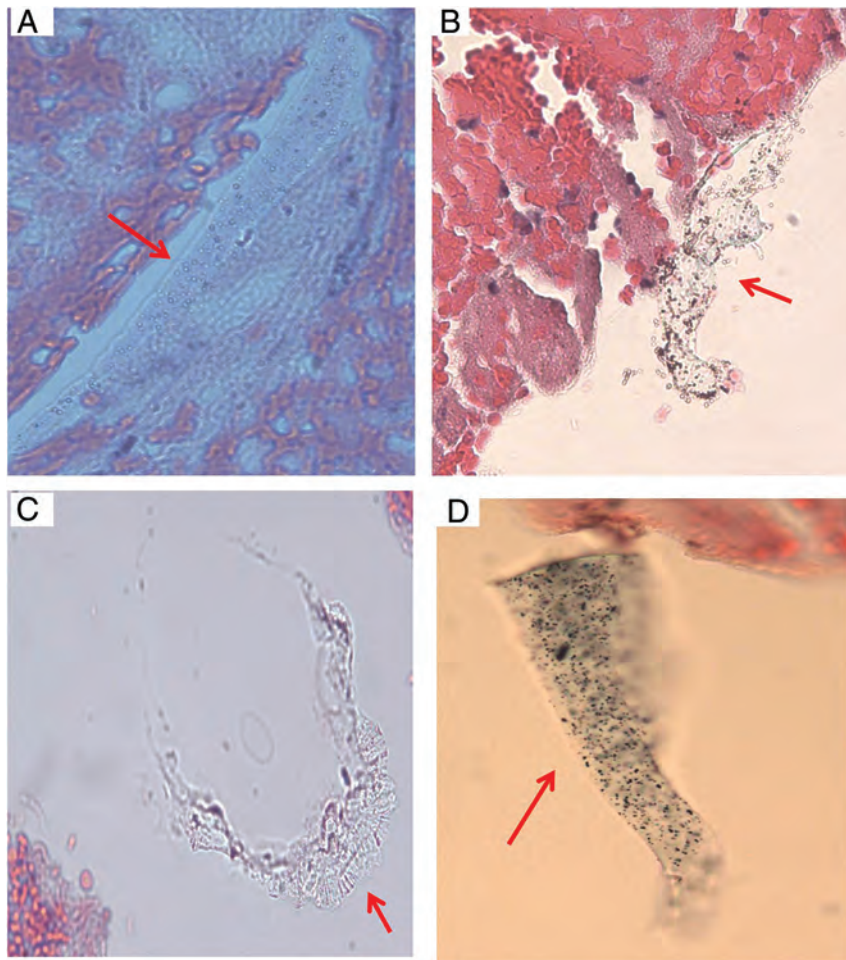


**FIG 7.** Representative microphotographs of type III foreign material found in patient clot tissue. *A*, A single, long, oval-like piece of foreign material embedded within clot tissue (*arrow*). The material is associated with multiple bubblelike particles, which are refracted under light microscopy. *B*, A single piece of irregular foreign material attaching to the clot tissue (*arrow*). It appears to be light green, associated dark/black and bubblelike, with refraction particles. *C*, Irregular piece of foreign material at the gap of clot tissue (*arrow*). It appears to be solid, homogeneous in texture with refraction, and light green. *D*, A piece of green, solid foreign material, associated diffused black, dotlike particles (*arrow*) (*A–D*, H&E, original magnification  $\times 400$ ). These materials presented in *A–D* are similar to the materials scratched from the catheters (Fig 3).

based on their microscopic appearance. The prevalence of each type of foreign materials was as follows:

Type I material was found in 49 (92%) of 53 cases that had foreign materials (Fig 5). The materials presented in different shapes, including tubular, short/long stripe, wormlike, or irregular pieces. They were scattered, single pieces, or clusters of varied size pieces. They were either located alongside the tissue border, at the gap between tissue masses, or were embedded within the clot tissue. These pieces measured from 6 to 1340  $\mu\text{m}$  in length. The average size of this type of material was  $64.9 \times 16.3 \mu\text{m}$  (length  $\times$  width).

Type II materials were found in 16 (30%) of 53 patient samples (Fig 6). They were embedded within thrombus tissue and presented as scattered or isolated separated pieces. They also gathered together as clusters. The pieces had various shapes, including cloudlike, honeycomblake, wormlike, cylinderlike, or

irregular. They measured 5 to 690  $\mu\text{m}$  in length. The average dimensions of type II material were  $110.5 \times 44.5 \mu\text{m}$  (length  $\times$  width).

Type III materials were found in 11 (21%) of 53 samples and were solitary in texture and irregular in shape (Fig 7). The material pieces were either located alongside the tissue section or embedded within the tissue. They measured 8 to 270  $\mu\text{m}$  in length. The measured average size for this material was  $93.8 \times 34 \mu\text{m}$  (length  $\times$  width).

Type IV materials were found in 8 (15%) of 53 samples (Fig 8). They were homogeneous in texture and lightly stained. They presented as snake or wormlike in shape. They were either located at gaps between tissues or embedded within thrombus tissue. They were measured 10 to 330  $\mu\text{m}$  in length. The average size of this type of material was  $126.4 \times 16.5 \mu\text{m}$  (length  $\times$  width).

Of the 53 samples that had polymer foreign material in the clot tissue, 29 (55%) cases showed type I material only in their clot tissue; and 20 (38%) cases had type I associated with other different types of materials. The frequency of each type of foreign material mentioned above, and the combinations of different types of material found in the clots are presented in Fig 9.

We found no inflammatory reactions to the foreign materials in thrombus specimens indicating the interaction of foreign materials with the tissue was acute.

#### **Histopathologic Features of Polymer Material from Catheters Used for MT**

The layers of the polymer material constructing the catheters are shown in Figs 1–3. The morphologic appearances of the PTFE liner material are shown in Fig 4. All types of foreign materials found in the thrombus samples retrieved from patients (Figs 5–8) in the current study demonstrated the same or similar morphologic features of materials that constructed the catheters in the scratched experiments (Figs 1–4). The inner layer of both catheters (Fig 2) and the inner PTFE material<sup>4</sup> both demonstrated the similar morphologic appearances of type I material found in the patient clots (Fig 5). The very outer surface coating material (Figs

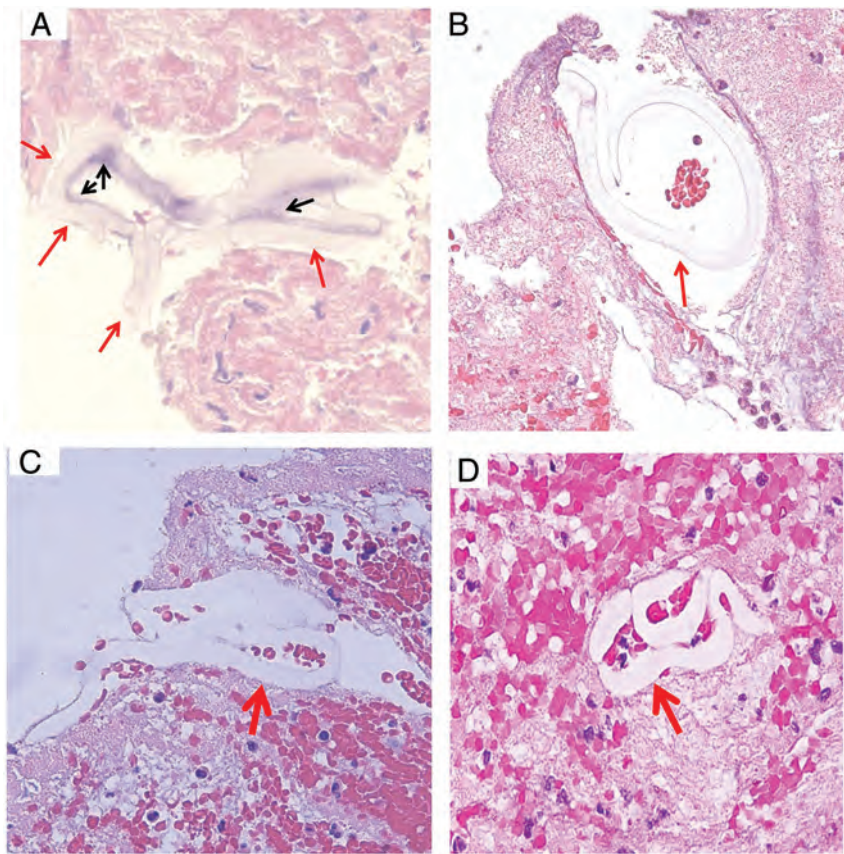


**FIG 8.** Representative microphotographs of type IV foreign material found in patient clot tissue. Different shapes of the type IV foreign material (red arrows) found in the clot tissue retrieved with MT. The foreign material is surrounded with clot tissue, appears to be homogeneous in texture, wormlike or snakelike in shape, and stained lightly. The residual, surface-coating material remains visible (A, black arrows) (A–D, H&E, original magnification  $\times 400$ ).

1 and 2) showed similar morphologic features of type II polymer material found in the retrieved thrombus samples (Fig 6). The rest of the other materials (type III and IV) found in the patient clot tissue (Figs 7 and 8) also had the similar features of other materials scratched from the catheters (Figs 1–3).

#### **Association of Thrombus Composition with the Presence of Foreign Materials**

The thrombus specimens had average histologic composition of 52.8% red blood cells, 3.5% white blood cells, 26.5% fibrin, and 15.0% platelets. The presence of foreign materials was not associated with thrombus composition ( $P > .05$ ).

#### **Association of the Presence of Foreign Material with MT Approach and Angiographic Outcome**

No association was found between the presence of foreign material and MT approaches ( $P = .58$ ) (Fig 10). In addition, there was no relation between final modified TICI reperfusion score and presence of foreign material in clot samples ( $P = .17$ ). A statistically significant correlation was not found between different types of polymer and final modified TICI reperfusion score ( $P = .49$ ).

In addition, the number of thrombectomy passes was not related to the presence of foreign materials ( $P = .34$ ).

#### **DISCUSSION**

Our study has a number of clinically relevant findings. First, we found that around half of the retrieved emboli had foreign material particles that shared similar morphologic features of polymer materials found in the neurovascular catheters, confirming the frequent release of debris from catheters during stroke intervention. Second, the polymer materials dislodging from catheters could be as long as 1.3 mm, and most of the particles were longer than  $10\ \mu\text{m}$ , the normal size of human capillaries. This phenomenon raises the concern of microinfarctions once these particles detach from the thrombus and embolize to the blood stream. Third, our results showed that the prevalence of foreign materials in thrombus specimens is not associated with the number of thrombectomy passes or thrombus composition. Fourth, we found no inflammatory reaction to foreign materials identified in the retrieved thrombi, suggesting the material interaction with tissue was an acute event and was from the MT procedure itself. Notably, the predominant foreign material was the PTFE liner, rather than the hydrophilic outer coating. The catheters including microcatheters, aspiration catheter, sheath, or any other devices with known PTFE liner, which were used with the MT operation (stent retriever, ASP, or stent retriever and ASP), could be one of the contributors. The shedding or tearing of the device lining and/or coating materials could happen when the stent retriever, guiding wire guiding catheters, and/or any other catheters were advancing to the target clot tissue; or as they were pulled back into the access catheter to be retrieved or dragged out of the patient's body. The circumstances mentioned here would have friction applied to the catheter materials resulting in their dislodgement.

This present study complements the current body of medical literature which, over the past decade, provides evidence that shearing of hydrophilic polymer coating materials is an under-recognized phenomenon during neuroendovascular procedures. In addition, our study found that the PTFE liner material was more frequently seen in the clot tissue associated with neurovascular procedure than the hydrophilic coating polymer. We present our results to enhance the awareness of this phenomenon among neurointerventionists and those studying retrieved thrombi. Our results are particularly important given the growing interest in the study of retrieved emboli in the stroke literature, as these materials could be identified during standard histologic analysis. Based on

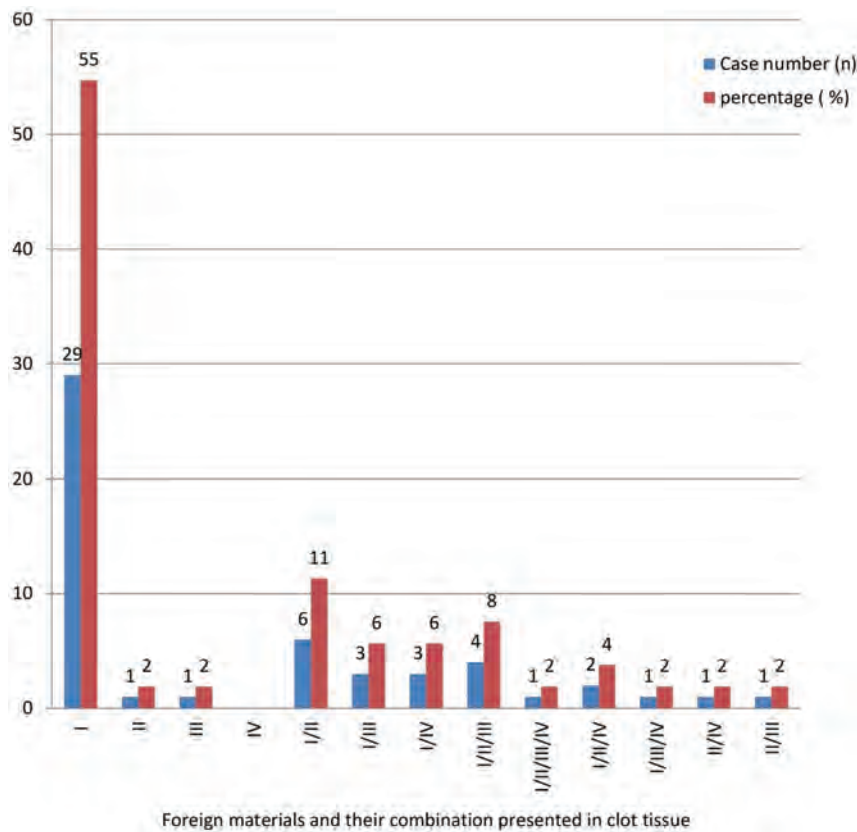


**FIG 9.** Foreign materials and varied combinations of different types found in patients with stroke treated with MT.

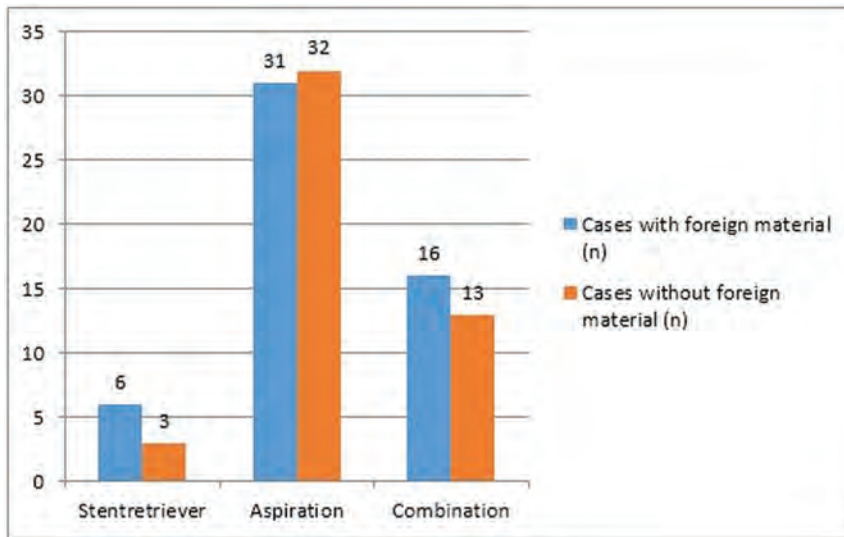


**FIG 10.** The association between foreign materials and MT approach.

this study, we still need to establish the significance of these dissociated materials in postinterventional clinical settings.

Numerous studies have reported neurologic tissue injuries due to the presence of various catheter coatings.<sup>1-3,8-11</sup> At present,

the clinical consequences associated with coating materials detaching from catheters include fever, inflammation, arteritis, vasculopathy, focal or multifocal hemorrhage, transient ischemia or microinfarction, and thrombosis, which can have a long-lasting effect and may result in irreversible tissue damage.<sup>2,3,8,12,13</sup> However, we suspect that the embolization of microscopic polymer materials is a relatively common phenomenon that does not routinely result in major clinical complications.

Distal embolization during MT is often clinically attributed to atheroemboli or thromboemboli; however, polymer embolism is now a well-documented event associated with endovascular procedures. One could speculate that the embolization of polymer materials may lead to occlusion of small intracranial arteries and subsequent microinfarctions. Chronic inflammation associated with the presence of foreign materials could potentially complicate microinfarctions further. Therefore, polymer embolism should be considered in the differential of unexpected ischemic or inflammatory events, as well as unexplained vasculopathies happening after endovascular procedures in patients.<sup>14</sup>

Our study has limitations. We do not have routine follow-up data on patients to see whether dislodged foreign materials can cause any significant complications. We suspect that the neurologic consequences from emboli of these polymers are generally limited. We did not quantify the number of foreign material particles in thrombus specimens because of technical limitations. Although harvested polymer materials from the Sofia, Fubuki catheter, and PTFE liners show similarity to the foreign materials found in the patients' retrieved thrombus specimens, chemistry analysis and Transmission Electron Microscopy examination are still necessary to show the details of the foreign material found in the patient clot tissue in the future. We assume the dislodging of catheter material could

happen along with device advancing during the clot removal, or when the device/clot was pulled back through catheters both inside and outside the human body. However, the current study cannot answer exactly when the shedding happened. In addition, our study sample size was small and included only a few brands of catheters currently used in clinical settings at our institution. More studies with larger sample sizes are needed to evaluate the occurrence rate and type of polymer materials that could detach from different catheters.

## CONCLUSIONS

Foreign polymer materials were found in around half of the thrombi collected from MT inpatients with large-vessel occlusion stroke. Our findings suggest that polymer materials are often separated from endovascular devices during thrombectomy; however, the clinical significance of this finding remains to be elucidated.

Disclosures: Yang Liu—UNRELATED: Consultancy: Endovascular Engineering Inc.; Comments: Scientific Board Member; Employment: Mayo Clinic Rochester; Luis Savastano—UNRELATED: Board Membership: Endovascular Engineering and VerAvanti; David Kallmes—UNRELATED: Board Membership: NoNO Inc, Vesalio Inc.; Comments: Data and Safety Monitoring Board membership; Grants/Grants Pending: Medtronic, MicroVention, Inera Therapeutics; Comments: Research support; Stock/Stock Options: Superior Medical Experts LLC, Marblehead Medical LLC; Comments: Founder/Owner; Other: Triticum Inc.; Comments: Advisory Board; Waleed Brinjikji—RELATED: Grant: National Institute of Neurological Disorders and Stroke, National Institutes of Health, \*Money paid to institution.

## REFERENCES

1. Fealey ME, Edwards WD, Giannini C, et al. **Complications of endovascular polymers associated with vascular introducer sheaths and metallic coils in 3 patients, with literature review.** *Am J Surg Pathol* 2008;32:1310–16 CrossRef Medline
2. Mehta RI, Mehta RI, Solis OE, et al. **Hydrophilic polymer emboli: an under-recognized iatrogenic cause of ischemia and infarct.** *Mod Pathol* 2010;23:921–30 CrossRef Medline
3. Mehta RI, Mehta RI, Fishbein MC, et al. **Intravascular polymer material after coil embolization of a giant cerebral aneurysm.** *Hum Pathol* 2009;40:1803–07 CrossRef Medline
4. Fitzgerald S, Wang S, Dai D, et al. **Orbit image analysis machine learning software can be used for the histological quantification of acute ischemic stroke blood clots.** *PLoS One* 2019;14:e0225841 CrossRef Medline
5. Fitzgerald ST, Wang S, Dai D, et al. **Platelet-rich clots as identified by Martius Scarlet Blue staining are isodense on NCCT.** *J Neurointerv Surg* 2019;11:1145–49 CrossRef Medline
6. Fitzgerald S, Dai D, Douglas AS, et al. **Abstract WP108: novel human acute ischemic stroke blood clot analogues for in-vitro testing.** Available at [https://www.ahajournals.org/doi/abs/10.1161/str.51.suppl\\_1.WP108](https://www.ahajournals.org/doi/abs/10.1161/str.51.suppl_1.WP108). Accessed October 1, 2020
7. Ward PA, Lentsch AB. **The acute inflammatory response and its regulation.** *Arch Surg* 1999;134:666–69 CrossRef Medline
8. Mehta RI, Mehta RI, Choi JM, et al. **Hydrophilic polymer embolism and associated vasculopathy of the lung: prevalence in a retrospective autopsy study.** *Hum Pathol* 2015;46:191–201 CrossRef Medline
9. Shapiro M, Ollenschleger M, Baccin C, et al. **Foreign body emboli following cerebrovascular interventions: clinical, radiographic, and histopathologic features.** *AJNR Am J Neuroradiol* 2015;36:2121–26 CrossRef Medline
10. Barnwell SL, D'Agostino AN, Shapiro SL, et al. **Foreign bodies in small arteries after use of an infusion microcatheter.** *AJNR Am J Neuroradiol* 1997;18:1886–89 Medline
11. Mehta RI, Mehta RI. **Polymer-induced central nervous system complications following vascular procedures: spectrum of iatrogenic injuries and review of outcomes.** *Hum Pathol* 2016;53:178–90 CrossRef Medline
12. Kozak M, Adams DR, Ioffreda MD, et al. **Sterile inflammation associated with transradial catheterization and hydrophilic sheaths.** *Catheter Cardiovasc Interv* 2003;59:207–13 CrossRef Medline
13. Mehta RI, Rai AT, Vos JA, et al. **Intrathrombus polymer coating deposition: a pilot study of 91 patients undergoing endovascular therapy for acute large vessel stroke, Part I: histologic frequency.** *J Neurointerv Surg* 2019;11:1191–96 CrossRef Medline
14. Mehta RI, Mehta RI. **Hydrophilic polymer embolism: an update for physicians.** *Am J Med* 2017;130:e287–e90 CrossRef Medline

# Novel Human Acute Ischemic Stroke Blood Clot Analogs for In Vitro Thrombectomy Testing

S.T. Fitzgerald, Y. Liu, D. Dai, O.M. Mereuta, M. Abbasi, J.L.A. Larco, A.S. Douglas, D.F. Kallmes, L. Savastano, K.M. Doyle, and W. Brinjikji



## ABSTRACT

**BACKGROUND AND PURPOSE:** Previous studies have successfully created blood clot analogs for in vitro endovascular device testing using animal blood of various species. Blood components vary greatly among species; therefore, creating clot analogs from human blood is likely a more accurate representation of thrombi formed in the human vasculature.

**MATERIALS AND METHODS:** Following approval from the Mayo Clinic institutional review board, human whole-blood and platelet donations were obtained from the blood transfusion service. Twelve clot analogs were created by combining different ratios of red blood cells + buffy coat, plasma, and platelets. Thrombin and calcium chloride were added to stimulate coagulation. Clot composition was assessed using histologic and immunohistochemical staining. To assess the similarities of mechanical properties to patient clots, 3 types of clot analogs (soft, elastic, and stiff) were selected for in vitro thrombectomy testing.

**RESULTS:** The range of histopathologic compositions produced is representative of clots removed during thrombectomy procedures. The red blood cell composition ranged from 8.9% to 91.4%, and fibrin composition ranged from 3.1% to 53.4%. Platelets (CD42b) and von Willebrand Factor ranged from 0.5% to 47.1% and 1.0% to 63.4%, respectively. The soft clots had the highest first-pass effect and successful revascularization rates followed by the elastic and stiff clots. Distal embolization events were observed when clot ingestion could not be achieved, requiring device pullback. The incidence rate of distal embolization was the highest for the stiff clots due to the weak clot/device integration.

**CONCLUSIONS:** Red blood cell-rich, fibrin-rich, and platelet-rich clot analogs that mimic clots retrieved from patients with acute ischemic stroke were created in vitro. Differing retrieval outcomes were confirmed using in vitro thrombectomy testing in a subset of clots.

**ABBREVIATIONS:** A = aspiration; AIS = acute ischemic stroke; DA = direct aspiration; FPE = first-pass effect; MSB = Martius Scarlett Blue; RBC = red blood cell; SR = successful revascularization; STR = Stent retriever; vWF = von Willebrand factor; WBC = white blood cell

In the treatment of acute ischemic stroke (AIS), the achievement of complete revascularization from a single mechanical thrombectomy attempt, termed first-pass effect (FPE), is associated with significantly improved outcomes for patients.<sup>1,2</sup> Removing the clot in a fragmented manner increases the potential of embolization to new territories, a major contributing factor to poor neurologic outcomes due to additional brain infarction.<sup>3-5</sup> Despite the advancement in the second-generation mechanical thrombectomy devices, the rates

of FPE remain low, as low as 29% in the recently reported Contact Aspiration vs Stent Retriever for Successful Revascularization (ASTER) trial.<sup>6</sup>

Previous studies have demonstrated that a wide variety of occlusive clots can cause large-vessel occlusion,<sup>7-11</sup> and clot composition has been shown to have a significant impact on the success of mechanical thrombectomy procedures.<sup>7,12,13</sup> These findings suggest that to further advance the success rates of stroke intervention, we must turn our attention to clot composition and compare

Received September 29, 2020; accepted after revision January 26, 2021.

From the Departments of Radiology (S.T.F., Y.L., D.D., O.M.M., M.A., D.F.K., W.B.) and Neurosurgery (J.L.A.L., L.S., W.B.), Mayo Clinic, Rochester, Minnesota; and Department of Physiology (S.T.F., O.M.M., A.S.D., K.M.D.) and SFI Centre for Research in Medical Devices (O.M.M., A.S.D., K.M.D.), National University of Ireland Galway, Galway, Ireland.

This work was supported by the National Institutes of Health grant No. R01 NS105853, the European Regional Development Fund and Science Foundation Ireland grant No. 13/RC/2073, and Enterprise Ireland (IP20190865).

Paper previously presented, in part, as a poster presentation at: International Stroke Conference, February 18–21, 2020; Los Angeles, California.

Please address correspondence to Seán Fitzgerald, PhD, Department of Physiology, Human Biology Building, National University of Ireland Galway, Galway, H91 TK33, Ireland; e-mail: Sean.Fitzgerald@nuigalway.ie; @FitzSeanT; @WBrinjikji

Indicates open access to non-subscribers at [www.ajnr.org](http://www.ajnr.org)

Indicates article with online supplemental data.

Indicates article with supplemental on-line videos.

<http://dx.doi.org/10.3174/ajnr.A7102>

**Table 1: Volume of components added to each clot analog type<sup>a</sup>**

Ratio	Platelets (μl)	Plasma (μl)	RBC + Buffy Coat (μl)
Plasma only			
1:5	2400	600	
1:10	0	2700	300
1:50	0	2940	60
1:100	0	2970	30
Platelets only			
1:5	2400	0	600
1:10	2700	0	300
1:50	2940	0	60
1:100	2970	0	30
Plasma and platelets			
1:5	1200	1200	600
1:10	1350	1350	300
1:50	1470	1470	60
1:100	1485	1485	30

<sup>a</sup> Three microliters of thrombin (1 NIH/mL) and 300 μL of 5% CaCl<sub>2</sub> were added to stimulate coagulation.

treatment strategies using in vitro thrombectomy models of the cerebral vasculature. Previous studies have successfully created blood clot analogs for in vitro testing using animal blood of various species, which have significantly advanced our understanding of clot biomechanics and imaging characteristics.<sup>13-19</sup> However, blood components and blood groups vary among species;<sup>20</sup> thus, creating clot analogs with human blood is likely a more accurate representation of thrombi formed in the human vasculature.

The hypothesis of the study was that the diverse range of clots retrieved from patients with AIS can be accurately replicated using human blood by mimicking the process by which clots form in vivo. The rationale for this study is that because the success of mechanical thrombectomy procedures is influenced by the composition of the clot, creating human clot analogs that accurately represent the different phenotypes retrieved from patients and testing them in an in vitro thrombectomy system will allow us to compare the performance of different thrombectomy devices and techniques. We will be able to determine the optimum treatment approach for each clot phenotype, thereby optimizing the chances of achieving the desired first-pass TICI 3 outcome in the clinical setting.<sup>1</sup> To assess the similarities of mechanical properties to patient clots, we selected 3 types of clot analogs (soft, elastic, and stiff) for in vitro thrombectomy testing.

## MATERIALS AND METHODS

### Human Clot Analog Creation

This study received institutional review board approval from Mayo Clinic Rochester in accordance with the ethical standards of the Declaration of Helsinki. A total of 12 clot analog types were created as per Table 1. These clots analogs were selected to be representative of the previously identified phenotypes of clots retrieved from patients with AIS, including red blood cell (RBC)-rich, fibrin-rich, and platelet-rich clots.<sup>21</sup>

A human whole-blood donation and a human platelet donation from 2 separate donors were obtained from the Mayo Clinic blood transfusion service. The whole blood was centrifuged at 1200 rpm for 20 minutes at 20°C to separate it into its

constituents.<sup>22</sup> Plasma was harvested by pipetting, and the remaining RBCs and buffy coat were mixed together by inverting. Plasma and platelets were combined first as per Table 1; then, 3 μL of thrombin (1 NIH/mL, No. T6884; Roche Diagnostic) was added to activate platelets for a total of 1–2 minutes while continuously mixing. Three hundred microliters of 5% calcium chloride (CaCl<sub>2</sub>, No. C1016; Sigma Aldrich) solution was then added followed by the RBCs + buffy coat mixture. The tube was then quickly mixed by inversion 5 times and then, the clot analog mixture was drawn into a 3 mL syringe. The syringes were spun overnight at 20 rpm at room temperature to mimic the dynamic flow conditions of the human vasculature.

### Patient Cohort

Clots were collected from 100 patients who underwent mechanical thrombectomy for the treatment of AIS at Mayo Clinic Rochester. When greater than 1 procedural pass was needed to retrieve the occlusive clot, all fragments of clot were combined for histologic analysis. The inclusion criteria were patients 18 years of age or older and having undergone mechanical thrombectomy treatment for AIS with clot material available for analysis. A waiver of informed consent was granted for the purposes of collecting retrieved clot material from patients with AIS for this study.

### Histologic Processing and Staining

Gross photos were taken of each clot and analog before fixation overnight in 10% phosphate-buffered formalin. All clots and analogs were then processed using a standard tissue-processing protocol and embedded in paraffin. The formalin-fixed paraffin-embedded material was cut into 3-μm sections. The Martius Scarlett Blue (MSB) stain is now regarded as the criterion standard for assessing clot composition because it identifies platelet-rich regions of thrombi in addition to RBCs, white blood cells (WBCs), and fibrin.<sup>21,23</sup> Two representative slides were stained with MSB to identify the common clot constituents: RBCs, WBCs, fibrin, platelets/other, collagen, and calcification as described previously.<sup>21,23</sup> Clot phenotypes for both the clinical samples and the clot analogs were defined on the basis of the dominant component (in percentages) in each clot as determined by the MSB histologic staining.

### Immunohistochemistry

Platelet and von Willebrand factor (vWF) levels are useful additional hallmarks of clot composition.<sup>24-26</sup> Immunohistochemical staining for platelets (CD42b) and the vWF was performed on a Bond RX autostainer (Leica Biosystems). Antigen retrieval with Tris-EDTA was performed for platelet staining (anti-CD42b); no antigen retrieval was used for vWF staining. For the primary antibody (anti-CD42b, ab27669, 1:200 dilution [Abcam]; anti-vWF, A-0082, 1:200 dilution [Dako]), the incubation time was 30 minutes. Negative controls were performed by omission of the primary antibody step. A Bond Polymer Refine Red Detection system (Leica Biosystems), which incorporates a post-primary antibody, polymer reagent, Fast Red chromogen and hematoxylin counterstain, was used for visualization. Sections were washed in warm soapy water, dehydrated in increasing alcohol gradients, cleared in xylene, and mounted with DPX Mountant (Sigma-Aldrich).



**FIG 1.** Gross photographs of human blood clot analogs pre- and postfixation. Gross photographs of human blood clot analogs of various compositions were obtained pre- and postfixation in 10% neutral buffered formalin. Clot analogs were created using different ratios (1:5, 1:10, 1:50, and 1:100) of RBC+buffy coat and plasma only, platelets only, and plasma + platelets.

### Imaging and Quantification

Following staining, a representative slide of each stain was scanned at 20x magnification (EasyScan Pro; Motic Digital Pathology). Histologic quantification was performed on the digital slide using Image Analysis Software (Orbit; www.Orbit.bio) as described previously.<sup>21,25</sup> The percentage area of each component (RBC, WBC, fibrin, and platelet/other) within the clot was calculated for the histologic staining with MSB.<sup>21</sup> The percentage area of positive immunohistochemistry staining was calculated separately for CD42b and vWF.<sup>25</sup>

### Thrombectomy Testing in a Benchtop Stroke Platform

The mechanical properties of clots vary on the basis of their histologic composition; clot analogs with an increasing volume of platelets contract to a greater degree due to the force of platelet contraction, resulting in stiffer clot analogs.<sup>27</sup> Clot analogs that have a high RBC content will typically be softer, more friable clots, and clots made from plasma only will produce clot analogs with a network of thin fibrin strands. Three phenotypes of clot analogs with varying compositions of RBCs, plasma, and platelets were selected to represent prominent phenotypes of clots retrieved from patients with AIS during thrombectomy: soft (1:10 RBCs+buffy coat : plasma only), elastic (1:5 RBCs+buffy coat : platelets + plasma), and stiff (1:10 RBCs+buffy coat : platelets + plasma).

Thrombectomy testing was performed on these clots inside a benchtop stroke platform as previously described.<sup>28,29</sup> Briefly, a cerebrovascular glass model, in which the lumen resembles the intracranial internal carotid artery, the anterior cerebral artery, and the middle cerebral arteries, is connected to a customized flow system to deliver flow with a physiologically representative flow rate and pressure. Clot analogs measuring 6 mm in length were introduced into the flow system and embolized to the M1–M2 bifurcation.

Revascularization was performed using the following: 1) the direct aspiration (DA) technique with the Sofia 6F aspiration catheter (MicroVention), and 2) stent retriever with aspiration (stent retriever+A) technique with the Solitaire stent retriever (Medtronic) and the Sofia 6F aspiration catheter. For each type of clot analog and revascularization technique, 5 clot analogs were made to replicate large-vessel occlusion stroke. For each large-vessel occlusion case, 3 device passes were attempted before declaring failure. Revascularization results, number of passes, and embolization events were recorded for each test.

Ingestion was defined as complete ingestion of the clot into the catheter, FPE was defined as complete removal of the clot from the target artery in the first procedural pass, successful recanalization (SR) was defined as the complete removal of the clot from the target artery within 3 procedural passes, and distal embolization was defined as the occurrence of visible fragments of clots being dislodged and migrating distally from the target vessel. The thrombectomy processes were recorded, and the failure mechanisms, including the presence of distal embolization, were confirmed following the procedure.

### Statistical Analysis

All statistical correlations were assessed, and graphs were generated using GraphPad Prism 8 (GraphPad Software). MSB histologic composition was reported as the percentage of the total clot area. Positive immunohistochemistry staining (CD42b and vWF) was reported as the percentage of the total clot area. A Shapiro-Wilk test indicated that quantitative variables did not follow a standard normal distribution. The nonparametric Spearman  $\rho$  correlation was used to assess the similarity between clot analogs and clinical samples. A level of statistical significance for all analyses was set at  $P < 0.05$ .

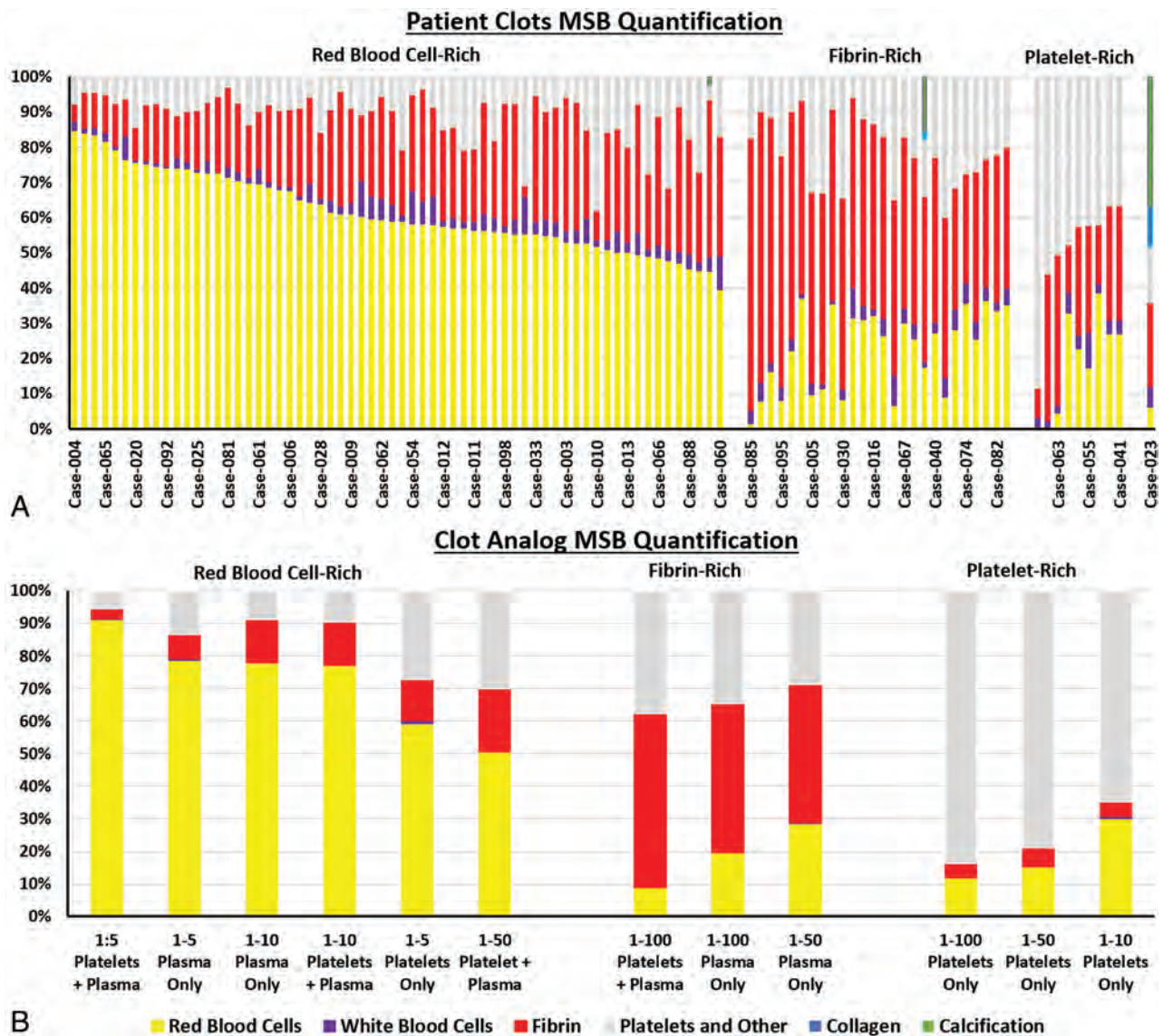


**FIG 2.** Histologic quantification of MSB-stained human clots retrieved from patients and human clot analogs created in vitro. **A**, The histologic composition of 100 various clots retrieved from patients was assessed using the MSB stain and grouped according to their dominant component, resulting in 3 main groups; RBC-rich, fibrin-rich, and platelet-rich. **B**, The histologic composition of various human clot analogs created in vitro was also assessed using the MSB stain and grouped according to their dominant component, resulting in the same 3 phenotypes; RBC-rich, fibrin-rich, and platelet-rich.

## RESULTS

### Clot Analog Appearance

The gross appearance of each of the human clot analogs after clot formation and also postfixation in 10% neutral buffered formalin is shown in Fig 1. Clot analogs that are rich in RBC clots (eg, 1:10 RBCs+buffy coat : plasma only) are dark red after creation and black postfixation. Clots that contain high platelet content (eg, 1:100 RBCs+buffy coat : platelets only) have white platelet-rich regions that are visible both pre- and postfixation. Clots that are fibrin-rich but not platelet-rich are light red after creation and brownish postfixation (eg, 1:50 RBCs+buffy coat : plasma only). The platelet-rich clots are smaller in clot volume due to the effect of platelet-stimulated contraction of the clots. The clot analogs produced have a gross appearance similar to that of clots extracted from patients during mechanical thrombectomy procedures for the treatment of AIS.

### Histologic Composition

The MSB stain was used to assess the histologic composition of the clot analogs (Online Supplemental Data) and of the clots retrieved from patients with AIS (Fig 2). RBC-rich, fibrin-rich, and platelet-rich clot analogs that mimic clots retrieved from patients with AIS were created. The range of histopathologic compositions of the clot analogs is similar to that of the clinical samples (Fig 2). The addition of a large volume of RBCs leads to an RBC-rich clot regardless of whether platelets and/or plasma were added (Fig 2). The RBC composition of the clot analogs ranged from 8.9% to 91.4%, and the clots retrieved from the patients ranged from <1% to 85%. There was a significant positive correlation between the RBC composition of the analogs and the clinical samples ( $r_s = 0.755$ ,  $P = .010^*$ ). The platelet composition of the clot analogs ranged from 5.4% to 83.7%, while the clinical samples ranged from 3% to 88% ( $r_s = 0.618$ ,  $P = .048^*$ ). Fibrin composition of the clot

analogues ranged from 3% to 53% and from 3% to 77% in the clinical samples ( $r_s = 0.136, P = .694$ ). WBCs are typically a minor component of clots and account for an average of 3.5% of clinical clots and 1% of clot analogs ( $r_s = 0.311, P = .345$ ). Each of these components is in line with the composition of AIS clots reported previously in the literature.<sup>7,21,30</sup>

### Immunohistochemical Composition

The composition of platelets (CD42b) varied from 0.5% to 47.1% of the total area, and the composition of vWF varied from 1.1% to 63.4% of the total area (Table 1). Clot analogs made with platelets only had the largest proportion of both CD42b and vWF present, while clot analogs made with plasma only had the lowest levels of both platelets and vWF. Clot analogs containing both platelets and plasma had moderate levels of both platelets and vWF present. An example of a clot analog closely resembling a clot retrieved from a patient with AIS is shown in Fig 3.

### Revascularization Results

The 3 types of clot analogs are associated with different revascularization outcomes (Table 2). The soft clots are associated with the highest ingestion, FPE, and successful recanalization rates,

followed by the elastic and stiff clots. The rate of distal embolization increased as the rate of ingestion decreased.

All of soft clots could be successfully removed with 1 pass, and no distal embolization was observed. By means of the DA technique, 80% (4 of 5) of clots were ingested (Supplemental Online Video S1), with 1 exception in which the catheter tip was corks by the clot. Using the stent retriever + A technique, all the clots could be pulled out without any distal embolization.

For the elastic clot and using the DA technique, only 40% (2 of 5) of the clots could be ingested and the other 3 clots were corks by the suction catheter and pulled out. During catheter pull, the clot was elongated under the tensional load applied by the vacuum suction and the pressure gradient across the clot. As the clot was moved to the internal carotid artery terminus, a temporary near-to-total obstruction of the flow increased the antegrade pressure gradient and eventually fractured the clot and caused distal embolization (Supplemental Online Video S2). In a similar fashion, the stent retriever + A technique also fractured the clot during device pull, causing distal embolization (Supplemental Online Video S3). Distal embolization of clot fragments is the main reason for repeat passes to recanalization.

For the stiff clots and using the DA technique, only 20% (1 of 5) of the clots could be ingested. During device pull, 80% (4 of 5) of the clots lost integration with the suction catheter due to the antegrade pressure gradient and resulted in failed revascularization. The integration of the clots to the stent retriever was stronger than the aspiration catheter alone, resulting in a lower distal embolization rate and higher revascularization rate (Table 2).

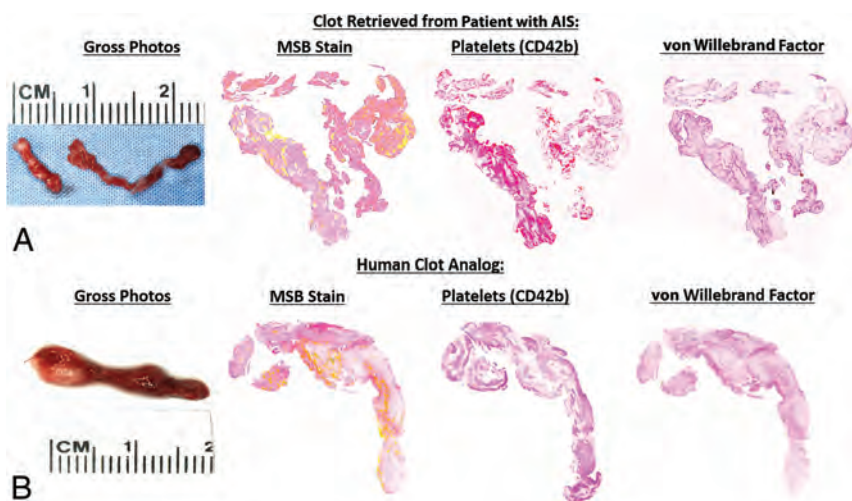


**FIG 3.** Histology and immunohistochemical-stained images of clots retrieved from a patient with AIS and of a human clot analog. A comparison of the similarity in terms of gross photographs, MSB stain, CD42b (platelets), and vWF between a clot retrieved from a patient with AIS (A) and a human clot analog (1:50 RBC + buffy coat/platelets) is shown (B). MSB stain: RBCs (yellow), WBCs (purple), fibrin (red), platelets/other (grey), and collagen (blue). Platelets (CD42b) and vWF; positive staining is red.

**Table 2: In vitro thrombectomy results**

Clot Type	Ingestion Rate	FPE Rate	SR Rate	Passes to Achieve SR	DE Rate
Soft					
DA	80%	100%	100%	1.0	0
STR + A	NA	100%	100%	1.0	0
Elastic					
DA	40%	100%	100%	1.0	20%
STR + A	NA	40%	100%	1.8	60%
Stiff					
DA	20%	40%	40%	1.0	80%
STR + A	NA	60%	80%	1.3	40%

**Note:**—DE indicates distal embolization; STR + A, stent retriever + aspiration; NA, not applicable.

### DISCUSSION

In this study, a range of novel in vitro human clot analogs that mimic the gross appearance and histologic composition of clots retrieved from patients with AIS was created. The composition of the clot analogs was confirmed using the MSB histologic stain for the main components and immunohistochemical staining for the identification of platelets and vWF. Furthermore, a subset of clot analogs were tested in an in vitro thrombectomy model and demonstrated that revascularization outcome is related to both the composition of the clots and the technique used to retrieve them. The results of this study are important because they prove that human clot analogs that accurately replicate the histologic composition of clots retrieved from patients can be created, and they demonstrate that these clot analogs can be used in an in vitro thrombectomy setup to compare the performance of

different treatment approaches, potentially leading to a clinical benefit for the patients.

The inability of second-generation thrombectomy aspiration and stent retriever devices to dramatically improve the rates of FPE following endovascular treatment of AIS suggests that the effect is not specifically device-related.<sup>6</sup> An understanding of clot histologic characteristics and recanalization outcomes is potentially of great importance in improving device selection and device development. There is a growing awareness of the importance of clot phenotypes, mechanical properties, clot-device interactions, and the interactions of clots with the surrounding vessel, factors that influence revascularization rates.<sup>1,27,31-34</sup> However, clinicians largely continue to treat patients using their preferred treatment strategy rather than tailoring their treatment strategy to suit the suspected clot composition because there have been few clinical studies comparing various thrombectomy techniques in their ability to retrieve different phenotypes of thrombi from patients with AIS.<sup>35</sup> The histologic composition of the clot analog phenotypes created in this study is in line with the range of clot compositions typically seen in AIS.<sup>21</sup> Clots retrieved from patients can generally be stratified into 3 main phenotypes based on their histologic composition: RBC-rich, fibrin-rich, and platelet-rich. Each of these phenotypes was successfully replicated in vitro in this study.

The novel clot analogs described herein used in conjunction with human vascular replicator systems that can accurately replicate the intracranial vasculature, cardiac cycle, and intracranial blood pressure may enable the optimization of techniques and treatment strategies. A recent study using similar human clot analogs in an in vitro thrombectomy system also demonstrated that the composition of the clot analogs significantly affects the outcome of the procedure.<sup>36</sup> By assessing the success rate of all of the various thrombectomy devices and techniques in retrieving different phenotypes of clots as described, we can arrive at a better understanding of how to improve the rates of FPE. The use of human clot analogs and accurate in vitro thrombectomy systems could be a valuable training resource for educating physicians on the potential clinical significance of tailoring their treatment strategy to optimize their chances of achieving complete revascularization. In addition to their use in in vitro thrombectomy testing, human clot analogs can also be used to investigate the ability of novel diagnostic imaging methods to identify the composition of the occlusive clot.<sup>37,38</sup>

For the DA technique, the FPE is associated with successful clot ingestion and depends on the clot mechanical properties. Of the 15 clots tested, FPEs were achieved for 12 clots, and 7 (58%) of them were due to successful ingestion. The ingestion rates were 80%, 40%, and 20% for the soft, elastic, and stiff clots, respectively. Clots with a higher composition of platelets and fibrin have a higher stiffness and friction coefficient,<sup>17,39</sup> making them difficult to deform into the catheter tip and be ingested. For the 8 clots without successful ingestion, 6 (75%) of them presented with distal embolization and resulted in repeat device passes or failed revascularization. Suction catheters that can generate a large suction force to deform the clots and overcome the clot friction to ingest the clots could be beneficial.<sup>40</sup> However, the thrombectomy tests are performed in a glass phantom, and

the arterial response to suction was not captured. Under suction, the vessel could collapse due to the reduced intraluminal pressure and evacuation of fluid, hypothetically related to the more severe vessel injuries using suction catheters rather than the stent retrievers.<sup>41</sup> The safety profile of the new-generation large-bore suction catheters needs to be further validated.

When we compared the stent retriever + A technique with the DA technique, the FPE rate was the same (100%) for the soft clots, lower (40% versus 100%) for the elastic clots, and higher (60% versus 40%) than the DA technique for the stiff clots, showing a clear relation with the clot mechanical properties. For both the DA and the stent retriever + A techniques in which the FPE was not achieved, the failure mechanism was the poor clot/device integration with downstream migration of emboli, similar to that found in a whole human brain thrombectomy platform.<sup>42</sup> During clot retrieval by device pull (stent retriever or suction catheter without clot ingestion), the clot/device integration has to fight against the tensional force generated by the device and the antegrade pressure gradient. Compared with the DA technique in which the clot was engaged with the suction catheter only at the clot "head" (Supplemental Online Video S2), in the stent retriever + A technique, the clot integration was stronger as the clot was grabbed by the stent tines along the clot length (Supplemental Online Video S3). This result could be the reason for higher FPE and successful revascularization rates for the stiff clot analogs. On the other hand, the clot/stent integration was still weak, with multiple passes needed to revascularize. Future stent technologies should enable better clot integration, especially for stiff clots.

This study has some limitations. First, the whole-blood and platelet donations were not collected from the same patient, and the blood phenotypes of each were not available. Second, blood phenotype has been shown to impact coagulation, and this method may need to be adjusted slightly for each blood phenotype. Finally, the thrombectomy tests were performed in a glass phantom, and the arterial response to suction was not captured.

## CONCLUSIONS

RBC-rich, fibrin-rich, and platelet-rich clot analogs that mimic clots retrieved from patients with AIS were created in vitro. Differing retrieval outcomes were confirmed using in vitro thrombectomy testing in a subset of clots. The use of human clot analogs and accurate in vitro thrombectomy systems could be a valuable training resource for physicians to optimize their chances of achieving complete revascularization for every clot phenotype.

Disclosures: Sean T. Fitzgerald—*RELATED: Grant:* National Institutes of Health, *Comments:* This work was supported by the National Institutes of Health grant No. R01 NS105853; the European Regional Development Fund and Science Foundation Ireland grant No. 13/RC/2073; and Enterprise Ireland (IP20190865).\* Yang Liu—*RELATED: Grant:* National Institutes of Health, *Comments:* R01 NS105853 to Waleed Brinjikji\*; *UNRELATED: Employment:* Mayo Clinic, Rochester; *Stock/Stock Options:* Endovascular Engineering Inc, *Comments:* Endovascular Engineering Inc is developing thrombectomy devices, and I serve on the Scientific Advisory Board, paid by stock options. Oana Madalina Mereuta—*RELATED: Grant:* National Institutes of Health, the European Regional Development Fund and Science Foundation Ireland, *Comments:* This work was supported by the National Institutes of Health grant No. R01NS105853, the European Regional Development Fund, and Science Foundation Ireland (grant No. 13/RC/2073).\* Andrew S. Douglas—*RELATED: Grant:* National Institutes of Health, the European Regional Development Fund and Science Foundation

Ireland, and Enterprise Ireland. *Comments:* This work was supported by the National Institutes of Health grant No. R01 NS105853, the European Regional Development Fund and Science Foundation Ireland grant No. 13/RC/2073, and Enterprise Ireland (IP20190865). \* David F. Kallmes—*RELATED: Grant:* National Institutes of Health: National Institute of Neurological Disorders and Stroke. *Comments:* R01 NS105853\*; *UNRELATED: Board Membership:* Triticum, Vesalio, *Comments:* Advisory Board, Data and Safety Monitoring Board\*; *Grants/Grants Pending:* Cerenovus, MiVi Neurovascular\*; *Patents (Planned, Pending or Issued):* Mayo Clinic\*; *Stock/Stock Options:* Marblehead Medical, LLC, Superior Medical Experts, LLC. Karen M. Doyle—*RELATED: Grant:* Science Foundation Ireland, *Comments:* This work was supported by the European Regional Development Fund and Science Foundation Ireland grant No. 13/RC/2073\*; *UNRELATED: Employment:* National University of Ireland Galway; *Grants/Grants Pending:* Cerenovus.\* Waleed Brinjikji—*RELATED: Grant:* National Institutes of Health: National Institute of Neurological Disorders and Stroke.\* \*Money paid to the institution.

## REFERENCES

- Zaidat OO, Castonguay AC, Linfante I, et al. **First pass effect.** *Stroke* 2018;49:660–66 CrossRef Medline
- Nikoubashman O, Dekeyser S, Riabikin A, et al. **True first-pass effect.** *Stroke* 2019;50:2140–46 CrossRef Medline
- Todo A, Minaeian A, Sahni R, et al. **Incidence and outcome of procedural distal emboli using the Penumbra thrombectomy for acute stroke.** *J Neurointerv Surg* 2013;5:135–38 CrossRef Medline
- Kurre W, Vorlaender K, Aguilar-Pérez M, et al. **Frequency and relevance of anterior cerebral artery embolism caused by mechanical thrombectomy of middle cerebral artery occlusion.** *AJNR Am J Neuroradiol* 2013;34:1606–11 CrossRef Medline
- Jindal G, Carvalho HD, Wessell A, et al. **Beyond the first pass: revascularization remains critical in stroke thrombectomy.** *J Neurointerv Surg* 2019;11:1095–99 CrossRef Medline
- Ducroux C, Ptiotin M, Gory B, et al; ASTER Trial Investigators. **First pass effect with contact aspiration and stent retrievers in the Aspiration versus Stent Retriever (ASTER) trial.** *J Neurointerv Surg* 2020;12:386–91 CrossRef Medline
- Hashimoto T, Hayakawa M, Funatsu N, et al. **Histopathologic analysis of retrieved thrombi associated with successful reperfusion after acute stroke thrombectomy.** *Stroke* 2016;47:3035–37 CrossRef Medline
- Liebeskind DS, Sanossian N, Yong WH, et al. **CT and MRI early vessel signs reflect clot composition in acute stroke.** *Stroke* 2011;42:1237–43 CrossRef Medline
- Maegerlein C, Friedrich B, Berndt M, et al. **Impact of histological thrombus composition on preinterventional thrombus migration in patients with acute occlusions of the middle cerebral artery.** *Interv Neuroradiol* 2018;24:70–75 CrossRef Medline
- Saver JL, Goyal M, Bonafe A, et al; SWIFT PRIME Investigators. **Stent-retriever thrombectomy after intravenous t-PA vs. t-PA alone in stroke.** *N Engl J Med* 2015;372:2285–95 CrossRef Medline
- Staessens S, Denorme F, François O, et al. **Structural analysis of ischemic stroke thrombi: histological indications for therapy resistance.** *Haematologica* 2020;105:498–507 CrossRef Medline
- Boeckh-Behrens T, Schubert M, Förtschler A, et al. **The impact of histological clot composition in embolic stroke.** *Clin Neuroradiol* 2016;26:189–97 CrossRef Medline
- Chueh JY, Wakhloo AK, Hendricks GH, et al. **Mechanical characterization of thromboemboli in acute ischemic stroke and laboratory embolus analogs.** *AJNR Am J Neuroradiol* 2011;32:1237–44 CrossRef Medline
- Preut A, Laughlin M, Jensen H, et al. **Novel method for emboli analog formation towards improved stroke retrieval devices.** *J Biomech* 2018;80:121–28 CrossRef Medline
- Duffy S, Farrell M, McArdle K, et al. **Novel methodology to replicate clot analogs with diverse composition in acute ischemic stroke.** *J Neurointerv Surg* 2017;9:486–91 CrossRef Medline
- Ren M, Lin Z-J, Qian H, et al. **Embolus middle cerebral artery occlusion model using thrombin and fibrinogen composed clots in rat.** *J Neurosci Methods* 2012;211:296–304 CrossRef Medline
- Gunning GM, McArdle K, Mirza M, et al. **Clot friction variation with fibrin content; implications for resistance to thrombectomy.** *J Neurointerv Surg* 2018;10:34–38 CrossRef Medline
- Bretzner M, Lopes R, McCarthy R, et al. **Texture parameters of R2\* maps are correlated with iron concentration and red blood cells count in clot analogs: a 7-T micro-MRI study.** *J Neuroradiol* 2020;47:306–11 CrossRef Medline
- Gonzalez AV, Buerke B, Görlich D, et al. **Clot analog attenuation in non-contrast CT predicts histology: an experimental study using machine learning.** *Transl Stroke Res* 2020;11:940–49 CrossRef Medline
- Stormont CJ. **Blood groups in animals.** *J Am Vet Med Assoc* 1982;181:1120–24 Medline
- Fitzgerald ST, Wang S, Dai D, et al. **Platelet-rich clots as identified by Martius Scarlet Blue staining are isodense on NCCT.** *J Neurointerv Surg* 2019;11:1145–49 CrossRef Medline
- Van Wie BJ, Sofer SS. **Experimental considerations for the centrifugal separation of blood cell components.** *Int J Artif Organs*. 1986;9(1):49–58 Medline
- Staessens S, Fitzgerald S, Andersson T, et al. **Histological stroke clot analysis after thrombectomy: technical aspects and recommendations.** *Int J Stroke* 2020;15:467–76 CrossRef Medline
- Staessens S, Denorme F, François O, et al. **Dense fibrin, von Willebrand factor and extracellular DNA are specific structural hallmarks of platelet-rich areas in ischemic stroke thrombi.** In: *Proceedings of the Congress of the International Society on Thrombosis and Haemostasis*. Melbourne, Australia. July 6–10, 2019
- Douglas A, Fitzgerald S, Mereuta OM, et al. **Platelet-rich emboli are associated with von Willebrand factor levels and have poorer revascularization outcomes.** *J Neurointerv Surg* 2020;12:557–62 CrossRef Medline
- Mereuta OM, Fitzgerald S, Abbasi M, et al. **Abstract WP268: von Willebrand factor expression in various subtypes of acute ischemic stroke.** *Stroke* 2020;51:AWP268 [https://www.ahajournals.org/doi/10.1161/str.51.suppl\\_1.WP268](https://www.ahajournals.org/doi/10.1161/str.51.suppl_1.WP268). Accessed March 06, 2020
- Johnson S, Chueh J, Gounis MJ, et al. **Mechanical behavior of in vitro blood clots and the implications for acute ischemic stroke treatment.** *J Neurointerv Surg* 2020;12:853–57 CrossRef Medline
- Reddy AS, Liu Y, Cockrum J, et al. **Construction of a comprehensive endovascular test bed for research and device development in mechanical thrombectomy in stroke.** *J Neurosurg* 2020;1:1–8 CrossRef Medline
- Liu Y, Zheng Y, Reddy AS, et al. **Analysis of human emboli and thrombectomy forces in large-vessel occlusion stroke.** *J Neurosurg* 2020;1:1–9 CrossRef Medline
- Ye G, Gao Q, Qi P, et al. **The role of diabetes mellitus on the thrombus composition in patients with acute ischemic stroke.** *Interv Neuroradiol* 2020;26:329–36 CrossRef Medline
- Eng W, Kim M, Pham S, et al. **Micromechanics of blood clots.** *Arteriosclerosis, Thrombosis, and Vascular Biology* 2018;38(Suppl 1) CrossRef
- van der Marel K, Chueh JY, Brooks OW, et al. **Quantitative assessment of device-clot interaction for stent retriever thrombectomy.** *J Neurointerv Surg* 2016;8:1278–82 CrossRef Medline
- Fitzgerald S, Mereuta OM, Doyle KM, et al. **Correlation of imaging and histopathology of thrombi in acute ischemic stroke with etiology and outcome.** *J Neurosurg Sci* 2019;63:292–300 CrossRef Medline
- Sporns PB, Jeibmann A, Minnerup J, et al. **Histological clot composition is associated with preinterventional clot migration in acute stroke patients.** *Stroke* 2019;50:2065–71 CrossRef Medline
- Mohammaden MH, Haussen DC, Camara Cp D, et al. **Hyperdense vessel sign as a potential guide for the choice of stent retriever versus contact aspiration as first-line thrombectomy strategy.** *J Neurointerv Surg* 2020 Jul 31. [Epub ahead of print] CrossRef Medline
- Fitzgerald S, Ryan D, Thornton J, et al. **Preclinical evaluation of Millipede 088 intracranial aspiration catheter in cadaver and in vitro thrombectomy models.** *J Neurointerv Surg* 2020 Jun 30. [Epub ahead of print] CrossRef Medline
- Liu HC, Abbasi M, Ding YH, et al. **Characterizing thrombus with multiple red blood cell compositions by optical coherence tomography**

- attenuation coefficient.** *J Biophotonics* 2020 Dec 31. [Epub ahead of print] CrossRef Medline
38. Liu HC, Abbasi M, Ding YH, et al. **Characterizing blood clots using acoustic radiation force optical coherence elastography and ultrasound shear wave elastography.** *Phys Med Biol* 2021;66:035013 CrossRef Medline
39. Liu Y, Reddy AS, Cockrum J, et al. **Standardized fabrication method of human-derived emboli with histologic and mechanical quantification for stroke research.** *J Stroke Cerebrovasc Dis* 2020;29:105205 CrossRef Medline
40. Fitzgerald S, Ryan D, Thornton J, et al. **Preclinical evaluation of Millipede 088 intracranial aspiration catheter in cadaver and in vitro thrombectomy models.** *J Neurointerv Surg* 2020 Jun 30. [Epub ahead of print] CrossRef Medline
41. Gory B, Bresson D, Kessler I, et al. **Histopathologic evaluation of arterial wall response to 5 neurovascular mechanical thrombectomy devices in a swine model.** *AJNR Am J Neuroradiol* 2013;34:2192–98 CrossRef Medline
42. Gebrezgiabhier D, Liu Y, Reddy AS, et al. **A human brain test bed for research in large vessel occlusion stroke.** *J Neurosurg* 2021 Jan;22:1–9 CrossRef Medline

# Refractory Stroke Thrombectomy: Prevalence, Etiology, and Adjunctive Treatment in a North American Cohort

 R.N. Abdalla,  D.R. Cantrell,  A. Shaibani,  M.C. Hurley,  B.S. Jahromi,  M.B. Potts, and  S.A. Ansari



## ABSTRACT

**BACKGROUND AND PURPOSE:** Acute stroke intervention refractory to mechanical thrombectomy may be due to underlying vessel wall pathology including intracranial atherosclerotic disease and intracranial arterial dissection or recalcitrant emboli. We studied the prevalence and etiology of refractory thrombectomy, the safety and efficacy of adjunctive interventions in a North American–based cohort.

**MATERIALS AND METHODS:** We performed a multicenter, retrospective study of refractory thrombectomy, defined as unsuccessful recanalization, vessel reocclusion in <72 hours, or required adjunctive antiplatelet glycoprotein IIb/IIIa inhibitors, intracranial angioplasty and/or stenting to achieve and maintain reperfusion. Clinical and imaging criteria differentiated etiologies for refractory thrombectomy. Baseline demographics, cerebrovascular risk factors, technical/clinical outcomes, and procedural safety/complications were compared between refractory and standard thrombectomy groups. Multivariable logistic regression analysis was performed to determine independent predictors of refractory thrombectomy.

**RESULTS:** Refractory thrombectomy was identified in 25/302 cases (8.3%), correlated with diabetes (44% versus 22%,  $P = .02$ ) as an independent predictor with OR = 2.72 (95% CI, 1.05–7.09;  $P = .04$ ) and inversely correlated with atrial fibrillation (16% versus 45.7%,  $P = .005$ ). Refractory etiologies were secondary to recalcitrant emboli (20%), intracranial atherosclerotic disease (60%), and/or intracranial arterial dissection (44%). Four (16%) patients were diagnosed with early vessel reocclusion, and 21 patients underwent adjunctive salvage interventions with glycoprotein IIb/IIIa inhibitor infusion alone (32%) or intracranial angioplasty and/or stenting (52%). There were no significant differences in TICI 2b/3 reperfusion efficacy (85.7% versus 90.9%,  $P = .48$ ), symptomatic intracranial hemorrhage rates (0% versus 9%,  $P = .24$ ), favorable clinical outcomes (39.1% versus 48.3%,  $P = .51$ ), or mortality (13% versus 28.3%,  $P = .14$ ) versus standard thrombectomy.

**CONCLUSIONS:** Refractory stroke thrombectomy is encountered in <10% of cases, independently associated with diabetes, and related to underlying vessel wall pathology (intracranial atherosclerotic disease and/or intracranial arterial dissection) or, less commonly, recalcitrant emboli. Emergent salvage interventions with glycoprotein IIb/IIIa inhibitors or intracranial angioplasty and/or stenting are safe and effective adjunctive treatments.

**ABBREVIATIONS:** AIS = acute ischemic stroke; DAC = distal access catheter; ELVO = emergent large-vessel occlusion; GPI = glycoprotein IIb/IIIa inhibitors; IAD = intracranial arterial dissection; ICAD = intracranial atherosclerotic disease; sICH = symptomatic intracranial hemorrhage

Multiple randomized controlled trials have established mechanical thrombectomy as the standard of care treatment for acute ischemic stroke (AIS), secondary to an emergent large-vessel occlusion (ELVO).<sup>1</sup> Successful recanalization has been shown to be an independent predictor of favorable functional outcomes, with studies emphasizing near-complete reperfusion for

optimal outcomes.<sup>2,3</sup> However, in the Highly Effective Reperfusion evaluated in Multiple Endovascular Stroke Trials (HERMES) meta-analysis of 5 randomized controlled trials constituting 634 endovascular cases, successful thrombectomy was achieved in 71% of cases with nearly 30% of cases failing to achieve successful revascularization.<sup>1</sup>

Several causes have been postulated for the failure of thrombectomy, including anatomic difficulty, suboptimal devices, clot

Received November 18, 2020; accepted after revision January 26, 2021.

From the Departments of Radiology (R.N.A., D.R.C., A.S., M.C.H., B.S.J., M.B.P., S.A.A.), Neurology (S.A.A.), and Neurological Surgery (R.N.A., D.R.C., A.S., M.C.H., B.S.J., M.B.P., S.A.A.), Northwestern University, Feinberg School of Medicine, Chicago, Illinois; and Department of Radiology (R.N.A.), Ain Shams University, Cairo, Egypt.

Paper previously presented at: Annual Meeting of the American Society of Neuroradiology, May 18–23, 2019; Boston, Massachusetts, in preliminary format: Abdalla RN, Darwish M, Shokuhfar T, Hurley M, Shaibani A, Jahromi BS, Potts MB, Ansari SA. Safety and Efficacy of Adjuvant Endovascular Interventions in Refractory Anterior Circulation Thrombectomies.

Please address correspondence to Sameer A. Ansari, MD, PhD, Departments of Radiology, Neurology, and Neurological Surgery, Northwestern University, Feinberg School of Medicine, 676 N St. Clair St, Suite 800, Chicago, IL 60611-2927; e-mail: s-ansari@northwestern.edu

 Indicates article with online supplemental data.  
<http://dx.doi.org/10.3174/ajnr.A7124>

burden or composition, and underlying vessel wall pathology.<sup>4</sup> The mechanism of vessel occlusion (embolic-versus-thrombotic) and underlying vascular pathology determines the response to mechanical thrombectomy.<sup>5</sup> Multiple studies from Asia have described intracranial atherosclerotic disease (ICAD) as an important underlying etiology of refractory thrombectomy encountered in 15%–20% of cases,<sup>6–8</sup> with fewer studies describing spontaneous intracranial arterial dissection (IAD) or recalcitrant emboli as other causes.<sup>9–11</sup> In refractory cases, in which there is a failure of recanalization or progressive reocclusion after mechanical thrombectomy, the use of adjunctive medical treatment with antiplatelet glycoprotein IIb/IIIa inhibitors (GPI) and endovascular interventions with intracranial angioplasty and/or stenting have been described.<sup>7,12</sup>

To our knowledge, no studies have characterized the prevalence of refractory stroke thrombectomy and its underlying etiologies in a North American–based population. In our study, we aimed to investigate the predictors of refractory thrombectomy in patients presenting with AIS secondary to ELVO. We also describe clinical and imaging features used to differentiate etiologies of underlying vessel wall pathology (ICAD and/or IAD) or recalcitrant emboli. Finally, we assess the safety and efficacy of adjunctive medical and endovascular treatment techniques in our refractory thrombectomy cohort relative to patients undergoing standard thrombectomy.

## MATERIALS AND METHODS

### Patient Population

Between January 2015 and December 2019, we identified consecutive patients with AIS who underwent endovascular mechanical thrombectomy for an ELVO at 3 Northwestern University affiliated comprehensive stroke centers. An institutional review board (IRB) approved retrospective study was conducted via a prospectively maintained multi-institutional neurointerventional database. Emergent off-label use of Humanitarian Device Exemption (HDE) intracranial stents were reported to the IRB and device manufacturers as required.

Patient and imaging criteria for mechanical thrombectomy were the following: age >18 years; prestroke mRS score of <2; presenting NIHSS score of  $\geq 6$  within 24 hours from last known well; ASPECTS  $\geq 6$ ; and CTA/MRA demonstrating anterior or posterior circulation ELVO including the ICA, M1–M2 MCA, basilar artery, or the P1 segment of the posterior cerebral artery. Patients presenting within 6–24 hours with anterior circulation occlusions were treated if they fulfilled CTP/MRI and DWI-PWI criteria (measured by RAPID post-processing software; iSchemaView) as per the Triage of Wake-Up and Late Presenting Strokes Undergoing Neurointervention with Trevo (DAWN) and/or Endovascular Therapy Following Imaging Evaluation for Ischemic Stroke 3 (DEFUSE) 3 trials.<sup>13,14</sup>

### Mechanical Thrombectomy Procedures and Adjunctive Treatment of Refractory Cases

All procedures were attempted initially via transfemoral puncture using 6F, 80- to 100-cm-long guide sheaths placed in the cervical ICA or vertebral artery. Nearly all used a triaxial system with coaxial advancement of large-bore (0.054- to 0.072-inch inner diameter) distal access catheters (DACs) and 0.021- to 0.027-inch

microcatheters using 0.014- to 0.016-inch microwires to cross the thromboembolus for stent retriever deployment. Mechanical thrombectomy was performed with DAC advancement to the proximal aspect of the clot under continuous vacuum aspiration during stent retriever deployment across the thromboembolus. Next, the stent-delivery microcatheter was removed to maximize the DAC vacuum aspiration force and stent retriever engagement of the clot for ~5 minutes, and the combined stent retriever–DAC aspiration complex was retracted into the cervical or distal guide sheath under manual syringe aspiration. In a minority of cases, mechanical thrombectomy was performed with a large-bore DAC reperfusion catheter under vacuum aspiration without stent retriever use.

Refractory thrombectomy was defined as unsuccessful recanalization (TICI 0–1 reperfusion) after at least 3 passes or vessel reocclusion identified within 72 hours of presumed successful thrombectomy. In addition, residual or recalcitrant emboli or underlying intracranial vessel wall pathology (atherosclerotic plaque and/or an unstable dissection flap) that resulted in severe flow-limiting stenoses with impending or progressive reocclusion on immediate postthrombectomy angiograms were characterized as refractory thrombectomy. In these refractory thrombectomy cases, adjunctive rescue treatment was attempted with either GPI (eptifibatide 180 mcg/kg or abciximab 0.25 mg/kg in a single patient) intracranial angioplasty and/or stenting at the discretion of the neurointerventionalist. Following IV GPI infusion, serial cerebral angiography assessed interval improvement in vessel stability and patency for at least 15 minutes. In cases of persisting flow limitation or reocclusion despite GPI treatment, further salvage with intracranial angioplasty and/or stenting was performed. If intracranial stenting was the primary intervention, it was performed with either concomitant GPI infusion, antiplatelet loading, or in the setting of pre-existing dual-antiplatelet therapy.<sup>15</sup>

All patients having experienced refractory thrombectomy and adjunctive interventions were placed on at least aspirin >300 mg daily (300 mg rectal or 325 mg oral, depending on the patient's ability to swallow or the presence of a nasogastric tube) antiplatelet therapy postprocedure. If intracranial stenting required dual-antiplatelet loading, a 600-mg loading bolus of clopidogrel was provided (Siemens) with 75-mg daily therapy after an intraprocedural cone beam CT or postprocedure CT head study excluded intracranial hemorrhage complications. Patients receiving clopidogrel for intracranial stenting were followed with P2Y<sub>12</sub> assays (VerifyNow, Acumetrics, San Diego, CA) within 12 hours to ensure an adequate antiplatelet response. All standard and refractory thrombectomy cases had early (<72 hours) CTA and/or MR imaging/MRA follow-up available to identify early vessel reocclusion or stable vessel patency.

### Etiology Assessment of Refractory Thrombectomy Cases

We developed criteria to differentiate 3 potential etiologies for refractory thrombectomy: 1) ICAD, 2) IAD, or 3) recalcitrant embolus (Table). We used demographics (age), presentations (headache/neck pain, trauma, recent cardiac surgery), type and number of vascular risk factors (atrial fibrillation versus hypertension, diabetes mellitus, hyperlipidemia, prior stroke/TIA, and smoking), cross-sectional (CT/MR imaging) and angiographic (CTA/MRA/DSA) imaging findings (multivessel disease/peripheral vascular calcifications, intimal flap/subintimal contrast, double lumen,

### Clinical and Imaging Diagnostic Criteria to Differentiate Etiologies of Refractory Thrombectomy

	ICAD	IAD	Recalcitrant Embolus
Demographics	Age $\geq$ 65 Years	Age $\leq$ 55 Years	Any age
Presentations/Risk Factors	$\geq$ 3 Vascular risk factors: hypertension, diabetes mellitus, hyperlipidemia, prior stroke/TIA, smoking	Trauma, acute headache, neck pain	Atrial fibrillation Embolus infarcts: >1 Vascular territory Cardiac surgery Calcified embolus
Imaging Findings	Multivessel disease Peripheral vascular calcifications (extracranial and intracranial ICA)	Intimal flap Double lumen	
Interventional Findings	No stent normalization Residual stenosis >50%	Stent normalization Residual stenosis <50%	No stent normalization Residual stenosis >50% >3 Passes

calcified embolus, embolic distribution of infarcts >1 vascular territory), interventional angiographic findings following stent retriever deployment for thrombectomy, GPI infusion, intracranial angioplasty and/or stenting (>3 passes, stent normalization, degree of residual stenosis). Two independent neurointerventionalists classified each refractory thrombectomy case into at least 1 of the 3 underlying etiologies using this preset criteria (patients did not need to meet all criteria to be classified into 1 category). IAD cases were further classified into spontaneous/iatrogenic dissections versus superimposed IAD related to underlying ICAD pathology (if patients satisfied crossover criteria of both categories). Consensus was achieved in all cases.

#### Data and Outcome Analysis

We analyzed patient demographics (age, sex, race/ethnicity), NIHSS presentations, vascular risk factors, ASPECTS, and ELVO locations in the anterior (ICA and/or MCA) versus posterior (basilar artery/P1 segment of the PCA) circulation. Interventions were studied with respect to, IV tPA utilization, endovascular times to treatment (last known well to puncture or successful reperfusion), procedural times (puncture to reperfusion), angiographic outcomes (reperfusion grade, device passes, first pass reperfusion), major (neurovascular) or minor complications, and symptomatic intracranial hemorrhage (sICH) as per the European Cooperative Acute Stroke Study (ECASS-3) criteria on 1- to 3-day follow-up CT/MR imaging.<sup>16</sup> Clinical outcomes were assessed using the mRS and mortality at 90 days.

We adjudicated both angiographic and clinical outcomes to assess procedural efficacy. Reported angiographic outcomes were regraded using the modified TICI score and confirmed by a neurointerventionalist blinded to the interventions.<sup>17</sup> Successful reperfusion efficacy was defined as modified TICI  $\geq$ 2b, and complete reperfusion was defined as modified TICI 2c/3. Favorable clinical outcomes were defined as mRS  $\leq$  2, consistent with an independent or functional neurologic status requiring concordance of separate assessments by both stroke neurology and neurointerventional surgery practitioners at 90-day follow-up in the outpatient clinic and/or by telephone. In cases of disagreement, the lower modified TICI and higher mRS scores were used to record angiographic and clinical outcomes, respectively. Safety was assessed by comparing major procedural complications, sICH, and mortality at 90 days in the refractory thrombectomy cohort relative to the standard thrombectomy control group.

#### Statistical Analysis

All statistical analyses were performed using SPSS software (Version 24.0, IBM). Continuous variables are presented as medians (minimum-maximum) except for the number of thrombectomy passes that are presented as mean (SD), while discrete and categorical variables are presented as counts and percentages. Continuous variables were compared using the Mann-Whitney test, while categorical and binary variables were compared using the Fisher exact or the  $\chi^2$  test. Univariate analyses compared baseline demographics and procedural, angiographic, and clinical outcomes between standard and refractory thrombectomy groups. Multivariate analysis was performed to identify independent predictors of refractory thrombectomy with the patient's age and vascular risk factors used as variables for a logistic regression model. A *P* value of <.05 was considered statistically significant.

#### RESULTS

Mechanical stroke thrombectomy for an anterior or posterior circulation ELVO was performed in 302 consecutive patients (median age, 70 years; range, 20–98 years; 162 women and 140 men), with 25/302 (8.3%) meeting defined criteria for refractory thrombectomy. The Online Supplemental Data provides details on baseline demographics, vascular risk factors, presentations, technical and clinical outcomes of the refractory thrombectomy cohort in comparison with the standard thrombectomy group (*n* = 277/302).

Although there were presentation trends toward younger age (66 versus 71 years, *P* = .09) and lower NIHSS scores (15 versus 17, *P* = .11) in patients experiencing refractory thrombectomy, these did not reach statistical significance. There were no significant differences in presentation times, IV tPA use, ELVO locations, or anterior-versus-posterior circulation occlusions. With respect to vascular risk factors, diabetes was significantly associated with refractory thrombectomy (44% versus 22%; *P* = .02) and the only independent predictor on logistic regression analysis (OR = 2.72; 95% CI, 1.05–7.09; *P* = .04). Conversely, atrial fibrillation was inversely correlated with refractory thrombectomy (16% versus 45.7%; *P* = .005), accounting for the predominant etiology of intracranial vessel wall pathology (ICAD and/or IAD) over recalcitrant/calcified emboli.

Two independent observers classified underlying etiologies for refractory thrombectomy and achieved consensus as per the predefined criteria (Table). ICAD was the most common vessel

wall pathology associated with refractory thrombectomy in 15/25 (60%) patients, an isolated finding in 9 patients, and with superimposed IAD pathology in 6 patients. Five separate spontaneous or iatrogenic intracranial dissections (5/25 or 20%) were identified for a total of 11/25 (44%) IAD etiologies. A minority of refractory cases were determined to be secondary to recalcitrant/calcified emboli in 5/25 (20%).

In the refractory cohort, 4 of 25 (16%) patients were diagnosed with vessel reocclusion within 72 hours after presumed successful thrombectomy without an opportunity for vessel salvage. Despite adjunctive interventions in only 21/25 patients, with GPI in 8/25 (32%), intracranial angioplasty and/or stenting in 13/25 (54%), there were no significant differences in procedural times, successful reperfusion (87.5% versus 90.9%,  $P = .48$ ), complete or first-pass reperfusion, complications, sICH (0% versus 9%,  $P = .24$ ), favorable clinical outcomes (39% versus 48%,  $P = .51$ ), or mortality (13% versus 28.3%,  $P = .14$ ) at 90 days in comparison with the standard thrombectomy group, respectively (Online Supplemental Data). Only 1 patient receiving GPI and rescue intracranial stenting for a recalcitrant embolus developed a minor groin hematoma complication that resolved with conservative management.

In refractory thrombectomy cases that underwent adjunctive interventions, 5 of 8 (62%) patients with isolated ICAD were treated with intracranial angioplasty and/or stenting including 3 patients treated initially with angioplasty alone (2 of whom required rescue stenting for reocclusions either immediately or post-operatively at 2 months). In relatively equivalent proportions, 5/9 (56%) patients with IAD were adequately managed with GPI without intracranial stenting, including 4/6 (67%) IAD patients with underlying ICAD (Online Supplemental Data). However, all 4/4 (100%) patients with recalcitrant/calcified emboli that were eligible for salvage interventions required intracranial stenting, including 1 rescue stent placement after a failed attempt with GPI. At early CTA/MRA follow-up, most adjunctive interventions maintained vessel patency, except for 2/21 (9.5%) patients that were treated with intracranial stenting, but suffered vessel reocclusion or in-stent thrombosis.

## DISCUSSION

Our study indicates that refractory stroke thrombectomy occurs in approximately 8–9% of cases of a representative North American population, a lower prevalence than in previously reported Asian studies.<sup>4</sup> Patients with cerebrovascular risk factors including diabetes and hyperlipidemia may be prone to refractory thrombectomy due to underlying vessel wall pathology such as ICAD and/or IAD versus the less common etiology of recalcitrant emboli.<sup>5</sup> Antiplatelet GPI, intracranial angioplasty and/or stenting are safe and effective adjunctive treatments for vessel salvage, resulting in equivalent clinical outcomes compared with patients undergoing standard thrombectomy.<sup>8,18</sup>

ICAD is a common cause of AIS, accounting for nearly 15%–20% of ELVOs in Asian populations, and it often requires adjunctive treatment to obtain successful recanalization or maintain vessel patency in cases refractory to mechanical thrombectomy.<sup>8,19,20</sup> Lee et al<sup>5</sup> reported a series of patients having undergone thrombectomy, including 24 patients with underlying ICAD, and

identified independent predictors of male sex, hypercholesterolemia, and posterior circulation occlusions. In a smaller series of 14 patients with ELVO related to ICAD, Suh et al<sup>20</sup> also showed a predilection for younger patients, male sex, smoking, and involvement of the M1 segment of the MCA in 93% of cases. Our study supports these statistical trends for younger patients; cerebrovascular risk factors, especially diabetes as an independent predictor of refractory thrombectomy; and an inverse correlation with atrial fibrillation consistent with the nonembolic stroke etiology of in situ vessel wall pathologies (ICAD or IAD). Although there were no significant differences in the prevalence of anterior-versus-posterior circulation occlusions, the MCA remained the most commonly affected vessel in 76% of refractory cases.

Despite extracranial cervical dissections being responsible for 10%–25% of strokes in young and middle-aged patients,<sup>21</sup> IAD is a rare diagnosis accounting for <2% of all AIS.<sup>22,23</sup> However, IAD is an important consideration in cases of refractory thrombectomy secondary to spontaneous or iatrogenic/traumatic etiologies and is probably under-recognized when superimposed in the setting of an acutely ruptured atherosclerotic plaque. Differentiating IAD from ICAD is not always possible during emergent thrombectomy, with significant imaging overlap of both vessel wall pathologies. In a French study, spontaneous IAD was observed in 3% of all mechanical thrombectomy cases; the authors described complete normalization of vessel caliber after stent retriever deployment without irregular clot visualization or extraction as an imaging feature suggestive of IAD pathology.<sup>9</sup> In contrast, Suh et al<sup>20</sup> reported the need for angioplasty and/or stent placement to achieve vessel recanalization, persistent residual stenosis (>70%), and the absence of a dissection (intimal flap on final angiography as imaging criteria indicative of ICAD). While these paradigms may differentiate uncomplicated cases, not all refractory thrombectomy cases conform to a binary classification. In our study, we developed comprehensive criteria, including patient demographics, clinical risk factors, and additional imaging criteria, to improve the assessment and diagnosis of refractory thrombectomy etiologies, including recalcitrant emboli. Cases with overlapping findings were deemed superimposed IAD in the setting of ICAD. Twenty of 25 (80%) refractory thrombectomy cases were attributable to either IAD or ICAD; 6 were diagnosed as combined IAD/ICAD pathology.

Two large cohort Korean studies by Baek et al<sup>18</sup> and Kang et al<sup>24</sup> studied the management of refractory thrombectomy secondary to ICAD, demonstrating that >70% of patients initially fail stent retriever thrombectomy and require adjunctive treatment. Both antiplatelet GPI and intracranial angioplasty/stenting were shown to be safe and effective with equivalent rates of successful reperfusion, functional clinical outcomes, sICH, and mortality in comparison with patients negative for ICAD undergoing standard thrombectomy. Patients treated with GPI required rescue stenting in 9%–46% of cases, and angioplasty and/or stenting groups underwent permanent stenting in 64%–94% of cases. Balloon angioplasty alone in the treatment of symptomatic ICAD is controversial, with some studies suggesting that it is a safe and effective alternative that obviates the need for dual-antiplatelet therapy in the immediate postthrombectomy period of intracranial hemorrhage risk.<sup>25,26</sup> Other studies compared the durability

of endovascular treatment strategies for symptomatic ICAD and identified higher rates of immediate lesion recoil, delayed restenosis (50% versus 7.5%), and iatrogenic dissections with angioplasty alone versus angioplasty in conjunction with stenting.<sup>27</sup> In our cohort, 14 patients experiencing refractory thrombectomy with underlying ICAD (including 6 patients with superimposed IAD) were equivocally salvaged with either GPI or angioplasty and/or stenting. However, in 3 patients who underwent angioplasty alone, 2 required rescue stent placement for immediate or delayed restenosis/occlusion.

Few studies have evaluated treatment options for spontaneous IAD in the setting of ELVO, and suggest the superiority of intracranial stenting over mechanical thrombectomy alone.<sup>9,28,29</sup> Labeyrie et al<sup>9</sup> demonstrated improved recanalization rates and lower rates of residual dissection-related stenosis with intracranial stenting, but >50% rescue recanalization in patients managed conservatively. In our study, 9 patients with IAD (6 with underlying ICAD, 2 iatrogenic, and 1 spontaneous) were managed equivocally with antiplatelet GPI or intracranial stenting and no patients treated with GPI required rescue stenting.

Another less common cause of intracranial ELVO and refractory thrombectomy is recalcitrant/calcified emboli that may be spontaneous or iatrogenic with increasing cardiovascular catheterization procedures in patients with calcified aortic/cervical atherosclerotic plaques or cardiac valves.<sup>30</sup> In a large multicenter European retrospective study, Maurer et al<sup>31</sup> reported a 1.3% (40/2969) prevalence for calcified emboli and noted worse angiographic  $\text{TICI} \geq 2\text{b}$  reperfusion rates (57.5%), functional outcomes (mRS 0–2, 26.5%), and mortality (55.9%) at 90 days. These recalcitrant/calcified emboli are less likely to respond to standard mechanical thrombectomy techniques and often require adjunctive intracranial stenting for successful revascularization.<sup>10,11</sup> In fact, all 4 patients who were eligible for salvage interventions in our cohort of 5 patients with recalcitrant emboli etiologies required intracranial stenting. We suspect that the prevalence of recalcitrant emboli causing refractory thrombectomy may continue to decline with advancements in the technology of flexible distal guide sheaths, large-bore aspiration catheters, and clot-retrieval devices.<sup>32</sup>

Using GPI or thienopyridine P2Y<sub>12</sub> inhibitors during or after stroke thrombolysis/thrombectomy is concerning, with a risk of intracranial hemorrhagic complications from reperfusion or core infarct transformation. However, single (aspirin) and often dual-antiplatelet loading (for intracranial stenting) are mandatory after adjunctive interventions for refractory thrombectomy to maintain vessel recanalization and prevent in-stent thrombosis or reocclusion via platelet aggregation across an acutely ruptured atherosclerotic plaque or dissection flap. In our study, 2/12 patients treated with intracranial stents reoccluded, possibly due to in-stent thrombosis complications from inadequate or delayed antiplatelet loading. This is consistent with previously published literature suggesting an 87% patency rate for rescue stenting after failed mechanical thrombectomy.<sup>33</sup> Immediate and adequate antiplatelet loading should be initiated in refractory thrombectomy interventions, with early P2Y<sub>12</sub> testing recommended to confirm antiplatelet efficacy. Furthermore, novel intravenous P2Y<sub>12</sub> inhibitors such as cangrelor may offer improved therapeutic transition to oral

antiplatelet loading agents and safety over GPI. Several studies have shown no increased incidence of sICH after intracranial stenting and suggest that the benefit of recanalization outweighs the risk of hemorrhage.<sup>8,12,34</sup> Although no patients in our refractory thrombectomy cohort developed sICH complications, the risk should not be underestimated. This may have been partly due to our patient or imaging selection of small-core infarct volumes, intraprocedural cone beam CT scanning to exclude hemorrhagic complications prior to adjunctive interventions with GPI or intracranial angioplasty and/or stenting, and strict hemodynamic control afterwards to limit reperfusion complications.

Our study had several limitations, due to the inherent methodologic weaknesses of retrospective and small sample size studies, to assess rare pathologies such as ICAD, IAD, and recalcitrant/calcified emboli presenting with ELVO. Furthermore, patients experiencing refractory thrombectomy were managed at the discretion of treating neurointerventionalists without a formal protocol or randomization to adjunctive interventions of GPI versus intracranial angioplasty and/or stenting. Hence, we deferred direct comparisons of either underlying etiologies or treatment protocols for refractory thrombectomy. We limited our aims to assessing the prevalence of refractory thrombectomy in a North American population not previously described in the literature and identifying specific etiologies using a comprehensive diagnostic clinical and imaging evaluation. Finally, we compared the safety and efficacy of adjunctive interventions for vessel salvage in patients experiencing refractory thrombectomy with the standard thrombectomy cohort.

## CONCLUSIONS

Refractory stroke thrombectomy occurs with a prevalence of ~8–9% in a North American population, less than in reported Asian populations. Various cerebrovascular risk factors have been associated with refractory thrombectomy. In the current study, diabetes mellitus was shown to be associated with and an independent predictor of refractory thrombectomy and its underlying vessel wall pathologies. ICAD and/or IAD are presumably the most common etiologies for ELVO presentations refractory to mechanical thrombectomy and, less commonly, recalcitrant/calcified emboli. Both antiplatelet GPI and intracranial angioplasty/stenting are safe and effective adjunctive interventions for vessel salvage in the refractory thrombectomy setting, with equivalent clinical outcomes to standard thrombectomy.

## REFERENCES

1. Goyal M, Menon BK, van Zwam WH, et al. HERMES Collaborators. **Endovascular thrombectomy after large-vessel ischaemic stroke: a meta-analysis of individual patient data from five randomised trials.** *Lancet* 2016;387:1723–31 CrossRef Medline
2. Kaesmacher J, Dobrocky T, Heldner MR, et al. **Systematic review and meta-analysis on outcome differences among patients with  $\text{TICI}2\text{b}$  versus  $\text{TICI}3$  reperfusion: success revisited.** *J Neurosurg Neurosurg Psychiatry* 2018;89:910–17 CrossRef Medline
3. Dargazanli C, Consoli A, Barral M, et al. **Impact of modified  $\text{TICI}3$  versus modified  $\text{TICI}2\text{b}$  reperfusion score to predict good outcome following endovascular therapy.** *AJNR Am J Neuroradiol* 2017;38:90–96 CrossRef Medline
4. Kim BM. **Causes and solutions of endovascular treatment failure.** *J Stroke* 2017;19:131–42 CrossRef Medline

5. Lee JS, Hong JM, Lee KS, et al. **Endovascular therapy of cerebral arterial occlusions: intracranial atherosclerosis versus embolism.** *J Stroke Cerebrovasc Dis* 2015;24:2074–80 CrossRef Medline
6. Lee JS, Hong JM, Lee KS, et al. **Primary stent retrieval for acute intracranial large artery occlusion due to atherosclerotic disease.** *J Stroke* 2016;18:96–101 CrossRef Medline
7. Kang DH, Kim YW, Hwang YH, et al. **Instant reocclusion following mechanical thrombectomy of in situ thromboocclusion and the role of low-dose intra-arterial tirofiban.** *Cerebrovasc Dis* 2014;37:350–55 CrossRef Medline
8. Yoon W, Kim SK, Park MS, et al. **Endovascular treatment and the outcomes of atherosclerotic intracranial stenosis in patients with hyperacute stroke.** *Neurosurgery* 2015;76:680–86; discussion 86 CrossRef Medline
9. Labeyrie MA, Civelli V, Reiner P, et al. **Prevalence and treatment of spontaneous intracranial artery dissections in patients with acute stroke due to intracranial large vessel occlusion.** *J Neurointerv Surg* 2018;10:761–64 CrossRef Medline
10. Potts MB, da Matta L, Abdalla RN, et al. **Stenting of mobile calcified emboli after failed thrombectomy in acute ischemic stroke: case report and literature review.** *World Neurosurg* 2020;135:245–51 CrossRef Medline
11. Dobrocky T, Piechowiak E, Cianfoni A, et al. **Thrombectomy of calcified emboli in stroke: does histology of thrombi influence the effectiveness of thrombectomy?** *J Neurointerv Surg* 2018;10:345–50 CrossRef Medline
12. Baek JH, Kim BM, Kim DJ, et al. **Stenting as a rescue treatment after failure of mechanical thrombectomy for anterior circulation large artery occlusion.** *Stroke* 2016;47:2360–63 CrossRef Medline
13. Nogueira RG, Jadhav AP, Haussen DC, et al. DAWN Trial Investigators. **Thrombectomy 6 to 24 hours after stroke with a mismatch between deficit and infarct.** *N Engl J Med* 2018;378:11–21 CrossRef Medline
14. Albers GW, Marks MP, Kemp S, et al. DEFUSE 3 Investigators. **Thrombectomy for stroke at 6 to 16 hours with selection by perfusion imaging.** *N Engl J Med* 2018;378:708–18 CrossRef Medline
15. Gandhi CD, Bulsara KR, Fifi J, et al. SNIS Standards and Guidelines Committee. **Platelet function inhibitors and platelet function testing in neurointerventional procedures.** *J Neurointerv Surg* 2014;6:567–77 CrossRef Medline
16. Hacke W, Kaste M, Bluhmki E, et al. ECASS Investigators. **Thrombolysis with alteplase 3 to 4.5 hours after acute ischemic stroke.** *N Engl J Med* 2008;359:1317–29 CrossRef Medline
17. Goyal M, Fargen KM, Turk AS, et al. **2C or not 2C: defining an improved revascularization grading scale and the need for standardization of angiography outcomes in stroke trials.** *J Neurointerv Surg* 2014;6:83–86 CrossRef Medline
18. Baek JH, Kim BM, Heo JH, et al. **Outcomes of endovascular treatment for acute intracranial atherosclerosis-related large vessel occlusion.** *Stroke* 2018;49:2699–705 CrossRef Medline
19. Okawa M, Tateshima S, Liebeskind D, et al. **Early loss of immediate reperfusion while stent retriever in place predicts successful final reperfusion in acute ischemic stroke patients.** *Stroke* 2015;46:3266–69 CrossRef Medline
20. Suh HI, Hong JM, Lee KS, et al. **Imaging predictors for atherosclerosis-related intracranial large artery occlusions in acute anterior circulation stroke.** *J Stroke* 2016;18:352–54 CrossRef Medline
21. Schievink WI. **Spontaneous dissection of the carotid and vertebral arteries.** *N Engl J Med* 2001;344:898–906 CrossRef Medline
22. Debette S, Compter A, Labeyrie M-A, et al. **Epidemiology, pathophysiology, diagnosis, and management of intracranial artery dissection.** *Lancet Neurol* 2015;14:640–54 CrossRef Medline
23. Giannini N, Ulivi L, Maccarrone M, et al. **Epidemiology and cerebrovascular events related to cervical and intracranial arteries dissection: the experience of the city of Pisa.** *Neurol Sci* 2017;38:1985–91 CrossRef Medline
24. Kang DH, Yoon W, Kim SK, et al. **Endovascular treatment for emergent large vessel occlusion due to severe intracranial atherosclerotic stenosis.** *J Neurosurg* 2018 Jun 1. [Epub ahead of print] CrossRef Medline
25. Nguyen TN, Zaidat OO, Gupta R, et al. **Balloon angioplasty for intracranial atherosclerotic disease: periprocedural risks and short-term outcomes in a multicenter study.** *Stroke* 2011;42:107–11 CrossRef Medline
26. Marks MP, Marcellus ML, Do HM, et al. **Intracranial angioplasty without stenting for symptomatic atherosclerotic stenosis: long-term follow-up.** *AJNR Am J Neuroradiol* 2005;26:525–30 Medline
27. Mazighi M, Yadav JS, Abou-Chebl A. **Durability of endovascular therapy for symptomatic intracranial atherosclerosis.** *Stroke* 2008;39:1766–69 CrossRef Medline
28. Suh SH, Kim BM, Roh HG, et al. **Self-expanding stent for recanalization of acute embolic or dissecting intracranial artery occlusion.** *AJNR Am J Neuroradiol* 2010;31:459–63 CrossRef Medline
29. Kim BM. **Refractory occlusion to stentriever thrombectomy: etiological considerations and suggested solutions.** In: Park J, ed. *Acute Ischemic Stroke: Medical, Endovascular, and Surgical Techniques.* Singapore Springer; 2017:13–226
30. Walker BS, Shah LM, Osborn AG. **Calcified cerebral emboli, a do not miss imaging diagnosis: 22 new cases and review of the literature.** *AJNR Am J Neuroradiol* 2014;35:1515–19 CrossRef Medline
31. Maurer CJ, Dobrocky T, Joachimski F, et al. **Endovascular thrombectomy of calcified emboli in acute ischemic stroke: a multicenter study.** *AJNR Am J Neuroradiol* 2020;41:464–68 CrossRef Medline
32. Ansari SA, Darwish M, Abdalla RN, et al. **GUide sheath Advancement and aspiRation in the Distal petrocavernous internal carotid artery (GUARD) technique during thrombectomy improves reperfusion and clinical outcomes.** *AJNR Am J Neuroradiol* 2019;40:1356–62 CrossRef Medline
33. Chang Y, Kim BM, Bang OY, et al. **Rescue stenting for failed mechanical thrombectomy in acute ischemic stroke: a multicenter experience.** *Stroke* 2018;49:958–64 CrossRef Medline
34. Zaidat OO, Wolfe T, Hussain SI, et al. **Interventional acute ischemic stroke therapy with intracranial self-expanding stent.** *Stroke* 2008;39:2392–95 CrossRef Medline

# Carotid Stenting without Embolic Protection Increases Major Adverse Events: Analysis of the National Surgical Quality Improvement Program

P. Nazari, P. Golnari, M.C. Hurley, A. Shaibani, S.A. Ansari, M.B. Potts, and B.S. Jahromi



## ABSTRACT

**BACKGROUND AND PURPOSE:** Published data regarding embolic protection device efficacy is mixed, and its use during carotid artery stent placement remains variable. We, therefore, examined the frequency of embolic protection device use and its association with outcomes after carotid artery stent placement using a national quality improvement data base.

**MATERIALS AND METHODS:** Patients undergoing carotid artery stent placement with or without embolic protection devices were identified in the American College of Surgeons National Surgical Quality Improvement Program data base. The primary outcome was the incidence of major adverse cardiovascular events (defined as death, stroke, or myocardial infarction/arrhythmia) within 30 days. Propensity scoring was used to create 2 matching cohorts of patients using demographic and baseline variables.

**RESULTS:** Between 2011 and 2018, among 1200 adult patients undergoing carotid artery stent placement, 23.8% did not have embolic protection devices. There was no trend toward increased embolic protection device use with time. Patients without embolic protection device use received preoperative antiplatelets less frequently (90.6% versus 94.6%,  $P = .02$ ), underwent more emergent carotid artery stent placement (7.2% versus 3.6%,  $P = .01$ ), and had a higher incidence of major adverse cardiovascular events (OR = 1.81; 95% CI, 1.1–2.94) and stroke (OR = 3.31; 95% CI, 1.71–6.39). After compensating for baseline imbalances using propensity-matched cohorts ( $n = 261$  for both), carotid artery stent placement without an embolic protection device remained associated with increased major adverse cardiovascular events (9.2% versus 4.2%; OR = 2.30; 95% CI, 1.10–4.80) and stroke (6.5% versus 1.5%; OR = 4.48; 95% CI, 1.49–13.49).

**CONCLUSIONS:** Lack of embolic protection device use during carotid artery stent placement is associated with a 4-fold increase in the likelihood of perioperative stroke. Nevertheless, nearly one-quarter of patients in the American College of Surgeons National Surgical Quality Improvement Program underwent unprotected carotid artery stent placement. Efforts targeting improved embolic protection device use during carotid artery stent placement are warranted.

**ABBREVIATIONS:** ACS-NSQIP = American College of Surgeons National Surgical Quality Improvement Program; CAS = carotid artery stent placement; EPD = embolic protection device; MACE = major adverse cardiovascular events

Carotid artery stent placement (CAS) has developed rapidly during the past 30 years to become a viable option for carotid revascularization, especially in patients at high-risk for carotid endarterectomy.<sup>1</sup> One of the major remaining concerns about CAS is the risk of embolic stroke caused by mobilization and migration of plaque fragments during stent placement.<sup>2</sup> Embolic protection

devices (EPDs) have been developed to reduce the risk of distal embolization.<sup>3</sup> In 2011, guidelines from the American Stroke Association suggested that the use of EPDs during CAS can be beneficial to reduce the risk of stroke when the risk of vascular injury is low.<sup>4</sup> Nevertheless, randomized trials, systematic reviews, and meta-analyses offer conflicting evidence regarding the frequency and efficacy of EPD use, with some showing diminished rates of postoperative stroke and death when an EPD was used,<sup>5–8</sup> whereas others have not supported the benefit of an EPD during CAS.<sup>9–12</sup> We, therefore, examined the American College of Surgeons National Surgical Quality Improvement Program (ACS-NSQIP) data base to determine the frequency of EPD use during CAS and compared preoperative and postoperative characteristics, complications, and outcomes of patients undergoing CAS with and without an EPD.

Received December 15, 2020; accepted after revision January 26, 2021.

From the Departments of Neurological Surgery and Radiology Northwestern Memorial Hospital, Northwestern University Feinberg School of Medicine, Chicago, Illinois.

Please address correspondence to Babak S. Jahromi, MD, PhD, Departments of Neurological Surgery and Radiology, Northwestern University Feinberg School of Medicine, 676 North St. Clair St, Suite 2210, Chicago, IL 60611; e-mail: babak.jahromi@northwestern.edu; @babaksjahromi

Indicates open access to non-subscribers at www.ajnr.org

Indicates article with online supplemental data.

<http://dx.doi.org/10.3174/ajnr.A7108>

## MATERIALS AND METHODS

Our retrospective observational study did not require institutional review board approval or patient consent because the ACS-NSQIP is a publicly available, de-identified data base.

### Data Base

Patients who underwent CAS were identified using the vascular-targeted ACS-NSQIP Participant Use Data Files from 2011 (when targeted data bases were introduced) to 2018 (the latest data base available at time of analysis, spanning 98 hospitals). The ACS-NSQIP is a multi-institutional collaboration that collects information, including preoperative risk factors, intraoperative variables, and 30-day morbidity and mortality. The CAS-targeted module provides additional information including symptom status, anatomic and physiologic high-risk factors, preoperative antiplatelet medications, and the degree of carotid artery stenosis. Previous studies have shown the reliability of this data base.<sup>13,14</sup> Patients with complete ipsilateral carotid occlusion and patients who underwent thrombectomy at the same admission were excluded. Included patients were divided into 2 groups (CAS with EPD and CAS without EPD). General risk factors such as age, sex, race, body mass index, smoking, diabetes mellitus, preoperative dialysis, hypertension, history of chronic obstructive pulmonary disease and congestive heart failure, preoperative functional status, and emergency procedure status were obtained from the main ACS-NSQIP dataset. Anatomic high-risk factors were defined by the ACS-NSQIP to include recurrent stenosis, radical neck dissection, contralateral occlusion, prior neck radiation, contralateral laryngeal nerve injury/palsy, and a high anatomic lesion (C2 or higher). Physiologic high-risk factors were defined by the ACS-NSQIP as New York Heart Association congestive heart failure class III/IV, left ventricular ejection fraction <30%, unstable angina, and recent (within 30 days) myocardial infarction. Ipsilateral carotid stenosis was divided into 3 groups based on the baseline Doppler sonography or angiography: mild (estimate of <50%), moderate (estimate of 50%–79%), and severe (estimate of 80%–99%) stenosis. A list of all variable definitions captured by the ACS-NSQIP can be found in the data user guides.<sup>15,16</sup>

### Outcomes

The primary outcome was the occurrence of major adverse cardiovascular events (MACE), defined as the composite of death, stroke, and myocardial infarction/arrhythmia. Secondary outcomes included individual components of MACE as well as TIA, length of stay > 2 days, nonroutine discharge, and unplanned readmission within 30 days postoperatively. Discharge disposition to any hospital or facility other than home was designated as nonroutine discharge. All outcomes used prespecified variables in ACS-NSQIP.

### Missing Data and Propensity Matching

The percentage of missing values across all variables varied between 0% and 4.9%. In total, 184 of 1200 records (15%) were incomplete. We used multiple imputation with fully-conditional specification using all covariates and outcome variables to create and analyze 20 multiple imputed datasets. This method is widely

considered to improve accuracy and statistical power relative to other missing-data techniques.<sup>17</sup> To address potential confounding nonrandom differences between patients who underwent CAS with EPD versus those who underwent CAS without EPD, we used propensity scoring techniques to create 2 cohorts of patients from the entire study population who were matched on their propensity for undergoing CAS with EPD versus without EPD. In this analysis, a logistic regression model was created for each of the 20 imputed datasets to estimate the likelihood of undergoing CAS without EPD (rather than CAS with EPD) using all demographic and baseline variables as potential predictors. The logit coefficients from this model were then used to create a propensity score for undergoing CAS without EPD for each patient from the entire study population that ranged from 0 to 1 and represented the likelihood of undergoing CAS without EPD rather than CAS with EPD. We then averaged the 20 propensity scores for each case across the completed datasets<sup>18</sup> and performed nearest-neighbor matching (with a caliper distance of 0.05) with these averaged scores to create 2 evenly matched cohorts of CAS with EPD and CAS without EPD by a caliper-matching algorithm, with patients being used only once in the matching.

### Statistical Analysis

Baseline patient- and procedure-related characteristics of patients undergoing CAS with and without EPD were compared across both the entire study population and the propensity score-matched groups using  $\chi^2$  and Fisher exact (when appropriate) tests in the imputed dataset. For comparison, we also performed the analysis on the subset of available cases before imputation. The trend of EPD use was assessed during the entire time period by annual percentage change estimates using the Joinpoint Regression Program (Version 4.6.0.0; Statistical Methodology and Application Branch, Surveillance Research Program, National Cancer Institute, Bethesda, Maryland).<sup>19</sup> Logistic regression was performed on pre- and postmatched imputed datasets to assess the effect of EPD on postprocedural outcomes. Propensity score matching was performed using R statistical and computing software, Version 4.0.2 (<http://www.r-project.org>) and the MatchIt<sup>20</sup> package for R (<https://cran.r-project.org/web/packages/MatchIt/MatchIt.pdf>). Multiple imputation and statistical analyses were performed using SPSS Statistics for Windows, Version 26 (IBM), and statistical significance was defined as  $P < .05$ .

## RESULTS

### Demographics and Clinical Characteristics

Overall, 1200 adult patients undergoing CAS in the vascular-targeted ACS-NSQIP dataset between 2011 to 2018 met the criteria for analysis, of whom 277 (23.8%) underwent CAS without an EPD. The frequency of EPD use did not show any significant trend (annual percentage change,  $-0.74$ ; 95% CI,  $-3.61$ – $2.23$ ;  $P = .56$ ) during the study period (Fig 1). Demographics and characteristics of the study cohorts (before and after propensity score matching) are shown in the Online Supplemental Data. Use of multiple imputation to account for missing variables (0%–4.9% across the dataset) did not significantly affect the results (Online Supplemental Data); hence, subsequent analyses

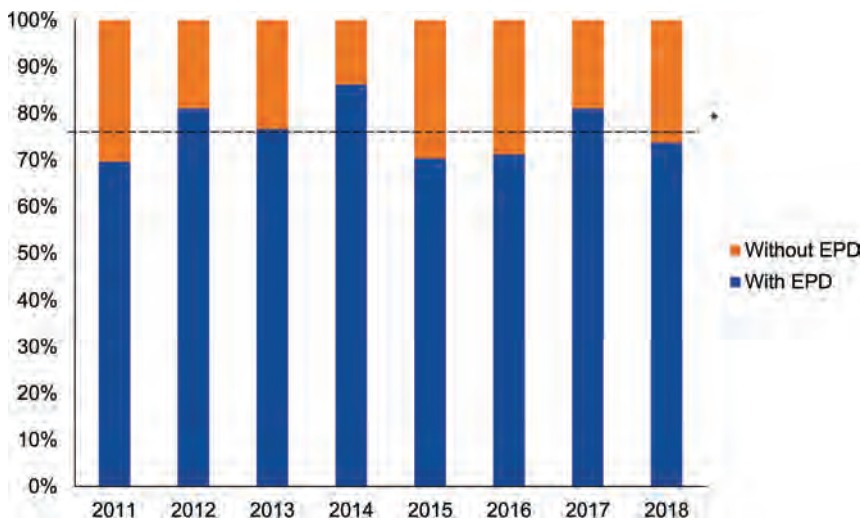


**FIG 1.** Annual proportion of EPD use during CAS (ACS-NSQIP CAS-targeted module, 2011–2018). Asterisk indicates mean percentage use of an EPD during the entire study period.

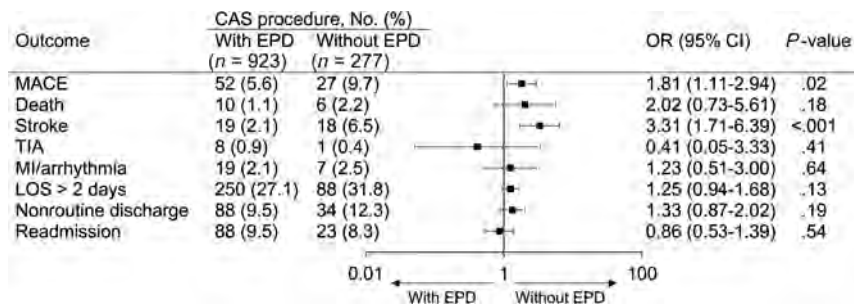


**FIG 2.** OR of outcomes in all patients undergoing CAS with or without EPD (ACS-NSQIP CAS-targeted module, 2011–2018). LOS indicates length of stay.

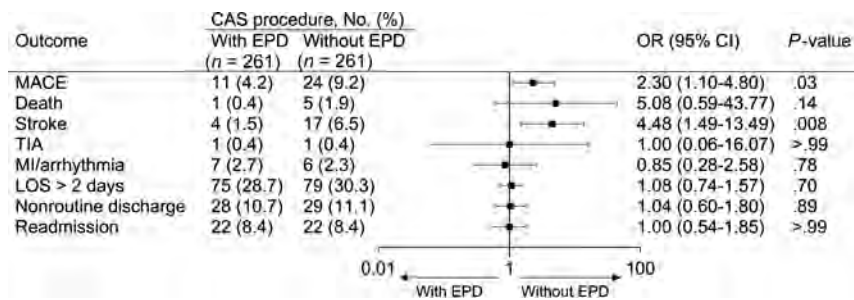


**FIG 3.** OR of outcomes in propensity-matched cohorts of patients undergoing CAS with or without EPD (ACS-NSQIP CAS-targeted module, 2011–2018). LOS indicates length of stay.

used the imputed dataset. There were no significant differences between 2 groups in age, sex, race, body mass index, preoperative comorbidities, functional dependency, American Society of Anesthesiologists classification, symptom status, or anatomic or physiologic high-risk factors before matching. However, stenosis categories were differently distributed across the 2 groups ( $P = .02$ ), and preoperative antiplatelet medication was administered more often in patients who had CAS with EPD (94.6% versus 90.6%,  $P = .02$ ). Subgroup

analysis showed that the proportion of patients who did not receive preoperative antiplatelets was higher in emergency cases compared with nonemergency cases (43.4% versus 4.6%,  $P < .001$ ). Finally, CAS without an EPD was more likely to have been performed emergently compared with CAS with an EPD (7.2% versus 3.6%,  $P = .01$ ). These baseline differences were no longer seen after propensity score matching (Online Supplemental Data).

### Clinical Outcomes before and after Matching

The 30-day postoperative outcomes of the entire cohort (before matching) are shown in Fig 2. The incidence of MACE was higher in CAS without EPD than in the group with EPD (OR = 1.81; 95% CI, 1.11–2.94;  $P = .02$ ), and was unrelated to the degree of stenosis being treated ( $P = .68$  and  $P = .16$  for CAS with and without EPD, respectively). Analysis of secondary outcomes revealed CAS without an EPD had a higher incidence of stroke compared with CAS with an EPD (OR = 3.31; 95% CI, 1.71–6.39;  $P < .001$ ). Other secondary outcomes did not show any differences between the 2 groups.

To account for potential confounders and baseline imbalances when comparing CAS with and without EPD, we performed propensity score matching between the 2 groups, yielding 261 patients in each matched cohort. After propensity score matching, no significant differences remained in baseline demographics and characteristics between the 2 cohorts (including stenosis categories, proportion of CAS performed emergently, and antiplatelet use), confirming that the cohorts were well-matched (Online Supplemental Data). Outcomes after matching are shown in Fig 3. The incidence of MACE remained higher in CAS without EPD compared with CAS with EPD (OR = 2.30; 95% CI, 1.10–4.80;  $P = .03$ ) as did stroke (OR = 4.48; 95% CI, 1.49–13.49;  $P = .008$ ). Other secondary outcomes were not significantly different between the matched cohorts.

### DISCUSSION

Our analysis of carotid stent placement records from the most recent 8 years of the ACS-NSQIP data base (2011–2018) found that approximately one-quarter of CAS was performed without an EPD each year and that this practice is associated with significantly

higher odds of MACE and stroke, even after adjusting for baseline imbalances between cohorts using propensity-matched analyses. These conclusions are strengthened by the relative size of the prospective ACS-NSQIP targeted registry being studied (rivaling the prespecified combined analysis of the Endarterectomy versus Angioplasty in Patients with Symptomatic Severe Carotid Stenosis [EVA-3S], Stent-Protected Angioplasty versus Carotid Endarterectomy [SPACE], and International Carotid Stenting Study [ICSS] trials by the Carotid Stenosis Trialists Collaboration)<sup>12</sup> and are in keeping with data from the Vascular Quality Initiative regarding variations in EPD use during CAS,<sup>21</sup> despite its efficacy.<sup>22</sup> These findings imply that a substantial portion of CAS remains unprotected (despite the consequences), a practice pattern that runs counter to the 2011 multisociety consensus guidelines, noting the benefit of EPD during CAS,<sup>4</sup> and to the directions from the US Centers for Medicare and Medicaid Services,<sup>23</sup> which list intraprocedural use of an EPD as a necessary condition for reimbursement of CAS.

The reasons for lack of EPD use in approximately one-quarter of CAS cases in the ACS-NSQIP targeted registry are unclear and do not appear to be explained by any differences in anatomic high-risk factors in patients undergoing CAS with or without EPD. One potential reason may be that while EPD use during CAS has been favored in a number of meta-analyses<sup>6,7</sup> and national data base reviews,<sup>8</sup> definitive evidence has not emerged from more recent randomized trials to support its use. For example, of the 5 major recent carotid revascularization trials comparing carotid endarterectomy with CAS, only 2 (Carotid Revascularization Endarterectomy versus Stenting Trial [CREST]<sup>24</sup> and Asymptomatic Carotid Trial [Randomized Trial of Stent versus Surgery for Asymptomatic Carotid Stenosis - ACT I]<sup>25</sup>) mandated EPD use with CAS. Of the remaining 3, the SPACE trial found no difference in 30-day ipsilateral stroke or death in patients undergoing CAS with and without an EPD (8.3% versus 6.2%;  $P = .40$ ),<sup>26</sup> and the ICSS trial found a trend toward more MACE after CAS with an EPD (8.5% versus 4.6%;  $P = .056$ ).<sup>27</sup> Only the EVA-3S trial found EPD use to be associated with fewer strokes or death (7.9% versus 20.6%; relative risk, 0.38; 95% CI, 0.17–0.85), though this trial was criticized for higher complication rates and operator inexperience.<sup>28</sup> Finally, a prespecified pooled analysis of individual patient data from 3 trials (SPACE, EVA-3S, ICSS) found stroke and death after CAS to be related to stent cell design and unrelated to EPD, even after adjusting for age, qualifying event, history of prior stroke, baseline disability, and operator experience.<sup>11</sup> Use of DWI as a surrogate measure of EPD efficacy has also not yielded evidence in favor of its use, with the ICSS trial finding more ischemic brain lesions on MR imaging after CAS with-versus-without an EPD (68% versus 35%;  $P = .003$ )<sup>29</sup> and Barbato et al<sup>11</sup> similarly finding more DWI lesions in patients having undergone CAS randomized to EPD versus to no EPD.

How EPD may counterintuitively increase stroke risk during CAS or lead to more ischemic changes on MR imaging has not been fully explained. Thrombus may form on the distal filter surface, on the tip of the EPD wire, or from microtrauma to the vascular wall and plaque during EPD placement, and microemboli may pass through the micropores of the EPD or through gaps that exist between the EPD and the vascular wall.<sup>30</sup> Other challenges related to use of an EPD during CAS may be the additional

technical difficulty of EPD navigation and placement, especially in severely stenotic and/or highly tortuous anatomy. To overcome some of these issues, a variety of EPDs have been developed to improve the safety of CAS, including proximal protection devices represented by proximal balloon occlusion and flow-reversal devices.<sup>31</sup> Nevertheless, even CAS using proximal protection with flow reversal has been associated with DWI lesions, though fewer than those seen with traditional distal EPDs.<sup>32</sup>

Given the above discussion, our finding that CAS without EPD is associated with a significantly higher risk of stroke and MACE (in both primary and matched-cohort analyses), while intuitive, may still come as a surprise. For example, a prior analysis of ACS-NSQIP did not find any significant differences in the number of major adverse events between CAS with and without an EPD.<sup>33</sup> However, the time span of this prior study (4 years) was much shorter than that in our dataset, and it is likely that our use of the largest targeted ACS-NSQIP dataset available to date may have accounted for our positive results. Most important, none of the prior studies randomized patients to EPD use, raising concern for potential confounding differences between cohorts with and without EPD that might mask significant differences despite multivariable regression analysis. For example, patients without an EPD in the ACS-NSQIP were more likely to have CAS performed emergently and less likely to have had preoperative antiplatelets. We, therefore, further adjusted for potential confounding differences between cohorts with EPD and without EPD by use of propensity score matching, which further confirmed the increased risk of stroke and MACE seen after CAS without EPD on our primary multivariable analysis.

There are limitations to our study, most important, that multivariable analysis, with or without propensity score matching, cannot eliminate biases inherent in retrospective data base analysis or replace a prospective randomized trial of CAS with or without EPD. However, it appears increasingly unlikely that such a trial will ever be undertaken, and prospective registries such as ACS-NSQIP, while not as comprehensive as desired, may be the next best alternative to randomized trial data. Nevertheless, the ACS-NSQIP does not provide granular periprocedural data that would permit analysis of factors such as the etiology of stenosis or the use of pre-/postangioplasty during CAS. Similarly, the ACS-NSQIP data base may not be representative of national practice, but it does identify periprocedural stroke more accurately than national administrative datasets.<sup>14</sup> Last, the ACS-NSQIP study population is largely from CAS using a distal rather than proximal EPD, and transcarotid artery revascularization was not part of this dataset. Use of transcarotid artery revascularization has been associated with exceptionally low rates of stroke and death after CAS in the Vascular Quality Initiative,<sup>34</sup> and increased use of proximal protection and/or flow-reversal techniques may further increase the performance gap between CAS with and without an EPD in the future.

## CONCLUSIONS

Analysis of the vascular-targeted ACS-NSQIP data base reveals that nearly one-quarter of CAS is performed without an EPD. This has not significantly changed between 2011 and 2018 and is associated with a more than a 2-fold increase in the likelihood of

MACE, and a 4-fold increase in the likelihood of periprocedural stroke. Quality improvement efforts targeting increased use of an EPD during CAS may, therefore, yield substantial benefit toward patient outcomes.

## REFERENCES

- Lichtman JH, Jones MR, Leifheit EC, et al. **Carotid endarterectomy and carotid artery stenting in the US Medicare population, 1999–2014.** *JAMA* 2017;318:1035–46 CrossRef Medline
- Tallarita T, Rabinstein AA, Cloft H, et al. **Are distal protection devices ‘protective’ during carotid angioplasty and stenting?** *Stroke* 2011;42:1962–66 CrossRef Medline
- Zahn R, Mark B, Niedermaier N, et al. Arbeitsgemeinschaft Leitende Kardiologische Krankenhausärzte (ALKK). **Embolic protection devices for carotid artery stenting: better results than stenting without protection?** *Eur Heart J* 2004;25:1550–58 CrossRef Medline
- Brott TG, Halperin JL, Abbara S, et al. 2011 **ASA/ACCF/AHA/AANN/AANS/ACR/ASNR/CNS/SAIP/SCAI/SIR/SNIS/SVM/SVS guideline on the management of patients with extracranial carotid and vertebral artery disease: executive summary—a report of the American College of Cardiology Foundation/American Heart Association Task Force on Practice Guidelines, and the American Stroke Association, American Association of Neuroscience Nurses, American Association of Neurological Surgeons, American College of Radiology, American Society of Neuroradiology, Congress of Neurological Surgeons, Society of Atherosclerosis Imaging and Prevention, Society for Cardiovascular Angiography and Interventions, Society of Interventional Radiology, Society of Neuro-Interventional Surgery, Society for Vascular Medicine, and Society for Vascular Surgery.** Developed in collaboration with the American Academy of Neurology and Society of Cardiovascular Computed Tomography. *Catheter Cardiovasc Interv* 2013;81:E76–123 CrossRef Medline
- Mas JL, Chatellier G, Beyssen B, EVA-3S Investigators, et al. **Endarterectomy versus stenting in patients with symptomatic severe carotid stenosis.** *N Engl J Med* 2006;355:1660–71 CrossRef Medline
- Touzé E, Trinquart L, Chatellier G, et al. **Systematic review of the perioperative risks of stroke or death after carotid angioplasty and stenting.** *Stroke* 2009;40:e683–93 CrossRef Medline
- Garg N, Karagiorgos N, Pisimisis GT, et al. **Cerebral protection devices reduce periprocedural strokes during carotid angioplasty and stenting: a systematic review of the current literature.** *J Endovasc Ther* 2009;16:412–27 CrossRef Medline
- Knappich C, Kuehnl A, Tsantilas P, et al. **The use of embolic protection devices is associated with a lower stroke and death rate after carotid stenting.** *JACC Cardiovasc Interv* 2017;10:1257–65 CrossRef Medline
- Ringleb PA, Allenberg J, Brückmann H, et al. SPACE Collaborative Group. **30 day results from the SPACE trial of stent-protected angioplasty versus carotid endarterectomy in symptomatic patients: a randomised non-inferiority trial.** *Lancet* 2006;368:1239–47 CrossRef Medline
- Gensicke H, Zumbunn T, Jongen LM, et al. ICSS-MRI Substudy Investigators. **Characteristics of ischemic brain lesions after stenting or endarterectomy for symptomatic carotid artery stenosis: results from the international carotid stenting study-magnetic resonance imaging substudy.** *Stroke* 2013;44:80–86 CrossRef Medline
- Barbato JE, Dillavou E, Horowitz MB, et al. **A randomized trial of carotid artery stenting with and without cerebral protection.** *J Vasc Surg* 2008;47:760–65 CrossRef Medline
- Wodarg F, Turner EL, Dobson J, et al. Carotid Stenosis Trialists’ Collaboration. **Influence of stent design and use of protection devices on outcome of carotid artery stenting: a pooled analysis of individual patient data.** *J Neurointerv Surg* 2018;10:1149–54 CrossRef Medline
- Shiloach M, Frencher SK Jr, Steeger JE, et al. **Toward robust information: data quality and inter-rater reliability in the American College of Surgeons National Surgical Quality Improvement Program.** *J Am Coll Surg* 2010;210:6–16 CrossRef Medline
- Bensley RP, Yoshida S, Lo RC, et al. **Accuracy of administrative data versus clinical data to evaluate carotid endarterectomy and carotid stenting.** *J Vasc Surg* 2013;58:412–19 CrossRef Medline
- User Guide for the 2018 ACS NSQIP Participant Use Data File (PUF). **American College of Surgeons National Surgical Quality Improvement Program.** 2019. [https://www.facs.org/-/media/files/quality-programs/nsqip/nsqip\\_puf\\_userguide\\_2018.ashx](https://www.facs.org/-/media/files/quality-programs/nsqip/nsqip_puf_userguide_2018.ashx). Accessed July 20, 2020
- User Guide for the 2018 ACS NSQIP Procedure Targeted Participant Use Data File (PUF). **American College of Surgeons National Surgical Quality Improvement Program.** 2018. [https://www.facs.org/-/media/files/quality-programs/nsqip/pt\\_nsqip\\_puf\\_userguide\\_2018.ashx](https://www.facs.org/-/media/files/quality-programs/nsqip/pt_nsqip_puf_userguide_2018.ashx). Accessed July 20, 2020
- Schafer JL, Graham JW. **Missing data: our view of the state of the art.** *Psychol Methods* 2002;7:147–77 CrossRef Medline
- Mitra R, Reiter JP. **A comparison of two methods of estimating propensity scores after multiple imputation.** *Stat Methods Med Res* 2016;25:188–204 CrossRef Medline
- Kim HJ, Fay MP, Feuer EJ, et al. **Permutation tests for joinpoint regression with applications to cancer rates.** *Statist Med* 2000;19:335–51 CrossRef Medline
- Ho D, Imai K, King G, et al. **MatchIt: nonparametric preprocessing for parametric causal inference.** *J Stat Softw* 2011;42:1–28
- Shean KE, McCallum JC, Soden PA, et al. Society for Vascular Surgery Vascular Quality Initiative. **Regional variation in patient selection and treatment for carotid artery disease in the Vascular Quality Initiative.** *J Vasc Surg* 2017;66:112–21 CrossRef Medline
- Obeid T, Arhuidese I, Gaidry A, et al. **Beta-blocker use is associated with lower stroke and death after carotid artery stenting.** *J Vasc Surg* 2016;63:363–69 CrossRef Medline
- Decision memo for carotid artery stenting (CAG-00085R.). Centers for Medicare and Medicaid Services. <https://www.cms.gov/medicare-coverage-database/details/nca-decision-memo.aspx?NCAId=157>. Accessed July 27, 2020
- Brott TG, Hobson RW 2nd, Howard G, et al. CREST Investigators. **Stenting versus endarterectomy for treatment of carotid-artery stenosis.** *N Engl J Med* 2010;363:11–23 CrossRef Medline
- Rosenfield K, Matsumura JS, Chaturvedi S, et al. ACT I Investigators. **Randomized trial of stent versus surgery for asymptomatic carotid stenosis.** *N Engl J Med* 2016;374:1011–20 CrossRef Medline
- Jansen O, Fiehler J, Hartmann M, et al. **Protection or nonprotection in carotid stent angioplasty: the influence of interventional techniques on outcome data from the SPACE Trial.** *Stroke* 2009;40:841–46 CrossRef Medline
- Doig D, Turner EL, Dobson J, et al. ICSS Investigators. **Predictors of stroke, myocardial infarction or death within 30 days of carotid artery stenting: results from the International Carotid Stenting Study.** *Eur J Vasc Endovasc Surg* 2016;51:327–34 CrossRef Medline
- Young KC, Jain A, Jain M, et al. **Evidence-based treatment of carotid artery stenosis.** *Neurosurg Focus* 2011;30:E2 CrossRef Medline
- Bonati LH, Jongen LM, Haller S, et al. ICSS-MRI Study Group. **New ischaemic brain lesions on MRI after stenting or endarterectomy for symptomatic carotid stenosis: a substudy of the International Carotid Stenting Study (ICSS).** *Lancet Neurol* 2010;9:353–62 CrossRef Medline
- Vos JA, van den Berg JC, Ernst SM, et al. **Carotid angioplasty and stent placement: comparison of transcranial Doppler US data and clinical outcome with and without filtering cerebral protection devices in 509 patients.** *Radiology* 2005;234:493–99 CrossRef Medline
- Texakalidis P, Letsos A, Kokkinidis DG, et al. **Proximal embolic protection versus distal filter protection versus combined protection in carotid artery stenting: a systematic review and meta-analysis.** *Cardiovasc Revasc Med* 2018;19:545–52 CrossRef Medline

32. Leal JJ, Orgaz A, Fontcuberta J, et al. **A prospective evaluation of cerebral infarction following transcervical carotid stenting with carotid flow reversal.** *Eur J Vasc Endovasc Surg* 2010;39:661–66 CrossRef Medline
33. Bennett KM, Hoch JR, Scarborough JE. **Predictors of 30-day postoperative major adverse clinical events after carotid artery stenting: an analysis of the procedure-targeted American College of Surgeons National Surgical Quality Improvement Program.** *J Vasc Surg* 2017;66:1093–99 CrossRef Medline
34. Schermerhorn ML, Liang P, Eldrup-Jorgensen J, et al. **Association of transcarotid artery revascularization vs transfemoral carotid artery stenting with stroke or death among patients with carotid artery stenosis.** *JAMA* 2019;322:2313–22 CrossRef Medline

# Pressure Cooker Technique for Endovascular Treatment of Spinal Arteriovenous Fistulas: Experience in 15 Cases

F. Clarençon, C.P. Stracke, E. Shotar, M. Wallocha, P.J. Mosimann, A.-L. Boch, N. Sourour, and R. Chapot



## ABSTRACT

**BACKGROUND AND PURPOSE:** Spinal arteriovenous fistulas are challenging to cure by endovascular means, with a risk of incomplete occlusion or delayed recurrence. The authors report herein their preliminary experience using the pressure cooker technique for the embolization of spinal arteriovenous fistulas.

**MATERIALS AND METHODS:** Fifteen patients (8 men; mean age, 60.3 years) underwent an endovascular treatment of a spinal arteriovenous fistula (12 dural spinal arteriovenous fistulas and 3 epidural spinal arteriovenous fistulas) in 2 different institutions using the pressure cooker technique. Two microcatheters could be navigated in the segmental artery in all patients using 2 guiding catheters. A proximal plug was achieved with highly concentrated cyanoacrylate  $\pm$  coils. The liquid embolic agent injected to cure the fistula was diluted cyanoacrylate ( $n = 11$ ) or ethylene-vinyl alcohol ( $n = 4$ ). Technical and clinical complications were systematically recorded. Clinical and angiographic outcomes were systematically evaluated at follow-up.

**RESULTS:** One (6.7%) procedure-related complication was recorded, which consisted of a transient radicular deficit, related to nerve root ischemia. Clinical improvement was observed in 10/14 (71%) patients for whom clinical follow-up was available. Complete spinal arteriovenous fistula occlusion on a follow-up angiography was observed in 11/12 patients (91.7%) for whom angiographic follow-up was available. One patient (8.3%) presented with a delayed recurrence at 29 months.

**CONCLUSIONS:** The pressure cooker technique is feasible, with either glue or ethylene-vinyl alcohol, for the embolization of spinal arteriovenous fistulas. Our results suggest the safety and effectiveness of this technique.

**ABBREVIATIONS:** EVOH = ethylene-vinyl alcohol; IQR = interquartile range; PCT = pressure cooker technique; SAVF = spinal arteriovenous fistula

Spinal arteriovenous fistulas (SAVFs) are rare vascular malformations involving the spinal cord and corresponding to an abnormal arteriovenous shunt between spinal dural arteries and a radicular vein or the epidural venous plexus, which “contaminates” secondarily the spinal venous drainage.<sup>1,2</sup> Most of these SAVFs are clinically revealed by a venous congestion, responsible for progressive sensory and/or motor deficits of the inferior limbs, often associated with sphincter disturbance (ie, urinary/fecal incontinence, sexual impotence).<sup>3</sup>

The best treatment option for SAVFs is still a matter of debate because no randomized controlled trial has compared endovascular treatment and surgery. Even if it is minimally invasive, the main drawback of the endovascular treatment is the risk of incomplete occlusion of the shunt point, which may lead to treatment failure or recurrence.<sup>4</sup>

The pressure cooker technique (PCT) has been developed to improve the penetration of liquid embolic agents in the embolization of brain AVMs, increasing the occlusion rate in the endovascular treatment of brain AVMs.<sup>5</sup>

The purpose of our study was to report our experience with the PCT for the endovascular treatment of SAVFs.

## MATERIALS AND METHODS

### Patient Selection

All patients treated for an SAVF in 2 institutions (Alfried Krupp Krankenhaus, Essen, Germany, and Pitié-Salpêtrière Hospital, Paris, France) from 2012 to 2020 by endovascular means were systematically reviewed. Patient demographics (age, sex) as well

Received October 26, 2020; accepted after revision January 12, 2021.

From the Departments of Neuroradiology (F.C., E.S., N.S.) and Neurosurgery (A.-L.B.), Assistance Publique–Hôpitaux de Paris, Pitié-Salpêtrière Hospital, Paris, France; Sorbonne University (F.C.), Paris, France; Groupe de Recherche Clinique BIOFAST (F.C.), Paris VI University, Paris, France; and Department of Interventional Neuroradiology (C.P.S., M.W., P.J.M., R.C.), Alfried Krupp Krankenhaus, Essen, Germany. Data are available upon request from the corresponding author.

Please address correspondence to Frédéric Clarençon, MD, PhD, Department of Neuroradiology, Pitié-Salpêtrière Hospital, 47, Boulevard de l'Hôpital, 75013, Paris, France; e-mail: frederic.clarencon@aphp.fr

Indicates article with online supplemental data.

<http://dx.doi.org/10.3174/ajnr.A7078>

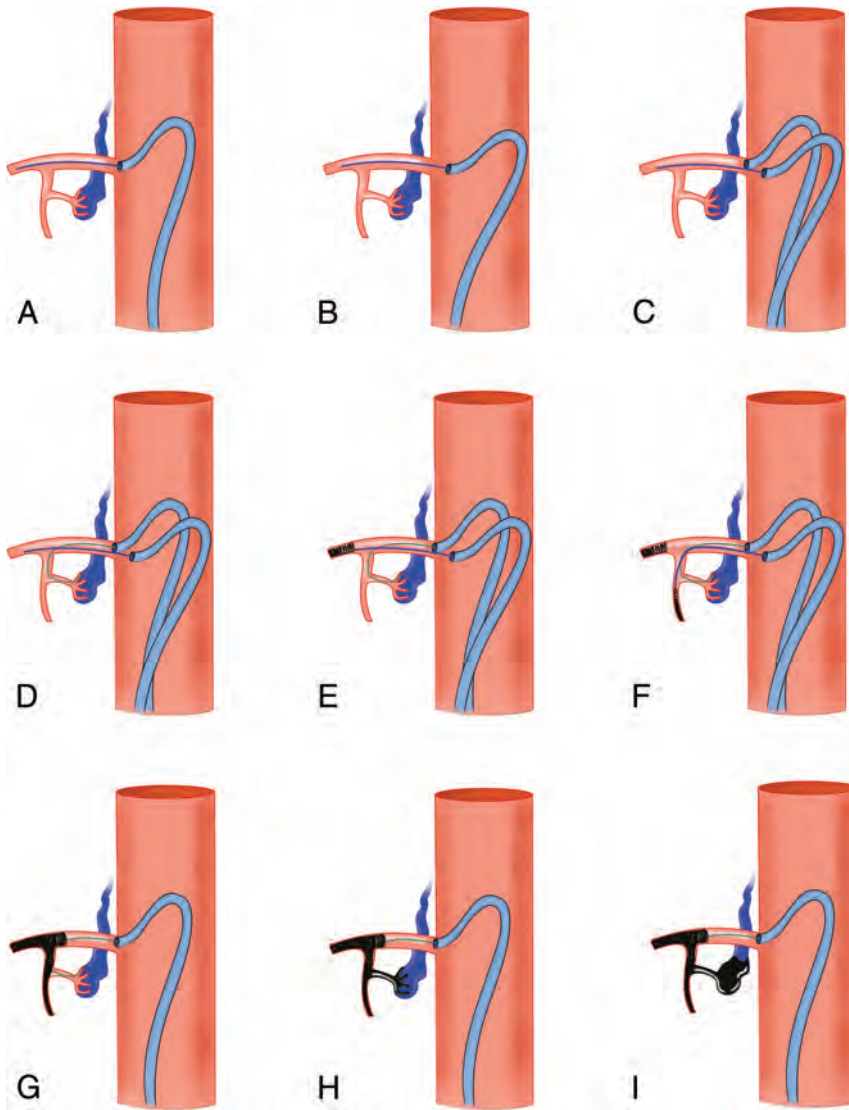


**FIG 1.** Drawing summarizing the different steps for the PCT in spinal vascular malformation embolization. A, Positioning the microcatheter No. 1 (for coiling) distally in the main trunk of the segmental artery, via the guiding catheter No. 1. B, The guiding catheter No. 1 is disengaged from the segmental artery ostium. C, The guiding catheter No. 2 is subsequently positioned at the ostium of the segmental artery. D, The microcatheter No. 2 (dedicated to the liquid embolic agent injection for the arteriovenous fistula treatment) is navigated via the guiding catheter No. 2 as close as possible to the shunt point. E, Coiling of the main trunk is performed via microcatheter No. 1 until occlusion. F and G, The dorsal branch and then the dorsospinal trunk are subsequently coiled until occlusion via the microcatheter No. 1 to obtain the proximal plug of the pressure cooker. H and I, Liquid embolic injection via the microcatheter No. 2 is performed until the filling of the origin of the draining vein.

as clinically revealing symptoms and the time interval between symptom onset and endovascular treatment were systematically recorded.

#### Clinical Evaluation

A pretreatment clinical examination was systematically performed by a neurologist who was not directly involved in the endovascular treatment. Clinical symptoms, as well as the duration between symptom appearance and SAVF diagnosis,

were systematically recorded. Symptom severity was evaluated using the Aminoff-Logue instability scale.<sup>6</sup>

#### Endovascular Procedures

All patients were treated under general anesthesia, via a bilateral 5F femoral access under full anticoagulation. A first 5F catheter (usually a Cobra Small catheter; Cook; or a Simmons [1 or 2] catheter; Merit Medical) was positioned at the ostium of the segmental artery feeding the SAVF. A microcatheter (1.2F or 0.017 inch) was navigated into the segmental artery. The 5F catheter was then disengaged from the ostium of the segmental artery but kept at that level. A second 5F guiding catheter was positioned at the ostium of the same segmental artery. A second microcatheter was then navigated into the segmental and later into the radiculomeningeal artery as close as possible to the shunt point. To reduce the risk of embolic agent migration, we placed coils through the first microcatheter in the main trunk of the segmental artery, distal to the origin of the dorsospinal trunk and/or the dorsal branch of the segmental artery. Afterward, a proximal plug was performed using high-concentrated *n*-BCA (ie, 50% *n*-BCA in combination with Lipiodol; Guerbet) (Fig 1). The fistula was then occluded by injection of low-concentrated *n*-BCA (20% *n*-BCA, 80% Lipiodol) ( $n = 11$ ) (Fig 2) or an ethylene-vinyl alcohol (EVOH) copolymer ( $n = 4$ ) (Fig 3) through the second microcatheter. Injection was maintained until occlusion of the origin of the draining vein.

For SAVFs embolized with the PCT using glue as a liquid embolic agent, microcatheters without detachable tip were used (Echelon 10 [Medtronic] or the Marathon [Medtronic]). On the contrary, when EVOH was used to occlude the fistula, a detachable-tip microcatheter was systematically used (Apollo Medtronic).

#### Feasibility and Safety

Technical failures and complications were systematically recorded. Complications were systematically assessed and graded using the Cardiovascular and Interventional Radiological Society of Europe and Society of Interventional Radiology complication guidelines.<sup>7</sup> Briefly, this classification is a 6-scale grading system evaluating the severity of the complication: grade 3 being a complication requiring

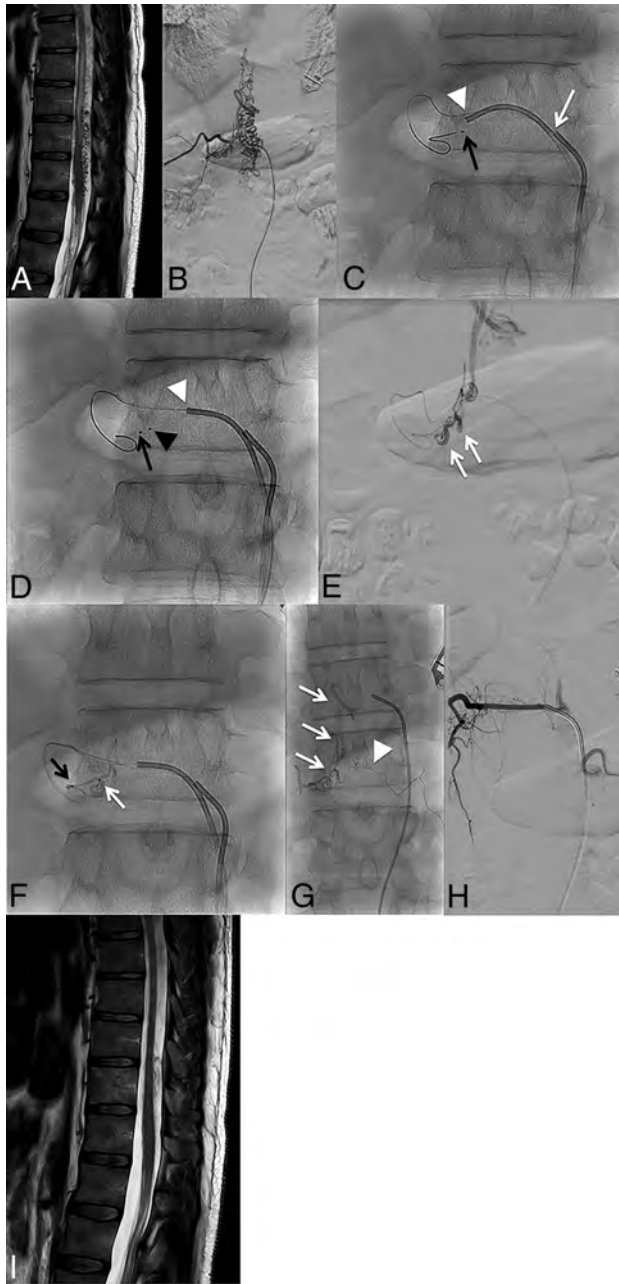


**FIG 2.** Patient in his or her 40's presenting with lower limb paresthesia, constipation, and bladder disturbance lasting for 36 months. *A*, Spinal cord MR imaging. T2WI, sagittal section, shows the hyperintense signal of the spinal cord extending up to T8 and multiple flow void signals in the enlarged spinal veins. *B*, Spinal DSA. Right T11 angiogram in a postero-anterior projection shows a spinal arteriovenous fistula with both ascending and descending venous drainage. *C*, Navigation of the microcatheter No. 1 (dedicated to the PCT plug) (black arrow). Then, the guiding catheter No. 1 is disengaged from the right T11 intercostal artery (white arrow). The guiding catheter No. 2 is subsequently positioned at the ostium of the segmental artery (white arrowhead). *D*, Navigation of the second microcatheter (No. 2) (black arrowhead) from the guiding catheter No. 2 (white arrowhead) as close as possible to the shunt point. Note the tip of microcatheter No. 1, located proximal to the tip of microcatheter No. 2. *E*, Ultraselective angiogram in a postero-anterior projection from microcatheter No. 2. The origin of the main draining vein (radicular vein) is clearly seen (double white arrow). *F*, PCT. Injection of 50% *n*-BCA through microcatheter No. 1 to create the proximal plug (black arrow). Then, injection of a 20% dilution of *n*-BCA is performed to embolize the fistula (white arrow). *G*, Plain x-ray in a postero-anterior projection shows the glue cast. Note the filling of the origin of the radicular vein (white arrows) and also progression of the liquid embolic agent through the retrocorporeal anastomosis (white arrowhead). *H*, Right T11 angiogram at the end of the procedure shows complete occlusion of the fistula. *I*, Spinal cord MR imaging 14 months after embolization. T2WI, sagittal section, shows complete resolution of the spinal cord edema.

additional postprocedural therapy or prolonged hospital stay (48 hours) but with no sequelae; grade 4 being a complication causing permanent mild sequelae; and grade 5 being a complication causing permanent severe sequelae.

### Clinical and Imaging Follow-up

The clinical examination was performed  $\geq 3$  months after the procedure, in most cases by the operator who performed the procedure. Spinal DSA was performed systematically at  $\geq 3$  months to rule out a SAVF recurrence.

### Statistical Analysis

Data were reported as mean [SD] for continuous variables and median with interquartile range (IQR) for noncontinuous variables. All tests were calculated using STATA software (Stata/IC 13.1 for Mac; StataCorp); *P* values  $< .05$  were considered statistically significant.

### Ethics Statement

The choice to treat these patients by endovascular means was made through a multidisciplinary meeting, including neurosurgeons and interventional neuroradiologists. Patients were informed before each treatment of the strategy that was chosen and gave an oral consent.

This work received approval from both institutional review board (institutional review approval No. HH 16\_4\_20b). The need for patients' informed consent for retrospective analyses of records and imaging data was waived by our institutional review board. This work adheres to the World Medical Association's Declaration of Helsinki.

## RESULTS

### Patient Demographics

Among the patients treated for a spinal arteriovenous fistula in the 2 institutions during the inclusion period, 15 patients (8 men [53%]; mean age, 60.3 [SD, 16.7] years) were treated using the PCT (Online Supplemental Data). The PCT was chosen in these patients due to the inability to bring the microcatheter into a wedge flow position with a risk of poor progression of the liquid embolic agent beyond the shunt. In 2/15 cases

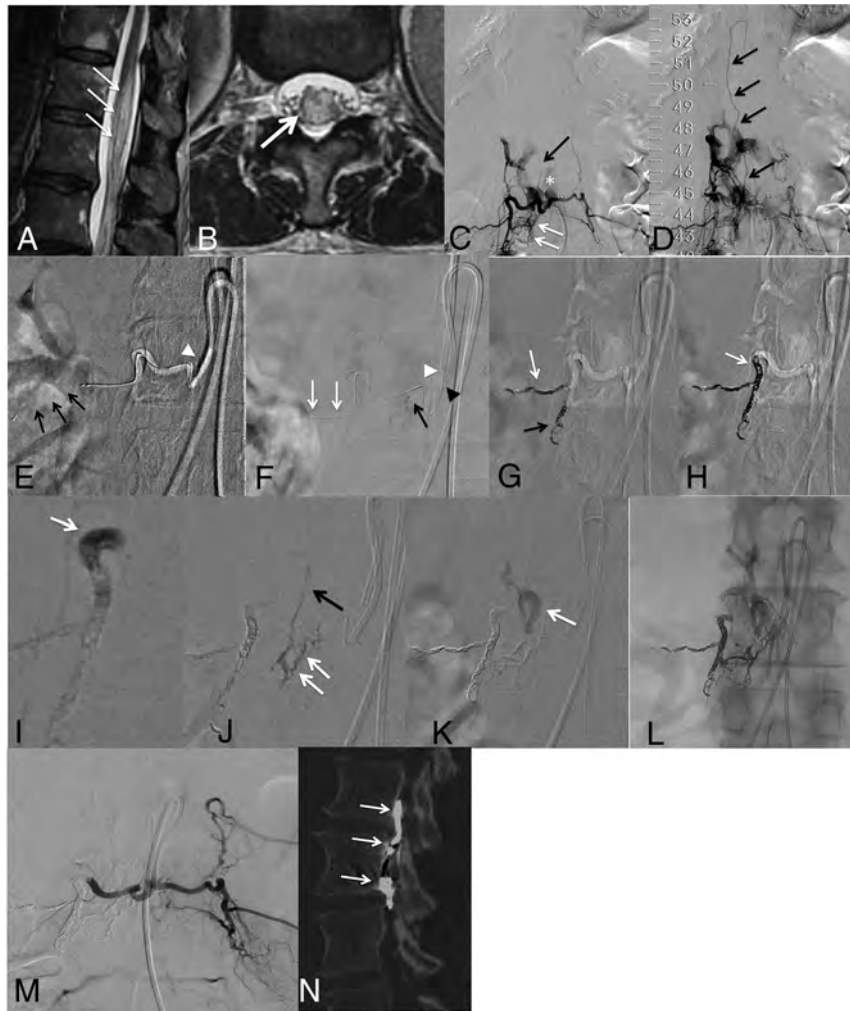


**FIG 3.** Patient in his or her 60's presenting with a 4-year history of paresthesia of the inferior limbs, bladder disturbance, and constipation. Spinal cord MR imaging, T2WI, sagittal (A) and axial (B) slices show a centromedullar hyperintense signal (white arrows) and lumbar spinal cord enlargement. Spinal DSA. Right L3 selective angiogram in a postero-anterior projection at an early phase (C) and intermediate phase (D). Numerous dural branches from the right L3 spinal trunk are depicted (C, white arrows), with abnormal connection with the right aspect of the epidural plexus (C, asterisk). Reflux from the anterior epidural plexus to a radicular vein is seen (C and D, black arrows), with an ascending drainage. E, Navigation of a 0.017-inch microcatheter via a 5F Simmons 1 catheter (white arrowhead). The microcatheter is stabilized by deploying a Catch Mini stent retriever (black arrows); then the guiding catheter is gently pulled away from the right L3 ostium. F, An Apollo (5-cm detachable tip) microcatheter is then navigated in the spinal trunk of the right L3 artery, as close as possible to the shunt point (black arrow). Selective DSA via the Apollo microcatheter in a postero-anterior projection. Note the guiding catheter (5F Simmons 1) at the ostium of the right L3 artery (black arrowhead), while the second one is stabilized in front of it (white arrowhead). Note the second 0.017-inch microcatheter that has been left in the main trunk of right L3 artery (white arrows). Coiling, via the 0.017-inch microcatheter, of the main L3 trunk (G, white arrow), then the dorsospinal trunk (G, black arrow) and the arterial segment before arising from the dorsospinal trunk (H, white arrow) to obtain the proximal plug of the pressure cooker. Finally, a 50% dilution *n*-BCA injection was performed at the proximal aspect of the cast of the coils through the 0.017-inch microcatheter (I, white arrow) to ensure that the proximal plug would be occlusive. Then, Squid 12 (Balt) was injected under a blank roadmap through the Apollo catheter until occlusion of the shunt point along the anterior epidural venous plexus (J and K, white arrows) and filling of the origin of the radicular vein (J, black arrow). L, Plain x-ray in a postero-anterior projection at the end of the Squid 12 injection shows the EVOH cast. M, Final control DSA in a postero-anterior projection via the common trunk feeding both the right and left L3 arteries, showing complete occlusion of the fistula. N, Postprocedural unenhanced CT scan, bone windowing. Sagittal reconstruction shows the EVOH cast in the anterior epidural venous plexus (white arrows).

(13.3%), the embolization was performed after a recurrence in patients previously treated by *n*-BCA injection without the PCT. Most interesting, 2 patients (13.3%) were previously treated surgically for a spinal canal stenosis.

In 60% of the patients (9/15), sensory symptoms (paresthesia, dysesthesia) were recorded; genitourinary dysfunction (fecal and/or urinary retention) was observed in 53.3% of the cases (8/15). Inferior limb motor weakness was observed in 40% of the cases (6/15). Finally, in 2 cases (13.3%), lumbar pain was recorded, for which there was no clear relationship with the SAVF.

The median Aminoff-Logue disability scale<sup>6</sup> score before exclusion treatment was 3 (IQR, 2–4.5) (sensory signs: median = 2 [IQR, 1.5–2.5]; micturition: median = 1 [IQR, 0–2]).

#### Angiographic Features of the SAVF

Most SAVFs were dural AVFs (12/15, 80%); the 3 remaining patients (20%) had epidural AVFs (Online Supplemental Data). Most SAVFs were located at the thoracic level (9/15, 60%), 3 SAVFs (20%) were located at the lumbar level, and 3 (20%) were sacral dural AVFs. In 46.7% of the patients (7/15), the venous drainage was purely ascending; in 7/15 patients (46.7%), it was both ascending and descending; and in the remaining one (7%), it was purely descending.

#### Feasibility and Safety

No catheterization failure was recorded. Two guiding catheters could be successively placed in the segmental artery, and a microcatheter was further navigated in all patients. The embolic agent could be brought up to the vein in 14/15 patients (93.3%). The retrieval of all microcatheters was uneventful. Specifically, no glued microcatheter or reflux of embolic agent in the aorta was reported.

No major complication was recorded in our series. Only 1 minor complication (grade 3 in the Cardiovascular and Interventional Radiological Society of Europe/Society of Interventional Radiology classification<sup>7</sup>) was observed, which consisted of an L3 nerve root lesion revealed by pain and motor deficit

in an L3 epidural AVF. This complication was reversible; the patient recovered under anti-inflammatory medication with no sequelae.

### **Immediate Angiographic Outcome/Imaging Follow-up**

Immediate complete occlusion of the SAVF was observed in 15/15 patients. No residual shunt was depicted at the end of the procedure in any case. Follow-up spinal DSA was available in 12/15 patients (80%) at a mean time interval of 6.7 [SD, 7.6] months from the procedure (range, 3–29 months). Complete persistent occlusion of the AVF was observed 11/12 patients (91.7%).

### **Clinical Follow-up**

Clinical follow-up was available in 14/15 patients (93.3%), with a mean time interval of 7.3 [SD, 8.4] months (range, 3–29 months). One patient died at 1 month from a myocardial infarction.

Patients experienced clinical improvement in 71.4% (10/14) of cases. Three patients (21.4%) were stable, and 1 patient (7.2%) presented with a delayed clinical worsening at 29 months, related to a SAVF recurrence, which was subsequently treated by microsurgery.

The median Aminoff-Logue distability scale<sup>6</sup> score at clinical follow-up was 2.5 (IQR, 1–4.5) (sensory signs: median = 1.5 [IQR, 0.25–2.75]; micturition: median = 0 [IQR, 0–1.75]).

## **DISCUSSION**

Embolization of dural/epidural arteriovenous fistulas may be challenging. The 2 major drawbacks for SAVF embolization are the following: 1) the noncontrolled embolic agent migration into a radiculomedullary artery, potentially responsible for neurologic complications, and 2) incomplete occlusion of the shunt point, with an unrecognized persistent SAVF and clinical worsening. This delay may finally hamper the recovery of the patient's symptoms.<sup>8</sup> A recent meta-analysis<sup>9</sup> showed that among patients treated for SAVFs, a surgical operation had better results in terms of complete occlusion and clinical outcome compared with endovascular embolization. Indeed, SAVF recurrence was observed, ranging up to 3.7% of patients with surgical treatment versus up to 40% with embolization.<sup>9</sup> Additionally, in patients treated by endovascular means, the same meta-analysis showed that the risk of failure/late recurrence was higher with EVOH than with *n*-BCA (OR = 3.87; 95% CI, 1.73–8.68;  $P < .001$ ).<sup>9</sup> Indeed, the chance to penetrate distally when using EVOH is lower (without using a PCT) because important reflux is often seen, toward the aorta, prompting the operator to stop the injection, despite non-occlusion of the shunt point. These results lead some interventional neuroradiologists to discourage the endovascular option as a first-line treatment and to prefer a surgical operation.<sup>10</sup> Our experience in the embolization of intracranial vascular malformations using the PCT led us to use this technique in SAVF.

The pressure cooker technique was first described for the embolization of intracranial vascular malformations.<sup>5</sup> Its principle is to combine 2 liquid embolic agents that do not interact. The goal is first to avoid an excessive and uncontrolled retrograde reflux of embolic agent and second to increase the distal diffusion of the embolic agent. The potential of the PCT for the embolization of spinal vascular malformations (SVM) has been assessed only in oral presentations up to now.<sup>11</sup>

Unlike in the initial description of the PCT, we did not use only EVOH but also low-concentrated *n*-BCA as an embolic agent for the SVM. This was left to the discretion of the operator. The advantage of using the EVOH copolymer is its better visibility under a blank roadmap. On the other hand, the advantage of using *n*-BCA is that there is no need for dimethyl-sulfoxide; thus, non-dimethyl-sulfoxide-compatible microcatheters like Magic 1.2 (Balt Extrusion) can be used for embolization. In our opinion, the type of embolic agent used for the fistula embolization is not of major importance, as long as it does not dissolve the plug and has a high ability to diffuse, as with EVOH or low-concentrated *n*-BCA.

For SAVFs embolized with the PCT using glue as a liquid embolic agent, no detachable-tip microcatheters were used. The retrieval of microcatheters in the segmental arteries was uneventful, without elongation of arteries and high retraction forces. Neither excessive force nor rupture of the microcatheter tip occurred when retrieving the nondetachable microcatheters, despite the proximal plug of polymerized high-concentrated *n*-BCA. In our previous experience using the pressure cooker technique outside pial cerebral vessels, we noticed that retrieval of microcatheters was uneventful, such as in the meningeal or occipital arteries. We attribute the ease of retrieval to the combination of a short length of the plug and a straight course of the microcatheter. The Echelon microcatheter is braided but the Marathon is not, so ease of retrieval cannot be attributed to the braiding. On the contrary, a detachable-tip microcatheter should be used systematically for PCT in the pial branches. Indeed, the cerebral gyri are responsible for the tortuous course of the cerebral pial arteries. This course is straightened during the retraction of a microcatheter, even more so if its tip has been trapped by EVOH or *n*-BCA, potentially inducing bleeding from ruptured transmedullary arteries.

For SAVFs treated with EVOH, detachable-tip microcatheters were used to avoid trapping, because the EVOH was injected during a long time period, with a significant proximal reflux.

The main technical drawback for the use of the PCT in SAVFs is the need for 2 microcatheters. Because the segmental arteries are usually too narrow to allow cannulation with a regular 6F guiding catheter, which would allow 2 microcatheters, two 5F-guiding catheters are required for the PCT. Thus, after placement of the first microcatheter in the segmental artery, the guiding catheter has to be disengaged from the ostium for the second guiding catheter to be positioned at the origin of the segmental artery for navigation with the second microcatheter (Fig 1). The use of a Catch Mini stent retriever (Balt), compatible with a 0.017-inch microcatheter, was helpful to stabilize the first microcatheter and the first guiding catheter in some patients (Fig 3).

The use of a dual-lumen balloon may be an alternative to PCT for SAVF embolization.<sup>12</sup> It may help to overcome the limitation of using 2 guiding catheters. However, the dual-lumen balloons available on the market may be difficult to navigate in small and tortuous vessels, as can be the case with the segmental arteries. Smaller dual-lumen balloons with a low profile may help overcome this limitation.

### **Feasibility, Safety, and Effectiveness**

Embolization of SAVFs was feasible using the PCT in all cases; no technical failure was recorded. It was possible to navigate 2

microcatheters in all patients, including elderly patients up to 91 years of age. It was possible to fill the origin of the main draining vein in 14/15 patients (93.3%). Only 1 minor complication (6.6%) was recorded, consisting of a transient nerve root lesion, probably related to an ischemic mechanism. No major complication was recorded. Occlusion of the fistula was observed in all cases (15/15) at the end of the procedure.

At angiographic follow-up (available in 12/15 patients, 80%; average time interval, 6.7 [SD, 7.6] months), a persistent complete occlusion was found in 11/12 (91.7%) patients. A recurrence occurred only in the patient with an epidural SAVF in whom the embolic agent did not completely reach the vein.

The filling of the origin of the draining vein with embolic agent seems, therefore, to be the main criterion to assess an endovascular cure.

The avoidance of reflux, as achieved with the PCT, allows an increased diffusion of the embolic agent. The ability to see the opening of anastomoses is reduced by respiratory artifacts, which alter the quality of the blank roadmap used during injection. Therefore, additional precautions, such as for prolonged apnea, may be taken during injection. This is especially important in case of a spinal artery arising from the contralateral segmental artery or from a segmental artery 1 level below or above the SAVF. In these situations, migration of embolic agent toward a radiculomedullary artery may occur because retrocorporeal or intersegmental anastomoses are always present.<sup>13</sup> To prevent such uncontrolled embolic agent migration, preventive selective coiling of these anastomoses may be performed before liquid embolic agent injection.

### Limitations of the Study

The main limitations of our study are the retrospective design and the limited number of patients and centers included. Additionally, comparison with the standard therapy (ie, microsurgery) for the curative treatment of SVMs is lacking. Moreover, the SVMs treated in our series were heterogeneous, including both dural and epidural AVFs. Techniques used were also slightly heterogeneous because in some patients, the liquid embolic agent used was diluted *n*-BCA and in others, EVOH. Moreover, angiographic follow-up missing in 20% of the patients is another limitation of our study.

### CONCLUSIONS

The PCT to treat spinal arteriovenous fistulas, either with glue or EVOH, may improve the rate of complete endovascular cure. A prospective head-to-head comparison with microsurgery appears warranted.

### ACKNOWLEDGMENT

The authors kindly thank Mme Bénédicte Ibert-Clarençon for her help in the editing the drawings.

Disclosures: Frédéric Clarençon—UNRELATED: Board Membership: Artedrone; Grants/Grants Pending: Assistance Publique-Hôpitaux de Paris, Comments: national grant for the Emprotect trial\*; Payment for Lectures Including Service on Speakers Bureaus: Medtronic, Guerbet, Balt Extrusion, Penumbra. Christian P. Stracke—UNRELATED: Consultancy: Acandis, Comments: consultancy agreement; Expert Testimony: Balt; Payment for Lectures Including Service on Speakers Bureaus: MicroVention, Rapid Medical. Nader Sourour—RELATED: Consulting Fee or Honorarium: Medtronic, Balt. Rene Chapot—UNRELATED: Payment for Lectures Including Service on Speakers Bureaus: Balt, Medtronic, MicroVention, Siemens, Stryker; Travel/Accommodations/Meeting Expenses Unrelated to Activities Listed: Stryker, Balt, Siemens. \*Money paid to the Institution.

### REFERENCES

1. Krings T, Geibprasert S. **Spinal dural arteriovenous fistulas.** *AJNR Am J Neuroradiol* 2009;30:639–48 CrossRef Medline
2. Lenck S, Nicholson P, Tymianski R, et al. **Spinal and paraspinous arteriovenous lesions.** *Stroke* 2019;50:2259–69 CrossRef Medline
3. Donghai W, Ning Y, Peng Z, et al. **The diagnosis of spinal dural arteriovenous fistulas.** *Spine (Phila Pa 1976)* 2013;38:E546–53 CrossRef Medline
4. Bakker NA, Uyttenboogaart M, Luijckx GJ, et al. **Recurrence rates after surgical or endovascular treatment of spinal dural arteriovenous fistulas: a meta-analysis.** *Neurosurgery* 2015;77:137–44; discussion 44 CrossRef Medline
5. Chapot R, Stracke P, Velasco A, et al. **The pressure cooker technique for the treatment of brain AVMs.** *J Neuroradiol* 2014;41:87–91 CrossRef Medline
6. Aminoff MJ, Logue V. **Clinical features of spinal vascular malformations.** *Brain* 1974;97:197–210 CrossRef Medline
7. Filippidis DK, Binkert C, Pellerin O, et al. **Cirsc Quality Assurance Document and Standards for Classification of Complications: the Cirsc Classification System.** *Cardiovasc Intervent Radiol* 2017;40:1141–46 CrossRef Medline
8. Bretonnier M, Henaux PL, Gaberel T, et al. **Spinal dural arteriovenous fistulas: clinical outcome after surgery versus embolization: a retrospective study.** *World Neurosurg* 2019;127:e943–49 CrossRef Medline
9. Goyal A, Cesare J, Lu VM, et al. **Outcomes following surgical versus endovascular treatment of spinal dural arteriovenous fistula: a systematic review and meta-analysis.** *J Neurol Neurosurg Psychiatry* 2019;90:1139–46 CrossRef Medline
10. Houdart E. **The debate on the technique of treatment of spinal dural AVFs: Almost all must be treated by surgery.** In: *Proceedings of the Annual Meeting of the World Federation of Interventional and Therapeutic Neuroradiology Congress, Naples, Italy.* October 21–24, 2019
11. Chapot R, Stracke P. **Use of the pressure cooker technique in a spinal dural fistula: case report.** In: *Proceedings of the Annual Meeting of ABC WIN: Anatomy-Biology-Clinical correlations-Working group in Interventional Neuroradiology, Val d'Isère, France.* January 18–23, 2015
12. Nakae R, Nagaishi M, Hyodo A, et al. **Embolization of a spinal dural arteriovenous fistula with ethylene-vinyl alcohol copolymer (Onyx) using a dual-lumen microballoon catheter and buddy wire technique.** *Surg Neurol Int* 2017;8:166 CrossRef Medline
13. Lasjaunias P, Berenstein A, Ter Brugge K. **Spinal and spinal cord arteries and veins.** In: *Clinical Vascular Anatomy and Variations.* Springer-Verlag; 2001; 89–92

# Endovascular Treatment of Small and Very Small Intracranial Aneurysms with the Woven EndoBridge Device

J.-B. Girot, J. Caroff, J. Cortese, C. Mihalea, A. Rouchaud, V. Da Ros, J.V. Martinez, L. Contreras, L. Ikka, V. Chalumeau, A. Ozanne, G.B.D. Aguiar, S. Gallas, J. Moret, and L. Spelle



## ABSTRACT

**BACKGROUND AND PURPOSE:** The Woven EndoBridge has proved to be a safe and effective treatment, especially for wide-neck intracranial aneurysms. The recent fifth-generation Woven EndoBridge came with smaller devices. The purpose of this study was to assess the safety and efficiency of Woven EndoBridge treatment of small and very small aneurysms.

**MATERIALS AND METHODS:** Between September 2017 and March 2020, all consecutive patients treated with a 3- or 3.5-mm-width Woven EndoBridge device were included in this retrospective intention-to-treat study. Clinical and radiologic findings were evaluated at immediate and last-available follow-up. Angiographic outcome was assessed by an external expert reader.

**RESULTS:** One hundred twenty-eight aneurysms were treated with a fifth-generation Woven EndoBridge device including 29 with a width of  $\leq 3.5$  mm. Ten aneurysms were ruptured (34%). In 3 cases (10%), Woven EndoBridge treatment could not be performed because the aneurysm was still too small for the smallest available Woven EndoBridge device and another endovascular strategy was chosen. The median follow-up time was 11.2 months. Complete and adequate occlusion was obtained in 71% and 90% of the treated aneurysms, respectively. Retreatment was needed in 2 cases (10%). Symptomatic ischemic complications leading to transient neurologic deficits occurred in 2 cases (7%) (1 procedure-related and 1 device-related) but with full spontaneous recovery at discharge.

**CONCLUSIONS:** The fifth-generation Woven EndoBridge device seems to be a safe and technically feasible treatment for both ruptured and unruptured small and very small intracranial aneurysms, with satisfactory occlusion rates on midterm follow-up. However, further study is needed to evaluate longer-term efficiency.

**ABBREVIATIONS:** SL = single-layer; WEB = Woven EndoBridge

Since the publications of the results of the International Subarachnoid Aneurysm Trial (ISAT), in many centers, endovascular therapy has become the first-line treatment for intracranial aneurysms.<sup>1,2</sup> With an annual rupture rate of 0.36% per year, the

treatment of small, unruptured, intracranial aneurysms remains disputable.<sup>3</sup> However, independent predictors of rupture such as a history of subarachnoid hemorrhage, active smoking, location on the anterior communicating artery, and aneurysm multiplicity were identified, providing selection criteria for potential treatment.<sup>4-7</sup>

The treatment of small and very small aneurysms is often challenging, especially for ruptured cases, in which therapeutic options are limited.<sup>8-10</sup> Conceived as an intrasaccular flow-disruption device, the Woven EndoBridge aneurysm embolization system (WEB; MicroVention) has proved to be a safe and effective treatment for bifurcation aneurysms.<sup>11-14</sup> The absence of systematic use of antiplatelet therapy in a hemorrhagic context makes the WEB therapy particularly interesting for ruptured wide-neck aneurysms.<sup>15-17</sup>

Since 2010, the device progressively evolved from an initial double-layer version to single-layer (SL-WEB) and single-layer spherical versions. Recently, the fifth-generation WEBs became available outside the United States,<sup>18</sup> compatible with a new and smaller delivery catheter (VIA 17; MicroVention), facilitating the

Received November 19, 2020; accepted after revision January 11, 2021.

From the Department of Interventional Neuroradiology-NEURI Brain Vascular Center (J.-B.G., J. Caroff, J. Cortese, C.M., J.V.M., L.C., L.I., V.C., A.O., G.B.D.A., S.G., J.M., L.S.), Bicêtre Hospital, Le Kremlin-Bicêtre, France; Radiology Department (J.-B.G.), Angers University Hospital, Angers, France; Department of Radiology (A.R.), Centre Hospitalier et Universitaire Dupuytren, Centre National de la Recherche Scientifique, XLIM, Unité Mixte de Recherche Limoges, France; Department of Biomedicine and Prevention (V.D.R.), University Hospital of Rome Tor Vergata, Rome, Italy; Department of Neurosurgery (L.C.), Hospital Clínico Universidad de Chile, Santiago, Chile; Department of Surgery, Discipline Neurosurgery (G.B.D.A.), Santa Casa de Sao Paulo School of Medical Sciences, São Paulo, Brazil; and Université Paris Sud, Faculté de Médecine (J.M., L.S.), Le Kremlin-Bicêtre, France.

J.-B. Girot and J. Caroff contributed equally to this work.

Please address correspondence to Jildaz Caroff, MD, Department of Interventional Neuroradiology-NEURI Brain Vascular Center, Bicêtre Hospital, 78 Rue du General Leclerc, 94270 Le Kremlin-Bicêtre, France; e-mail: Jildaz.caroff@aphp.fr; @jildazz



Indicates article with supplemental online video.

<http://dx.doi.org/10.3174/ajnr.A7115>

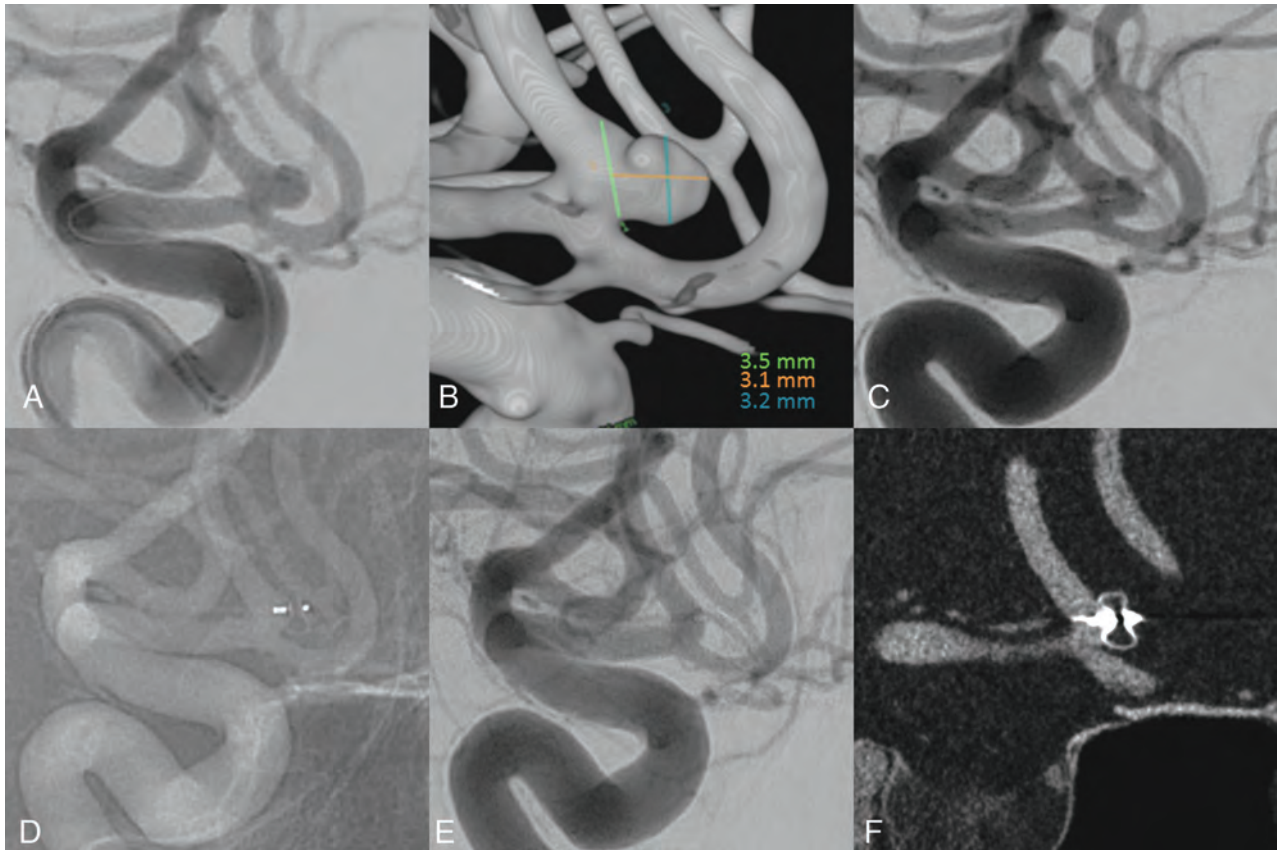


**FIG 1.** Ruptured anterior communicating artery aneurysm treatment using an SL 3.5 × 2 mm WEB. *A*, Left internal carotid angiogram shows the aneurysm. *B*, 3D rotational angiography with aneurysm measurement. *C*, A postdeployment angiogram shows a good filling of the aneurysmal sac with persistent opacification inside the WEB. *D* and *E*, Three-month follow-up angiogram shows complete exclusion of the aneurysm. *F*, Three-month follow-up VasoCT confirms the aneurysm exclusion, with slight WEB compaction.

treatment of smaller and more distal aneurysms. The changes in the braiding design allowed the development of smaller devices (3- and 3.5-mm width).

The WEB device has been evaluated in many Good clinical practice (GCP) studies, but the smaller fifth-generation devices were not included at that time.<sup>11,19,20</sup> The purpose of this study was to report the follow-up results of ruptured and unruptured small and very small intracranial aneurysms treated using the new, smaller fifth-generation WEB devices.

## MATERIALS AND METHODS

Between September 2017 and March 2020, all patients treated for an intracranial aneurysm in Department of Interventional Neuroradiology (NEURI Brain Vascular Center, Bicêtre Hospital, Le Kremlin Bicêtre, France) neurovascular center were retrospectively reviewed. All cases that had the intention to treat with a WEB as a first-line strategy were included. The collected data base was notified to the French Data Protection Authority. All patients gave informed consent before inclusion.

### Inclusion Criteria

Every patient in whom an SL 3 or SL 3.5 WEB was used to attempt to treat an intracranial aneurysm was included. Patients with both ruptured or unruptured aneurysms were included. No

exclusion criteria were defined. Technical failures were included but were not considered for follow-up evaluations.

### Indications

Embolization indications for unruptured small aneurysms were all discussed in a local multidisciplinary meeting with neuroradiologists and neurosurgeons.

Among the 19 small and very small unruptured aneurysms, 7 were treated due to a personal or familial history of aneurysm rupture; 5 were treated due to multiple aneurysms locations; 2 due to both personal history of aneurysm rupture and multiple aneurysm locations, 4 due to irregular aneurysm shape combined with patient anxiety; and 1, due to aneurysm modifications with time.

In most cases, the WEB was selected as a first-line strategy because of wide-neck lesions. Wide-neck aneurysms were defined as aneurysms with an aspect ratio inferior or equal to 1.2.<sup>21</sup> Treatment was performed on a biplane angiographic system (Azurion; Philips Healthcare).

### Antiplatelet Therapy

Patients with unruptured aneurysms were administered a dual-antiplatelet therapy (acetylsalicylic acid, 160 mg, and ticagrelor, 90 mg) 24 hours before the intervention in case an additional stent placement would be required. No antiplatelet therapy was administered for patients with ruptured aneurysms. Postoperative antiplatelet

therapy was specifically prescribed only in cases of major protrusion (generally aspirin for 1 month).

### Procedures

All procedures were performed with the patient under general anesthesia and systemic heparinization. After puncture, a long delivery catheter and a guiding catheter were positioned in the internal carotid artery or the vertebral artery according to the case. A 3D rotational angiography was then systematically performed for WEB sizing. The WEB device was usually slightly oversized in width.

Aneurysm catheterization was then performed using the VIA 17 microcatheter, and the selected WEB was deployed. Prior to detachment, a control VasoCT (Philips Healthcare)<sup>22</sup> was performed to evaluate the WEB positioning (Fig 1). If needed, the device could then be repositioned or replaced (Supplemental Online Video).

### Follow-up Evaluation

Clinical evaluation was based on the mRS and evaluated before every follow-up angiography, which were routinely scheduled at 6, 18, and 42 months or 3, 15, and 39 months after treatment for unruptured and ruptured aneurysms, respectively.

For every patient, the last available follow-up angiography was retrospectively reviewed by an external expert neurointerventional radiologist. Angiographic results were classified according to the Bicêtre Occlusion Scale Score.<sup>23</sup> Complete occlusion was defined as grades 0 or 0'; adequate occlusion was defined as grades 0, 0', 1, or 2; and other grades were considered to be aneurysm remnants. Aneurysms that required retreatment were systematically considered to be aneurysm remnants, irrespective of Core Lab evaluation.

## RESULTS

### Patients

Between September 2017 and March 2020, one hundred twenty-eight aneurysms were embolized in our center with a fifth-generation WEB device. Twenty-seven patients with 29 aneurysms were treated using an SL 3 or a SL 3.5 WEB. Two patients were treated for 2 distinct aneurysms. Ten (34%) of the 29 aneurysms were ruptured aneurysms. The mean age was 54 years (median, 55 years; range, 32–90 years of age), and 18 (67%) patients were women. A history of hypertension and dyslipidemia was found in 7 (26%) and 4 (15%) patients, respectively. Eight (30%) patients were active smokers, and 6 (22%) had a history of smoking.

Aneurysm locations were the following: middle cerebral artery (15 aneurysms, 52%), anterior communicating artery (8 aneurysms, 28%), basilar tip (3 aneurysms, 11%), carotid tip (1 aneurysm, 3%), anterior cerebral artery (1 aneurysm, 3%), and posterior communicating artery (1 aneurysm, 3%). The overall mean width and height were 2.8 mm (range, 1.7–4.8 mm) and 2.9 mm (range, 2.1–4.4 mm), respectively. Eighteen aneurysms (62%) were considered wide-neck. The mean aspect ratio was 1.2 (range, 0.7–2.0) (Table).

### Technical Results and Adverse Events

Technical success with satisfactory WEB deployment was achieved in 26 aneurysms (90%). In 2 cases, even the SL 3 WEB (the smallest

### Baseline characteristics and angiographic outcomes<sup>a</sup>

Treated Intracranial Aneurysms	All (n = 29)
Baseline demographic characteristics	All (n = 27)
Age (mean) (yr)	54 (SD, 11.5)
Female	18 (67)
Hypertension	7 (26)
Dyslipidemia	4 (15)
Smoking	
Global	14 (52)
Active	8 (30)
History	6 (22)
Baseline aneurysm characteristics	All (n = 29)
Aneurysm location	
Middle cerebral artery	15 (52)
Anterior communicating artery	8 (28)
Basilar tip	3 (11)
Carotid tip	1 (3)
Anterior cerebral artery	1 (3)
Posterior communicating artery	1 (3)
Acutely ruptured	10 (34)
Maximum diameter (mean) (mm)	3.8 (SD, 0.9)
Aneurysm height (mean) (mm)	2.9 (SD, 0.6)
Aneurysm width (mean) (mm)	2.8 (SD, 0.6)
Aneurysm neck (mean) (mm)	2.6 (SD, 0.5)
Aspect ratio (height/neck) (mean)	1.2 (SD, 0.4)
Width/neck ratio (mean)	1.1 (SD, 0.2)
Wide neck	18 (62)
Baseline treatment characteristics	All (n = 29)
WEB	
SL 3	17 (59)
SL 3.5	9 (31)
Technical failure	3 (10)
Angiographic outcomes	All (n = 21)
Adequate occlusion	19 (90)
Complete occlusion	15 (71)
Aneurysm remnant	2 (10)

<sup>a</sup> Data are number of subjects (and percentage) for qualitative variables, and mean (and standard deviation) for quantitative variables.

existing WEB) was considered too large on the control VasoCT before detachment, with device protrusion inside the parent artery. In 1 anterior communicating artery aneurysm, the angulation did not allow proper deployment of the WEB. These 3 patients were successfully treated using coils.

Among patients successfully treated with a WEB, no perioperative rupture was reported. Thromboembolic complications occurred in 4 cases, of which 3 were intraoperative thromboembolism. Of those 3, complete recanalization was achieved during the final angiography in 2 patients after intra-arterial abciximab injection. In the third case, owing to the excellent leptomeningeal collateral circulation, we decided not to perform any endovascular treatment and no deficit was observed after the intervention.

A postoperative neurologic deficit was depicted in 2 cases, and DWI revealed small punctiform ischemic spots. The first patient was treated with abciximab, and DWI spots were located in the territory of the branch where the clot had been seen. In the second case, no intraoperative thromboembolic complications were depicted, and MR imaging revealed 4 DWI spots in the middle cerebral artery territory. Deficits were all completely regressive at the patients' discharge.

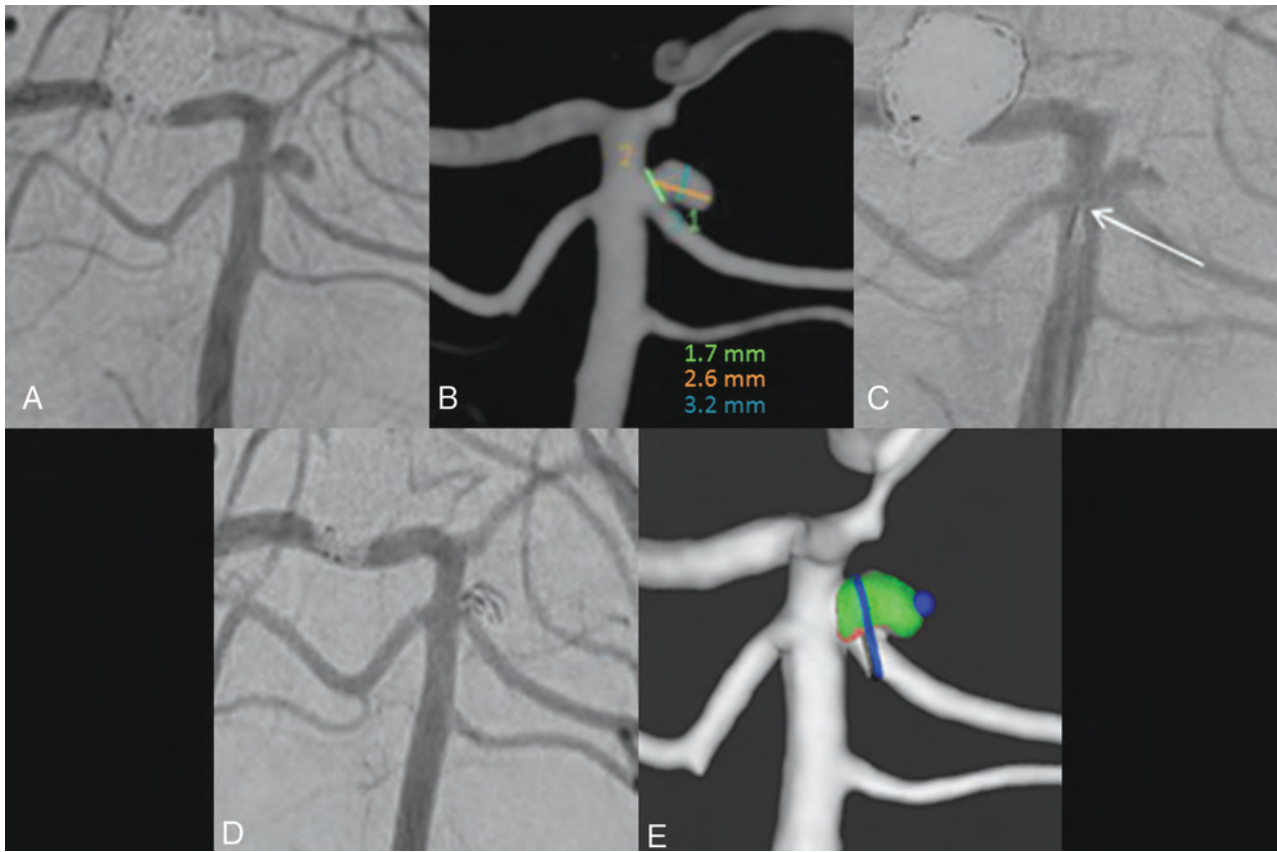


**FIG 2.** Technical failure in a left superior cerebellar artery with an SL 3 × 2 WEB. *A*, A left vertebral angiogram shows the left cerebellar aneurysm. *B*, 3D rotational angiography with aneurysm measurement. *C*, WEB deployment attempt, with the proximal marker (*white arrow*) protruding into the basilar trunk. *D*, Final angiogram after coiling. *E*, Retrospective Sim&Cure simulation showing SL 3 WEB protrusion into the superior cerebellar artery and basilar trunk.

### Clinical Outcome

Clinical worsening defined as a higher mRS score at the final control than before treatment was observed in 3 patients (10%). These patients were treated for ruptured aneurysms. In 2 of these patients, initial subarachnoid hemorrhage was associated with intraparenchymal hematoma, resulting in a persistent neurologic deficit in 1 patient and a persistent psychomotor slowdown in the other. In the latter case, clinical worsening was due to persistent asthenia and headache at 11 months after the initial rupture. At discharge, no procedure-related morbidity or mortality was reported. During the follow-up period, none of the ruptured aneurysms treated with a WEB rebled.

### Angiographic Outcome

Twenty-one aneurysms (72%) had at least 1 angiographic evaluation at the time of this study. Mean follow-up was 10.9 months (range, 3.1–22.3 months). Complete occlusion was obtained in 15 aneurysms (71%), and adequate occlusion, in 19 aneurysms (90%). Retreatment was needed in 2 patients (Table).

## DISCUSSION

Twenty-nine individual aneurysms were treated using 3- and 3.5-mm SL WEBs in this retrospective study. The median follow-up was 11.2 months. Technical success was achieved in 90% of the cases, with complete and adequate occlusion rates in 71% and 90%

of aneurysms, respectively. Four patients experienced periprocedural thrombotic events, with 2 ischemic complications leading to full recovery at discharge. No perioperative rupture was reported.

### Treatment Feasibility and Angiographic Efficiency

Technical success was achieved in 90% of the treatments. However, the WEB could not be deployed in 3 cases. In 2 of the 3 technical failures, successful treatment could not be achieved owing to the WEB size. With an average aneurysm width of 1.7 and 2.2 mm and an average height of 2.3 and 2.1 mm, respectively, the SL 3 size was chosen. In each case, the WEB was protruding into the parent artery and had to be removed. Indeed, in some cases and especially in small, irregular aneurysms, the choice of the device size can be challenging. A postoperative evaluation using the IDsize software (Sim&Cure) showed that this situation could have been predicted (Fig 2). In the future, a systematic preoperative software simulation might improve device selection and success rates.

Previous studies reported increased difficulties for endovascular treatment of smaller aneurysms using only coils. With less space in the aneurysmal sac for a proper placement of the microcatheter, coil deployment is indeed more challenging with an increased risk of protrusion into the parent artery and aneurysmal rupture. Thus, in the prospective Analysis of Treatment by Endovascular Approach of Nonruptured Aneurysms (ATENA) multicenter study, the rate of technical failure was significantly

different in 1- to 6-mm aneurysms (5.7%) and in 7- to 15-mm aneurysms (2.3%).<sup>8</sup> In a 2016 meta-analysis evaluating endovascular treatment with coils for  $\leq 3$  mm aneurysms, technical success was obtained in 92% of the coiled intracranial aneurysms, fairly close to the results obtained in this study.<sup>24</sup> The 91% rate of “complete and near-complete” occlusion reported in this meta-analysis was also quite similar to the adequate occlusion rate of 90% described in this study. The technical success and angiographic efficiency of coil treatment in the 2016 meta-analysis were improved using stent-assisted techniques in 8% of the aneurysms, particularly in wide-neck lesions.<sup>25</sup> However, with mandatory postoperative antiplatelet therapy, stent-assisted techniques are limited by hemorrhage risk in ruptured cases. Applicable in both wide-neck and ruptured small aneurysms, WEBS seem to be a viable alternative treatment.

### Treatment Safety

Small and very small ruptured aneurysms have been associated with higher procedure-related rupture when treated by coils.<sup>26</sup> The 2016 meta-analysis<sup>24</sup> of endovascular treatment for  $\leq 3$ -mm aneurysms found intraprocedural rupture rates of 7% of the coiling procedures, while thromboembolic events occurred in 4%. No perioperative rupture was reported in this study. Ischemic complications occurred in 2 patients (7%) (1 device-related and 1 procedure-related); however, neurologic deficits were spontaneously completely regressive at discharge, and no clinical worsening was attributed to WEB embolization on long-term follow-up. However, considering the risk associated with endovascular treatment and the 0.36% annual rupture rate in unruptured intracranial small aneurysms, treatment should be performed only in selected cases, taking into account the history of SAH, age, hypertension, or location of the aneurysm.<sup>3,6</sup>

### Limitations

We decided not to perform a case-control study comparing WEB treatments with coiling because of potential biases. Indeed, most of the aneurysms treated here were wide-neck and ruptured so that endovascular coiling might not have been a feasible option. Also, since 2017, the WEB device is our favored first-line strategy so that our physician team has grown in experience since older coiling was performed.

This study is limited by its retrospective design and the small number of patients included, but until now, only a few articles have reported the use of the fifth-generation WEB device, including very few of the smallest WEBS.<sup>18,27</sup>

### CONCLUSIONS

The fifth-generation WEB seems to be a technically feasible treatment for both ruptured and unruptured small and very small intracranial aneurysms, with satisfactory occlusion rates on midterm follow-up and acceptable complication rates. However, further study is needed to evaluate longer-term efficiency.

Disclosures: Jacques Moret—UNRELATED: Consultancy: Medtronic, MicroVention, Stryker, Balt. Laurent Spelle—UNRELATED: Consultancy: Medtronic, MicroVention, Stryker, Balt.

### REFERENCES

- Molyneux AJ, Kerr RSC, Yu LM, et al. International Subarachnoid Aneurysm Trial (ISAT) Collaborative Group. **International Subarachnoid Aneurysm Trial (ISAT) of neurosurgical clipping versus endovascular coiling in 2143 patients with ruptured intracranial aneurysms: a randomised comparison of effects on survival, dependency, seizures, rebleeding, subgroups, and aneurysm occlusion.** *Lancet* 2005;366:809–17 CrossRef Medline
- Abecassis IJ, Zeeshan Q, Ghodke BV, et al. **Surgical versus endovascular management of ruptured and unruptured intracranial aneurysms: emergent issues and future directions.** *World Neurosurg* 2020;136:17–27 CrossRef Medline
- UCAS Japan Investigators, Morita A, Kirino T, et al. **The natural course of unruptured cerebral aneurysms in a Japanese cohort.** *N Engl J Med* 2012;366:2474–82 CrossRef Medline
- Korja M, Lehto H, Juvela S. **Lifelong rupture risk of intracranial aneurysms depends on risk factors: a prospective Finnish cohort study.** *Stroke* 2014;45:1958–63 CrossRef Medline
- Salih M, Harris D, Moore J, et al. **Current management of small unruptured intracranial aneurysms in the United States: results of a national survey.** *World Neurosurg* 2021;146:e631–38 CrossRef Medline
- Ikawa F, Morita A, Tominari S, et al. Japan Neurosurgical Society for UCAS Japan Investigators. **Rupture risk of small unruptured cerebral aneurysms.** *J Neurosurg* 2019 Jan 25. [Epub ahead of print] CrossRef Medline
- Choi JH, Park HS. **The incidence and characteristics of patients with small ruptured aneurysms (<5 mm) in subarachnoid hemorrhage.** *J Korean Neurosurg Soc* 2017;60:424–32 CrossRef Medline
- Pierot L, Spelle L, Vitry F; ATENA Investigators. **Immediate clinical outcome of patients harboring unruptured intracranial aneurysms treated by endovascular approach: results of the ATENA study.** *Stroke* 2008;39:2497–504 CrossRef Medline
- Cognard C, Pierot L, Anxionnat R, et al. Clarity Study Group. **Results of embolization used as the first treatment choice in a consecutive nonselected population of ruptured aneurysms: clinical results of the Clarity GDC study.** *Neurosurgery* 2011;69:837–41; discussion 842 CrossRef Medline
- Malhotra A, Wu X, Forman HP, et al. **Management of tiny unruptured intracranial aneurysms: a comparative effectiveness analysis.** *JAMA Neurol* 2018;75:27–34 CrossRef Medline
- Pierot L, Gubucz I, Buhk JH, et al. **Safety and efficacy of aneurysm treatment with the WEB: results of the WEBCAST 2 study.** *AJNR Am J Neuroradiol* 2017;38:1151–55 CrossRef Medline
- Pierot L, Costalat V, Moret J, et al. **Safety and efficacy of aneurysm treatment with WEB: results of the WEBCAST study.** *J Neurosurg* 2016;124:1250–56 CrossRef Medline
- Pierot L, Moret J, Turjman F, et al. **WEB treatment of intracranial aneurysms: clinical and anatomic results in the French Observatory.** *AJNR Am J Neuroradiol* 2016;37:655–59 CrossRef Medline
- Sivan-Hoffmann R, Gory B, Riva R, et al. **One-year angiographic follow-up after WEB-SL endovascular treatment of wide-neck bifurcation intracranial aneurysms.** *AJNR Am J Neuroradiol* 2015;36:2320–24 CrossRef Medline
- Da Ros V, Bozzi A, Comelli C, et al. **Ruptured intracranial aneurysms treated with Woven Endobridge intrasaccular flow disruptor: a multicenter experience.** *World Neurosurg* 2019;122:e498–505 CrossRef Medline
- Caroff J, Mihalea C, Dargento F, et al. **Woven Endobridge (WEB) device for endovascular treatment of ruptured intracranial wide-neck aneurysms: a single-center experience.** *Neuroradiology* 2014;56:755–61 CrossRef Medline
- Lubicz B, Mine B, Collignon L, et al. **WEB device for endovascular treatment of wide-neck bifurcation aneurysms.** *AJNR Am J Neuroradiol* 2013;34:1209–14 CrossRef Medline
- Mihalea C, Caroff J, Pagiola I, et al. **Safety and efficiency of the fifth generation Woven EndoBridge device: technical note.** *J Neurointerv Surg* 2019;11:511–55 CrossRef Medline

19. Pierot L, Moret J, Barreau X, et al. **Aneurysm treatment with Woven EndoBridge in the cumulative population of three prospective, multicenter series: 2-year follow-up.** *Neurosurgery* 2020;87:357–67 CrossRef
20. Arthur AS, Molyneux A, Coon AL, et al. WEB-IT Study investigators. **The safety and effectiveness of the Woven EndoBridge (WEB) system for the treatment of wide-necked bifurcation aneurysms: final 12-month results of the pivotal WEB Intrasaccular Therapy (WEB-IT) study.** *J Neurointerv Surg* 2019;11:924–30 CrossRef Medline
21. Brinjikji W, Cloft HJ, Kallmes DF. **Difficult aneurysms for endovascular treatment: overdue or undertall?** *AJNR Am J Neuroradiol* 2009;30:1513–17 CrossRef Medline
22. Caroff J, Mihalea C, Neki H, et al. **Role of C-arm VasoCT in the use of endovascular WEB flow disruption in intracranial aneurysm treatment.** *AJNR Am J Neuroradiol* 2014;35:1353–57 CrossRef Medline
23. Caroff J, Mihalea C, Tuilier T, et al. **Occlusion assessment of intracranial aneurysms treated with the WEB device.** *Neuroradiology* 2016;58:887–91 CrossRef Medline
24. Yamaki VN, Brinjikji W, Murad MH, et al. **Endovascular treatment of very small intracranial aneurysms: meta-analysis.** *AJNR Am J Neuroradiol* 2016;37:862–67 CrossRef Medline
25. Zheng Y, Song Y, Liu D, et al. **Stent-assisted coiling embolization of tiny, wide-necked intracranial aneurysms.** *Acta Neurochir (Wien)* 2017;159:93–100 CrossRef Medline
26. Nguyen TN, Raymond J, Guilbert F, et al. **Association of endovascular therapy of very small ruptured aneurysms with higher rates of procedure-related rupture.** *J Neurosurg* 2008;108:1088–92 CrossRef Medline
27. Goertz L, Liebig T, Siebert E, et al. **Low-profile intra-aneurysmal flow disruptor WEB 17 versus WEB predecessor systems for treatment of small intracranial aneurysms: comparative analysis of procedural safety and feasibility.** *AJNR Am J Neuroradiol* 2019;40:1766–72 CrossRef Medline

# Arterial and Venous 3D Fusion AV-3D-DSA: A Novel Approach to Cerebrovascular Neuroimaging

E. Raz, M. Shapiro, O. Mir, E. Nossek, and P.K. Nelson

## ABSTRACT

**SUMMARY:** DSA is the standard imaging technique for evaluation of cerebrovascular conditions. However, One drawback is its limitation in depicting a single angiographic phase at a time. We describe a new 3D-DSA algorithm, which we call arterial and venous-3D-DSA, which allows the concurrent yet distinct display of the arterial and venous structures, which may be useful for different clinical and educational purposes.

**ABBREVIATION:** AV-3D-DSA = arterial and venous 3D-DSA

DSA is the gold standard imaging technique for evaluation of cerebrovascular diseases.<sup>1</sup> The 3D reconstructions of the vasculature acquired with rotational DSA are a routine tool used by neurointerventionalists for multiple purposes, enabling improved interpretation of complex vascular lesions, particularly before endovascular or surgical management.<sup>2,3</sup> One limitation of traditional 3D-DSA is the ability to visualize only 1 angiographic phase. Recently, 4D-DSA was implemented, enabling visualization of different temporal phases from different angles; however, this technique does not allow proper separation of normal phase arteries and veins and their anatomic relationships.<sup>4</sup> We describe a new 3D-DSA acquisition and reconstruction protocol, which we call arterial and venous-3D-DSA (AV-3D-DSA). This allows concurrent yet separate display of arterial and venous cerebral vasculature.

## Technical Report

After obtaining institutional review board approval, we retrospectively reviewed the angiograms performed in our institution, in which we obtained the AV-3D-DSA as part of routine care.

## Acquisition

We used a routine arterial approach with 5F diagnostic catheters and a biplane DSA machine (Artis Q pure VD11C biplane, Siemens), and nonionic iodinated contrast agent (Isovue 300,

Bracco Diagnostics) injected through a Mark V ProVis injector (Medrad). Rotational angiographic data were obtained with 2 separate (arterial and venous) 5-second DSA protocol acquisitions by using 42-cm FOV with 200° rotation of the anteroposterior x-ray tube around the patient's head (angular velocity, 40° per second). Arterial acquisition parameters for the 3D rotational angiography were as follows: internal carotid artery (flow: 3 mL/s; volume: 18 mL; delay: 1.5 seconds) and vertebral artery (flow: 3 mL/s; volume: 18 mL; delay: 1.5 seconds). Venous rotational acquisition parameters were as follows: internal carotid artery (flow: 3.5 mL/s; volume: 15 mL; delay: 5 seconds); vertebral artery (flow: 3 mL/s; volume: 18 mL; delay: 5 seconds). The datasets were then reconstructed using Syngo X-workplace VD20B (Siemens), a commercially available 3D angiography software.

## Postprocessing

From each 3D-DSA, 3 volume datasets are obtained: the mask, fill, and subtracted-fill volumes. The 2 subtracted volumes of both injections (called "3D Head Sub Full EE Smooth Mo [AX3D]" in Syngo) are selected and loaded together into the Syngo via the Inspace 4D module. The 2 subtracted-fill arterial and venous datasets then are optimized separately by choosing the best contrast, windowing, and color coding. Based on tradition, we chose red for arteries and blue for veins. Subsequently, the 2 subtracted datasets were merged and the fused AV volume was obtained, similar to what would be used to obtain dual-volume images.

## Case Illustrations

1) In a woman presenting with subarachnoid hemorrhage, DSA revealed a right carotid terminus aneurysm. Rotational angiography of the right ICA was performed as part of routine preoperative

Received December 6, 2020; accepted after revision February 5, 2021.

From the Departments of Radiology (E.R., M.S., O.M., P.K.N.) and Neurosurgery (E.N.), NYU Langone Health, New York, New York.

Please address correspondence to Eytan Raz, MD, PhD, Department of Radiology, NYU Langone Health, 550 First Ave, New York, NY, 10016; e-mail: eytan.raz@gmail.com; @eytanraz  
<http://dx.doi.org/10.3174/ajnr.A7103>

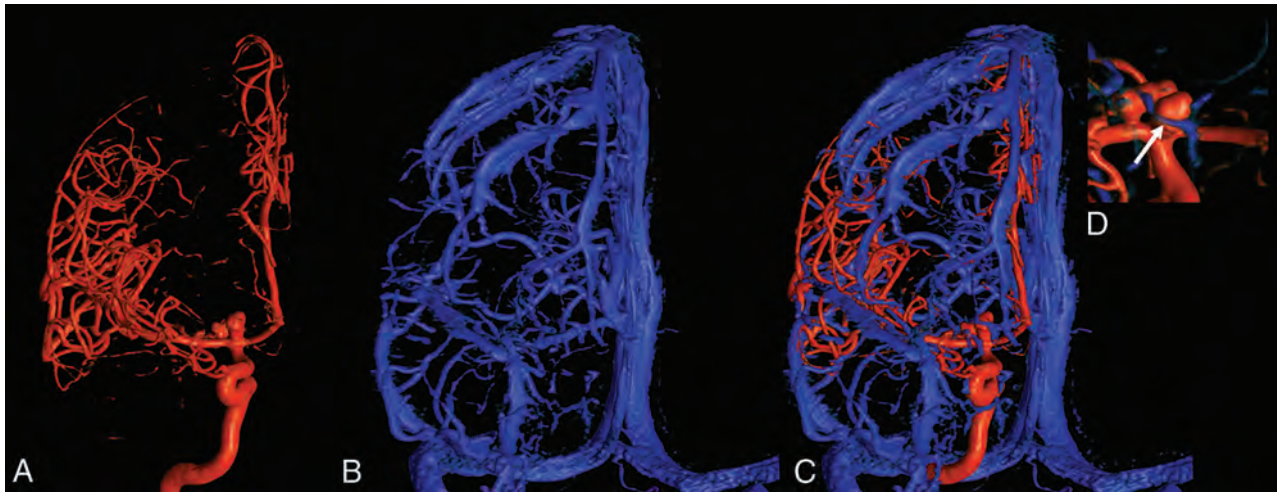


**FIG 1.** A, Frontal view arterial 3D-DSA of the right internal carotid artery injection demonstrating a multilobulated carotid terminus aneurysm. B, Frontal view venous 3D-DSA of the right internal carotid artery injection showing the venous outflow of the right hemisphere using mainly a deep middle cerebral vein draining toward the pterygoid plexus through the foramen ovale. C, Fused AV-3D-DSA demonstrating the relationship between the arteries and the veins. Specifically, note the presence of a vein running adjacent to the anterior aneurysm dome (arrow) better demonstrated in the insert (D).

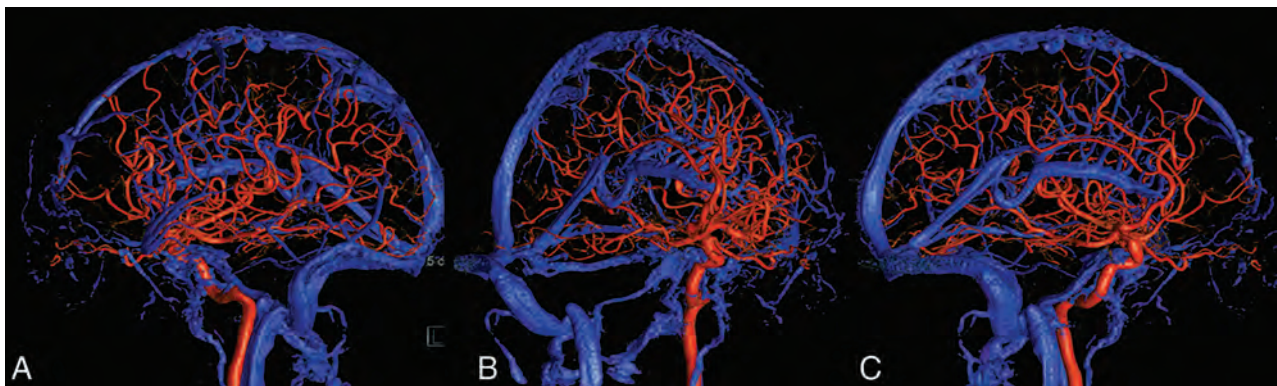


**FIG 2.** Left lateral (A), right anterior oblique (B), and right lateral (C) views of AV-3D-DSA of the left internal carotid artery injection demonstrating a large developmental venous anomaly draining most of the left frontal hemisphere toward the left internal cerebral vein, which likely developed in association with atretic anterior superior sagittal sinus. Notice also the hypertrophied right inferior petrosal sinus and the plexus of Rektorzik surrounding the left ICA.

evaluation of the aneurysm (Fig 1A). Given the patient's preference to be treated with clipping, venous 3D also was obtained (Fig 1B) to demonstrate the venous anatomy, especially around the Sylvian fissure, for surgical planning. The 2 subtracted volumes were then fused to show concomitant representation of the arteries and veins (Fig 1C).

2) In a woman presenting with small centrum semiovale hemorrhage, arterial DSA with rotational angiography revealed no evidence of aneurysm or AVM. Rather, it showed a large developmental venous anomaly and, for better visualization, a venous 3D DSA was also obtained. The 2 subtracted volumes were then fused to show concomitant representation of the arteries and veins (Fig 2).

3) In a man presenting with Moyamoya disease, full arterial and venous angiography was performed for surgical planning in anticipation of a possible direct bypass. As part of the cerebral angiogram, a vertebrobasilar AV-3D-DSA was obtained (Fig 3).

## DISCUSSION

In this technical note, we describe how to obtain simultaneously merged AV-3D-DSA visualization by using 2 separate, appropriately timed, rotational acquisitions with postprocessing. While there has been description of concomitant arterial and venous-3D reconstruction in cross-sectional imaging by using 2 separate CTA acquisitions, this has not previously been done by using DSA to our knowledge.<sup>5,6</sup> Our protocol can be considered a variant of the 2-color 3D-3D fusion of selective rotational cerebral angiograms used to visualize concurrently 2 different arterial territories.<sup>7</sup> Notably, this technique can be applied to any volume of interest as demonstrated by the insert in the case 1 illustration.

Other DSA methods to examine concomitant vessels in different phases are, for example, the acquisition of 4D-DSA, which is excellent to analyze the fast inflow and outflow of AVMs, but has the limitation of not distinctly separating arteries and veins in the same volume.<sup>4</sup> Another method is the so-called "sequential

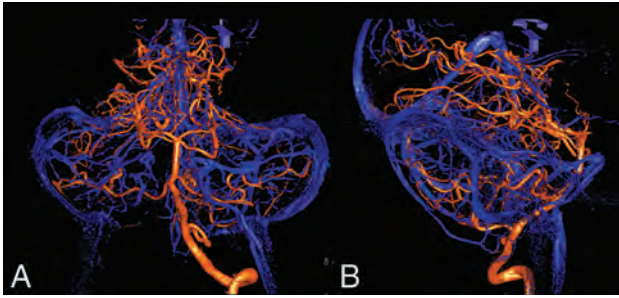


**FIG 3.** Frontal (A) and lateral (B) fused AV-3D-DSA of left vertebral artery injection demonstrating well the relationship between the petrosal veins and the vertebrobasilar system.

subtraction,” which uses 2 different masks, one for the bone and a negative one for the veins. Described in 1974, this is a useful technique to show the relationships between the arteries and veins but is limited only to 2D-DSA.<sup>8</sup> With another technique, cone beam CT, the 20sDSA DynaCT (Siemens) protocol is long enough to depict both arteries and veins in the same volume, but the technique is not able to separate them for differential visualization.

Obtaining AV-3D-DSA has multiple potential purposes. Because it allows depiction of the relationship between the arteries and the veins in a 3D environment, the technique can be useful in planning open cerebrovascular surgery. It can help the surgeon understand the relevant “angioarchitecture” of a particular situation (depicting arteries and veins in their relationship to one another from the perspective of the surgical window) to better prepare for surgical exploration of cerebrovascular lesions, such as dissection and a clip reconstruction of a complex cerebral aneurysm. Other potential specific applications are its use to distinguish the venous drainage of an AVM or dural AVF from the venous drainage of the adjacent normal parenchyma. Moreover, it has also been extremely useful as a teaching tool for residents and fellows allowing a better understanding of neurovascular anatomy.

In this report, we demonstrate the technique used for the internal carotid and vertebrobasilar territories, but theoretically this can be applied to any vascular territory, granted that the arterial and venous injection protocols are appropriately modified to better set the pertinent flow, volume, and delay of the contrast injection. 2D-DSA images are used to establish appropriate rate, volume, and injection delay settings.

While volumetric MR imaging with 3D-T1 and 3D-T2 can demonstrate the vasculature, both sequences are poor in terms of differentiating arteries compared with veins, and the differentiation may be important for the surgical planning or other purposes.

The method is simple and the main disadvantage is the need to obtain 2 separate 3D-DSAs to obtain the dataset, which means double the amount of radiation and double the contrast volume. For this reason, we recommend strategic use of this technique when clinically necessary to answer specific questions. Theoretically, to

obtain the dataset, the 2 phases may potentially be acquired with the same contrast injection, but that is not possible with the software/hardware capability of current Siemens angiographic equipment. Current protocol requires the subject not to move between and during acquisitions. We have obtained excellent quality images in cooperative subjects who were awake (images from Fig 2 were obtained in an awake patient) and patients under general anesthesia.

To conclude, in this technical note we describe how to obtain a simultaneous arterial and venous 3D-DSA visualization by using 2 separate, appropriately timed rotational acquisitions followed by dedicated, straightforward postprocessing, the results of which may be useful for different clinical and educational purposes.

## ACKNOWLEDGMENTS

We thank our lead tech Safia Syed for her invaluable relentless support. We also want to acknowledge Zia Shamsi, Osiris Galan, and Duane Thomas from Siemens AG for their 24/7 across campus availability to assist with image quality.

Disclosures: Eytan Raz—UNRELATED: *Expert Testimony*: Various law firms; *Royalties*: Springer; *Stock/Stock Options*: Siemens stocks; *Comments*: personal portfolio; *Travel/Accommodations/Meeting Expenses Unrelated to Activities Listed*: MicroVention, Rapid Medical, Stryker. Erez Nossek—UNRELATED: *Consultancy*: Rapid Medical; *Stock/Stock Options*: Rapid Medical.

## REFERENCES

- Jayaraman MV, Mayo-Smith WW, Tung GA, et al. **Detection of intracranial aneurysms: multi-detector row CT angiography compared with DSA.** *Radiology* 2004;230:510–18 CrossRef Medline
- Anxionnat R, Bracard S, Ducrocq X, et al. **Intracranial aneurysms: clinical value of 3D digital subtraction angiography in the therapeutic decision and endovascular treatment.** *Radiology* 2001;218:799–808 CrossRef Medline
- Hochmuth A, Spetzger U, Schumacher M. **Comparison of three-dimensional rotational angiography with digital subtraction angiography in the assessment of ruptured cerebral aneurysms.** *AJNR Am J Neuroradiol* 2002;23:1199–205 Medline
- Lang S, Gölitz P, Struffert T, et al. **4D DSA for dynamic visualization of cerebral vasculature: a single-center experience in 26 cases.** *AJNR Am J Neuroradiol* 2017;38:1169–76 CrossRef Medline
- Kasuya H, Matsumoto M, Munakata R, et al. **Separate demonstration of arterial- and venous-phase by 3D-CT angiography for brain tumors using 64-multidetector row CT: 3D-CT arteriography and 3D-CT venography.** *Fukushima J Med Sci* 2009;55:7–22 CrossRef Medline
- Matsumoto M, Kodama N, Sakuma J, et al. **3D-CT arteriography and 3D-CT venography: the separate demonstration of arterial-phase and venous-phase on 3D-CT angiography in a single procedure.** *AJNR Am J Neuroradiol* 2005;26:635–41 Medline
- Jalali A, Srinivasan VM, Chinnadurai P, et al. **Two-color 3D-3D fusion of selective rotational cerebral angiograms: a novel approach to imaging in cerebrovascular neurosurgery.** *J Neurointerv Surg* 2016;8:1056–60 CrossRef Medline
- Rivoir R, Huber P. **Sequential subtraction.** *Neuroradiology* 1974;7:85–89 CrossRef Medline

# Carotid Intraplaque Hemorrhage and Stenosis: At What Stage of Plaque Progression Does Intraplaque Hemorrhage Occur, and When is It Most Likely to Be Associated with Symptoms?

 A.S. Larson,  W. Brinjikji,  L. Savastano,  A.A. Rabinstein,  L. Saba,  J. Huston, and  J.C. Benson

## ABSTRACT

**BACKGROUND AND PURPOSE:** The relationship between carotid intraplaque hemorrhage and luminal stenosis severity is not well-established. We sought to determine whether intraplaque hemorrhage is related to carotid stenosis and at what degree of stenosis intraplaque hemorrhage most likely contributes to ischemic symptoms.

**MATERIALS AND METHODS:** Consecutive patients who underwent MR carotid plaque imaging with MPRAGE sequences to identify intraplaque hemorrhage were retrospectively reviewed. Degrees of stenoses were categorized as minimal (<30%), moderate (30%–69%), and severe (>70%). Arteries were categorized into 2 groups: symptomatic (ipsilateral to a cerebral ischemic event) and asymptomatic (from a patient without an ischemic event). Multiple regression analyses were used to determine independent associations between the degree of stenosis and intraplaque hemorrhage and the presence of intraplaque hemorrhage with symptoms among categories of stenosis.

**RESULTS:** We included 449 patients with 449 carotid arteries: Two hundred twenty-five (50.1%) were symptomatic, and 224 (49.9%) were asymptomatic. An increasing degree of stenosis was independently associated with the presence of intraplaque hemorrhage (OR = 1.02; 95% confidence interval, 1.01–1.03). Intraplaque hemorrhage was independently associated with ischemic events in arteries with <30% stenosis (OR = 5.68; 95% CI, 1.49–21.69). No such association was observed in arteries with >30% stenosis. Of symptomatic arteries with minimal stenosis, 8.7% had intraplaque hemorrhage versus 1.7% of asymptomatic arteries ( $P = .02$ ). No differences in intraplaque hemorrhage prevalence were found between symptomatic and asymptomatic groups with moderate ( $P = .18$ ) and severe stenoses ( $P = .99$ ).

**CONCLUSIONS:** The presence of intraplaque hemorrhage on high-resolution plaque imaging is likely most useful in identifying symptomatic plaques in cases of minimal stenosis.

**ABBREVIATION:** IPH = intraplaque hemorrhage

Carotid artery disease is a well-known risk factor for cerebral ischemic events such as stroke, transient ischemic attack, and retinal ischemia. It has been estimated that 18%–25% of all strokes result from carotid artery atherosclerotic disease.<sup>1</sup> Conventional features of carotid atherosclerosis, such as the degree of luminal stenosis and surface irregularities, have been used as predictors of ischemic events.<sup>2–4</sup> The severity of luminal narrowing, specifically, has long served a central role in determining whether medical or surgical intervention is indicated to treat such lesions.<sup>5–7</sup> However,

in recent years, attention has been drawn to strokes in patients with mild or moderate carotid artery stenosis, calling into question the reliance on luminal stenosis as the primary prognosticator for ischemic events.<sup>8,9</sup> Instead, interest has turned to the morphologic characteristics of plaques, with the presumption that identifiable vulnerable features may provide crucial information regarding the stability of a plaque.<sup>10,11</sup>

The advent of high-resolution MR plaque imaging has enabled the detection of various carotid plaque components, including intraplaque hemorrhage (IPH), lipid-rich necrotic core, and various plaque characteristics, including neovascularization and inflammation.<sup>12</sup> Of these, IPH is a particularly well-documented risk factor for stroke.<sup>13–15</sup> Prior studies have found patients with carotid IPH to be at increased risk of thromboembolic events in the context of both mild-to-moderate<sup>13,16,17</sup> and severe arterial stenosis.<sup>15</sup> Nevertheless, the degree of stenosis at which IPH is likely to

Received June 23, 2020; accepted after revision February 8, 2021.

From the Departments of Radiology (A.S.L., W.B., J.H., J.C.B.), Neurosurgery (A.S.L., W.B., L. Savastano), and Neurology (A.A.R.), Mayo Clinic, Rochester, Minnesota; and Department of Radiology (L. Saba), University of Cagliari, Cagliari, Italy.

Please address correspondence to Anthony Larson, BS, Mayo Clinic Department of Radiology, 200 First St SW, Rochester, MN 55905; e-mail: lars4689@umn.edu; @TonyLarsonBS; @WBrinjikji; @SavastanoPH  
<http://dx.doi.org/10.3174/ajnr.A7133>

contribute most to ischemic symptoms remains largely uncertain. This information would provide clinicians with the ability to identify symptomatic IPHs that are likely contributing to ischemic events.

The objective of this study was to determine the relationship between IPH and the degree of carotid stenosis by answering following questions: 1) Are increasing degrees of stenosis independently associated with the presence of IPH, and 2) does the prevalence of IPH vary across categories of luminal stenosis? Furthermore, we also sought to determine whether carotid IPH was independently associated with ipsilateral ischemic events among varying degrees of luminal stenosis and to compare the prevalence of IPH between symptomatic and asymptomatic arteries on the basis of the degree of stenosis.

## **MATERIALS AND METHODS**

### **Study Population and Patient Groups**

This was a cross-sectional, retrospective study. Mayo Clinic Institutional review board approval was obtained before the initiation of this study. All patients provided written informed consent for participation in research activities at our institution. All patients from our institution who had a neck MRA with high-resolution carotid vessel wall imaging with MPRAGE sequences from 2015 to 2020 were retrospectively reviewed. Patients were excluded for the following reasons: 1) The MRA protocol did not include MPRAGE sequences, 2) acquired images were of poor quality and/or substantially degraded by artifacts (eg, motion), and 3) radiology reports were incomplete (ie, did not comment on the presence of atherosclerotic plaque) or were unavailable.

All patients underwent an initial evaluation by a staff neurologist, cardiologist, or neurosurgeon at our institution. Neck MRAs with MPRAGE sequences were performed within 6 weeks after an initial evaluation. This evaluation included an assessment for clinical signs of cerebral ischemic events including stroke or TIA as well as any ischemic ophthalmologic events, including retinal artery occlusion or amaurosis fugax. In cases in which patients were found to have an ischemic event (as described below), an assessment for potential cardioembolic sources was pursued with an electrocardiogram, telemetry monitoring, echocardiogram, and Holter monitoring.

Next, patients were first categorized into 2 groups: symptomatic and asymptomatic. Symptomatic patients were defined as those having one of the following unilateral anterior circulation ischemic events: ischemic stroke diagnosed with either MR imaging or CT perfusion studies, TIA as diagnosed by a neurologist, ophthalmologically diagnosed central or branch retinal artery occlusion, or amaurosis fugax as diagnosed by a neurologist or ophthalmologist. Patients with posterior circulation strokes and bilateral anterior circulation strokes were excluded from analysis. Patients with a documented history of atrial fibrillation were excluded from the symptomatic group. Asymptomatic patients were those without a history of one of the preceding ischemic events. Most asymptomatic patients underwent neck MRA for symptoms thought to possibly be related to carotid artery pathology but were ultimately not diagnosed with ischemic stroke, TIA, retinal artery occlusion, or amaurosis fugax. Other indications for neck MRA in asymptomatic patients included follow-up for connective tissue diseases (Ehlers-

Danlos syndrome, Marfan syndrome, and so forth), a history of neoplasm of the neck, fibromuscular dysplasia, or dissection. Patients with connective tissue diseases underwent neck MRAs with MPRAGE sequences at our institution to more thoroughly assess any potential carotid vessel wall abnormalities.

To determine the potential association between carotid stenosis and IPH with ischemic events, we analyzed carotid arteries from each patient group on a per-artery basis. In symptomatic patients, only the artery located ipsilateral to the anterior circulation ischemic event was considered. In asymptomatic patients, the carotid artery with the highest degree of stenosis was selected for analysis. In cases of asymptomatic patients with equivalent degrees of stenosis in each carotid artery (including those without any stenosis at all), an artery was randomly selected using the RANDBETWEEN function in Excel (Microsoft), in which each patient was assigned a number at random (0 or 1). The right carotid artery was used in patients who were assigned a value of 0, and the left was used in patients assigned a value of 1.

### **MR Imaging Protocol**

Neck MR imaging was performed similar to a previously reported protocol.<sup>18</sup> Carotid vessel wall imaging was performed on a 3T MR imaging scanner (750; GE Healthcare) using a 16-channel head/neck/spine coil and included 3 sequences: 1) 2D TOF; 2) 3D inversion recovery fast-spoiled gradient recalled imaging acquired in the coronal plane; and 3) gadolinium bolus carotid MR imaging acquired in the coronal plane. A 3D MPRAGE sequence was used as previously described.<sup>19</sup> The parameters were the following: TR/TE = 13.2/3.2 ms, flip angle = 15°, in-plane spatial resolution = 0.63 × 0.63 mm, reconstructed resolution = 0.31 × 0.31 mm, section thickness = 1 mm, number of excitations = 2, TI = 304 ms, TR with respect to the nonselective inversion = 568 ms, acquisition time = 3 minutes 50 seconds.

### **MR Imaging Review Criteria**

Data relating to neck MRAs were abstracted from the original radiology reports. Reports were made by multiple neuroradiologists from our institution who were blinded to the research question, but not to the clinical scenario. Carotid arteries were assessed for the presence and laterality of atherosclerotic plaques, the presence or absence of IPH, and the degree of carotid stenosis. Atherosclerotic plaque was identified on the basis of the presence of circumferential or eccentric wall thickening. Intraplaque hemorrhage was defined as being hyperintense on MPRAGE, with intralésional signal intensity >150% of the ipsilateral sternocleidomastoid muscle. The degree of carotid stenosis was calculated on the basis of the NASCET criteria and was categorized as minimal (<30%), moderate (30%–69%), or severe (>70%).<sup>5</sup>

### **Statistical Analysis**

To determine whether the degree of carotid stenosis was independently associated with the presence of IPH, we performed multiple regression analysis that used several vascular risk factors as independent variables in addition to the degree of ipsilateral luminal stenosis. The outcome variable was the presence or absence of IPH.

To elucidate any potential independent associations with ischemic events, we performed 3 separate multiple logistic regression

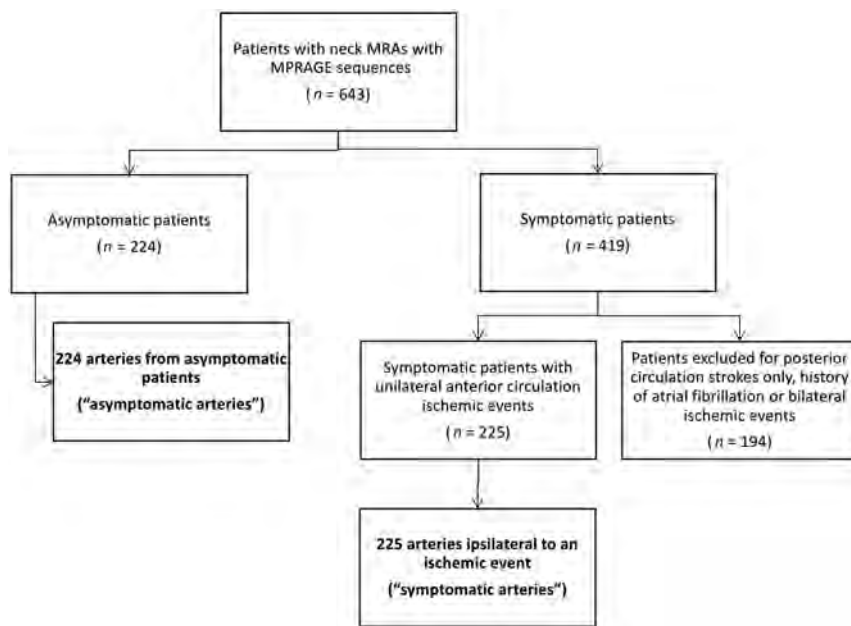


FIGURE. Patient- and artery-selection process.

Table 1: Patient characteristics<sup>a</sup>

	Overall	Symptomatic	Asymptomatic	P Value
Total patients included	449	225	224	
Total arteries included	449	225	224	
Mean age (SD) (yr)	66.4 (16.3)	67.2 (13.1)	65.6 (18.9)	.30
Male (No.) (%)	245 (54.6)	150 (66.7)	95 (42.4)	<.0001
Comorbidities				
Coronary artery disease (No.) (%)	110 (24.5)	69 (30.7)	41 (18.3)	.003
Hypertension (No.) (%)	269 (59.9)	154 (68.4)	115 (51.3)	.0002
Hyperlipidemia (No.) (%)	287 (63.9)	177 (78.7)	110 (49.1)	<.0001
Diabetes mellitus (No.) (%)	82 (18.3)	56 (28.9)	26 (11.6)	.0003
Peripheral artery disease (No.) (%)	29 (6.5)	17 (7.6)	12 (5.4)	.44
Obstructive sleep apnea (No.) (%)	85 (18.9)	17 (7.6)	12 (5.4)	.44
Ever smoker (No.) (%)	203 (45.2)	125 (55.6)	78 (34.8)	<.0001
Current smoker (No.) (%)	45 (10.0)	29 (12.9)	16 (7.1)	.06
Mean body mass index (SD)	28.3 (5.3)	28.5 (4.8)	28.1 (5.7)	.39
Imaging characteristics				
Arteries without presence of atherosclerotic plaque <sup>b</sup> (No.) (%)	202 (45.0)	47 (20.9)	155 (69.2)	<.0001
Mean degree of stenosis <sup>c</sup> (SD)	23.8 (33.6)	33.5 (35.2)	14.0 (28.8)	<.0001
Presence of IPH <sup>d</sup> (No.) (%)	71 (15.8)	55 (24.4)	16 (7.1)	<.0001

<sup>a</sup>P values pertain to the differences in values between asymptomatic and symptomatic groups.

<sup>b</sup>As mentioned by radiology reports.

<sup>c</sup>Degrees of stenosis were based on NASCET criteria.<sup>5</sup>

<sup>d</sup>Intraplaque hemorrhage was defined as being hyperintense on MPRAGE with intralésional signal intensity of >150% of the ipsilateral sternocleidomastoid muscle.

analyses in which arteries were stratified by the following degrees of ipsilateral stenosis: <30%, 30%–69% stenosis, and >70%. Input variables were those that differed between symptomatic and asymptomatic patients, with a *P* value of ≤ .30 on univariate analysis. The outcome variable was a unilateral anterior circulation ischemic event as described above. The prevalence of IPH in each category of luminal stenosis was calculated for all patients included, as well as symptomatic and asymptomatic patients separately.

Means (SDs) were calculated for continuous variables including age and body mass index. Percentages were calculated for binary variables including sex, comorbidities, the prevalence of ischemic symptoms, the prevalence of each degree of carotid stenosis, and the prevalence of IPH. Each of the aforementioned descriptive statistics was calculated in Excel. The Fisher exact probability test was used to determine the significance among categorical baseline variables between asymptomatic and symptomatic patients and to determine the difference in prevalence of IPH in each category of stenosis between symptomatic and asymptomatic patients. The Student 2-tailed *t* test was used to determine significance among continuous variables. Any *P* values < .05 were considered statistically significant. Each of the aforementioned statistical tests was calculated using STATA statistical software, Version 14.1 (StataCorp).

## RESULTS

### Patients

Our patient and artery-selection process is outlined in the Figure. The final patient cohort comprised 449 patients, yielding 449 carotid arteries. There were 224 asymptomatic patients (49.9%) and 225 symptomatic patients (50.1%). Accordingly, there were 224 asymptomatic carotid arteries (49.9%), and 225 symptomatic arteries (50.1%).

Baseline data from symptomatic and asymptomatic patients are summarized in Table 1. The mean age of all included patients was 66.4 (SD, 16.3) years, and 245 (54.6%) were men.

Regarding ischemic symptoms, 171 of 225 patients (76.0%) were diagnosed with an ischemic stroke; 69 (30.7%), with a TIA; 16 (7.1%), with retinal artery occlusion; and 20 (8.9%), with amaurosis fugax (these numbers

do not add up to 100% because multiple patients had multiple events).

### Intraplaque Hemorrhage and Degree of Stenosis

Increasing degrees of carotid stenosis were independently associated with the presence of ipsilateral IPH (OR = 1.02; 95% CI, 1.01–1.03). Other variables that were independently associated with carotid IPH were male sex (OR = 2.7; 95% CI, 1.43–5.04)

and hyperlipidemia (OR = 4.03; 95% CI, 1.58–10.32). These data are further summarized in Table 2.

On stratified multiple regression analysis, ipsilateral carotid IPH was found to be independently associated with ipsilateral anterior circulation ischemic events in arteries that had <30% stenosis (OR = 5.68; 95% CI, 1.49–21.69). This association was not observed in arteries with 30%–69% or >70% stenosis. In arteries with <30% stenosis, male sex (OR = 1.92, 95% CI, 1.12–3.32), and hyperlipidemia (OR = 2.1; 95% CI, 1.17–3.79) were also found to be independently associated with ischemic events. These data are summarized in Table 3.

The prevalence of IPH in the setting of varying degrees of carotid stenosis is summarized in Table 4. Intraplaque hemorrhage was identified in 71 arteries in total (15.8%), 55 of which (77.5%) were ipsilateral to an ischemic event; 8.7% of symptomatic arteries with minimal (<30%) stenosis had IPH, compared with 1.7% of asymptomatic arteries with minimal stenosis ( $P = .02$ ).

**Table 2: Multiple regression analysis to determine independent associations with the presence of carotid intraplaque hemorrhage<sup>a</sup>**

Variable	OR (95% CI)
Ipsilateral stenosis	1.02 (1.01–1.03)
Male sex	2.70 (1.43–5.04)
Coronary artery disease	1.24 (0.68–2.25)
Hypertension	1.21 (0.61–2.42)
Hyperlipidemia	4.03 (1.58–10.32)
Diabetes mellitus	0.89 (0.47–1.70)
Current smoker	1.16 (0.47–2.83)
Ever smoker	1.06 (0.58–1.94)

<sup>a</sup> All independent variables are listed in the table. The outcome variable was the presence or absence of carotid intraplaque hemorrhage.

**Table 3: Stratified multiple regression analyses to determine independent associations with the presence of an anterior circulation ischemic event<sup>a</sup>**

Variable	OR (95% CI)		
	<30% Stenosis	30%–69% Stenosis	>70% Stenosis
Ipsilateral IPH	5.68 (1.49–21.69)	2.38 (0.67–8.43)	0.95 (0.32–2.80)
Age	0.99 (0.97–1.0)	0.99 (0.95–1.03)	1.02 (0.98–1.06)
Male sex	1.92 (1.12–3.32)	1.64 (0.46–5.90)	2.04 (0.69–6.06)
Coronary artery disease	0.74 (0.33–1.66)	0.75 (0.24–2.35)	0.68 (0.21–2.19)
Hypertension	0.93 (0.50–1.70)	0.93 (0.09–2.95)	0.82 (0.20–3.35)
Hyperlipidemia	2.10 (1.17–3.79)	0.57 (0.05–6.45)	1.25 (0.26–6.02)
Diabetes mellitus	1.51 (0.66–3.49)	1.56 (0.43–5.92)	2.34 (0.59–9.24)
Current smoker	1.68 (0.66–4.28)	1.82 (1.68–19.83)	1.07 (0.25–4.53)
Ever smoker	1.59 (0.87–2.91)	1.33 (0.41–4.41)	0.65 (0.17–2.43)

<sup>a</sup> All independent variables are listed in the table.

**Table 4: Degree of carotid artery stenosis and prevalence of intraplaque hemorrhage in asymptomatic-versus-symptomatic arteries<sup>a</sup>**

Degree of Stenosis <sup>c</sup>	Prevalence of Intraplaque Hemorrhage <sup>b</sup> (%)			P Value
	All (n = 449 Total)	Asymptomatic (n = 224 Total)	Symptomatic (n = 225 Total)	
<30% (n = 295 total)	13/295 (4.4)	3/180 (1.7)	10/115 (8.7)	.02
30%–69% (n = 79 total)	33/79 (41.8)	5/19 (26.3)	28/60 (46.7)	.18
70%+ (n = 75 total)	25/75 (33.3)	8/25 (32.0)	17/50 (34.0)	.99

<sup>a</sup>P values pertain to the difference in the prevalence of IPH between asymptomatic and symptomatic groups and were calculated using the Fisher exact test. Data are number of arteries per group with intraplaque hemorrhage.

<sup>b</sup>Intraplaque hemorrhage was defined as being hyperintense on MPRAGE with intralesional signal intensity of >150% of the ipsilateral sternocleidomastoid muscle.

<sup>c</sup>Degrees of stenosis were based on the NASCET criteria.<sup>5</sup>

Symptomatic arteries with moderate stenosis (30%–69%) had an IPH prevalence of 46.7%, compared with a prevalence of 26.3% in the asymptomatic group, though this finding did not reach statistical significance ( $P = .18$ ). In arteries with severe (>70%) stenosis, there was no difference in the prevalence of IPH between symptomatic (34.0%) and asymptomatic groups (32.0%,  $P = .99$ ).

## DISCUSSION

The current study has 2 primary findings: First, increasing degrees of carotid stenosis were found to be independently associated with the presence of IPH. This finding corresponds to a higher prevalence of IPH that was observed in all arteries with >30% stenosis compared with arteries with <30% stenosis. Second, ipsilateral IPH was independently associated with symptoms in carotid arteries with <30% stenosis, a finding that was accompanied by a higher prevalence of IPH in symptomatic-versus-asymptomatic patients with ipsilateral stenosis of <30%. Such findings were not observed for arteries with >30% stenosis. Taken together, these results suggest that first, carotid IPH is more likely to be observed in arteries with increasing degrees of luminal stenosis. However, the presence of IPH may be less useful in differentiating symptomatic from asymptomatic plaques in the context of greater degrees of luminal stenosis: IPH is likely most useful in distinguishing between symptomatic and asymptomatic plaques in cases of <30% stenosis. However, large differences were evident in the number of arteries between each degree of stenosis. For example, there were 295 total arteries in the <30% category, while only 154 arteries made up the total of the remaining categories. These smaller sample sizes in arteries with greater degrees of stenosis may have precluded statistical significance from being reached.

Already, IPH is a known risk factor for symptomatic ischemic events in the context of less severe degrees of carotid stenosis. Altaf et al<sup>13</sup> performed a longitudinal prospective study involving a total of 64 symptomatic patients with 30%–69% carotid artery stenosis during a mean follow-up period of 28 months. Fourteen ipsilateral ischemic events were noted on follow-up, 13 of which occurred in patients found to have ipsilateral IPH. Similarly, Singh et al<sup>16</sup> reported a case-control study in which 36 of 98 carotid arteries with 50%–70% stenosis had IPH (75 patients in total). At a minimum follow-up of 1 year, 6 ipsilateral ischemic events occurred in patients with IPH, and no events occurred in patients without evidence of IPH.

The results of this study have a rationale based on the expected histopathologic progression of most plaques. IPH represents a well-described vulnerable feature of atherosclerotic plaques and is associated with a sudden increase in plaque size, thrombosis, and

embolism. Such changes in the setting of nonsevere stenoses might be expected to contribute to symptoms in previously asymptomatic lesions. Plaques resulting in severe stenosis but without IPH, conversely, are often symptomatic likely due to the presence of additional vulnerable characteristics such as increased plaque volume, lipid-rich necrotic core, neovascularization, or inflammation. Hence, it stands to reason that IPH has a larger impact on the development of neurologic symptoms in less severe plaques. Thus, dedicated MR plaque imaging in symptomatic patients with milder stenoses may be particularly useful.

Because IPH was found to be prevalent in a wide range of luminal stenoses, the results of this study provide imaging evidence that plaques of higher histologic grades (and therefore increased vulnerability) do not always exist exclusively in the context of higher degrees of luminal stenosis. Such findings are consistent with several prior reports that have demonstrated the imaging evidence of IPH across the spectrum of carotid stenoses.<sup>13,15,16</sup> This phenomenon is further supported by histologic evidence. A postmortem histopathologic study of specimens with carotid artery disease by Svindland and Torvik<sup>20</sup> noted the presence of IPH in various degrees of carotid stenosis, ranging from 35% to 88%, and they also found that hemorrhage was more commonly seen in arteries with greater stenosis. Albuquerque et al<sup>21</sup> found IPH to be equally prevalent across varying degrees of stenosis ranging from 50% to >90%. Taken together with the results of the current study, these data indicate that IPH may be present in all severities of carotid artery stenosis. Although MR plaque imaging protocols are likely useful in detecting symptomatic plaques with IPH in cases of less-than-severe stenosis, further study is necessary for confirmation.

The current study is limited in its single-center, retrospective design. It is uncertain how many patients from our institution did not provide informed consent for involvement in research; therefore this potential for selection bias cannot be excluded. It is possible that arteries with minimal atherosclerotic plaque may have been excluded from the study on the basis of radiology reports because this may not have been commented on by the reading radiologist. Other, noncarotid sources of cerebral ischemia were not explicitly ruled out in each symptomatic patient, though this potential confounding factor was mitigated by excluding patients with atrial fibrillation. Most cases of IPH were detected within 4 weeks of the ischemic event; however, we did not control for the timeframe of IPH detection relative to the ischemic event in each case, nor was the age of the IPH considered. Prior studies have implied that IPH signals may persist for up to 24 months.<sup>22</sup> It is, therefore, uncertain how the age and evolution of IPH may contribute to ischemic symptoms, and further study is required to address these issues. We used a definition of carotid IPH as being a hyperintensity that is >150% of the adjacent musculature in accordance with prior reports.<sup>13,16</sup> However, other studies have used a hyperintensity threshold of 200%, which may increase the specificity of carotid IPH detection.<sup>23</sup> In this study, IPH and carotid stenosis were the sole plaque features that were evaluated, and other important plaque features such as ulceration, cap thickness, or the presence of a lipid-rich necrotic core were not evaluated, all of which may play confounding roles. Future studies may also consider the size of the plaque because larger plaques are likely at higher risk of developing IPH.

## CONCLUSIONS

Carotid artery IPH is independently associated with the degree of arterial stenosis. Carotid IPH is also independently associated with the presence of ipsilateral symptoms in cases of minimal arterial stenosis. Symptomatic carotid arteries with minimal stenosis also tended to have a higher prevalence of IPH compared with asymptomatic arteries. The presence of IPH on high-resolution plaque imaging is likely most useful in identifying symptomatic plaques in cases of minimal stenosis. However, carotid artery IPH was observed in all degrees of luminal stenosis. High-resolution carotid plaque imaging should, therefore, be considered in patients with suspected carotid artery atherosclerosis regardless of the degree of stenosis.

Disclosures: Alejandro Rabinstein—UNRELATED: Royalties: Elsevier, Wolters Kluwer, Springer; Payment for Development of Educational Presentations: Univadis, Medscape; Other: adverse event adjudicator, Comments: for trials funded by Boston Scientific and Boehringer Ingelheim.

## REFERENCES

1. Ooi YC, Gonzalez NR. **Management of extracranial carotid artery disease.** *Cardiol Clin* 2015;33:1–35 CrossRef Medline
2. Troyer A, Saloner D, Pan XM, et al. Assessment of Carotid Stenosis by Comparison with Endarterectomy Plaque Trial Investigators. **Major carotid plaque surface irregularities correlate with neurologic symptoms.** *J Vasc Surg* 2002;35:741–47 CrossRef Medline
3. Prabhakaran S, Rundek T, Ramas R, et al. **Carotid plaque surface irregularity predicts ischemic stroke: the Northern Manhattan Study.** *Stroke* 2006;37:2696–2701 CrossRef Medline
4. Autret A, Pourcelot L, Saudeau D, et al. **Stroke risk in patients with carotid stenosis.** *Lancet* 1987;1:888–90 CrossRef Medline
5. Barnett HJ, Taylor DW, Haynes RB, et al. North American Symptomatic Carotid Endarterectomy Trial Collaborators. **Beneficial effect of carotid endarterectomy in symptomatic patients with high-grade carotid stenosis.** *N Engl J Med* 1991;325:445–53 CrossRef Medline
6. **Endarterectomy for asymptomatic carotid artery stenosis: Executive Committee for the Asymptomatic Carotid Atherosclerosis Study.** *JAMA* 1995;273:1421–28 Medline
7. **MRC European Carotid Surgery Trial: interim results for symptomatic patients with severe (70–99%) or with mild (0–29%) carotid stenosis—European Carotid Surgery Trialists' Collaborative Group.** *Lancet* 1991;337:1235–43 Medline
8. Freilinger TM, Schindler A, Schmidt C, et al. **Prevalence of nonstenosing, complicated atherosclerotic plaques in cryptogenic stroke.** *JACC Cardiovasc Imaging* 2012;5:397–405 CrossRef Medline
9. Wasserman BA, Wityk RJ, Trout HH 3rd, et al. **Low-grade carotid stenosis: looking beyond the lumen with MRI.** *Stroke* 2005;36:2504–13 CrossRef Medline
10. Lovett JK, Gallagher PJ, Hands LJ, et al. **Histological correlates of carotid plaque surface morphology on lumen contrast imaging.** *Circulation* 2004;110:2190–97 CrossRef Medline
11. Lovett JK, Gallagher PJ, Rothwell PM. **Reproducibility of histological assessment of carotid plaque: implications for studies of carotid imaging.** *Cerebrovasc Dis* 2004;18:117–23 CrossRef Medline
12. Saba L, Yuan C, Hatsukami TS, et al. Vessel Wall Imaging Study Group of the American Society of Neuroradiology. **Carotid Artery Wall Imaging: Perspective and Guidelines from the ASNR Vessel Wall Imaging Study Group and Expert Consensus Recommendations of the American Society of Neuroradiology.** *AJNR Am J Neuroradiol* 2018;39:E9–31 CrossRef Medline
13. Altaf N, Daniels L, Morgan PS, et al. **Detection of intraplaque hemorrhage by magnetic resonance imaging in symptomatic patients with mild to moderate carotid stenosis predicts recurrent neurological events.** *J Vasc Surg* 2008;47:337–42 CrossRef Medline

14. Takaya N, Yuan C, Chu B, et al. **Association between carotid plaque characteristics and subsequent ischemic cerebrovascular events: a prospective assessment with MRI—initial results.** *Stroke* 2006;37:818–23 CrossRef Medline
15. Altaf N, MacSweeney ST, Gladman J, et al. **Carotid intraplaque hemorrhage predicts recurrent symptoms in patients with high-grade carotid stenosis.** *Stroke* 2007;38:1633–35 CrossRef Medline
16. Singh N, Moody AR, Gladstone DJ, et al. **Moderate carotid artery stenosis: MR imaging-depicted intraplaque hemorrhage predicts risk of cerebrovascular ischemic events in asymptomatic men.** *Radiology* 2009;252:502–08 CrossRef Medline
17. Schindler A, Schinner R, Altaf N, et al. **Prediction of stroke risk by detection of hemorrhage in carotid plaques: meta-analysis of individual patient data.** *JACC Cardiovasc Imaging* 2020;13:395–406 CrossRef Medline
18. Brinjikji W, DeMarco JK, Shih R, et al. **Diagnostic accuracy of a clinical carotid plaque MR protocol using a neurovascular coil compared to a surface coil protocol.** *J Magn Reson Imaging* 2018;48:1264–72 CrossRef Medline
19. Zhu DC, Ferguson MS, DeMarco JK. **An optimized 3D inversion recovery prepared fast spoiled gradient recalled sequence for carotid plaque hemorrhage imaging at 3.0 T.** *Magn Reson Imaging* 2008;26:1360–66 CrossRef Medline
20. Svindland A, Torvik A. **Atherosclerotic carotid disease in asymptomatic individuals: an histological study of 53 cases.** *Acta Neurol Scand* 1988;78:506–17 CrossRef Medline
21. Albuquerque LC, Narvaes LB, Maciel AA, et al. **Intraplaque hemorrhage assessed by high-resolution magnetic resonance imaging and C-reactive protein in carotid atherosclerosis.** *J Vasc Surg* 2007;46:1130–37 CrossRef Medline
22. Simpson R, Akwei S, Hosseini A, et al. **MR imaging-detected carotid plaque hemorrhage is stable for 2 years and a marker for stenosis progression.** *AJNR Am J Neuroradiol* 2015;36:1171–75 CrossRef Medline
23. McNally JS, McLaughlin MS, Hinckley PJ, et al. **Intraluminal thrombus, intraplaque hemorrhage, plaque thickness, and current smoking optimally predict carotid stroke.** *Stroke* 2015;46:84–90 CrossRef Medline

## Another Step toward the Understanding of Carotid Artery Pathology

Approximately 18%–25% of strokes are caused by atherosclerotic carotid disease.<sup>1</sup> For the past 20 years, we have witnessed substantial technological progress resulting in a paradigm shift for carotid artery imaging.<sup>1</sup> Using carotid sonography with Doppler to assess the degree of arterial stenosis is still the primary technique used in everyday clinical practice because of the low cost and the low risk-to-benefit ratio. However, different imaging modalities exploring carotid plaque in-depth have identified a few features that may be connected to the high risk of plaque rupture and consequential ischemic events.<sup>1</sup>

Currently, MR imaging is the technique of choice for direct plaque imaging.<sup>2</sup> The best-known vulnerable plaque characteristic is the presence of intraplaque hemorrhage (IPH). The individual patient data meta-analysis of 696 patients with carotid stenosis (560 symptomatic and 136 asymptomatic) concluded that IPH is an independent predictor of ipsilateral stroke (hazard ratio = 11.0; 95% CI, 4.8–25.1), which is more robust than any known clinical risk factor.<sup>3</sup> Currently, it is clinically feasible to add the MPRAGE sequence for visualizing carotid plaque in detail to the standard vessel/neck imaging protocol, as it adds only 4–6 minutes to the scan time and requires neither nonstandard coils nor additional contrast agent.<sup>2</sup>

The natural history of asymptomatic carotid atherosclerotic disease is not yet fully understood; thus, it can be a problem to stratify the prognosis and guide treatment (optimized medical therapy, carotid endarterectomy, or carotid stent placement). A recent meta-analysis, including more than 20,000 participants from 64 studies, showed that the vulnerable plaque detected by MR imaging increased the risk of an ipsilateral stroke (OR = 3.0; 95% CI, 2.1–4.3) during a median observation period of 3 years.<sup>4</sup> The OR was similar (3.2; 95% CI, 1.7–5.9) among patients with severe stenosis. It suggests that the plaque characteristics visualized by advanced imaging may play a more important role than the degree of stenosis severity.<sup>4,5</sup>

In this issue of the *American Journal of Neuroradiology*, Larson et al<sup>6</sup> describe a cohort of 449 patients with or without ischemic events who underwent risk stratification with both the assessment of carotid stenosis degree and the presence of IPH.

First, they found that the IPH is independently associated with carotid stenosis—the narrower the vessel, the more unstable the plaque. Second, they have observed among a group with mild stenosis (< 30%) that IPH was more frequently present in the symptomatic than the asymptomatic group. This led to the hypothesis based on the available data that the presence of IPH is particularly relevant for ischemic events risk prediction among patients with mild stenosis.

It is important to recognize the existing research and implement it into current guidelines. For example, the European Society of Cardiology recommended in their 2017 Guidelines to consider revascularization of the carotid artery for patients without prior symptoms, with moderate-to-severe stenosis (60%–99%), with a life expectancy of more than 5 years, and the presence of vulnerable plaque characteristics on advanced imaging (IPH or lipid-rich necrotic core).<sup>7</sup> It reinforces the message that plaque composition should be considered in clinical decision-making. With their latest revision in February 2021, the US Preventive Services Task Force advised against asymptomatic carotid artery screening in the general population because of possible harm.<sup>8</sup> Although we would support their call for rigorous up-to-date trials with long-term follow-up, we would argue that screening itself is not harmful, and rather than directly guiding a patient toward the invasive procedure, it should lead to the multidisciplinary team discussion.<sup>9</sup> Moreover, a lack of carotid artery disease recognition in the first place leads to a lack of any treatment, including optimized medical therapy.

The question is not if we should screen for asymptomatic carotid stenosis, but rather how to establish the most effective multimodal screening protocol. There is an urgent need for collective work and randomized clinical trials selecting patients for different treatment modalities so that we can understand their efficacy and safety based on carotid plaque MR imaging or other extended imaging. The work by Larson et al<sup>6</sup> further supports the use of MR plaque imaging in this endeavor. For now, we need to embrace available evidence with its inherent limitations and treat our patients the best we can with an individual approach.<sup>5</sup>

## REFERENCES

1. Saba L, Yuan C, Hatsukami TS, et al. **Carotid artery wall imaging: perspective and guidelines from the ASNR Vessel Wall Imaging Study Group and expert consensus recommendations of the American Society of Neuroradiology.** *AJNR Am J Neuroradiol* 2018;39:E9–31 CrossRef Medline
2. Saba L, Saam T, Jäger HR, et al. **Imaging biomarkers of vulnerable carotid plaques for stroke risk prediction and their potential clinical implications.** *Lancet Neurol* 2019;18:559–72 CrossRef Medline
3. Schindler A, Schinner R, Altaf N, et al. **Prediction of stroke risk by detection of hemorrhage in carotid plaques: meta-analysis of individual patient data.** *JACC Cardiovasc Imaging* 2020;13:395–406 CrossRef Medline
4. Kamtchum-Tatuene J, Noubiap JJ, Wilman AH, et al. **Prevalence of high-risk plaques and risk of stroke in patients with asymptomatic carotid stenosis: a meta-analysis.** *JAMA Neurol* 2020;77:1524–35 CrossRef Medline
5. Podlasek A, Grunwald IQ, Musialek P. **The evolution from an “average” study patient to patient-specific characteristics to guide interventions in vascular medicine.** *Pol Arch Intern Med* 2021;131:5–8 CrossRef Medline
6. Larson A, Brinjikji W, Savastano L, et al. **Carotid intraplaque hemorrhage and stenosis: At what stage of plaque progression does intraplaque hemorrhage occur, and when is it most likely to be associated with symptoms?** *AJNR Am J Neuroradiol* 2021. [Epub ahead of print] CrossRef
7. Aboyans V, Ricco JB, Bartelink MLEL, et al. **2017 ESC guidelines on the diagnosis and treatment of peripheral arterial diseases, in collaboration with the European Society for Vascular Surgery (ESVS).** *Eur Heart J* 2018;39:763–816 CrossRef Medline
8. Krist AH, Davidson KW, Mangione CM, et al. **Screening for asymptomatic carotid artery stenosis.** *JAMA* 2021;325:476–81 CrossRef Medline
9. Paraskevas KI, Eckstein HH, Mikhailidis DP, et al. **Rationale for screening selected patients for asymptomatic carotid artery stenosis.** *Curr Med Res Opin* 2020;36:361–65 CrossRef Medline

© **A. Podlasek**

National Institute for Health Research Nottingham Biomedical Research Centre  
University of Nottingham  
Nottingham, United Kingdom  
Clinical Radiology  
Nottingham University Hospitals National Health Service Trust  
Nottingham, United Kingdom

© **R.J. Simpson**

Department of Vascular and Endovascular Surgery  
Nottingham University Hospitals National Health Service Trust  
Nottingham, United Kingdom

<http://dx.doi.org/10.3174/ajnr.A7137>

# Asynchrony in Peritumoral Resting-State Blood Oxygen Level–Dependent fMRI Predicts Meningioma Grade and Invasion

P.B. Wu, D.S. Chow, P.D. Petridis, M.B. Sisti, J.N. Bruce, P.D. Canoll, and J. Grinband



## ABSTRACT

**BACKGROUND AND PURPOSE:** Meningioma grade is determined by histologic analysis, with detectable brain invasion resulting in a diagnosis of grade II or III tumor. However, tissue undersampling is a common problem, and invasive parts of the tumor can be missed, resulting in the incorrect assignment of a lower grade. Radiographic biomarkers may be able to improve the diagnosis of grade and identify targets for biopsy. Prior work in patients with gliomas has shown that the resting-state blood oxygen level–dependent fMRI signal within these tumors is not synchronous with normal brain. We hypothesized that blood oxygen level–dependent asynchrony, a functional marker of vascular dysregulation, could predict meningioma grade.

**MATERIALS AND METHODS:** We identified 25 patients with grade I and 11 patients with grade II or III meningiomas. Blood oxygen level–dependent time-series were extracted from the tumor and the radiographically normal control hemisphere and were included as predictors in a multiple linear regression to generate a blood oxygen level–dependent asynchrony map, in which negative values signify synchronous and positive values signify asynchronous activity relative to healthy brain. Masks of blood oxygen level–dependent asynchrony were created for each patient, and the fraction of the mask that extended beyond the contrast-enhancing tumor was computed.

**RESULTS:** The spatial extent of blood oxygen level–dependent asynchrony was greater in high (grades II and III) than in low (I) grade tumors ( $P < 0.001$ ) and could discriminate grade with high accuracy (area under the curve = 0.88).

**CONCLUSIONS:** Blood oxygen level–dependent asynchrony radiographically discriminates meningioma grade and may provide targets for biopsy collection to aid in histologic diagnosis.

**ABBREVIATIONS:** AUC = area under the curve; BOF = BOLD outside fraction; BOLD = blood oxygen level–dependent; FOF = FLAIR outside fraction

The 2016 World Health Organization guidelines for meningiomas were notable for the inclusion of brain invasion as a criterion sufficient for assignment to “high-grade” status (ie, grade II or III) and may explain the greater incidence of high-grade meningiomas since 2016.<sup>1</sup> In addition to brain invasion, a meningioma is considered grade II or III if it demonstrates an elevated mitotic index and  $\geq 3$  aggressive histologic features or demonstrates a loss of meningeothelial differentiation.<sup>2</sup> While roughly 80% of all meningiomas are grade I, with excellent prognosis

following surgical resection, the remaining 20% are grade II or III and more likely to recur.<sup>3</sup> Furthermore, grade I tumors have a 10-year survival of 83%, compared with 61% for grade II and III tumors,<sup>4</sup> making the accurate determination of meningioma grade important for both prognostic and treatment purposes.

Histologic assessment remains the criterion standard for grading meningiomas; however, an accurate noninvasive prediction of tumor grade could benefit both clinicians and patients by improving preoperative planning and patient counseling and potentially guiding difficult management decisions. Furthermore, routine surgical biopsy may undersample regions that have histologic features, such as invasion, that are diagnostic for grade II or III meningioma, resulting in possible misdiagnosis. Identifying radiographic features that correlate with tumor invasion would, therefore, be useful for guiding biopsy location. Prior studies using standard-of-care structural imaging have attempted to predict meningioma grade by evaluating a mix of objective radiographic features, such as mean voxel intensity, and subjective radiographic features, such as the presence of hyperostosis.<sup>5</sup> Peritumoral edema detected by T2-FLAIR has also

Received October 11, 2020; accepted after revision January 14, 2021.

From the Vagelos College of Physicians and Surgeons (P.B.W.) and Departments of Neurological Surgery (P.B.W., M.B.S., J.N.B.), Pathology and Cell Biology (P.D.C.), Radiology (J.G.), and Psychiatry (J.G.), Columbia University, New York, New York; Department of Radiological Sciences (D.S.C.), University of California Irvine, Irvine, California; and Department of Psychiatry (P.D.P.), New York University, New York, New York.

Please address correspondence to Jack Grinband, PhD, New York State Psychiatric Institute, 1051 Riverside Drive, Room 6-103, New York, NY 10032; e-mail: jg2269@cumc.columbia.edu

Indicates article with online supplemental data.

<http://dx.doi.org/10.3174/ajnr.A7154>

been associated with higher-grade meningiomas.<sup>6,7</sup> Additionally, histogram analysis of diffusion tensor imaging has also been shown to correlate with tumor grade and tumor subtype in meningiomas.<sup>8</sup> However, it would be beneficial to develop a single, simple, visual criterion that could be easily applied by radiologists and surgeons to predict meningioma grade with high accuracy.

Prior work using resting-state blood oxygen level—dependent (BOLD) fMRI in diffuse glioma has revealed that the BOLD signal in and around the tumor is temporally asynchronous with radiographically normal parts of the brain.<sup>9</sup> BOLD asynchrony maps provide a quantitation of this phenomenon and are generated by comparing each voxel with the mean global signal intensity of both the contralateral hemisphere and the contrast-enhancing tumor. Stereotactically localized biopsies collected from peritumoral regions have demonstrated that the degree of BOLD asynchrony correlates with local tumor burden.<sup>10</sup> Furthermore, the spatial extent of the asynchrony can discriminate *IDH* wild-type and *IDH*-mutated gliomas with high fidelity.<sup>11</sup>

Meningiomas have also been shown to cause disruptions in vascular function observable with resting-state BOLD fMRI.<sup>11</sup> We, therefore, hypothesized that brain invasion, a common feature of high-grade meningiomas, would be detectable using BOLD asynchrony maps derived from resting-state BOLD fMRI and that the spatial extent of BOLD asynchrony could be used to discriminate meningioma grade. Furthermore, we evaluated whether combining the spatial features of BOLD asynchrony and T2-FLAIR hyperintensity could improve tumor grading accuracy over either measure alone.

## MATERIALS AND METHODS

### Patient Selection and Clinical Data Acquisition

All aspects of this single-center study were conducted in compliance with the Health Insurance Portability and Accountability Act regulations and approved by the institutional review board of Columbia University. Demographic and clinical data were retrospectively collected from the medical records of patients diagnosed with meningiomas and treated at our institution between 2010 and 2020. Pathology reports generated before the release of the 2016 World Health Organization criteria were re-evaluated to ensure that all tumors were graded correctly according to the updated 2016 criteria. Patients were included in the study if they were at least 18 years of age, had histologically proved meningiomas, and had preoperative structural MR imaging and resting-state BOLD fMRI available. The reported patient age was dated from the time the BOLD fMRI scan was acquired. Because our cohort included only a single patient with grade III, this patient was grouped with grade II patients into a “high-grade” meningioma group. All patients had preoperative standard-of-care T1 postcontrast and T2-FLAIR sequences, in addition to resting-state BOLD fMRI. Imaging parameters are listed in the Online Supplemental Data. Contrast-enhanced images were obtained with intravenous gadobenate dimeglumine (MultiHance; Bracco Diagnostics) dosed by weight at 0.2 mL/kg. BOLD images were obtained before contrast administration.

### Structural ROIs

Tumor masks were defined by contrast enhancement on T1-weighted imaging and were hand-drawn by a board-certified neuroradiologist with 10 years of experience (D.S.C.) as described previously in Chow et al.<sup>9</sup> In this study, normal brain comprised the cerebral hemisphere contralateral to the tumor with any contrast enhancement or T2-FLAIR hyperintensity crossing the midline removed. Masks of peritumoral edema were also drawn from each patient’s corresponding T2-FLAIR imaging after being affine-registered with 6 *df* to their corresponding T1-post-contrast image using the FMRIB Linear Image Registration Tool, Version 5.0.6 (FLIRT; <http://www.fmrib.ox.ac.uk/fslwiki/FLIRT>).<sup>12</sup> Registrations were visually inspected to ensure high-quality alignment. All masks were drawn in a blinded manner with the neuroradiologist unaware of the histologic subtype of the tumor or the radiographic features present on other sequences.

### BOLD Asynchrony Maps

**Overview.** Global signal intensity refers to the mean BOLD signal across the entire brain and is related to cardiac pulsations and respiration-related changes in arterial carbon dioxide (CO<sub>2</sub>)<sup>12–14</sup> as well as whole-brain neural fluctuations.<sup>15</sup> Vascular sources account for ~25%–27% of the variance, and neural sources account for ~5%–6% of the variance in the global signal.<sup>16,17</sup> Also, by means of functional connectivity measures, the 2 hemispheres are >95% symmetric.<sup>18</sup> This signal is often considered a nuisance variable that is removed as part of standard BOLD preprocessing.<sup>19,20</sup> In the current study, the global signal of the control mask is used as a temporal signature of healthy hemodynamics reflecting normal responses to cardiac pulsatility, respiration-related CO<sub>2</sub> changes, and neuronal fluctuations common across the whole brain. The mean signal from the tumor mask produces a temporal signature of unhealthy hemodynamics. Voxelwise regression using these 2 signatures produces 2 *Z*-statistic maps that represent the similarity of each voxel to tumor and normal brain. Furthermore, because the tumor and control time-series are temporally uncorrelated, subtracting the 2 maps further enhances the difference between the 2 tissue types and results in a map of BOLD asynchrony.<sup>9</sup> The degree of asynchrony has been shown to predict tumor burden, thus providing an indirect measure of glioma brain invasion.<sup>10</sup>

**Preprocessing.** Resting-state BOLD fMRI data were preprocessed as previously described.<sup>9</sup> Briefly, the imaging data were brain-extracted, motion-corrected, slice timing-corrected, spatially smoothed (Gaussian filter, full width at half maximum = 5 mm), high-pass-filtered, and coregistered (linear, 6 *df*) to the T1-postcontrast image using FSL (<http://www.fmrib.ox.ac.uk/fsl>).<sup>21</sup> Independent-components analysis (MELODIC-FIX; <https://fsl.fmrib.ox.ac.uk/fsl/fslwiki/MELODIC>; <https://fsl.fmrib.ox.ac.uk/fsl/fslwiki/FIX>) was used to remove artifacts due to scanner noise and head motion.

**Mask Generation.** Multiple linear regression was performed on each subject’s native resting-state BOLD data using time-series extracted from the contrast-enhancing tumor mask and control hemisphere mask. The model also included 6 motion confound

regressors (3 translations and 3 rotations). Two Z-statistic images were then generated, indicating the similarity of each voxel's dynamics to the dynamics of the contrast-enhancing mask and the control hemisphere mask. Because the time-series from the 2 masks are uncorrelated, they can be combined to improve the signal-to-noise properties of the BOLD asynchrony metric.<sup>9</sup> Thus, BOLD asynchrony was defined as the difference of the 2 Z-statistic images ( $z_{tumor} - z_{control}$ ) so that values are negative (blue) in normal brain and positive (red) in regions of tumor-related vascular dysregulation. Moreover, a positive BOLD asynchrony value in a voxel denotes BOLD dynamics that are asynchronous with normal cardiovascular fluctuations. BOLD asynchrony maps were thresholded at  $Z > 1.68$  (corresponding to a  $P$  value  $< .05$  on a standardized normal distribution) to denote voxels with abnormal values, as described previously.<sup>9</sup>

### Spatial Decay

To compute the spatial rate of change in the BOLD asynchrony and T2-FLAIR images, we extracted all voxels within a 3-cm radius of the contrast-enhancing tumor and contained within the skull and fit them to an exponential decay of the form

$$N(t) = N_0 e^{-\lambda t},$$

where  $N$  represents BOLD asynchrony or T2-FLAIR values.

### BOLD and FLAIR Outside Fraction

The BOLD outside fraction (BOF) represents how much of the BOLD asynchronous region is found outside the contrast-enhancing tumor and is calculated by dividing the volume of the BOLD asynchrony mask that extends outside the region of contrast enhancement by the total volume of the BOLD asynchrony mask,

$$BOF = \frac{|BOLD \notin TUMOR|}{|BOLD|}.$$

FLAIR outside fraction (FOF) was computed in a similar way, denoting the fraction of T2-FLAIR hyperintensity outside the contrast-enhancing tumor.

### Statistical Analysis

All statistical tests were performed in Matlab 2019a (MathWorks) and thresholded for significance at  $P < .05$ . The Pearson correlation was calculated using a linear model. Two-tailed Student  $t$  tests were used for all paired comparisons. All proportion data were first transformed using the arcsine transform for fractions.

## RESULTS

### Patient Demographics

We identified 36 patients who underwent standard-of-care imaging with additional resting-state BOLD fMRI before a histologic tumor diagnosis of meningioma. Of these patients, 25 (69%) were diagnosed with grade I meningioma and 11 (31%) were diagnosed with grade II or III meningioma. For this study, the grade II and III meningiomas were grouped together as "high-grade" meningiomas, while grade I tumors were considered "low-grade." The median age of the patients with low-grade tumors was 67 years (range, 29–85 years), and 72%

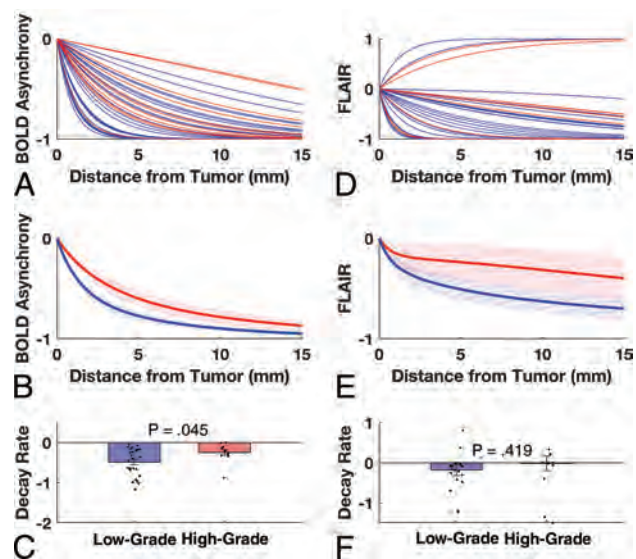


**FIG 1.** BOLD asynchrony decreases with distance from the tumor. *A*, Exponential fits were made to BOLD asynchrony values across all voxels within a 3-cm radius as a function of distance from the tumor for each patient. *Blue lines* represent individual patients with low-grade tumors; *red lines* represent individual patients with high-grade tumors. *B*, The mean BOLD asynchrony is greater for high-grade than low-grade tumors at comparable distances from the tumor. *Shading* represents standard error of the mean. *C*, *Bars* represent the median spatial decay for the low- (blue) and high-grade (red) tumors; *dots* represent decay constants for individual patients. High-grade meningiomas have significantly slower spatial decay rates, indicating that high-grade tumors caused a larger disruption to surrounding vasculature. *D–F*, FLAIR signal did not differ significantly between groups. Note, the *error bars* are very large and extend beyond the visible range.

were women; the median age of patients with high-grade tumors was 59 years (range, 41–78 years), and 45% were women.

### Spatial Decay of BOLD Asynchrony Differs between Low- and High-Grade Meningiomas

We first tested whether there were objective differences in the spatial extent of BOLD asynchrony between low- and high-grade meningiomas. Tumor-related disruption of vascular function in surrounding tissue should result in higher BOLD asynchrony values. To this end, we plotted the BOLD asynchrony signal in each voxel as a function of distance from contrast-enhancing tumor or all brain voxels in a 3-cm radius around the tumor. BOLD asynchrony decreased as a function of distance for all patients (Fig 1A) but decreased faster in low-grade tumors (Fig 1B). A comparison of decay rates showed a significant difference between the 2 groups, with high-grade meningiomas showing a smaller rate (ie, slower spatial decay) than low-grade tumors (high-grade:  $-0.25$ ; low-grade:  $-0.49$ ;  $t$  test,  $P = .045$ ) (Fig 1C). The T2 FLAIR signal also showed a slower decay in high-grade tumors, though this difference was not significant (high-grade:  $-0.25$ ; low-grade:  $-0.45$ ;  $t$  test,  $P = .42$ ) (Fig 1D–F).

### Extent of BOLD Asynchrony and T2-FLAIR Hyperintensity Discriminate Meningioma Grade

Although the spatial-decay analysis is objective, an arbitrary 3-cm margin is likely to include voxels affected and unaffected by

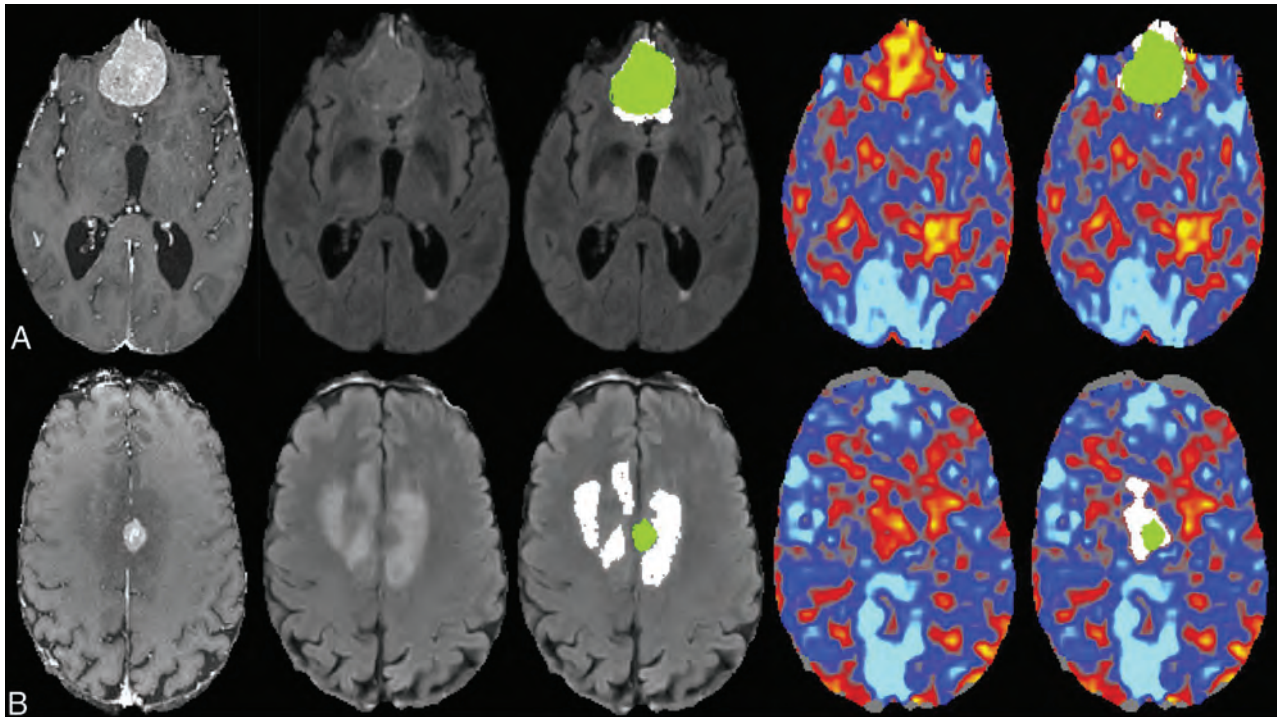


**FIG 2.** Representative axial slices from a 77-year-old male patient (A) with a grade I meningioma and a 75-year-old male patient (B) with a grade II meningioma. The first 3 columns show the T1-weighted postcontrast image, the T2-FLAIR, and the T2-FLAIR with overlaid masks representing the contrast enhancement (green) and the T2-FLAIR hyperintensity outside the tumor (white). The fourth and fifth columns show the BOLD asynchrony map and the BOLD asynchrony map with overlaid masks representing the contrast enhancement (green) and the BOLD asynchrony outside the tumor (white). The high-grade tumor (B) has BOLD asynchrony extending further outside the region of contrast enhancement than the low-grade tumor.

tumor, resulting in a mixture of low and high decay rates, which may underestimate differences between groups. To address this issue, we used subjective, expert-drawn masks of the elevated BOLD asynchrony to estimate the size of the tumor-related increases in BOLD asynchrony and determine whether it differed across grades. Sample T1-weighted postcontrast, T2-FLAIR, and BOLD asynchrony images from patients with grade I and II tumors are shown in Fig 2. The BOF and FOF are greater in the high-grade tumor than in the low-grade tumor.

The mean BOF across subjects was significantly greater in the high-grade than the low-grade meningiomas (high-grade: 0.33; low-grade: 0.17;  $t$  test,  $P < .001$ ) (Fig 3A). We also found that the mean FOF was higher in the high-grade tumors (0.43 versus 0.23,  $P = .092$ ), though this did not reach significance (Fig 3B). A receiver-operating characteristic curve was generated for the BOF (Fig 3C) and FOF (Fig 3D) to assess how well these 2 measures can discriminate between the 2 groups. The area under the curve (AUC) for the BOF was 0.88, while for FOF, it was 0.67. Sample cases in which BOF and FOF were discordant in their tumor-grade prediction are shown in the Online Supplemental Data.

### Combining Structural and Functional Imaging Improves Discrimination

BOLD asynchrony and T2-FLAIR hyperintensity discriminate meningioma grade through fundamentally different processes, ie,

vascular function versus edema, and in fact, the 2 measures were not significantly correlated ( $r = 0.12$ ,  $P = .50$ ). This finding suggests that combining the 2 measures could improve discriminability over either measure alone. A weighted mean fit showed that the best model ( $0.86 \times \text{BOF} + 0.14 \times \text{FOF}$ ) resulted in a modest improvement in discriminability (high-grade mean: 0.34; low-grade mean: 0.18;  $t$  test,  $P < .001$ ) (Fig 4A) with an area under the curve of 0.90 (Fig 4B).

### DISCUSSION

Accurate preoperative prediction of tumor grade enhances patient counseling and may inform clinical decision-making regarding treatment of patients when there is clinical equipoise. For instance, a suspected high-grade meningioma may merit more aggressive treatment than a suspected low-grade meningioma and advanced knowledge that a tumor shows brain invasion might alter the surgical approach. Furthermore, current pathologic diagnosis of brain invasion is limited by sampling error. A radiographic biomarker of brain invasion could greatly increase the likelihood of successfully sampling invasive tissue and correctly grading the tumor.

In this study, we looked at the patterns of BOLD asynchrony and T2-FLAIR hyperintensity in grade I, II, and III meningiomas. The spatial decay rate of BOLD asynchrony was significantly different in low- and high-grade meningiomas. Furthermore, because brain invasion is often focal and not uniformly distributed, we used expert-drawn masks to

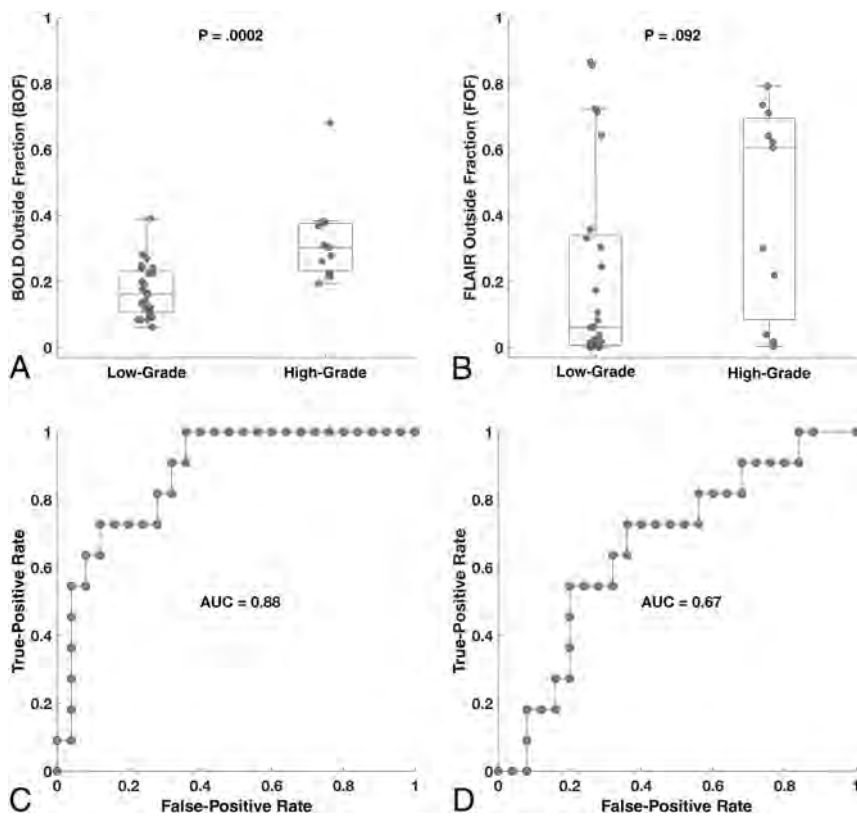


**FIG 3.** Boxplots demonstrate that high-grade meningiomas are characterized by greater BOF values than low-grade meningiomas (A). B, FOF values were higher in high-grade meningiomas, though this did not reach significance. Receiver operating characteristic curves for BOF show high discriminability for grade (C), while FOF demonstrates marginal discriminability (D).

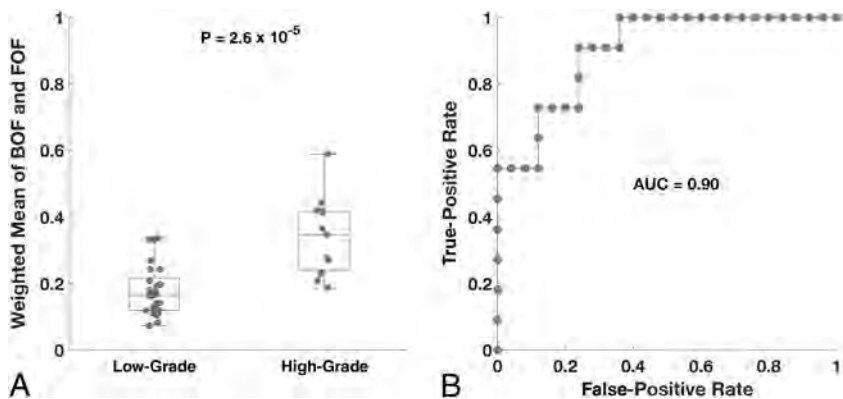


**FIG 4.** A, The weighted mean of BOF and FOF shows a difference comparable with the BOF alone. B, The discriminability of the weighted model is better, though only marginally, than the BOF alone.

measure the extent of BOLD asynchrony outside the contrast-enhancing tumor (BOF) and found even better discriminability between low- and high-grade meningiomas. Previous work<sup>6,7</sup> has suggested that peritumoral edema is associated with high-grade meningiomas; however, in our sample, the FOF was not significantly different between the 2 tumor groups.

BOF and FOF have areas under the curve of 0.88 and 0.67, respectively, suggesting that BOLD asynchrony is superior to T2-FLAIR hyperintensity for discriminating tumor grade. When combining the 2, the area under the curve improves slightly to 0.90. This outcome is consistent with our understanding that T2-FLAIR and BOLD asynchrony measure independent physiologic processes—edema for T2-FLAIR hyperintensity and abnormal vascular function for BOLD asynchrony. This discrimination accuracy is comparable with previously published values of AUC = 0.946 for DTI histogram analysis and AUC = 0.86 for multiple standard-of-care imaging features.<sup>5,8</sup> Although generating a weighted mean estimate would likely be impractical for a typical clinician, visual inspection of the T2-FLAIR and BOLD asynchrony maps may allow a fast and accurate determination of tumor grade by a trained neuroradiologist or neurosurgeon. Prospective application of this methodology for predicting grade will be needed to determine its true efficacy, accessibility, and value to clinicians.

Prior work in glioma has shown that BOLD asynchrony correlates with tumor burden in gliomas, suggesting that the presence of local tumor cells causes vascular dysregulation.<sup>10</sup> However, all patients with grade I meningiomas in our cohort had a BOF greater than 0, despite having no evidence of histologic brain invasion. Although the lack of detectable invasion may be at least partly due to tissue-sampling error, the positive BOFs suggest that BOLD asynchrony outside of the region of contrast enhancement is not solely caused by local tumor burden but also by other physiologic mechanisms such as the compression of peritumoral small vessels, compression of large vessels that supply peritumoral small vessels, or compression of local neurons that lead to vascular dysregulation.

One limitation of this study is its retrospective nature and relatively small sample size, which prevented the use of a subset of patients as an independent validation set. Furthermore, due to their rarity, grade III meningiomas could not be analyzed separately from grade II tumors; thus, it is unknown whether BOLD asynchrony can differentiate grade II and III tumors. Finally, future studies using MR imaging–

localized biopsies will be necessary to assess how accurately BOLD asynchrony can predict local tumor burden and whether it can be used as a tool for identifying the locations of putative invasion.

## CONCLUSIONS

This study provides preliminary evidence that BOLD asynchrony maps are a useful adjunct for discriminating grade and brain invasion in meningiomas through both the spatial decay rate and BOF.

Disclosures: Daniel S. Chow—UNRELATED: Consultancy: Canon Medical; Employment: University of California, Irvine; Grants/Grants Pending: Novocure.\* Peter D. Canoll—UNRELATED: Employment: Columbia University. Jack Grinband—UNRELATED: Employment: Columbia University. \*Money paid to the institution.

## REFERENCES

1. Kshetry VR, Ostrom QT, Kruchko C, et al. **Descriptive epidemiology of World Health Organization grades II and III intracranial meningiomas in the United States.** *Neuro Oncol* 2015;17:1166–73 CrossRef Medline
2. Louis DN, Perry A, Reifenberger G, et al. **The 2016 World Health Organization Classification of Tumors of the Central Nervous System: a summary.** *Acta Neuropathol* 2016;131:803–20 CrossRef Medline
3. Willis J, Smith C, Ironside JW, et al. **The accuracy of meningioma grading: a 10-year retrospective audit.** *Neuropathol Appl Neurobiol* 2005;31:141–49 CrossRef Medline
4. Ostrom QT, Cioffi G, Gittleman H, et al. **CBTRUS Statistical Report: Primary Brain and Other Central Nervous System Tumors Diagnosed in the United States in 2012–2016.** *Neuro Oncol* 2019;21:v1–100 CrossRef Medline
5. Coroller TP, Bi WL, Huynh E, et al. **Radiographic prediction of meningioma grade by semantic and radiomic features.** *PLoS One* 2017;12:e0187908 CrossRef Medline
6. Kim BW, Kim MS, Kim SW, et al. **Peritumoral brain edema in meningiomas: correlation of radiologic and pathologic features.** *J Korean Neurosurg Soc* 2011;49:26–30 CrossRef Medline
7. Adeli A, Hess K, Mawrin C, et al. **Prediction of brain invasion in patients with meningiomas using preoperative magnetic resonance imaging.** *Oncotarget* 2018;9:35974–82 CrossRef Medline
8. Wang S, Kim S, Zhang Y, et al. **Determination of grade and subtype of meningiomas by using histogram analysis of diffusion-tensor imaging metrics.** *Radiology* 2012;262:584–92 CrossRef Medline
9. Chow DS, Horenstein CI, Canoll P, et al. **Glioblastoma induces vascular dysregulation in nonenhancing peritumoral regions in humans.** *AJR Am J Roentgenol* 2016;206:1073–81 CrossRef Medline
10. Bowden SG, Gill BJ, Englander ZK, et al. **Local glioma cells are associated with vascular dysregulation.** *AJNR Am J Neuroradiol* 2018;39:507–14 CrossRef Medline
11. Jiang Z, Krainik A, David O, et al. **Impaired fMRI activation in patients with primary brain tumors.** *Neuroimage* 2010;52:538–48 CrossRef Medline
12. Murphy K, Birn RM, Handwerker DA, et al. **The impact of global signal regression on resting state correlations: are anti-correlated networks introduced?** *Neuroimage* 2009;44:893–905 CrossRef Medline
13. Shmueli K, van Gelderen P, de Zwart JA, et al. **Low-frequency fluctuations in the cardiac rate as a source of variance in the resting-state fMRI BOLD signal.** *Neuroimage* 2007;38:306–20 CrossRef Medline
14. Birn RM, Murphy K, Bandettini PA. **The effect of respiration variations on independent component analysis results of resting state functional connectivity.** *Hum Brain Mapp* 2008;29:740–50 CrossRef Medline
15. Scholvinck ML, Maier A, Ye FQ, et al. **Neural basis of global resting-state fMRI activity.** *Proc Natl Acad Sci U S A* 2010;107:10238–43 CrossRef Medline
16. Power JD, Plitt M, Laumann TO, et al. **Sources and implications of whole-brain fMRI signals in humans.** *Neuroimage* 2017;146:609–25 CrossRef Medline
17. Glasser MF, Coalson TS, Bijsterbosch JD, et al. **Using temporal ICA to selectively remove global noise while preserving global signal in functional MRI data.** *Neuroimage* 2018;181:692–717 CrossRef Medline
18. Raemaekers M, Schellekens W, Petridou N, et al. **Knowing left from right: asymmetric functional connectivity during resting state.** *Brain Struct Funct* 2018;223:1909–22 CrossRef Medline
19. Murphy K, Birn RM, Bandettini PA. **Resting-state fMRI confounds and cleanup.** *Neuroimage* 2013;80:349–59 CrossRef Medline
20. Desjardins AE, Kiehl KA, Liddle PF. **Removal of confounding effects of global signal in functional MRI analyses.** *Neuroimage* 2001;13:751–58 CrossRef Medline
21. Jenkinson M, Beckmann CF, Behrens TE, et al. **FSL.** *Neuroimage* 2012;62:782–90 CrossRef Medline

# Resting-State Functional MRI for Determining Language Lateralization in Children with Drug-Resistant Epilepsy

N.L. Phillips, A.S. Shatil, C. Go, A. Robertson, and E. Widjaja



## ABSTRACT

**BACKGROUND AND PURPOSE:** Task-based fMRI is a noninvasive method of determining language dominance; however, not all children can complete language tasks due to age, cognitive/intellectual, or language barriers. Task-free approaches such as resting-state fMRI offer an alternative method. This study evaluated resting-state fMRI for predicting language laterality in children with drug-resistant epilepsy.

**MATERIALS AND METHODS:** A retrospective review of 43 children with drug-resistant epilepsy who had undergone resting-state fMRI and task-based fMRI during presurgical evaluation was conducted. Independent component analysis of resting-state fMRI was used to identify language networks by comparing the independent components with a language network template. Concordance rates in language laterality between resting-state fMRI and each of the 4 task-based fMRI language paradigms (auditory description decision, auditory category, verbal fluency, and silent word generation tasks) were calculated.

**RESULTS:** Concordance ranged from 0.64 (95% CI, 0.48–0.65) to 0.73 (95% CI, 0.58–0.87), depending on the language paradigm, with the highest concordance found for the auditory description decision task. Most (78%–83%) patients identified as left-lateralized on task-based fMRI were correctly classified as left-lateralized on resting-state fMRI. No patients classified as right-lateralized or bilateral on task-based fMRI were correctly classified by resting-state fMRI.

**CONCLUSIONS:** While resting-state fMRI correctly classified most patients who had typical (left) language dominance, its ability to correctly classify patients with atypical (right or bilateral) language dominance was poor. Further study is required before resting-state fMRI can be used clinically for language mapping in the context of epilepsy surgery evaluation in children with drug-resistant epilepsy.

**ABBREVIATIONS:** ACT = auditory category task; ADDT = auditory description decision task; DRE = drug-resistant epilepsy; IC = independent component; ICA = independent component analysis; LI = laterality index; rs-fMRI = resting-state fMRI; SWG = silent word generation; tb-fMRI = task-based fMRI; VF = verbal fluency.

Pediatric drug-resistant epilepsy (DRE) is defined as poorly controlled seizures despite treatment on  $\geq 2$  appropriately used antiseizure medications.<sup>1</sup> Surgery is recommended when seizures have not responded to treatment with antiseizure medications.

Received September 25, 2020; accepted after revision February 16, 2021.

From the Neurosciences and Mental Health Program (N.L.P., A.S.S., A.R., E.W.), The Hospital for Sick Children, Peter Gilgan Centre for Research and Learning, Toronto, Ontario, Canada; and Department of Psychology (N.L.P.), Division of Neurology (C.G., E.W.), and Department of Diagnostic Imaging (E.W.), The Hospital for Sick Children, Toronto, Ontario, Canada

The opinions, results, and conclusions are those of the authors, and no endorsement by the Ontario Brain Institute is intended or should be inferred.

This research was supported by EpLink, the Epilepsy Research Program of the Ontario Brain Institute. The Ontario Brain Institute is an independent nonprofit corporation, funded partially by the Ontario government.

Please address correspondence to E. Widjaja, MD, Diagnostic Imaging, Hospital for Sick Children, 555 University Ave, Toronto, ON M5G 1X8, Canada; e-mail: elysa.widjaja@sickkids.ca

Indicates article with online supplemental data.

<http://dx.doi.org/10.3174/ajnr.A7110>

Surgery could result in seizure freedom in up to 90% of children with DRE.<sup>2,3</sup> The risk of language impairment is a key consideration in determining surgical candidacy and surgical planning. In neurologically intact individuals, language is supported by a predominantly left-lateralized frontal-temporal network. Up to 25% of children and adults with epilepsy have atypical language dominance (ie, language lateralized to the right hemisphere or bilaterally across both the left and right hemispheres) compared with only 3% of healthy children and adults.<sup>4</sup> Hence, determining hemispheric language dominance during presurgical evaluation is critical in preventing postsurgical language deficits in children with DRE.

The intracarotid amobarbital procedure, previously known as the Wada test, is currently the criterion standard for determining language laterality. Electrical stimulation mapping is also considered the criterion standard for functional localization. More recently, however, task-based fMRI (tb-fMRI) has been commonly used for establishing language laterality in clinical practice

**Table 1: Language task-based fMRI tasks**

Language Task	Description (Task and Control Condition)
ADDT	Task: decide whether a sentence is true or false and taps leg if correct. Control: listen to reverse speech and taps leg each time in response to hearing a beep
ACT	Task: decide whether a list of words falls into a previously presented category (eg, animals) and taps leg when target word matches category. Control: listen to reverse speech and taps leg each time in response to hearing a beep
VF	Task: generate words from a series of letters, ie, must generate as many words covertly/silently in head that begin with a particular letter (5 letters presented per task block via MR imaging goggle system). Control: constant right hand tapping during each 30-minute control block
SWG	Task: generate verbs from a series of nouns, ie, must generate as many verbs covertly/silently from each noun presented (5 nouns presented per task block via MR imaging goggle system). Control: constant left hand tapping during each 30-minute control block

because it is less invasive and carries less risk. Tb-fMRI has shown good concordance with the intracarotid amobarbital procedure, with concordance rates of 87% and 81% in adults with medial-temporal and extratemporal epilepsy, respectively.<sup>5</sup> Concordance rates in pediatric epilepsy have been slightly lower, with a recent meta-analysis of 21 studies finding an overall concordance rate between the intracarotid amobarbital procedure and tb-fMRI of 76% and sensitivity and specificity of 0.72 and 0.60, respectively, in correctly classifying typical-versus-atypical language lateralization.<sup>6</sup> However, not all children are suitable for tb-fMRI. Children who are very young or have cognitive/intellectual disabilities cannot always complete the tasks necessary for tb-fMRI. Task-free approaches such as resting-state fMRI (rs-fMRI) may offer an alternative to task-based approaches, especially for children in whom tb-fMRI is contraindicated.

Preliminary evidence suggests that rs-fMRI is promising for lateralizing language in healthy<sup>7,8</sup> and clinical populations of adults with tumor<sup>9,10</sup> and epilepsy,<sup>11,12</sup> though concordance rates are highly variable across studies. Only 2 studies have examined the use of rs-fMRI to determine language dominance in children with epilepsy compared with tb-fMRI,<sup>13,14</sup> and these 2 studies were limited by the use of visual assessment for classifying language laterality and/or small sample size, and in 1 study, bilateral language lateralization was excluded. This study aimed to evaluate the validity of rs-fMRI in predicting language laterality compared with tb-fMRI in children with DRE.

## MATERIALS AND METHODS

### Participants

This retrospective study included 51 children with DRE (7–18 years of age) who were undergoing epilepsy surgery evaluation at the Hospital for Sick Children, Toronto, Ontario, Canada. We excluded 8 children: Seven did not have tb-fMRI, and in 1 case, the rs-fMRI data were excluded due to motion. This study included 43 children who had data on rs-fMRI and at least 1 of 4 language tb-fMRI paradigms. Ethics approval was obtained from the local research ethics board. The baseline characteristics of the sample are shown in the Online Supplemental Data.

### MR Imaging

MR imaging was performed using a 3T scanner (Achieva, Philips Healthcare,  $n = 27$ , or Magnetom Skyra, Siemens,  $n = 16$ ). The rs-fMRI and tb-fMRI were acquired using gradient EPI. The scan

parameters for rs-fMRI and tb-fMRI on the Achieva scanner were the following: TR = 2000 ms, TE = 30 ms, flip angle = 90°, FOV = 220 mm, voxel size = 2.5 × 2.5 × 3.5 mm, and 180 volumes. The scan parameters for rs-fMRI and tb-fMRI on Magnetom Skyra were the following: TR = 2000 ms, TE = 30 ms, flip angle = 90°, FOV = 220 mm, voxel size = 2.3 × 2.3 × 2.0 mm, and 180 volumes. Rs-fMRI required children to lie still with their eyes closed for the duration of the 6-minute scan. All patients also underwent volumetric T1-weighted imaging. Rs-fMRI was acquired before the tb-fMRI.

A block design consisting of alternating 30-second blocks of experimental and control conditions was used. Each task consisted of 12 blocks (6 task blocks and 6 control blocks) with a total task time of 6 minutes. Auditory stimuli were presented via headphones. Visual stimuli were presented via MR imaging goggles.

### Tb-fMRI Language Paradigms

The tb-fMRI involved 4 standard language paradigms: verbal fluency (VF), silent word generation (SWG), auditory description decision task (ADDT), and auditory category task (ACT) (Table 1).

### Rs-fMRI Data Preprocessing

Rs-fMRI images were processed with FSL software (<http://www.fmrib.ox.ac.uk/fsl>). Nonbrain regions including the skull were removed from all structural T1 images by the FSL Brain Extraction Tool (<http://fsl.fmrib.ox.ac.uk/fsl/fslwiki/BET>)<sup>15</sup> with a fractional intensity threshold of 0.1. Images were motion-corrected using the FSL motion correction of functional images using the Linear Image Registration Tool (FLIRT; <https://fsl.fmrib.ox.ac.uk/fsl/fslwiki/FLIRT>).<sup>16</sup> Data were scrubbed by removing images showing root mean square relative displacement of >0.25 mm or root mean square absolute displacement of >2.5 mm.<sup>17</sup> All scrubbed data were post-processed using the MELODIC 3.0 tool (<https://fsl.fmrib.ox.ac.uk/fsl/fslwiki/MELODIC>).<sup>18</sup> To eliminate noise due to slow temporal drifts, we used a high-pass filter with the default cutoff value 100 seconds (0.01 Hz). Spatial smoothing was performed by the full width at half maximum Gaussian kernel of 5 mm. All functional images were linearly coregistered to the structural image using FLIRT<sup>16,19</sup> affine transformation with 7 degrees of freedom ( $df$ ). Later, spatial registration of fMRI to the high-resolution standard Montreal Neurological Institute 152 T1 template was performed with 12  $df$ .

## Independent Component Analysis

Single-subject independent component analysis (ICA) was performed to extract language networks from resting-state data. For each subject, the maximum (mean = 51 [SD, 10]) possible independent components (ICs) were extracted. IC spatial maps were thresholded with the alternative hypothesis tested at a voxel-based  $P$  value  $> .5$  for true activation (signal) versus null (noise). An automated algorithm was used to select “signal” from “noise” ICs. First, an expert (N.L.P.) manually hand-labeled IC maps from 23 subjects as signal or noise based on overlap with gray matter, number, and dimensions of clusters; extent of overlap with brain boundaries; and temporal features of the ICs.<sup>20</sup> Labeled signal ICs were then used to train the FMRIB ICA-based X-noiseifier (FIX; <https://fsl.fmrib.ox.ac.uk/fsl/fslwiki/FIX>) hierarchical classifier.<sup>21,22</sup> Using the study-specific training dataset, we chose a threshold of 40 for categorizing the ICs in the remaining 20 subjects, accurately based on 2 accuracy parameters: the highest true-positive rate (proportion of signal components correctly labeled) and the lowest true-negative rate (proportion of noise components correctly labeled). The ICs that were selected as signal by the algorithm were visually inspected to confirm that they were signal ICs.

To select the language IC from denoised data, we calculated<sup>9</sup> Dice coefficients—ie,  $Dice = \frac{|X \cap Y|}{|X + Y|}$  were used to measure the degree of overlap between ICs and language regions, including the inferior frontal gyrus, middle temporal gyrus, superior temporal gyrus, angular gyrus, and supramarginal gyrus, identified using the Willard atlas.<sup>23,24</sup> The IC with the highest Dice coefficient (range, 0–1, with 1 indicating the greatest spatial overlap) was selected as the language IC for each participant. These components were then converted into  $z$  score maps using the following thresholds:  $z = 1.5$ , 2.5, and 3 (ie,  $P = .05$ , .01, and .001). Visual identification of noise components and subsequent identification and ranking of language ICs were conducted by 2 authors (N.L.P. and E.W.,  $\kappa = 0.84$ ), to validate and ensure the accuracy of the automated procedures described above.

## Tb-fMRI Analysis

Tb-fMRI images were processed using Analysis of Functional Neuro Images (AFNI; <http://afni.nimh.nih.gov/afni>). Preprocessing included registering the raw EPI volumes to the EPI base volume, outlier detection and censoring outlier time points, and section-timing correction. The images were then smoothed with a 5.0-mm full width at half maximum Gaussian kernel. For each task, activation maps were generated using the FSL General Linear Model (<http://fsl.fmrib.ox.ac.uk/fsl/fslwiki/GLM>) analysis.

## Language Laterality

The laterality index (LI) was calculated for rs-fMRI and tb-fMRI data using the standard formula,  $LI = (Left - Right) / (Left + Right)$ ,<sup>25</sup> where Left and Right are the number of voxels in the left and right hemispheres in the given ROIs for each threshold, respectively. The LI values ranged from  $-1$  (right-dominant) to  $+1$  (left-dominant) with a cutoff of  $\pm 0.2$ . The LIs of selected ICs from rs-fMRI were calculated at a  $z$ -threshold ( $z = 1.5$ , 2.5, and 3). The LI for tb-fMRI was first calculated at 3 thresholds:  $t = 2$  ( $P = .05$ ),  $t = 2.5$  ( $P = .01$ ), and  $t = 3.5$  ( $P = .001$ ). If laterality

**Table 2: Language laterality based on resting-state and task-based fMRI**

Study	Laterality					
	Left		Right		Bilateral	
	No.	%	No.	%	No.	%
Rs-fMRI <sup>a</sup>						
$z = 1.5$	36	84%	3	7%	4	9%
$z = 2.5$	34	79%	3	7%	6	14%
$z = 3$	35	81%	3	7%	5	12%
Tb-fMRI <sup>a</sup>						
ADDT, $n = 40$	36	90%	1	3%	3	8%
ACT, $n = 43$	36	84%	2	5%	5	12%
VF, $n = 40$	32	80%	1	3%	7	18%
SWG, $n = 42$	35	83%	1	2%	6	14%

<sup>a</sup> LI calculated with a cutoff score  $\pm 0.2$ .

differed across the 3 thresholds for a task, the most common classification was chosen (eg, if a subject was classified as bilateral on the ADDT language paradigm at  $t = 2$  but left-lateralized at  $t = 2.5$  and  $t = 3.5$ , he or she was classified as left-lateralized for the ADDT paradigm). This approach is consistent with that of a previous study.<sup>26</sup>

## Statistical Analysis

Data were analyzed using SPSS Statistics (Version 26.0; IBM). Concordance between the 4 tb-fMRI language paradigms and rs-fMRI at each threshold was calculated using the following: 1) descriptive statistics (frequencies) by laterality (left, right, bilateral), and 2) the overall agreement rate with 95% CIs. Subgroup analyses were conducted comparing the agreement between rs-fMRI and tb-fMRI based on scanner type, age (younger than 13 years of age or 13 years of age or older), sex, side of seizure onset, and handedness. The agreement between the LI and visual inspection of rs-fMRI language hemispheric dominance was also assessed.

## RESULTS

Language laterality findings for tb-fMRI and rs-fMRI are presented in Table 2.

Across the 4 language tasks, tb-fMRI suggested left dominance in 80%–90%, right dominance in 2% to 5%, and bilateral language dominance in 8%–14% of patients. Rs-fMRI suggested left dominance in 79%–84%, right dominance in 7%, and bilateral language dominance in 9%–14% of patients, depending on the  $z$ -threshold.

The Online Supplemental Data show concordance between the 4 language tb-fMRI paradigms and rs-fMRI at each  $z$ -threshold. Overall, concordance rates for language laterality between rs-fMRI and tb-fMRI were highest for the ADDT paradigm and ranged from 0.73 (95% CI, 0.58–0.87) to 0.70 (95% CI, 0.55–0.85), with higher concordance rates found at rs-fMRI thresholds of  $z = 1.5$  and  $z = 3$ , compared with  $z = 2.5$ . With respect to the ACT paradigm, concordance was highest with rs-fMRI at a threshold of  $z = 1.5$ , with an agreement rate of 0.70 (95% CI, 0.55–0.84). Concordance rates for the VF paradigm were the lowest of the tb-fMRI paradigms and ranged from 0.64 (95% CI, 0.48–0.80) to 0.65 (95% CI, 0.50–0.80). Last, concordance between the rs-fMRI and SWG paradigms, which was highest at

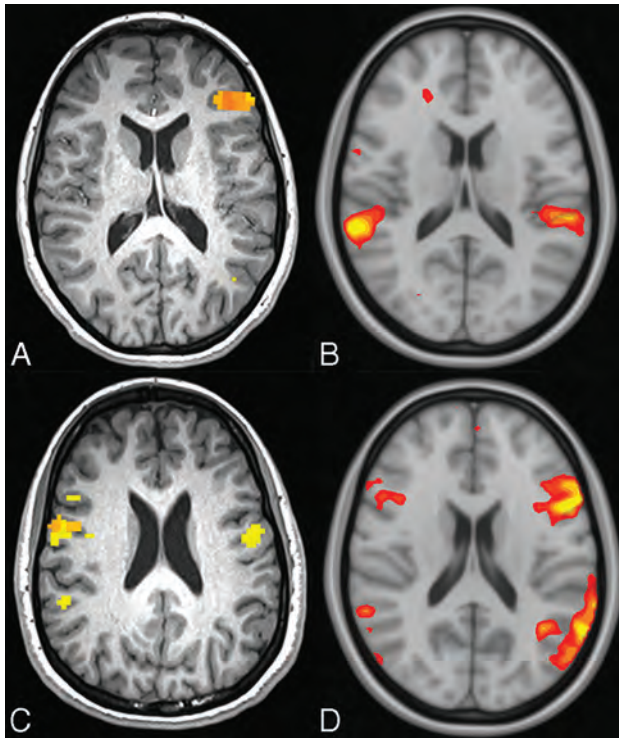


**FIGURE.** An 11-year-old child (A and B) with left-lateralized language on tb-fMRI and bilateral language on rs-fMRI. A 14-year-old adolescent (C and D) with bilateral language on tb-fMRI and left-lateralized language on rs-fMRI.

the most stringent rs-fMRI threshold of  $z = 3$ , ranged from 0.69 (95% CI, 0.54–0.84) to 0.66 (95% CI, 0.52–0.8)

Between 78% and 83% of patients identified as left-lateralized on tb-fMRI were correctly classified as left-lateralized on rs-fMRI. In contrast, no patients identified as right-lateralized on tb-fMRI were correctly classified. Instead, all patients were classified as left-lateralized on rs-fMRI. No patients identified as bilateral on tb-fMRI were classified correctly. Most were classified as left-lateralized (80%–100%) (Figure), while the rest were classified as right-lateralized (0%–20%; Online Supplemental Data).

Subgroup analyses showed that there were no significant differences in agreement between rs-fMRI and tb-fMRI based on scanner type, age, sex, side of seizure onset, or handedness (all  $P > .05$ ) (Online Supplemental Data).

Concordance between the LI and visual inspection of rs-fMRI language hemispheric dominance was highest at a threshold of  $z = 2.5$ ; (0.79; 95% CI, 0.78–0.80), followed by  $z = 3$  (0.73; 95% CI, 0.72–0.74) and lowest at  $z = 1.5$  (0.66; 95% CI, 0.65–0.67). Four patients identified as left-lateralized on rs-fMRI LI were classified as bilateral on visual inspection.

## DISCUSSION

This study examined the validity of rs-fMRI for predicting language laterality in children with DRE by comparing rs-fMRI with a panel of established tb-fMRI language paradigms. We found concordance rates of 64%–73% between rs-fMRI and tb-fMRI. While rs-fMRI correctly identified most patients with left-lateralization, it did not correctly classify those with bilateral or right

dominance. A small group of patients was classified as having language dominance in the contralateral hemisphere on rs-fMRI compared with tb-fMRI. Specifically, all patients classified as right-lateralized for language on tb-fMRI were classified as left-lateralized on rs-fMRI, and those who were classified as left-lateralized on tb-fMRI were right-lateralized on rs-fMRI, albeit the number of cases was small.

Earlier studies<sup>13,14</sup> involving pediatric DRE found higher concordance rates between rs-fMRI and tb-fMRI compared with our study. Desai et al<sup>13</sup> found a concordance rate of 93% in 28 children with DRE. Rs-fMRI correctly classified 23 (92%) patients as left- and 3 (100%) patients as right-lateralized for language. However, the authors relied on visual inspection by a neuroradiologist to make a clinical judgment regarding the following: 1) identification of each patient's rs-fMRI language networks extracted using ICA, and 2) classification of language laterality on tb-fMRI and rs-fMRI. Visual inspection of individual ICs is time- and labor-intensive and potentially less replicable. In contrast, we have developed an automated approach for selecting signal from noise ICs and then used a data-driven approach to select the IC that contained the language network by comparing our signal ICs with a standard language network template using the Dice coefficient measure. This approach is automated and can be consistently and objectively applied across studies and clinical samples. Nath et al<sup>14</sup> found a concordance rate of 80% between rs-fMRI (using a seed-based approach to identify language networks) and traditional methods of language lateralization (tb-fMRI, intracarotid amobarbital procedure, or cortical-stimulation mapping) in children with epilepsy. Nevertheless, the sample size was small, and patients with bilateral language lateralization were excluded. Hence, the results do not extend to children with bilateral language lateralization. In addition, language lateralization for tb-fMRI was based on frontal (Broca) seed regions rather than frontal-temporal seed regions, and only 5 participants had tb-fMRI data, which was based on only 1 language paradigm (verb generation). This finding is important because language lateralization determined across several paradigms is considered more reliable, especially in those with bilateral lateralization.<sup>27</sup>

A recent study of adults with DRE<sup>11</sup> found that language dominance was less lateralized on seed-based rs-fMRI data compared with tb-fMRI. The authors also found concordance rates of between 20% and 63%, with the highest concordance rate found when using a frontal-temporal mask (compared with just frontal or temporal) and at the top 10% threshold of connections.<sup>11</sup> Furthermore, they showed that the method for calculating LI for rs-fMRI influenced the classification of language lateralization, with concordance of dominance classifications ranging from 20% to 30% for the intrahemispheric LI method and 50%–63% for the intrahemispheric-minus-interhemispheric difference LI method. We have used the commonly used intrahemispheric LI method to evaluate language laterality. While we found higher concordance rates using the intrahemispheric LI approach compared with Rolinski et al,<sup>11</sup> our overall concordance rate was within a similar range. Rolinski et al also found that 40% of patients who were left-dominant on tb-fMRI showed bilateral language dominance on rs-fMRI. While we found similar numbers of bilateral language dominance on rs-fMRI relative to tb-fMRI, all of those

that were found to have bilateral dominance on rs-fMRI were left-lateralized on tb-fMRI, and most who were bilateral-dominant on tb-fMRI were left-lateralized on rs-fMRI.

In our study, the concordance rate between rs-fMRI and tb-fMRI was variable, depending on the tb-fMRI language paradigm, with the highest concordance rates found for ADDT. Most previous studies have compared rs-fMRI with just 1 language paradigm.

However, different language paradigms have been shown to activate different brain regions, possibly accounting for the variable concordance rates. The ADDT is the most reliable activator of the frontal (inferior frontal gyrus, prefrontal cortex) and temporal (superior and middle temporal gyri) language networks,<sup>28</sup> possibly explaining the higher concordance rate found in our study. In contrast, the remaining language paradigms were largely frontal- or temporal-dominant tasks. Our results highlight the need to validate rs-fMRI against a battery of tb-fMRI language paradigms in research as well as clinical practice because results may vary.

This study has important clinical implications for the use of rs-fMRI in presurgical planning for children with DRE. There is a growing trend of using rs-fMRI to lateralize language in patients who are not cooperative or may require light sedation. We found that there was greater agreement with typical language lateralization but high discordance for atypical language lateralization with tb-fMRI. Our findings suggest that rs-fMRI should not be used as the sole method for lateralizing language in uncooperative or sedated patients in clinical practice and should not replace tb-fMRI for lateralizing language. Further work is required to compare rs-fMRI language lateralization with the intracarotid amobarbital procedure and to validate our findings across institutions.

The 2 commonly used methods for analyzing rs-fMRI to lateralize language are ICA<sup>9,12,13,29</sup> or seed-based<sup>11</sup> approaches. ICA is data-driven and can be performed without any a priori assumptions. A disadvantage of the ICA approach is that individual IC maps may not depict the entirety of a network if the ICA order is too high—that is, splitting of a network into subnetworks tends to occur at a high ICA order. It is possible that different ICs depicted right- and left-lateral aspects of the language network. We have used the IC with the highest Dice coefficient as the language IC, which could potentially have failed to identify additional ICs that represent language subnetworks, thereby misclassifying language laterality. However, this approach has been used by several investigators for assessing language IC.<sup>3,12,29</sup> Branco et al<sup>9</sup> have extracted a mean of 66.3 ICs, which was higher than the number of ICs in our study, and showed that for each subject, 1 IC was identified as the language component with high confidence by an expert. They also found that there was good agreement between the IC with the highest ranked Dice coefficient and the expert-selected language component. The main advantage of a seed-based approach is that the computation is simple and the interpretation of the results is intuitive.<sup>30</sup> However, the position of the seed region could affect the resulting patterns of the functional system such as the language network. Studies using a seed-based approach have reported lower concordance rates compared with those using the ICA approach. However, there has been no

direct comparison of ICA and seed-based methods. Future study comparing different methods of analyzing rs-fMRI, including-but-not-limited-to seed-based and ICA approaches, may clarify the optimum approach for language lateralization using rs-fMRI.

We compared rs-fMRI with tb-fMRI as the reference standard, but there are limitations with tb-fMRI. A meta-analysis found that tb-fMRI correctly classified 94% of patients with epilepsy as having typical language lateralization based on the intracarotid amobarbital procedure, but only 51% of patients were correctly classified as having atypical language lateralization.<sup>31</sup> Hence, tb-fMRI works well when patients have typical language lateralization but not when patients have atypical language lateralization. While it would have been ideal to compare rs-fMRI with the intracarotid amobarbital procedure (the criterion standard) or electrophysiologic mapping with intracranial electrodes, both procedures are performed only occasionally in clinical practice in children with DRE. Hence, we were unable to compare with these 2 methods in the current study. We considered the whole language network, but a portion of patients with epilepsy are known to demonstrate cross-dominant language laterality and, thus, discordant lateralization between expressive and receptive language regions. This finding could impact calculation of the LI and, therefore, concordance between rs-fMRI and tb-fMRI. The language network in the Willard atlas does not include secondary language areas such as the dorsolateral prefrontal cortex, presupplementary motor area, visual word form area, and basal temporal language area. Hence, these areas were not considered when assessing language laterality, which may potentially impact subsequent classification of hemispheric dominance. Future studies assessing language laterality with rs-fMRI should consider using a language template that incorporates secondary language areas. Finally, we did not consider the dynamic functional connectivity of rs-fMRI, which would have accounted for a time-varying language network connectivity and may impact LI assessment. Hence, both static and dynamic functional connectivity of language networks should be evaluated in future studies determining language lateralization.

## CONCLUSIONS

The current study found only modest concordance of rs-fMRI with tb-fMRI in determining language lateralization in children with DRE. While accuracy rates were reasonably high when children were left-lateralized for language, rs-fMRI was poor at correctly lateralizing language in children who had atypical language dominance compared with tb-fMRI as the reference standard. As such, based on the findings of the current study, caution is recommended if using rs-fMRI to lateralize language function in children with DRE undergoing presurgical evaluation. Further studies comparing rs-fMRI with the intracarotid amobarbital procedure or electrophysiologic mapping, as well as addressing the limitations of the current study, are required to confirm the use of rs-fMRI in presurgical mapping of children with epilepsy.

Disclosures: Anwar S. Shatil—UNRELATED: Employment: The Hospital for Sick Children, Peter Gilgan Centre for Research and Learning. Cristina Go—UNRELATED: Employment: The Hospital for Sick Children, Division of Neurology. Elysa Widjaja—RELATED: Grant: Ontario Brain Institute.\* \*Money paid to the institution.

## REFERENCES

1. Kwan P, Arzimanoglou A, Berg AT, et al. **Definition of drug resistant epilepsy: consensus proposal by the ad hoc Task Force of the ILAE Commission on Therapeutic Strategies.** *Epilepsia* 2010;51:1069–77 CrossRef Medline
2. Ryvlin P, Cross JH, Rheims S. **Epilepsy surgery in children and adults.** *Lancet Neurol* 2014;13:114–26 CrossRef Medline
3. Spencer S, Huh L. **Outcomes of epilepsy surgery in adults and children.** *Lancet Neurol* 2008;7:525–37 CrossRef Medline
4. Berl MB, Zimmaro LA, Khan OI, et al. **Characterization of atypical language activation patterns in focal epilepsy.** *Ann Neurol* 2014;75:33–42 CrossRef Medline
5. Szaflarski JP, Gloss D, Binder JR, et al. **Practice guideline summary: use of fMRI in the presurgical evaluation of patients with epilepsy: report of the Guideline Development, Dissemination, and Implementation Subcommittee of the American Academy of Neurology.** *Neurology* 2017;88:395–402 CrossRef Medline
6. Collinge S, Prendergast G, Mayers ST, et al. **Pre-surgical mapping of eloquent cortex for paediatric epilepsy surgery candidates: evidence from a review of advanced functional neuroimaging.** *Seizure* 2017;26:136–46 CrossRef Medline
7. Tie Y, Rigolo L, Norton IH, et al. **Defining language networks from resting-state fMRI for surgical planning: a feasibility study.** *Hum Brain Mapp* 2014;35:1018–30 CrossRef Medline
8. Smitha KA, Arun KM, Rajesh PG, et al. **Resting-state seed-based analysis: an alternative to task-based language fMRI and its laterality index.** *AJNR Am J Neuroradiol* 2017;38:1187–92 CrossRef Medline
9. Branco P, Seixas D, Deprez S, et al. **Resting-state functional magnetic resonance imaging for language preoperative planning.** *Front Hum Neurosci* 2016;10:11 CrossRef Medline
10. Gohel S, Laino ME, Rajeev-Kumar G, et al. **Resting-state functional connectivity of the middle frontal gyrus can predict language lateralization in patients with brain tumors.** *AJNR Am J Neuroradiol* 2019;40:319–35 CrossRef Medline
11. Rolinski R, You X, Gonzalez-Castillo J, et al. **Language lateralization from task-based and resting state functional MRI in patients with epilepsy.** *Hum Brain Mapp* 2020;41:3133–46 CrossRef Medline
12. Smitha KA, Arun KM, Rajesh PG, et al. **Resting fMRI as an alternative for task-based fMRI for language lateralization in temporal lobe epilepsy patients: a study using independent component analysis.** *Neuroradiology* 2019;61:803–10 CrossRef Medline
13. Desai VR, Vedantam A, Lam SK, et al. **Language lateralization with resting-state and task-based functional MRI in pediatric epilepsy.** *J Neurosurg Pediatr* 2018;23:171–77 CrossRef Medline
14. Nath A, Robinson M, Magnotti J, et al. **Determination of differences in seed-based resting state functional magnetic resonance imaging language networks in pediatric patients with left- and right-lateralized language: a pilot study.** *J Epilepsy Res* 2019;9:93–102 CrossRef Medline
15. Jenkinson M, Pechaud M, Smith S. **BET2: MR-based estimation of brain, skull and scalp surfaces.** In: *Proceedings of the Annual Meeting of the Organization for Human Brain Mapping*; June 12–16, 2005; Toronto, Ontario, Canada
16. Jenkinson M, Bannister P, Brady JM, et al. **Improved optimization for the robust and accurate linear registration and motion correction of brain images.** *Neuroimage* 2002;17:825–41 CrossRef Medline
17. Mongerson CRL, Jennings RW, Borsook D, et al. **Resting-state functional connectivity in the infant brain: methods, pitfalls, and potentiality.** *Front Pediatr* 2017;5:159 CrossRef Medline
18. Beckmann CF, Smith SM. **Probabilistic independent component analysis for functional magnetic resonance imaging.** *IEEE Trans Med Imaging* 2004;23:137–52 CrossRef Medline
19. Jenkinson M, Smith SM. **A global optimization method for robust affine registration of brain images.** *Med Image Anal* 2001;5:143–56 CrossRef
20. Griffanti L, Douaud G, Bijsterbosch J, et al. **Hand classification of fMRI ICA noise components.** *Neuroimage* 2017;154:188–205 CrossRef Medline
21. Griffanti L, Salimi-Khorshidi G, Beckmann CF, et al. **ICA-based artifact removal and accelerated fMRI acquisition for improved resting state network imaging.** *Neuroimage* 2014;95:232–47 CrossRef Medline
22. Salimi-Khorshidi G, Douaud G, Beckmann CF, et al. **Automatic denoising of functional MRI data: combining independent component analysis and hierarchical fusion of classifiers.** *Neuroimage* 2014;90:449–68 CrossRef Medline
23. Altmann A, Ng B, Landau S, et al. **Alzheimer's Disease Neuroimaging Initiative. Regional brain hypometabolism is unrelated to regional amyloid plaque burden.** *Brain* 2015;138:3734–46 CrossRef Medline
24. Shirer WR, Ryali S, Rykhlevskaia E, et al. **Decoding subject-driven cognitive states with whole-brain connectivity patterns.** *Cereb Cortex* 2012;22:158–65 CrossRef Medline
25. Seghier ML. **Laterality index in functional MRI: methodological issues.** *Magn Reson Imaging* 2008;26:594–601 CrossRef Medline
26. Austermuehle A, Cocjin J, Reynolds RC, et al. **Language functional MRI and direct cortical stimulation in epilepsy preoperative planning.** *Ann Neurol* 2017;81:526–37 CrossRef Medline
27. Ruten GJ, Ramsey NF, van Rijen PC, et al. **fMRI-determined language lateralization in patients with unilateral or mixed language dominance according to the Wada test.** *Neuroimage* 2002;17:447–60 CrossRef Medline
28. Vannest J, Karunanayaka PR, Schmithorst VJ, et al. **Language networks in children: evidence from functional MRI studies.** *AJR Am J Roentgenol* 2009;192:1190–96 CrossRef Medline
29. DeSalvo MN, Tanaka N, Douw L, et al. **Resting-state functional MR imaging for determining language laterality in intractable epilepsy.** *Radiology* 2016;281:264–69 CrossRef Medline
30. Lv H, Wang Z, Tong E, et al. **Resting-state functional MRI: everything that nonexperts have always wanted to know.** *AJNR Am J Neuroradiol* 2018;39:1390–99 CrossRef Medline
31. Bauer PR, Reitsma JB, Houweling BM, et al. **Can fMRI safely replace the Wada test for preoperative assessment of language lateralisation? A meta-analysis and systematic review.** *J Neurol Neurosurg Psychiatry* 2014;85:581–88 CrossRef Medline

# Comparison of Readout-Segmented Echo-Planar Imaging and Single-Shot TSE DWI for Cholesteatoma Diagnostics

 M. Wiesmueller,  W. Wuest,  M.S. May,  S. Ellmann,  R. Heiss,  M. Saake,  R. Janka,  M. Uder, and  F.B. Laun



## ABSTRACT

**BACKGROUND AND PURPOSE:** The high diagnostic value of DWI for cholesteatoma diagnostics is undisputed. This study compares the diagnostic value of readout-segmented echo-planar DWI and single-shot TSE DWI for cholesteatoma diagnostics.

**MATERIALS AND METHODS:** Thirty patients with newly suspected cholesteatoma were examined with a dedicated protocol, including readout-segmented echo-planar DWI and single-shot TSE DWI at 1.5T. Acquisition parameters of both diffusion-weighted sequences were as follows:  $b=1000$  s/mm<sup>2</sup> axial and coronal section orientations, and section thickness of 3 mm. Image quality was evaluated by 2 readers on a 5-point Likert scale with respect to lesion conspicuity, the presence of susceptibility artifacts mimicking cholesteatomas, and overall subjective image quality. Sensitivity and specificity were calculated using histology results as the gold standard.

**RESULTS:** Twenty-five cases of histologically confirmed cholesteatomas were included in the study group. Lesion conspicuity was higher and fewer artifacts were found when using TSE DWI (both  $P < .001$ ). The overall subjective image quality, however, was better with readout-segmented DWI. For TSE DWI, the sensitivity for readers 1 and 2 was 92% (95% CI, 74%–99%) and 88% (95% CI, 69%–97%), respectively, while the specificity for both readers was 80% (95% CI, 28%–99%). For readout-segmented DWI, the sensitivity for readers 1 and 2 was 76% (95% CI, 55%–91%) and 68% (95% CI, 46%–85%), while the specificity for both readers was 60% (95% CI, 15%–95%).

**CONCLUSIONS:** The use of TSE DWI is advisable for cholesteatoma diagnostics and preferable over readout-segmented DWI.

**ABBREVIATIONS:** rsDWI = readout-segmented echo-planar DWI; tseDWI = TSE DWI

Cholesteatoma is a common non-neoplastic disease in otology, characterized by collections of trapped keratinous debris within a sack of stratified epithelium, typically found in the middle ear and capable of causing a progressive inflammatory process.<sup>1</sup> Clinical complications include the destruction of adjacent bone and ossicular structures, which can lead to conductive or sensorineural hearing loss.<sup>2,3</sup> Cholesteatoma is commonly treated with

surgery, ranging from focal excision to radical mastoidectomy.<sup>4</sup> A second-look surgery procedure is typically performed within the first 2 years after the initial surgery to identify residual or recurrent cholesteatoma foci. Unlike canal wall down mastoidectomy, visual inspection of canal wall up mastoidectomy can be challenging; hence, a reliable diagnostic imaging tool is desirable for accurate follow-up diagnosis and treatment.<sup>5–7</sup> Preoperative high-resolution CT is the method of choice for the detection of osseous disintegration and is sufficient for diagnosis; however, for recurrent cholesteatoma after surgery, its role may be more limited.<sup>8</sup> MR imaging is suitable for the assessment pre- and postsurgery using DWI and delayed postcontrast T1-weighted spin-echo imaging, which enable differentiation between keratinous debris and noncholesteatoma findings such as granulation tissue or scar.<sup>9</sup>

The value of DWI in cholesteatoma diagnostics was initially shown using echo-planar DWI sequences.<sup>10–12</sup> Alternative approaches have been proposed for cholesteatoma diagnostics such as diffusion-sensitized driven-equilibrium DWI<sup>13</sup> and PROPELLER TSE DWI (tseDWI).<sup>14</sup> Notably, tseDWI techniques introduce radiofrequency refocusing pulses between the  $k$ -space

Received October 10, 2020; accepted after revision January 23, 2021.

From the Institute of Radiology (M.W., W.W., M.S.M., S.E., R.H., M.S., R.J., M.U., F.B.L.) and Image Science Institute (M.W., W.W., M.S.M., R.H., M.S., R.J., M.U.), University Hospital Erlangen, Friedrich-Alexander-Universität Erlangen-Nürnberg, Erlangen, Germany.

Paper previously presented, in part, at: Annual Meeting of the Radiological Society of North America, November 29 to December 5, 2020; Virtual.

The position of the F.B. Laun was funded by the Deutsche Forschungsgemeinschaft (LA 2804/6-1 and LA 2804/12-1).

Please address correspondence to Marco Wiesmueller, MD, Institute of Radiology, University Hospital Erlangen, Friedrich-Alexander-University Erlangen-Nuremberg (FAU), Maximiliansplatz 3, 91054 Erlangen, Germany; e-mail: marco.wiesmueller@uk-erlangen.de

 Indicates open access to non-subscribers at [www.ajnr.org](http://www.ajnr.org)

<http://dx.doi.org/10.3174/ajnr.A7112>

**Table 1: DWI sequence parameters**

Sequence	tseDWI	rsDWI
TR (ms)	2000	4000
TE (ms)	103	66 (and 91 for phase-correction scan)
Voxel size (mm <sup>3</sup> )	1.1 × 1.5 × 3	1.4 × 1.4 × 3
FOV (mm <sup>2</sup> )	220	230
FOV in-phase direction	100%	65%
Phase direction	Anterior-posterior (axial), right to center (coronal)	Right to center (axial and coronal)
Phase resolution	75%	100%
Partial Fourier	50% (phase)	87.5% (readout)
Matrix	192 × 144	160 × 104
Section distance	10%	10%
No. of slices	13 (axial) 11 (coronal)	13 (axial) 11 (coronal)
Parallel imaging	GRAPPA × 2	GRAPPA × 2
Bandwidth (Hz/pixel)	554	977
Echo spacing (ms)	4.48	0.36
Readout segments	1	5
Flip angle	150°	180°
b-values (s/mm <sup>2</sup> )	1000	0, 1000
Averages	10	1 (for b=0 s/mm <sup>2</sup> ), 2 (for b=1000 s/mm <sup>2</sup> )
Diffusion mode	3D diagonal	4-scan trace
Diffusion scheme	Bipolar	Bipolar
Acquisition time (minute:second)	4:22 (axial), 3:42 (coronal)	3:06

**Note:**—GRAPPA indicates generalized autocalibrating partially parallel acquisition.

lines and are, therefore, not able to easily fulfill the Carr-Purcell-Meibom-Gill Sequence condition if diffusion encoding is applied—an issue that must be addressed in the sequence design and essentially often degrades the image quality.<sup>15</sup> Nonetheless, several studies have suggested single-shot tseDWI to be superior in terms of diagnostic accuracy compared with single-shot echo-planar DWI.<sup>16-18</sup> The image quality of EPI in the temporal region is often degraded due to the inhomogeneous magnetic environment at the skull base. Moreover, regions adjacent to bone- or air-filled spaces can artificially appear hyperintense, which can be misleading and result in false-positive findings.

Readout-segmented echo-planar DWI (rsDWI)<sup>19</sup> as a derivative of conventional echo-planar DWI can be used to minimize the geometric distortions to improve both image quality and diagnostic accuracy.<sup>20,21</sup> In a recently published work by Algin et al,<sup>21</sup> rsDWI proved to be superior to single-shot EPI sequences for cholesteatoma diagnostics. Hence, this study sought to compare rsDWI and tseDWI, focusing on image quality and performance in cholesteatoma diagnostics.

## MATERIALS AND METHODS

### Patient Population and Study Procedure

On the basis of the findings of a clinical assessment performed by a consultant physician for otorhinolaryngology, only patients with a newly suspected cholesteatoma were prospectively included into this study. In total, 30 patients underwent MR imaging to detect cholesteatoma and to evaluate its extension.

Patients with contraindications for MR imaging (such as a pacemaker, metal fragments, unsuitable implants, or claustrophobia) were excluded. All patients underwent a surgery after their respective MR imaging examinations, and histologic findings served as the gold standard for the presence of a cholesteatoma. Institutional review board approval was obtained, and all patients gave written informed consent.

### Image Acquisition

All MR imaging examinations were performed on a 1.5T MR imaging scanner (Magnetom Aera; Siemens) with a dedicated 20-channel head and neck coil using a routine examination protocol for cholesteatoma and additional rsDWI sequences as stated below.

Our routine examination protocol for cholesteatoma of the temporal region consists of a T1-weighted sequence in axial-section orientation with a 2-mm section thickness; a T2-weighted CISS sequence in axial-section orientation with an isotropic 0.8-mm voxel size; and a

postcontrast T1-weighted sequence with spectral fat saturation in axial- and coronal-section orientations, each with a 2-mm section thickness. The complete neurocranium was imaged with a T2-weighted FLAIR sequence in an axial-section orientation with a 5-mm section thickness.

A HASTE DWI sequence (tseDWI) and a rsDWI (readout segmentation of long variable echo trains<sup>19</sup>) sequence of the temporal region were measured in axial- and coronal-section orientations (see Table 1 for detailed sequence parameters). The tseDWI sequence is part of our institution's routine cholesteatoma protocol. The rsDWI sequence was added at the end of the protocol. The vendor-provided prescan normalize option was used for both DWI sequences to correct for spatially varying coil-sensitivity profiles and to ensure homogeneous image signal intensity. The tseDWI was interpolated to a doubled matrix size using the vendor-provided standard settings.

### Image Analysis

The image analysis was independently performed by 2 experienced radiologists (reader 1 with 6 years of experience and reader 2 with 9 years of experience in head and neck MR imaging, respectively) who were blinded to information on patient status and additional imaging data. First, each reader evaluated only tseDWI data in a random order. Then, a few days later, rsDWI data were assessed in a different order to avoid recall bias. In the readers' opinions, if both ears were affected, further documentation referred to only the left ear. The histopathologic reference was unknown at the time of assessment.

Both readers rated the image quality for each of the 4 diffusion-weighted sequences (ie, tseDWI axial, tseDWI coronal,

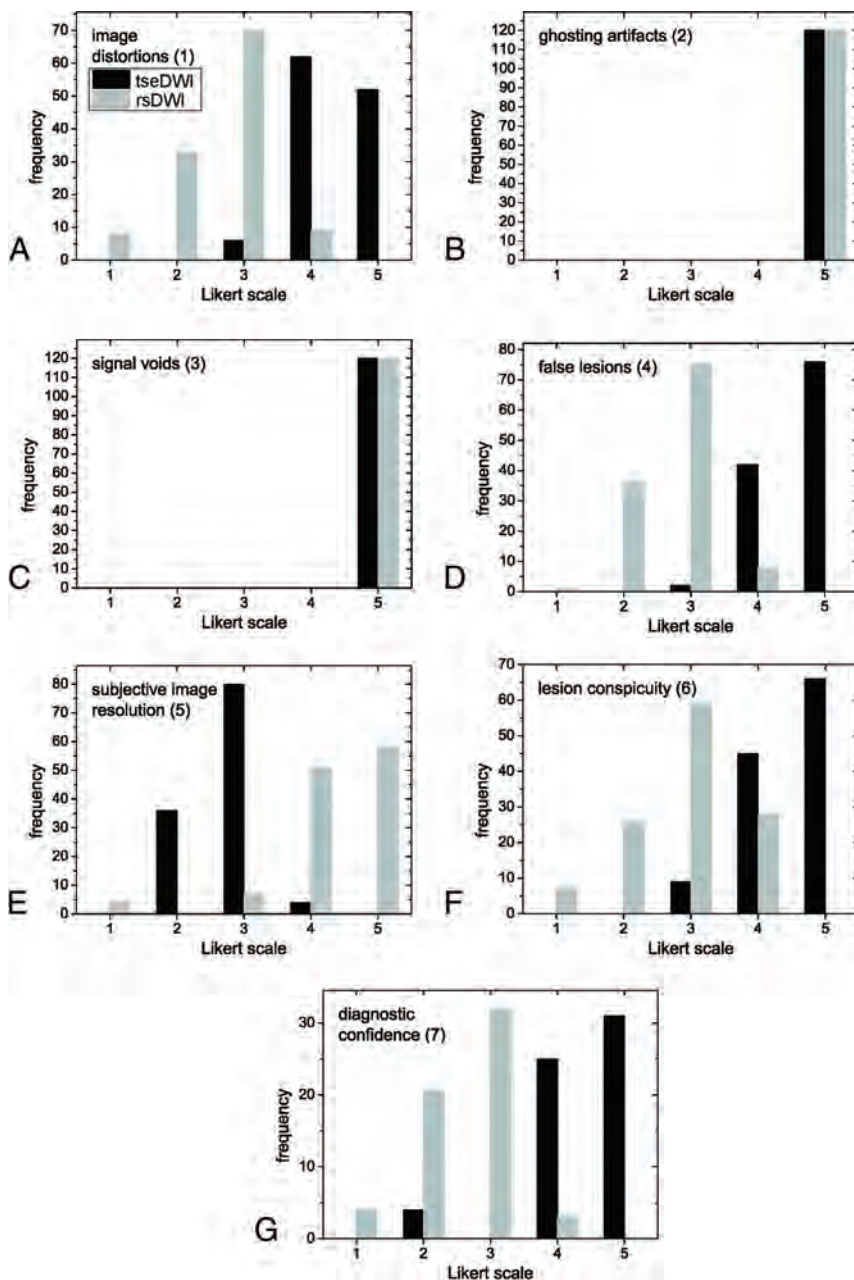


**FIG 1.** Histograms displaying Likert scale scores ranging from 1 (worst) to 5 (best) points. The histograms show the combined frequencies of both readers. The frequencies of axial and coronal images were added.

rsDWI axial, and rsDWI coronal) using the following categories on a 5-point Likert scale:

1) Prominence of geometric image distortions in the relevant temporal region, ie, inner ear, middle ear, and outer auditory canal (1 = very strong, 2 = strong, 3 = medium, 4 = small, and 5 = negligible).

2) Prominence of ghosting artifacts in the relevant temporal region (1 = very strong, 2 = strong, 3 = medium, 4 = small, and 5 = negligible).

3) Prominence of signal voids or other artifacts in the relevant temporal region (1 = very strong, 2 = strong, 3 = medium, 4 =

small, and 5 = negligible)—notably, signal voids might originate from pulsatile motion.

4) Presence of bright-appearing regions that might be mistaken for a true lesion (1 = present and not distinguishable from a true lesion, 2 = present and hardly distinguishable from the true lesion, 3 = present but clearly distinguishable, 4 = hardly present, and 5 = not present).

5) Subjective rating of image resolution (1 = very low, 2 = low, 3 = medium, 4 = good, and 5 = very good).

Additionally, the readers evaluated the diagnostic properties of the datasets (ie, lesion conspicuity) as follows, also using a 5-point Likert scale:

6) Lesion conspicuity (1 = very bad, 2 = bad, 3 = medium, 4 = good, 5 = very good). Each reader provided 1 rating each for the axial and coronal datasets, respectively.

Then, the readers rated the 2 tseDWI datasets (axial and coronal combined) and the 2 rsDWI datasets (axial and coronal combined):

7) Diagnostic confidence (1 = very low, 2 = low, 3 = medium, 4 = high, and 5 = very high).

8) Each reader had to decide whether a cholesteatoma was present or not (yes/no). This decision was made on the basis of the signal intensity in a supposed lesion relative to that of the adjacent brain tissue. The decision was “yes” if a hyperintense signal could be detected and “no” otherwise.

Subsequently, in a second independent assessment cycle, tseDWI and rsDWI data were simultaneously compared. The readers rated the 2 tseDWI datasets (axial and coronal combined) versus the 2 rsDWI datasets (axial and coronal combined) regarding the following:

9) Lesion conspicuity when comparing tseDWI versus rsDWI (2 = much better with tseDWI, 1 = better with tseDWI, 0 = equal, -1 = better with rsDWI, and -2 = much better with rsDWI).

10) Subjective diagnostic confidence (2 = much better with tseDWI, 1 = better with tseDWI, 0 = equal, -1 = better with rsDWI, and -2 = much better with rsDWI).

### Statistics

Statistical analysis was performed individually for each reader and for each image dataset, calculating (separately for the 2

**Table 2: Likert score evaluation per reader**

Category	Coronal/Axial	tseDWI (Likert Categories 4 and 5)		rsDWI (Likert Categories 4 and 5)		Mean Difference (tseDWI and rsDWI)	
		Reader 1	Reader 2	Reader 1	Reader 2	Reader 1	Reader 2
1) Geometric image distortion	Cor	97%	97%	0%	0%	1.9	2
1) Geometric image distortion	Ax	93%	93%	17%	13%	1.5	1.5
2) Ghosting artifacts	Cor	100%	100%	100%	100%	0	0
2) Ghosting artifacts	Ax	100%	100%	100%	100%	0	0
3) Signal voids or other artifacts	Cor	100%	100%	100%	100%	0	0
3) Signal voids or other artifacts	Ax	100%	100%	100%	100%	0	0
4) Bright-appearing region	Cor	97%	97%	0%	0%	2	2
4) Bright-appearing region	Ax	100%	100%	13%	13%	1.7	1.8
5) Subjective image resolution	Cor	3%	3%	90%	90%	-1.6	-1.7
5) Subjective image resolution	Ax	3%	3%	90%	93%	-1.5	-1.6
6) Lesion conspicuity	Cor	97%	93%	33%	23%	1.6	1.7
6) Lesion conspicuity	Ax	90%	90%	20%	17%	1.5	1.5
7) Diagnostic confidence	Cor/Ax	93%	93%	7%	3%	1.8	1.8

**Note:**—Cor indicates coronal; Ax, axial.

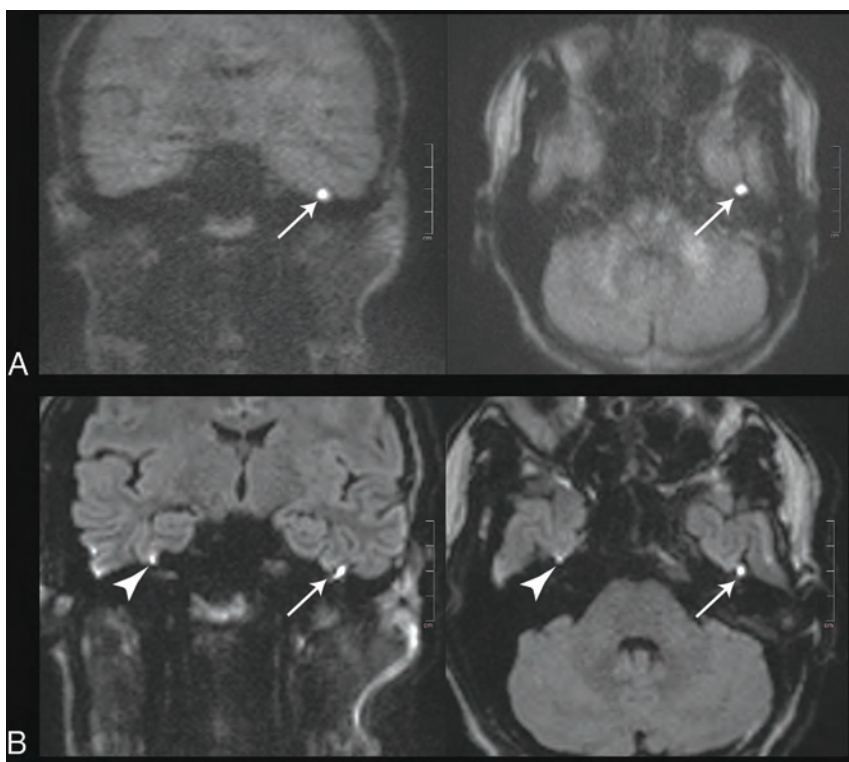


**FIG 2.** Images of a 20-year-old patient with a left-sided cholesteatoma (white arrows). A, tseDWI. B, rsDWI. The lesion can be seen clearly in tseDWI and rsDWI. It is, however, not spheric in the coronal rsDWI but rather is elongated and tilted due to image distortions in phase directions. Field inhomogeneities generate a bright spot in the rsDWI that might be mistaken for a lesion (arrowheads). The tseDWI displayed in A is more blurred than the rsDWI and shows less contrast in the brain. For example, unlike in the rsDWI, both white matter and gray matter are not discernible in the tseDWI.

groups of patients with histologically proved cholesteatomas and no cholesteatomas, respectively) the sensitivity and specificity with 95% confidence intervals using the Clopper-Pearson method. Furthermore, the McNemar test was performed to compare the 2 MR imaging sequences per these

measures of diagnostic accuracy, while interrater agreement was evaluated using the Cohen  $\kappa$  value; in this context,  $\kappa$  was interpreted as follows:  $0 < \kappa \leq 0.2$  indicated slight agreement,  $0.2 < \kappa \leq 0.4$  indicated fair agreement,  $0.4 < \kappa \leq 0.6$  indicated moderate agreement,  $0.6 < \kappa \leq 0.8$  indicated substantial agreement,  $0.8 < \kappa \leq 1.0$  indicated almost perfect agreement, and  $\kappa = 1$  indicated perfect agreement. A comparison between tseDWI and rsDWI ratings was performed using a nonparametric Wilcoxon rank sum test. Significance was accepted for  $P$  values  $< .05$ . Statistical analysis was performed using SPSS Statistics, Version 24 (IBM) and R statistical and computing software, Version 3.5.3 (<http://www.r-project.org/>).

## RESULTS

### Patient Population

The study population consisted of 13 female and 17 male patients with a mean age of 46 (SD, 16) years (range, 18–79 years). Twenty-five of the 30 included patients (83%) were diagnosed with cholesteatoma after surgical excision and histopathologic confirmation, with 22 of 25 patients (88%) with unilateral cholesteatoma and 3 patients with bilateral cholesteatoma (12%). The mean lesion diameter was 0.6 (SD, 0.4) cm (median, 0.5 cm; range, 0.1–1.6 cm).

### Diagnostic Performance

Regarding the 25 patients with cholesteatoma, reader 1 found 23 cholesteatomas with tseDWI and 19 with rsDWI, with 18 being

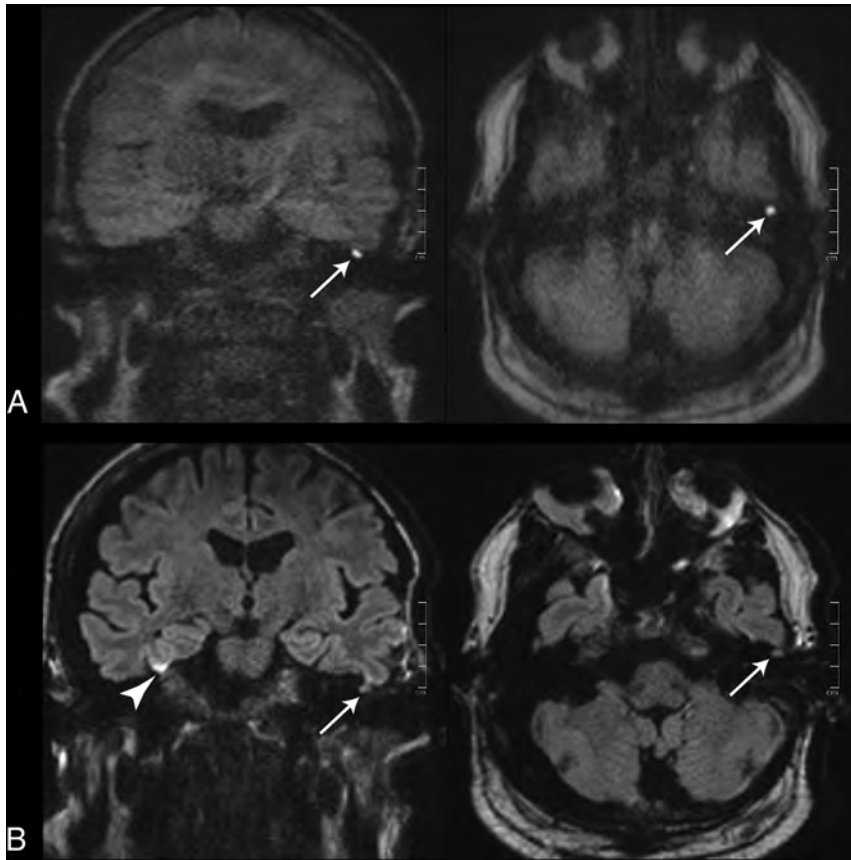


**FIG 3.** Images of a 55-year-old patient with a left-sided cholesteatoma (white arrows). A, tseDWI. B, rsDWI. The lesion can be seen clearly in the tseDWI. In the rsDWI, however, the lesion is displayed with reduced contrast and is hardly visible; therefore, both readers did not diagnose a cholesteatoma in this case in the rsDWI dataset. Again, a bright spot is present in the coronal rsDWI next to the temporal bone on the right side due to field inhomogeneities, which might be mistaken for a true lesion (arrowhead).

concordantly found with both sequences. The sensitivity for tseDWI and rsDWI in this case was 92% (95% CI, 74%–99%) and 76% (95% CI, 55%–91%) (McNemar  $P = .22$ ). Reader 2 correctly found 22 cholesteatomas with tseDWI and 17 with rsDWI, with 16 being concordantly found with both sequences. The sensitivity for tseDWI and rsDWI was 88% (95% CI, 69%–97%) and 68% (95% CI, 46%–85%) (McNemar  $P = .13$ ).

Regarding the 5 patients without cholesteatomas, reader 1 negatively diagnosed 4 patients by tseDWI; 3 patients were ultimately also classified correctly by rsDWI, leading to specificities of 80% (95% CI, 28%–99%) and 60% (95% CI, 15%–95%), respectively (McNemar  $P = 1$ ). Reader 2 classified 2 patients concordantly correctly negative with both sequences. Meanwhile, 2 patients were correctly classified with tseDWI but not with rsDWI, and 1 patient was correctly classified by rsDWI but not by tseDWI. Thus, the specificity for tseDWI was 80% (95% CI, 28%–99%), and for rsDWI, it was 60% (95% CI, 15%–95%) (McNemar  $P = 1$ ).

The overall agreement between both readers concerning the presence of a cholesteatoma was 97% ( $\kappa = 0.9$ ) for tseDWI and 87% ( $\kappa = 0.7$ ) for rsDWI, respectively.

### Likert Score Ratings

Frequencies of Likert scores per category are summarized in Fig 1 and Table 2. Relevant ghosting artifacts and signal voids were not observed by the readers for both rsDWI and tseDWI. rsDWI outperformed tseDWI only in terms of the subjective image resolution, while tseDWI performed much better in terms of handling image distortions and lesion conspicuity. For rsDWI, the readers more frequently observed the presence of bright-appearing regions outside the lesion that might be mistaken for a true lesion. The diagnostic confidence was higher for tseDWI. Representative images are provided in Figs 2–4.

Figure 5 shows the comparative reader evaluations performed with possible Likert scores ranging from –2 to 2 points (categories 9 and 10). Notably, tseDWI always performed equal to or even better than rsDWI; the readers assigned better lesion conspicuity in 91% of cases and better diagnostic confidence in 95% of cases for tseDWI, respectively.

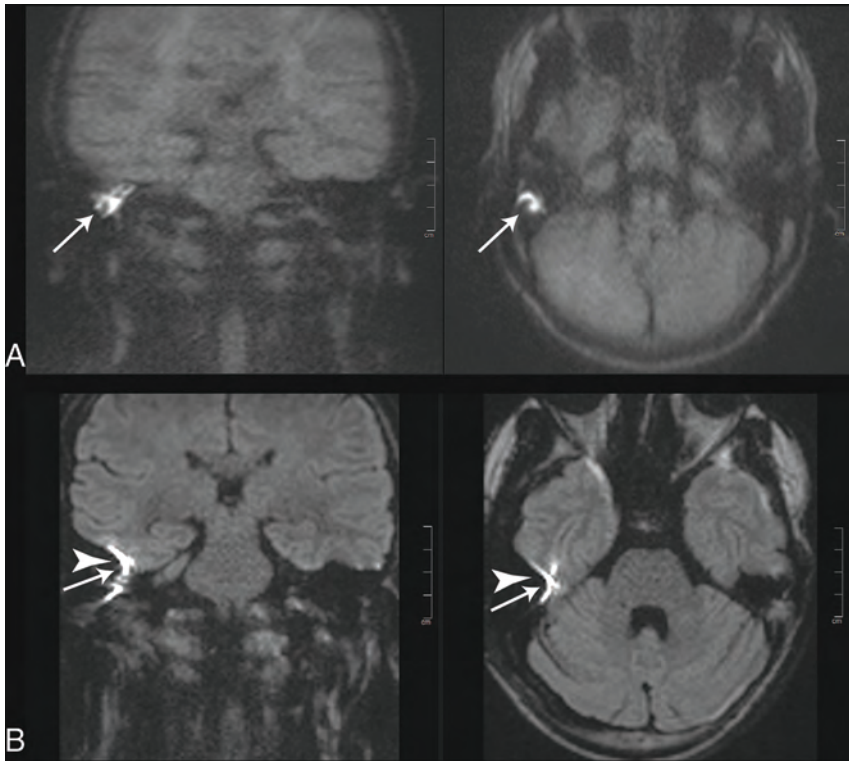
The differences between tseDWI and rsDWI were significant ( $P < .001$ ) in all cases, ie, for all section orientations and both readers, except with regard to signal voids and ghosting artifacts ( $P = 1$ ).

Table 3 summarizes the  $\kappa$  values. A moderate-to-perfect degree of interreader agreement was observed for all evaluations.

### DISCUSSION

In this study, we found that single-shot tseDWI outperformed rsDWI with respect to diagnostic performance, lesion conspicuity, the presence of false-positive findings, and subjective diagnostic confidence for imaging cholesteatomas. tseDWI showed greater sensitivity and specificity compared with rsDWI, albeit without verifiable statistical significance. Notably, the better subjective image resolution of rsDWI did not translate into a generally improved level of performance in comparison with tseDWI. So far, to our knowledge, only a few studies have evaluated the impact of rsDWI in cholesteatoma diagnostics.

The reductions in susceptibility artifacts that we observed with tseDWI in comparison with rsDWI are in line with the technical considerations that can be made for the 2 sequences. For multishot EPI, the susceptibility-induced distortion is  $\Delta r_{\text{EPI}} = \frac{t_{\text{line}} \cdot \Delta \nu}{N_{\text{shot}}} \times \text{FoV}_{\text{phase}}$ , with the acquisition duration of 1 k-space line reflected as  $t_{\text{line}}$ , the susceptibility-induced off-



**FIG 4.** Images of a 38-year-old patient with a recurrent cholesteatoma (white arrows). A stapes prosthesis implant caused major image distortions in the rsDWI (arrowheads).

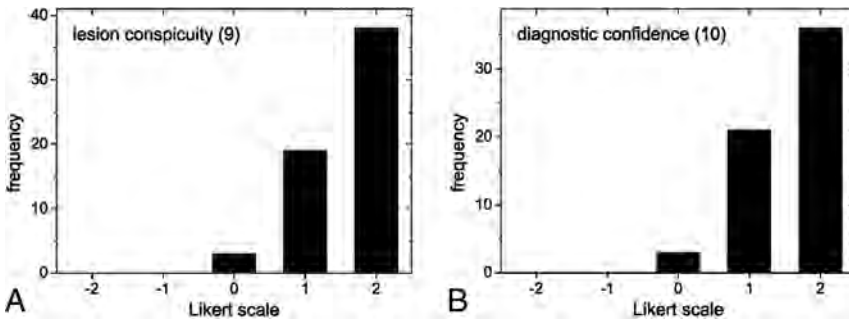


**FIG 5.** Histograms displaying the scores obtained with Likert scores ranging from  $-2$  (rsDWI much better than tseDWI) to 2 points (tseDWI much better than rsDWI). The histograms show the added frequencies of both readers.

resonance stated as  $\Delta\nu$ , and the number of shots represented as  $N_{\text{shot}}$ .<sup>22</sup> This relation highlights the advantage of multishot EPI techniques in comparison with single-shot EPI, for which  $N_{\text{shot}} = 1$ . Meanwhile, the susceptibility-induced distortion in tseDWI is  $\Delta r_{\text{tseDWI}} = \frac{h_{\text{line}} \Delta\nu}{N_{\text{voxel, read}}} \times \text{FoV}_{\text{read}}$ , with the number of voxels in the read direction being  $N_{\text{voxel, read}}$ .<sup>23</sup> Because  $N_{\text{voxel, read}}$  is less than  $N_{\text{shot}}$  in our setting, the image distortions for tseDWI are technically expected to be much smaller than those for rsDWI. We used a longer TE value for tseDWI (103 ms), which might explain the better visibility of lesions assessed with tseDWI than with rsDWI. This setting for rsDWI was chosen using the vendor-provided standard option for rsDWI, which minimizes the TE and is not variable. This contrast

issue might be addressed by prolonging the TE for rsDWI, but this would not solve the problem of false-positive hyperintense susceptibility artifacts due to adjacent bone and air interfaces in the temporal region in rsDWI. These are caused by field inhomogeneities and do not depend on TE.<sup>22</sup>

We could not confirm the high sensitivity and specificity values for rsDWI reported by both Fischer et al<sup>24</sup> and Algin et al.<sup>21</sup> In contrast to in our study, Algin et al used longer TEs for rsDWI (91–124 versus 66 ms). This might increase the T2 hyperintense signal of cholesteatomas, which could possibly lead to a higher detection rate.<sup>25</sup> Another difference that might explain a higher detection rate is the greater size of cholesteatomas in their study group (median, 0.8 versus 0.5 cm). Because we were not able to track and compare all sequence parameters and lesion sizes of Fischer et al and Algin et al, we found it difficult to make statements on the origin of the observed differences.

Dudau et al<sup>26</sup> recently conducted a similar study comparing tseDWI and rsDWI, and several of their findings are in line with ours. In particular, these authors reported a good overall agreement between the 2 sequences with similar levels of diagnostic performance for rsDWI and tseDWI (positive predictive value = 93% versus 92.5%, negative predictive value = 70% versus 80%), while we observed a drop in the diagnostic performance for the rsDWI sequence. Furthermore, concerning discrepancies between tseDWI and rsDWI, they found a greater proportion of false-negative results for rsDWI, which is in line with our results. Many of the settings that Dudau et al used are quite similar to

ours (eg, same scanner, sequence, similar TEs). They used a smaller voxel size for rsDWI acquisitions than we did ( $1.2 \times 1.2 \times 2 \text{ mm}^3$  versus  $1.4 \times 1.4 \times 3 \text{ mm}^3$ ). This may have been beneficial during imaging because it reduces partial volume effects and thus can make small lesions appear brighter. However, they did not report the lesion sizes, which might be different from those in our study. Moreover, their main detection criterion was also the presence of signal hyperintensity, but perhaps, they also used a better reading strategy, potentially classifying smaller hyperintensities as lesions. On the one hand, this could indicate that an improvement of our reading strategy might be possible, while on the other, it might also indicate that the diagnostic performance of

**Table 3: Cohen  $\kappa$  values quantifying the interreader agreement**

	$\kappa$ (tseDWI, Axial)	$\kappa$ (tseDWI, Coronal)	$\kappa$ (rsDWI, Axial)	$\kappa$ (rsDWI, Coronal)
1) Geometric image distortion	0.64	0.62	0.83	0.58
2) Ghosting artifacts	1	1	1	1
3) Signal voids	1	1	1	1
4) Bright-appearing region	0.79	0.78	0.82	0.78
5) Subjective image resolution	0.79	0.78	0.71	0.77
6) Lesion conspicuity	0.71	0.62	0.83	0.53
7) Diagnostic confidence with $\kappa$ (tseDWI, axial and coronal combined) and $\kappa$ (rsDWI, axial and coronal combined)	$\kappa$ (tseDWI) 0.82	$\kappa$ (rsDWI) 0.77		
9) Lesion conspicuity with $\kappa$ (tseDWI vs. rsDWI)	$\kappa$ (tseDWI vs. rsDWI) 0.80			
10) Subjective diagnostic confidence	0.68			

tseDWI is more robust when used in different centers and that its use would thus be recommendable.

As stated above, tseDWI revealed more true-positive findings compared with rsDWI, but we also observed false-negative findings within the tseDWI datasets. In the literature, this deficiency is reported to be due to motion artifacts or empty retraction pockets.<sup>27,28</sup> According to histopathologic results, all patients with false-negative MR imaging results in our study had only residual portions of cholesteatomas measuring <2 mm. This is in line with the results published by De Foer et al,<sup>17</sup> who proposed 2 mm as a size limit for accurate diagnosis when using single-shot tseDWI. Furthermore, the lack of a clear visualization of anatomic landmarks in single-shot tseDWI sequences can be considered a major limitation that could prevent the exact spatial description of a cholesteatoma in the temporal bone.<sup>17</sup> Thus, a substantially better depiction of anatomic details would potentially help to overcome this diagnostic limitation, especially in patients with residual cholesteatoma before second-look surgery. In 2 recently published studies, it has been shown that coregistration of DWI data with CT or T2-weighted cisternography may help in this regard.<sup>29,30</sup> In theory, a promising approach would be rsDWI, with its better ability to depict anatomic details—if the drawbacks described in our study can be overcome.

Several possibilities exist to achieve further improvement in the performance of the rsDWI sequence, which aims to reduce the susceptibility-induced artifacts. The use of higher parallel imaging acceleration factors might become possible with the use of head coils with 64, 96, or more channels,<sup>31</sup> which could reduce susceptibility-induced image distortions. These distortions might also be reduced by involving postprocessing schemes.<sup>32</sup> We used a scanner with a maximal gradient strength of 40 mT/m; in comparison, newer whole-body scanners can provide values of 80 mT/m, while dedicated head scanners offer 300 mT/m of gradient strength.<sup>33</sup> Using such systems might allow very high-acquisition bandwidths, which could decrease the severity of susceptibility-induced image distortions. Also, a further approach to minimize such distortions may be the use of reduced-FOV excitations.<sup>34,35</sup>

In our setting, the acquisition time of the rsDWI sequence was shorter than that of the routine tseDWI sequence. Most important, we used the vendor-provided setting for tseDWI, which involves the acquisition of 10 averages and prolongs the acquisition time more than the acquisition of multiple segments with rsDWI ( $n = 5$  in our study).

Our study has several limitations. A quantitative evaluation of imaging features such as the signal-to-noise ratio was not performed. With multichannel coils, an evaluation of the signal-to-noise ratio would have necessitated the acquisition of >1 dataset for each setting,<sup>36</sup> which contrasted with our desire to limit the total acquisition time. Furthermore, we did not run a quality-assurance program with dedicated phantoms<sup>37</sup> during the study, and we did not evaluate computed b-value images, possibly constituting additional steps to improve the final diagnostic performance.<sup>38</sup>

## CONCLUSIONS

In cholesteatoma diagnostics, the use of single-shot tseDWI is recommended instead of echo-planar rsDWI.

Disclosures: Wolfgang Wuest—UNRELATED: Consultancy: Siemens; Payment for Lectures Including Service on Speakers Bureaus: Siemens. Matthias S. May—UNRELATED: Payment for Lectures Including Service on Speakers Bureaus: Siemens, Comments: lectures, services on speakers bureau. Rafael Heiss—UNRELATED: Payment for Lectures Including Service on Speakers Bureaus: Siemens. Marc Saake—UNRELATED: Payment for Lectures Including Service on Speakers Bureaus: Siemens. Rolf Janka—UNRELATED: Payment for Lectures Including Service on Speakers Bureaus: Siemens, Bracco Diagnostics. Frederik B. Laun—RELATED: Grant: Deutsche Forschungsgemeinschaft, Comments: DFG LA 2804/6-1 and LA 2804/12-1.\* \*Money paid to the institution.

## REFERENCES

- Swartz JD. **Cholesteatomas of the middle ear: diagnosis, etiology, and complications.** *Radiol Clin North Am* 1984;22:15–35 Medline
- Yung M, Tono T, Olszewska E, et al. **EAONO/JOS Joint Consensus Statements on the Definitions, Classification and Staging of Middle Ear Cholesteatoma.** *J Int Adv Otol* 2017;13:1–8 CrossRef Medline
- Suzuki C, Ohtani I. **Bone destruction resulting from rupture of a cholesteatoma sac: temporal bone pathology.** *Otol Neurotol* 2004;25:674–77 Medline
- Prasad SC, Piras G, Piccirillo E, et al. **Surgical strategy and facial nerve outcomes in petrous bone cholesteatoma.** *Audiol Neurootol* 2016;21:275–85 CrossRef Medline
- Foti G, Beltramello A, Minerva G, et al. **Identification of residual-recurrent cholesteatoma in operated ears: diagnostic accuracy of dual-energy CT and MRI.** *Radiol Med* 2019;124:478–86 CrossRef Medline
- Bazzi K, Wong E, Jufas N, et al. **Diffusion-weighted magnetic resonance imaging in the detection of residual and recurrent cholesteatoma in children: a systematic review and meta-analysis.** *Int J Pediatr Otorhinolaryngol* 2019;118:90–96 CrossRef Medline

7. Gouda M, Nasr WF, Elbary ME, et al. **MRI as an alternative to second look mastoid surgery.** *Indian J Otolaryngol Head Neck Surg* 2018;70:410–14 CrossRef Medline
8. Migirov L, Tal S, Eyal A, et al. **MRI, not CT, to rule out recurrent cholesteatoma and avoid unnecessary second-look mastoidectomy.** *Isr Med Assoc J* 2009;11:144–146 Medline
9. Williams MT, Ayache D, Alberti C, et al. **Detection of postoperative residual cholesteatoma with delayed contrast-enhanced MR imaging: initial findings.** *Eur Radiol* 2003;13:169–74 CrossRef Medline
10. Maheshwari S, Mukherji SK. **Diffusion-weighted imaging for differentiating recurrent cholesteatoma from granulation tissue after mastoidectomy: case report.** *AJNR Am J Neuroradiol* 2002;23:847–49 Medline
11. Aikele P, Kittner T, Offergeld C, et al. **Diffusion-weighted MR imaging of cholesteatoma in pediatric and adult patients who have undergone middle ear surgery.** *AJR Am J Roentgenol* 2003;181:261–65 CrossRef Medline
12. Vercausse JP, De Foer B, Pouillon M, et al. **The value of diffusion-weighted MR imaging in the diagnosis of primary acquired and residual cholesteatoma: a surgical verified study of 100 patients.** *Eur Radiol* 2006;16:1461–67 CrossRef Medline
13. Yamashita K, Yoshiura T, Hiwatashi A, et al. **High-resolution three-dimensional diffusion-weighted imaging of middle ear cholesteatoma at 3.0 T MRI: usefulness of 3D turbo field-echo with diffusion-sensitized driven-equilibrium preparation (TFE-DSDE) compared to single-shot echo-planar imaging.** *Eur J Radiol* 2013;82:e471–75 CrossRef Medline
14. Kasbekar AV, Scoffings DJ, Kenway B, et al. **Non echo planar, diffusion-weighted magnetic resonance imaging (periodically rotated overlapping parallel lines with enhanced reconstruction sequence) compared with echo planar imaging for the detection of middle-ear cholesteatoma.** *J Laryngol Otol* 2011;125:376–80 CrossRef Medline
15. Alsop DC. **Phase insensitive preparation of single-shot RARE: application to diffusion imaging in humans.** *Magn Reson Med* 1997;38:527–33 CrossRef Medline
16. Dubrulle F, Souillard R, Chechin D, et al. **Diffusion-weighted MR imaging sequence in the detection of postoperative recurrent cholesteatoma.** *Radiology* 2006;238:604–10 CrossRef Medline
17. De Foer B, Vercausse JP, Bernaerts A, et al. **The value of single-shot turbo spin-echo diffusion-weighted MR imaging in the detection of middle ear cholesteatoma.** *Neuroradiology* 2007;49:841–48 CrossRef Medline
18. Pizzini FB, Barbieri F, Beltramello A, et al. **HASTE diffusion-weighted 3-Tesla magnetic resonance imaging in the diagnosis of primary and relapsing cholesteatoma.** *Otol Neurotol* 2010;31:596–602 CrossRef Medline
19. Porter DA, Heidemann RM. **High resolution diffusion-weighted imaging using readout-segmented echo-planar imaging, parallel imaging and a two-dimensional navigator-based reacquisition.** *Magn Reson Med* 2009;62:468–75 CrossRef Medline
20. Yamashita K, Yoshiura T, Hiwatashi A, et al. **Detection of middle ear cholesteatoma by diffusion-weighted MR imaging: multishot echo-planar imaging compared with single-shot echo-planar imaging.** *AJNR Am J Neuroradiol* 2011;32:1915–18 CrossRef Medline
21. Algin O, Aydin H, Ozmen E, et al. **Detection of cholesteatoma: high-resolution DWI using RS-EPI and parallel imaging at 3 Tesla.** *J Neuroradiol* 2017;44:388–94 CrossRef Medline
22. Jones DK. *Diffusion MRI: Theory, Methods, and Applications.* Oxford University Press; 2011
23. Emmerich J, Laun FB, Pfaffenberger A, et al. **Technical Note: on the size of susceptibility-induced MR image distortions in prostate and cervix in the context of MR-guided radiation therapy.** *Med Phys* 2018;45:1586–93 CrossRef Medline
24. Fischer N, Scharfingher VH, Dejaco D, et al. **Readout-segmented echo-planar DWI for the detection of cholesteatomas: correlation with surgical validation.** *AJNR Am J Neuroradiol* 2019;40:1055–59 CrossRef Medline
25. Fitzek C, Mewes T, Fitzek S, et al. **Diffusion-weighted MRI of cholesteatomas of the petrous bone.** *J Magn Reson Imaging* 2002;15:636–41 CrossRef Medline
26. Dudau C, Draper A, Gkagkanasiou M, et al. **Cholesteatoma: multi-shot echo-planar vs non echo-planar diffusion-weighted MRI for the prediction of middle ear and mastoid cholesteatoma.** *BJR Open* 2019;1:20180015 CrossRef Medline
27. Henninger B, Kremser C. **Diffusion-weighted imaging for the detection and evaluation of cholesteatoma.** *World J Radiol* 2017;9:217–22 CrossRef Medline
28. Dremmen MH, Hofman PA, Hof JR, et al. **The diagnostic accuracy of non-echo-planar diffusion-weighted imaging in the detection of residual and/or recurrent cholesteatoma of the temporal bone.** *AJNR Am J Neuroradiol* 2012;33:439–44 CrossRef Medline
29. Locketz GD, Li PM, Fischbein NJ, et al. **Fusion of computed tomography and PROPELLER diffusion-weighted magnetic resonance imaging for the detection and localization of middle ear cholesteatoma.** *JAMA Otolaryngol Head Neck Surg* 2016;142:947–53 CrossRef Medline
30. Benson JC, Carlson ML, Yin L, et al. **Cholesteatoma localization using fused diffusion-weighted images and thin-slice T2 weighted images.** *Laryngoscope* 2020 Nov 3. [Epub ahead of print] CrossRef Medline
31. Wiggins GC, Polimeni JR, Potthast A, et al. **96-Channel receive-only head coil for 3 Tesla: design optimization and evaluation.** *Magn Reson Med* 2009;62:754–62 CrossRef Medline
32. Andersson JLR, Skare S, Ashburner J. **How to correct susceptibility distortions in spin-echo echo-planar images: application to diffusion tensor imaging.** *Neuroimage* 2003;20:870–88 CrossRef Medline
33. Setsompop K, Kimmlingen R, Eberlein E, et al. **Pushing the limits of in vivo diffusion MRI for the Human Connectome Project.** *Neuroimage* 2013;80:220–33 CrossRef Medline
34. Dowell NG, Jenkins TM, Ciccarelli O, et al. **Contiguous-slice zonally oblique multislice (CO-ZOOM) diffusion tensor imaging: examples of in vivo spinal cord and optic nerve applications.** *J Magn Reson Imaging* 2009;29:454–60 CrossRef Medline
35. Laun F, Stieltjes B, Schluter M, et al. **Reproducible evaluation of spinal cord DTI using an optimized inner volume sequence in combination with probabilistic ROI analysis.** *Z Med Phys* 2009;19:11–20 CrossRef Medline
36. Goerner FL, Clarke GD. **Measuring signal-to-noise ratio in partially parallel imaging MRI.** *Med Phys* 2011;38:5049–57 CrossRef Medline
37. Wagner F, Laun FB, Kuder TA, et al. **Temperature and concentration calibration of aqueous polyvinylpyrrolidone (PVP) solutions for isotropic diffusion MRI phantoms.** *PLoS One* 2017;12:e0179276 CrossRef Medline
38. Yamashita K, Hiwatashi A, Togao O, et al. **Improved visualization of middle ear cholesteatoma with computed diffusion-weighted imaging.** *Magn Reson Med Sci* 2019;18:233–37 CrossRef Medline

# Optimal Duration of MRI Follow-up to Safely Identify Middle Ear Residual Cholesteatoma

 A.-L. Fourez,  M. Akkari,  G. Gascou,  P.-H. Lefevre,  C. Duflos,  A. Kaderbay,  M. Mondain, and  F. Venail



## ABSTRACT

**BACKGROUND AND PURPOSE:** Previous studies have demonstrated the usefulness of non-EPI DWI for detection of residual cholesteatoma. However, limited data are available to determine the suitable duration of imaging follow-up after a first MR imaging with normal findings has been obtained. The present study aimed to determine the optimal duration of non-EPI DWI follow-up for residual cholesteatoma.

**MATERIALS AND METHODS:** A retrospective, monocentric study was performed between 2013 and 2019 and included all participants followed up after canal wall up tympanoplasty with at least 2 non-EPI DWI examinations performed on the same 1.5T MR imaging scanner. MR images were reviewed independently by 2 radiologists. Sensitivity and specificity values were calculated as a function of time after the operation. Receiver operating characteristic curves were analyzed to determine the optimal follow-up duration.

**RESULTS:** We analyzed 47 MRIs from 17 participants. At the end of the individual follow-up period, a residual cholesteatoma had been found in 41.1% of cases. The follow-up duration ranged from 20 to 198 months (mean, 65.9 [SD, 43.9] months). Participants underwent between 2 and 5 non-EPI DWI examinations. Analyses of the receiver operating characteristic curves revealed that the optimal diagnostic value of non-EPI DWI occurred 56 months after the operation when the first MR imaging performed a mean of 17.3 (SD, 6.8) months after the operation had normal findings (sensitivity = 0.71; specificity = 0.7, Youden index = 0.43).

**CONCLUSIONS:** Repeat non-EPI DWI is required to detect slow-growing middle ear residual cholesteatomas. We, therefore, recommend performing non-EPI DWI for at least the first 5 years after the initial operation.

The development of DWI has profoundly changed the management of middle ear cholesteatomas. An increasing number of surgeons no longer systematically perform second-look surgery, and MR imaging follow-up is performed if revision surgery is not needed to treat conductive hearing loss. Numerous studies have evaluated the sensitivity and specificity of EPI DWI and non-EPI DWI sequences for the detection of residual cholesteatoma. Non-EPI DWI sequences offer the best sensitivity and specificity and are suitable for the detection of residual cholesteatomas as small as 2 mm.<sup>1</sup> A recent meta-analysis of 26 studies concerning non-EPI DWI showed a pooled sensitivity and

specificity of 0.91 (95% CI, 0.87–0.95) and 0.92 (95% CI, 0.86–0.96), respectively.<sup>1</sup> Another meta-analysis reported a similar pooled sensitivity and specificity of 0.89 (95% CI, 0.52–0.99) and 0.93 (95% CI, 0.81–0.98), respectively.<sup>2</sup>

However, data on the diagnostic value of non-EPI DWI sequences regarding the optimal timing after the initial operation remain limited. Lingam et al<sup>3</sup> reported a sensitivity of 0.91 (95% CI, 0.79–0.97) and a specificity of 0.88 (95% CI, 0.69–0.97) with a median time to MR imaging of 5.4 months after the operation. Khemani et al<sup>4</sup> found a sensitivity of 0.82 (95% CI, 0.63–0.94) and a specificity of 0.90 (95% CI, 0.55–1.00) when MR imaging was performed 10–24 months after the operation.

Most authors agree that imaging follow-up should not start <12 months postsurgery,<sup>5–8</sup> to reduce the number of false-negatives due to residual cholesteatomas measuring <2 mm.<sup>9</sup> Nevertheless, the optimal duration of follow-up necessary to exclude the existence of a residual cholesteatoma if the findings of the first MR imaging are considered normal is unclear. In a recent retrospective series, follow-up non-EPI DWI detected residual cholesteatoma in 12 of 88 patients only after a mean interval of 3.8 years after the initial cholesteatoma surgery (median, 3.7 years; range, 1.6–7.9 years).<sup>10</sup> Pai et al<sup>10</sup> suggested that

Received June 11, 2020; accepted after revision February 15, 2021.

From the Departments of ENT and Head and Neck Surgery (A.-L.F., M.A., A.K., M.M., F.V.) and Neuroradiology (G.G., P.-H.L.), University Hospital Gui de Chauliac, and Department of Medical Information and Biostatistics (C.D.), University Hospital La Colombière, University of Montpellier, Montpellier, France; and Institute for Neurosciences de Montpellier (F.V.), Institut National de la Santé et de la Recherche Médicale U1051 and University of Montpellier, Montpellier, France.

Please address correspondence to Frederic Venail, MD, PhD, Department of ENT and Neck Surgery, University Hospital Gui de Chauliac, 80 Avenue Augustin Fliche, 34295 Montpellier Cedex 5, France; e-mail: f-venail@chu-montpellier.fr

 Indicates article with online supplemental data.

<http://dx.doi.org/10.3174/ajnr.A7116>

imaging follow-up should be performed for a minimum of 5 years postoperatively, without defining how this was calculated.

To provide more information on the optimal imaging follow-up duration, we describe the long-term follow-up imaging of participants with  $\geq 2$  non-EPI DWI examinations for residual middle ear cholesteatoma. The sensitivity and specificity values were calculated as a function of the duration of the follow-up, and the receiver operating characteristic curves were analyzed to determine the optimal follow-up time.

## MATERIALS AND METHODS

### Design and Settings

This retrospective, monocentric study was performed in the Ear, Nose, and Throat Department of University Hospital Gui de Chauliac tertiary referral center, with approval from the local ethics committee of our institution (IRB-MTP\_2020\_04\_202000448). Data were collected from participants regularly followed up between January 2003 and December 2019 in our department.

Participants assessed in this study were regularly followed up for middle ear cholesteatoma and underwent  $\geq 2$  non-EPI DWI examinations, which were performed with the same 1.5T MR imaging scanner. All participants underwent canal wall up tympanoplasty. Those with incomplete removal of the cholesteatoma during the first operation or congenital cholesteatomas, or those having undergone tympanoplasty with the canal wall down technique without reconstruction or in whom residual cholesteatoma was suspected on the first MR imaging follow-up were not considered for the study.

All MRIs were performed in the neuroradiology department using a 1.5T scanner with a standard head coil. We used the following protocols: axial TSE T2-weighted sequences (TR = 4.56 seconds; TE = 0.097 seconds; section thickness = 5 mm; matrix =  $426 \times 448$ ; FOV = 230 mm; total duration 1 minute 2.4 seconds); 3D CISS sequences (TR = 0.01 seconds; TE = 0.005 seconds; section thickness = 0.7 mm; matrix =  $350 \times 448$ ; FOV = 210 mm; total duration = 6 minutes 28.2 seconds); coronal spin-echo T1-weighted sequences (TR = 0.5 seconds; TE = 0.009 seconds; section thickness = 2 mm; matrix =  $128 \times 128$ ; FOV = 190 mm; total duration = 2 minutes 25.8 seconds); and axial HASTE DWI sequences (TR = 2.8 seconds; TE = 0.122 seconds; b factor = 0, 1000 s/mm<sup>2</sup>; section thickness = 2.5 mm; matrix =  $256 \times 256$ ; FOV = 300 mm; total duration = 1 minute 8.4 seconds).

The radiologist classified the images as “suspicion” or “no suspicion” of residual cholesteatoma based on all imaging sequences acquired. The surgeon then made a decision as to whether to perform revision surgery on the basis of the imaging diagnosis and/or clinical assessment.

In the event of revision surgery, MR imaging follow-up was interrupted. If not, additional MRIs could be performed if requested by the surgeon. Because no official recommendations are available, the decision regarding the number of MRIs and the interval between any 2 was left to the surgeon’s discretion.

Data were collected and analyzed 3–12 years after the initial operation. Non-EPI DWI sequences were retrieved and anonymized. Two senior neuroradiologists, blinded to the diagnosis, retrospectively and independently evaluated all sequences and

classified them as “no residual cholesteatoma” or “residual cholesteatoma.” In cases of disagreement, both neuroradiologists performed a third review of the images until consensus was reached.

Medical charts and surgical records were analyzed; when revision surgery occurred, any residual cholesteatoma was reported. If no revision surgery was performed and the imaging showed no residual cholesteatoma, the patient was considered disease-free.

The initial localization and staging of the cholesteatoma were assessed with the STAM classification.<sup>11</sup>

### Statistical Analyses

The interobserver agreement between the 2 radiologists was evaluated using the  $\kappa$  coefficient, computed on the 29 available MR imaging examinations (second, third, fourth, and fifth MRIs). Differences in staging and initial localization between residual and no residual cases were analyzed using the Fisher exact test.

Receiver operating characteristic curves were used to determine the cutoff of the optimal follow-up duration. This cutoff was then used to optimize the sensitivity and specificity of non-EPI DWI using the Youden index. The performance associated with residual cholesteatoma detection was reported in terms of sensitivity and specificity. Each MR imaging was considered a separate event and associated with a time point. Due to the reduction in analyzed participants each time follow-up was discontinued (revision surgery or end of MR imaging follow-up), the diagnostic values of sensitivity and specificity were recalculated for every new event. Using this method, we generated sensitivity and specificity values for censored data as a function of time.

## RESULTS

### Study Population

The study included 17 participants with a sex ratio of 7:10 (females/males) and a mean age of 30.2 (SD, 22.2) years (range, 6–79 years) at the time of the second MR imaging. Eight (47%) were pediatric cases. Ten (58.8%) presented with left-ear cholesteatoma, and 7 (41.2%), with right-ear cholesteatoma at the time of initial operation. The Online Supplemental Data present clinical, MR imaging, and surgical findings.

The mean time between the initial operation and the first MR imaging was 17.3 (SD, 6.8) months (range, 9–32 months). The mean time between the first and second MR imaging was 24.9 (SD, 20.2) months (range, 8–94 months). The mean time between the initial operation and the second MR imaging was 42.7 (SD, 22.9) months (range, 20–119 months).

### MR Imaging Follow-up and Revision Surgery Findings

We analyzed 47 non-EPI DWI MR images from all participants. Figure 1 presents the flowchart of participant inclusion and MR imaging follow-up. On the basis of the second MR imaging, 5 participants underwent revision surgery, 3 had residual cholesteatoma, and the other 2 participants had false-positive diagnoses. Imaging follow-up was discontinued after the second MR imaging for 3 other participants at 20, 45, and 68 months after the initial operation.

A third MR imaging was performed in 9 participants with a mean interval of 68.2 (SD, 32.6) months (range, 43–147 months)

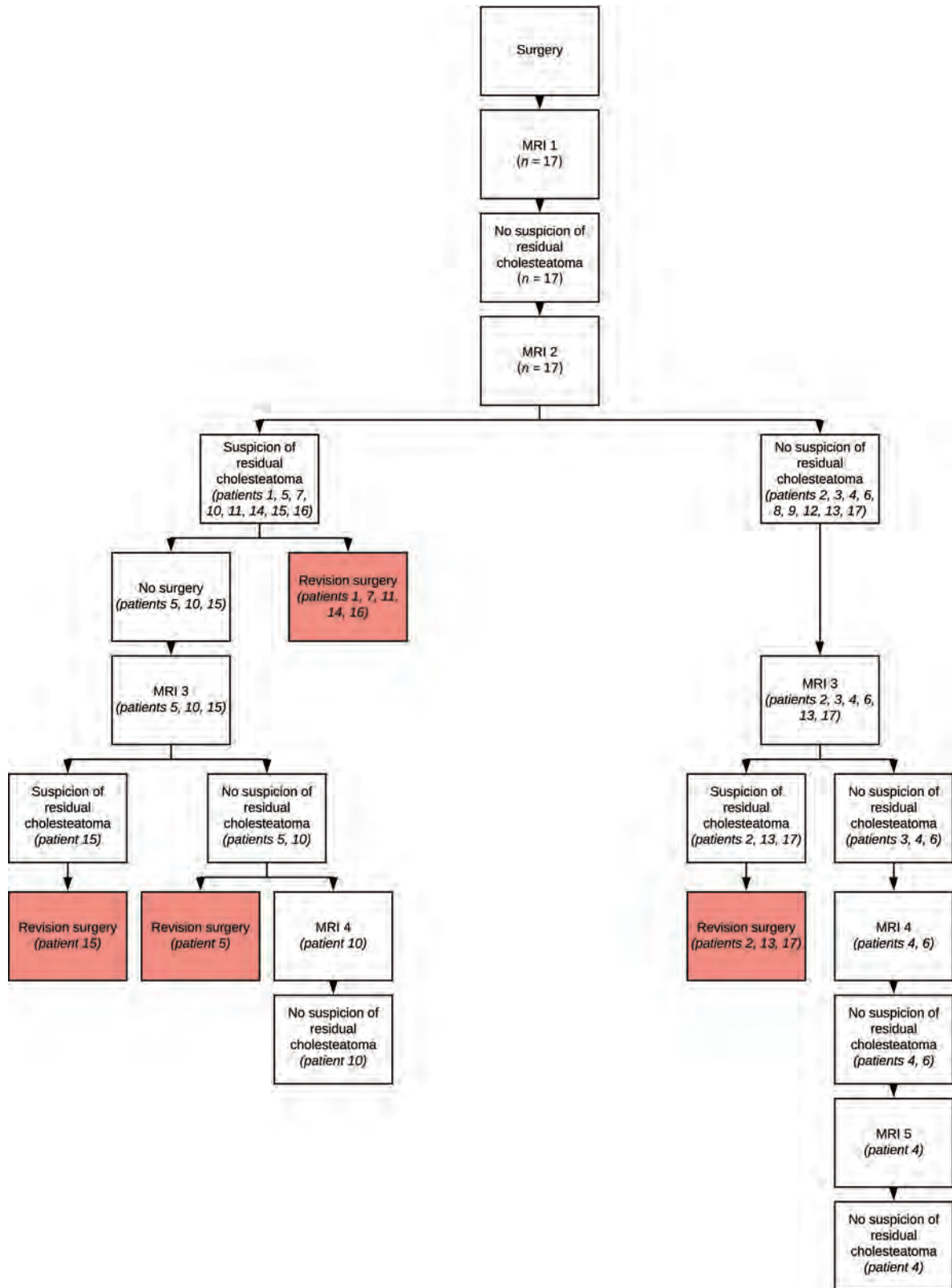


**FIG 1.** Flowchart of patient inclusion and follow-up imaging.

from the initial operation and 24.4 (SD, 12.3) months (range 11–44 months) between second and third MRIs. Five participants underwent revision surgery based on the third MR imaging. Four had residual cholesteatomas, and a fifth had an operation after

conductive hearing loss. One participant ended the follow-up after the findings of the third MR imaging were considered normal.

A fourth MR imaging was performed in the 3 remaining participants with a mean interval of 115 (SD, 72.5) months (range,

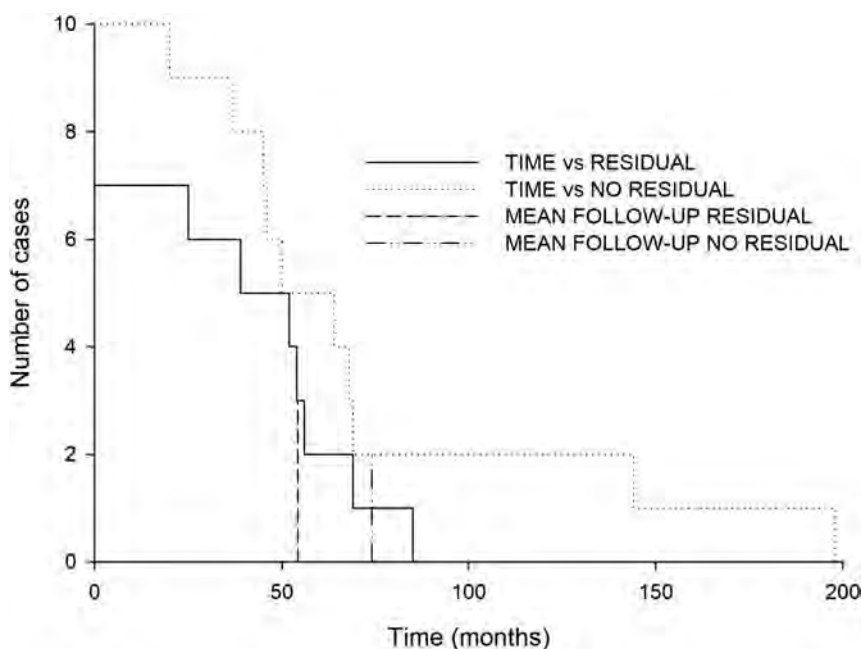


**FIG 2.** Duration of follow-up in participants with or without residual cholesteatoma. Solid and dotted lines depict participants with or without residual cholesteatoma, respectively, followed up across time in months. The mean duration of follow-up is 54.3 months in the residual cholesteatoma group and 74.1 months in the no residual cholesteatoma group.

64–198 months) from the initial operation and 36.7 (SD, 16.3) months (range, 19–51 months) between the third and fourth MRIs. No MR images from these participants indicated the need for revision surgery.

Finally, 1 participant underwent a fifth MR imaging 144 months after the initial operation and 60 months after the fourth MR imaging. No revision surgery was performed on this participant.

We detected a residual cholesteatoma in 41.1% of all participants (7/17) after the initial operation. The mean interval between the initial operation and the MR imaging classified as suspicious for residual cholesteatoma was 54.28 (SD, 19.4) months (median interval, 54 months). Among these, 43% were classified as stage I (1 location) and 57% were classified as stage II (2 locations) according to STAM classification. The location of the initial cholesteatoma was the attic in 85.7% of cases, mesotympanic in 42.8%, retrotympanic in 28.6%, and into the mastoid in 28.6% of cases. Participants with residual cholesteatomas were 14–74 years of age (mean, 32.3 years). Participants without residual cholesteatomas were 6–79 years of age (mean, 28.8 years). Follow-up duration ranged from 20 to 198 months (mean, 65.9 [SD, 43.9] months). The mean time between initial and revision surgery (when performed) was 53.8 (SD, 17.4) months (range, 28–85 months). Ten revision surgeries were performed (58.8%) for 7 residual cholesteatomas and 2 false-positives. The average follow-up duration from the initial operation to the last MR imaging was 65.9 (SD, 43.9) months (range, 20–198 months). The follow-up duration was longer in the group without a residual cholesteatoma (including false-positive cases with unnecessary surgery, 74.1 [SD, 54.7] months) than in the residual cholesteatoma group (54.3 [SD, 19.4] months) (Fig 2).

Three of 7 residual cholesteatomas were diagnosed on the second MR imaging (42.9%); the other 4 were discovered on the third MR imaging (57.1%). The residual cholesteatomas diagnosed on the second MR imaging were found 25, 39, and 52 months post-surgery. In those cases, the first MR imaging, considered to have normal findings, was performed 14, 12, and 20 months, respectively, after the initial operation. The residual cholesteatomas diagnosed during the third MR imaging were found at 54, 56, 69, and 85 months. In these cases, the second MR imaging, considered to have normal findings, was performed 29, 45, 37, and 40 months, respectively, after the initial operation. Their first MR imaging was performed 10, 24, 15, and 32 months, respectively, after the initial operation.

For the participants without identified residual cholesteatoma ( $n = 10$ ), 30% of initial cholesteatomas were classified as stage I and 70% were classified as stage II. Forty percent of the initial cholesteatomas were (fully or not) in the attic; 80%, mesotympanic; 20%, retrotympanic; 20%, paratympanic; and 40%, located in the mastoid. No differences in stage or location were found between the residual and no residual groups ( $P > .05$ , Fisher exact test).

#### Diagnostic Value of Non-EPI DWI as a Function of Time

Interobserver agreement based on the evaluation of non-EPI DWI MR imaging was high between the 2 senior neuroradiologists with a  $\kappa$  of 1 (perfect agreement).

The sensitivity and specificity of MR imaging were calculated as a function of time to determine the time at which non-EPI DWI had the best diagnostic value for detecting residual cholesteatoma after a first MR imaging showing no sign of residual cholesteatoma (Fig 3). Thus, the calculation was performed from the second MR imaging, including all subsequent imaging.

The sensitivity increased from 0 to 1 by 85 months postoperatively. The specificity went from 1 for MRIs performed up to 45 months to 0 for those performed from 198 months after the operation. Analyses of receiver operating characteristic curves showed that non-EPI DWI had the best diagnostic value 56 months after the initial operation (sensitivity = 0.71, specificity = 0.71, Youden index = 0.43).

#### DISCUSSION

Our results suggest that the optimal diagnostic value of repeat non-EPI DWI (sensitivity = 0.71 and specificity = 0.71) is reached 56 months (4.7 years) after the initial operation when a first MR imaging examination performed a mean of 17.3 (SD, 6.8) months after the operation does not detect residual cholesteatoma. This recommendation is based on analysis of

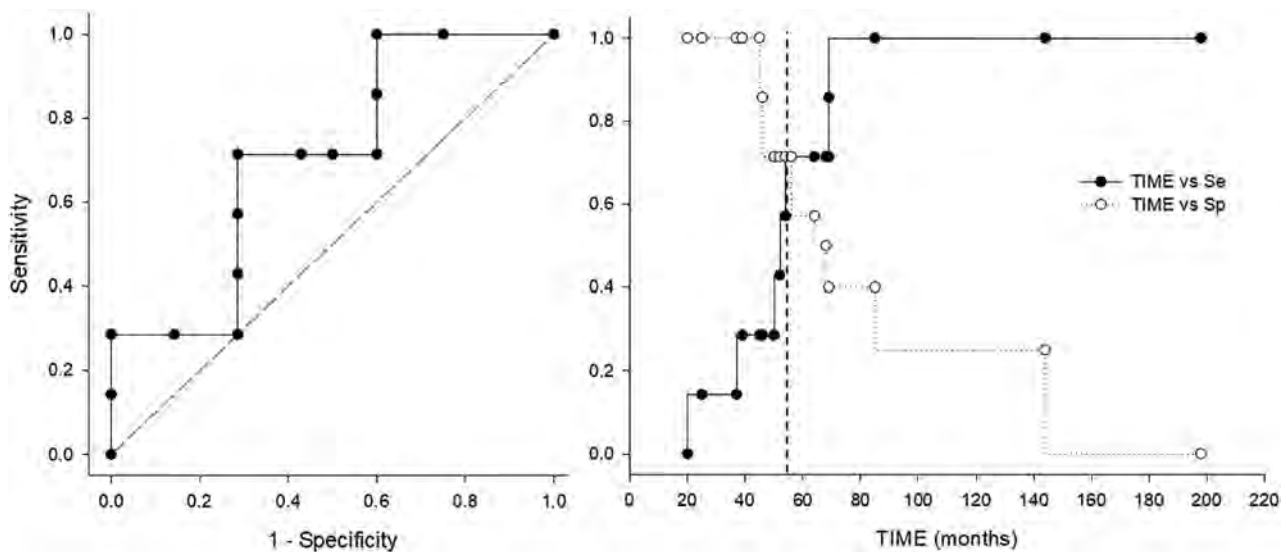


**FIG 3.** Diagnostic value of non-EPI DWI as a function of time. The *left panel* shows the receiver operating characteristic curve of sensitivity according to 1-specificity. The best diagnostic values (sensitivity = 0.71, specificity = 0.71, Youden index = 0.43) are reached at 56 months postoperatively. The *right panel* shows the values of sensitivity and specificity as a function of time. Sensitivity increases from 0 to 1 by 85 months postoperatively. Specificity changes from 1 for MRIs performed up to 45 months to 0 for those performed from 198 months after the operation. Se indicates sensitivity; sp, specificity.

participants who underwent complete macroscopic removal during the first operation. A different follow-up may be relevant in cases of incomplete removal, but our study did not address this issue.

This proposal is consistent with that of Pai et al,<sup>10</sup> who reported residual cholesteatoma detection by non-EPI DWI 3.8 years after the initial operation (median, 3.7 years; range, 1.6–7.9 years) and 2.5 years after the first negative imaging findings (median, 2.0 years; range, 0.9–5.1 years). Similarly, in a cohort of 45, Steens et al<sup>12</sup> reported 8 cases of residual cholesteatoma detected a mean of 3 (SD, 1.1) years after the initial operation and 2 (SD, 1) years after the first MR imaging; 2 cases were detected after a third MR imaging. In our study, the mean time between the first and second MR imaging was 24.9 (SD, 20.2) months or 2.08 (SD, 1.68) years, and between the initial and revision operations, it was a mean of 53.8 (SD, 17.4) months or 4.5 (SD, 1.4) years.

Knowing the mean interval between the operation and detection of a residual cholesteatoma is interesting, but the question of when to start and finish performing repeat MRIs remains unsolved. Thus, we performed a longitudinal analysis of all participants' MRIs and calculated the sensitivity and specificity values to optimize the number and the time of repeat MR imaging. Indeed, our recommendation relies on sensitivity and specificity analyses that are more robust than calculating the average time of residual detection, which, by its nature, does not consider cases without residual cholesteatoma or false-positive cases.

Despite being concordant with other long-term follow-up imaging studies (Pai et al<sup>10</sup> and Steens et al<sup>12</sup>), our results ended with lower sensitivity and specificity values than most reported studies that considered non-EPI DWI performed only once shortly after the operation.

The difference between short-term studies (using 1.5T or 3T scanners) and long-term studies (1.5T for Pai et al<sup>10</sup> and Steens et

al<sup>12</sup> and our study) cannot be explained by the type of MR imaging scanner used. Indeed, Lincot et al,<sup>13</sup> in 2015, demonstrated that 1.5T and 3T scanners could be used with no implications for diagnostic accuracy during short-term follow-up. The sensitivity and specificity of non-EPI DWI sequences used alone were 90.5%–100% and 68.4%–100%, respectively, depending on the reader. Conversely and unexpectedly, Lips et al,<sup>14</sup> in 2020, concluded that the sensitivity and specificity were lower at 3T than at 1.5T for non-EPI DWI sequences, irrespective of whether additional T1- and T2-weighted sequences were used. For non-EPI DWI sequences used alone, expert readers had a sensitivity and specificity of 96% and 59% at 1.5T, and 80% and 46% at 3T, respectively.<sup>14</sup>

Thus, technical aspects cannot explain the differences in diagnostic values obtained in long-term follow-up studies, including ours, and 2 meta-analyses by Lingam et al<sup>1</sup> (26 studies including 1152 participants) and Bazzi et al<sup>2</sup> (10 studies including 141 participants), which demonstrated very high diagnostic values (sensitivity = 0.82–0.91 and specificity = 0.88–0.90). Considering that the size limit for MR imaging detection of cholesteatomas is 2 mm, One main limitation of most of these studies was the lack of systematic revision surgery to ensure that no small residual cholesteatoma was left in the middle ear but missed by imaging.

One hypothesis that could explain the differences in diagnostic values is the variable growth rates among residual cholesteatomas. In 1976, Gristwood and Venables<sup>15</sup> reported varying growth rates of residual cholesteatomas, depending on the site (epitympanic versus mastoid) and other parameters such as tubal function, vascularization, or size of initial cholesteatoma. Pai et al<sup>10</sup> reported growth rates of 0–18 mm/year, with a mean of 4 mm/year; data computed by Venail et al<sup>16</sup> showed a mean growth rate of 2.74 mm/year. Faster-growing residual cholesteatomas may be detected during early and first non-EPI DWI; hence, they explain the high diagnostic values reported in the short term while

supporting the notion that slow-growing lesions require prolonged follow-up imaging to be detected.

Our imaging strategy, like those of Pai et al<sup>10</sup> and Steens et al<sup>12</sup> (including participants for whom the first MR imaging findings were considered negative) allowed us to rule out including any residual cholesteatomas with a high growth rate. The population remaining after removing those with a fast-growing residual cholesteatoma identified on the first examination showed high rates of residual cholesteatomas (31% for Steens et al<sup>12</sup> and 41.1% in our study), even though absolute numbers were limited (12 residual cholesteatoma cases for Pai et al,<sup>10</sup> 8 cases for Steens et al,<sup>12</sup> and 7 cases in this study).

These data seem to support the need for long-term follow-up. Pai et al<sup>10</sup> and Geven et al<sup>17</sup> recommended imaging follow-up of 5 years. Because our participants were followed up with different numbers of MRIs performed at several timepoints, we were able to calculate sensitivity and specificity values according to the follow-up duration. Our receiver operating characteristic curve analysis suggests the need for follow-up for 5 years. Indeed, in our study, the best diagnostic values of non-EPI DWI occurred 4.7 years after the initial operation.

A main limitation of long-term follow-up studies, including ours, is the limited number of participants who have undergone repeat MR imaging. Another limitation of our study is the lack of systematic surgical revision, which did not allow the accurate determination of the true sensitivity of MR imaging because late cholesteatoma recurrence can occur and be missed by imaging. To reduce limitations relating to technical issues, we chose to include only those participants operated on in our tertiary care center (same surgical team) and to use only MR imaging performed on the same device at a tertiary referral center and images interpreted by the same radiologist team. While this practice effectively reduced potential technical bias, it also limited the number of participants eligible for the study. Even if the true sensitivity of non-EPI DWI cannot be calculated using such a study design, the mean follow-up in the group with no identified residual cholesteatoma (including false-positive cases with unnecessary revision surgery) was 74.1 (SD, 54.7) months (6.2 years). This duration is, thus, longer than the 5-year follow-up suggested on the basis of our analyses. It would have been interesting to compare initial localization and staging between residual and no residual groups and late and early residual disease, but our sample size was too small to address these points.

The cost of repeat MR imaging for cholesteatoma follow-up has not been considered here. Choi et al<sup>18</sup> compared second-look surgery with a single non-EPI DWI in Canada. The cost analysis favored non-EPI DWI (difference of CAD\$390.66 [95% CI, CAD\$381.52–\$399.80]) for a single MR imaging examination, but this analysis needs re-evaluating for repeat imaging assessments. As we showed, MR imaging 5 years after the initial operation provides the best diagnostic values, but the question of whether to add an intermediate MR imaging around 3 years after the operation remains. Our clinical experience was that a third MR imaging was performed around 3.5 years after the operation. The advantage is the potential to prevent excessive growth of a residual lesion between the first MR imaging and the 5-year MR imaging, but this additional MR imaging comes with an extra

cost and a risk of poor sensitivity (<0.3) in our study. Indeed, the MR imaging at 3.5 years was clearly not sufficient for optimal follow-up, and an MR imaging at 5 years was needed. Because no major complications related to residual cholesteatoma growth (labyrinthine fistula, meningitis) were observed during our prolonged follow-up study, the absolute need for an intermediate MR imaging before 5 years is questionable and deserves further investigation, including cost-utility analyses.

## CONCLUSIONS

Repeat non-EPI DWI is an effective method to detect middle ear residual cholesteatoma. Prolonged follow-up is needed to identify slowly growing lesions. On the basis of our results, we suggest performing non-EPI DWI at 18 months and 3.5 years after the initial operation. If the second non-EPI DWI shows no sign of cholesteatoma, a third and last MR imaging should be performed 5 years after the initial operation to safely exclude or identify residual tumors. Follow-up should be adapted depending on the initial localization and extent of the cholesteatoma and on the quality of the initial operation.

Disclosures: Pierre-Henri Lefevre—UNRELATED: Payment for Development of Educational Presentations: Medtronic, Frederic Venail—UNRELATED: Grants/Grants Pending: Cochlear SAS\*; Travel/Accommodations/Meeting Expenses Unrelated to Activities Listed: international and national ear, nose and throat meeting unrelated to the work submitted. \*Money paid to the institution.

## REFERENCES

1. Lingam RK, Bassett P. **A meta-analysis on the diagnostic performance of non-echo-planar diffusion-weighted imaging in detecting middle ear cholesteatoma: 10 years on.** *Otol Neurotol* 2017;38:521–28 CrossRef Medline
2. Bazzi K, Wong E, Jufas N, et al. **Diffusion-weighted magnetic resonance imaging in the detection of residual and recurrent cholesteatoma in children: a systematic review and meta-analysis.** *Int J Pediatr Otorhinolaryngol* 2019;118:90–96 CrossRef Medline
3. Lingam RK, Khatri P, Hughes J, et al. **Apparent diffusion coefficients for detection of postoperative middle ear cholesteatoma on non-echo-planar diffusion-weighted images.** *Radiology* 2013;269:504–10 CrossRef Medline
4. Khemani S, Lingam RK, Kalan A, et al. **The value of non-echo planar HASTE diffusion-weighted MR imaging in the detection, localisation and prediction of extent of postoperative cholesteatoma.** *Clin Otolaryngol* 2011;36:306–12 CrossRef Medline
5. Akkari M, Gabrillargues J, Saroul N, et al. **Contribution of magnetic resonance imaging to the diagnosis of middle ear cholesteatoma: analysis of a series of 97 cases.** *Eur Ann Otorhinolaryngol Head Neck Dis* 2014;131:153–58 CrossRef Medline
6. Gaillardin L, Lescanne E, Moriniere S, et al. **Residual cholesteatoma: prevalence and location: follow-up strategy in adults.** *Eur Ann Otorhinolaryngol Head Neck Dis* 2012;129:136–40 CrossRef Medline
7. Horn RJ, Gratama JW, van der Zaag-Loonen HJ, et al. **Negative predictive value of non-echo-planar diffusion weighted MR imaging for the detection of residual cholesteatoma done at 9 months after primary surgery is not high enough to omit second look surgery.** *Otol Neurotol* 2019;40:911–19 CrossRef Medline
8. Lecler A, Lenoir M, Peron J, et al. **Magnetic resonance imaging at one year for detection of postoperative residual cholesteatoma in children: is it too early?** *Int J Pediatr Otorhinolaryngol* 2015;79:1268–74 CrossRef Medline
9. De Foer B, Vercrucyse JP, Bernaerts A, et al. **Detection of postoperative residual cholesteatoma with non-echo-planar diffusion-weighted magnetic resonance imaging.** *Otol Neurotol* 2008;29:513–17 CrossRef Medline

10. Pai I, Crossley E, Lancer H, et al. **Growth and late detection of post-operative cholesteatoma on long term follow-up with diffusion weighted magnetic resonance imaging (DWI MRI): a retrospective analysis from a single UK centre.** *Otol Neurotol* 2019;40:638–44 CrossRef Medline
11. Yung M, Tono T, Olszewska E, et al. **EAONO/JOS joint consensus statements on the definitions, classification and staging of middle ear cholesteatoma.** *J Int Adv Otol* 2017;13:1–8 CrossRef Medline
12. Steens S, Venderink W, Kunst D, et al. **Repeated postoperative follow-up diffusion-weighted magnetic resonance imaging to detect residual or recurrent cholesteatoma.** *Otol Neurotol* 2016;37:356–61 CrossRef Medline
13. Lincot J, Veillon F, Riehm S, et al. **Middle ear cholesteatoma: compared diagnostic performances of two incremental MRI protocols including non-echo planar diffusion-weighted imaging acquired on 3T and 1.5T scanners.** *J Neuroradiol* 2015;42:193–201 CrossRef Medline
14. Lips LM, Nelemans PJ, Theunissen FM, et al. **The diagnostic accuracy of 1.5 T versus 3 T non-echo-planar diffusion-weighted imaging in the detection of residual or recurrent cholesteatoma in the middle ear and mastoid.** *J Neuroradiol* 2020;47:433–40 CrossRef Medline
15. Gristwood RE, Venables WN. **Growth rate and recurrence of residual epidermoid cholesteatoma after tympanoplasty.** *Clin Otolaryngol Allied Sci* 1976;1:169–82 CrossRef Medline
16. Venail F, Bonafe A, Poirrier V, et al. **Comparison of echo-planar diffusion-weighted imaging and delayed postcontrast T1-weighted MR imaging for the detection of residual cholesteatoma.** *AJNR Am J Neuroradiol* 2008;29:1363–68 CrossRef Medline
17. Geven LI, Mulder JJ, Graamans K. **Giant cholesteatoma: recommendations for follow-up.** *Skull Base* 2008;18:353–59 CrossRef Medline
18. Choi DL, Gupta MK, Rebello R, et al. **Cost-comparison analysis of diffusion weighted magnetic resonance imaging (DWMRI) versus second look surgery for the detection of residual and recurrent cholesteatoma.** *J Otolaryngol Head Neck Surg* 2019;48:58 CrossRef Medline

# Assessment of MR Imaging and CT in Differentiating Hereditary and Nonhereditary Paragangliomas

 Y. Ota,  S. Naganawa,  R. Kurokawa,  J.R. Bapuraj,  A. Capizzano,  J. Kim,  T. Moritani, and  A. Srinivasan



## ABSTRACT

**BACKGROUND AND PURPOSE:** Head and neck paragangliomas have been reported to be associated with mutations of the succinate dehydrogenase enzyme family. The aim of this study was to assess whether radiologic features could differentiate between paragangliomas in the head and neck positive and negative for the succinate dehydrogenase mutation.

**MATERIALS AND METHODS:** This single-center retrospective review from January 2015 to January 2020 included 40 patients with 48 paragangliomas (30 tumors positive for succinate dehydrogenase mutation in 23 patients and 18 tumors negative for the succinate dehydrogenase mutation in 17 patients). ADC values and tumor characteristics on CT and MR imaging were evaluated by 2 radiologists. Differences between the 2 cohorts in the diagnostic performance of ADC and normalized ADC (ratio to ADC in the medulla oblongata) values were evaluated using the independent samples *t* test. *P* < .05 was considered significant.

**RESULTS:** ADC<sub>mean</sub> (1.07 [SD, 0.25]/1.04 [SD, 0.12] versus 1.31 [SD, 0.16]/1.30 [SD, 0.20] × 10<sup>-3</sup> mm<sup>2</sup>/s by radiologists 1 and 2; *P* < .001), ADC<sub>maximum</sub> (1.49 [SD, 0.27]/1.49 [SD, 0.20] versus 2.01 [SD, 0.16]/1.87 [SD, 0.20] × 10<sup>-3</sup> mm<sup>2</sup>/s; *P* < .001), normalized ADC<sub>mean</sub> (1.40 [SD, 0.33]/1.37 [SD, 0.16] versus 1.73 [SD, 0.22]/1.74 [SD, 0.27]; *P* < .001), and normalized ADC<sub>maximum</sub> (1.95 [SD, 0.37]/1.97 [SD, 0.27] versus 2.64 [SD, 0.22]/2.48 [SD, 0.28]; *P* < .001) were significantly lower in succinate dehydrogenase mutation–positive than mutation–negative tumors. ADC<sub>minimum</sub>, normalized ADC<sub>minimum</sub>, and tumor characteristics were not statistically significant.

**CONCLUSIONS:** ADC is a promising imaging biomarker that can help differentiate succinate dehydrogenase mutation–positive from mutation–negative paragangliomas in the head and neck.

**ABBREVIATIONS:** nADC = normalized ADC; SDH = succinate dehydrogenase

Paragangliomas are uncommon neuroendocrine tumors with an estimated annual incidence of 3–8 cases per 1 million people in the general population.<sup>1</sup> They arise from the sympathetic and parasympathetic autonomic system and occur anywhere from the base of the skull to the pelvis, with 70% of extra-adrenal paragangliomas arising in the head and neck region. The typical clinical sites are the carotid artery bifurcation, middle ear, and jugular fossa.<sup>1–3</sup> Clinical manifestations include hypertension, palpitations, headache, excessive

sweating, and pallor, which vary depending on the tumor size, location, and biochemical activity.<sup>1,4</sup>

There has been an increasing interest in the genetic basis for paragangliomas. Although head and neck paragangliomas often occur as sporadic tumors, it is now recognized that approximately 30%–40% of head and neck paragangliomas are associated with autosomal dominant hereditary tumor syndromes.<sup>1,2,5</sup> Succinate dehydrogenase (SDH), a multiprotein complex composed of SDH subunit A, B, C, and D proteins, is an important enzyme in the Krebs cycle and electron transport chain in the mitochondria for energy production. The loss of SDH function results in less efficiency of these processes. Moreover, these altered pathways allow the tumor cells to grow even in a low-oxygen environment.<sup>6</sup> Therefore, deactivation in any of the subunits will result in tumors positive for the SDH mutation.

Familial paraganglioma syndromes associated with SDH gene mutations have now been recognized as the primary cause of hereditary paragangliomas in the head and neck. Twenty-five percent of all paragangliomas and pheochromocytomas are related

Received November 17, 2020; accepted after revision February 15, 2021.

From the Division of Neuroradiology (Y.O., S.N., J.R.B., A.C., J.K., T.M., A.S.), Department of Radiology, University of Michigan, Ann Arbor, Michigan; and Department of Radiology (R.K.), Graduate School of Medicine, The University of Tokyo, Tokyo, Japan.

Please address correspondence to Yoshiaki Ota, MD, 1500 E Medical Center Dr, UH B2, Ann Arbor, MI 48109; e-mail: yoshiako@med.umich.edu

 Indicates open access to non-subscribers at [www.ajnr.org](http://www.ajnr.org)

 Indicates article with online supplemental data.

<http://dx.doi.org/10.3174/ajnr.A7166>

to genetic mutations in different subunits of the SDH protein, each with different tendencies toward different tumor locations, different numbers of lesions, and different potentials for malignancy.<sup>1</sup> For example, familial paragangliomas with *SDH subunit D* (*SDHD*) mutation are more likely to be multifocal in the head and neck, and paragangliomas with *SDH subunit B* (*SDHB*) mutations are prone to malignant transformation.<sup>1</sup> Therefore, establishment of genetic screening of individuals and life-long surveillance of patients at high risk for developing paragangliomas are important.

The typical imaging appearances of head and neck paragangliomas on CT and MR imaging include well-circumscribed lesions showing avid contrast enhancement.<sup>7-9</sup> Prior studies have demonstrated that DWI and ADC parameters can be used for diagnosis, staging, and follow-up of head and neck tumors.<sup>10</sup> As for paragangliomas, ADC values have been used in the past to differentiate these tumors from other head and neck lesions, with variable results.<sup>11</sup> Because paragangliomas can have genetic mutations and a variety of histologic patterns,<sup>12</sup> the variability of ADC values on MR imaging studies may be secondary to the heterogeneous genotype of these lesions. The aim of our study, therefore, was to evaluate the differences in ADC values between SDH mutation-positive and SDH mutation-negative head and neck paragangliomas to assess the utility of ADC as an imaging biomarker.

## MATERIALS AND METHODS

The institutional review board of University of Michigan approved this retrospective single-center study and waived the requirement for informed consent. Data were acquired in compliance with all applicable Health Insurance Portability and Accountability Act regulations.

### Study Population

We retrospectively reviewed 579 consecutive patients from January 2015 to January 2020 who were suspected of having head and neck paragangliomas from head and neck CT/MR imaging findings and clinical information. Among them, 94 patients had been diagnosed with paragangliomas histopathologically or clinically by elevated plasma fractionated metanephrines or elevated 24-hour urinary fractionated metanephrines, findings of head and neck CT and MR imaging, and PET with 2-Deoxy-2-[<sup>18</sup>F] fluoro-d-glucose integrated with CT or indium-111 (<sup>111</sup>In) pentetreotide SPECT. We excluded patients who had previously undergone an operation, had undergone radiation therapy, did not have pretreatment CT/MR imaging ( $n = 28$ ), or did not have prior genetic testing for *SDH* mutations ( $n = 26$ ). Forty patients (49.3 [SD, 14.9] years of age; 9 men; 31 women) with 48 paragangliomas constituted the final study cohort.

### Genetic Testing

Genetic testing was by the PGLNext panel (Ambry Genetics), which requires collecting blood or saliva samples by an appropriate kit. PGLNext analyzes 12 genes including *SDHA*, *SDH subunits AF2* (*SDHAF2*), *SDHB*, *SDHC*, and *SDHD*. This test is designed and validated to detect >99% of the gene mutations noted above.

This cohort was further divided into 2 groups: the *SDH* mutation-positive group and *SDH* mutation-negative group.

In the *SDH* mutation-positive group, there were 30 paragangliomas in 23 patients (mutations of the *SDH subunits A*, *B*, *C*, and *D* were  $n = 2$ , 8, 5 and 15, respectively). Nineteen lesions were pathologically proved, and 11 lesions were clinically diagnosed. Three patients with the *SDHD* mutation had 2 lesions each, 1 patient with an *SDHD* mutation had 4 lesions, and 1 patient with an *SDHB* mutation had 2 lesions.

In the *SDH* mutation-negative group, there were 18 paragangliomas in 17 patients. Eleven lesions were pathologically proved, and 7 lesions were clinically diagnosed. One patient had 2 lesions.

### MR Imaging Acquisition

MR imaging studies were acquired on multiple scanners including 1.5T scanners (Ingenia,  $n = 10$ , and Achieva,  $n = 10$ ; Philips Healthcare; Signa Excite,  $n = 4$ , and GoldSeal Signa HDxt,  $n = 4$ ; GE Healthcare) and 3T scanners (Magnetom Vida,  $n = 5$ ; Siemens; and Ingenia,  $n = 15$ ; Philips Healthcare). MR imaging sequences and parameters were summarized in the Online Supplemental Data. These parameters were modified depending on the field strength and manufacturers.

### CT Acquisition

Contrast-enhanced CT neck examinations were acquired on a multislice 64-detector CT scanners (HD 750; GE Healthcare) with the following scan parameters: 120–140 kV(peak), 80–295 mA, skull base to thoracic inlet, 125 mL of iopamidol (Isovue 300; Bracco). The parameters of neck CT were as follows: plane = axial, FOV = 96 mm, section thickness = 0.625 mm, window level and width = 400 and 3200 HU, phase = 45 seconds, delayed phase.

### Image Analysis

**Conventional Imaging Analysis.** Two board-certified neuroradiologists with 6 and 9 years of experience interpreted all radiologic images independently. They were blinded to the mutation status of the lesions. Both radiologists recorded the following metrics:

1. Maximum axial diameter of the tumor on postcontrast T1-weighted images.
2. The presence of necrotic or cystic changes and salt-and-pepper appearance (flow voids) evaluated on T2-weighted and pre- and postcontrast T1-weighted images. These were recorded as binary variables (yes/no). Cystic changes were defined as nonenhancing, predominantly T1-hypointense and T2-hyperintense areas; necrotic changes, as nonenhancing, predominantly T1-hypointense and heterogeneously T2-hyperintense areas; and salt-and-pepper appearance, as nonenhancing T1-hypointense and T2-hypointense vessel structures within the tumors.
3. Erosions of adjacent bony structures evaluated on CT. The axial plane was used. These were recorded as binary variables (yes/no).
4. Glomus jugulare and glomus jugulotympanicum were classified into head lesions; and carotid body tumors and glomus vagale, into neck lesion as for location.

**ADC Analysis.** ADC maps were constructed by a monoexponential fitting model using the commercially available

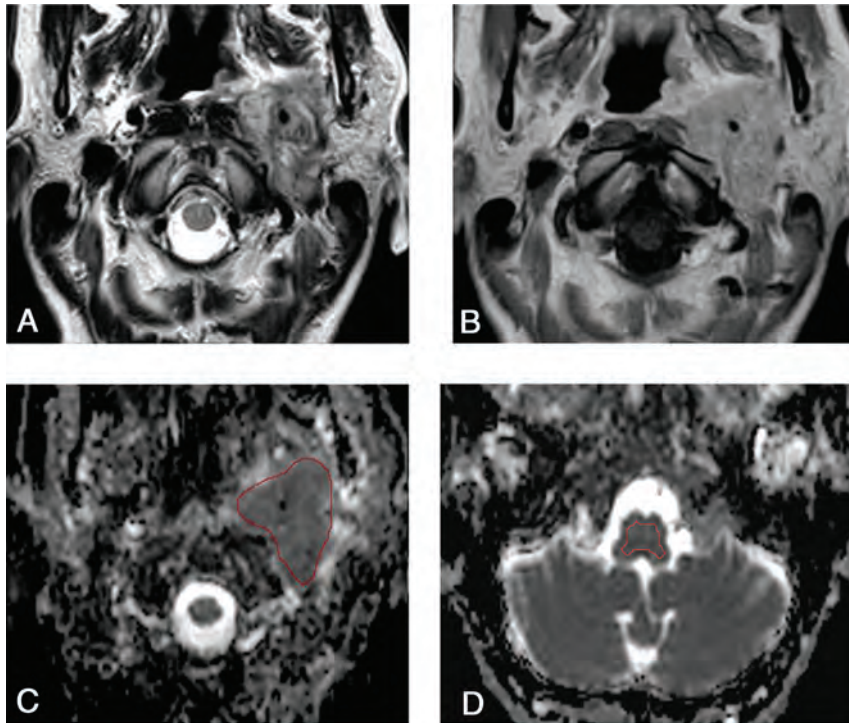


**FIG 1.** A 48-year-old woman positive for the *SDHC* mutation with a paraganglioma in the left jugular foramen. *A* and *B*, Axial T2-weighted and contrast-enhanced T1-weighted images demonstrate a heterogeneously enhancing, irregularly shaped tumor with flow voids in the left jugular foramen. *C*, An ROI is placed on the lesion on the ADC map. The mean ADC, maximum ADC, and minimum ADC values of reader 1 are  $1.06$ ,  $1.47$ , and  $0.53 \times 10^{-3} \text{ mm}^2/\text{s}$ , respectively. *D*, Another ROI for an internal standard is placed on the medulla as an internal control (mean ADC,  $0.75 \times 10^{-3} \text{ mm}^2/\text{s}$ ). The mean nADC, maximum nADC, and minimum nADC are  $1.41$ ,  $1.96$ , and  $0.71 \times 10^{-3} \text{ mm}^2/\text{s}$ , respectively.

software Olea Sphere (Olea Medical). The 2 neuroradiologists independently outlined the tumors on an axial post-contrast T1-weighted image and transposed the freehand ROI to the ADC map. The axial images that predominantly showed solid enhancing portions without cystic or necrotic areas on postcontrast T1-weighted images were selected. The ROIs spared the peripheral 2-mm margin of the lesions to avoid volume averaging (Fig 1C).<sup>13</sup> When geometric distortion was observed, the location and size were adjusted on the ADC map so that the ROI could be included within the tumor. A separate ROI was placed in the center of the medulla oblongata at the level of the foramen of Lushcka as an internal reference standard (Fig 1D).<sup>14</sup> A normalized ADC (nADC) ratio was calculated by dividing each ADC value of the lesion by the mean ADC value of the medulla oblongata.

### Statistical Analysis

Patient demographic characteristics including sex (ratio of male to female) and age, number of lesions, tumor characteristics of maximum diameter of tumor, presence or absence of salt-and-pepper appearance, location (ratio of head/neck lesion), adjacent skull destructive changes, and necrotic changes were compared between the 2 groups. Age was compared by *t* tests and was described as mean (SD). The maximum diameter of the tumor

was compared using the Mann-Whitney *U* test and described as median (interquartile range). The categorical variables such as sex (ratio of male to female), presence or absence of salt-and-pepper appearance, adjacent skull destructive change and necrotic change, and location (ratio of head/neck lesion) were compared using the Fisher exact test.

The  $ADC_{\text{mean}}$ ,  $ADC_{\text{maximum}}$ , and  $ADC_{\text{minimum}}$  values and  $nADC_{\text{mean}}$ ,  $nADC_{\text{maximum}}$ , and  $nADC_{\text{minimum}}$  ratios for the 2 readers were analyzed separately using the independent samples *t* test. For the metrics that showed a statistically significant difference, diagnostic performances were calculated on the basis of receiver operating characteristic curve analysis. The optimal cutoff values in receiver operating characteristic analysis were determined as a value to maximize the Youden index (sensitivity + specificity - 1).

As for tumor characteristics, inter-reader agreement was assessed by  $\kappa$  analysis, which was interpreted as follows:  $<0.40$ , poor-to-fair agreement;  $0.41$ – $0.60$ , moderate agreement;  $0.61$ – $0.80$ , substantial agreement; and  $0.81$ – $1.00$ , almost perfect agreement.<sup>15</sup>

All statistical calculations were conducted with JMP Pro, Version 15.0.0 (SAS Institute). Variables with

$P < .05$  were considered statistically significant.

## RESULTS

Patient demographics and tumor characteristics are shown in Table 1. Patients who were in the *SDH* mutation-positive group were significantly younger than those in the *SDH* mutation-negative group ( $43.9$  [SD,  $16.2$ ] years versus  $56.9$  [SD,  $10.7$ ] years;  $P = .007$ ).

In the *SDH* mutation-positive group, 4 patients with *SDHD* mutations had multiple lesions in the head and neck (1 with 4 lesions, 1 with 3 lesions, and 2 with 2 lesions each) and 1 patient with an *SDHB* mutation had 2 lesions. There were 13 head lesions (7 glomus jugulare and 6 glomus jugulotympanicum lesions), and 17 neck lesions (16 carotid body tumors and 1 glomus vagale) in this group.

In the *SDH* mutation-negative group, there were 13 head lesions (12 glomus jugulare and 1 jugulotympanicum) and 5 neck lesions (5 carotid body tumors).

There were no significant differences between the 2 groups in the maximum diameter of tumor, the presence or absence of salt-and-pepper appearance, adjacent skull erosions, necrotic changes, or location (ratio of head/neck region).

### Reader 1 Results

$ADC_{\text{mean}}$  ( $1.07$  [SD,  $0.25$ ] versus  $1.31$  [SD,  $0.16$ ]  $\times 10^{-3} \text{ mm}^2/\text{s}$ ;  $P < .001$ ),  $ADC_{\text{maximum}}$  ( $1.49$  [SD,  $0.27$ ] versus  $2.01$  [SD,

**Table 1: Demographic and tumor characteristics patients with head and neck paragangliomas**

	SDH Mutation–Positive	SDH Mutation–Negative	P Value
No. of lesions	30	18	NA
Sex (male/female)	7:16	2:15	.37
Age (mean) (yr)	43.9 (SD, 16.2) (23 patients)	56.9 (SD, 10.7) (17 patients)	.007
Maximum diameter (median) (IQR) (mm)	26.5 (20.6–33.0)	24.4 (21.2–36.0)	.68
Salt-and-pepper appearance	24/30	13/18	.72
Ratio of head/neck region	13:17	13:5	.07
Adjacent osseous erosive changes of head region	13:13	12:13	1
Necrotic or cystic changes	18/30	10/18	.77

Note:—NA indicates not applicable; IQR, interquartile range.

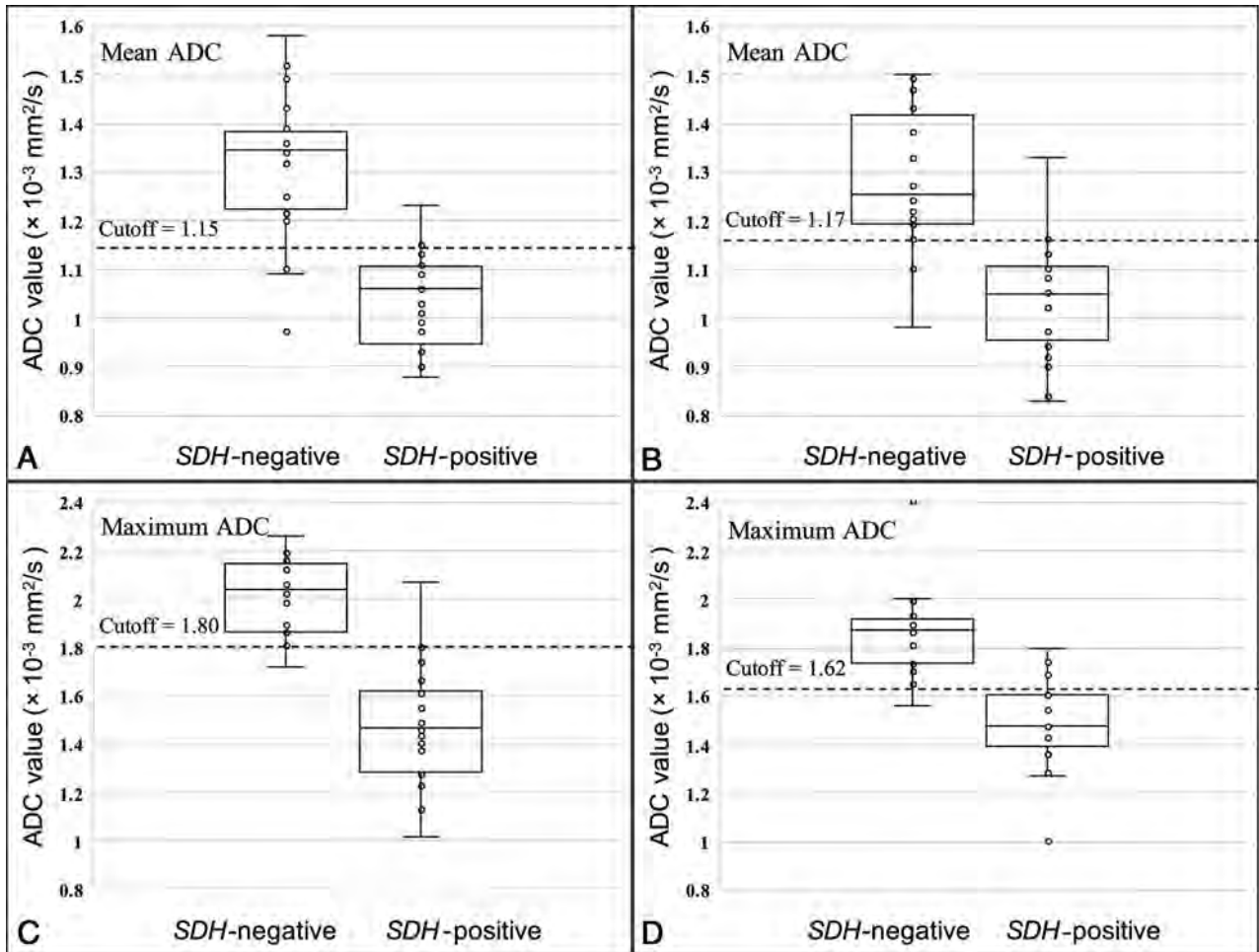


**FIG 2.** Comparison of mean and maximum ADC values between the SDH mutation–negative group and the SDH mutation–positive group (A and C, result of reader 1; B and D, result of reader 2).

$0.16] \times 10^{-3} \text{ mm}^2/\text{s}$ ;  $P < .001$ ,  $nADC_{\text{mean}}$  (1.40 [SD, 0.33] versus 1.73 [SD, 0.22];  $P < .001$ ), and  $nADC_{\text{maximum}}$  (1.95 [SD, 0.37] versus 2.64 [SD, 0.22];  $P < .001$ ) were significantly lower in the SDH mutation–positive group than in SDH mutation–negative group (Online Supplemental Data and Fig 2A, -C). The size of the ROI was 313 (SD, 259) mm.

#### Reader 2 Results

$ADC_{\text{mean}}$  (1.04 [SD, 0.12] versus 1.30 [SD, 0.20]  $\times 10^{-3} \text{ mm}^2/\text{s}$ ;  $P < .001$ ),  $ADC_{\text{maximum}}$  (1.49 [SD, 0.20] versus 1.87 [SD,

$0.20] \times 10^{-3} \text{ mm}^2/\text{s}$ ;  $P < .001$ ),  $nADC_{\text{mean}}$  (1.37 [SD, 0.16] versus 1.74 [SD, 0.27];  $P < .001$ ), and  $nADC_{\text{maximum}}$  (1.97 [SD, 0.27] versus 2.48 [SD, 0.28];  $P < .001$ ) were significantly lower in the SDH mutation–positive group than in SDH mutation–negative group (Online Supplemental Data and Fig 2B, -D). The size of the ROI was 291 (SD, 229) mm.

There were no significant statistical differences in  $ADC_{\text{minimum}}$  and  $nADC_{\text{minimum}}$  data for both readers. Representative cases of an SDH mutation–positive paraganglioma and an SDH mutation–negative paraganglioma are shown in Figs 3 and 4, respectively.

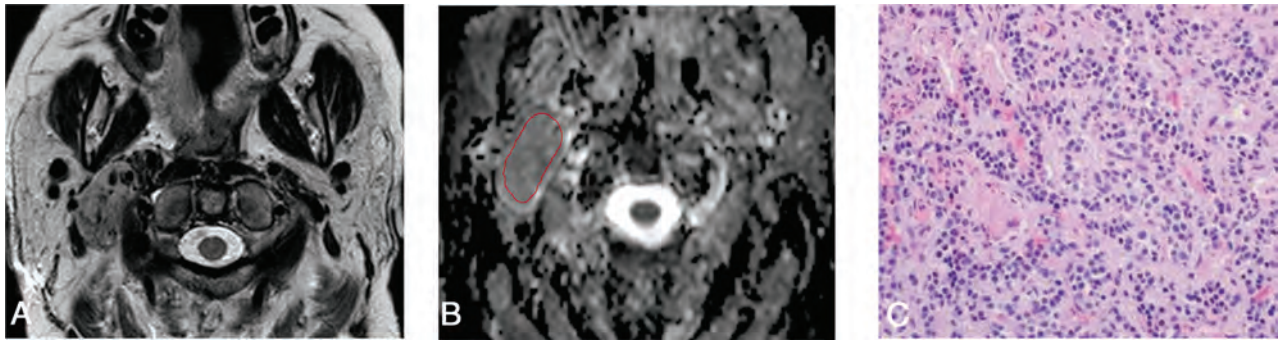


**FIG 3.** A 62-year-old woman negative for the *SDH* mutation with a paraganglioma in the right carotid space. *A*, Axial T2-weighted image demonstrates a heterogeneous well-defined tumor with flow voids in the right carotid space. *B*, The freehand ROI is placed on the lesion on the ADC map. Mean ADC, maximum ADC, and minimum ADC values of reader 1 are 1.31, 1.61, and  $0.71 \times 10^{-3} \text{ mm}^2/\text{s}$ , respectively. *C*, The resection specimen shows chief cells forming variable-size clusters in the zellballen pattern (H&E,  $\times 40$ ).

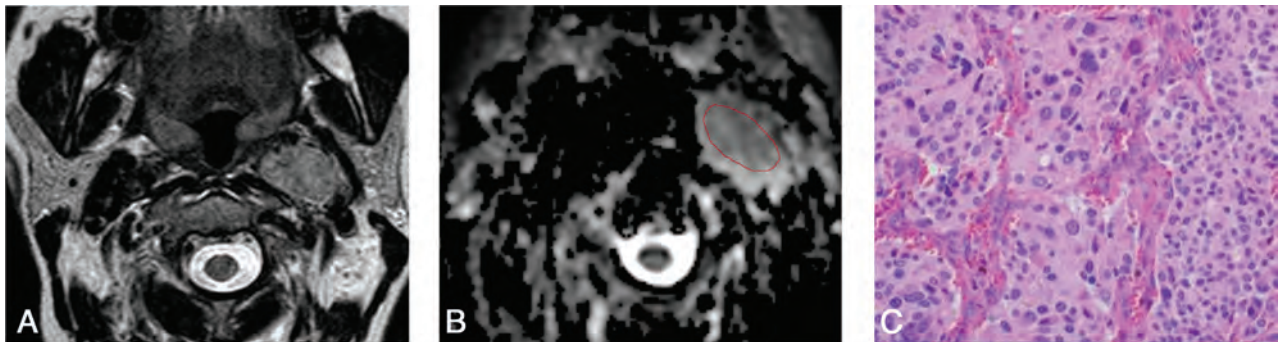


**FIG 4.** A 52-year-old woman positive for the *SDHD* mutation with a paraganglioma in the left carotid space. *A*, Axial T2-weighted image demonstrates a heterogeneous tumor with flow voids. *B*, The freehand ROI is placed on this lesion on the ADC map. The mean ADC, maximum ADC, and minimum ADC of reader 1 are 1.13, 1.57, and  $0.51 \times 10^{-3} \text{ mm}^2/\text{s}$ , respectively. *C*, The resection specimen shows a large and irregular cell nest and prominent vascularity (H&E,  $\times 40$ ).

Table 2 depicts the areas under the curve and diagnostic performances of the  $\text{ADC}_{\text{mean}}$ ,  $\text{ADC}_{\text{maximum}}$ ,  $\text{nADC}_{\text{mean}}$ , and  $\text{nADC}_{\text{maximum}}$  for both readers.

Interreader agreement for tumor characteristics was substantial-to-almost perfect ( $\kappa = 0.625\text{--}1$ ).

## DISCUSSION

Our study aimed to evaluate the utility of ADC values and tumor characteristics on CT and MR imaging in differentiating *SDH* mutation-positive versus mutation-negative head and neck paragangliomas. While the *SDH* mutation could not be identified by tumor characteristics interpreted on the basis of conventional imaging features, ADC values were significantly different between the 2 cohorts, with the diagnostic performances of areas under the curves from 0.87 to 0.94.

Prior studies focusing on ADC values in paragangliomas<sup>11,16,17</sup> showed mean ADC values ranging between  $0.89 \times 10^{-3}$  and  $1.30 \times 10^{-3} \text{ mm}^2/\text{s}$ .<sup>11,16</sup> Our study revealed mean ADC values of 1.07/1.04, 1.31/1.30, and  $1.16/1.17 \times 10^{-3} \text{ mm}^2/\text{s}$  for *SDH* mutation-positive, mutation-negative, and total paragangliomas; thus, the relatively wide range of ADC values reported in past literature may be due to differences in the proportion of *SDH* mutations in the study populations.

In our study, the mean and maximum ADC values of the *SDH* mutation-positive group were significantly lower than those of *SDH* mutation-negative group. It has been recognized that paragangliomas show different tumor cell morphology and cellularity and various histologic patterns, such as nests of tumor cells separated by peripheral capillaries (zellballen pattern) or large and irregular cell nest patterns.<sup>12</sup> This histopathologic background may result in lower mean and maximum ADC values in the *SDH* mutation-positive group. A histologic study suggested that no difference is to be expected in benign and malignant paragangliomas,<sup>18</sup> but to the best of our knowledge, there have not been studies about pathologic differences based on *SDH*-mutation status. In another study, *SDH* mutation-positive paragangliomas have been reported to show prominent vascularization.<sup>6</sup> Prominent signal voids from higher arterial vascularity can result in T2 blackout on DWI and low ADC values within the high-flow arteries, which could contribute to a decrease in the overall ADC values.<sup>19</sup> Therefore, differences in vascularity between the *SDH* mutation-positive group and the *SDH* mutation-negative group may also result in differences of mean and maximum ADCs.

There was no significant difference in minimum ADC values between the 2 groups. This can be because paragangliomas have

**Table 2: Diagnostic performance of ADC values in differentiating groups positive for the SDH mutation from those negative for it (both readers' results)**

	ADC Mean ( $\times 10^{-3}$ mm <sup>2</sup> /s)	ADC Maximum ( $\times 10^{-3}$ mm <sup>2</sup> /s)	nADC Mean	nADC Maximum
Cutoff	1.15/1.17	1.80/1.62	1.52/1.53	2.32/2.07
Sensitivity	0.90/0.95	0.93/0.79	0.90/0.95	0.93/0.68
Specificity	0.83/0.78	0.94/0.94	0.83/0.83	0.94/1.00
PPV	0.90/0.82	0.97/0.94	0.90/0.86	0.97/1.00
NPV	0.83/0.93	0.90/0.81	0.83/0.94	0.90/0.75
Accuracy	0.88/0.87	0.94/0.87	0.88/0.89	0.94/0.84
AUC	0.87/0.91	0.94/0.94	0.87/0.91	0.94/0.94

**Note:**—PPV indicates positive predictive value; NPV, negative predictive value; AUC, area under the curve.

abundant arterial supply. We postulate that the very fast arterial flow in the lesion could show a signal void in both  $b = 1000$  and  $b = 0$  images, resulting in a very low value on the calculated ADC map, which affects the minimum ADC values.<sup>19</sup> Moreover, in this study, there was no statistical difference in the presence of flow voids between the *SDH* mutation-positive and *SDH* mutation-negative groups.

Genetic testing is recommended for patients with paragangliomas who are diagnosed at a young age, have a family history, or demonstrate multifocal paragangliomas. Our results show that ADC values have high sensitivity and specificity in predicting *SDH*-mutation status, thereby suggesting that referring providers may be able to suggest close follow-up based on the ADC when genetic testing is not possible or feasible. Moreover, this result of ADC values may be useful in the early detection of *SDH* mutations when patients who are *SDH* mutation-positive do not show the implication of the mutations such as young age, family history, and multiplicity. Early detection is important, especially in the case of *SDHB* mutation, which is prone to malignant transformation. Clinicians can also suggest genetic testing to patients whose mean ADC values are low.

We chose to evaluate the ADC values on a single axial section instead of the entire tumor volume because prior studies using volumetric ADC analyses showed no better ability than single-axial-section evaluations.<sup>20,21</sup> The consistency between the results of both readers further supports the single-section method. Additionally, we normalized the ADC values of the tumors to those of the medulla oblongata to minimize variations due to differences in scan techniques or imaging platforms. The medulla is usually visualized within the FOV of head and neck imaging studies, and it is less affected by intrinsic signal abnormalities due to changes of chronic microvascular disease or direct tumor invasion. Given our strategy for standardization with ADC values of the medulla, we believe that our results are validated and robust.

Our study has several limitations. First, this was a retrospective study with a small cohort of patients from a single institution. This small cohort was due not only to the low incidence rate but also to the strict inclusion criteria of patients with genetic testing results. In our institution, genetic testing is currently recommended for patients who are suspected of hereditary paragangliomas, so prior probability of genetic mutation in our study population may be higher than that in the overall population of paragangliomas that have been reported before. Second, we also included the patients who were not evaluated histopathologically

but were diagnosed on the basis of accepted and established diagnostic tests such as elevated plasma or urinary fractionated metanephrines and findings of head and neck CT and MR imaging and PET with 2-Deoxy-2-[<sup>18</sup>F] fluoro-d-glucose integrated with CT and <sup>111</sup>In pentetreotide SPECT.<sup>1,4,22,23</sup> Therefore, we believe that despite lack of histopathologic evidence, the diagnosis of paraganglioma was validated in all our patients. Last, we included multiple lesions from the

same patients. We believe that this is reasonable according to a previous study indicating that the ADC value and vascularity of paragangliomas may depend on the location of tumor.<sup>16</sup>

## CONCLUSIONS

Our study shows that ADC values can be promising as a noninvasive imaging biomarker to predict *SDH* mutation in head and neck paragangliomas.

## ACKNOWLEDGMENTS

We thank Dr Jonathan McHugh, Department of Pathology, Division of Neuropathology, University of Michigan, for his assistance in reviewing the sections pertaining to the histopathology of the tumors.

## REFERENCES

1. Withey SJ, Perrio S, Christodoulou D, et al. **Imaging features of succinate dehydrogenase-deficient pheochromocytoma-paraganglioma syndromes.** *Radiographics* 2019;39:1393–1410 CrossRef Medline
2. Williams MD, Rich TA. **Paragangliomas arising in the head and neck: a morphologic review and genetic update.** *Surg Pathol Clin* 2014;7:543–57 CrossRef Medline
3. Patel D, Phay JE, Yen TWF, et al. **Update on pheochromocytoma and paraganglioma from the SSO Endocrine/Head and Neck Disease-Site Work Group, Part 1 of 2: advances in pathogenesis and diagnosis of pheochromocytoma and paraganglioma.** *Ann Surg Oncol* 2020;27:1329–37 CrossRef Medline
4. Farrugia FA, Martikos G, Tzanetis P, et al. **Pheochromocytoma, diagnosis and treatment: review of the literature.** *Endocr Regul* 2017;51:168–81 CrossRef Medline
5. Neumann HP, Bausch B, McWhinney SR, et al. **Germ-line mutations in nonsyndromic pheochromocytoma.** *N Engl J Med* 2002;346:1459–66 CrossRef Medline
6. Williams MD. **Paragangliomas of the head and neck: an overview from diagnosis to genetics.** *Head Neck Pathol* 2017;11:278–87 CrossRef Medline
7. Offergeld C, Brase C, Yaremchuk S, et al. **Head and neck paragangliomas: clinical and molecular genetic classification.** *Clinics (Sao Paulo)* 2012;67:(Suppl 1):19–28 CrossRef Medline
8. Woolen S, Gemmete JJ. **Paragangliomas of the head and neck.** *Neuroimaging Clin N Am* 2016;26:259–78 CrossRef Medline
9. van Gils AP, van den Berg R, Falke TH, et al. **MR diagnosis of paraganglioma of the head and neck: value of contrast enhancement.** *AJR Am J Roentgenol* 1994;162:147–53 CrossRef Medline
10. Thoeny HC, De KF, King AD. **Diffusion-weighted MR imaging in the head and neck.** *Radiology* 2012;263:19–32 CrossRef Medline

11. Aschenbach R, Basche S, Vogl TJ, et al. **Diffusion-weighted imaging and ADC mapping of head-and-neck paragangliomas: initial experience.** *Clin Neuroradiol* 2009;19:215–19 CrossRef Medline
12. Tischler AS, deKrijger RR. **15 years of paraganglioma: pathology of pheochromocytoma and paraganglioma.** *Endocr Relat Cancer* 2015;22:123c33 CrossRef Medline
13. Srinivasan A, Dvorak R, Perni K, et al. **Differentiation of benign and malignant pathology in the head and neck using 3T apparent diffusion coefficient values: early experience.** *AJNR Am J Neuroradiol* 2008;29:40–44 CrossRef Medline
14. Koontz NA, Wiggins RH 3rd. **Differentiation of benign and malignant head and neck lesions with diffusion tensor imaging and DWI.** *AJR Am J Roentgenol* 2017;208:1110–15 CrossRef Medline
15. Landis JR, Koch GG. **The measurement of observer agreement for categorical data.** *Biometrics* 1977;33:159–74 CrossRef Medline
16. Güneş A, Ozgen B, Bulut E, et al. **Magnetic resonance and diffusion weighted imaging findings of head and neck paragangliomas.** *Acta Oncologica Turcica* 2019;52:416–23 CrossRef
17. Yuan Y, Shi H, Tao X. **Head and neck paragangliomas: diffusion weighted and dynamic contrast enhanced magnetic resonance imaging characteristics.** *BMC Med Imaging* 2016;16:12 CrossRef Medline
18. Feng N, Zhang WY, Wu XT. **Clinicopathological analysis of paraganglioma with literature review.** *World J Gastroenterol* 2009;15:3003–08 CrossRef Medline
19. Hiwatashi A, Kinoshita T, Moritani T, et al. **Hypointensity on diffusion-weighted MRI of the brain related to T2 shortening and susceptibility effects.** *AJR Am J Roentgenol* 2003;181:1705–09 CrossRef Medline
20. Ahlawat S, Khandheria P, Grande FD, et al. **Interobserver variability of selective region-of-interest measurement protocols for quantitative diffusion weighted imaging in soft tissue masses: comparison with whole tumor volume measurements.** *J Magn Reson Imaging* 2016;43:446–54 CrossRef Medline
21. Han X, Suo S, Sun Y, et al. **Apparent diffusion coefficient measurement in glioma: influence of region-of-interest determination methods on apparent diffusion coefficient values, interobserver variability, time efficiency, and diagnostic ability.** *J Magn Reson Imaging* 2017;45:722–30 CrossRef Medline
22. Chang CA, Pattison DA, Tothill RW, et al. **Ga-DOTATATE and (18)F-FDG PET/CT in paraganglioma and pheochromocytoma: utility, patterns and heterogeneity.** *Cancer Imaging* 2016;16:68:22 CrossRef Medline
23. Telischi FF, Bustillo A, Whiteman ML, et al. **Octreotide scintigraphy for the detection of paragangliomas.** *Otolaryngol Head Neck Surg* 2000;122:358–62 CrossRef Medline

# Quantitative Susceptibility Mapping of Venous Vessels in Neonates with Perinatal Asphyxia

 A.M. Weber,  Y. Zhang,  C. Kames, and  A. Rauscher



## ABSTRACT

**BACKGROUND AND PURPOSE:** Cerebral venous oxygen saturation can be used as an indirect measure of brain health, yet it often requires either an invasive procedure or a noninvasive technique with poor sensitivity. We aimed to test whether cerebral venous oxygen saturation could be measured using quantitative susceptibility mapping, an MR imaging technique, in 3 distinct groups: healthy term neonates, injured term neonates, and preterm neonates.

**MATERIALS AND METHODS:** We acquired multiecho gradient-echo MR imaging data in 16 neonates with perinatal asphyxia and moderate or severe hypoxic-ischemic encephalopathy (8 term age: average, 40.0 [SD, 0.8] weeks' gestational age; 8 preterm, 33.5 [SD, 2.0] weeks' gestational age) and in 8 healthy term-age controls (39.3 [SD, 0.6] weeks, for a total of  $n = 24$ ). Data were postprocessed as quantitative susceptibility mapping images, and magnetic susceptibility was measured in cerebral veins by thresholding out 99.95% of lower magnetic susceptibility values.

**RESULTS:** The mean magnetic susceptibility value of the cerebral veins was found to be 0.36 (SD, 0.04) ppm in healthy term neonates, 0.36 (SD, 0.06) ppm in term injured neonates, and 0.29 (SD, 0.04) ppm in preterm injured neonates. Correspondingly, the derived cerebral venous oxygen saturation values were 73.6% (SD, 2.8%), 71.5% (SD, 7.4%), and 72.2% (SD, 5.9%). There was no statistically significant difference in cerebral venous oxygen saturation among the 3 groups ( $P = .751$ ).

**CONCLUSIONS:** Quantitative susceptibility mapping–derived oxygen saturation values in preterm and term neonates agreed well with values in past literature. Cerebral venous oxygen saturation in preterm and term neonates with hypoxic-ischemic encephalopathy, however, was not found to be significantly different between neonates or healthy controls.

**ABBREVIATIONS:**  $\chi$  = magnetic susceptibility; CSaO<sub>2</sub> = cerebral arterial oxygen saturation; CSvO<sub>2</sub> = cerebral venous oxygen saturation; Hct = hematocrit; HIE = hypoxic-ischemic encephalopathy; NIRS = near-infrared resonance spectroscopy; QSM = quantitative susceptibility mapping; SSS = superior sagittal sinus; TRUST = T2-relaxation-under-spin tagging

Perinatal asphyxia is the condition resulting from the deprivation of oxygen to a neonate and can lead to brain tissue damage or death. Asphyxia at birth can affect virtually any organ, but the brain is of the highest concern because it is the least likely to quickly or completely heal.<sup>1</sup> Hypoxic-ischemic encephalopathy (HIE) occurs when the entire brain is deprived of an adequate supply of oxygen and can result in neurologic disability, such as cerebral palsy, mental retardation, and epilepsy. HIE occurs in

1.5 per 1000 live births<sup>2</sup> and is the fifth leading cause of death worldwide in children younger than 5 years of age (8%).<sup>3</sup>

Currently, the severity of HIE is mainly assessed by clinical parameters and conventional MR imaging and can be classified into mild, moderate, or severe categories.<sup>4,5</sup> While identifying HIE in term infants is generally well-characterized, its identification in preterm infants remains complex, with variable inclusion criteria being discussed and reported.<sup>6–9</sup> More accurate markers would be useful

Received December 7, 2020; accepted after revision January 14, 2021.

From the Division of Neurology (A.M.W., A.R.), Department of Pediatrics and University of British Columbia MRI Research Centre (A.M.W., C.K., A.R.), Department of Physics and Astronomy (C.K., A.R.), and Department of Radiology (A.R.), University of British Columbia, Vancouver, British Columbia, Canada; Department of Radiology (Y.Z.), Children's Hospital of Chongqing Medical University, Chongqing, China; Ministry of Education Key Laboratory of Child Development and Disorders (Y.Z.), Chongqing, China; Key Laboratory of Pediatrics in Chongqing (Y.Z.), Chongqing, China; Chongqing International Science and Technology Cooperation Center for Child Development and Disorders (Y.Z.), Chongqing, China.

A.M. Weber and Y. Zhang contributed equally to this work.

A.M. Weber was supported by a British Columbia Children's Hospital Research Institute, M.I.N.D. postdoctoral fellowship. A. Rauscher is supported by Canada Research Chairs and a Natural Sciences and Engineering Council of Canada grant (402039-2011, RGPIN-2016-05371).

Please address correspondence to Alexander Mark Weber, PhD, BC Children's Hospital Research Institute, Variety Building, Room 370B, 950 West 28th Ave, Vancouver, BC, Canada V5Z 4H4; e-mail: alex.weber@ubc.ca; @AlexMarkWeber

 Indicates open access to non-subscribers at [www.ajnr.org](http://www.ajnr.org)

 Indicates article with online supplemental data.

<http://dx.doi.org/10.3174/ajnr.A7086>

for detection, classification, early therapeutic interventions, and predictors of long-term outcome. Several studies have investigated various alternative methods for measuring HIE, such as DWI,<sup>10</sup> MR spectroscopy,<sup>11,12</sup> urinary nuclear MR metabolomic profiling,<sup>13</sup> and visual evoked potentials,<sup>14</sup> with varying levels of reported success.

Cerebral venous oxygen saturation (CSvO<sub>2</sub>) is the amount of leftover oxygen in the veins after oxygen delivery and extraction by the brain and can act as a surrogate of brain oxygen consumption. The oxygen supply is of critical importance to brain function because neurons rely predominantly on aerobic metabolism for their energy demands. In infants who have experienced birth asphyxia, CBF has been reported to be markedly elevated.<sup>15</sup> When the brain is hyperperfused like this, elevated CSvO<sub>2</sub> values would signal a “luxury perfusion” state, suggesting serious brain damage.<sup>16</sup> Normal CSvO<sub>2</sub> values, meanwhile, would suggest intact coupling between CBF and metabolic needs.<sup>17</sup> Thus, knowing the CSvO<sub>2</sub> in preterm and term infants who are suspected of having HIE could provide clinicians with invaluable information. Unfortunately, the 2 current methods for measuring CSvO<sub>2</sub> require either the invasive insertion of an internal jugular vein catheter for co-oximetry or a blood gas analyzer, or the noninvasive use of near-infrared resonance spectroscopy (NIRS). NIRS, however, has been shown to have poor sensitivity at low CSvO<sub>2</sub> compared with co-oximetry and can reach a depth of only a few millimeters.<sup>18</sup>

Quantitative susceptibility mapping (QSM)<sup>19,20</sup> examines gradient-echo phase data, usually acquired with SWI,<sup>21</sup> to determine local tissue magnetic susceptibility ( $\chi$ ). Because deoxyhemoglobin in the venous blood is paramagnetic, a decrease in  $\chi$  of venous blood compared with the surrounding brain tissue will indicate increased CSvO<sub>2</sub>. Thus, QSM, a noninvasive method, may provide an indirect measure of CSvO<sub>2</sub>.<sup>22,23</sup> For example, Doshi et al,<sup>24</sup> in 2015, reported increased CSvO<sub>2</sub> in adults following mild traumatic brain injury. Similarly, Chai et al,<sup>25</sup> in 2017, reported increased CSvO<sub>2</sub> in subjects with mild traumatic brain injury compared with healthy controls, but they also reported a positive correlation of CSvO<sub>2</sub> with postconcussive symptoms. Chai et al,<sup>26</sup> in 2020, also reported reduced CSvO<sub>2</sub> in patients undergoing hemodialysis, which also correlated with cognitive scores ( $r = 0.492, P = .02$ ).

Thus, we set out to determine how well CSvO<sub>2</sub> could be measured using QSM and hematocrit (Hct) from blood samples in term and preterm neonates with moderate or severe HIE and to compare those values with those of healthy term controls. We hypothesized that after perinatal asphyxia, both preterm and term neonates with moderate or severe HIE would demonstrate increased CSvO<sub>2</sub> through decreased cerebral vein magnetic susceptibility compared with healthy term controls.

## MATERIALS AND METHODS

### Patients

Between January 2017 and January 2018, preterm and term neonates with a clinical history of perinatal asphyxia and moderate or severe HIE who were transferred to Children’s Hospital of Chongqing Medical University intensive care nursery were enrolled in a study evaluating the detection of brain injury by MR imaging, in accordance with The Code of Ethics of the World Medical Association (Declaration of Helsinki). Recruitment and

scanning ended due to the neonatal ward of the hospital moving to a new branch of the hospital, where their scanners were from a different vendor, and there were no Phillips Healthcare scanners. The institution’s Committee on Clinical Research Ethics approved the study protocol, and informed consent was obtained from the parents. The inclusion criteria were determined on the basis of the definition of perinatal asphyxia and moderate or severe HIE as follows: 1) evidence of perinatal asphyxia (Apgar score of  $\leq 7$  for  $>5$  minutes after birth or a history of acute perinatal event, placental abruption, cord prolapse, or the need for ventilation for at least 10 minutes after birth<sup>27</sup>); 2) evidence of moderate or severe HIE distinguished by using the Sarnat and Sarnat clinical stages<sup>5</sup> for term infants and infants between 33 and 37 weeks’ gestation and significant changes in neurologic examination findings and/or seizures for infants younger than 33 weeks gestation;<sup>28</sup> and 3) abnormal MR imaging findings in all patients on T1-weighted, T2-weighted, and FLAIR images, mainly but not only in the basal ganglia/thalamic region, watershed region, and periventricular white matter caused by HIE.<sup>29,30</sup> Subjects were sedated using 5 mg/kg of phenobarbital (intramuscular injection). Neonates with high motion or image artifacts were excluded. In total, 8 term neonates and 8 preterm neonates who were determined to have perinatal asphyxia and moderate or severe HIE were included for further study. Eight term neonates with hyperbilirubinemia who were free of other neonatal complications, such as congenital and chromosomal abnormalities and with normal MR imaging findings were recruited prospectively as healthy controls. Hct values were obtained as part of the regular clinical work-up.

### MR Imaging Acquisition

Brain MR images were obtained on a 3T system (Achieva; Philips Healthcare) using an 8-channel sensitivity encoding head coil. Data for QSM were collected using a 3D gradient-echo sequence with 5 echoes (TR = 30 ms, TE1 = 4.5 ms, echo spacing = 5.5 ms, flip angle = 17°, FOV = 196 × 154 × 103 mm<sup>3</sup>, acquired voxel size = 0.50 × 0.5 × 1.0 mm<sup>3</sup>, reconstructed voxel size = 0.5 × 0.5 × 0.5 mm<sup>3</sup>, scan time = 5 minutes 9 seconds).<sup>31</sup> Other scans included the following: inversion recovery turbo spin-echo T1-weighted (TR/TI = 7000/600 ms, TE = 15 ms, section thickness = 5 mm, FOV = 160 × 151 × 98 mm<sup>3</sup>, acquisition matrix = 220 × 163, scan time = 2 minutes 17 seconds); turbo spin-echo T2-weighted (TR = 5000 ms, TE = 100 ms, section thickness = 5 mm, FOV = 160 × 149 × 98 mm<sup>3</sup>, acquisition matrix = 332 × 205, scan time = 1 minute 38 seconds); and fast FLAIR images (TR/TI = 12,000/2850 ms, TE = 140 ms, section thickness = 5 mm, FOV = 160 × 149 × 98 mm<sup>3</sup>, acquisition matrix = 176 × 144, scan time = 3 minutes 55 seconds). The total acquisition time was 13 minutes 23 seconds.

### MR Imaging Analysis

QSM images of all 5 echoes were postprocessed from the phase data of the multi-gradient-echo scans. Phase unwrapping was achieved using a 3D Laplacian algorithm,<sup>32</sup> while the background field was removed using the variable sophisticated harmonic artifact reduction for phase method.<sup>33</sup> A Gaussian filter ( $\sigma = 0.5$ ) was applied to the normalized field maps to smooth out high-frequency errors originating from the reconstruction steps before

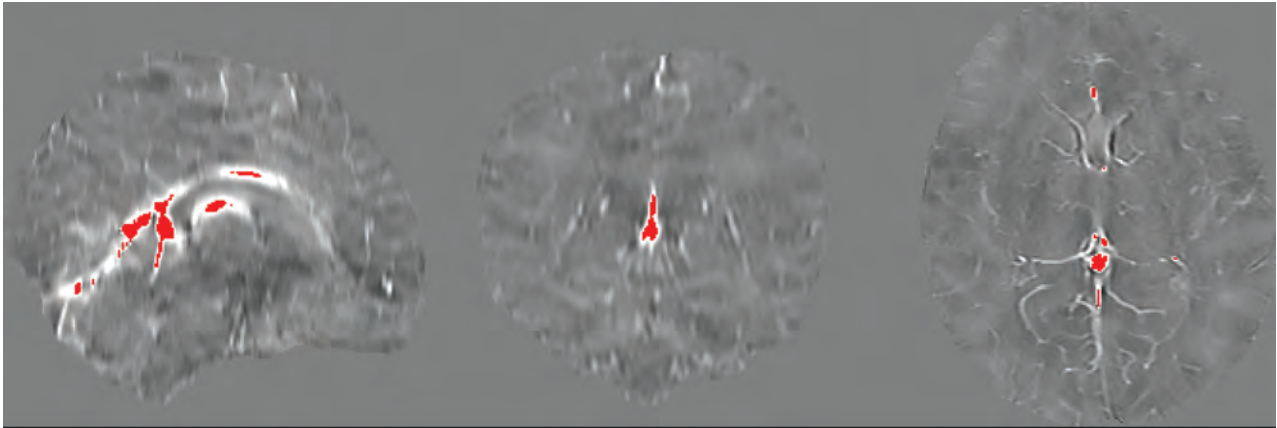


**FIG 1.** Sample internal veins selected after thresholding out the lower 99.95%  $\chi$  values. As can be seen in these sagittal, coronal, and axial views from a sample healthy term neonate, the major veins that were left over include the straight sinus, inferior sagittal sinus, and the internal cerebral vein. Note the weak contrast between gray and white matter and the basal ganglia due to the low myelin and iron content of the neonate brain.

the inversion. A 2-step dipole inversion algorithm<sup>34</sup> was used to solve the dipole inversion problem. The last echo was used to obtain the brain mask, which effectively removed the external cerebral veins. Using the last echo to generate the brain mask reliably removed artifacts from air-tissue and bone-tissue interfaces, eg, sinuses, especially in the later echoes, without the need for manual erosion. This QSM algorithm can be freely accessed at <https://github.com/kamesy/QSM.m>. Finally, only the fourth echo (TE = 21 ms) was used for measuring  $\chi$  values because even echoes were flow-compensated along the readout direction and the second echo (TE = 10 ms) had a poor contrast-to-noise ratio.

The  $\chi$  of cerebral veins was measured by thresholding out the lowest 99.95% values of the whole brain. In the absence of intracranial hemorrhage and because neonates have very low brain iron content, voxels that reside entirely inside veins reflect the structures with the highest magnetic susceptibility values. Total blood volume is about 3%.<sup>35,36</sup> Venous blood volume is about two-thirds of total blood volume. For a voxel to be free of partial volume effects and given the spatial resolution of  $0.5 \times 0.5 \times 1 \text{ mm}^3$  of the scan, only veins with an inner diameter of at least 1 mm could be included in the analysis. After thresholding, images were assessed by A.M.W. to ensure that only veins remained (Fig 1). The remaining 0.25% of  $\chi$  values was then averaged to give the mean cerebral  $\chi$  value for each subject. ROIs were also drawn manually on nonvein tissue by A.M.W. to calculate  $\Delta\chi$ . Visual inspection did not reveal any germinal matrix bleeding in the deep cerebral veins.

### Calculating CSvO<sub>2</sub>

CSvO<sub>2</sub> was calculated using the following equation:

$$\Delta\chi = \Delta\chi_{do} \times HCT \times (1 - CSvO_2),$$

where  $\Delta\chi$  is the susceptibility difference between venous blood and surrounding tissue,  $\Delta\chi_{do}$  is the susceptibility difference per unit hematocrit between fully deoxygenated and fully oxygenated blood, Hct is the individual fractional hematocrit, and CSvO<sub>2</sub> is the blood oxygen saturation.  $\Delta\chi_{do}$  was taken to be  $4 \times \pi \times 0.21$ , or 2.64 ppm.<sup>37,38</sup>

### Statistical Analysis

Statistical analysis was performed using R 3.4.2 (2017; <http://www.r-project.org/>). The relationship between calculated CSvO<sub>2</sub> and condition (healthy control, preterm injury, and term injury) was investigated using a 1-way ANOVA. Visual inspection of residual plots did not reveal any obvious deviations from homoscedasticity or normality.

## RESULTS

### Patient Characteristics

Demographic data and clinical characteristics for both groups (8 healthy controls, 8 term neonates, and 8 preterm neonates with perinatal asphyxia and moderate or severe HIE) are summarized in Table 1. No significant differences were found in gestational age, corrected gestational age at MR imaging, time interval between age at birth and age at MR imaging, birth weight, or sex between healthy controls and term neonates with HIE. No significant differences were found in sex, time interval between age at birth and age at MR imaging, clinical history, and symptoms and signs between term neonates and preterm neonates with perinatal asphyxia and moderate or severe HIE. As expected, a significant difference ( $P < .05$ ) was found in the Apgar grade between healthy term neonates and term neonates with HIE. Between term and preterm neonates with HIE, significant differences ( $P < .05$ ) were found only in gestational age, corrected gestational age at MR imaging, and birth weight, as would be expected.

### CSvO<sub>2</sub> Analysis

The mean  $\chi$  value of the internal cerebral veins in healthy controls and term and preterm injured neonates was found to be 0.36 (SD, 0.04) ppm, 0.36 (SD, 0.06) ppm, and 0.29 (SD, 0.04) ppm, respectively, while the mean fractional Hct values were 0.52 (SD, 0.03), 0.49 (SD, 0.07), and 0.42 (SD, 0.06), respectively. Correspondingly, the derived mean CSvO<sub>2</sub> values were 73.6% (SD, 2.8%), 71.5% (SD, 7.4%), and 72.2% (SD, 6.0%), respectively. The Cohen D effect size between each group was found to be 0.38 for healthy controls and term injured neonates; 0.30 for healthy controls and preterm neonates; and 0.10 between term injured neonates and preterm

**Table 1: Demographic data and clinical characteristics of the 3 groups<sup>a</sup>**

Characteristics	Healthy Controls (n = 8)	Term Neonates with HIE (n = 8)	P Value between Controls and Term HIE	Preterm Neonates with HIE (n = 8)	P Value between Term and Preterm HIE
Gestational age (mean) (wk)	39.3 (SD, 0.6)	40.0 (SD, 0.8)	.056	33.5 (SD, 2.1)	<.001
Corrected gestational age at MRI (mean) (wk)	41.3 (SD, 1.1)	41.9 (SD, 0.7)	.166	35.7 (SD, 2.6)	<.001
Time interval between age at birth and age at MR imaging (mean) (wk)	2.0 (SD, 0.7)	1.9 (SD, 0.6)	.819	2.2 (SD, 0.9)	.404
Birth weight (mean) (g)	3306.3 (SD, 353.1)	3430.6 (SD, 471.4)	.560	1926.3 (SD, 350.3)	<.001
No. of male neonates (No.) (%)	4 (50)	5 (62.5)	1.000	4 (50)	1.000
Apgar grade (median) (IQR)	10 (10–10)	6.5 (4–7)	<.001	6 (2–7)	.543
Umbilical cord around the neck (No.) (%)	2 (25)	1 (12.5)	1.000	1 (12.5)	1.000
Oxygen inhalation (No.) (%)	0	4 (50)	NA	7 (87.5)	1.000
Pulse oximetry (%)	95–100	90–95	<.001	90–95	.122
Meconium-stained amniotic fluid (No.) (%)	0	3 (37.5)	NA	1 (12.5)	.569
Premature rupture of fetal membranes (No.) (%)	0	3 (37.5)	NA	5 (62.5)	.619
Placental abruption (No.) (%)	0	0	NA	2 (25)	NA
Cord prolapse (No.) (%)	0	0	NA	1 (12.5)	NA
Fetal intrauterine distress (No.) (%)	0	7 (87.5)	NA	2 (25)	.119
Neonatal asphyxia resuscitation (No.) (%)	0	8 (100)	NA	8 (100)	NA
Respiratory failure and ventilation (No.) (%)	0	2 (25)	NA	5 (62.5)	.315
Obtundation (No.) (%)	0	7 (87.5)	NA	6 (75)	1.000
Stuporous (No.) (%)	0	1 (12.5)	NA	2 (25)	1.000
Inhibited primitive reflexes (No.) (%)	0	7 (87.5)	NA	6 (75)	1.000
Disappeared primitive reflexes (No.) (%)	0	1 (12.5)	NA	2 (25)	1.000
Hypotonia (No.) (%)	0	2 (25)	NA	4 (50)	.608
Flaccid (No.) (%)	0	1 (12.5)	NA	2 (25)	1.000
Seizures (No.) (%)	0	2 (25)	NA	3 (37.5)	1.000
Therapeutic hypothermia (No.) (%)	0	2 (25)	NA	1 (12.5)	1.000

Note:—IQR indicates interquartile range; NA, not applicable.

<sup>a</sup> P values were from the  $\chi^2$  test or Fisher exact test for categorical variables or the Student t test for continuous variables.

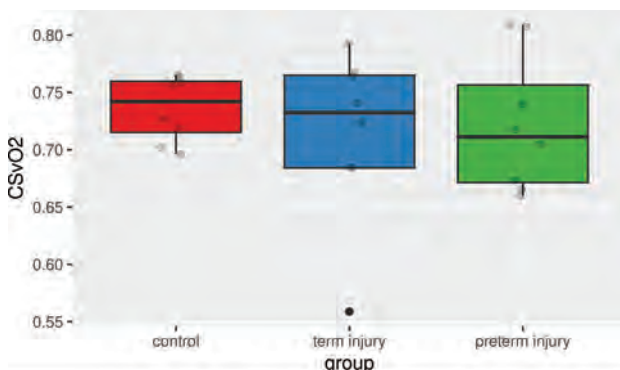


**FIG 2.** Boxplot of CSvO<sub>2</sub> percentages by group. Gray circles are the ROI measurements from each subject.

neonates. A CSvO<sub>2</sub> boxplot among the 3 groups with individual points for each subject is shown in Fig 2. One-way ANOVA analysis did not reveal that the condition (healthy control, preterm injury, and term injury) made a significant difference among groups ( $P > .05$ ). Boxplots of  $\chi$  and Hct values in each group, with individual points for each subject are included in the Online Supplementary Data.

## DISCUSSION

In this study, we quantified CSvO<sub>2</sub> from  $\chi$  values in the internal cerebral veins of preterm and term neonates with HIE and healthy term controls. Moderate-to-severe HIE caused by intrapartum or late antepartum hypoxic-ischemic events may lead to neurodevelopmental disability.<sup>1</sup> It is of great importance to examine cerebral hemodynamic changes in neonates with moderate or severe HIE because this examination may lead to a better understanding of the cerebral oxygen metabolism of brain injury in HIE and early therapeutic interventions. Although no statistical difference in CSvO<sub>2</sub> values was found between healthy term controls and preterm and term infants with moderate or severe HIE, to the best of our knowledge, this is one of the first studies measuring CSvO<sub>2</sub> using QSM in healthy term neonates, as well as the first to do so in term and preterm neonates with moderate or severe HIE. Thus, our reported values for healthy neonates as well as injured preterm and term neonates may be used in future studies for comparison purposes. These values agree well with previously reported values using other methods (Table 2).

Noninvasive measurements of CSvO<sub>2</sub> in neonates has historically been quite difficult. The current best practice, NIRS, does not provide robust and reliable measurements due to several limitations,<sup>39,40</sup> including contamination from extracerebral tissue

**Table 2: Comparison of CSvO<sub>2</sub> percentages in fetuses and neonates in the literature**

Study	CSvO <sub>2</sub> (mean) (%)	Method	Subjects	Region
van der Hoeven et al <sup>57</sup>	73.56 (SD, 5.25)	Fiber optic catheter	Healthy neonates	
Buchvald et al <sup>58</sup>	64.12 (SD, 4.6)	NIRS	Healthy neonates	Frontotemporal region
Wintermark et al <sup>59</sup>	77.3 (SD, 4.7)	NIRS	Hypothermia therapy (moderate) in neonatal HIE	Frontal lobe
Wintermark et al <sup>59</sup>	77.6 (SD, 6.6)	NIRS	Hypothermia therapy (severe) in neonatal HIE	Frontal lobe
De Vis et al <sup>60</sup>	65.0 (SD, 13.0)	T2-TRIR	Healthy neonates	SSS
Shetty et al <sup>48</sup>	73.2 (SD, 5.5)	TRUST	Hypothermia therapy in neonatal HIE	SSS
Shetty et al <sup>48</sup>	68.5 (SD, 9.6)	TRUST	Post-hypothermia therapy in neonatal HIE	SSS
Liu et al <sup>49</sup>	62.6 (SD, 8.3)	TRUST	Healthy neonates	SSS
Yadav et al <sup>44</sup>	67 (SD, 7)	QSM	Healthy fetuses (~31 wk)	SSS
Jain et al <sup>45</sup>	55.2	Susceptometry	Neonates with congenital heart disease	SSS
Yadav et al <sup>46</sup>	62.6 (SD, 3.25)	Susceptometry	Healthy fetuses (~31 wk)	SSS
Neelavalli et al <sup>47</sup>	66 (SD, 9.4)	Susceptometry	Healthy fetuses (~34 wk)	SSS
Average	68.12			

**Note:**—T2-TRIR indicates T2-prepared tissue relaxation inversion recovery; SSS, superior sagittal sinus; TRUST, T2-relaxation-under-spin tagging; QSM, quantitative susceptibility mapping; NIRS, near infrared resonance spectroscopy.

and arterial blood (generally 30% but can vary considerably among subjects)<sup>41</sup> and an insensitivity to low CSvO<sub>2</sub> levels.<sup>18</sup> QSM, meanwhile, is a relatively new technique, which fully quantifies  $\chi$  using MR imaging phase data. Because oxyhemoglobin is diamagnetic and deoxyhemoglobin is paramagnetic, a reduction in deoxyhemoglobin and an increase in oxyhemoglobin will be reflected as a decrease in the  $\chi$  of venous blood. Using Hct values obtained from blood samples, one can then calculate the CSvO<sub>2</sub>.

Recently, several studies have been published demonstrating the promise<sup>22,42,43</sup> of using QSM to quantify CSvO<sub>2</sub> changes in brain injuries of adults.<sup>24,25</sup> Doshi et al<sup>24</sup> and Chai et al<sup>25</sup> reported CSvO<sub>2</sub> differences between adult healthy controls and subjects with mild traumatic brain injury by measuring the  $\chi$  of cerebral major veins. Doshi et al found decreases in venous  $\chi$  in the left thalamostriate vein and right basal vein, while Chai et al found decreases in venous  $\chi$  in the straight sinus. Both of these studies suggested increased CSvO<sub>2</sub> after a mild traumatic brain injury, with different conclusions as to what this might suggest. Doshi et al also obtained CBF measurements and found injured subjects to have significantly increased CBF postinjury. Along with the increase in CSvO<sub>2</sub>, they suggested that the brain responds to traumatic injuries by trying to protect brain tissue via the supply of more oxygen than the tissue requires. Whereas Chai et al did not acquire CBF measures but did look at the correlation of  $\chi$  reductions with the amount of time post-trauma, they reported a positive correlation between the 2 measures, which indicates recovery to normal levels of oxygenation with time. Chai et al suggested that QSM can thus be used as a biomarker and to monitor progress.

Closer to our study, Yadav et al<sup>44</sup> used QSM to measure CSvO<sub>2</sub> in healthy fetuses ( $n = 21$ , median week of pregnancy = 31.3). They reported a mean CSvO<sub>2</sub> of 67% (SD, 7%) in the superior sagittal sinus (SSS) vein, an external cerebral vein that is less than our reported values in internal cerebral veins in healthy controls (73.6% [SD, 2.84%]). Similarly, several studies have used a method analogous to QSM, known as MR susceptometry, which uses a susceptibility-weighted image to measure  $\chi$  values on the basis of geometric assumptions (such as the SSS vein being an infinitely long cylinder). These studies reported CSvO<sub>2</sub> values in the SSS ranging from 55.2% in neonates with congenital heart disease<sup>45</sup> to 66% in 34-week-old healthy fetuses (Table 2).<sup>46,47</sup>

Along with the susceptibility-based methods of measuring CSvO<sub>2</sub> in neonates and fetuses, there have been other MR imaging-related techniques worth mentioning. One such method is known as T2-relaxation-under-spin tagging (TRUST). For instance, Shetty et al,<sup>48</sup> in 2019, reported CSvO<sub>2</sub> changes during and after therapeutic hypothermia in neonatal HIE using TRUST. The CSvO<sub>2</sub> was calculated by measuring  $1/T_2$  ( $R_2$ ) of the SSS. They examined CSvO<sub>2</sub> values during early hypothermia treatment (18–24 hours after initiating treatment) and after and found posttreatment CSvO<sub>2</sub> to have been reduced from 73.2% (SD, 5.5%) (during treatment) to 68.5% (SD, 9.6%) (posttreatment). These posttreatment values agreed well with a previous study that reported 62.6% (SD, 8.3%) in healthy infants using the same method.<sup>49</sup> While these initial reports of measuring CSvO<sub>2</sub> using TRUST are promising, some drawbacks should be considered. On the one hand, the measurement of  $R_2$  is relatively easier to postprocess than QSM because it requires only a few simple steps. On the other hand, unlike QSM, the measurement of  $R_2$  has confounding factors such as fat, fibrosis, and edema,<sup>50</sup> along with saturation and blooming artifacts. Additionally, the scan required for QSM provides a wealth of additional information such as  $R_2^*$  maps and SWI, which can be used to better characterize lesions.<sup>51</sup> In fact, SWI is already often used in clinical settings to detect intracranial hemorrhages and other brain abnormalities and is often part of the neonatal and pediatric MR imaging protocols.<sup>52–54</sup> The scan is fast (<3 minutes on modern scanners) even at high spatial resolution (<1 mm<sup>3</sup>). Disadvantages in QSM include a range of different approaches for background field removal, dipole inversion, and referencing to other tissue.

The results of our study indicate that CSvO<sub>2</sub> values were not found to be significantly different in injured preterm and term neonates compared with healthy term controls. One reason for this finding could be that preterm and term infants with moderate or severe HIE could have reduced CBF, which, along with a reduced oxygen metabolism, would result in CSvO<sub>2</sub> similar to that in healthy controls. In this case, injured neonates would have reduced oxygen metabolism and, thus, compromised brain health. To test these 2 opposing theories, however, we would require additional information, such as CBF and cerebral arterial oxygen saturation (CSaO<sub>2</sub>). For instance, the oxygen extraction

fraction, the percentage of oxygen used from the blood as it passes through the capillary network, can be calculated by subtracting the fraction of oxygen saturation in the cerebral arteries (CSaO<sub>2</sub>) from the fraction of oxygen saturation in the cerebral veins (CSvO<sub>2</sub>).<sup>22,23</sup> While CSaO<sub>2</sub> can be easily and noninvasively measured using a pulse oxygen monitor and CBF can be acquired using another MR imaging scan such as arterial spin-labeling or phase contrast,<sup>55</sup> our study, unfortunately, did not acquire these data because they were not part of the original study design. Thus, we cannot make more conclusive statements regarding preterm and term injured brain health. An alternative explanation could be because our data show premature rupture of fetal membranes in >60% of the preterm infants, which is higher than usual. It is possible that these infants have adapted to the outside world and have CSvO<sub>2</sub> values closer to term infants.

Two strengths of our method are as follows: The QSM algorithm is available for free on-line at <https://github.com/kamesy/QSM.m> for researchers and clinicians to download and use. Furthermore, our method of selecting venous susceptibility values (looking at the highest 0.25%) helps reduce human error using a completely data-driven process.

There are several limitations to the current study. Only 8 subjects from each group were examined, limiting our statistical power. We did not acquire CSaO<sub>2</sub> or CBF measurements, which would have allowed us to examine why both preterm and term infants with moderate or severe HIE did not show statistically significant differences in CSvO<sub>2</sub> compared with healthy controls. Furthermore, no follow-up with these patients was attempted, such as cognitive scores, which could have been used to investigate any correlations with CSvO<sub>2</sub>. In the future, we hope to add more subjects, acquire CSaO<sub>2</sub> and CBF measurements (such as arterial spin-labeling), and perform cognitive measurements as the infants develop later in life. One piece of advice the authors wish to pass on to future researchers is the importance of acquiring and using Hct values in calculating CSvO<sub>2</sub>. Had we used a constant value for Hct, the preterm group would have been found to have a statistically significant difference in CSvO<sub>2</sub>. However, by using acquired Hct from each subject, this difference was no longer seen because Hct increases with gestational age and preterm infants were scanned at a younger gestational age.<sup>56</sup>

## CONCLUSIONS

We were able to measure CSvO<sub>2</sub> in the internal cerebral veins in healthy term, preterm, and term injured neonates. These values agree well with previously reported values in the literature. However, we did not see a difference in CSvO<sub>2</sub>, despite the presence of HIE in the term injured and preterm infants. More studies should be performed in preterm and term infants with moderate or severe HIE, while acquiring other brain oxygen metrics such as CBF and CSaO<sub>2</sub> along with cognitive metrics as the infants develop later in life.

## REFERENCES

1. Ferriero DM. Neonatal brain injury. *N Engl J Med* 2004;351:1985–95 CrossRef Medline
2. Kurinczuk JJ, White-Koning M, Badawi N. Epidemiology of neonatal encephalopathy and hypoxic-ischaemic encephalopathy. *Early Hum Dev* 2010;86:329–38 CrossRef Medline
3. Bryce J, Boschi-Pinto C, Shibuya K, et al. WHO estimates of the causes of death in children. *Lancet* 2005;365:1147–52 CrossRef Medline
4. Barkovich AJ, Hajnal BL, Vigneron D, et al. Prediction of neuromotor outcome in perinatal asphyxia: evaluation of MR scoring systems. *AJNR Am J Neuroradiol* 1998;19:143–49 Medline
5. Sarnat HB, Sarnat MS. Neonatal encephalopathy following fetal distress: a clinical and electroencephalographic study. *Arch Neurol* 1976;33:696–705 CrossRef Medline
6. Chalak LF, Rollins N, Morriss MC, et al. Perinatal acidosis and hypoxic-ischemic encephalopathy in preterm infants of 33 to 35 weeks' gestation. *J Pediatr* 2012;160:388–94 CrossRef Medline
7. Logitharajah P, Rutherford MA, Cowan FM. Hypoxic-ischemic encephalopathy in preterm infants: antecedent factors, brain imaging, and outcome. *Pediatr Res* 2009;66:222–29 CrossRef Medline
8. Lupton AR. Birth asphyxia and hypoxic-ischemic brain injury in the preterm infant. *Clin Perinatol* 2016;43:529–45 CrossRef Medline
9. Salhab WA, Perlman JM. Severe fetal acidemia and subsequent neonatal encephalopathy in the larger premature infant. *Pediatr Neurol* 2005;32:25–29 CrossRef Medline
10. Rana L, Sood D, Chauhan R, et al. MR imaging of hypoxic ischemic encephalopathy: distribution patterns and ADC value correlations. *Eur J Radiol Open* 2018;5:215–20 CrossRef Medline
11. Azzopardi D, Edwards AD. Magnetic resonance biomarkers of neuroprotective effects in infants with hypoxic ischemic encephalopathy. *Semin Fetal Neonatal Med* 2010;15:261–69 CrossRef Medline
12. Thayyil S, Chandrasekaran M, Taylor A, et al. Cerebral magnetic resonance biomarkers in neonatal encephalopathy: a meta-analysis. *Pediatrics* 2010;125:e382–395 CrossRef Medline
13. Skappak C, Regush S, Cheung P-Y, et al. Identifying hypoxia in a newborn piglet model using urinary NMR metabolomic profiling. *PLoS ONE* 2013;8:e65035 CrossRef Medline
14. Cainelli E, Trevisanuto D, Cavallin F, et al. Evoked potentials predict psychomotor development in neonates with normal MRI after hypothermia for hypoxic-ischemic encephalopathy. *Clin Neurophysiol* 2018;129:1300–06 CrossRef Medline
15. Pryds O, Greisen G, Lou H, et al. Vasoparalysis associated with brain damage in asphyxiated term infants. *J Pediatr* 1990;117:119–25 CrossRef Medline
16. Lassen NA. The luxury-perfusion syndrome and its possible relation to acute metabolic acidosis localised within the brain. *Lancet* 1966;2:1113–15 CrossRef Medline
17. Skov L, Pryds O, Greisen G, et al. Estimation of cerebral venous saturation in newborn infants by near infrared spectroscopy. *Pediatr Res* 1993;33:52–55 CrossRef Medline
18. Rescoe E, Tang X, Perry DA, et al. Cerebral near-infrared spectroscopy insensitively detects low cerebral venous oxygen saturations after stage 1 palliation. *J Thorac Cardiovasc Surg* 2017;154:1056–62 CrossRef Medline
19. Shmueli K, de Zwart JA, van Gelderen P, et al. Magnetic susceptibility mapping of brain tissue in vivo using MRI phase data. *Magn Reson Med* 2009;62:1510–22 CrossRef Medline
20. Deistung A, Schweser F, Reichenbach JR. Overview of quantitative susceptibility mapping. *NMR Biomed* 2017;30:e3569 CrossRef Medline
21. Haacke EM, Xu Y, Cheng Y-CN, et al. Susceptibility-weighted imaging (SWI). *Magn Reson Med* 2004;52:612–18 CrossRef Medline
22. Haacke EM, Tang J, Neelavalli J, et al. Susceptibility mapping as a means to visualize veins and quantify oxygen saturation. *J Magn Reson Imaging* 2010;32:663–76 CrossRef Medline
23. Tang J, Liu S, Neelavalli J, et al. Improving susceptibility mapping using a threshold-based K-space/image domain iterative reconstruction approach. *Magn Reson Med* 2013;69:1396–1407 CrossRef Medline
24. Doshi H, Wiseman N, Liu J, et al. Cerebral hemodynamic changes of mild traumatic brain injury at the acute stage. *PLoS One* 2015;10:e0118061 CrossRef Medline

25. Chai C, Guo R, Zuo C, et al. **Decreased susceptibility of major veins in mild traumatic brain injury is correlated with post-concussive symptoms: a quantitative susceptibility mapping study.** *Neuroimage Clin* 2017;15:625–32 CrossRef Medline
26. Chai C, Wang H, Chu Z, et al. **Reduced regional cerebral venous oxygen saturation is a risk factor for the cognitive impairment in hemodialysis patients: a quantitative susceptibility mapping study.** *Brain Imaging Behav* 2020;14:1339–49 CrossRef Medline
27. Antonucci R, Porcella A, Pilloni MD. **Perinatal asphyxia in the term newborn.** *Journal of Pediatric and Neonatal Individualized Medicine* 2014;3:e030269 CrossRef
28. Gopagondanahalli KR, Li J, Fahey MC, et al. **Preterm hypoxic-ischemic encephalopathy.** *Front Pediatr* 2016;4:114 CrossRef Medline
29. Sie LT, van der Knaap MS, Oosting J, et al. **MR patterns of hypoxic-ischemic brain damage after prenatal, perinatal or postnatal asphyxia.** *Neuropediatrics* 2000;31:128–36 CrossRef Medline
30. Barkovich AJ, Sargent SK. **Profound asphyxia in the premature infant: imaging findings.** *AJNR Am J Neuroradiol* 1995;16:1837–46 Medline
31. Denk C, Rauscher A. **Susceptibility weighted imaging with multiple echoes.** *J Magn Reson Imaging* 2010;31:185–91 CrossRef Medline
32. Schofield MA, Zhu Y. **Fast phase unwrapping algorithm for interferometric applications.** *Opt Lett* 2003;28:1194–96 CrossRef Medline
33. Li W, Wu B, Liu C. **Quantitative susceptibility mapping of human brain reflects spatial variation in tissue composition.** *Neuroimage* 2011;55:1645–56 CrossRef Medline
34. Kames C, Wiggemann V, Rauscher A. **Rapid two-step dipole inversion for susceptibility mapping with sparsity priors.** *Neuroimage* 2018;167:276–83 CrossRef Medline
35. Leenders KL, Perani D, Lammertsma AA, et al. **Cerebral blood flow, blood volume and oxygen utilization normal values and effect of age.** *Brain* 1990;113:27–47 CrossRef Medline
36. Doucette J, Wei L, Hernández-Torres E, et al. **Rapid solution of the Bloch-Torrey equation in anisotropic tissue: application to dynamic susceptibility contrast MRI of cerebral white matter.** *Neuroimage* 2019;185:198–207 CrossRef Medline
37. Sedlacik J, Rauscher A, Reichenbach JR. **Obtaining blood oxygenation levels from MR signal behavior in the presence of single venous vessels.** *Magn Reson Med* 2007;58:1035–44 CrossRef Medline
38. Portnoy S, Milligan N, Seed M, et al. **Human umbilical cord blood relaxation times and susceptibility at 3 T: human umbilical cord blood relaxation times and susceptibility at 3 T.** *Magn Reson Med* 2018;79:3194–3206 CrossRef Medline
39. Ferrari M, Mottola L, Quaresima V. **Principles, techniques, and limitations of near infrared spectroscopy.** *Can J Appl Physiol* 2004;29:463–87 CrossRef Medline
40. Davies DJ, Su Z, Clancy MT, et al. **Near-infrared spectroscopy in the monitoring of adult traumatic brain injury: a review.** *J Neurotrauma* 2015;32:933–41 CrossRef Medline
41. Murkin JM, Arango M. **Near-infrared spectroscopy as an index of brain and tissue oxygenation.** *Br J Anaes* 2009;103(Suppl 1):i3–13 CrossRef Medline
42. Fan AP, Bilgic B, Gagnon L, et al. **Quantitative oxygenation venography from MRI phase.** *Magn Reson Med* 2014;72:149–59 CrossRef Medline
43. Liu S, Buch S, Chen Y, et al. **Susceptibility-weighted imaging: current status and future directions.** *NMR Biomed* 2017;30:10.1002/nbm.3552 CrossRef Medline
44. Yadav BK, Buch S, Krishnamurthy U, et al. **Quantitative susceptibility mapping in the human fetus to measure blood oxygenation in the superior sagittal sinus.** *Eur Radiol* 2019;29:2017–26 CrossRef Medline
45. Jain V, Buckley EM, Licht DJ, et al. **Cerebral oxygen metabolism in neonates with congenital heart disease quantified by MRI and optics.** *J Cereb Blood Flow Metab* 2014;34:380–88 CrossRef Medline
46. Yadav BK, Krishnamurthy U, Buch S, et al. **Imaging putative foetal cerebral blood oxygenation using susceptibility weighted imaging (SWI).** *Eur Radiol* 2018;28:1884–90 CrossRef Medline
47. Neelavalli J, Jella PK, Krishnamurthy U, et al. **Measuring venous blood oxygenation in fetal brain using susceptibility-weighted imaging.** *J Magn Reson Imaging* 2014;39:998–1006 CrossRef Medline
48. Shetty AN, Lucke AM, Liu P, et al. **Cerebral oxygen metabolism during and after therapeutic hypothermia in neonatal hypoxic-ischemic encephalopathy: a feasibility study using magnetic resonance imaging.** *Pediatr Radiol* 2019;49:224–33 CrossRef Medline
49. Liu P, Huang H, Rollins N, et al. **Quantitative assessment of global cerebral metabolic rate of oxygen (CMRO<sub>2</sub>) in neonates using MRI.** *NMR Biomed* 2014;27:332–40 CrossRef Medline
50. Wang Y, Spincemaille P, Liu Z, et al. **Clinical quantitative susceptibility mapping (QSM): biometal imaging and its emerging roles in patient care.** *J Magn Reson Imaging* 2017;46:951–71 CrossRef Medline
51. Zhang Y, Rauscher A, Kames C, et al. **Quantitative analysis of punctate white matter lesions in neonates using quantitative susceptibility mapping and R2\* relaxation.** *AJNR Am J Neuroradiol* 2019;40:1221–26 CrossRef Medline
52. Bosemani T, Poretti A, Huisman TA. **Susceptibility-weighted imaging in pediatric neuroimaging.** *J Magn Reson Imaging* 2014;40:530–44 CrossRef Medline
53. Tortora D, Severino M, Malova M, et al. **Variability of cerebral deep venous system in preterm and term neonates evaluated on MR SWI venography.** *AJNR Am J Neuroradiol* 2016;37:2144–49 CrossRef Medline
54. Albayram MS, Smith G, Tufan F, et al. **Frequency, extent, and correlates of superficial siderosis and ependymal siderosis in premature infants with germinal matrix hemorrhage: an SWI study.** *AJNR Am J Neuroradiol* 2020;41:331–37 CrossRef Medline
55. Dolui S, Wang Z, Wang DJ, et al. **Comparison of non-invasive MRI measurements of cerebral blood flow in a large multisite cohort.** *J Cereb Blood Flow Metab* 2016;36:1244–56 CrossRef Medline
56. Jopling J, Henry E, Wiedmeier SE, et al. **Reference ranges for hematocrit and blood hemoglobin concentration during the neonatal period: data from a multihospital health care system.** *Pediatrics* 2009;123:e333–37 CrossRef Medline
57. van der Hoeven MA, Maertzdorf WJ, Blanco CE. **Continuous central venous oxygen saturation (ScvO<sub>2</sub>) measurement using a fiber optic catheter in newborn infants.** *Arch Dis Child Fetal Neonatal Ed* 1996;74:F177–81 CrossRef Medline
58. Buchvald FF, Kesje K, Greisen G. **Measurement of cerebral oxyhaemoglobin saturation and jugular blood flow in term healthy newborn infants by near-infrared spectroscopy and jugular venous occlusion.** *Biol Neonate* 1999;75:97–103 CrossRef Medline
59. Wintermark P, Hansen A, Warfield SK, et al. **Near-infrared spectroscopy versus magnetic resonance imaging to study brain perfusion in newborns with hypoxic-ischemic encephalopathy treated with hypothermia.** *Neuroimage* 2014;85:287–93 CrossRef Medline
60. De Vis JB, Petersen ET, Alderliesten T, et al. **Non-invasive MRI measurements of venous oxygenation, oxygen extraction fraction and oxygen consumption in neonates.** *Neuroimage* 2014;95:185–92 CrossRef Medline

# Imaging Patterns Characterizing Mitochondrial Leukodystrophies

 S.D. Roosendaal,  T. van de Brug,  C.A.P.F. Alves,  S. Blaser,  A. Vanderver,  N.I. Wolf, and  M.S. van der Knaap



## ABSTRACT

**BACKGROUND AND PURPOSE:** Achieving a specific diagnosis in leukodystrophies is often difficult due to clinical and genetic heterogeneity. Mitochondrial defects cause 5%–10% of leukodystrophies. Our objective was to define MR imaging features commonly shared by mitochondrial leukodystrophies and to distinguish MR imaging patterns related to specific genetic defects.

**MATERIALS AND METHODS:** One hundred thirty-two patients with a mitochondrial leukodystrophy with known genetic defects were identified in the data base of the Amsterdam Leukodystrophy Center. Numerous anatomic structures were systematically assessed on brain MR imaging. Additionally, lesion characteristics were scored. Statistical group analysis was performed for 57 MR imaging features by hierarchic testing on clustered genetic subgroups.

**RESULTS:** MR imaging features indicative of mitochondrial disease that were frequently found included white matter rarefaction ( $n = 50$  patients), well-delineated cysts ( $n = 20$  patients), T2 hyperintensity of the middle blade of the corpus callosum ( $n = 85$  patients), and symmetric abnormalities in deep gray matter structures ( $n = 42$  patients). Several disorders or clusters of disorders had characteristic features. The combination of T2 hyperintensity in the brain stem, middle cerebellar peduncles, and thalami was associated with complex 2 deficiency. Predominantly periventricular localization of T2 hyperintensities and cystic lesions with a distinct border was associated with defects in complexes 3 and 4. T2-hyperintense signal of the cerebellar cortex was specifically associated with variants in the gene *NUBPL*. T2 hyperintensities predominantly affecting the directly subcortical cerebral white matter, globus pallidus, and substantia nigra were associated with Kearns-Sayre syndrome.

**CONCLUSIONS:** In a large group of patients with a mitochondrial leukodystrophy, general MR imaging features suggestive of mitochondrial disease were found. Additionally, we identified several MR imaging patterns correlating with specific genotypes. Recognition of these patterns facilitates the diagnosis in future patients.

**ABBREVIATIONS:** KSS = Kearns-Sayre syndrome; SDH = Succinate dehydrogenase; MELAS = mitochondrial encephalopathy, lactic acidosis, and stroke-like episodes syndrome; MNGIE = mitochondrial neurogastrointestinal encephalopathy

Leukodystrophies are genetic disorders predominantly involving the white matter of the CNS.<sup>1</sup> Clinical and genetic heterogeneity complicate establishing a specific molecular diagnosis, which becomes more effective when clinical, radiologic, and genetic parameters are combined.<sup>1</sup> Most leukodystrophies are

characterized by a specific combination of affected structures on MR imaging, constituting a recognizable pattern. Recent diagnostic algorithms for leukodystrophies acknowledge the central role of MR imaging pattern recognition.<sup>1,2</sup>

A subset of leukodystrophies, involving 5%–10%, is caused by mitochondrial defects.<sup>3,4</sup> Mitochondrial diseases comprise a group of disorders with genetic defects in mitochondrial oxidative energy metabolism. Mitochondria are cellular organelles that produce energy via oxidative phosphorylation (Online Supplemental Data). The oxidative phosphorylation system consists of 5 respiratory

Received November 17, 2020; accepted after revision January 14, 2021.

From the Departments of Radiology (S.D.R.) and Epidemiology and Biostatistics (T.v.d.B.), Amsterdam UMC, Amsterdam, the Netherlands; Division of Neuroradiology (C.A.P.F.A.), and Department of Radiology and Division of Neurology (A.V.), The Children's Hospital of Philadelphia, Philadelphia, Pennsylvania; Division of Neuroradiology (S.B.), Department of Diagnostic Imaging, Hospital for Sick Children, University of Toronto, Toronto, Ontario, Canada; Department of Pediatric Neurology (M.S.v.d.K., N.I.W.), Emma Children's Hospital, Amsterdam Leukodystrophy Center, Amsterdam UMC, Vrije Universiteit and Amsterdam Neuroscience, Amsterdam, the Netherlands; and Department of Functional Genomics (M.S.v.d.K.), Center for Neurogenomics and Cognitive Research, VU University, Amsterdam, the Netherlands.

The following authors are members of the European Reference Network for Rare Neurological Disorders, project ID 739510: M.S. van der Knaap and N.I. Wolf.

Please address correspondence to Stefan D. Roosendaal, MD, PhD, Amsterdam UMC, Department of Radiology, Meibergdreef 9, 1105 AZ Amsterdam, the Netherlands; e-mail: stefan.roosendaal@amsterdamumc.nl

 Indicates open access to non-subscribers at [www.ajnr.org](http://www.ajnr.org)

 Indicates article with online supplemental data.

<http://dx.doi.org/10.3174/ajnr.A7097>

chain complexes in the mitochondrial membrane. Human cells possess 2 different genomes: the nuclear genome, containing approximately 20,000 genes, and the mitochondrial genome, containing 37 genes. Although mitochondria have functions in addition to energy metabolism, mitochondrial diseases are typically regarded as disorders of oxidative phosphorylation.<sup>5</sup> They are caused by variants in either mitochondrial genes or, much more frequently, nuclear genes encoding proteins necessary for mitochondrial function.<sup>5</sup> Concerning the high number of associated gene defects, it is not surprising that mitochondrial disorders have a striking clinical heterogeneity,<sup>5</sup> the high energy demand of the CNS explains it being the most commonly affected organ.<sup>5</sup>

Some mitochondrial encephalopathies predominantly manifest with lesions of gray matter structures (eg, mitochondrial encephalopathy, lactic acidosis, and stroke-like episodes syndrome (MELAS); Alpers syndrome; and Leigh syndrome).<sup>6</sup> Another category manifests as leukodystrophy.<sup>7</sup> The leukoencephalopathy in Kearns-Sayre syndrome (KSS)<sup>8</sup> and mitochondrial neurogastrointestinal encephalopathy syndrome (MNGIE)<sup>9</sup> has been known for a long time, but more recently, next-generation genetic sequencing techniques have revealed that numerous unsolved cases of leukodystrophy have a mitochondrial cause, and MR imaging patterns of new mitochondrial leukodystrophies were added.<sup>10</sup> Patient selection by specific MR imaging patterns was pivotal in the detection of the novel leukodystrophies caused by defects in the genes *LYRM7*, *APOPT1*, *NUBPL*, and *CLPP*.<sup>11-14</sup> However, systematic studies on MR imaging patterns in larger groups of patients with different mitochondrial leukodystrophies are lacking, and information on the associated MR imaging patterns is lacking in recent leukodystrophy diagnostic algorithms.<sup>1,2</sup>

In the current study, we systematically analyzed MRIs of a large group of patients with mitochondrial leukodystrophy. In all patients, the causative gene defect was known. The study aims were to describe MR imaging features suggesting a mitochondrial leukodystrophy in general and to distinguish MR imaging patterns related to particular gene defects.

## MATERIALS AND METHODS

### Patients

In the MR imaging data base of the Amsterdam Leukodystrophy Center, comprising more than 4000 patients, 132 patients with a mitochondrial leukodystrophy and a known gene defect were identified. Patients with defects in genes encoding mitochondrial transfer RNA synthetases were excluded because the MR imaging patterns associated with the respective disorders have been well-described in separate studies and their high numbers in the data base would dominate the current study.<sup>15-18</sup> The retrospective phenotype analysis study was approved by the Ethics Committee of the VU University Medical Center.

Of the 132 patients, 43 had a respiratory chain complex 1 defect: 22 with variants in the genes *NDUFV1*, 1 in *NDUFV2*, 10 in *NDUFS1*, 2 in *NDUFS3*, 2 in *NDUFS4*, 1 in *NDUFS6*, 1 in *NDUFS7*, 3 in *NDUFS8*, and 1 in *NDUFAF5*. Complex 2 deficiency was present in 22 patients: 4 with variants in *SDHA*, 5 in *SDHB*, and 10 in *SDHAF1*; in 3 patients with biochemical evidence of complex 2 deficiency, the gene defect was not determined, and in one of them the *SDHA* protein expression was reduced. Most of these patients were part of a previous study on complex 2 deficiency.<sup>19</sup> Complex 3

deficiency was present in 10 patients, all with variants in *LYRM7*. Some were part of a previous study on *LYRM7*.<sup>14</sup> Complex 4 deficiency was present in 9 patients: 7 with variants in *APOPT1*, 1 with variants in *COX6B*, and 1 with variants in *COX10*. Most patients with *APOPT1* variants were part of a previous study on *APOPT1*.<sup>12</sup> Iron-sulfur cluster assembly pathway variants were present in 33 patients: 9 with variants in *NUBPL*, 8 in *IBA57*, 7 in *ISCA2*, 5 in *FDX1L*, 3 in *BOLA3*, and 1 in *CDK5RAP1*. Descriptions of some of the patients with *NUBPL*,<sup>11</sup> *IBA57*,<sup>20</sup> and *FDX1L*<sup>21</sup> variants were published before. A large mitochondrial DNA deletion was present in 6 patients, all presenting with the KSS phenotype. Additionally, 4 patients had *TYMP* variants, indicative of MNGIE, and 5 patients had *CLPP* variants; descriptions of some of the latter have been published before.<sup>13</sup>

### MR Imaging Evaluation

At least 1 brain MR imaging was available for each patient. When multiple MRIs were available, the first was used for analysis. MR sequences and image quality were variable because the MRIs were acquired at multiple institutions. T2-weighted and nonenhanced T1-weighted sequences were available for every patient; FLAIR was available for 115 patients. These images were used to systematically score numerous white and gray matter structures as normal or abnormal, and specific features of the abnormalities were scored, as described in van der Knaap et al.<sup>22</sup> More salient features of this scoring system were as follows: The white matter was divided into 3 zones—directly subcortical white matter (ie, arcuate fibers), deep white matter, and periventricular white matter. The corpus callosum was divided into inner, middle, and outer blades (or layers) and anterior, middle, and posterior parts. Cysts were strictly scored as lesions with a signal intensity identical to that of CSF on FLAIR images, whereas lesions having a signal intensity on FLAIR intermediate between normal white matter and CSF were defined as rarefaction. The caudate nucleus, putamen, globus pallidus, thalamus, dentate nucleus, substantia nigra, cerebral cortex, and cerebellar cortex were individually evaluated.

### Statistical Analysis

Group analysis was performed with 57 MR imaging features. We first analyzed which abnormalities were most commonly observed among our 132 patients.

Considering the large number of different genetic subgroups, it was unlikely that specific patterns would survive multiple comparison analysis. We therefore clustered genetic subgroups. First, patients were clustered in 9 groups: complex 1; complex 2; complex 3; complex 4; iron-sulfur cluster defects excluding *NUBPL*; *NUBPL*; MNGIE; KSS; and *CLPP*. This clustering was partly on the basis of the type of mitochondrial defect and partly on the basis of prior knowledge from personal experience and reviewing the MRIs. To further reduce the number of subgroups, we visually inspected a heat map of the data, in which the patients were ordered by genetic subtype and the features were clustered using unsupervised hierarchical cluster analysis. No differences were observed between defects of complexes 3 and 4, and they were clustered. *NUBPL* and KSS were considered separately. Complex 1 defects were clustered

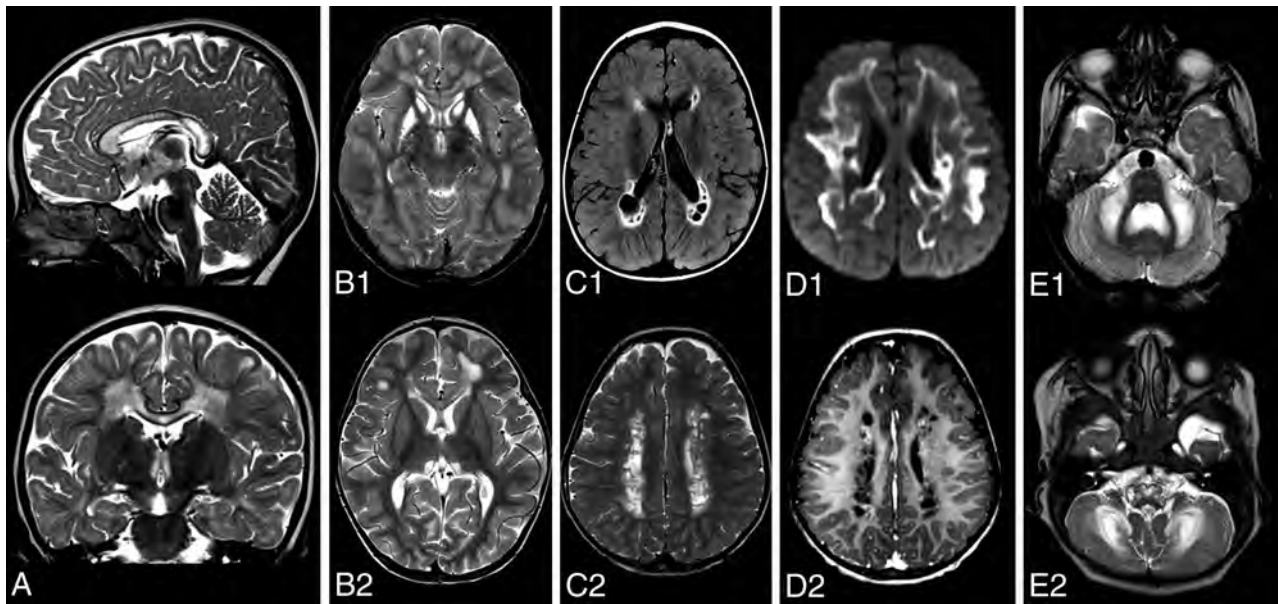


**FIG 1.** MR imaging features suggestive of mitochondrial leukodystrophy. *A*, Sagittal and coronal T2-weighted images of a patient with a complex 2 deficiency show longitudinal T2 hyperintensity affecting the middle blade of the corpus callosum while sparing the inner and outer blades. *B*, Axial T2-weighted images of 2 patients. *B1*, Symmetric involvement of the striatum in a patient with *NDUFV1* variants. *B2*, Symmetric hyperintensity in the thalami in a patient with *NDUFA5* variants. *C1*, FLAIR image of a patient with *LYRM7* variants shows small cysts in the periventricular and deep cerebral white matter. *C2*, T2-weighted image shows the well-defined border of cysts in a different patient with *LYRM7* variants. *D1*, Axial diffusion trace images show extensive diffusion restriction at the edge of the lesions in a patient with *BOLA3* variants. *D2*, Postcontrast T1-weighted image shows subtle enhancement at the edge of cysts in the same patient as in *C2*. *E1* and *E2*, Axial T2-weighted images. *E1*, Symmetric hyperintensity of the middle cerebellar peduncles and cerebellar white matter in a patient with *ISCA2* variants. *E2*, Hyperintensity of the medulla oblongata, middle cerebellar peduncles, and cerebellar white matter in a patient with *IBA57* variants.

together with the remaining genetic subgroups, so, patients were clustered in 5 groups: complex 2; complexes 3 and 4; *NUBPL*; *KSS*; and other.

To identify which MR imaging features correlated with the 5 subgroups, we performed hierarchical testing. First, the association of each feature with the overall group structure was tested. Then, for each significant feature, the association with each of the 5 subgroups was tested. Fisher exact tests were used with Holm-Bonferroni correction for multiple testing to control the maximum family-wise error rate at 0.05.

## RESULTS

### MR Imaging Findings

The age of patients at the time of their first available MR image ranged from the first month of life to 46 years of age.

T2 hyperintensity affecting the middle blade of the corpus callosum, while sparing thin inner and outer blades, was noted in 85 of our 132 patients (Fig 1). Brain stem lesions were found in 66 patients (Fig 1). These included selective involvement of certain tracts, such as part of the corticospinal tracts in 32 patients but also more diffuse or ill-defined brain stem lesions. Symmetric T2 hyperintensity in the middle cerebellar peduncles was found in 42 patients (Fig 1). Rarefaction of white matter lesions was found in 50 patients; cystic lesions were found in an additional 20 patients. These cysts were typically well-delineated (Fig 1). Symmetric abnormalities of deep gray matter structures were found in 42 patients (Fig 1), more specifically in the thalamus in 34,

substantia nigra in 13, globus pallidus in 9, putamen in 8, and caudate nucleus in 5. Cerebellar atrophy was found in 23 patients. Multifocal enhancement was found in 31 of 66 patients with contrast-enhanced images, most frequently at the edges of lesions (Fig 1). Multifocal diffusion restriction was found in 68 of 84 patients with diffusion-weighted images, again, most frequently at the lesion edges (Fig 1). Elevated lactate levels were found in 31 of 49 patients with MR spectroscopy.

Brain stem lesions were, in particular, common in succinate dehydrogenase (SDH) deficiency (19 of 22 patients) and *KSS* (all 6 patients). Symmetric T2 hyperintensity in the middle cerebellar peduncles was more commonly seen in SDH deficiency (14 of 22 patients) and *KSS* (5 of 6 patients), but also in patients with *NDUFS1* variants (5 of 10 patients). Cystic lesions were most commonly observed in patients with *APOPT1* variants (5 of 7 patients), patients with *LYRM7* variants (6 of 10 patients), and also in patients with both *COX6B* and *COX10* variants.

We investigated whether certain MR imaging abnormalities or combinations of abnormalities were specific for particular disorders or clusters of disorders. Complex 2 deficiency was characterized by T2 hyperintensity in the brain stem, more specifically in the transverse pontine fibers, and T2-hyperintense abnormality in the middle cerebellar peduncles and the thalami (Fig 2). Defects in complexes 3 and 4 were characterized by predominantly periventricular localization of T2 hyperintensities and well-defined cystic lesions with distinct borders (Fig 3). Patients with *NUBPL* variants had a unique

combination of T2-hyperintense signal of the cerebellar cortex bilaterally and supratentorial white matter abnormalities (Fig 4). Patients with KSS had T2-hyperintense abnormalities predominantly affecting the directly subcortical cerebral white matter, in combination with T2-hyperintense abnormalities in the globus pallidus and substantia nigra (Fig 5).

## DISCUSSION

We investigated the MRIs of patients with leukodystrophies caused by a genetic defect affecting the mitochondrial respiratory chain function, except for mitochondrial transfer RNA synthetase defects. Several MR imaging features were relatively frequent among all patients and therefore suggestive of a possible mitochondrial cause when observed.

Additionally, we found 4 MR imaging patterns specific for the following defects: 1) SDH deficiency, 2) *LYRM7* or *APOPT1* or *COX10* or *COX6B* variants, 3) *NUBPL* variants, and 4) KSS.

### MR Imaging Features Suggestive of a Mitochondrial Leukodystrophy

In the diagnostic work-up of patients with leukodystrophy, several MR imaging features suggest an underlying mitochondrial defect (Table 1 and illustrated in Fig 1).

We observed longitudinal T2 hyperintensity of the middle blade of the corpus callosum in most of our patients, with sparing of inner and outer blades. In metachromatic leukodystrophy, Krabbe disease, and adrenoleukodystrophy, all layers of the corpus callosum are typically affected,<sup>23</sup> while in vanishing white matter, the inner blade is involved.<sup>24</sup> Marchiafava-Bignami disease<sup>23</sup> and Susac syndrome<sup>25</sup> also selectively affect the middle blade of the corpus callosum, in Marchiafava-Bignami disease in a longitudinal fashion; but in Susac syndrome, the lesions are round and multifocal.<sup>25</sup> Thus, longitudinal selective involvement of the middle layer should be regarded as a red flag for possible mitochondrial disease.

White matter rarefaction and cystic degeneration, most accurately visualized in FLAIR sequences, were common in our patients. The cysts were usually multifocal and well-delineated and mainly located in the periventricular and deep white matter and not in the subcortical regions. Diffusion restriction and contrast enhancement often specifically involved the rims of the cysts. By contrast, in Alexander disease, cysts are mainly located in the deep frontal white matter and may become quite large.<sup>23</sup> In megalencephalic leukoencephalopathy with subcortical cysts, the cysts are

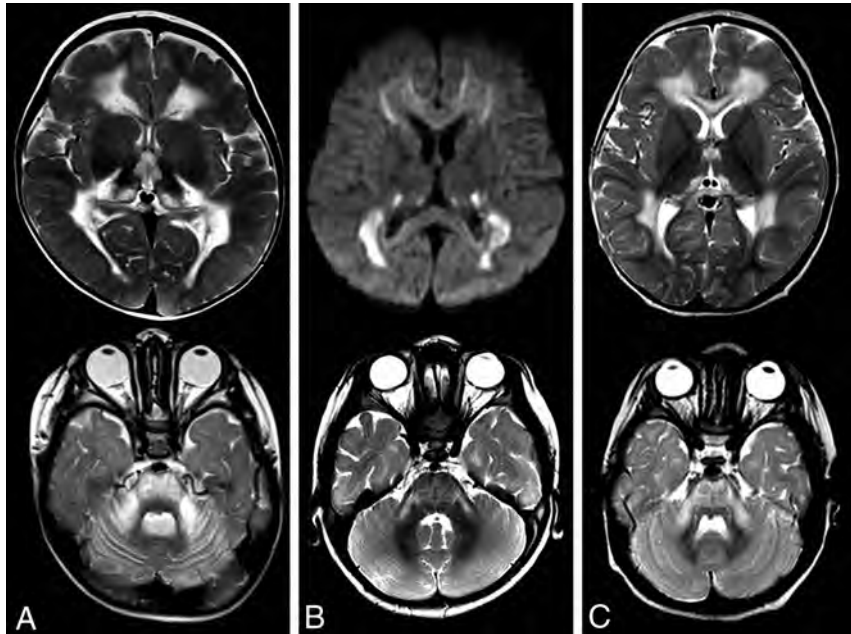


**FIG 2.** Features characteristic of SDH deficiency in 3 patients (A–C) showing symmetric thalamic involvement and pontine and middle cerebellar hyperintensities on T2-weighted images. B, Note the diffusion restriction.

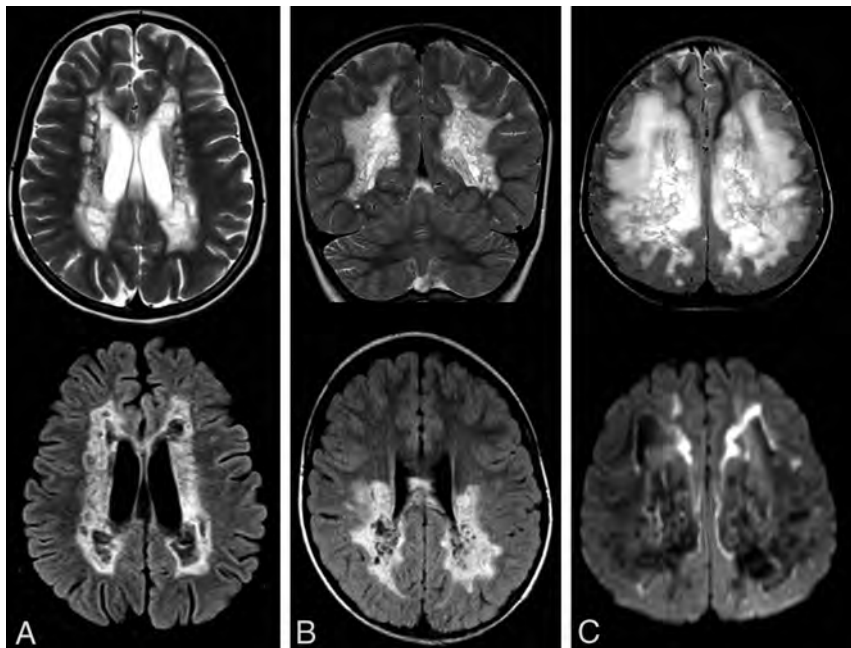


**FIG 3.** Characteristic features of defects in complexes 3 (A) and 4 (B and C). Upper rows are T2-weighted images; lower rows show FLAIR images and a diffusion trace image. Predominantly periventricular T2 hyperintensities, well-defined cystic lesions with a distinct border. Diffusion restriction at the edge of the lesions.

located in the directly subcortical white matter.<sup>23</sup> Seldom, patients with Canavan disease may exhibit multiple small cysts throughout the white matter.<sup>26</sup> Bilateral anterior temporal lobe localization of the cysts, often seen in megalencephalic leukoencephalopathy with subcortical cysts, congenital cytomegalovirus infection, and Aicardi-Goutières syndrome,<sup>23</sup> was not observed in our patient cohort,

though this localization has been reported in a mitochondrial disorder caused by *RMND1* variants.<sup>27</sup> In vanishing white matter, the cerebral white matter rarefaction and cystic degeneration are diffuse and without well-defined rims.<sup>23,24</sup> Therefore, the appearance and location of the white matter cysts are indicative of the type of leukodystrophy.

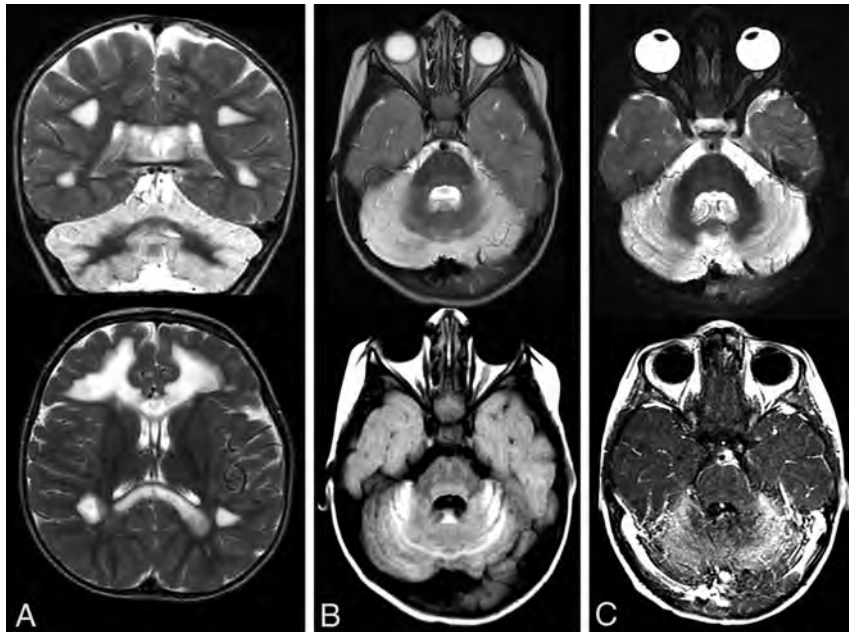


**FIG 4.** Characteristic features of *NUBPL* variants shown in 3 patients (A–C). The T2-weighted images show hyperintensity of the cerebellum, which is also hyperintense on FLAIR (B) and enhances (C). Involvement of supratentorial white matter can be extensive (A).

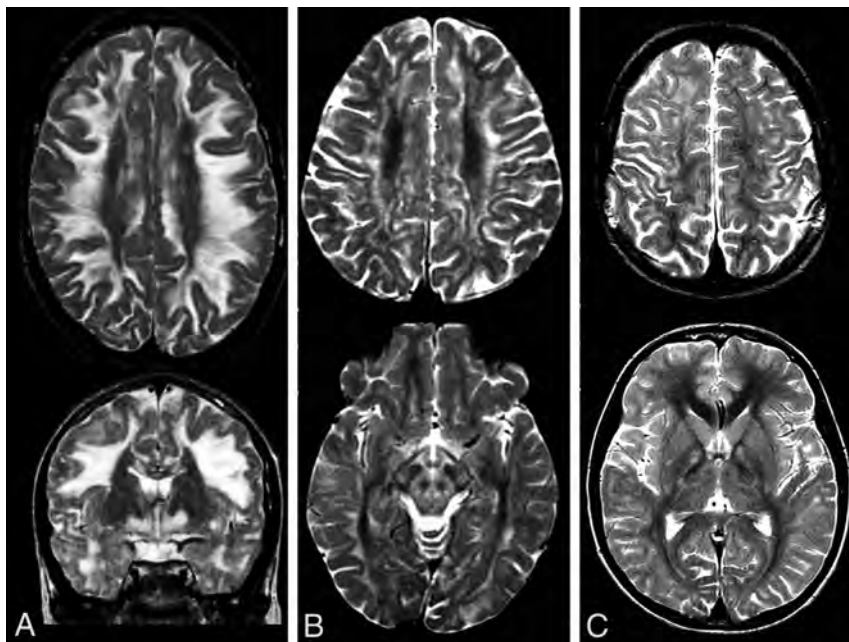


**FIG 5.** T2-weighted images of 3 patients with KSS (A–C) showing hyperintensity affecting (predominantly the subcortical and also deep) white matter. A and C, In the lower panel, hyperintensities in the globus pallidus exist. B, Involvement of the substantia nigra and, in this case, larger areas of the midbrain are shown.

Symmetric deep gray matter involvement was common in our patients, the thalamus being most frequently involved. In Wilson disease, white matter abnormalities are uncommon but may be extensive in exceptional patients.<sup>28</sup> In Alexander disease, signal changes and mild swelling, followed by atrophy, occur in the caudate nucleus and putamen.<sup>23</sup> The globus pallidus and thalamus are commonly involved in Canavan disease with sparing of the putamen and caudate nucleus.<sup>23</sup> Other defects in amino acid and organic acid metabolism may present with white and deep gray matter abnormalities,<sup>23</sup> as well as in certain types of neurodegeneration with brain iron accumulation.<sup>29</sup> Therefore, the combination of white matter abnormalities and changes in deep gray matter nuclei comes with a long differential diagnosis, of which mitochondrial defects should be part.

Brain stem abnormalities were seen in half of our patients, involving both brain stem tracts and the pontine nuclei. The brain stem abnormalities in leukoencephalopathy with brain stem and spinal cord involvement and high lactate are distinct, involving the pyramidal tracts, medial lemniscus, cerebellar connections, and intraparenchymal trigeminal nerves.<sup>15</sup> In peroxisomal disorders, brain stem abnormalities commonly occur together with abnormal signal of the cerebellar and parieto-occipital or frontal white matter.<sup>23</sup> In Wilson disease, abnormalities frequently diffusely affect the pontine tegmentum and midbrain tectum and tegmentum, creating the so-called “face of the giant panda.”<sup>30</sup> Diffuse or multifocal enhancing brain stem lesions occur in Alexander disease, particularly in the medulla and midbrain.<sup>23</sup> In dentatorubral-pallidoluysian atrophy, T2 hyperintensity exists in the midbrain and pons and often also in the globus pallidus and thalamus.<sup>23</sup> In adult patients, adult polyglucosan body

**Table 1: MR imaging features suggestive of a mitochondrial leukodystrophy**

Imaging Features
Selective longitudinal involvement of the middle blade of the corpus callosum
Cerebral white matter rarefaction and cysts with a well-delineated rim, which may show contrast enhancement and diffusion restriction
Symmetric deep gray matter abnormalities
Brain stem abnormalities
Symmetric abnormalities in the middle cerebellar peduncles

**Table 2: Diagnostic MR imaging patterns in mitochondrial leukodystrophies**

MR Imaging Patterns
Succinate dehydrogenase (complex 2) deficiency
Abnormalities in the brain stem, more specifically in the transverse pontine fibers
Abnormalities in the middle cerebellar peduncles
Abnormalities in the thalami
Succinate in MR spectroscopy
Complex 3 and 4 defects
Numerous small cysts with well-defined borders in the periventricular and deep cerebral white matter
Kearns-Sayre syndrome
Abnormalities predominantly affecting the directly subcortical cerebral white matter plus abnormalities in the globus pallidus and substantia nigra
<i>NUBPL</i> defects
T2 hyperintensity of the cerebellar cortex plus cerebral white matter abnormalities

disease and autosomal dominant leukodystrophy with autonomic disease may be considered.<sup>31,32</sup>

Symmetric T2 hyperintensity in the middle cerebellar peduncles was frequently seen in our patients, especially in SDH deficiency and KSS, and in those with *NDUFS1* variants. It has also been described in Wilson disease and adrenoleukodystrophy.<sup>33</sup> In adult patients with symmetric middle cerebellar peduncle involvement, autosomal dominant leukodystrophy with autonomic disease,<sup>32</sup> fragile X-associated tremor/ataxia syndrome,<sup>23</sup> and multiple system atrophy can be considered.<sup>33,34</sup>

### Diagnostic MR Imaging Patterns

In some cases, the MR imaging pattern is specific for or strongly suggestive of a particular disorder or group of disorders and therefore quite helpful in the diagnosis (Table 2).

We found that patients with SDH deficiency could be diagnosed by the following MR imaging features: T2 hyperintensity in the brain stem (more specifically the transverse pontine fibers), the middle cerebellar peduncles, and thalami, as reported previously.<sup>19</sup> Obviously, a succinate peak in MR spectroscopy is specific for SDH deficiency,<sup>19</sup> but spectroscopy is not always available.

The presence of numerous small cystic lesions with a well-defined border in the periventricular and deep cerebral white matter was associated with complex 3 or 4 defects. In line with this association, the MR imaging findings previously described in patients with *LYRM7* variants<sup>14</sup> are similar to those described in patients with *APOPT1* variants.<sup>12</sup> There are no previous descriptions of MR imaging abnormalities in patients with *COX10* or *COX6B* variants.

The combination of FLAIR or T2 hyperintensity of the cerebellar cortex and cerebral white matter involvement is unique for *NUBPL* variants.<sup>11</sup> Cerebellar cortical T2 hyperintensity has

been infrequently reported in other mitochondrial diseases,<sup>35</sup> but without cerebral white matter abnormalities. In several other diseases known for cerebellar cortical hyperintensity and volume loss,<sup>36</sup> typically no leukoencephalopathy exists.

A pattern of T2-hyperintense abnormalities predominantly affecting the U-fibers, the globus pallidus, and the substantia nigra was associated with KSS. Calcifications in the globus pallidus and substantia nigra may be visible. Brain stem and symmetric middle cerebellar peduncle abnormalities were also frequently observed in patients with KSS. However, these 2 features did not survive our statistical analysis, probably due to the small number of patients with KSS and the presence of these abnormalities in patients with SDH deficiency.

### Study Limitations

A limitation of our study is its retrospective nature. Most important, this limited the availability of important MR images, such as spectroscopy and contrast-enhanced images. Furthermore, a larger patient group would have increased the statistical power and may have led to the distinction of a higher number of specific MR imaging patterns. A strength of our study is that in all our patients, the causative gene defect was known. Still, it is difficult to estimate the generalizability of our results for new patients, though it is reassuring that similar, though limited, observations have been published before.<sup>11-14,19</sup>

### CONCLUSIONS

In patients with leukodystrophy, MR imaging findings are very helpful in directing the diagnostic process. In some cases, the pattern of MR imaging abnormalities is diagnostic, facilitating rapid genetic confirmation. This finding is also true for some mitochondrial leukodystrophies. In many of our patients, the MR imaging pattern was not specific for a particular mitochondrial defect, also in these patients MR imaging abnormalities suggestive of mitochondrial disease were commonly present.

### ACKNOWLEDGMENTS

We thank the numerous colleagues who sent us MR imaging scans of their patients for review and provided us with the definitive diagnosis.

Disclosures: Adeline Vanderver—UNRELATED: Board Membership: Biogen, Takeda Pharmaceutical Company, Homology Medicines, Orchard Therapeutics, European Leukodystrophy Association (ELA) Foundation, United Leukodystrophy Foundation (ULF), Yaya Foundation, Metachromatic Leukodystrophy (MLD) Foundation, Ionis Pharmaceuticals, Passage Bio\*; Grants/Grants Pending: National Institutes of Health, Takeda Pharmaceutical Company, Homology Medicines, Eli Lilly, Biogen, Ionis Pharmaceuticals, Pelizaeus Merzbacher Disease (PMD) Foundation, Foundation to Fight to Hypomyelination with Atrophy of the Basal Ganglia (H-ABC)\*; Patents (Planned, Pending or Issued): Aicardi-Goutieres Syndrome (AGS)

scale, Hypomyelination with Atrophy of the Basal Ganglia (H-ABC) Therapeutics.\* Nicole I. Wolf—UNRELATED: Consultancy: Shire/Takeda Pharmaceutical Company, Orchard Therapeutics, Ionis Pharmaceuticals, Passage Bio\*; Grants/Grants Pending: ZonMW\*; Travel/Accommodations/Meeting Expenses Unrelated to Activities Listed: European Society of Magnetic Resonance in Neuropediatrics. Marjo van der Knaap—UNRELATED: Grants/Grants Pending: ZonMw, European Leukodystrophy Association (ELA) Foundation, Hersenstichting, Vanishing White Matter Foundation, Chloe Saxby and Vanishing White Matter Disease Incorporated, and Vanishing White Matter Families Foundation Inc. Comments: ZonMw Top grant 91217006, European Leukodystrophy Foundation grant 2017-02712, European Leukodystrophy Foundation grant 2019-P001, Hersenstichting grant DR-2019-00285, Vanishing White Matter Foundation, Chloe Saxby and Vanishing White Matter Disease Incorporated, and Vanishing White Matter Families Foundation Inc; Patents (Planned, Pending or Issued): I have a patent, PI12686CA00, on the therapeutic effects of Guanabenz treatment in vanishing white matter, pending to VU University Medical Center. \*Money paid to the institution.

## REFERENCES

- van der Knaap MS, Schiffmann R, Mochel F, et al. **Diagnosis, prognosis, and treatment of leukodystrophies.** *Lancet Neurol* 2019;18:962–72 CrossRef Medline
- Köhler W, Curiel J, Vanderver A. **Adulthood leukodystrophies.** *Nat Rev Neurol* 2018;14:94–105 CrossRef Medline
- Stellitano LA, Winstone AM, van der Knaap MS, et al. **Leukodystrophies and genetic leukoencephalopathies in childhood.** *Dev Med Child Neurol* 2016;58:680–89 CrossRef Medline
- Bonkowsky JL, Nelson C, Kingston JL, et al. **The burden of inherited leukodystrophies in children.** *Neurology* 2010;75:718–25 CrossRef Medline
- Area-Gomez E, Schon EA. **Mitochondrial genetics and disease.** *J Child Neurol* 2014;29:1208–15 CrossRef Medline
- Baertling F, Klee D, Haack TB, et al. **The many faces of paediatric mitochondrial disease on neuroimaging.** *Childs Nerv Syst* 2016;32:2077–83 CrossRef Medline
- Morató L, Bertini E, Verrigni D, et al. **Mitochondrial dysfunction in CNS white matter disorders.** *Glia* 2014;62:1878–94 CrossRef Medline
- Chu BC, Terae S, Takahashi C, et al. **MRI of the brain in Kearns-Sayre syndrome.** *Neuroradiology* 1999;41:759–64 CrossRef Medline
- Millar WS, Lignelli A, Hirano M. **MRI of five patients with mitochondrial neurogastrointestinal encephalomyopathy.** *AJR Am J Roentgenol* 2004;182:1537–41 CrossRef Medline
- Kevelam S, Steenweg M, Srivastava S, et al. **Update on leukodystrophies: historical perspective and adapted definition.** *Neuropediatrics* 2016;47:349–54 CrossRef Medline
- Kevelam SH, Rodenburg RJ, Wolf NI, et al. **NUBPL mutations in patients with complex I deficiency and a distinct MRI pattern.** *Neurology* 2013;80:1577–83 CrossRef Medline
- Melchionda L, Haack TB, Hardy S, et al. **Mutations in APOPT1, encoding a mitochondrial protein, cause cavitating leukoencephalopathy with cytochrome c oxidase deficiency.** *Am J Hum Genet* 2014;95:315–25 CrossRef Medline
- Theunissen TE, Szklarczyk R, Gerards M, et al. **Specific MRI abnormalities reveal severe Perrault syndrome due to CLPP defects.** *Front Neurol* 2016;7:203 CrossRef Medline
- Dallabona C, Abbink TE, Carrozzo R, et al. **LYRM7 mutations cause a multifocal cavitating leukoencephalopathy with distinct MRI appearance.** *Brain* 2016;139:782–94 CrossRef Medline
- van Berge L, Hamilton EM, Linnankivi T, et al. **LBSL Research Group. Leukoencephalopathy with brainstem and spinal cord involvement and lactate elevation.** *Brain* 2014;137:1019–29 CrossRef Medline
- van der Knaap MS, Bugiani M, Mendes MI, et al. **Biallelic variants in LARS2 and KARS cause deafness and (ovario)leukodystrophy.** *Neurology* 2019;92:e1225–37 CrossRef Medline
- Steenweg ME, Ghezzi D, Haack T, et al. **Leukoencephalopathy with thalamus and brainstem involvement and high lactate 'LTBL' caused by EARS2 mutations.** *Brain* 2012;135:1387–94 CrossRef Medline
- Dallabona C, Diodato D, Kevelam SH, et al. **Novel (ovario)leukodystrophy related to AARS2 mutations.** *Neurology* 2014;82:2063–71 CrossRef Medline
- Helman G, Caldovic L, Whitehead MT, et al. **SDH Study Group. MRI spectrum of succinate dehydrogenase-related infantile leukoencephalopathy.** *Ann Neurol* 2016;79:379–86 CrossRef Medline
- Torraco A, Ardisson A, Invernizzi F, et al. **Novel mutations in IBA57 are associated with leukodystrophy and variable clinical phenotypes.** *J Neurol* 2017;264:102–11 CrossRef Medline
- Gurgel-Giannetti J, Lynch DS, Paiva A. D, et al. **Novel complex neurological phenotype due to a homozygous mutation in FDX2.** *Brain* 2018;141:2289–98 CrossRef Medline
- van der Knaap MS, Breiter SN, Naidu S, et al. **Defining and categorizing leukoencephalopathies of unknown origin: MR imaging approach.** *Radiology* 1999;213:121–33 CrossRef Medline
- van der Knaap MS, Valk J. *Magnetic Resonance of Myelination and Myelin Disorders.* Springer-Verlag; 2005
- van der Lei H, Steenweg M, Barkhof F, et al. **Characteristics of early MRI in vanishing white matter.** *Neuropediatrics* 2012;43:22–26 CrossRef Medline
- Bourekas EC, Varakis K, Bruns D, et al. **Lesions of the corpus callosum: MRI and differential considerations in adults and children.** *AJR Am J Roentgenol* 2002;179:251–57 CrossRef Medline
- Drenckhahn A, Schuelke M, Knierim E. **Leukodystrophy with multiple beaded periventricular cysts in Canavan disease.** *J Inherit Metab Dis* 2015;38:983–84 CrossRef Medline
- Ulrick N, Goldstein A, Simons C, et al. **RMND1-related leukoencephalopathy with temporal lobe cysts and hearing loss.** *Pediatr Neurol* 2017;66:59–62 CrossRef Medline
- Trocello JM, Woimant F, El Balkhi S, et al. **Extensive striatal, cortical, and white matter brain MRI abnormalities in Wilson disease.** *Neurology* 2013;81:1557–57 CrossRef Medline
- Krueger MC, Boddaert N, Schneider A, et al. **Neuroimaging features of neurodegeneration with brain iron accumulation.** *AJNR Am J Neuroradiol* 2012;33:407–14 CrossRef Medline
- Hitoshi S, Iwata M, Yoshikawa K. **Mid-brain pathology of Wilson's disease.** *J Neurol Neurosurg Psychiatry* 1991;54:624–26 CrossRef Medline
- Mochel F, Schiffmann R, Steenweg ME, et al. **Adult polyglucosan body disease: natural history and key MRI findings.** *Ann Neurol* 2012;72:433–41 CrossRef Medline
- Melberg A, Hallberg L, Kalimo H, et al. **MR characteristics and neuropathology in adult-onset autosomal dominant leukodystrophy with autonomic symptoms.** *AJNR Am J Neuroradiol* 2006;27:904–11 Medline
- Okamoto K, Tokiguchi S, Furusawa T, et al. **MR features of diseases involving bilateral middle cerebellar peduncles.** *AJNR Am J Neuroradiol* 2003;24:1946–54 Medline
- Shrivastava A. **The hot cross bun sign.** *Radiology* 2007;245:606–07 CrossRef Medline
- Tan AP, Robles C, Mankad K. **Cerebellar atrophy with T2/FLAIR hyperintense cerebellar cortex.** *Childs Nerv Syst* 2018;34:601–03 CrossRef Medline
- Poretti T, Wolf N, Boltshauser E. **Differential diagnosis of cerebellar atrophy in childhood: an update.** *Neuropediatrics* 2015;46:359–70 CrossRef Medline

# CT Cervical Spine Fracture Detection Using a Convolutional Neural Network

J.E. Small, P. Osler, A.B. Paul, and M. Kunst

## ABSTRACT

**BACKGROUND AND PURPOSE:** Multidetector CT has emerged as the standard of care imaging technique to evaluate cervical spine trauma. Our aim was to evaluate the performance of a convolutional neural network in the detection of cervical spine fractures on CT.

**MATERIALS AND METHODS:** We evaluated C-spine, an FDA-approved convolutional neural network developed by Aidoc to detect cervical spine fractures on CT. A total of 665 examinations were included in our analysis. Ground truth was established by retrospective visualization of a fracture on CT by using all available CT, MR imaging, and convolutional neural network output information. The  $\kappa$  coefficients, sensitivity, specificity, and positive and negative predictive values were calculated with 95% CIs comparing diagnostic accuracy and agreement of the convolutional neural network and radiologist ratings, respectively, compared with ground truth.

**RESULTS:** Convolutional neural network accuracy in cervical spine fracture detection was 92% (95% CI, 90%–94%), with 76% (95% CI, 68%–83%) sensitivity and 97% (95% CI, 95%–98%) specificity. The radiologist accuracy was 95% (95% CI, 94%–97%), with 93% (95% CI, 88%–97%) sensitivity and 96% (95% CI, 94%–98%) specificity. Fractures missed by the convolutional neural network and by radiologists were similar by level and location and included fractured anterior osteophytes, transverse processes, and spinous processes, as well as lower cervical spine fractures that are often obscured by CT beam attenuation.

**CONCLUSIONS:** The convolutional neural network holds promise at both worklist prioritization and assisting radiologists in cervical spine fracture detection on CT. Understanding the strengths and weaknesses of the convolutional neural network is essential before its successful incorporation into clinical practice. Further refinements in sensitivity will improve convolutional neural network diagnostic utility.

**ABBREVIATIONS:** AI = artificial intelligence; CNN = convolutional neural network; NPV = negative predictive value; PPV = positive predictive value

A variety of studies have been conducted evaluating the performance of artificial intelligence (AI) to detect fractures. AI has been used to detect hip,<sup>1–3</sup> humeral,<sup>4</sup> distal radius,<sup>5</sup> wrist,<sup>6–8</sup> hand,<sup>8</sup> and ankle fractures<sup>8</sup> on radiographs, as well as thoracic and lumbar spine fractures on dual x-ray absorptiometry.<sup>9</sup> In addition, AI has been used to detect calcaneal<sup>10</sup> and thoracic and lumbar vertebral body fractures<sup>11–13</sup> on CT. To our knowledge, no studies evaluating AI in detecting cervical spine fractures on CT have been published.

Cervical spine injury is common with greater than 3 million patients per year being evaluated for cervical spine injury in North

America,<sup>14</sup> and greater than 1 million patients with blunt trauma with suspected cervical spine injury per year being evaluated in the United States.<sup>15</sup> Cervical spine injury can be associated with high morbidity and mortality,<sup>16</sup> and a delay in diagnosis of an unstable fracture leading to inadequate immobilization may result in a catastrophic decline in neurologic function with devastating consequences.<sup>17–20</sup> Clearing the cervical spine through imaging is therefore a critical first step in the evaluation of patients with trauma, and multidetector CT has emerged as the standard of care imaging technique to evaluate cervical spine trauma.<sup>21</sup> Morbidity and mortality in patients with cervical spine injury can be reduced through rapid diagnosis and intervention.

The aim of this study is to evaluate the performance of a convolutional neural network (CNN) developed by Aidoc ([www.aidoc.com](http://www.aidoc.com)) for the detection of cervical spine fractures on CT. We establish the presence of fractures based on retrospective clinical diagnosis and compare the CNN performance with that of radiologists. Aidoc's CNN currently runs continuously on our

Received August 21, 2020; accepted after revision January 25, 2021.

From the Departments of Neuroradiology (J.E.S., A.B.P., M.K.) and Radiology (P.O.), Lahey Hospital and Medical Center, Burlington, Massachusetts.

Paper previously presented as a poster at: Annual Meeting of the American Society of Neuroradiology, May 30 to June 4, 2020; Virtual.

Please address correspondence to Juan E. Small, MD, Lahey Hospital and Medical Center, 41 Mall Rd, Burlington, MA 01805; e-mail: [Juan.E.Small@Lahey.org](mailto:Juan.E.Small@Lahey.org)  
<http://dx.doi.org/10.3174/ajnr.A7094>

hospital system and functions as a triage and notification software for analysis and detection of cervical spine fractures. However, we purposefully conducted a retrospective study on cervical spine studies performed before system-wide deployment, as we wanted to compare CNN performance to radiologist performance without the aid of the tool. A proficient algorithm may help identify and triage studies for the radiologist to review more urgently, helping to ensure faster diagnoses.

## MATERIALS AND METHODS

After approval by our institutional review board, we conducted a retrospective analysis of the predictions of an FDA-approved CNN developed by Aidoc for the identification of cervical spine fractures based on CT. We compared these predictions to the unaided diagnoses made by radiologists of different levels of expertise and training. Our criterion standard for the presence or absence of cervical spine fractures was based on retrospective consensus review by 2 fellowship-trained neuroradiologists after evaluating all available CT, MR imaging, and CNN data.

### CNN Algorithm Development

We evaluated an FDA-approved CNN developed by Aidoc for cervical spine fracture detection on CT. The CNN is designed to detect linear bony lucency in patterns consistent with fracture (including compression), does not distinguish between acute and chronic fractures, and is limited to the cervical spine (C1–7).

The hardware used for developing and validating the CNN included 8 GPUs, 64 CPUs, 488 GB of RAM, and 128 GB of GPU memory. Validation was based on retrospective, blinded data from 47 clinical sites evaluating approximately 8000 examinations. Nearly equal amounts of positive and negative examinations were included in the analysis. Validation sensitivity was 95.8% (95% CI, 95.7%–95.9%) and specificity was 98.5% (95% CI, 98.5%–98.5%). Approximately 12,000 studies from 83 clinical sites were used for training the algorithm, and 80% of them were positive. The CNN training data base was made from datasets from all commercially available CT scanners, and included all available imaging planes (axial, coronal, and sagittal) and kernels (bone and soft tissue). The training data base labeling was based on manual review and annotation of fractures by neuroradiologists experienced in spine trauma.

The cervical spine fracture detection model consists of 2 stages: a region proposal stage and a false-positive reduction stage. The first stage is a 3D fully convolutional deep neural network. The architecture is based on the Residual Network architecture, which consists of repeated blocks of several convolutional layers with skip connections between them, and is followed by a pooling layer that reduces the dimensions of the output. This network is trained on segmented scans and produces a 3D segmentation map. The model was trained from scratch, with no pretraining from additional datasets. From the segmentation map, region proposals are extracted and passed as input to the second stage of the algorithm. The second stage classifies each region as positive or negative. Two sets of features are extracted from each region, fused together, and used for the final decision. The first are learned features from a multilayered, classification head that receives the features from the last layer of the 3D segmentation network for the proposed regions

as input. The second are nonlearned engineered features obtained from traditional image-processing methods that operate on the proposed regions. These features are combined through an additional neural network, which classifies each proposal as a fracture or not.

### Validation Dataset

We queried the PACS for cervical spine CT studies performed between January 3, 2015, and December 30, 2018 (a time before system-wide deployment of the CNN algorithm at our institution), in patients who also had a short interval follow-up cervical spine MR imaging (<48 hours). In particular, we limited the analysis to cervical spine CT studies with a short interval follow-up MR imaging so that the MR imaging data could aid in the retrospective criterion standard determination of acute fractures. Of note, examinations at our institution have cervical spine MR imaging after a CT when there is a persistent clinical concern for cervical spine trauma despite a negative cervical spine CT, or in patients with positive cervical spine CT findings for trauma to evaluate for cord contusion, ligamentous injury, or epidural hemorrhage.

The CNN validation was made of datasets acquired from multiple institutions on all commercially available CT scanners with differences in FOV and section thickness. Similarly, the study group included datasets acquired on different commercially available CT scanners at both Lahey Hospital and Medical Center and affiliate institutions with differences in FOV and section thickness. MR images used to troubleshoot examinations were performed at both 1.5T and 3T and were not evaluated by the CNN. The finalized cervical spine CT reports were simultaneously independently reviewed by 2 fellowship-trained neuroradiologists. To achieve labeling consensus maximizing ground truth assessment in our study, the decision was made to have 2 neuroradiologists who had each completed a 2-year neuroradiology fellowship and obtained the Certificate of Added Qualification review each report. Results were classified as positive or negative for fracture.

### Error Analysis

The cervical spine CTs were interpreted and dictated at the time of patient presentation by a diverse group of radiologists. This group consisted of neuroradiologists (some of whom had obtained the Certificate of Added Qualification), emergency department radiologists, general private practice radiologists from affiliate hospitals, and remote overnight coverage night-hawk radiologists (some of whom had completed fellowship training in neuroradiology). Meaningful analysis and conclusions comparing the CNN to different-level radiologists was not feasible because of the wide variety of training backgrounds and small number of radiologists within some of the groups. Research data analysis was performed by neuroradiologists who had completed a 2-year neuroradiology fellowship and obtained the Certificate of Added Qualification. Ground truth labeling was obtained by retrospective visualization of a fracture on CT after using all available CT, MR imaging, and CNN information and was performed independently by 2 fellowship-trained neuroradiologists. Discrepant CNN positive

examinations were reviewed both on a custom web-based viewer and in the PACS. The finalized CT reports and primary CNN output were graded against the ground truth.

Only fractures involving the cervical spine (C1–7), as well as both acute and chronic fractures, were labeled true-positives to match the design of the CNN. Postsurgical changes, congenital fusion anomalies, nutrient foramina, degenerative changes, and artifact were labeled negative for fracture. Traumatic disc injuries were labeled true-negatives as they do not match the design of the CNN by failing to contain a linear bony lucency in a pattern consistent with fracture.

Our study data base included datasets from several referring institutions with different scanner manufacturers and techniques mimicking the heterogeneity of the CNN training data base. Most of the examinations at our institution were performed on an Ingenuity CT scanner (Philips Healthcare) with 1.5 mm axial section thickness and 1 mm coronal and sagittal reformats.

Diagnostic accuracy and agreement between the radiologist and the ground truth, and between the CNN and ground truth, was evaluated by using  $\kappa$  coefficients, sensitivity/specificity, positive predictive value (PPV), and negative predictive value (NPV). The 95% confidence intervals were calculated for each estimate.

## RESULTS

A total of 869 cervical spine CT examinations were initially identified. The patient age range was 16–98 years, with an average of 60.28 years and a median of 61 years. A total of 379 patients were men (54.5%) and 316

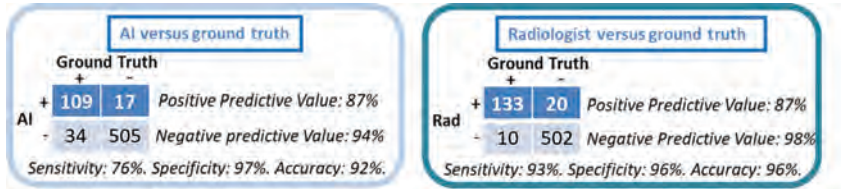


FIG 1. CNN and radiologist performance.

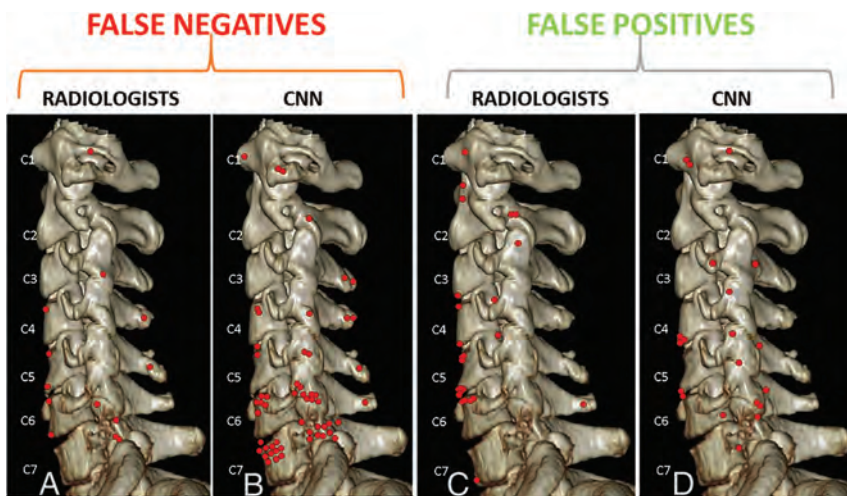
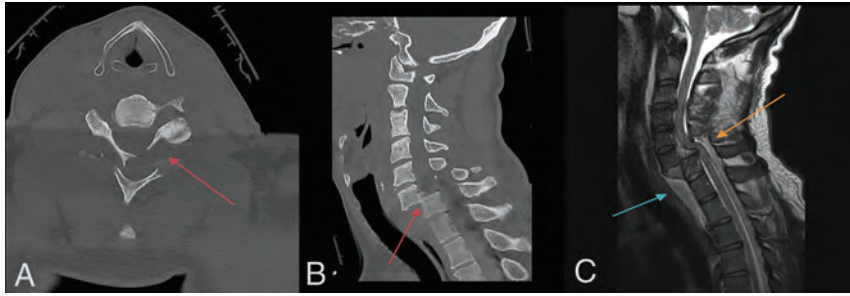


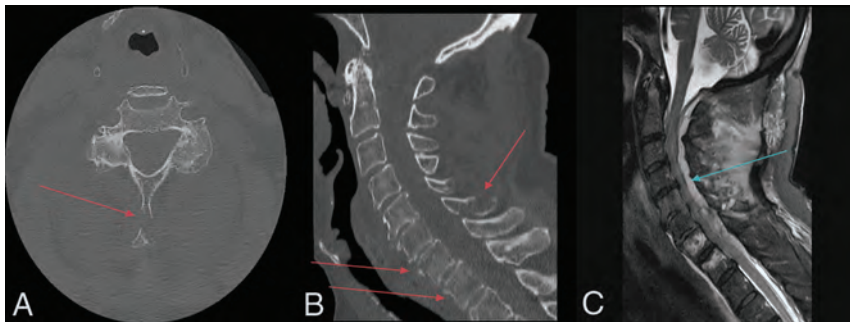
FIG 2. Location of false-negative and false-positive fractures for the radiologists and the CNN. Each location instance is marked by a red dot. False-negative fractures by radiologists (A) and the CNN (B) were similar in site and distribution. Although both the radiologists and CNN missed fractures more commonly along the lower cervical spine, errors were more numerous for the CNN. False-positive fracture sites noted by radiologists (C) and the CNN (D) can also be compared side-by-side. Numerous findings can mimic fractures on CT, most commonly degenerative changes or nutrient foramina. These fracture mimics were misinterpreted by both radiologists and the CNN. False-positive fractures along the anterior corners of vertebral bodies were slightly more commonly noted by radiologists and false-positive fractures along the facets and transverse processes were more commonly identified by the CNN.



FIG 3. Fracture-positive, radiologist false-negative, CNN false-negative case example. Axial (A), sagittal (B), and coronal (C) cervical spine CT images, and sagittal fat-saturated T2-weighted cervical spine MR image (D) demonstrate a minimally displaced C4 spinous process fracture. Red arrows demarcate fracture lines, the blue arrow demarcates prevertebral edema, and the orange arrow demarcates interspinous and supraspinous ligamentous injury. This case example illustrates a subtle fracture missed by both the radiologist and CNN that was identified in retrospect with the help of MR imaging because of the presence of secondary signs, such as prevertebral edema and ligamentous injury.



**FIG 4.** Fracture-positive, radiologist true-positive, CNN false-negative case example. Axial (A) and sagittal (B) cervical spine CT images, and sagittal fat-saturated T2-weighted cervical spine MR image (C) demonstrate a C6–7 fracture-dislocation with cord compression. *Red arrows* demarcate fracture-dislocation, the *blue arrow* demarcates prevertebral edema, and the *orange arrow* demarcates cord compression. This case example illustrates an important drawback of the CNN to overlook areas of gross bony translation, as it was only designed to detect linear bony lucency in patterns consistent with fractures.



**FIG 5.** Fracture-positive, radiologist true-positive, CNN false-negative case example. Axial (A) and sagittal (B) cervical spine CT images, and sagittal fat-saturated T2-weighted cervical spine MR image (C) demonstrate multiple fractures involving the C7 and T1 vertebral bodies and C6 spinous process with epidural hematoma and associated cord compression. *Red arrows* demarcate fracture lines and the *blue arrow* demarcates epidural hematoma. This case example illustrates important drawbacks of the algorithm to miss fractures characterized more by distraction rather than linear bony lucency, fractures involving the distal aspects of the spinous processes that may be mistaken for nuchal ligament calcification or ossification, and fractures located in the lower cervical spine where fine bony detail becomes poor from CT beam attenuation.

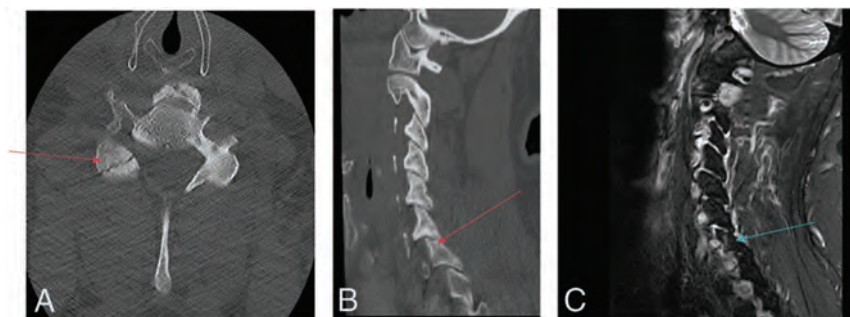


**FIG 6.** Fracture-positive, radiologist false negative, CNN true positive case example. Axial (A) and sagittal (B) cervical spine CT images and sagittal (C) STIR cervical spine MR image demonstrate a minimally displaced right C7 superior articular facet fracture. *Red and blue arrows* demarcate fracture lines. This case example illustrates the strength of the algorithm to detect subtle fractures when they conform to linear bony lucencies.

were women (45.5%). Twelve examinations were duplicates and 162 examinations could not be processed by the CNN. A total of 157 of the 162 excluded examinations could not be retrieved from the PACS by the CNN because they were imported from an outside hospital without an identifiable DICOM header. The remaining 5 of the 162 excluded examinations could not be analyzed by the CNN because of technical issues with the datasets. These technical issues related to a few preprocessing steps of the CNN orchestrator, which assure that the study is technically adequate for analysis. These include inconsistent DICOM tags or missing slices that would compromise the processing. The fracture prevalence in the excluded dataset is similar to the fracture prevalence in the included dataset. For example, 35 of the 162 excluded examinations were positive for fracture (22%) compared with 143 of the 695 included examinations (21%). Because this was a retrospective study of datasets acquired before CNN implementation, the percentage of excluded examinations on datasets acquired after CNN implementation is likely to be much smaller based on the availability of technical support from the CNN developer and the presence of reliable DICOM tags. Consequently, we feel the true accuracy of the CNN to be comparable with the accuracy demonstrated in our study. Out of the 695 remaining examinations, 30 examinations had fractures outside of the cervical spine (C1–7) and were excluded from our analysis, for a final sample size of 665 examinations. A total of 143 examinations were labeled positive for fracture and 522 examinations were labeled negative for fracture by ground truth analysis.

For the radiologists, there were 133 examinations labeled true-positive in which fractures were noted in the report and 502 examinations labeled true-negative in which no fractures were noted in the report. There were 20 examinations labeled false-positive in which a fracture was mentioned in the report but both MR imaging and CNN output were negative for fracture. There were 10 examinations labeled false-negative in which no fracture was

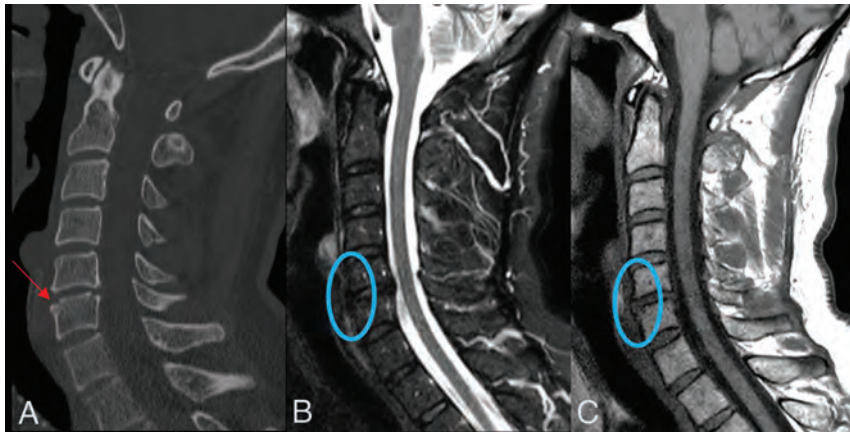


**FIG 7.** Fracture-negative, radiologist false positive, CNN false positive case example. Sagittal (A) cervical spine CT image and sagittal (B) STIR and sagittal (C) T1-weighted cervical spine MR images demonstrate a small depression along the anterosuperior margin of the C6 vertebral body (red arrow) without associated bone marrow edema, prevertebral edema, or disc space widening (blue circles). This case example illustrates how both the radiologist and CNN algorithm are capable of ignoring the absence of secondary signs, such as prevertebral edema and disc space widening when incorrectly identifying a fracture.

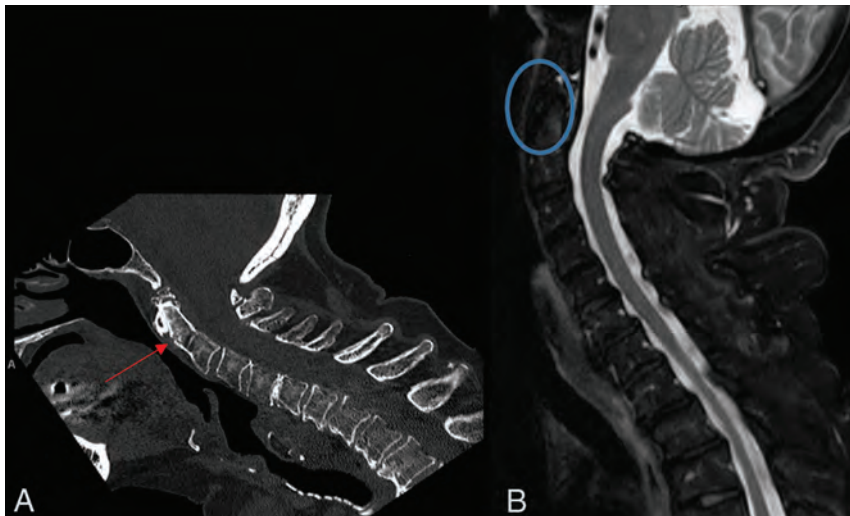


**FIG 8.** Fracture-negative, radiologist false positive, CNN true negative case example. Sagittal (A) cervical spine CT image and sagittal (B) STIR cervical spine MR image demonstrate a nutrient foramen/trabecular variant within the dens (red arrow) without associated bone marrow edema (blue circle). This case example illustrates the ability of the AI algorithm to exclude those linear bony lucencies that contain sclerotic margins inconsistent with fracture.

mentioned in the report but either MR imaging or CNN output were positive for fracture and the fracture could be visualized in retrospect on the cervical spine CT. The PPV and NPV for the radiologist was 87% (95% CI, 81%–92%) and 98% (95% CI, 96%–99%), respectively. The sensitivity, specificity, and percent agreement were 93% (95% CI, 88%–97%), 96% (95% CI, 94%–98%), and 95.5% (95% CI, 94%–97%), respectively. The  $\kappa$  coefficient was 0.87 (95% CI, 0.82–0.92). The time from acquisition until a finalized report for the radiologist ranged from 33 to 43 minutes.

For the CNN, there were 109 examinations labeled true-positive and 505 examinations labeled true-negative that matched ground truth labeling. There were 17 examinations labeled false-positive in which the CNN detected a fracture, but both the radiologist and MR imaging reports were negative for fracture. There were 34 examinations labeled false-negative in which the CNN failed to detect a fracture that was seen in both the radiologist and MR imaging reports. The PPVs and NPVs for the CNN were 87% (95% CI, 79%–92%) and 94% (95% CI, 91%–96%), respectively. The sensitivity, specificity, and percent agreement for the CNN was 76% (95% CI, 68%–83%), 97% (95%–98%), and 92% (95% CI, 90%–94%), respectively. The  $\kappa$  coefficient was 0.76 (95% CI, 0.70–0.82). The time from acquisition until a CNN analysis report ranged from 3 to 8 minutes.

To address the concern of selection bias in our sample (with an incidence of 21.5%), extrapolation to a population with an incidence of 1.9% as reported by Inaba et al<sup>16</sup> of cervical fracture was conducted. With the same sample size and values of sensitivity and specificity as found above, estimated PPVs and NPVs for the radiologist's ratings were 32% (95% CI, 18%–50%) and 99.9% (95% CI, 99%–100%), and for the CNN's ratings, they were 30% (95% CI, 15%–49%) and 99.5% (95% CI, 99%–100%).

In 7 examinations labeled true-positive, the CNN detected a fracture that the radiologist missed on CT and MR imaging. In 4 examinations labeled true-positive, the fracture detected by the CNN was chronic.

The results for CNN-versus-radiologist performance are summarized in

Fig 1. The location of false-negative and false-positive fractures for the CNN and radiologist are compared in Fig 2. Several instructive examples are depicted in Figs 3–10.

## DISCUSSION

We evaluated the performance of a CNN designed to detect cervical spine fractures on CT and compared it to that of radiologists. Our dataset contained a high fracture prevalence because of our decision to limit our analysis to only those examinations that

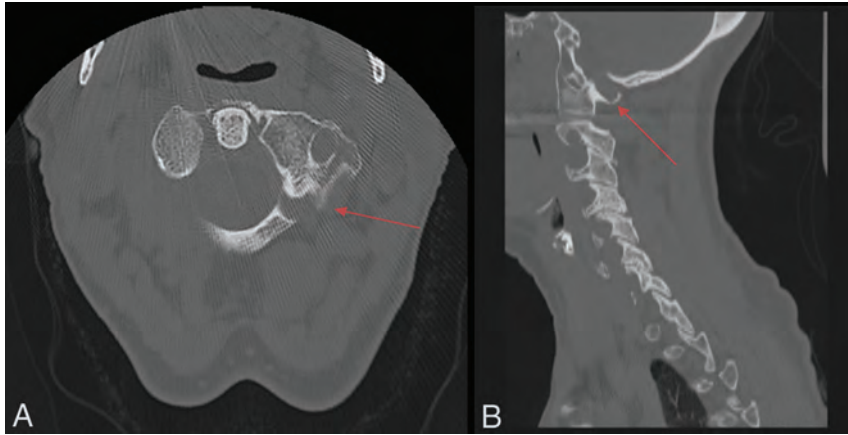


**FIG 9.** Fracture-negative, radiologist true negative, CNN false positive case example. Axial (A) and sagittal (B) cervical spine CT images demonstrate congenital thinning and incomplete fusion of the left C1 lamina. Red arrows demarcate congenital thinning and incomplete fusion. This case example illustrates a limitation of the AI algorithm to mistake common congenital anomalies for fractures if the image contains linear bony lucency extending into the cortex.



**FIG 10.** Fracture-negative, radiologist true-negative, CNN false-positive case example. Axial cervical spine CT image demonstrates a post-surgical defect involving the right lamina secondary to laminoplasty. Red arrow demarcates postsurgical defect. This case example illustrates a drawback of the algorithm to fail to differentiate postsurgical changes from fractures.

contained a short interval follow-up cervical spine MR imaging. This decision was made to ensure the veracity of our ground truth analysis because the group of interpreting radiologists in our study was diverse and had individuals with various experience in cervical spine trauma evaluation.

The CNN in our study demonstrated an accuracy of 92% compared with 96% for the radiologists, underscoring the capability of the CNN at fracture detection. In addition, time from image acquisition to CNN analysis was considerably shorter than the time from image acquisition to radiologist report finalization emphasizing the value of the CNN in worklist prioritization. This benefit would be of greater value to high-volume practices that may have even longer radiology interpretation times. There is tremendous potential for worklist prioritization to improve patient outcomes by decreasing time to diagnosis and therapeutic intervention for unstable fractures.

The sensitivity of the CNN (79%) is lower than that of the radiologists (93%). CNN output should therefore be appraised after the radiologist's imaging review. Further work to improve CNN sensitivity is particularly important if CNNs are to become widely accepted as valuable worklist prioritization tools. Importantly, the clinically more useful parameters of PPV and NPV were comparable between the CNN and radiologists in our dataset consisting of a high fracture prevalence.

Our review of the few CNN false-negative examinations demonstrates that the locations of CNN misses closely match those of radiologists. Knowledge of this is important as radiologists need to be aware of the locations where the CNN performs poorly in order to subject these locations to additional scrutiny before report finalization. The few instances in which the CNN detected a fracture that the radiologist missed underscores the ability of the CNN to function as a valuable complementary tool in fracture detection that should be reviewed by the radiologist before report finalization to maximize overall fracture detection sensitivity.

Discrepant examinations reveal important limitations of the CNN. As noted in Fig 4, a severe fracture-dislocation was missed by the CNN algorithm. In addition, as noted in Fig 5, fractures characterized more by distraction rather than linear bony lucency, fractures involving the distal aspects of the spinous processes that may be mistaken for nuchal ligament calcification or ossification, and fractures located in the lower cervical spine where fine bony detail becomes poor from CT beam attenuation were also missed by the CNN. Fractures of these types must be added to the CNN training dataset as they will need to be detected if CNNs are to become increasingly valuable worklist prioritization tools.

Study design and selection bias are important limitations to our study, diminishing the generalizability of our findings. Most scans were performed at a single primary site and therefore a prospective, multicenter trial will need to be pursued next. In addition, our dataset contained a high fracture prevalence minimizing the number of clinically occult fractures and potentially falsely elevating our reported CNN and radiologist sensitivity. If

we extrapolate our sample size and values for sensitivity and specificity to a dataset that contains a much lower fracture prevalence on par with that observed in previously reported multi-institutional cervical spine trauma trials, the PPVs for the CNN and radiologist drop below the threshold of clinical utility. Consequently, we view our results as an important first step to demonstrate CNN effectiveness in cervical spine fracture detection in a dataset with a high fracture prevalence with robust ground truth analysis, which will need to be replicated in a dataset with a lower fracture prevalence similar to routine clinical practice.

## CONCLUSIONS

The CNN holds promise at both worklist prioritization and assisting radiologists in cervical spine fracture detection on CT. CNN plays an important role in prioritizing fracture-positive examinations on the worklist. Further refinements in sensitivity will improve CNN diagnostic utility. Understanding the strengths and weaknesses of the CNN is essential before its successful incorporation into clinical practice. In the evaluation of individual examinations, the current role of the CNN in fracture detection is secondary to a thorough review by a radiologist and should always be reviewed before report finalization.

Disclosures: Juan Small—UNRELATED: Royalties: Elsevier book royalties.

## REFERENCES

- Adams M, Chen W, Holcdorf D, et al. **Computer vs human: Deep learning versus perceptual training for the detection of neck of femur fractures.** *J Med Imaging Radiat Oncol* 2019;63:27–32 CrossRef Medline
- Urakawa T, Tanaka Y, Goto S, et al. **Detecting intertrochanteric hip fractures with orthopedist-level accuracy using a deep convolutional neural network.** *Skeletal Radiol* 2019;48:239–44 CrossRef Medline
- Cheng CT, Ho TY, Lee TY, et al. **Application of a deep learning algorithm for detection and visualization of hip fractures on plain pelvic radiographs.** *Eur Radiol* 2019;29:5469–77 CrossRef Medline
- Chung SW, Han SS, Lee JW, et al. **Automated detection and classification of the proximal humerus fracture by using deep learning algorithm.** *Acta Orthop* 2018;89:468–73 CrossRef Medline
- Gan K, Xu D, Lin Y, et al. **Artificial intelligence detection of distal radius fractures: a comparison between the convolutional neural network and professional assessments.** *Acta Orthop* 2019;90:394–400 CrossRef Medline
- Kim DH, MacKinnon T. **Artificial intelligence in fracture detection: transfer learning from deep convolutional neural networks.** *Clin Radiol* 2018;73:439–45 CrossRef Medline
- Lindsey R, Daluiski A, Chopra S, et al. **Deep neural network improves fracture detection by clinicians.** *Proc Natl Acad Sci U S A* 2018;115:11591–96 CrossRef Medline
- Olczak J, Fahlberg N, Maki A, et al. **Artificial intelligence for analyzing orthopedic trauma radiographs.** *Acta Orthop* 2017;88:581–86 CrossRef Medline
- Derkatch S, Kirby C, Kimelman D, et al. **Identification of vertebral fractures by convolutional neural networks to predict nonvertebral and hip fractures: a registry-based cohort study of dual x-ray absorptiometry.** *Radiology* 2019;293:405–11 CrossRef Medline
- Pranata YD, Wang KC, Wang JC, et al. **Deep learning and SURF for automated classification and detection of calcaneus fractures in CT images.** *Comput Methods Programs Biomed* 2019;171:27–37 CrossRef Medline
- Burns JE, Yao J, Summers RM. **Vertebral body compression fractures and bone density: automated detection and classification on CT images.** *Radiology* 2017;284:788–97 CrossRef Medline
- Tomita N, Cheung YY, Hassanpour S. **Deep neural networks for automatic detection of osteoporotic vertebral fractures on CT scans.** *Comput Biol Med* 2018;98:8–15 CrossRef Medline
- Muehlethaler UJ, Mannil M, Becker AS, et al. **Vertebral body insufficiency fractures: detection of vertebrae at risk on standard CT images using texture analysis and machine learning.** *Eur Radiol* 2019;29:2207–17 CrossRef Medline
- Milby AH, Halpern CH, Guo W, et al. **Prevalence of cervical spinal injury in trauma.** *Neurosurg Focus* 2008;25:E10 CrossRef Medline
- Minja FJ, Mehta KY, Mian AY. **Current challenges in the use of computed tomography and MR imaging in suspected cervical spine trauma.** *Neuroimaging Clin N Am* 2018;28:483–93 CrossRef Medline
- Inaba K, Byerly S, Bush LD, et al. **Cervical spinal clearance: a prospective Western Trauma Association multi-institutional trial.** *J Trauma Acute Care Surg* 2016;81:1122–30 CrossRef Medline
- Poonnoose PM, Ravichandran G, McClelland MR. **Missed and mismanaged injuries of the spinal cord.** *J Trauma* 2002;53:314–20 CrossRef Medline
- Izzo R, Popolizio T, Balzano RF, et al. **Imaging of cervical spine traumas.** *Eur J Radiol* 2019;117:75–88 CrossRef Medline
- Khanpara S, Ruiz-Pardo D, Spence SC, et al. **Incidence of cervical spine fractures on CT: a study in a large level I trauma center.** *Emerg Radiol* 2020;27:1–8 CrossRef Medline
- Alessandrino F, Bono CM, Potter CA, et al. **Spectrum of diagnostic errors in cervical spine trauma imaging and their clinical significance.** *Emerg Radiol* 2019;26:409–16 CrossRef Medline
- Bernstein MP, Young MG, Baxter AB. **Imaging of spine trauma.** *Radiol Clin North Am* 2019;57:767–85 CrossRef Medline

# T1 Mapping for Microstructural Assessment of the Cervical Spinal Cord in the Evaluation of Patients with Degenerative Cervical Myelopathy

G. Baucher, H. Rasoanandrianina, S. Levy, L. Pini, L. Troude, P.-H. Roche, and V. Callot



## ABSTRACT

**BACKGROUND AND PURPOSE:** Although current radiologic evaluation of degenerative cervical myelopathy by conventional MR imaging accurately demonstrates spondylosis or degenerative disc disease causing spinal cord dysfunction, conventional MR imaging still fails to provide satisfactory anatomic and clinical correlations. In this context, we assessed the potential value of quantitative cervical spinal cord T1 mapping regarding the evaluation of patients with degenerative cervical myelopathy.

**MATERIALS AND METHODS:** Twenty patients diagnosed with mild and moderate-to-severe degenerative cervical myelopathy and 10 healthy subjects were enrolled in a multiparametric MR imaging protocol. Cervical spinal cord T1 mapping was performed with the MP2RAGE sequence procedure. Retrieved data were processed and analyzed regarding the global spinal cord and white and anterior gray matter on the basis of the clinical severity and the spinal canal stenosis grading.

**RESULTS:** Noncompressed levels in healthy controls demonstrated significantly lower T1 values than noncompressed, mild, moderate, and severe stenotic levels in patients. Concerning the entire spinal cord T1 mapping, patients with moderate-to-severe degenerative cervical myelopathy had higher T1 values compared with healthy controls. Regarding the specific levels, patients with moderate-to-severe degenerative cervical myelopathy demonstrated a T1 value increase at C1, C7, and the level of maximal compression compared with healthy controls. Patients with mild degenerative cervical myelopathy had lower T1 values than those with moderate-to-severe degenerative cervical myelopathy at the level of maximal compression. Analyses of white and anterior gray matter confirmed similar results. Strong negative correlations between individual modified Japanese Orthopaedic Association scores and T1 values were also observed.

**CONCLUSIONS:** In this preliminary study, 3D-MP2RAGE T1 mapping demonstrated increased T1 values in the pathology tissue samples, with diffuse medullary alterations in all patients with degenerative cervical myelopathy, especially relevant at C1 (nonstenotic level) and at the maximal compression level. Encouraging correlations observed with the modified Japanese Orthopaedic Association score make this novel approach a potential quantitative biomarker related to clinical severity in degenerative cervical myelopathy. Nevertheless, patients with mild degenerative cervical myelopathy demonstrated nonsignificant results compared with healthy controls and should now be studied in multicenter studies with larger patient populations.

**ABBREVIATIONS:** DCM = degenerative cervical myelopathy; Cmax = maximal compression; HC = healthy controls; mJOA = modified Japanese Orthopaedic Association; OSS = overall stenosis score; SC = spinal cord

Degenerative cervical myelopathy (DCM) currently covers the various cervical spine pathologic conditions potentially causing spinal cord (SC) impairment, including cervical spondylosis and degenerative disc disease.<sup>1</sup> The wide range of severity of clinical

presentations makes the disability caused by DCM widely variable but usually substantially associated with a reduction in the quality of life.<sup>2,3</sup> DCM is generally considered the first cause of SC dysfunction among adults,<sup>4</sup> and the epidemiology of DCM remains complex to estimate because of frequent diagnostic delays.<sup>1</sup> Cervical spondylosis and degenerative disc disease are currently found in approximately 70% of individuals older than 65 years of age and 70% of

Received March 11, 2020; accepted after revision February 7, 2021.

From the Neurochirurgie Adulte (G.B., L.T., P.-H.R.), Assistance Publique-Hôpitaux de Marseille, Hôpital Universitaire Nord, Marseille, France; Center for Magnetic Resonance in Biology and Medicine (G.B., H.R., L.P., S.L., V.C.), Assistance Publique-Hôpitaux de Marseille, Hôpital Universitaire Timone, Marseille, France; Center for Metabolic Exploration in Biology and Medicine (H.R., L.P., S.L., V.C.), Aix-Marseille Université, Centre National de la Recherche Scientifique, Marseille, France; and iLab-Spine International Associated Laboratory (G.B., H.R., S.L., P.-H.R., V.C.), Marseille-Montreal, France-Canada.

This work was supported by the Institut Carnot Star and Centre National de la Recherche Scientifique.

Please address correspondence to Virginie Callot, PhD, CRMBM-CEMEREM, UMR7339, CNRS, Aix-Marseille Université, 27 Boulevard Jean Moulin, 13385 Marseille Cedex 05, France; e-mail: virginie.callot@univ-amu.fr

Indicates open access to non-subscribers at [www.ajnr.org](http://www.ajnr.org)

Indicates article with online supplemental data.

<http://dx.doi.org/10.3174/ajnr.A7157>

asymptomatic individuals.<sup>5,6</sup> In addition to a disposition to a further evolution toward progressive symptomatic myelopathy, these conditions also expose patients to the risk of acute neurologic deterioration in cases of traumatic hyperextension or hyperflexion, notably illustrated by the central cord syndrome.<sup>7-9</sup>

Once the diagnosis of DCM is suspected, the role of MR imaging is obviously useful for demonstrating cervical spinal degenerative changes and signs of SC impairment.<sup>10</sup> First, MR imaging provides direct information about spinal canal size and the structural causes responsible for its narrowing.<sup>11</sup> Second, conventional T2WI and T1WI highlight intramedullary signal intensity changes, which are associated with postoperative functional outcome.<sup>10</sup>

Nevertheless, the major discrepancy between clinical severity and the radiologic degree of stenosis is an important issue for the neurosurgeon. Several advanced MR imaging techniques have, thus, been proposed as potential biomarkers of DCM, attempting to more accurately assess the microstructural and functional organization of the SC. DTI, measuring directional diffusivity of water within each voxel,<sup>12,13</sup> appears to be the most studied and promising technique. However, it currently remains complex to apply in daily practice due to difficulties in establishing standardized protocols, such as an appropriate anatomic level of acquisition and surgery-predictive cutoff values.<sup>14</sup>

Although longitudinal relaxation time T1 is an essential parameter in MR imaging, T1 mapping has not been used in clinical routine practice due to its long scan time. Due to faster techniques of acquisition,<sup>15-18</sup> it now appears as another option to help analyze pathologic SC and, more particularly highly myelinated tissue associated with low T1 values.<sup>19-21</sup> Water content, axonal size, and iron concentration also influence T1, explaining the sensitivity of this approach to pathologic microstructural changes in neural tissue, despite a lack of specificity.<sup>22-24</sup> Used in the brain to study alterations in white and gray matter in both lesions and tissue with a normal appearance, T1 values demonstrated an interesting clinical correlation with cognitive dysfunction.<sup>25,26</sup> Although it has been rarely used in the SC until recently, studies have now outlined fast and reproducible methods to measure T1 in cervical SC in healthy subjects using 3D-MP2RAGE,<sup>27</sup> 2D multisection inversion recovery zonally oblique-magnified multislice EPI,<sup>18</sup> or 2D single-section inversion recovery radial gradient-echo<sup>28</sup> sequences. This latter procedure, recently applied in patients presenting with mild and moderate cervical spinal canal stenosis,<sup>28</sup> demonstrated decreased T1 values in the SC at the compression site, with a more pronounced decrease in the higher-grade stenosis. To the best of our knowledge, this is, to date, the only quantitative T1 investigation in a pathologic context.

The aim of the current study was, therefore, to go further and pursue the investigation of microstructural alterations in patients with diagnosed DCM, by performing routine T1 mapping of the entire cervical SC (ie, not restricted to the level of maximal compression) using the 3D-MP2RAGE sequence (for the first time in the pathologic SC) and evaluating both white and gray matter compartments (instead of the SC alone). In this study, we compared T1 values collected in the healthy cervical SC with compressed levels and levels of normal appearance in patients with DCM, and using the correlation with clinical features, we explored the potential diagnostic contribution of T1 mapping.

## MATERIALS AND METHODS

### Subject Recruitment and Clinical Assessment

In this prospective single-center study, 20 volunteer patients presenting with clinical and radiologic signs of DCM were recruited in an adult neurosurgery department (Hôpital Nord, AP-HM). Ten healthy subjects with no clinical signs of myelopathy were enrolled in parallel as a control group. Exclusion criteria were contraindications for MR imaging and intolerance of the supine position. The study was approved by the local ethics committee (South Mediterranean Committee for the Protection of Individuals), and written informed consent was routinely obtained before MR imaging for all patients and healthy controls (HC). Clinical presentation was assessed using the modified Japanese Orthopaedic Association (mJOA) scale, with scores ranging from 0 to 17.<sup>29</sup> Patients were separated into mild DCM (mJOA score from 15 to 17) and moderate-to-severe DCM (mJOA score of  $\leq 14$ ) groups.<sup>30</sup> The clinical onset of the symptoms was classified as acute or chronic.

### MR Imaging Protocol

MR imaging examinations were performed on a 3T system (Magnetom Verio; Siemens) using standard 12-channel head, 4-channel neck, and 24-channel spine matrix coils for signal reception. Subjects were placed in a supine position with the neck fixed in a neutral position using a cervical brace to prevent any movement during the procedure. The protocol included a 3D T2 sagittal sampling perfection with application-optimized contrasts by using different flip angle evolution (SPACE sequence; Siemens) and MP2RAGE acquisitions. The MP2RAGE<sup>31</sup> sequence was optimized for the SC as in Rasoanandrianina et al<sup>27</sup> (TE = 2.48 ms, TR = 4 seconds, generalized autocalibrating partially parallel acquisition = 2, isotropic resolution = 0.9 mm) and covered both brain and C1-C7 vertebral levels (Fig 1). This sequence provided both anatomic imaging and quantitative T1 mapping. In fact, normally the MP2RAGE sequence acquires two 3D gradient-echo volumes at 2 different TIs ( $T1_{inv1}$  and  $T1_{inv2}$ , here 65 and 2000 ms) with 2 different flip angles ( $\alpha_1$  and  $\alpha_2$ , here 4° and 5°) that are combined to obtain a composite “uniform” T1WI contrasted volume, called  $T1_{UNI}$ ,<sup>27</sup> from which a T1 map is subsequently derived. Because  $T1_{UNI}$  signal is partially altered by the transmitted  $B_1^+$  and received  $B_1^-$  field inhomogeneities (bias fields), leading to inaccurate T1 estimation, an additional magnetized-prepared turbo-FLASH  $B_1^+$  mapping sequence covering the whole cervical SC was acquired to correct bias fields during postprocessing. The total acquisition time was approximately 15 minutes.

### Data Postprocessing

The data postprocessing aimed at extracting corrected T1 values from  $T1_{UNI}$  acquisitions, at the level of the cervical SC, using the  $T1_{inv2}$  sequence as an anatomic reference. The postprocessing stages were performed using in-house Matlab codes (R2018a version; MathWorks).  $T1_{UNI}$  and  $B_1^+$  maps were first combined to offset bias fields, generating the adjusted  $T1_Q$ .<sup>27</sup> Denoising of  $T1_Q$  was achieved by Block-matching 4D filtering (BM4D).<sup>32</sup> The next stage consisted of cervical SC segmentation using the semi-automated processing pipeline PropSeg,<sup>33</sup> included in the Spinal Cord Toolbox.<sup>34</sup> Due to frequent difficulties of PropSeg in



**FIG 1.** Illustrative cases of cervical sagittal MP2RAGE views ( $T1_{inv2}$  and  $T1_Q$ ) acquired in healthy controls (upper row), patients with mild DCM (middle row), and moderate-to-severe DCM (lower row). M indicates mild; M&S, moderate and severe.

correctly projecting the SC beyond compressed levels, the obtained cord segmentation from the  $T1_{inv2}$  volume was systematically reviewed and manually corrected to match both  $T1_Q$  and  $T1_{inv2}$  (Fig 2). The  $T1_Q$  volume and its corresponding cord segmentation were then registered into the anatomic and probabilistic PAM50 space.<sup>35,36</sup> Vertebral labeling was derived from this process and routinely checked visually. SC GM, including anterior, intermediate, and dorsal GM, and WM delineations were also obtained using the PAM50 atlases. The binarization of the GM/WM segmentation was completed using 0.5 as a threshold for each voxel. Warping back of the cord segmentation and WM/GM masks into the subject space allowed new visual checking and correction in case of an anatomic defect. Using these masks and following a 2D erosion around the cord, we quantified T1 values within the entire SC, WM, and anterior and intermediate GM for each vertebral level from C1 to C7. Anterior and intermediate GM ROIs were merged into a single ROI. Posterior GM was intentionally excluded from the analysis to avoid a substantial risk of partial volume effects and erroneous results due to the small dimensions of the posterior horns at the

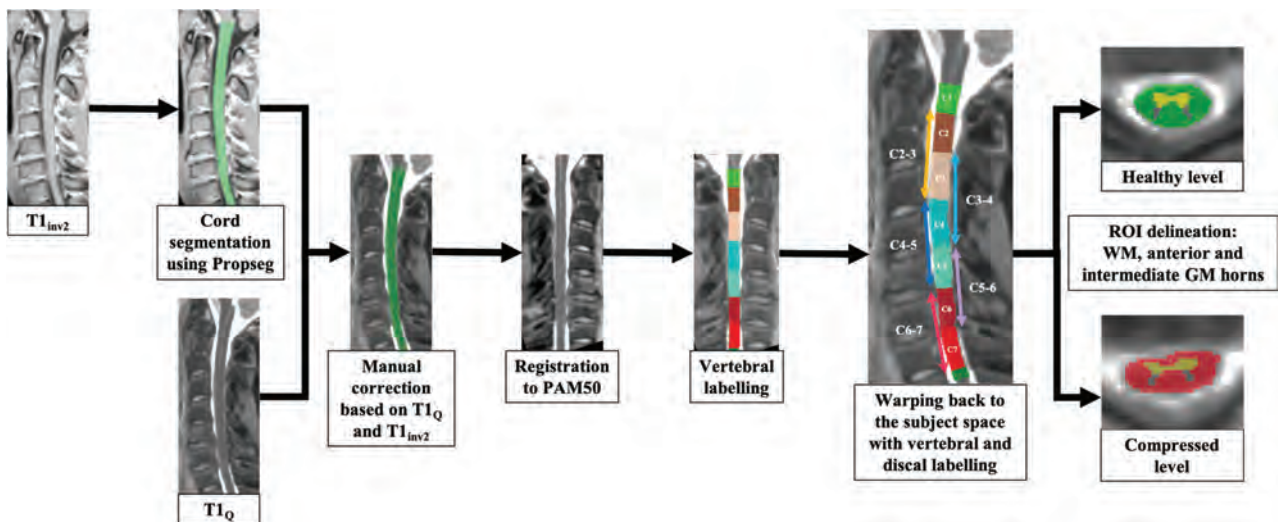


**FIG 2.** Postprocessing of the T1 data from cord segmentation to WM/GM ROI analysis, per vertebral and disc levels. A  $T1_Q$  threshold of 2 seconds was used to check the cord segmentation. Segmentation was performed using the PAM50 atlas.<sup>34,35</sup> Quantifications were performed in the subject space.

cervical level regarding the spatial resolution of the images at 3T.

### **Anatomic Assessment of the Spinal Stenosis**

Compression of the SC was assessed using axial and sagittal views of the anatomic T2-SPACE series, as usual in daily practice. We selected a qualitative scale of spinal canal stenosis, presenting satisfactory intraobserver and interobserver reliabilities (Online Supplemental Data).<sup>37,12</sup> This grading, ranging from 0 to 3, classified each disc level as normal, mildly, moderately, or severely compressed, respectively. The level of maximal compression was determined for each patient and termed "Cmax." These observations were routinely rated by an experienced neurosurgeon, blindly, from the clinical severity and before T1-mapping post-processing. An overall stenosis score (OSS) was additionally proposed for each subject by adding the single stenosis scores (from 0 to 3) for each disc level from C2–C3 to C6–C7. The obtained value, ranging from 0 to 15, was then used to define 3 grades of OSS severity based on the statistical distribution of the results: mild OSS (0–6) (first quartile, 5.8); moderate OSS (7–9); and severe OSS (10–15) (third quartile, 10). The presence of T2 signal hyperintensity at the level of maximal compression was evaluated as well.

### **Statistical Analysis**

All statistical analyses were performed using JMP 9 (SAS Institute), considering  $P$  values  $< .05$  as statistically significant. T1 values at the disc levels (C2–C3 to C6–C7) were calculated by averaging the 2 adjacent vertebral level T1 values from C2 to C7 for each subject. Due to the large number of compressed levels in both the mild and moderate-to-severe groups of patients, we decided to compare T1 values for C1, C7, and Cmax. Because C4–C5 and C5–C6 were the most frequent levels of maximal compression (respectively, 40% and 40% of all patients), we took the T1 value of the vertebral C5 level into account for the healthy subjects' group, to compare with the Cmax results of the groups of patients. T1 comparisons between the different groups (clinical severity, clinical onset, spinal canal stenosis) were performed using a linear analysis of covariance (age as a covariate), followed by a nonparametric Steel-Dwass test corrected for multiple comparisons. Age effect was reported when appropriate. The Spearman coefficients were calculated to study the correlation between clinical severity (preoperative mJOA score) and T1 values.

## **RESULTS**

### **Epidemiology**

The healthy control group included 10 subjects (mean, 45.1 [SD, 17.7] years of age; range, 22–66 years); the mild DCM group, 7 patients (mean, 41.3 [SD, 15.2] years of age; range, 25–71 years; mean mJOA, 16.3 [SD, 0.5]; range, 16–17); and the moderate-to-severe group, 13 patients (mean, 54.0 [SD, 14.2] years; range, 30–72 years; mean mJOA, 12.5 [SD, 1.7]; range, 9–14). There was no statistical difference concerning age among these 3 clinical groups. Four elderly subjects and 1 young healthy subject had moderate radiologic compression (grades 1–2) related to degenerative changes but remained in the control group due to their absence of symptoms and clinical signs of myelopathy. Details are presented in

the Online Supplemental Data. The maximal compression was primarily found at C5–C6 in the mild DCM group (71%) and at C4–C5 in the moderate-to-severe DCM group (54%). The mean number of compressed disc levels was 3.7 (SD, 1.1): 3.3 (SD, 1.6) in the mild DCM group and 3.8 (SD, 0.8) in the moderate-to-severe DCM group. The mean spinal canal stenosis score (from 0 to 3 for each disc level) for the compressed levels was 2.0 (SD, 0.9) for the mild DCM group, 2.1 (SD, 0.9) for the moderate-to-severe DCM group, and 2.9 (SD, 0.3) at Cmax (equal in both patient groups). Six patients (30%, 49.3 [SD, 13.4] years of age on average) had an acute onset of their neurologic signs, whereas 14 patients (70%, 49.6 [SD, 16.7] years of age) had a progressive appearance of their symptoms. Cervical spondylosis was the predominant cause of DCM, observed in 15 patients (75%) compared with 5 patients with degenerative disc disease (25%). Patients affected with degenerative disc disease were significantly younger (35.8 [SD, 7.5] years of age on average) than those with spondylosis (54.1 [SD, 14.8] years of age,  $P = .02$ ). Nevertheless, the mJOA score did not differ in the 2 etiologic entities (mean mJOA: 14.6 [SD, 2.8] for degenerative disc versus 13.6 [SD, 2.2] for spondylosis).

### **T1 Mapping and Clinical Onset**

The mJOA score between the patients presenting with an acute onset of their symptoms ( $n = 6$ , mean mJOA = 13.7 [SD, 2.5]) and those having a progressive neurologic course ( $n = 14$ , mean mJOA = 13.9 [SD, 2.3]) did not show any significant difference. Despite a slightly superior vertebral distribution of T1 values for acute onset, statistical analyses failed to show any significant difference between the 2 clinical entities at C1 (mean T1 for acute onset, 977.1 [SD, 36.4] ms; and chronic onset, 964.0 [SD, 27.3] ms), Cmax (1001.6 [SD, 88.4] ms and 981.0 [SD, 63.3] ms), and C7 (981.8 [SD, 47.6] ms and 958.0 [SD, 49.6] ms) levels.

### **T1 Mapping and Cervical Spinal Canal Stenosis**

When we compared noncompressed disc level T1 values in healthy controls (grade 0) with all disc level T1 values in patients (grade 0–3), an overall increased T1 value was observed for all patient grades (Fig 3), with a significant difference between healthy subject grade 0 and patient grade 0 ( $P < .001$ ), grade 1 ( $P = .003$ ), grade 2 ( $P = .03$ ), and grade 3 ( $P < .001$ , with an age effect ( $P = .04$ )). Overall (all subjects combined) increased T1 values in the cervical SC were observed in cases of spinal canal stenosis, with statistically significant differences between grades 3 and 0 ( $P < .001$ , age effect [ $P = .047$ ]) and grades 3 and 1 ( $P < .05$ ).

### **T1 Mapping and T2 Hyperintensity**

Among the 20 patients, 10 had medullary T2 hyperintensity (Online Supplemental Data), corresponding to a mean T1 value of 1037 [SD, 64] ms at the level of maximal compression (median = 1039 ms; minimum–maximum = 949–1157 ms). In comparison, the remaining 10 patients having a normal medullary T2 intensity had a statistically significant lower mean T1 value of 937 (SD, 25) ms (median = 935 ms; minimum–maximum = 905–990 ms) ( $P < .001$ ).

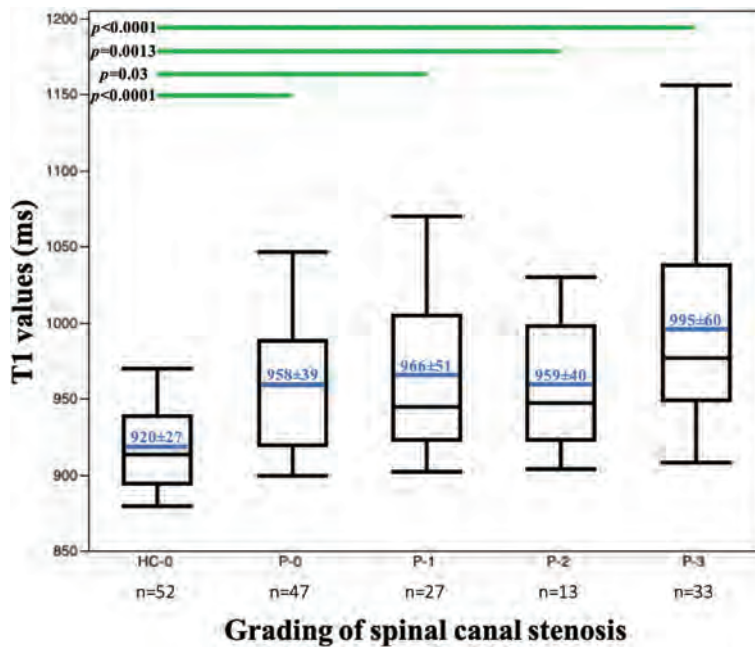


**FIG 3.** Boxplots of cervical spinal cord T1 values (in milliseconds) in noncompressed disc levels for the 10 healthy controls (HC-0 grade 0; mean T1, 920 [SD, 27] ms) compared with noncompressed (P-0 grade 0; mean T1, 958 [SD, 39] ms), mildly (P-1 grade I; mean T1, 966 [SD, 51] ms), moderately (P-2 grade II; mean T1, 959 [SD, 40] ms), and severely (P-3 grade III; mean T1, 995 [SD, 60] ms) compressed disc levels for the 20 patients. C1 and C2–C3 to C6–C7 disc levels were considered for each subject (6 levels in total). Grade 0 in patients and healthy controls were considered separately because they present statistical different values. The *horizontal blue lines* represent the mean value in each group. The *horizontal lines within and at the ends of the boxes* represent the median value and the first and third quartiles, respectively. The *whiskers* illustrate the minimum and maximum values. The *horizontal green lines* demonstrate statistically significant differences between the stenosis grades.

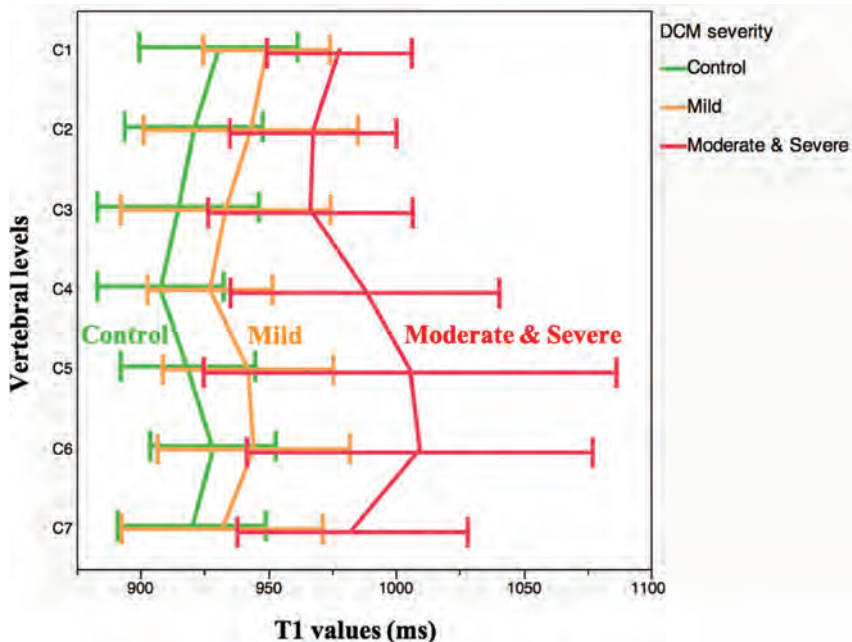


**FIG 4.** Distribution of the cervical spinal cord T1 values (milliseconds) according to the vertebral levels in the healthy subjects (green, no statistical difference between the different cervical levels) and patients with mild (orange) and moderate-to-severe (red) DCM. The *horizontal bars* represent the SD for each level.

### Global T1 Mapping and Overall Stenosis Score

Statistical analysis of the global SC T1 values in the 20 patients (single value for each subject, calculated by the mean T1 value for the whole cervical SC), regarding the OSS, demonstrated lower values in the mild OSS group (OSS = 1–6, seven patients; mean T1, 936.9 [SD, 35.7] ms) compared with the highest outcomes of the moderate OSS group (OSS = 7–9, nine patients; mean, 988.7 [SD, 40.9] ms) and with the severe OSS group (OSS = 10–15; four patients; mean, 968.6 [SD, 14.2] ms). Statistical analyses were not conclusive regarding differentiating the severe OSS group from the mild and moderate groups, though comparison between the moderate and the mild groups was significant ( $P = .02$ ).

### T1 Mapping and Clinical Severity

Cervical SC T1 mapping in the 3 clinical groups revealed increased T1 values in the moderate-to-severe group compared with the mild DCM group and healthy subjects (Fig 4). In comparison, the mild DCM group demonstrated slightly higher cord T1 distribution compared with the healthy control group. Global inflection of the 3 T1 curves could be observed around the C3 and C4 levels (but no statistical difference was observed among the different vertebral levels). Considering specifically the single global SC T1 value for each patient in the 3 clinical groups, patients with moderate-to-severe DCM had the highest mean SC T1 value (982.1 [SD, 39.4] ms), followed by the patients with mild DCM (937.7 [SD, 32.9] ms), and healthy subjects (920.1 [SD, 24.1] ms). A significant difference was found between the patients with moderate-to-severe DCM and healthy subjects ( $P = .002$ ). T1 values in the mild DCM and moderate-to-severe DCM groups were close to statistical significance ( $P = .06$ ), whereas no difference was observed between the patients with mild DCM and healthy subjects ( $P = .50$ ). Finally, a significant correlation between the single SC T1 values and the preoperative mJOA scores was observed ( $\rho = -0.68$  and  $P = .003$ ).

### Level-Specific T1 Mapping and Clinical Severity

When we compared the SC T1 values at the C1, Cmax, and C7 levels among the different clinical groups, a global increase was observed from the control group to the mild and then moderate-to-

severe DCM groups (Fig 5). Statistical analysis revealed significant differences between healthy subjects and the moderate-to-severe DCM group at each level ( $P = .005$ ,  $.003$ , and  $.007$ , at C1, Cmax, and C7, respectively). The relationships between the mild and the moderate-to-severe DCM groups showed a significant difference at Cmax ( $P = .04$ ). Comparisons between the healthy subjects and the mild DCM group failed to show any statistical relationship. When we considered individual z scores (each patient's T1 relative to the mean of healthy controls) at Cmax, 10/13 patients with moderate-to-severe DCM had values of  $>2$  (12/13 had z scores of  $>1$ ). For the patients with mild DCM, 4/7 had z scores of  $>1$ , but only one was above 2. Correlations between the preoperative mJOA score and T1 values at C1, Cmax, and C7 were also assessed using the Spearman coefficient and were consistently significant ( $\rho = -0.63$  and  $P = .01$ ;  $\rho = -0.71$  and  $P = .002$ ;  $\rho = -0.62$  and  $P = .01$ ).

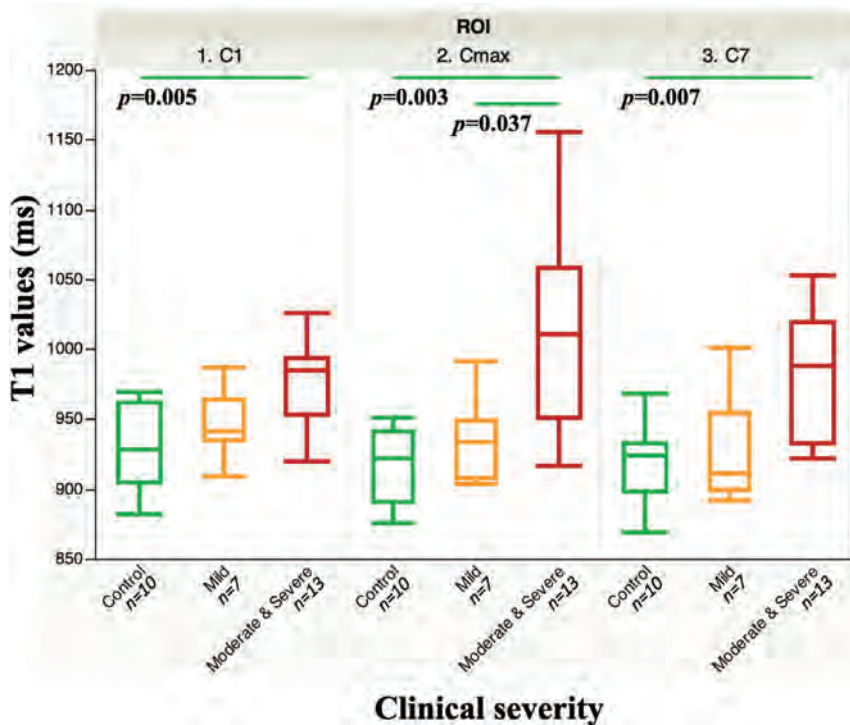


**FIG 5.** Boxplots of the T1 values at C1, Cmax, and C7 in the control (green), mild (orange), and moderate-to-severe (red) DCM groups. Horizontal green lines represent statistically significant differences among the clinical groups ( $P < .05$ ).

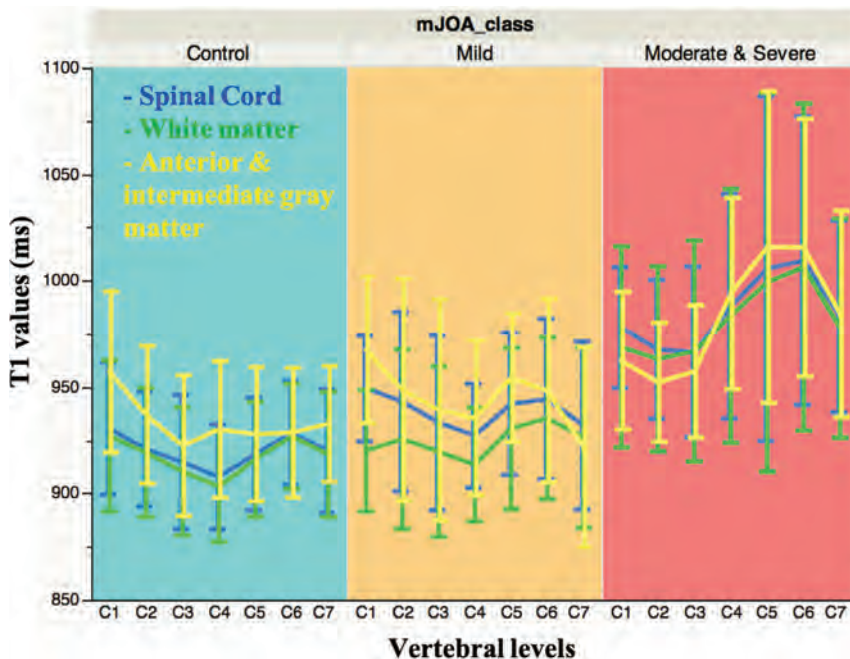


**FIG 6.** Distribution of the T1 values (milliseconds) for each clinical group according to the vertebral levels, in the entire spinal cord (blue), white matter (green), and anterior gray matter (yellow). Vertical bars represent the SD for each level.

### White Matter and Anterior Gray Matter T1 Mapping and Clinical Severity

Regarding the T1 mapping in more specific anatomic subdivisions, increased values were observed in the anterior and intermediate GM compared with WM and the entire SC in the healthy subjects (Fig 6). Anterior and intermediate GM T1 values remained the highest in the mild DCM group, with values close to those observed in the SC. Finally, anatomic distribution values in the moderate-to-severe DCM group appeared more erratic, without any clear hierarchic organization, but with very high values for both WM and GM, especially in the lower levels. Statistical comparisons of T1 values at the C1, Cmax, and C7 levels between the clinical groups globally demonstrated significant differences between healthy subjects and the moderate-to-severe group in WM at Cmax ( $P = .01$ ) and C7 ( $P < .05$ ), as well as at Cmax in the anterior GM ( $P = .002$ ). Results between patients with mild and moderate-to-severe DCM were conclusive at C1 ( $P < .05$ ) and Cmax ( $P = .04$ ) for WM and at Cmax ( $P = .01$ ) for anterior GM. None of the analyses

**Summary of the global observations and statistical analyses according to radiologic/clinical settings and regionalized T1-mapping**

Radiologic and Clinical Settings	Regionalized T1 Mapping	Global Observations	Statistical Significance
Clinical onset Cervical spinal canal stenosis	SC at C1, Cmax, C7 SC at disc levels	T1 values acute > chronic T1 values increase according to the severity of the stenosis ( $T1_{\text{grade0}} < T1_{\text{grade1}} < T1_{\text{grade3}}$ )	No Grades 3/0; 3/1 (considering all subjects) Grades 3/0 <sub>HC</sub> , 2/0 <sub>HC</sub> , 1/0 <sub>HC</sub> , 0/0 <sub>HC</sub> (differentiating patients and HC grade 0)
OSS	Entire cervical SC	Lower T1 values in the mild-stenosis group	Mild-vs-moderate OSS
Clinical severity	Entire cervical SC	T1 values increase according to the clinical severity ( $T1_{\text{control}} < T1_{\text{mild}} < T1_{\text{moderate-to-severe}}$ ) Inverse relationship between global T1 values and preoperative mJOA scores	HC and patients with moderate-to-severe DCM  Yes
	SC at C1, Cmax, C7	T1 values increase at C1, Cmax, C7 according to the clinical severity	HC and patients with moderate-to-severe DCM (C1, Cmax, and C7) Patients with mild and moderate-to-severe DCM (Cmax) No statistical difference between controls and patients with mild DCM
	WM, anterior and intermediate GM at C1, Cmax, C7	Global T1-value increase at C1, Cmax, C7 in the WM and GM according to the clinical severity	HC and patients with moderate-to-severe DCM (Cmax and C7 in WM and Cmax in GM) Patients with mild and moderate-to-severe DCM (C1 and Cmax in WM, Cmax in GM) No statistical difference between controls and patients with mild DCM

between the patients with mild DCM and HC were statistically significant.

**DISCUSSION**

T1 values are known to be directly affected by the degree of myelination, axonal diameter, and water content,<sup>24</sup> with the shorter T1s being associated with healthy tissue and longer T1s reflecting demyelination, axonal loss, and global microstructural medullary disorganization of myelopathy. The present study illustrates the potentialities of the MP2RAGE sequence in the context of patients with DCM, permitting medullary T1 mapping with valuable pathologic changes. The main findings related to the stenosis grading; clinical severity; and SC, GM, and WM ROIs are summarized in the Table and discussed further below.

**Clinical Correlation of Spinal Cord T1 Mapping**

A similar pattern of SC T1 mapping was found in the 3 clinical groups, shifted according to the severity of their symptoms (Fig 4). If occurrence of critical changes in T1 values at the level of maximal compression was not surprising, more remarkable were the important modifications of the T1 mapping at distal levels, simultaneously above and below the main compression. While standard anatomic MR imaging sequences primarily showed

focal alterations at compressed medullary levels, the quantitative MP2RAGE sequence emphasized a more diffuse structural deterioration of the SC, potentially related to Wallerian degeneration, proximal and distal to the compression zone.<sup>38</sup>

**Anatomic Considerations of Spinal Cord T1 Mapping**

In healthy subjects, the T1 mapping of the SC presented an inflection of the curve centered over the vertebral C4 level that was also observed in the mild DCM group, and in a less obvious shape in the moderate-to-severe DCM group (Fig 4). These lower T1 values at C4 could potentially be correlated to the upper limit of the cervical SC enlargement, anatomically corresponding to the motor output and sensory input of the upper limbs<sup>39</sup> and thus to the medullary zone where the bundles of WM are the most important and compact. Further studies according to the spinal levels (rather than vertebral) could be considered.<sup>40</sup> The distribution of T1 values according to the vertebral levels in WM was lower than that in the anterior GM in healthy subjects and patients with mild DCM (Fig 6), as previously reported.<sup>41</sup> This observation conforms to the bundles-network nature of the WM, with strong preferential orientation and functional organization in tracts in the SC.<sup>42</sup> In contrast, GM is characterized by a more lamellar and vascularized structure, containing the perikaryons of the medullary neurons.<sup>43</sup> Regarding

homogenization of WM and anterior GM values in the moderate-to-severe DCM group, it could indicate a medullary alteration predominant on WM in the more severe clinical cases, presumably related to important demyelination phenomena. The statistical comparisons of the WM and anterior GM T1 mapping among the different clinical groups at the C1, Cmax, and C7 levels provided close results to those estimated in the SC analysis (Table). Nevertheless, these conclusions should be accepted with caution because of both the persistent risk of partial volume effects and probabilistic estimations of the segmentation between WM and GM, especially in the atrophic and compressed SC of the patients with DCM.

### **Radiologic Correlation of Spinal Cord T1 Mapping**

The presence of T2 hypersignal was associated with increased T1 values at the level of maximal compression. This observation appeared consistent because both increased T1 values and the presence of T2 hypersignal may be linked to increased water content in extracellular space, inducing an increase in both T1- and T2-relaxation times. However, T2 hyperintensity in DCM (including our patients) is usually focal and located at the level of compression, as opposed to the diffuse medullary alterations demonstrated by T1 mapping (reaching the C1 level). Furthermore, T2 hyperintensities were associated with large global T1 values (Online Supplemental Data), but this association was not systematic, nor reciprocal. Consequently, this has not been further investigated but would probably require an analysis in a larger cohort.

Statistical analysis of the SC T1 mapping according to the severity of the spinal canal stenosis (Fig 3) showed a significant difference in T1 values between noncompressed levels (grade 0) in healthy subjects and all types of levels (grade 0–3) in patients (Fig 3). A trend toward a progressive increase of disc level T1 values according to the severity of the stenosis was observed for patients, except for grade 2. This latter observation was probably the repercussion of the smaller number of levels classified as moderately compressed (grade 2: 13 levels) compared with the mildly (grade 1: 27 levels) and severely (grade 3: 33 levels) compressed ones. Thus, T1 mapping in our study appears as a sensitive tool to differentiate symptomatic patients from healthy subjects but fails to correlate with the severity of the spinal stenosis, despite a progressive increase in values.

In their study, Maier et al<sup>28</sup> highlighted an inverse correlation of the T1 values with the severity of the spinal canal stenosis, demonstrating lower values in case of compression compared with “unaffected” segments above and below the compression. This should be further explored because MR imaging protocols, measurement techniques, and inclusion criteria (leading to different populations and pathophysiologic stages of DCM) differed.

### **Potential Role in DCM**

T1 mapping has shown its role in the brain for multiple sclerosis, demonstrating alterations in white and gray matter (including normal-appearing tissue) and a clinical correlation with cognitive dysfunction.<sup>44,45</sup> From the DCM perspective, the main interest of alternative MR imaging sequence studies resides in the exploration of the correlation with the preoperative clinical severity and the prediction of the postoperative outcomes. DTI parameters

showed, for example, a valuable association with the mJOA score across researches;<sup>46</sup> nevertheless, results fluctuate among other factors, according to age and vertebral levels.<sup>14</sup> Regarding T1 mapping, measurements at both the C1 and Cmax levels appear particularly relevant because they provide both focal and diffuse information on SC tissue alterations in DCM (even in the absence of compression, as observed here in the C1 and C7 levels). Longitudinal postoperative follow-ups should now be performed to investigate these potentialities. Given current investigations and observations, T1 mapping at the level of maximal compression appears to be the most promising metric because it clearly demonstrates higher values and the most obvious group stratification/discriminating potentialities (Fig 5).

The main limitation of this study is, first, the lack of statistically significant results for the mild DCM group due to its smaller population, which thus remains the most challenging to individualize, especially from healthy controls. Another difficulty is the variable performance of the semi-automated detection and projection of the cervical SC in the compressed levels of the DCM (here performed with PropSeg<sup>33</sup> but also tried with DeepDeg<sup>47</sup>) involving mandatory visual checking and manual correction in the postprocessing phase, which are sometimes time-consuming. Nonetheless, due to the feasibility and reproducibility of the protocol on the one hand<sup>27</sup> and partial correlation of the T1 values with the clinical severity on the other, this study confirms the already encouraging results of previous experiences.<sup>18,28</sup>

Consequently, orthcoming attention to T1 mapping in DCM will have to focus on diverse key points, starting with selecting the optimal technique of measurement to standardize it. Then, larger series will have to test the robustness of the correlation with preoperative clinical severity, in particular in patients with mild DCM, identifying corresponding intervals and thresholds of T1 values. Multivariate analysis at the different cord levels should also be investigated to analyze the patients on the individual scale and to, therefore, fully demonstrate clinical use potentiality. Future prospective studies will also have to assess T1 mapping as a feasible prognostic tool for postoperative outcome, the prediction of which persists in being partially unsolved. Eventually, confrontation with other alternative MR imaging sequences will have to identify the best option in terms of sensitivity and specificity for daily practice.

## **CONCLUSIONS**

In this preliminary study, cervical MP2RAGE-based T1 mapping in patients with DCM demonstrated diffuse medullary alterations, especially relevant at the level of maximal compression and upper (C1) levels, with promising-but-still-incomplete correlation with clinical severity. Contrary to the patients with moderate-to-severe DCM, analyses of T1 mapping of those with mild DCM notably failed to demonstrate significant differences from healthy controls, despite slightly higher T1 values. Nevertheless, SC T1 mapping appears to be a biomarker of interest, particularly concerning the clinical severity in DCM, which will now have to be explored in a number of larger series, especially including more patients with mild DCM, along with the ability to predict postoperative outcome.

## ACKNOWLEDGMENTS

The authors would like to thank T. Kober from Siemens for MP2RAGE sequence support, A. Massire and O. Girard for T1-postprocessing code support, as well as V. Gimenez, C. Costes, S. Confort-Gouny, V. Véla, M. Juge-Boulogne, and C. Laura for study logistics and R. Medeiros for editing the final manuscript version. The authors are also grateful to the 20 patients and 10 healthy subjects for their kind participation in this study. This work was performed within a laboratory member of France Life Imaging network (grant ANR-11-INBS-0006) and was supported by Institut Carnot Star and Centre National de la Recherche Scientifique.

## REFERENCES

1. Nouri A, Tetreault L, Singh A, et al. **Degenerative cervical myelopathy: epidemiology, genetics, and pathogenesis.** *Spine (Phila Pa 1976)* 2015;40:E675–93 CrossRef Medline
2. King JT, McGinnis KA, Roberts MS. **Quality of life assessment with the medical outcomes study short form-36 among patients with cervical spondylotic myelopathy.** *Neurosurgery* 2003;52:113–20; discussion 121 Medline
3. Kalsi-Ryan S, Karadimas SK, Fehlings MG. **Cervical spondylotic myelopathy: the clinical phenomenon and the current pathobiology of an increasingly prevalent and devastating disorder.** *Neuroscientist* 2013;19:409–21 CrossRef Medline
4. Nurick S. **The pathogenesis of the spinal cord disorder associated with cervical spondylosis.** *Brain* 1972;95:87–100 CrossRef Medline
5. Gore DR, Sepic SB, Gardner GM. **Roentgenographic findings of the cervical spine in asymptomatic people.** *Spine (Phila Pa 1976)* 1986;11:521–24 CrossRef Medline
6. Ernst CW, Stadnik TW, Peeters E, et al. **Prevalence of annular tears and disc herniations on MR images of the cervical spine in symptom free volunteers.** *Eur J Radiology* 2005;55:409–14 CrossRef Medline
7. Schneider RC, Cherry G, Pantek H. **The syndrome of acute central cervical spinal cord injury.** *J Neurosurg* 1954;11:546–77 CrossRef Medline
8. Aarabi B, Hadley MN, Dhall SS, et al. **Management of acute traumatic central cord syndrome (ATCCS).** *Neurosurgery* 2013;72 (Suppl 2):195–204 CrossRef Medline
9. Brooks NP. **Central cord syndrome.** *Neurosurg Clin N Am* 2017;28:41–47 CrossRef Medline
10. Martin AR, Tadokoro N, Tetreault L, et al. **Imaging evaluation of degenerative cervical myelopathy.** *Neurosurg Clin N Am* 2018;29:33–45 CrossRef Medline
11. Tracy JA, Bartleson JD. **Cervical spondylotic myelopathy.** *Neurologist* 2010;16:176–87 CrossRef Medline
12. Nouri A, Martin AR, Mikulis D, et al. **Magnetic resonance imaging assessment of degenerative cervical myelopathy: a review of structural changes and measurement techniques.** *Neurosurg Focus* 2016;40: E5 CrossRef Medline
13. Stroman PW, Wheeler-Kingshott C, Bacon M, et al. **The current state-of-the-art of spinal cord imaging: methods.** *Neuroimage* 2014;84:1070–81 CrossRef Medline
14. Rindler RS, Chokshi FH, Malcolm JG, et al. **Spinal diffusion tensor imaging in evaluation of preoperative and postoperative severity of cervical spondylotic myelopathy: systematic review of literature.** *World Neurosurg* 2017;99:150–58 CrossRef Medline
15. Henderson E, McKinnon G, Lee TY, et al. **A fast 3D look-locker method for volumetric T1 mapping.** *Magn Reson Imaging* 1999;17:1163–71 CrossRef Medline
16. Deoni SCL, Rutt BK, Peters TM. **Rapid combined T1 and T2 mapping using gradient recalled acquisition in the steady state.** *Magn Reson Med* 2003;49:515–26 CrossRef Medline
17. Wang X, Joseph AA, Kalentev O, et al. **High-resolution myocardial T1 mapping using single-shot inversion recovery fast low-angle shot MRI with radial undersampling and iterative reconstruction.** *Br J Radiol* 2016;89:20160255 CrossRef Medline
18. Battiston M, Schneider T, Prados F, et al. **Fast and reproducible in vivo T1 mapping of the human cervical spinal cord.** *Magn Reson Med* 2018;79:2142–48 CrossRef Medline
19. Koenig SH, Brown RD, Spiller M, et al. **Relaxometry of brain: why white matter appears bright in MRI.** *Magn Reson Med* 1990;14:482–95 CrossRef Medline
20. Does MD, Gore JC. **Compartmental study of T1 and T2 in rat brain and trigeminal nerve in vivo.** *Magn Reson Med* 2002;47:274–83 CrossRef Medline
21. Lancaster JL, Andrews T, Hardies LJ, et al. **Three-pool model of white matter.** *J Magn Reson Imaging* 2003;17:1–10 CrossRef Medline
22. Vymazal J, Righini A, Brooks RA, et al. **T1 and T2 in the brain of healthy subjects, patients with Parkinson disease, and patients with multiple system atrophy: relation to iron content.** *Radiology* 1999;211:489–95 CrossRef Medline
23. Gelman N, Ewing JR, Gorell JM, et al. **Interregional variation of longitudinal relaxation rates in human brain at 3.0 T: relation to estimated iron and water contents.** *Magn Reson Med* 2001;45:71–79 CrossRef Medline
24. Harkins KD, Xu J, Dula AN, et al. **The microstructural correlates of T1 in white matter.** *Magn Reson Med* 2016;75:1341–45 CrossRef Medline
25. Steenwijk MD, Vrenken H, Jonkman LE, et al. **High-resolution T1-relaxation time mapping displays subtle, clinically relevant, gray matter damage in long-standing multiple sclerosis.** *Mult Scler* 2016;22:1279–88 CrossRef Medline
26. Lommers E, Simon J, Reuter G, et al. **Multiparameter MRI quantification of microstructural tissue alterations in multiple sclerosis.** *Neuroimage Clin* 2019;23:101879 CrossRef Medline
27. Rasoanandrianina H, Massire A, Guye M, et al. **Fast and robust sub-millimetric 3D MP2RAGE-based T1 mapping of the entire cervical cord at 3T.** *NMR Biomed* 2019;32(11):e4142 CrossRef Medline
28. Maier IL, Hofer S, Joseph AA, et al. **Quantification of spinal cord compression using T1 mapping in patients with cervical spinal canal stenosis: preliminary experience.** *Neuroimage Clin* 2019;21:101639 CrossRef Medline
29. Chiles BW, Leonard MA, Choudhri HF, et al. **Cervical spondylotic myelopathy: patterns of neurological deficit and recovery after anterior cervical decompression.** *Neurosurgery* 1999;44:762–69; discussion 769–70 CrossRef Medline
30. Tetreault L, Kopjar B, Nouri A, et al. **The modified Japanese Orthopaedic Association scale: establishing criteria for mild, moderate and severe impairment in patients with degenerative cervical myelopathy.** *Eur Spine J* 2017;26:78–84 CrossRef Medline
31. Marques JP, Kober T, Krueger G, et al. **MP2RAGE, a self bias-field corrected sequence for improved segmentation and T1-mapping at high field.** *Neuroimage* 2010;49:1271–81 CrossRef Medline
32. Maggioni M, Katkovich V, Egiazarian K, et al. **Nonlocal transform-domain filter for volumetric data denoising and reconstruction.** *IEEE Trans Image Process* 2013;22:119–33 CrossRef Medline
33. De Leener B, Kadoury S, Cohen-Adad J. **Robust, accurate and fast automatic segmentation of the spinal cord.** *Neuroimage* 2014;98:528–36 CrossRef Medline
34. De Leener B, Lévy S, Dupont SM, et al. **SCT: Spinal Cord Toolbox, an open-source software for processing spinal cord MRI data.** *Neuroimage* 2017;145:24–43 CrossRef Medline
35. De Leener B, Fonov VS, Collins DL, et al. **PAM50: Unbiased multimodal template of the brainstem and spinal cord aligned with the ICBM152 space.** *NeuroImage* 2018;165:170–79 CrossRef Medline
36. Fonov VS, Le Troter A, Taso M, et al. **Framework for integrated MRI average of the spinal cord white and gray matter: the MNI-Poly-AMU template.** *Neuroimage* 2014;102:817–27 CrossRef Medline

37. Muhle C, Metzner J, Weinert D, et al. **Classification system based on kinematic MR imaging in cervical spondylitic myelopathy.** *AJNR Am J Neuroradiol* 1998;19:1763–71 Medline
38. Dolan RT, Butler JS, O'Byrne JM, et al. **Mechanical and cellular processes driving cervical myelopathy.** *World J Orthop* 2016;7:20–29 CrossRef Medline
39. Bican O, Minagar A, Pruitt AA. **The spinal cord: a review of the functional neuroanatomy.** *Neurol Clin* 2013;31:1–18 CrossRef Medline
40. Cadotte DW, Cadotte A, Cohen-Adad J, et al. **Characterizing the location of spinal and vertebral levels in the human cervical spinal cord.** *AJNR Am J Neuroradiol* 2015;36:803–10 CrossRef Medline
41. Smith SA, Edden RAE, Farrell JAD, et al. **Measurement of T1 and T2 in the cervical spinal cord at 3 Tesla.** *Magn Reson Med* 2008;60:213–19 CrossRef Medline
42. Cho TA. **Spinal cord functional anatomy.** *Continuum (Minneap Minn)* 2015;21:13–35 CrossRef Medline
43. Santillan A, Nacarino V, Greenberg E, et al. **Vascular anatomy of the spinal cord.** *J Neurointerv Surg* 2012;4:67–74 CrossRef Medline
44. Vrenken H, Geurts JJ, Knol DL, et al. **Whole-brain T1 mapping in multiple sclerosis: global changes of normal-appearing gray and white matter.** *Radiology* 2006;240:811–20 CrossRef Medline
45. Spini M, Choi S, Harrison D. **A comparison of FLAIR and T1 maps from MP2RAGE at 7T for quantifying lesion volume and its correlation to disability in multiple sclerosis.** *Neurology* 2019;92:P5.2–026
46. Guan X, Fan G, Wu X, et al. **Diffusion tensor imaging studies of cervical spondylotic myelopathy: a systemic review and meta-analysis.** *PLoS One* 2015;10:e0117707 CrossRef Medline
47. Gros C, De Leener B, Badji A, et al. **Automatic segmentation of the spinal cord and intramedullary multiple sclerosis lesions with convolutional neural networks.** *Neuroimage* 2019;184:901–15 CrossRef Medline

# Celebrating 35 Years of the AJNR

July 1986 edition

## Multiple Sclerosis: MRI and Clinical Correlation

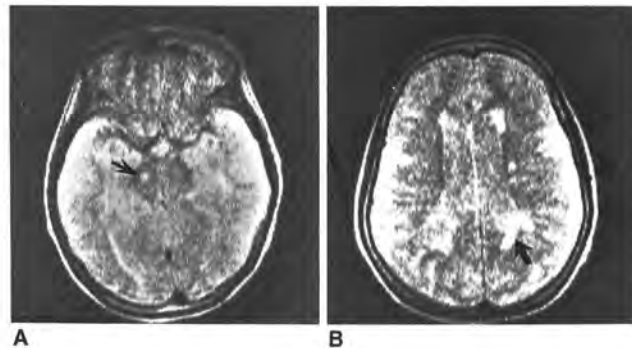
Mary K. Edwards<sup>1</sup>  
Martin R. Farlow<sup>2</sup>  
James C. Stevens<sup>3</sup>

Fifty-three consecutive patients with suspected multiple sclerosis were studied to determine if the extent of disease apparent on MRI correlated with the clinical severity of the disease. MRI images were evaluated and compared with an assessment of the patient's disability using three neurologic rating scales. The severity of the disease seen on MRI showed a strong statistically significant correlation ( $p < 0.0001$ ) with two of the three methods of clinical evaluation and a significant correlation ( $p < 0.01$ ) with the third rating scale. The severity of disease shown on MRI correlated only weakly ( $p = 0.05$ ) with the length of time the patients had been symptomatic. Normal controls did not show any abnormality characteristic of multiple sclerosis on MRI or on neurologic exam.

MRI has been recognized as a major advance in the diagnosis and evaluation of patients with multiple sclerosis (MS) [1-4]. Many more lesions are detected by MRI than by CT, and MRI has proved to be helpful in establishing the diagnosis of MS in cases where the clinical diagnosis is not definite [5-7]. Although MRI has made MS easier to diagnose at an early stage [7], the correlation between MRI results and the clinical course and disability has been questioned [8, 9].

### Subjects and Methods

Fifty-three patients with suspected MS were evaluated in the Department of Neurology at Indiana University using three different clinical scales. The patients were evaluated according to the McAlpine criteria as having either possible, probable, or definite MS [10]. The McAlpine criteria were converted to a numerical scale ranging from 1 (possible) to 3 (definite). Patients who did not qualify as having MS according to the McAlpine criteria were excluded from the study. The patients were also graded using the expanded disability status scale proposed by Kurtzke [11], which grades the patient's disability from 0 (normal) to 10 (death due to MS) at one-half step intervals. The Kurtzke scale is designed to grade the patient's functional disability. Cerebellar dysfunction, cranial nerve deficits, and difficulty ambulating are among



## CT and MR of Angiomatous Malformations of the Choroid Plexus in Patients with Sturge-Weber Disease

Gary K. Sliniac<sup>1</sup>  
Murray A. Solomon<sup>2</sup>  
T. H. Newton<sup>3</sup>

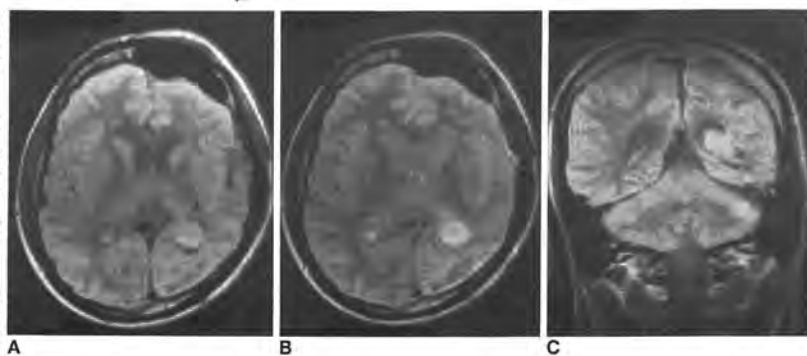
Eight patients with Sturge-Weber disease in one patient, or both (one patient). CT scans of head and increased enhancement of the choroid and intracranial lesions. MRI showed similar findings, seen in six of eight cases of Sturge-Weber disease. The presence of angiomatous malformations of common finding in this disease.

Sturge-Weber disease is a neurocutaneous, white stain (nevus flammeus) of the face, an disease has been extensively reviewed in the literature [1]. The disease is characterized by Sturge-Weber disease are venous angiomatous. These angiomatous have been seen in the pancreas, adrenal glands, pituitary, globe, and angiomatous have been noted in the neuropath of two cases, in the radiology literature [13] that we studied, six showed enlargement of the choroid plexus on the side affected by the face. We believe the choroid plexus is commonly

### Subjects and Methods

We reviewed eight cases of Sturge-Weber disease of the choroid plexus of the lateral ventricle with contrast material were performed using a GE on an Ohio Nuclear Delta CT scanner. A total of two patients. MRI using high-resolution technique was performed with TR-2 sec, TE-28 and 56 in thickness of 7 mm with a 3-mm interslice gap. Evaluated by at least two independent observers.

To determine whether the enhancement and extent of calcification of the choroid plexus in our patients was unusual, we examined CT scans of 107 patients who had no evidence of Sturge-Weber disease (most had experienced trauma or had metabolic disease). The transverse diameter of the calcification (on noncontrast scans) and the enhancement (on contrast scans) of the choroid plexus was measured with Vernier calipers and was corrected for magnification. Because CT slices were contiguous and the object of measurement (calcification or enhancement) was dense, partial volume errors were not encountered in these measurements. The size of the choroid plexus as identified by its intensity and by the anatomical borders at the trigone of the lateral ventricle was similarly measured on MRI. Partial volume errors could occur in the measurement of the choroid plexus on MRI scans due to the inferior gap of 3 mm, but in both our cases, the difference in size was obvious.



Received September 7, 1984; accepted after revision January 14, 1986.

<sup>1</sup>Department of Radiology, University of Washington, Seattle, WA 98195. Address reprint requests to G. K. Sliniac.

<sup>2</sup>Department of Radiology, San Jose MRI Center, San Jose, CA 95128.

<sup>3</sup>Department of Radiology, University of California, San Francisco, CA 94143.

AJNR 14:622-627, July/August 1986  
0195-9581/86/0704-0622  
© American Society of Neuroradiology

## Robert A. Zimmerman, MD

On February 23, 2021, the pediatric neuroradiology community lost our beloved colleague, master clinician, and mentor, Dr Robert “Bob” A. Zimmerman. He died peacefully at home, amid family.

Bob was born June 20, 1938, in Philadelphia, and he received his bachelor of arts degree in biology at Temple University in 1960. He graduated from Georgetown University Medical School summa cum laude in 1964.

He interned in internal medicine at Georgetown University Hospital and completed his radiology residency at the Hospital of the University of Pennsylvania (HUP). He then served in the military from 1969 to 1972, mostly in Europe. Bob returned to HUP, where he swiftly rose through the ranks to become full Professor of Radiology with a secondary appointment in neurosurgery. Dr. Zimmerman served as Chief of Neuroradiology at HUP from 1979 to 1985. He transitioned to the Children’s Hospital of Philadelphia (CHOP) and served as Chief of Pediatric Neuroradiology at CHOP until his retirement in 2018.

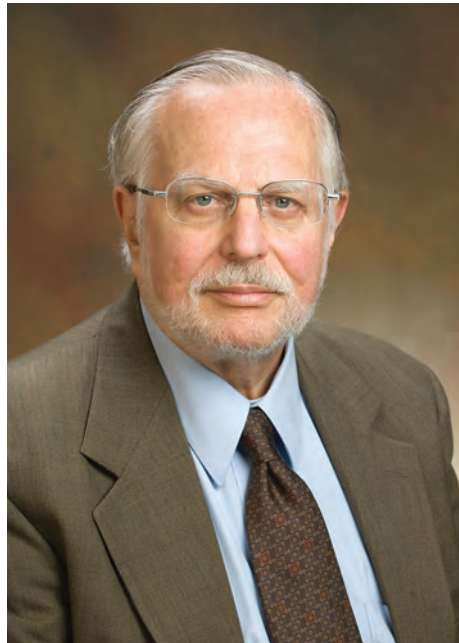
Dr. Zimmerman was a champion of interdisciplinary cooperation in aid of a child. With his colleagues in neurosurgery, neuropathology, and radiology, he helped to create and maintain the world-renowned Section of Pediatric Neuroradiology at CHOP. In honor of his extraordinary excellence and his years of dedication, CHOP created the Robert A. Zimmerman Endowed Chair in Pediatric Neuroradiology in 2018, presently held by Dr Larissa T. Bilaniuk.

Dr. Zimmerman’s research was recognized nationally and internationally. For decades, he was the featured speaker at national and international scientific meetings. For his work, Dr. Zimmerman received countless awards and honors, including the honorary membership of the Belgian Radiological Society in 2000 and the European Society of Neuroradiology in 2001, the American Society of Neuroradiology Special Achievement Award (later designated the Gold Medal) in 2002, the Award for Special Contributions in Research from the American Society of Neuroradiology in 2012, and the honorary membership of the Italian Neuroradiological Society in 2016.

Dr. Zimmerman authored more than 350 publications, edited 2 textbooks, reviewed for the major scientific journals in radiology, neuroradiology, neurosurgery, and neurology, and was a perennial member of the National Institutes of Health panel on sickle cell disease. From 1989 to 2005, he served as the United States Editor-in-Chief of *Neuroradiology*, the official journal of the European Society of Neuroradiology, the Japanese Society of Neuroradiology, and more than 20 national European neuroradiological societies.

Dr. Zimmerman was a founding member of the American Society of Pediatric Neuroradiology (ASPNR) and President of the ASPNR from 1995 to 1996.

Beyond his academic work, Bob was a loving husband, father, and grandfather. He met his future wife, Dianne, when they were both camp counselors, and they married in 1960, sixty-one years ago. He loved to read to his kids, and he became an avid gardener.



Because of his time in Europe, Bob became a connoisseur of fine food and wine. No matter which city hosted a scientific meeting, domestic or international, Bob had already scouted out where to dine and which vineyard to visit when the meeting ended.

Medicine is a tradition, perpetuated by mentoring across the generations. Beyond “academics,” your legacy is what you have passed on to those who follow. Dr. Zimmerman trained numerous residents and fellows in pediatric neuroradiology. His legacy may be summarized by the spontaneous outpouring of memories and love:

“He was such a giant in our field, and a kind and generous man.”

“He is so very present to us on a regular basis through his work; I can’t tell you how many times I refer to his many publications.”

“I was so privileged that he accepted me as a friend and that he has always been extremely supportive of me.”

“Many teach what you have to know. Bob taught us the joy of neuroradiology and the special honor it was to help to heal children.”

“I remember Bob as a gentle giant, a renaissance man who was always looking after you as a human, a colleague, a friend, a mentor, somebody who enjoyed shaping and supporting your career and who would always be there for advice. Because of him I will enjoy pediatric neuroradiology for the rest of my career.”

Dr. Zimmerman is survived by his loving wife Dianne, their beloved daughters Rachel and Sara, and their precious grandchildren, Ivan and Sasha Boyko. He will be remembered fondly by the many friends, colleagues, and trainees who loved him, respected him, and miss him sorely.

On behalf of all pediatric neuroradiologists around the globe.

T.P. Naidich  
T.A.G.M. Huisman

<http://dx.doi.org/10.3174/ajnr.A7173>

# Virtual Biopsy: A Reality Thanks to Advances in Radiology



It is fascinating when we can determine cause and effect in the topographic identification of intracranial lesions. Neurologic semiology was developed before neuroimaging existed to determine the exact location of the brain injury and its representation as a neurologic deficit or dysfunction observed during a physical examination of the patient.

A very curious symptom during the coronavirus disease 2019 (COVID-19) pandemic is a change in the sense of smell. We could consider this symptom as pathognomonic in the current context of the pandemic.

The explanation of the anosmia reported by patients with COVID-19 was controversial for some time, not always considering injury to the olfactory bulb as a probable cause. Nevertheless, with the help of neuroradiology, it is now possible to show that some patients with COVID-19 have lesions in the olfactory bulbs.

On June 1, 2020, our study was accepted, and we published 5 cases of patients with COVID-19 and injury to olfactory bulbs detected on MR imaging, which could represent microvascular injury with enhancement (breakdown of the blood-brain barrier) and/or probable hemorrhagic lesions (methemoglobin).<sup>1</sup> We were probably the first to show a microvascular phenomenon in the olfactory bulbs of patients with COVID-19.<sup>1</sup> However, there was an interpretation that considered these changes on MR imaging as artifacts,<sup>2</sup> and we had to explain why the findings in our study of the olfactory bulbs could not be artifacts. We showed another case with a lesion in the olfactory bulb on FLAIR and echo-spoiled gradient-echo T1WI, which could represent methemoglobin.<sup>3</sup> We finished our Reply saying, “We think all would agree that anatomopathologic studies are necessary to better define neuroradiologic interpretation.”<sup>3</sup> Finally, Lee et al<sup>4</sup> demonstrated, in an extremely elegant postmortem histopathology study using much more sophisticated tools (eg, an 11.7T scanner), what we had suggested in vivo previously on the 1.5T MR imaging.<sup>1</sup> The change of the sense of smell represents microvascular injury<sup>1,3</sup> (areas of fibrinogen leakage, thinned basal lamina, and hemorrhagic lesions in the brain and olfactory bulbs)<sup>4</sup> and not artifacts as is also shown in Figure.

In conclusion, once again, there is evidence that our neuroradiology tools can function as a virtual biopsy to correctly diagnose the topography of the lesion and discover the etiology, especially when it is not possible to obtain histopathological evidence.

## REFERENCES

1. Aragao MFVV, Leal MC, Cartaxo FO, et al. **Anosmia in COVID-19 associated with injury to the olfactory bulbs evident on MRI.** *AJNR Am J Neuroradiol* 2020;41:1703–06 CrossRef Medline
2. Mamourian A. **Seeing what we expect to see in COVID-19.** *AJNR Am J Neuroradiol* 2021;42:E1 CrossRef Medline
3. Aragao MFVV, Leal MC, Fonseca TM, et al. **Reply.** *AJNR Am J Neuroradiol* 2021;42:E2–E3 CrossRef Medline
4. Lee MH, Perl DP, Nair G, et al. **Microvascular injury in the brains of patients with Covid-19.** *N Engl J Med* 2021;384:481–83 CrossRef Medline

M.F.V.V. Aragao

Universidade Federal de Pernambuco  
Recife, Brazil

Multimagem Centro Diagnóstico  
Recife, Brazil

A.D.P. Oliveira

Universidade de Pernambuco  
Serra Talhada, Brazil

A.R.M.C. Lima

Universidade de Pernambuco  
Recife, Brazil

M.C. Leal

Universidade Federal de Pernambuco  
Recife, Brazil

Real Hospital Português de Beneficência em Pernambuco  
Recife, Brazil

M.M. Valença

Universidade Federal de Pernambuco  
Recife, Brazil

Indicates open access to non-subscribers at [www.ajnr.org](http://www.ajnr.org)

<http://dx.doi.org/10.3174/ajnr.A7092>

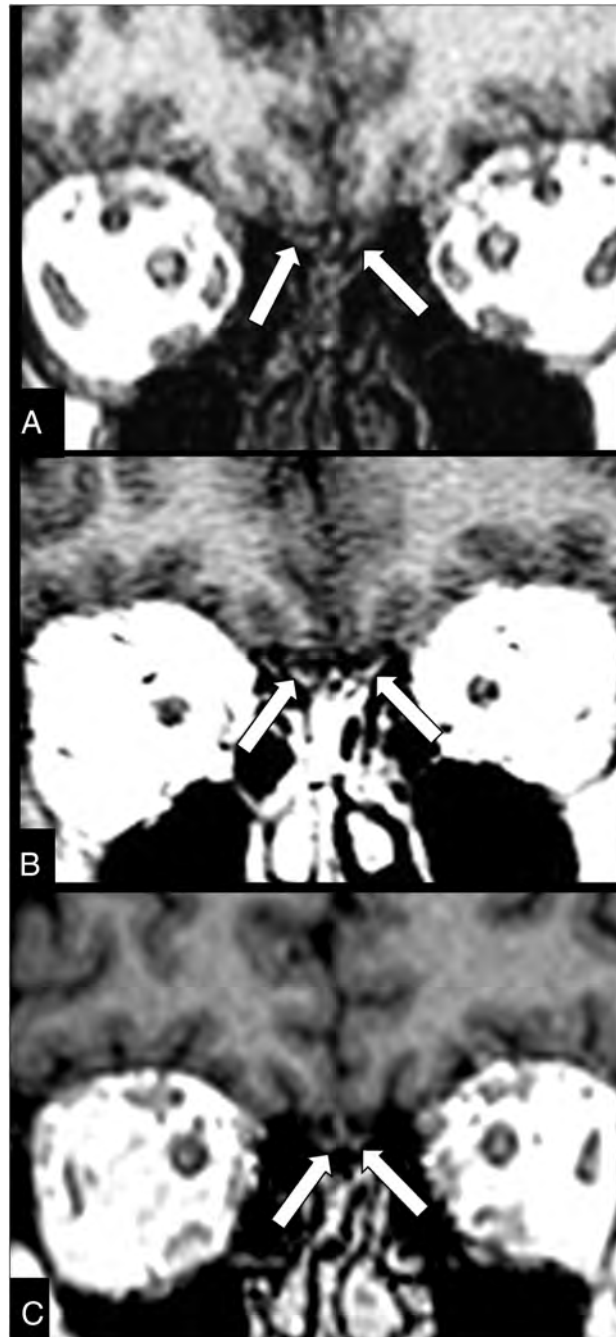


**FIGURE.** Brain MR imaging of a woman in her 40's with confirmed COVID-19 shows injury of the olfactory bulbs, within 7 days of onset of the disease. A real-time polymerase chain reaction of a nasopharyngeal swab detected Severe Acute Respiratory Syndrome coronavirus 2, which was negative on her CSF. The MR imaging shows that the olfactory bulbs are oval images with signal intensity similar to that of gray matter on precontrast T1WI (A, arrows), being hypointense. On postcontrast T1WI (B, arrows), the olfactory bulbs show abnormal enhancement and become hyperintense, suggesting injury with breakdown of the brain-blood barrier. Two months later, the follow-up MR imaging shows that the contrast enhancement of the olfactory bulbs has completely disappeared and they have a normal appearance, being hypointense and similar to the gray matter on coronal postcontrast T1WI (C, arrows).

# Leptomeningeal Enhancement Due to COVID-19 on 3D-FLAIR and T1 Black-Blood MR Imaging Sequences



We read with great interest the literature review by Gulko et al<sup>1</sup> that included 22 articles reporting the MR imaging brain findings of 126 patients with coronavirus disease 2019 (COVID 19). We agree with the authors that the most frequent diagnosis on MR imaging is acute and subacute infarct, which was reported in 32 of 126 patients. However, because of the different imaging techniques used in the original articles, the frequency of leptomeningeal involvement may be underestimated.

We observed great differences in the reported frequency of leptomeningeal enhancement in the articles included in this review. Helms et al<sup>2</sup> reported enhancement in leptomeningeal spaces in 8 patients (68%). On the other hand, leptomeningeal enhancement was absent (0%) in several other studies with similar patient samples.<sup>1</sup> This discrepancy may be attributed to the different imaging techniques used to evaluate leptomeningeal involvement. The contrast-enhanced 3D-FLAIR sequence was used by Helms et al,<sup>2</sup> while only conventional T1WI postcontrast sequences were performed in several other studies.

In our practice, 3D-FLAIR sequences or 3D T1 black-blood imaging or both are used to clearly demonstrate leptomeningeal enhancement. Leptomeningeal involvement seems to be a relatively common manifestation of CNS involvement in patients with COVID-19. Herein, we present a 68-year-old woman with COVID-19 who underwent brain MR imaging 2 weeks after extubation, because of confusion and muscle weakness in her limbs. Turbo spin-echo 3D-T1 black-blood and 3D-FLAIR sequences postcontrast administration revealed leptomeningeal enhancement in the left angular gyrus (Fig 1) and on both sides of the right parieto-occipital sulcus (Fig 2). Enhancement was not prominent on conventional (turbo-field echo) 3D-T1 images.

Leptomeningeal enhancement on FLAIR images is known to occur frequently in MS and non-MS inflammatory neurologic conditions, including encephalitis. In their systematic review Zurawski et al<sup>3</sup> suggested that contrast-enhanced FLAIR provided as much as 10-fold sensitivity compared with conventional T1 sequences in the detection of low concentration of contrast in the subarachnoid space.

The increased sensitivity of T1 black-blood imaging in detecting leptomeningeal enhancement has also been reported. Oh et al<sup>4</sup> compared contrast-enhanced gradient recalled-echo, contrast-enhanced spin-echo, and black-blood imaging for the detection of leptomeningeal carcinomatosis. According to their results, black-blood imaging had a significantly higher sensitivity than contrast-enhanced gradient recalled-echo and contrast-enhanced spin-echo (97.43%, 64.1%, and 66.67%, respectively) in identifying foci of leptomeningeal enhancement.

The possible underlying mechanism of focal leptomeningeal enhancement may include inflammation-related focal disruption of the blood-meninges barrier and associated fibrosis. Pathologist analysis in patients with MS showed leptomeningeal inflammation, which may lead to the up-regulation of reactive fibroblasts and collagen deposition causing local meningeal fibrosis.<sup>3</sup> Consequently, both fibrosis and inflammation may result in the trapping of low concentration of gadolinium-based contrast medium within the subarachnoid spaces.

Although contrast-enhanced 3D-FLAIR and T1 black-blood imaging are sensitive in detecting leptomeningeal enhancement, they are not routinely performed in patients with COVID-19 in many institutions. Including one or both sequences in MR imaging protocols for patients with COVID-19 with neurologic symptoms may help to avoid underestimation of leptomeningeal and CNS involvement.

## REFERENCES

1. Gulko E, Oleksk ML, Gomes W, et al. **MRI brain findings in 126 patients with COVID-19: initial observations from a descriptive literature review.** *AJNR Am J Neuroradiol* 2020;41:2199–203 CrossRef Medline
2. Helms J, Kremer S, Merdji H, et al. **Neurologic features in severe SARS-CoV-2 infection.** *N Engl J Med* 2020;382:2268–70 CrossRef Medline
3. Zurawski J, Lassmann H, Bakshi R. **Use of magnetic resonance imaging to visualize leptomeningeal inflammation in patients with multiple sclerosis: a review.** *JAMA Neurol* 2017;74:100–09 CrossRef Medline
4. Oh J, Choi SH, Lee E, et al. **Application of 3D fast spin-echo T1 black-blood imaging in the diagnosis and prognostic prediction of patients with leptomeningeal carcinomatosis.** *AJNR Am J Neuroradiol* 2018;39:1453–59 CrossRef Medline

Indicates open access to non-subscribers at [www.ajnr.org](http://dx.doi.org/10.3174/ajnr.A7104)  
<http://dx.doi.org/10.3174/ajnr.A7104>

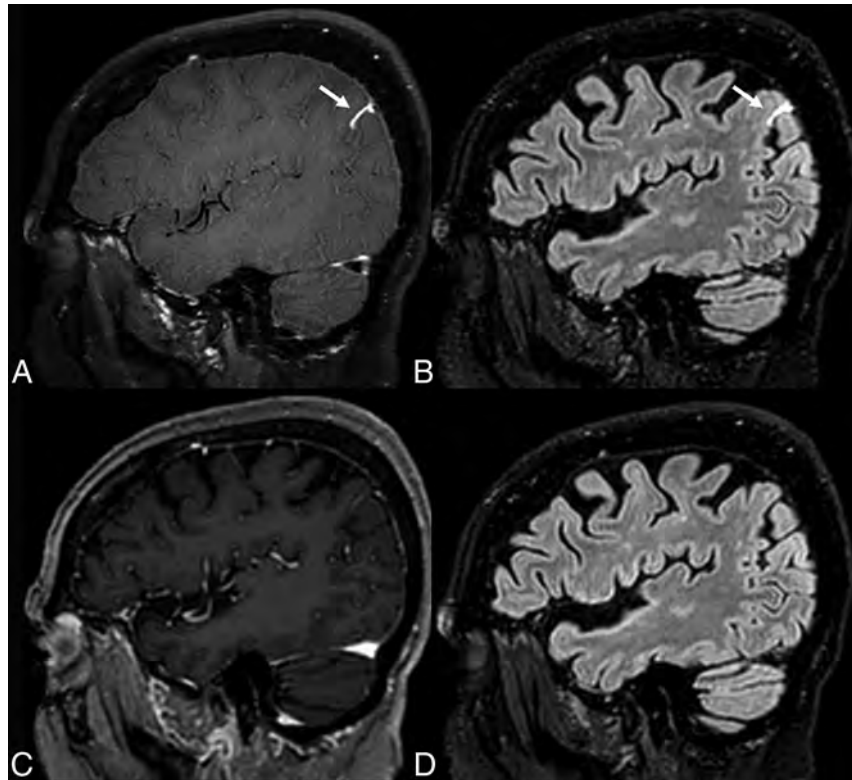


**FIG 1.** Sagittal 3D turbo spin-echo black-blood T1-weighted (A) and 3D-FLAIR (B) images, both postcontrast administration, reveal leptomeningeal enhancement in the left angular gyrus (arrows, A and B). Enhancement is not prominent on T1 contrast-enhanced images (C). There are no hyperintensities in this area on the sagittal 3D-FLAIR image without contrast (D).

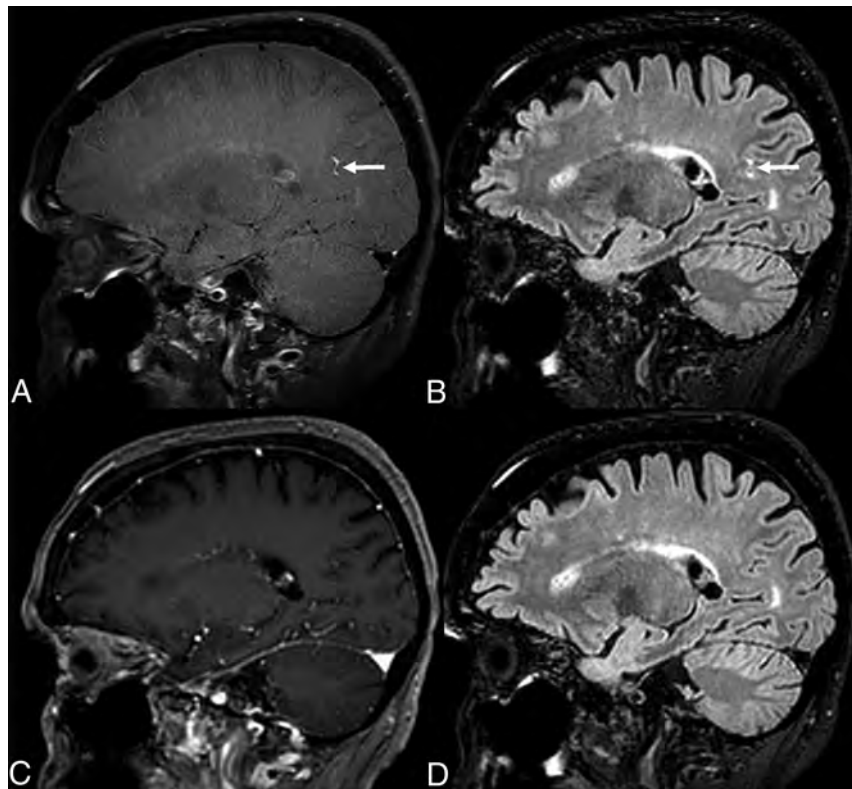


**FIG 2.** Leptomeningeal enhancement on both sides of the right parieto-occipital sulcus is more evident on sagittal 3D-T1 turbo spin-echo black-blood (A) and 3D-FLAIR (B) images (arrows, A and B), than on T1 postcontrast (C). No hyperintensities on 3D-FLAIR before contrast administration (D) are noticed in the right parieto-occipital sulcus.

 **G. Velonakis**

 **E. Karavasilis**

 **D.K. Filippiadis**

Research Unit of Radiology – 2nd Department of Radiology  
Medical School, National and Kapodistrian University of Athens  
Athens, Greece

 **M.P. Almyroudi**

Emergency Department  
Attikon University Hospital, National and Kapodistrian University of Athens  
Athens, Greece

 **E. Korompoki**

Department of Clinical Therapeutics  
Medical School, National and Kapodistrian University of Athens  
Athens, Greece

**REPLY:**



**W**e thank Drs Velonakis, Karavasilis, Almyroudi, Filippiadis, and Korompoki for the in-depth commentary on our article. We value the important observations they made regarding the differences in the rates of leptomeningeal contrast enhancement in patients with coronavirus disease 2019 among the included articles in our review. We agree that the large range may be in part because of the differences in MR imaging protocols. It is reasonable to assume that institutions using MR imaging sequences that are more sensitive for detecting leptomeningeal contrast enhancement would report more of it. Because the data included in our article came from around the world, another possibility for the great variability of neuroimaging findings, including leptomeningeal contrast enhancement, may be because of differences in patient population, disease severity, geographic location, and genetic variations of Severe Acute Respiratory Syndrome coronavirus 2. More

Indicates open access to non-subscribers at [www.ajnr.org](http://www.ajnr.org)

<http://dx.doi.org/10.3174/ajnr.A7159>

research is needed to account for all of the clinical and imaging presentations of this protean disease in the central nervous system.

**E. Gulko**

**W. Gomes**

**S. Ali**

**H. Mehta**

Department of Radiology, Division of Neuroradiology  
Westchester Medical Center  
Valhalla, New York

**M.L. Oleksk**

New York Medical College  
Valhalla, New York

**P. Overby**

Department of Pediatrics  
Westchester Medical Center  
Valhalla, New York

**F. Al-Mufti**

Department of Neurology, Westchester Medical Center  
Valhalla, New York

**A. Rozenshtein**

Department of Radiology, Division of Cardiothoracic Imaging  
Westchester Medical Center  
Valhalla, New York

## Expediting Care and Improving Patient Experience: Imaging after Subdural Contrast Injection during Myelography

We read the recent publication by Shlapak et al,<sup>1</sup> “Time to Resolution of Inadvertent Subdural Contrast Injection during a Myelogram: When Can the Study Be Reattempted?” with interest. The extrathecal injection of contrast during a spinal myelography generates frustration for the neuroradiologist, and more importantly, the patient. The authors provide much needed insight into the rapid physiologic “washout” of contrast and suggest that a repeat study can be performed as soon as the next day.

Unfortunately, even the proposed “next day” study requires a repeat invasive procedure. For outpatient procedures, there are additional inconveniences, including: the time and expense of travel; the need for additional time away from work and family; and for some patients, prolonged time off anticoagulation medication. These concerns may be amplified during the current pandemic, and we should strive to minimize the unnecessary burden on patients and on an already-strained health care system.

With these factors in mind, we wish to supplement the article with our experience imaging subdural contrast after a recent myelogram. As the patient had already traveled several hours for an evaluation of back pain, and with the aim of generating an expeditious diagnosis, we performed a repeat CT 1 hour after the first. The initial and follow-up CT images (Figure) demonstrate that the contrast rapidly exited the subdural space, with enough passing into the thecal sac to produce diagnostic imaging.

This obviated the need for a repeat procedure and suggests that even without an initially successful injection, there may be enough membranous disruption to allow effective contrast passage into the thecal sac. This type of contrast motion may not

occur in every case. Indeed, the precise localization of contrast after its initial nontarget injection likely depends on multiple factors. These factors include the following: the specific site of the initial injection (eg, subdural, extradural, or split); the technical factors (eg, patient positioning or timing of imaging); and the underlying diagnosis. With respect to the latter, pressure within the CSF space may define the path of least resistance for contrast and produce a gradient across which movement into the thecal sac is precluded.

Regardless of the specifics, our case illustrates 2 points. First, there is a need to better understand the dynamic physiology across the thecal sac. Second, and more importantly, we have an opportunity to facilitate patient care in frustrating scenarios. A same-day repeat CT may produce diagnostic information and facilitate expedient patient management. At worst, the presence of persistent subdural contrast would require a repeat procedure the next day. At best, sufficient intrathecal contrast would help to avoid an additional invasive procedure and would minimize the patient inconvenience.

### REFERENCE

1. Shlapak DP, Kim DK, Diehn FE, et al. **Time to resolution of inadvertent subdural contrast injection during a myelogram: when can the study be reattempted?** *AJNR Am J Neuroradiol* 2020;41:1958–62 CrossRef Medline

© M.U. Antonucci

© M. Yazdani

Department of Radiology & Radiological Science  
Medical University of South Carolina  
Charleston, South Carolina

<http://dx.doi.org/10.3174/ajnr.A7114>

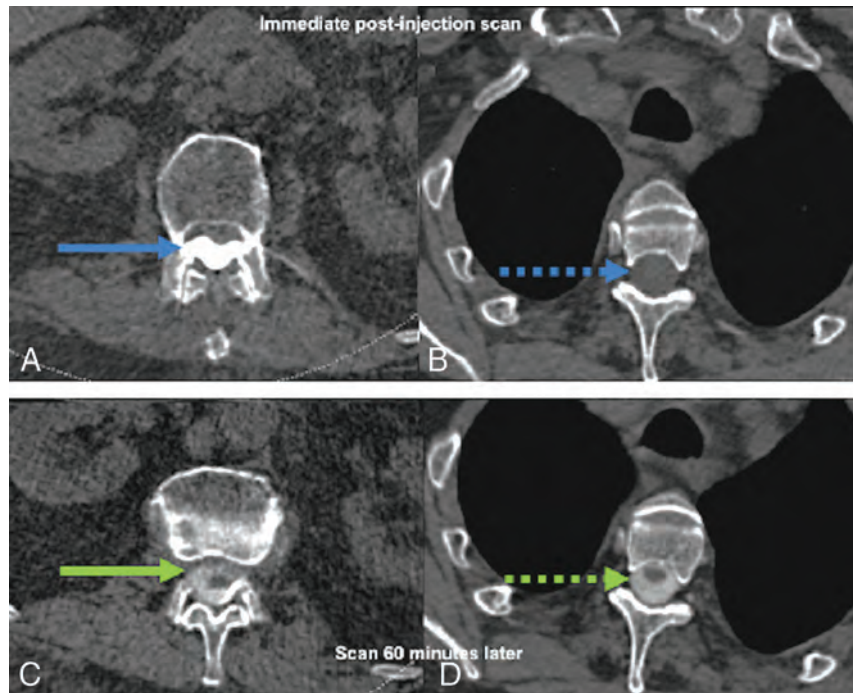


**FIGURE.** Following fluoroscopically guided lumbar puncture for thoracic myelogram, initial CT demonstrates contrast within the subdural space (A, blue arrow) with insufficient thoracic thecal sac enhancement (B, blue dashed arrow). One hour later, a repeat CT reveals contrast movement across the thecal sac (C, green arrow) with excellent thoracic myelography (D, green dashed arrow).

**REPLY:**

**T**hank you very much for such a thoughtful and timely letter. It brings up the important topic of CSF dynamics within the “subdural” space, which has not been fully elucidated. Diffusion of subdural contrast into the thecal sac is certainly interesting; we do not yet know if it is from the disruption of the inner layer at the puncture site, or if intrathecal distribution results from the natural egress passage of any subdural fluid.

In a typical CT myelogram for spinal stenosis evaluation, rescanning patients after an hour in cases of subdural injection to see whether the contrast diffuses intrathecally is a very acceptable option. This is especially true during the current pandemic setting, as the authors mentioned.

While most CT myelograms performed for spinal stenosis can be diagnostic if the CSF is appreciably denser than the neural elements, the evaluation of spinal CSF leaks on CT myelogram is extremely dependent on a high concentration of intrathecal contrast. This is especially true with CSF-venous fistulas, where the findings are often subtle even with maximal contrast attenuation. Therefore, waiting an hour for subdural injections to become intrathecal while contrast resorption from the CSF to the venous

system is occurring would likely result in submaximal opacification of intrathecal CSF and markedly decrease the diagnostic yield.

Thank you again for the letter and great efforts to optimize patient care in a difficult time for the medical community.

 **D. Shlapak**

Department of Radiology  
Mayo Clinic  
Rochester, Minnesota

 **D.K. Kim**

Department of Radiology  
Mayo Clinic  
Rochester, Minnesota

 **F.E. Diehn**

Department of Radiology  
Mayo Clinic  
Rochester, Minnesota

 **J.C. Benson**

Department of Radiology  
Mayo Clinic  
Rochester, Minnesota

 **V.T. Lehman**

Department of Radiology  
Mayo Clinic  
Rochester, Minnesota

 **G.B. Liebo**

Department of Radiology  
Mayo Clinic  
Rochester, Minnesota

 **J.M. Morris**

Department of Radiology  
Mayo Clinic  
Rochester, Minnesota

 **P.P. Morris**

Department of Radiology  
Mayo Clinic  
Rochester, Minnesota

 **J.T. Verdoom**

Department of Radiology  
Mayo Clinic  
Rochester, Minnesota

 **C.M. Carr**

Department of Radiology  
Mayo Clinic  
Rochester, Minnesota

<http://dx.doi.org/10.3174/ajnr.A7126>

## The True Potential of Artificial Intelligence for Detection of Large-Vessel Occlusion: The Role of M2 Occlusions

It is with great interest that we have read a recently published article by Yahav-Dovrat et al<sup>1</sup> investigating the diagnostic performance of a large-vessel occlusion (LVO) detection algorithm on CTA. With a sensitivity of 0.81 for detection of LVO, the authors indicate that the algorithm is suboptimal for use as a diagnostic tool. However, they state that the true potential lies in aiding radiologists in early detection of an LVO and accelerating decision-making. With respect to this statement, some methodologic aspects of their study merit further discussion.

The algorithm that was evaluated used a deep learning-based convolutional neural network to detect occlusions from the ICA terminus to the Sylvian fissure, which included both M1 and M2 segments of the MCA. In their analysis, the definition of LVO only included ICA terminus and M1, but not M2 occlusion. We argue that this definition does not adequately reflect the spectrum of LVOs that need to be targeted by these algorithms, and that M2 occlusion should also have been considered as an LVO. While current guidelines do not provide clear recommendations regarding endovascular treatment in patients with M2 occlusions, accumulating evidence is showing that these patients also benefit from this treatment.<sup>2</sup> As a result, in routine clinical practice, endovascular treatment is increasingly being performed in these patients.<sup>3</sup> In addition, M2 occlusions occur more commonly than is often thought and they constitute a substantial proportion of the real-world population who have had an acute ischemic stroke due to LVO. Accordingly, in the study of Yahav-Dovrat et al,<sup>1</sup> 75 patients were identified with an ICA terminus or M1 occlusion, and 44 patients had an occlusion in proximal M2 or distal M2–3 segments. As potential candidates for endovascular treatment, it is crucial that the latter occlusions are also identified quickly and accurately. Yet, it has been demonstrated that M2 occlusions are still frequently missed by radiologists at initial CTA evaluation, whereas the diagnostic error for ICA terminus and M1 occlusions is much lower.<sup>4</sup> Furthermore, detection of M2 occlusions by human readers is likely to be more time-consuming because of the smaller caliber, tortuosity, and anatomic variations of these vessels. This indicates a large potential for LVO detection algorithms to accelerate and improve the detection of mainly M2 occlusions and, to a lesser extent, ICA terminus and M1 occlusions.

Regrettably, this is where the current algorithm falls short. In 12 of 44 patients with proximal M2 or distal M2–3 occlusions, the algorithm indicated the presence of LVO. Further subdividing these results reveals a detection rate of 38% (8 of 21) for proximal M2 and 17% (4 of 23) for distal M2–3 occlusions. Considering these cases as non-LVOs and counting them as false-positives, as was done by Yahav-Dovrat et al,<sup>1</sup> simply inflates diagnostic performance, and leads to overestimating the potential of the algorithm for early and accurate identification of patients with LVO. Including M2 occlusion in the definition of LVO would have resulted in a considerably lower sensitivity of the algorithm for detection of LVO. However, this would provide a more reliable estimate of diagnostic performance in the population that is targeted for endovascular treatment in routine clinical practice.

Therefore, we strongly urge the need to consider M2 occlusion as LVO when evaluating the diagnostic performance of LVO detection algorithms for a more reliable estimation of their performance and true potential in a clinical setting.

### REFERENCES

1. Yahav-Dovrat A, Saban M, Merhav G, et al. **Evaluation of artificial intelligence-powered identification of large-vessel occlusions in a comprehensive stroke center.** *AJNR Am J Neuroradiol* 2021;42:247–54 CrossRef Medline
2. Menon BK, Hill MD, Davalos A, et al. **Efficacy of endovascular thrombectomy in patients with M2 segment middle cerebral artery occlusions: meta-analysis of data from the HERMES Collaboration.** *J Neurointerv Surg* 2019;11:1065–69 CrossRef Medline
3. Almekhlafi M, Ospel JM, Saposnik G, et al. **Endovascular treatment decisions in patients with M2 segment MCA occlusions.** *AJNR Am J Neuroradiol* 2020;41:280–85 CrossRef Medline
4. Fasen B, Heijboer RJJ, Hulsmans FH, et al. **CT angiography in evaluating large-vessel occlusion in acute anterior circulation ischemic stroke: factors associated with diagnostic error in clinical practice.** *AJNR Am J Neuroradiol* 2020;41:607–11 CrossRef Medline

✉ S.P.R. Luijten

✉ L. Wolff

✉ A. van der Lugt

Department of Radiology and Nuclear Medicine  
Erasmus MC University Medical Center  
Rotterdam, The Netherlands

<http://dx.doi.org/10.3174/ajnr.A7111>

## REPLY:

We would like to thank Dr Luijten et al at Erasmus MC University Medical Center for their interest in our article titled “Evaluation of Artificial Intelligence–Powered Identification of Large-Vessel Occlusions in a Comprehensive Stroke Center” and for their insightful comments.

In their letter, the authors suggested that distal occlusions should be considered positive cases for the purpose of evaluating the performance of artificial intelligence (AI) algorithms for detection of large-vessel occlusion (LVO) strokes. Indeed, recent studies suggest that endovascular treatment for these patients is safe and effective. These occlusions were even dubbed “MVOs” or middle-vessel occlusions to differentiate them from LVOs.<sup>1</sup>

We agree that this population is of great interest. As stated in our article, the potential clinical utility of a detection algorithm does not rely on its sensitivity alone. Although aiding radiologists in early detection is of great value, there is paramount importance for the positive predictive values of such systems. Avoiding an unacceptable burden on the application end-users due to multiple alerts is essential. While recent publications suggest the utility of treating MVOs, only the treatment of ICAs and M1 LVOs with endovascular techniques is currently supported by level 1 evidence from multiple randomized controlled trials.<sup>2</sup> As such, cutting-edge centers may choose to treat such patients, whereas many centers around the world might choose to strictly adhere to the American Heart Association and American Stroke Association guidelines. Typically, the less advanced and experienced centers stand to benefit the most from AI-driven detection and the triage of LVOs.<sup>3</sup> Any study of AI software should keep this audience in mind.

One of the great powers of neural network algorithms is the ability to improve in time as more data are used to train the algorithm. The study was performed 2 years ago, and as such, it is relevant to the version used at that time. Our study was conducted on a system intended to identify and alert LVOs, including ICA and M1. Therefore, identification of such occlusions was defined as the study's primary outcome. The identification of more distal occlusions is indeed of interest and was presented as a secondary outcome.

As more evidence for the safety and efficacy of endovascular treatment in M2 segment MCA occlusions becomes available, our recommendation to anyone considering or performing

similar studies would be to report both the overall sensitivity and specificity of the investigated device, as well as provide estimates of the sensitivity stratified by occlusion location. In addition, as various AI systems are being installed in different centers, studies reporting the effects on time, cost, or patient outcome before and after implementation of AI software<sup>4</sup> could be of great significance when evaluating the true benefit of such systems.

## REFERENCES

1. Saver JL, Chapot R, Agid R, et al. **Thrombectomy for distal, medium vessel occlusions: a consensus statement on present knowledge and promising directions.** *Stroke* 2020;51:2872–84 CrossRef Medline
2. Powers WJ, Rabinstein AA, Ackerson T, et al. **Guidelines for the early management of patients with acute ischemic stroke: a guideline for healthcare professionals from the American Heart Association/American Stroke Association.** *Stroke* 2018;49:e46–110 CrossRef Medline
3. Almekhlafi M, Ospel JM, Saposnik G, et al. **Endovascular treatment decisions in patients with M2 segment MCA occlusions.** *AJNR Am J Neuroradiol* 2020;41:280–85 CrossRef Medline
4. Hassan AE, Ringheanu VM, Rabah RR, et al. **Early experience utilizing artificial intelligence shows significant reduction in transfer times and length of stay in a hub and spoke model.** *Interv Neuroradiol* 2020;26:615–22 CrossRef Medline

 **A. Yahav-Dovrat**

 **G. Merhav**

 **A. Eran**

Department of Radiology  
Rambam Health Care Campus  
Haifa, Israel

 **R. Sivan-Hoffmann**

Department of Radiology  
Unit of Interventional Neuroradiology  
Rambam Health Care Campus  
Haifa, Israel

 **M. Saban**

Faculty of Social Health and Welfare  
Haifa University  
Haifa, Israel

 **E. Abergel**

Unit of Interventional Neuroradiology  
Rambam Health Care Campus  
Haifa, Israel

 **D. Tanne**

Stroke and Cognition Institute  
Rambam Health Care Campus  
Haifa, Israel

 **R.G. Nogueira**

Neuroendovascular Service, Marcus Stroke & Neuroscience Center  
Grady Memorial Hospital  
Atlanta, Georgia  
Neurology, Neurosurgery, and Radiology  
Emory University School of Medicine  
Atlanta, Georgia

<http://dx.doi.org/10.3174/ajnr.A7146>